2012

Forecasting Volcanic Activity Using An Event Tree Analysis System And Logistic Regression

William N. Junek
University of Central Florida

FORECASTING VOLCANIC ACTIVITY USING AN EVENT TREE ANALYSIS SYSTEM AND LOGISTIC REGRESSION

by

WILLIAM N. JUNEK
A.S. Engineering, Ocean County College, 1997
B.S. Electrical Engineering, Florida Institute of Technology, 1999
M.S. Electrical Engineering, University of Massachusetts, Amherst, 2003

A dissertation submitted in partial fulfillment of the requirements
for the degree of Doctor of Philosophy
in the Department of Electrical Engineering and Computer Science
in the College of Engineering and Computer Science
at the University of Central Florida
Orlando, Florida

Spring Term
2012

Major Professor: W. Linwood Jones

ABSTRACT

Forecasts of short term volcanic activity are generated using an event tree process that is driven by a set of empirical statistical models derived through logistic regression. Each of the logistic models are constructed from a sparse and geographically diverse dataset that was assembled from a collection of historic volcanic unrest episodes. The dataset consists of monitoring measurements (e.g. seismic), source modeling results, and historic eruption information. Incorporating this data into a single set of models provides a simple mechanism for simultaneously accounting for the geophysical changes occurring within the volcano and the historic behavior of analog volcanoes. A bootstrapping analysis of the training dataset allowed for the estimation of robust logistic model coefficients. Probabilities generated from the logistic models increase with positive modeling results, escalating seismicity, and high eruption frequency. The cross validation process produced a series of receiver operating characteristic (ROC) curves with areas ranging between 0.78 - 0.81, which indicate the algorithm has good predictive capabilities. In addition, ROC curves also allowed for the determination of a false positive rate and optimum detection threshold for each stage of the algorithm. The results demonstrate the logistic models are highly transportable and can compete with, and in some cases outperform, non-transportable empirical models trained with site specific information. The incorporation of source modeling results into the event tree's decision making process has begun the transition of volcano monitoring applications from simple mechanized pattern recognition algorithms to a physical model based forecasting system.

To Nicole, Jody, and Jacob Junek. Thank you for your love, patience, and support. This would not have been possible without your help.

ACKNOWLEDGMENTS

I would like to thank Dr. W. Linwood Jones for his guidance, assistance, and support in performing this research. In addition, I would also like to thank the Dr. Marwaan Simaan, Dr. Hassan Foroosh, and Dr. Mark T. Woods for serving on my dissertation committee and for their advise and assistance regarding my dissertation research. I am also grateful to Dr. Robert C. Kemerait, Dr. David R. Russell, Dr. Joe Schrodt, Dr. David B. Harris, Mr. John Dwyer, Mr. Jorge Roman-Nieves, Dr. Gene A. Ichinose, and Mr. David Sorter for their advice and assistance over the course of this work. I would also like to thank Dr. Chandan Saikia for many discussions regarding InSAR processing and the application of ROI PAC for deformation field mapping. The advise of Dr. Dale Anderson is greatly appreciated and was instrumental in the successful completion of the bootstrapping study and derivation of logistic coefficients. I am especially grateful to Dr. Michael Thursby, who gave me my first opportunity to perform research in the field of remote sensing and has been an outstanding mentor throughout my career.

This work would not have been possible without the multidisciplinary datasets acquired from a variety of organizations. A detailed overview of the providers of each data type is discussed in Section 3.6. Many of the maps shown in this dissertation were created with the Generic Mapping Tool (GMT) [1].

TABLE OF CONTENTS

LIST OF FIGURES

LIST OF TABLES

CHAPTER 1: INTRODUCTION

Volcanic eruptions have the potential to destroy entire communities, cripple critical infrastructure, and disrupt aviation traffic. Two examples of the destructive power and far reaching affect of volcanic activity are the 1995 eruption of the Soufriere Hills volcano on the island of Montserrat and the 2010 eruption of Eyjafjallajökull in Iceland. The Soufriere Hills eruption is one of the most dramatic examples of a volcanic eruption destroying a modern city. This volcano became active in 1995 after a long period of dormancy. Pyroclastic flows produced by a series of eruptions destroyed the capital city of Plymouth and left large sections of the island uninhabitable. Montserrat has become a laboratory for studying volcanic activity, where eruptions of the Soufriere Hills volcano continue to this day. In April 2010, global aviation traffic was disrupted by the explosive eruption of the Icelandic volcano known as Eyjafjallajökull. This eruption produced a massive ash cloud that halted Trans-Atlantic, European, and Asian air traffic for approximately six days and had a dramatic impact on an already weakened global economy.

There are approximately 169 geologically active volcanic centers in the United States [14], [15], [16], [2]. Many of these volcanic areas are located near densely populated areas and along heavily traveled air routes. Volcanoes in the Cascade Mountain range, such as Mount Saint Helens, which erupted violently in 1980, Mount Rainier and Mount Hood pose a significant threat to the population of the Pacific Northwest. An explosive eruption of an Alaskan or Aleutian Island volcano could significantly disrupt the air route between the Western United States and Eastern Asia. Thus, there is a significant need to monitor volcanic activity within the United States to ensure major population centers can be evacuated and air traffic diverted in the event of an eruption.

According to the Stafford Act (Public Law 93-288), the United States Geologic Survey (USGS) is responsible for issuing timely warnings of impending or potential volcanic eruptions to federal emergency management agencies. This responsibility is carried out by a series of volcano observatories that are primarily supported by the USGS Volcano Hazards Program in conjunction with universities and other federal agencies, such as the National Science Foundation (NSF) and the National Oceanic and Atmospheric Administration (NOAA). Each volcano observatory is tasked with monitoring volcanic activity in their distinct volcano-tectonic region. Each of these facilities independently operate or utilize a network of seismometers and GPS sensors to monitor activity at their respective volcanoes. However, the monitoring technologies and techniques developed since the eruption of Mount Saint Helens, approximately 30 years ago, are currently being applied on an ad hoc basis to volcanoes showing signs of heightened activity [16].

To combat this problem, the Consortium of U.S. Volcano Observatories (CUSVO) is working to develop a National Volcano Early Warning System (NVEWS), which will insure all of the high risk volcanoes in the United States are monitored at the appropriate level [16]. The NVEWS is outlined in a USGS open file report published in 2006 [16]. It will include a centralized "Watch Office" that will collect all of the monitoring data and issue the warnings to the appropriate federal emergency management agencies. A central part of this system will be the processing algorithm that analyzes incoming data. While the requirements for such an algorithm are not defined in [16], the report does state that "monitoring without research into the driving physico-chemical processes becomes mechanistic pattern recognition, an inadequate approach to phenomena as complex as volcanoes." Thus, there is a significant need for an automated volcano hazard assessment sys-

tem that uses a combination of source models, volcano monitoring data, and all available a priori information.

Volcanism is comprised of a combination of complex geophysical processes that vary in composition, duration, and intensity from location to location and episode to episode. Therefore, successful eruption forecasting will only be achieved through the use of methodologies that simultaneously weigh empirical experience and real-time interpretation of processes [17]. Event trees have proven to be useful tools for forecasting volcanic activity [18], [19], [20]. In 2002, Newhall and Hoblitt outlined a generic event tree structure for forecasting various types of volcanic activity and associated hazards. This process has been adopted and improved upon by a variety of researchers to forecast volcanic activity at various locations throughout the world (e.g., [21], [22], [23], [24], [25], [26], [27], [28]). However, previous event tree implementations require conditional probabilities or PDFs be manually derived on a volcano-by-volcano basis. This means every volcano being monitored will have a unique and unvalidated set of statistical functions driving the forecasting process. Thus, each instance of the algorithm uses subjectively selected detection thresholds that possess a unique and unquantified false positive rate. Moreover, these implementations have produced short-term forecasts largely from monitoring data only. To the best of the author's knowledge, there is no published method that combines near real-time source modeling results, monitoring data, and historic information to produce forecasts of short-term volcanic activity.

This research initiative aims to improve upon and standardize the event tree forecasting process. The method employed here also utilizes Newhall and Hoblitt's generic event tree infrastructure. However, its decision making process is augmented by a suite of empirical statistical

models that are derived through logistic regression. Each model is constructed from a geographically diverse dataset that was assembled from a collection of historic volcanic unrest episodes. The dataset consists of monitoring measurements (e.g. InSAR, seismic, GPS), source modeling results, and historic eruption information. The regression is performed using a generalized linear model routine (GLMR) that assumes a binominal response variable and employs a logit linking function, which is described in detail in Section 4.2.3. This process allows for trends in the relationship between modeling results, monitoring data, historic information, and the known outcome of the training events to drive the formulation of the statistical models. It yields a static set of logistic models that weight the contributions of modeling information, monitoring data and empirical experience relative to one another. The models estimate the probability of a particular event occurring based on the current values of a set of predefined explanatory variables and are transportable to a variety of different volcanoes. This provides a simple mechanism for simultaneously accounting for the geophysical changes occurring within the volcano and the historic behavior of analog volcanoes in short term forecasts. The methodology is easily extensible, where recalibration can be performed or new branches added to the decision making process with relative ease. In addition, a rigorous cross validation process is used to document the algorithm's performance, identify optimum detection thresholds, and quantify false positive rates. Moreover, the dataset used to train the algorithm is well documented and archived in a relational database, which ensures reproducibility of results. Such a system could aid federal, state, and locale emergency management officials in determining the proper response to an impending eruption and can be easily deployed by a NVEWS.

1.1 Dissertation Objectives

The specific objective of this research are as follows:

- Develop a simple process for forecasting short-term volcanic activity using monitoring data, source modeling results, and historic information, which can be easily deployed by a NVEWS.
- Derive empirical statistical models via logistic regression using a common dataset that is comprised of monitoring data, source modeling results, and historic eruption information acquired from collection of analog volcanoes.
- Estimate probable volcanic vent location using a two dimensional spatial probability density function derived from a combination of source modeling results and monitoring data, which is updated as new information becomes available.
- Characterize and document the performance of the forecasting algorithm using standard cross validation techniques.
- Quantify the false positive rate and identify the optimum detection threshold for each processing stage.
- Produce hazard assessments in terms of the USGS ground-based color code system.

1.2 Dissertation Overview

This dissertation is organized in the following manner. Chapter two, provides on overview of basic concepts in volcanology which is intended for readers not familiar with this science. Chapter three describes the volcano monitoring techniques employed in this research. Chapter four contains a detailed overview of the statistical development of the volcanic eruption forecasting algorithm, the empirical statistical models that drive it, and the cross validation process. Chapter five provides a detailed discussion of the results generated from the forecasting algorithm. Chapter 6 discusses the conclusions that can be drawn from this work and provides an overview of future research initiatives that may improve the algorithm's performance.

CHAPTER 2: CONCEPTS IN VOLCANOLOGY

According to the theory of plate tectonics, the upper most layers of the Earth's surface is comprised of a series of plates that move relative to one another on top of a semi-liquid mantle. These fragmented crustal layers and softer upper mantle layers are referred to as the Lithosphere and the Asthenosphere, see Figure 2.1. Plate motion is caused by mantle convection currents deep within the Earth. These currents drive molten material toward the surface, which applies a force on the lithospheric plates that either pulls them apart or pushes them together. Regions where plates are being forced apart are known as spreading ridges and areas where they are being driven beneath one another is known as a subduction zone. This process is responsible for continental drift and the configuration of landmasses we are familiar with today.

Volcanism typically occurs along or near the vicinity of a tectonic plate boundary. In fact, there are approximately 1500 active volcanoes on Earth today [15]. Roughly two-thirds of them are located along the plate margins that encircle the Pacific Ocean [15]. This region, known as the *Ring of Fire*, is shown in Figure 2.2. Other regions of intense volcanic activity include the sea mount chain along the Mid-Atlantic Ridge and the Mid-African Rift [3]. Volcanic activity occurring away from tectonic plate boundaries is known as intraplate volcanism. This phenomenon is thought to be caused by columns of hot molten material, know as a mantle plume, that originate from deep within the Earth and extend to shallow depths just below the Earth's surface. An area where intraplate volcanism occurs is known as a *hot spot*. The most commonly cited examples include the Hawaiian Islands and Yellowstone National Park.

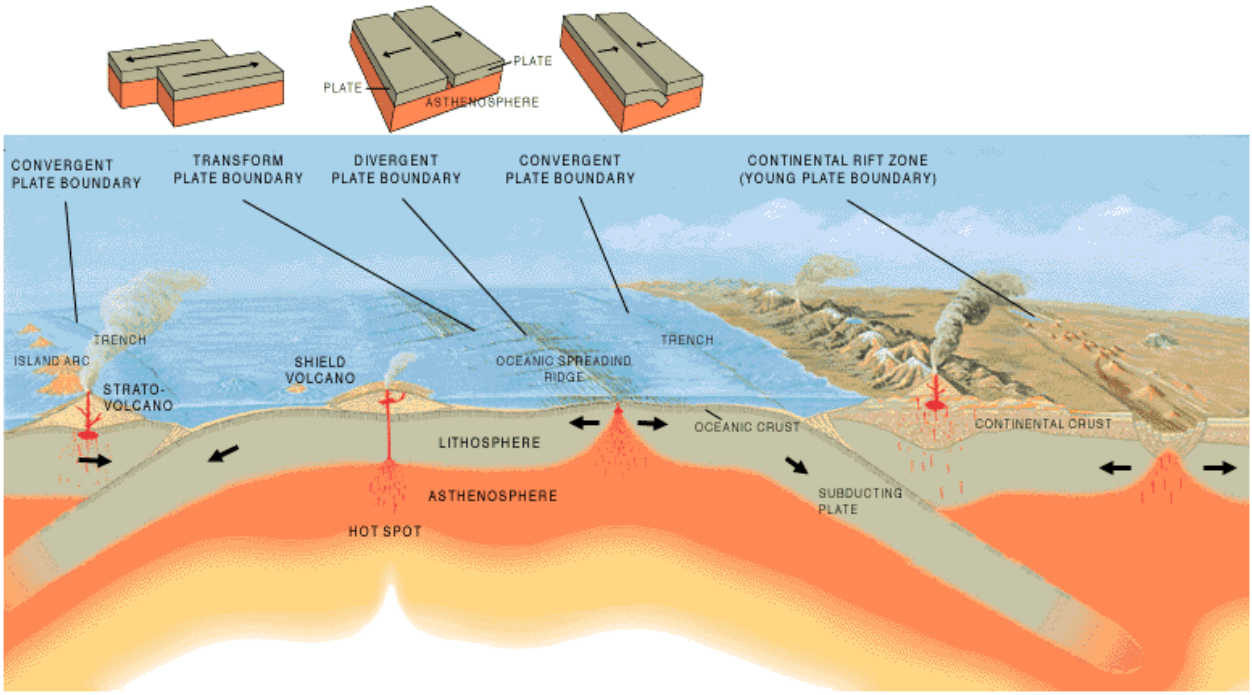

Figure 2.1: Diagram illustrating the different types of tectonic plate boundaries, Lithosphere and Asthenosphere. This figure was produced by the USGS Volcano Hazards Team and was obtained from [2].

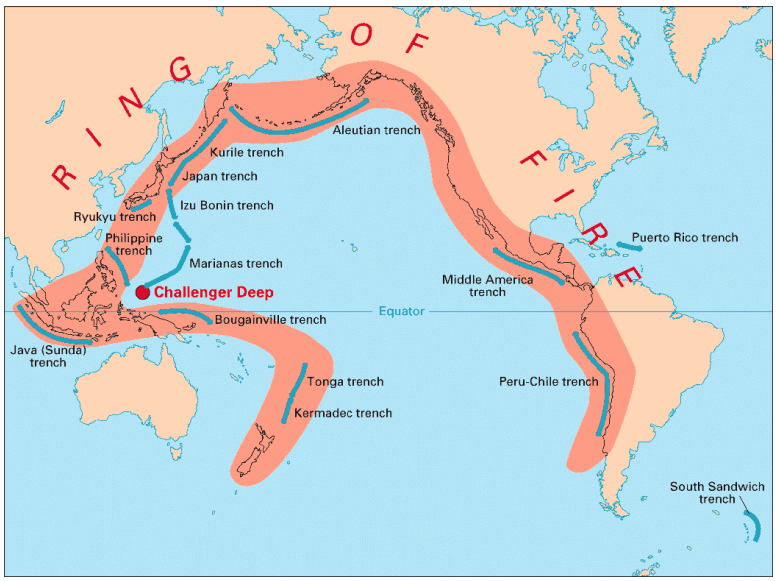

Figure 2.2: Map highlighting the location of the Ring of Fire. This figure was produced by the USGS Volcano Hazards Team and was obtained from [2].

2.1 Eruption Mechanics

A volcanic eruption is the result of a multi-stage process that can take months, years, or decades to culminate. The internal geophysical processes leading to an eruption are summarized in [3] as a simplified, four part, process which is illustrated in Figure 2.3 and is comprised of the following components:

- *Melt Generation* - The process of magma production occurs deep beneath the Earth's crust. High temperatures, decreased pressure, or hydration can cause rock to melt. The molten material begins to flow through pathways that exist at depth or are self generated. Since the density of the molten rock is less than that of the surrounding material, it needs to occupy a larger volume. As a result, pressure increases and the melt begins to fill all available space. Eventually the pressure increases to the point where the surrounding material fails. These failures produce fissures, known as dikes, that allow the magma to travel upward (see Figure 2.4 A) [3].

- *Magma Ascent* - The movement of magma through a series of dike intrusions that exist between the melt layer and an intermediate storage area or the surface. The velocity of the molten material is a function of its viscosity. The shape and size of dike intrusions is a function of the stresses driving the magma [3]. Upward motion of fluid typically induces seismic activity and or measurable surface deformation (uplift or subsidence). The onset of anomalous geologic activity caused by fluid motion within a volcano is known as volcanic unrest, which is a typical precursor to an eruption. Early detection and identification of unrest is key to producing timely volcanic hazard condition assessments.

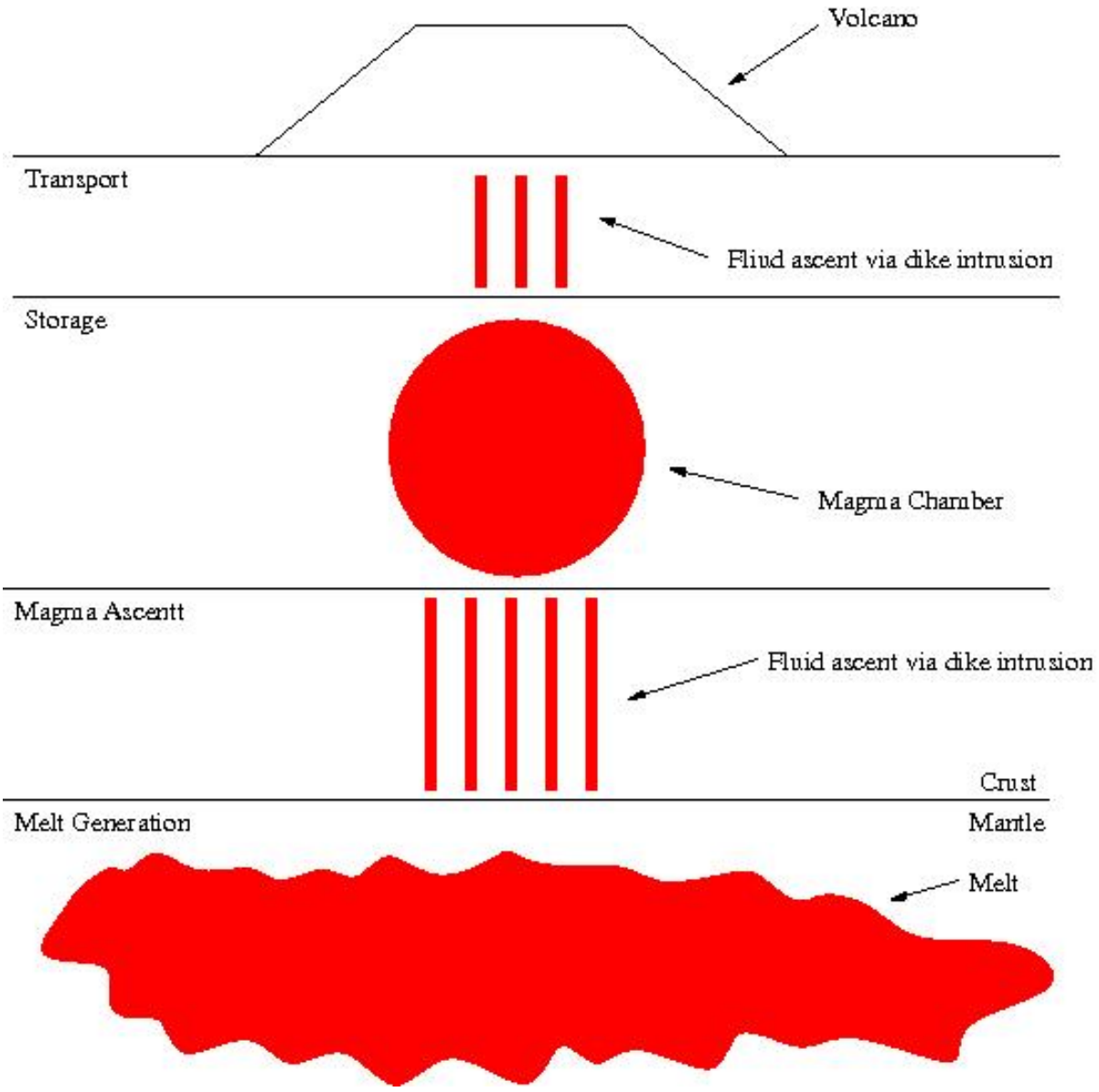

Figure 2.3: Schematic diagram describing the eruption process [3].

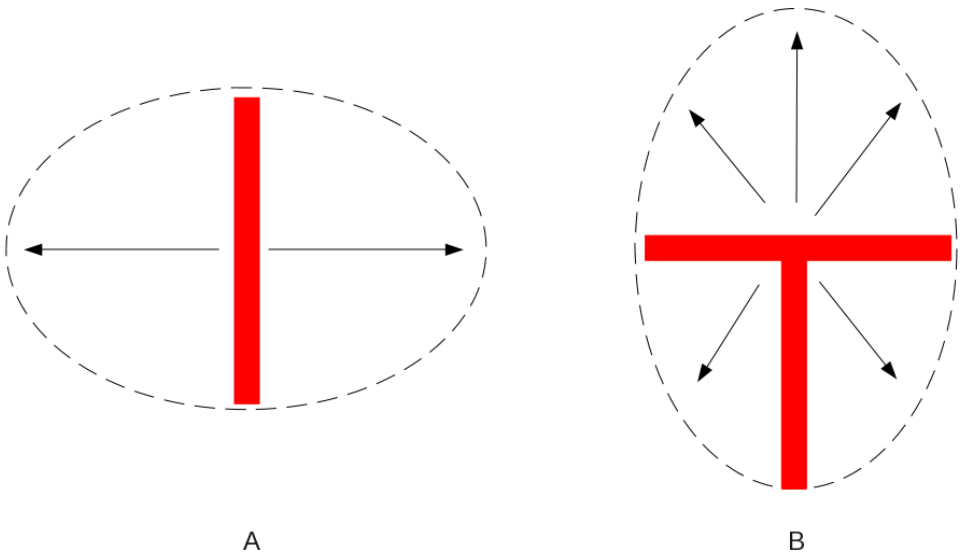

Figure 2.4: Schematic diagram illustrating the geometry of magmatic intrusions. Inflating dikes and sills can eventually produce large magma storage chambers. A) Inflating dike. B) Inflating sill that is fed by a horizontal dike.

- *Storage* - A shallow chamber that stores magma transported from underlying melts. Most chambers are spawned from the inflation of horizontal dike intrusions, known as sills (see Figure 2.4 B). The inflation process is another potential source of volcanic unrest. Eruption size and frequency is typically a function of the magma chamber's size. Small chambers usually produce small but frequent eruptions, while large chambers produce large intensity but less frequent eruptions. Eruption frequency is related to the fluid (e.g. magma or gas) replenishment rate or the time it takes for internal pressure to rebuild within the chamber [3].

- *Transport* - The process that delivers magma from the storage area to the surface. As new material is delivered to the chamber its internal pressure and dimensions increase. Eventually the chamber walls fail. The high internal pressure drives magma into the opening, which produces a series of dike intrusions that lead to the surface and often induces intense unrest.

Once the dike intrusions reach the surface, magma and volcanic gases erupt from the volcanic edifice.

2.2 Eruption Triggers

Eruptions can be triggered by a number of internal and external sources. A partial list of generally accepted mechanisms for inducing an eruption is as follows:

- *Magma Intrusions:* The ascent of fluid from depth continues until the pressure inside the magma storage vessel exceeds that of the country rock. This leads to the failure of the surrounding material and the opening of a pathway from the storage vessel to the surface.
- *Excessive Gas Pressure:* Pressure build up due to expanding gasses within the volcano exceeds the load bearing capability of the country rock. This can also lead to the failure of the surrounding material. Thus opening of a pathway from a magma storage vessel to the surface.
- *Local Earthquake Activity:* Local earthquake activity can induce an eruption through faulting, flank collapses, or gas pressure build up from intense ground shaking.
- *Loading Shifts:* Decrease of pressure that is equalizing pressure contained within the volcano. Examples include massive removal of material by landslides, lake drainage, and glacier reduction that remove surface load and causes internal pressure to fracture the surrounding country rock.

- *Earth Tides:* Some volcanoes have exhibited a statistical preference for erupting during the earth tide minimum or maximum [17].

2.3 Volcanic Explosivity Index

There are several techniques to quantify the intensity of a volcanic eruption. The method used in this research is known as the Volcanic Explosivity Index (VEI). It is derived from a combination of the volume of material expelled during the eruption, the column height, and a qualitative description of the event [3], [29]. This scale ranges between 0 and 8. Eruption intensity values increase one VEI unit when the volume of expelled material (tephra) increases one order of magnitude [17]. For example, an eruption that expels $10^6 m^3$ of tephra has a VEI of approximately 2. However, if the eruption produces $10^{12} m^3$ of tephra its VEI is approximately 8.

2.4 Surface Deformation

The surface deformation in the area surrounding a volcanic center is typically caused by the inflation or deflation of a shallow magma chamber. This behavior results from the influx or expulsion of magma, gases, or a mixture of the two. The volume change causes the size and or internal pressure (hydro-static) within the chamber to fluctuate. This imparts stress on the surrounding area, which changes the local topography by producing measurable uplift or subsidence. Surface deformation can be modeled using a simple spherical source in a semi-infinite elastic half

space, which is defined as

$$\Delta h(r) = \frac{3A^3P}{4\mu}\frac{d}{(r^2+d^2)^{\frac{3}{2}}} \tag{2.1}$$

$$\Delta r(r) = \frac{3A^3P}{4\mu}\frac{r}{(r^2+d^2)^{\frac{3}{2}}} \tag{2.2}$$

where $\Delta h(r)$ and $\Delta r(r)$ are the vertical and horizontal displacement estimates, P is the change in internal hydro-static pressure, A is the chamber radius, μ is the shear modulus, r is the radial distance from the source, and d is the chamber's depth [30]. If the radius of the chamber is small compared to the depth, the shape of the vertical and horizontal deformation curves are a function of depth and the values of displacement are a function of A, P, and μ [30]. A schematic diagram illustrating Mogi's spherical source model and the relative shapes of the vertical and horizontal displacement curves are shown in Figure 2.5 and Figure 2.6.

The number of free model parameters prohibits the formulation of a unique solution in the absence of a priori information about the chamber's location and geometry. In this situation, the A, P, and μ terms are set to a constant scale factor ,C, which is defined as

$$C = \frac{3A^3P}{4\mu} \tag{2.3}$$

and allows Equations 2.1 and 2.2 to be rewritten as

$$\Delta h(r) = C\frac{d}{(r^2+d^2)^{\frac{3}{2}}} \tag{2.4}$$

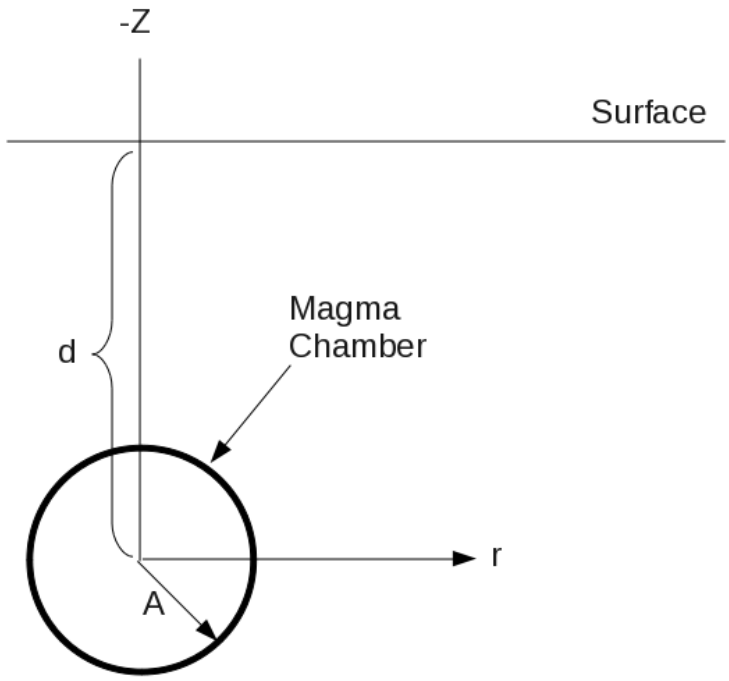

Figure 2.5: Schematic diagram illustrating the Mogi source assumptions.

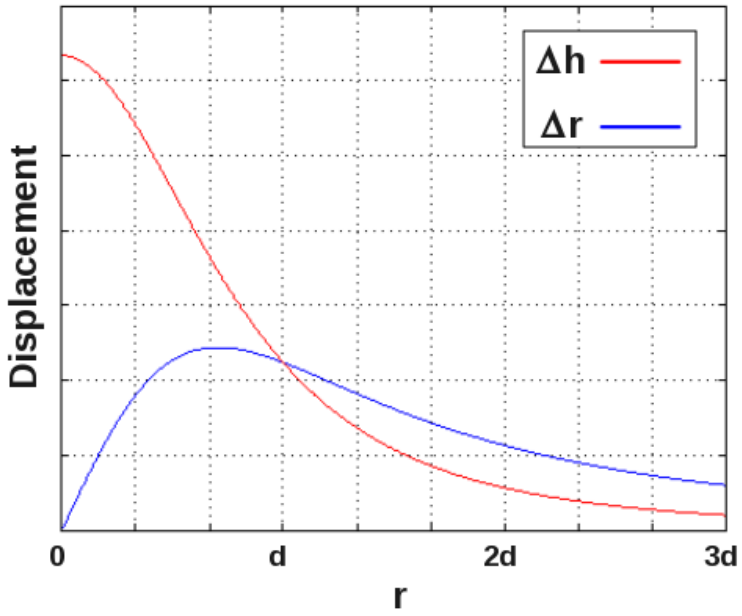

Figure 2.6: Mogi source ground displacement profiles.

$$\Delta r(r) = C\frac{r}{(r^2+d^2)^{\frac{3}{2}}} \tag{2.5}$$

The scale factor formulations shown in Equations 2.4 and 2.5 simplifies the model to a function of two independent variables, which reduces the non-uniqueness of the solution. If the chamber's depth is known *a priori*, then the model has a unique solution and only the value of C needs to be determined.

Once the value of C is established, it can be used to estimate the volume of magma displaced during an eruption [31], [32]. The volume of the deformed surface, assuming a Poisson solid (i.e., Lame's constant equals the shear modulus), is computed using

$$V = 2\pi\,|C| \tag{2.6}$$

and volumetric change in magma, ΔV, is equal to

$$\Delta V = \frac{2}{3}V \tag{2.7}$$

CHAPTER 3: VOLCANO MONITORING

Many volcanoes along the west coast of the United States, Alaska, and Hawaii are outfitted with an assortment of instruments to monitor volcanic unrest. Sensor suites typically include a combination of seismometers, GPS sensors, and tilt meters. These instruments acquire and process data in near real time to search for precursors that may signal the onset of an eruption. Sudden increases in seismic activity and/or surface deformation in the form of uplift or subsidence are the most common eruption precursors. Figure 3.1 illustrates the color code system adopted by the USGS in 2007 to identify the current hazard condition at a particular volcano. This system is designed to address both ground based and aviation hazards. The hazard condition of a volcano is determined by the scientific staff at the appropriate observatory based on the available monitoring data (seismic, GPS, etc.) and the current or expected level of activity [2]. Volcanoes designated as green are in the "normal" state, which indicates they are in a non-eruptive condition. Those labeled as yellow are in the "advisory" state, which indicates the volcano is displaying signs of heightened unrest. Volcanoes designated as orange, such as Kilauea in Hawaii, are in the "watch" state possibly due signs of escalating unrest or an ongoing eruption that does not pose any significant hazard. Locations labeled as red are in the "warning" state due the possibility of an impending eruption.

Volcanic eruptions produce a number of hazards that affect their surrounding area, population, and aviation traffic. The hazards most often produced by eruptions are illustrated in Figure 3.2 and are summarized below:

- *Volcanic Ash Clouds* - Eruption induced clouds of hot pulverized rock and volcanic gases that can travel approximately 10 to 20 km into the Earth's atmosphere [10]. Clouds that stay aloft

Figure 3.1: USGS volcanic hazard program color code system, where the top line defined the ground-based hazard conditions, the lower line shows the aviation warning levels, and normal, advisory, watch and warning declarations are signified by green, yellow, orange, and red respectively [2].

drift with the prevailing winds and can travel great distances. They pose a substantial hazard to aviation traffic. Ash material is highly abrasive and can seriously damage jet turbines and other vital air craft instrumentation and components.

- *Tephra* - Volcanic ash that precipitates from volcanic ash clouds and accumulates on the Earth's surface. Material dimensions can range from dust like particles to moderate size projectiles, which can cause substantial harm to machinery and make highways extremely slippery and difficult to navigate.

- *Pyroclastic Flows* - Extremely hot volcanic ash cloud that falls back to Earth and travels along the ground at high speed. Pyroclastic flows often destroy or kill everything in its path.

- *Lava Flows* - Molten rock that flows from volcanic vents and openings in the Earth's crust, where temperatures typically range between 700 - 1200 $^{\circ}C$ [3]. Flows can travel at various speeds depending on the material's viscosity and the slope of the terrain. Lava is extremely dangerous and can destroy or kill everything in its path.

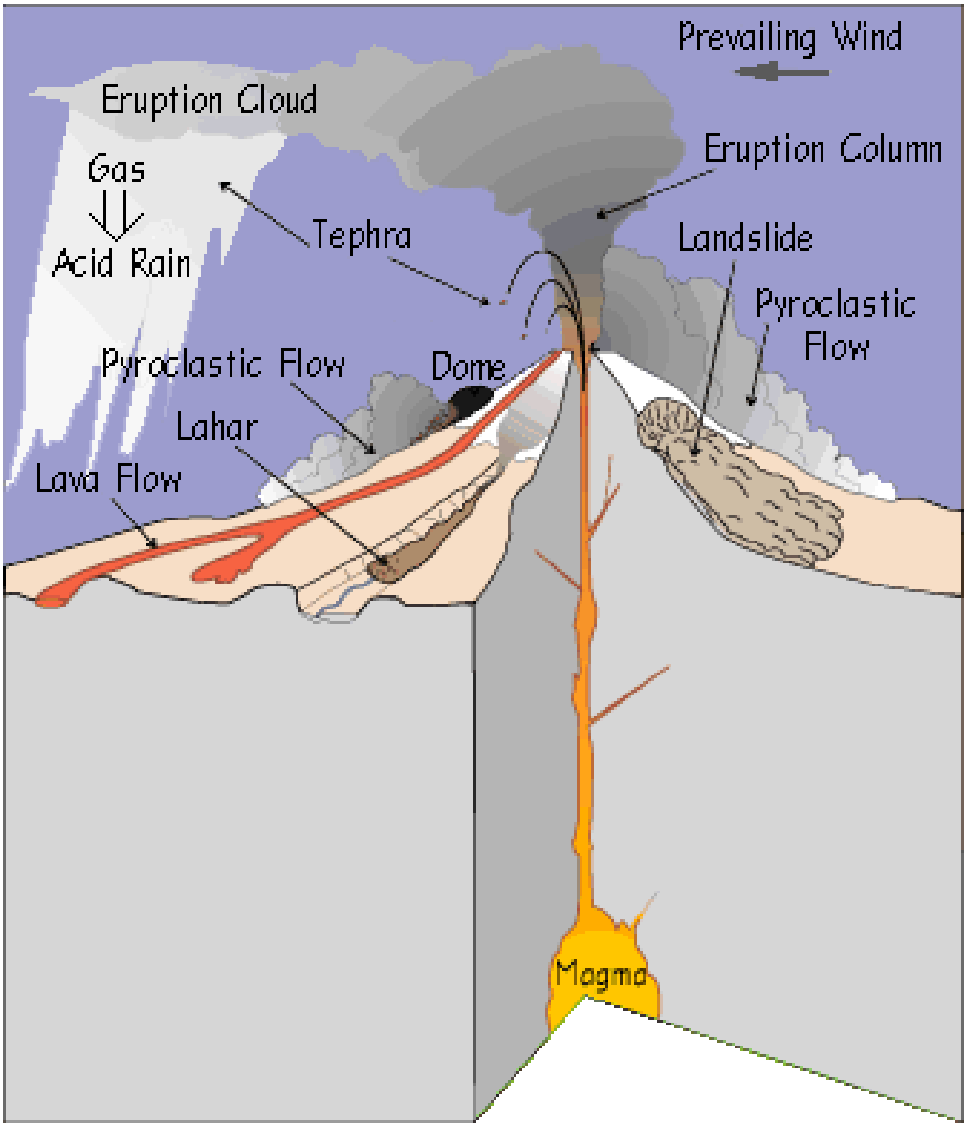

Figure 3.2: Illustration of various volcanic hazards. This figure was produced by the USGS Volcano Hazards Team and was obtained from [2].

- *Lahars* - A flash mud slide or flood that flows down the side of a volcano with little or no warning. They can cause substantial damage to property, destroy agriculture, and can cause bodily harm or loss of life.

- *Landslides* - An avalanche of rock and other material residing along the walls of a volcanic center or caldera. These events are typically caused by eruption induced ground displacement or explosions.

- *Volcanic Gases* - Hot steam or gases produced by volcanic eruptions or vented from near by fumerals. Gases are often invisible and may be highly toxic.

- *Directed Blasts* - Acoustic shockwave associated with a large explosive eruption. This is often the result of an extremely rapid release of internal pressure, which may be caused by a material failure within the volcano. The direct blast associated with the 1980 eruption of Mount St Helens was caused by an earthquake induced slope collapse that trigger an extremely large and violent explosion that permanently altered the shape of the mountain and the surrounding area.

- *Volcanic Tsunamis* - Tsunami caused by large fragments of material or pyroclastic flows that propagate into a large body of water, which can seriously damage the area along the opposing shore line.

- *Acid Rain* - Highly corrosive precipitation produced by a mixture of chemical compounds in volcanic clouds and water molecules in rain clouds, where pH values typically range between 3 and 4.

3.1 Monitoring Techniques

Most volcanoes are located in remote areas or extremely hostile environments that make them difficult to access on a regular basis. Therefore, it is preferable to study them with sensor technologies that can be deployed at stand-off distances and operate autonomously. A number of remote sensing and in-situ measurement techniques are often used to study active volcanoes.

3.2 Synthetic Aperture Radar

The importance of Synthetic Aperture Radar (SAR) as a scientific research tool has grown significantly over the last 50 years. Airborne and space based SAR platforms provide a means of studying remote areas of the Earth in a simple and non-invasive manner. They are used for a variety of scientific applications including, but not limited to, agriculture, forestry, oceanography, topographical mapping, glaciology, seismology, and volcanology[33], [4]. Since a SAR illuminates its scene with microwave energy, it is capable of producing high resolution images in day or night and in almost any weather condition.

SARs use the forward motion of its platform to produce the equivalent of a large aperture array from a relatively small antenna [5], [34], [35]. By directing the antenna beam perpendicular to the platform motion and summing the returns from successive pulses, a synthesized along track array can be constructed (see Figure 3.3a). The platform motion results in a path length difference between the returns collected by the synthesized array elements. This difference produces a phase variation across the length of the array, as shown in Figure 3.3b and c, that defocuses the final SAR

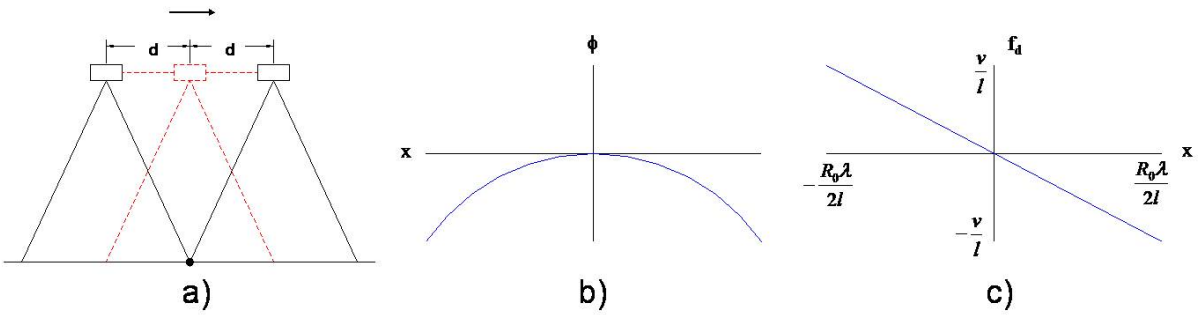

Figure 3.3: Synthetic Aperture Radar Concept: a) Platforms forward motion is used to construct a synthetic along track array. b) Phase variation across the array produced by the path length difference for returns observed along the length of the array, c) Frequency shift caused by path length difference across the array.

image. This phase variation is also referred to as a phase error, ϕ_n, and is defined as

$$\phi_n = -\frac{2d_n^2\pi}{\lambda R_0} \tag{3.1}$$

where d is the along-track distance from the center of the array to the n^{th} synthetic element and R_0 is the range to the area being studied. Fine azimuthal resolution can be achieved by applying a phase correction across the array to focus the image. A focused SAR is capable of an azimuthal resolution, Δx_f, as fine as half the length of the physical aperture of its antenna, L_{ap}, which is given by

$$\Delta x_f = \frac{L_{ap}}{2} \tag{3.2}$$

A traditional SAR resolves target locations in two dimensions. Range or cross-track measurements are derived from the radar pulse round trip travel time between the instrument and the target. Azimuthal or along track measurements are derived from the Doppler frequency of the target. Each two dimensional point corresponds to a range cell in space referred to as a pixel.

3.2.1 Interferometric Synthetic Aperture Radar

Three dimensional radar images are produced using Interferometric Synthetic Aperture Radar (InSAR) techniques. InSAR exploits the phase difference between two complex SAR images of the same scene that are displaced in either space or time. Three typical InSAR configurations are shown in Figure 3.4. Figure 3.4a shows the configuration of a cross track interferometer (CTI). The CTI generates a pair of complex SAR images using two coherent radar systems separated by a vertical distance referred to as the baseline, B. The construction of an along track interferometer (ATI) is shown in Figure 3.4b. The ATI consists of two coherent radars that are separated by a horizontal baseline extending in the along track direction. In this case, the image pairs are acquired from the same location but displaced in time rather than space. The temporal displacement of ATI images can be on the order of seconds, for oceanographic applications, or years for seismological or volcanological applications. An ATI is a specialized version of the repeat track interferometer (RTI) shown in Figure 3.4c. The RTI also acquires two complex SAR images of the same scene that are displaced in time and is the InSAR configuration most commonly used by space-based platforms[4].

The phase difference between complex SAR images is referred to as the interferometric phase, ϕ. It is caused by a path length difference between the backscattered signals from corresponding pixels in each complex SAR image and is a function of the interferometer geometry shown in Figure 3.5. The interferometric phase is defined as

$$\phi_{total} = \frac{-4\pi B sin(\theta - \alpha)}{\lambda} \tag{3.3}$$

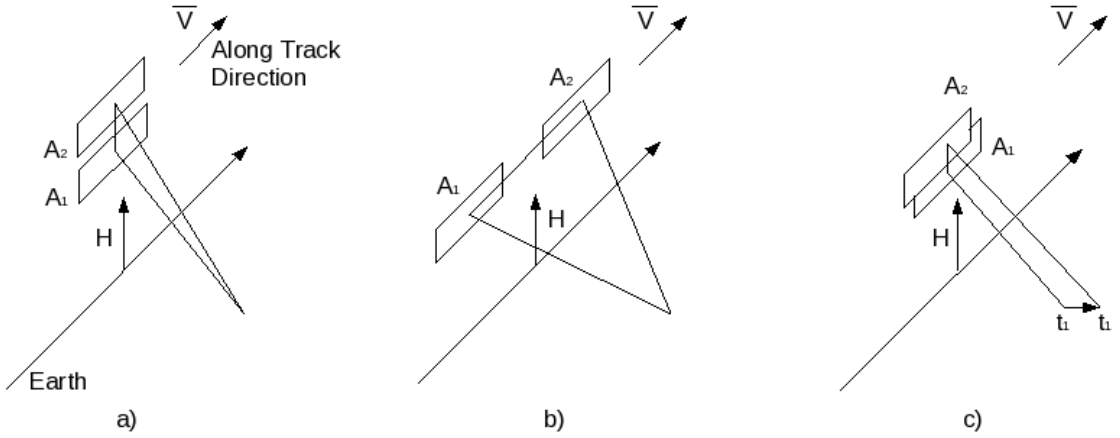

Figure 3.4: InSAR configurations, where A_1 and A_2 are the antenna locations for the first and second image acquisition, respectively, H is the platform height, and V is the velocity vector of the platform: a) Cross Track Interferometry (CTI), b) Along Track Interferometry (ATI), c) Repeat Pass Interferometry (RTI), where t_1 is the location of that point at each image acquisition [4].

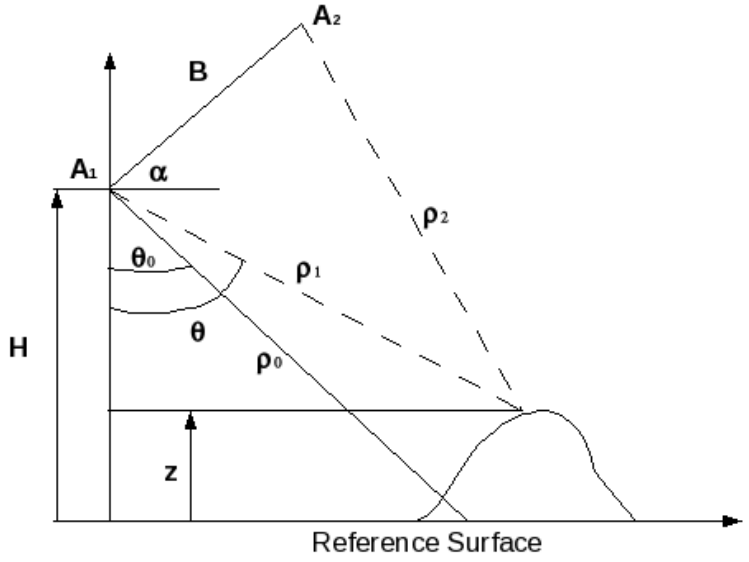

Figure 3.5: Typical cross track interferometer geometry in the plane normal to the flight direction, where θ is the look angle relative to the view point, z, θ_0 is the look angle relative to the reference surface, B is the baseline, A_1 and A_2 are the radar antennas, α is the baseline look angle, ρ_0 is the slant range to the reference surface, ρ_1 and ρ_2 are the slant ranges from antenna 1 and 2, respectively, to z, and H is the platform height [4] [5] [6].

where θ is the look angle and α is the baseline look angle. This phenomenon can be exploited to measure relative distances less than a fraction of the electromagnetic wavelength, λ. Interferometers have been used in a variety of applications, not just remote sensing, where highly accurate measurements of extremely small distances are required. In topographic mapping problems, InSARs measure the elevation of a scene as a function of interferometric phase. This application requires Equation 3.3 be expanded as

$$\phi_{total} = \phi_{flat} + \phi_{topo} \tag{3.4}$$

and rewritten in terms of the radar's operational parameters as

$$\phi_{total} = \frac{-4\pi B sin(\theta_0 - \alpha)}{\lambda} - \frac{4\pi z B cos(\theta_0 - \alpha)}{\lambda \rho_0 sin\theta_0} \tag{3.5}$$

where the first and second terms are the flat earth and topographic components of the interferometric phase [4], [6]. Topographic measurements are obtained from ϕ_{total} after the removal of the ϕ_{flat} component from the measurement (see Figure A.8).

An image illustrating the interferometric phase pattern over a geographic area is known as an interferogram. Each color cycle, or fringe, is equivalent to a complete phase revolution of 2π radians. The flat earth contribution causes a series of rapid phase revolutions, or wrapping, that increase in frequency as a function of increasing range. If the flat earth contribution is removed, the resulting fringe pattern represents the topographic elevation changes in the scene, in the line of sight direction. Displacement in the line of sight direction is represented by fringe patterns that increase or decrease as a function of the changing elevation. In this case, each complete phase

revolution is equivalent to an elevation change of h_a meters, which is referred to as the ambiguity height and is defined as

$$h_a = \frac{\lambda \rho sin\theta_0}{2Bcos(\theta_0 - \alpha)} \tag{3.6}$$

Elevation changes occurring over the time separation between SAR images is easily detected and measured using InSAR. These changes produce a new term in Equation (3.4), which is now defined as

$$\phi_{total} = \phi_{flat} + \phi_{topo} + \phi_{def} \tag{3.7}$$

where ϕ_{def} is the interferometric phase component caused by surface elevation changes between images (surface deformation) [4], [6]. This expression can be rewritten in terms of the radar's operational parameters as

$$\phi_{total} = \frac{-4\pi Bsin(\theta_0 - \alpha)}{\lambda} - \frac{4\pi z Bcos(\theta_0 - \alpha)}{\lambda \rho_0 sin\theta_0} + \frac{4\pi}{\lambda}\delta\rho_{disp} \tag{3.8}$$

where $\delta\rho_{disp}$ represents surface deformation in the line of site direction [4], [6]. Equation (3.8) shows that the total interferometric phase is far more sensitive to surface changes between images than any other contribution. Since one complete phase revolution occurs when the displacement component of equation (3.8) is equal to 2π, the elevation change associated with one interferometric fringe can be derived as follows

$$\phi_{def} = \frac{4\pi}{\lambda}\delta\rho_{disp} = \frac{4\pi}{\lambda}\frac{\lambda}{2} = 2\pi \tag{3.9}$$

As a result, once the topographic interferometric phase component is removed, each fringe in the interferogram is equivalent to a distance equal to half the electromagnetic wavelength, $\lambda/2$. Note that additional interferometric phase terms produced by atmospheric distortion and noise are assumed to be small and are neglected in this study.

A Differential InSAR (DInSAR) image is computed by removing the unwanted interferometric phase terms in Equation 3.7. A simple pictorial formula for computing a DInSAR image is shown in Figure 3.6 A - D. In order to remove the flat earth and topographic components from the interferogram, they must be simulated and subtracted from the total interferometric phase (Figure 3.6 A). Removal of the flat earth term is performed by subtracting a constant elevation surface from the image. This process leaves a fringe pattern dominated by topographic effects (Figure 3.6 B). In order to remove the topography from the image, a digital elevation model (DEM) of the area is required (Figure 3.6 C). The DEM is used to estimate the topography in the scene that must be simulated and removed [13], [12]. Once the topographic contribution is removed, the residual interferogram (ϕ_{def}) is the result of surface changes that have taken place over the elapsed time between images (Figure 3.6 D). True ground displacement measurements are obtained by unwrapping ϕ_{def}. Several algorithms have been developed to perform this task, such as the least squares and branch cut approaches, but is still an open area of research [4].

InSAR signal processing techniques have been studied extensively over the last twenty years (e.g., [36], [37], [4], [38], [39], [40], [34], [41], [42]). Since the subject of InSAR signal processing is not the primary focus of this research, the Repeat Orbit Interferometry Package (ROI PAC) is used to produce the interferograms necessary to preform this work. The ROI PAC is an open source InSAR processing application that was developed by Caltech and the JPL [43]. ROI

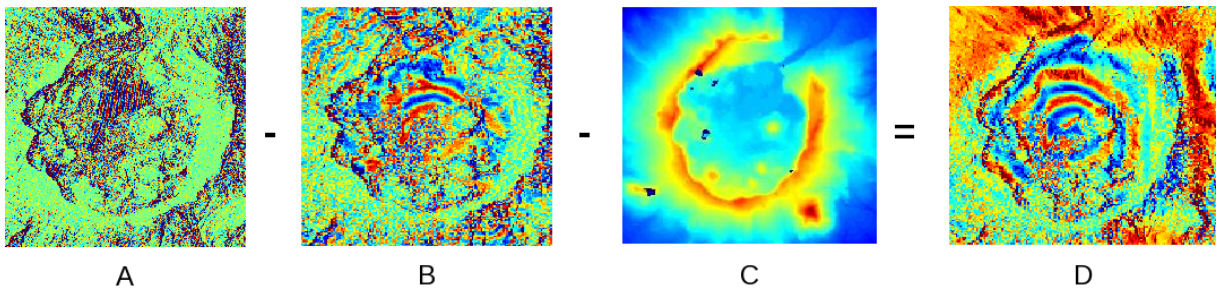

Figure 3.6: Pictorial formula for calculating a differential interferogram highlighting surface deformation inside the Okmok caldera using data acquired by ERS-1 and 2, where the operating parameters for these space based remote sensing platforms are listed in Table 3.1. In this example, Frame A shows the raw interferogram (ϕ_{total}), Frame B is the flattened interferogram, Frame C is the DEM, and Frame D is the final interferogram (ϕ_{def}) highlighting deformation inside the Okmok caldera between 1997 and 1998. Here frames B and C are subtracted from frame A and yields frame D where each fringe cycle represents 2.83 cm of ground displacement.

PAC is freely available for download from the Open Channel Foundation website [44]. The downloadable tar file contains source code and a collection of test data to determine if the compilation was successful. ROI PAC is essentially a collection of PERL scripts that call a series of C and FORTRAN functions that perform all of the computational heavy lifting. It handles all aspect of InSAR processing from the initial data formatting to the creation of geocoded DInSAR images. The software is controlled by a simple parameter file that points to two SAR images of the same scene, a DEM, Precision Orbit Information, and specifies the processing options the user wishes to invoke. A detailed overview of the ROI PAC and other open source SAR processors considered for this research is discussed in Appendix A.

3.2.2 Digital Elevation Model

A DEM, also referred to as a digital terrain model (DTM), is a digital representation of the topography of the earth. It should be noted that there is another type of digital terrain model known as a digital surface model (DSM), which includes all surface features such as vegetation and man-made objects, that will not be used in this study. As already stated in Section 3.2.1, DEM information is used to simulate ϕ_{topo} so it can be subtracted from ϕ_{total}. Once the topographic and flat earth components are removed, the residual interferometric phase is ϕ_{def}.

3.2.3 Precision Orbit Information

Precision Orbit Information (POI) for the satellite is required for each pass over the target area. Knowledge of the precise location of the platform is necessary for accurate baseline estimates, especially in the radial direction. Orbit errors translate directly into errors in topographic or deformation height estimates. This information is derived from a combination of tracking data, gravity models and physical models [40]. Tracking information is generated by a satellite laser ranging system (SLC) and precise range and range-rate equipment (PRARE) for ERS-1 and ERS-2, respectively. This information is collected by a sparse network of tracking stations that are non-uniformly distributed over the Earth. The gravity models, GEM-T2, PGM035, JGM 3, and DGM-E04, are used to determine orbital information between ground stations [40], [45]. The physical models account for atmospheric drag and solar radiation effects on the orbit.

Table 3.1: Space based radar platforms used in this study

Name	Launch	F_c(GHz)	H(km)	PRF(Hz)	F_s(MHz)	PL(μs)	ΔF(MHz)
ERS-1	June 1991	5.3	780	1679.9	18.962	37.12	15.55
ERS-2	April 1995	5.3	780	1679.9	18.962	37.12	15.55

3.2.4 Space Based Radar Platforms

The SAR data used in this study was acquired by European Remote Sensing (ERS) satellites 1 and 2. The ERS-1/2 satellites were developed by the ESA and launched in 1991 and 1995 [46]. They carry a suite of instrumentation designed to study the earth in great detail, which include a wind scatterometer, SAR, radar altimeter, microwave sounder and an infra-red radiometer. Both systems have similar operational parameters which are listed in Table 3.1. The common operational parameters allows ERS-1/2 to be used in tandem for InSAR applications.

3.3 Global Positioning System Measurements

GPS sensors are commonly used to measure the surface deformation (e.g. uplift and subsidence) around active volcanoes and urban areas. Position measurements acquired by GPS sensors are determined by triangulating the distance between several known locations. The reference points are defined by a constellation of satellites in orbit above the earth. These satellites transmit a series of timing signals (pseudoranges), L1 (1575.42 MHz) and L2 (1227.60 MHz), that are used to measure the one-way travel time between the sensor and the satellite [47].

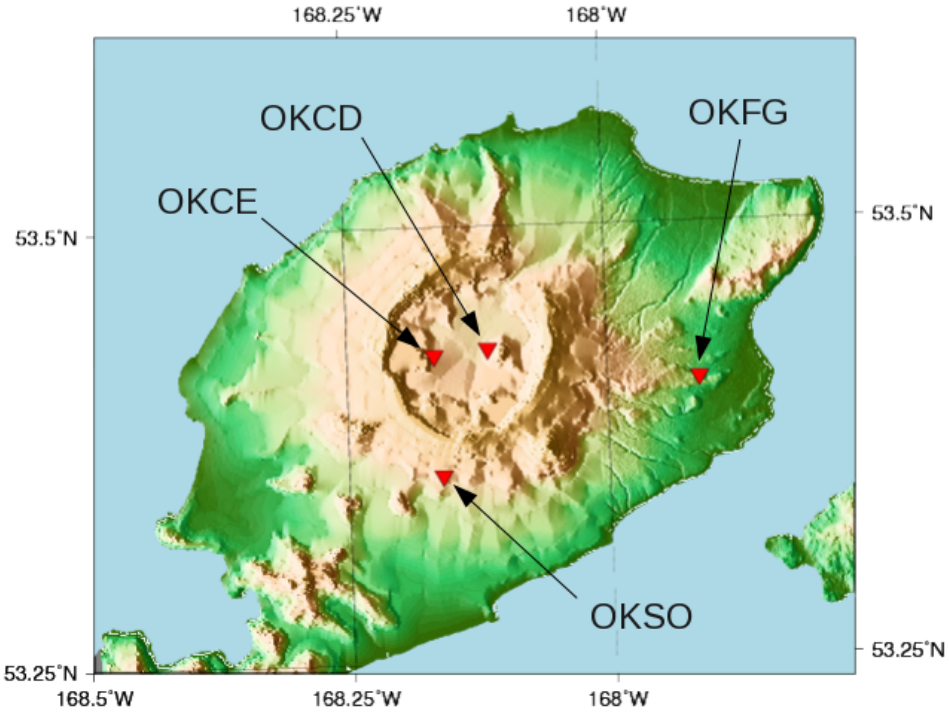

Figure 3.7: Umnak Island GPS Stations.

Many volcanoes are outfitted with a GPS network that measures changes in their topography. GPS sensors can provide unsurpassed temporal resolution for measuring topographic changes at a specific point and are also useful for offsetting the loss of spatial coverage in InSAR data due to decorrelation between images. For example, Umnak Island has four permanent GPS sensors located along and inside the Okmok caldera (see Figure 3.7). These sensors are managed by the Alaska Volcano Observatory (AVO) and have been in operation since 2002. Displacement measurements acquired by the available sensors (OKCD, OKCE, and OKFG) are shown in Figure E.1 - Figure E.3. The figures show subsidence occurring at OKCD and OKCE in mid 2004 and gradually transitioning to uplift by mid 2008. Measurements at OKFG appear to remain relatively flat between mid 2004 and mid 2008. Data for OKSO was not available.

3.4 Seismology

The study of volcano seismology is focused on understanding the dynamics and spatial extent of magmatic systems. A clear understanding of the physics that drive these systems will improve our ability to accurately determine volcanic hazard and identify seismic precursors that may signal an eruption. The motion of fluids within a volcano, such as magma or gas, generates two distinct families of seismic events: those produced by fluids and those generated by the fracture of solid rock. The detection of fluid induced seismicity is vital for eruption forecasting. However, the time span between the onset of seismic activity and an eruption varies dramatically from volcano to volcano. Seismicity can begin hours, days, weeks, months, years or decades before the start of an eruption. As a result, a large body of literature exists on the generation of volcano seismicity and its utility in eruption forecasting (e.g. [48],[49],[50],[51],[52],[53],[54]).

The first type of volcano seismicity is generated by disruptions in fluid motion within the volcanoes magma supply system. In this case, seismic energy is produced by pressure fluctuations occurring inside fluid filled cracks, conduits, or a resonating chamber. These phenomena can produce both long period (LP) seismic signals and continuous tremor. LP signals and those originating from tectonic activity share similar temporal characteristics but have significantly different spectra. Their spectral content is often comprised of a broadband onset followed by a low frequency or, in some cases, harmonic wavetrain. They are typically characterized by emergent P and S wave onsets and a substantial amount of energy below 5 Hz [48],[49]. Figure 3.8 and Figure 3.9 shows an example of a LP event produced by Okmok's 2008 eruption. Volcanic tremor is a long duration seismic signal whose spectral characteristics are typically defined by a series of

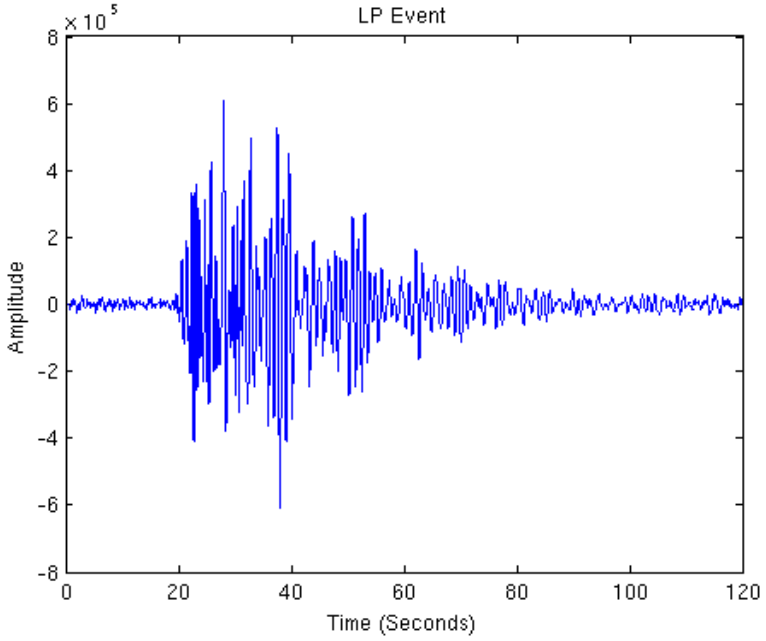

Figure 3.8: Time domain seismogram of LP Earthquake observed during Okmok's 2008 eruption.

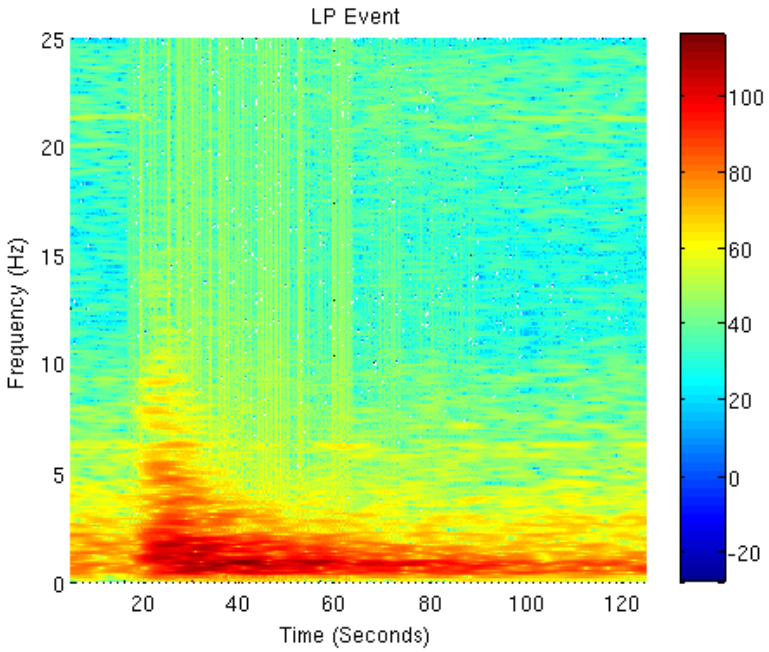

Figure 3.9: Spectrogram of LP Earthquake observed during Okmok's 2008 eruption.

narrow band peaks (harmonics). Figure 3.10 and Figure 3.11 shows an example of volcanic tremor produced by Okmok's 2008 eruption, where distinct spectral peaks occur at approximately 4 Hz, 5 Hz, 6Hz, 8 Hz and 18 Hz.

The second type of seismic activity originates within solid rock and is referred to as a volcano-tectonic (VT) earthquake. These events are similar to tectonic earthquakes in the sense that they share similar waveform characteristics and are caused by the failure of solid rock. In this case, stress is produced by pressure fluctuations that are occurring inside the volcano's magma supply system. Pressure changes impart stress on the surrounding material that eventually exceed its load bearing capability and is released in the form of an earthquake. VT events are useful for identifying regions of high stress concentration within the volcano and are typically the first sign of renewed unrest [48]. These events are generally characterized by impulsive P and S wave onsets and a substantial amount of energy above 5 Hz [48],[49]. Figure 3.12 and Figure 3.13 shows an example of a VT event produced by Okmok's 2008 eruption.

3.4.1 Seismicity Patterns

Earthquakes are routinely cataloged by the USGS for general seismological research purposes and seismic hazard studies. Statistical analysis of cataloged seismicity is often employed to map the location of magma chambers beneath active volcanoes. This is done by examining the frequency-magnitude distribution (FMD) of earthquakes in the area of interest. Earthquake FMDs

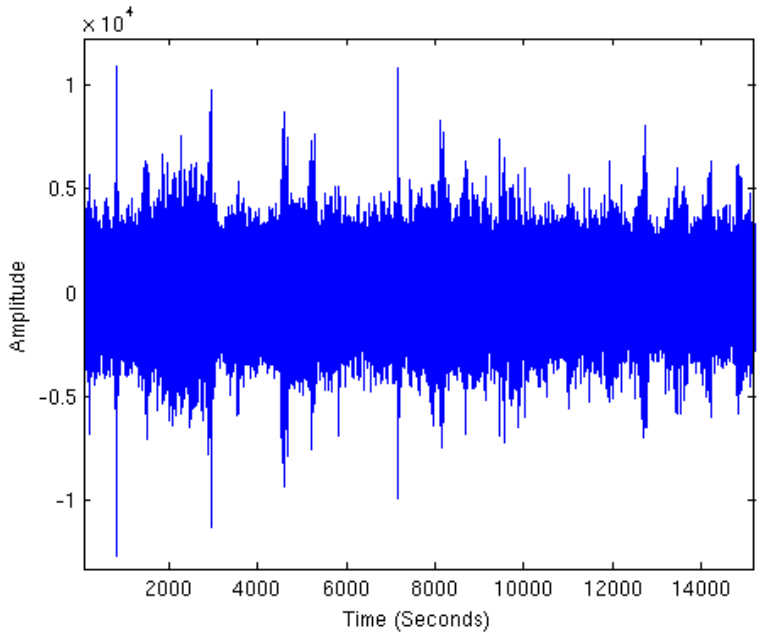

Figure 3.10: Time domain seismogram of volcanic tremor observed during Okmok's 2008 eruption.

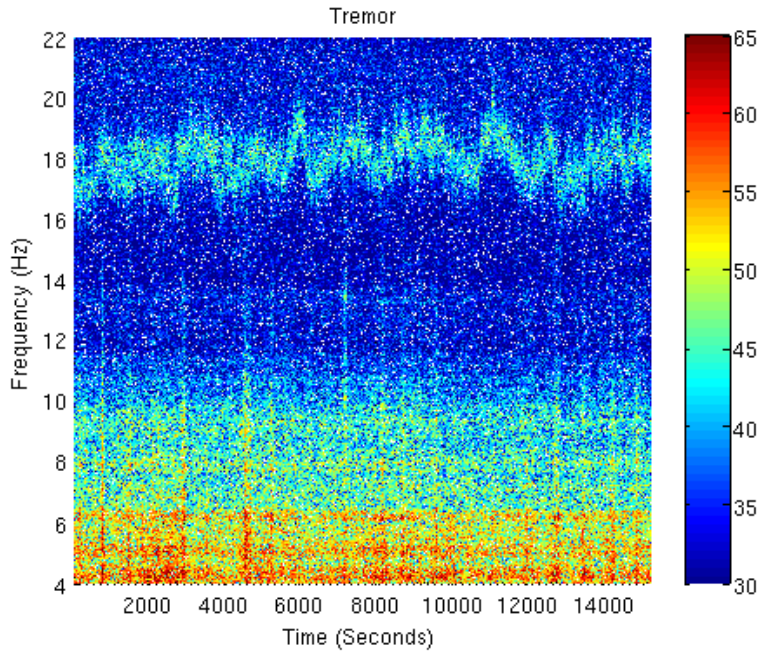

Figure 3.11: Spectrogram of volcanic tremor observed during Okmok's 2008 eruption.

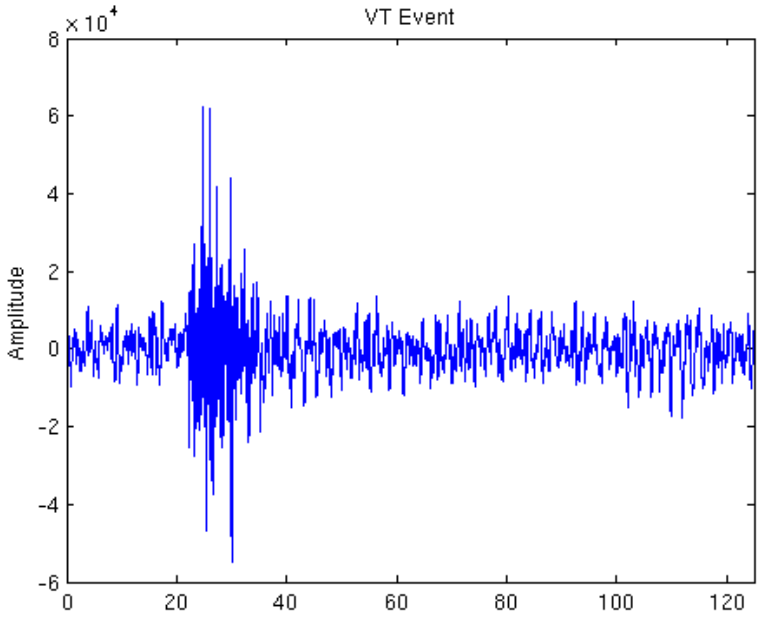

Figure 3.12: Time domain seismogram VT Earthquake observed during Okmok's 2008 eruption.

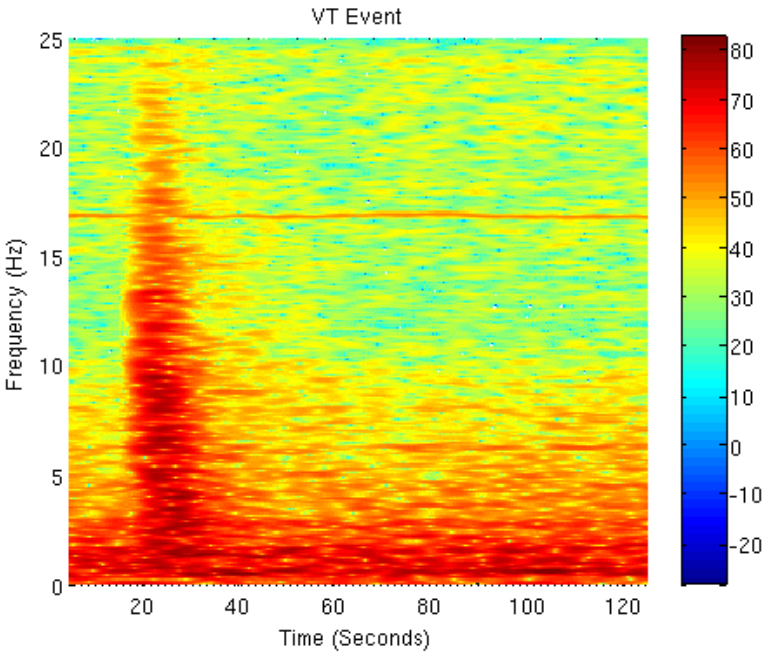

Figure 3.13: Spectrogram of VT Earthquake observed during Okmok's 2008 eruption.

are typically defined using a simple power law relationship of the form

$$log_{10}N(M) = a - bM \tag{3.10}$$

where M is the magnitude, N is the number of occurrence of a given magnitude, a is the productivity of the volume, b is the slope of the distribution [55], [56].

On average, b-values of 1.0 are observed in tectonic regions, while values greater than 1.0 are reported in volcanic areas. It has been shown that elevated b-values occur in the vicinity of magma, but remain close to 1.0 in its absence [57]. Numerous studies have employed b-value mapping as a means of locating active magma chambers (e.g. [58], [59], [57], [60], [61]). Various studies have identified a variety of mechanisms that produce elevated b-values; such as thermal gradients, strong material heterogeneity, increased pore pressure, and reduced effective stress [62], [63], [64], [57]. Typically, one or more of these conditions are prevalent in the vicinity of magma chambers residing in the upper crust [65].

The density of earthquakes within the area of interest provides additional information regarding the magma chamber location. Earthquakes do not occur within magma chambers or liquids. They tend to occur along the edges of the chamber, since the influx of magma or volatiles causes increased stress on the chamber walls. The lack of seismicity alone does not necessarily indicate the presence of a magma chamber. The presence, however, of high b-values and low earthquake density in an area with high seismicity is a strong indication that a magma chamber is present.

3.4.2 Seismic Moment

Seismic moment (M_0) relates earthquake size to a set of fundamental source parameters. This measurement is defined as

$$M_0 = \mu D S \tag{3.11}$$

where μ is the shear modules of the country rock, D is the average fault displacement (slip), S is the fault area. It is a more robust estimate of earthquake size since the defining parameters are not a function of azimuth or distance. Furthermore, it does not saturation at large values (¿ 5.5) like other magnitude scales [66]. These features led to the development of the seismic moment magnitude, M_w, which is defined as

$$M_0 = 10^{1.5(M_w+10.73)} \tag{3.12}$$

where M_0 is in terms of dyn-cm. Cumulative seismic moment has been shown to aid in the forecasting of volcanic activity [67].

In this study M_0 is estimated using body wave magnitude, m_b, measurements in lieu of M_w. This substitution is necessary since M_w is not generally reported in most seismic catalogs. The value of m_b and M_w tend to track one another fairly well up to approximately magnitude 5, where m_b begins to saturate. Since the earthquakes considered in this research are all below m_b 5, this substitution will suffice for M_w.

3.5 Magma Replenishment Rate

The magma replenishment rate is an estimate of the re-accumulation rate of fluid within a shallow storage chamber. It is evaluated by tracking the cumulative volumetric change in magma (ΔV) over time. Volumetric change is estimated by empirically matching a simulated surface deformation field to measurements acquired by InSAR platforms or GPS sensors. Synthetic deformation fields are created by substituting selected values of C and d into Equations 2.4 or 2.5. Modeled signal point displacements estimates or synthetic interferograms are compared to physical measurements and refined until the residual between the simulated and actual data is minimized. The newly derived value of C is used to compute ΔV via Equation 2.7.

This process is repeated using a time series of deformation measurements spanning the period of interest. Estimation of the cumulative increase in magma over time is computed relative to a single reference point (e.g., last eruption). If the amount of material expelled during the last eruption is known, the replenishment rate can be estimated, and the time required to recover the expelled material can be determined.

3.6 Data Sources

An abundance of multidisciplinary data was used throughout this research initiative. The source of each data type is listed below.

- SAR data was acquired from the ASF. The ASF and NASA grant researchers access to SAR data, free of charge, upon the approval of a written data request. This request can be

submitted at any time and takes approximately 4 to 6 weeks to be reviewed. The proposal guidelines can be found at [68]. A total of 600, level 0, Synthetic Aperture Radar (SAR) frames from the ERS-1, ERS-2, JERS-1, and RADARSAT data archives dating back as far as 1992 to the present day were requested. The Display Earth Remote Sensing Swath Coverage for Windows (DESCW) tool, developed and distributed by the ESA, is used to select suitable SAR image pairs for interferometric processing. This data request was granted in its entirety on April 15, 2010.

- POI for the ERS-2 platform was acquired from ESA. ESA archives this information and freely distributes it principle investigators with registered projects. Registration is obtained through an approved Category-1 registration application. The application requires a very short summary of the project, the names and affiliations of the PI and co-PIs, and some additional information about the nature of the research. Once the registration is granted, the PI is given a login to an ESA ftp server and can download the required data over the Internet. Mr. Junek's Category-1 registration application was submitted and approved in February 2010.

- ERS-1/2 POI was also obtained from the Department of Earth Observation and Space Systems at Delft University of Technology. Orbit specific files can be freely download via the internet. The binary files are referred to as orbital data records (ODRs) and contain 5.5 days of orbit information that overlap other files by 2 days. ODR files can be read using the $Getorb$ software package developed by Delft, which is freely available at [69]. Each ODR file contains time in UTC seconds past January 1, 1985, geodetic latitude and longitude in micro degrees, and height of the platform center of mass above the GRS80 reference ellip-

soid (mm) [45]. Additional information regarding the composition of ODR files is available at [70].

- The seismic data used in this study was acquired from a number of sources. Seismic event catalogs were derived from open catalogs posted on the internet by the USGS, AVO, Icelandic Meteorological Office, and the Instituto Nazionale di Geofisica e Vulcanologia (INGV). Waveform data was acquired from the IRIS data management center, which freely provides seismic data to the scientific community. IRIS is a consortium of over 100 universities that are actively involved in acquiring, studying, and disturbing seismic data [71]. They have a number of automated data request and distribution tools on their web site. Typically, data is requested via email and is delivered through IRIS's FTP site.

- GPS data from many of the sensors located in North America are freely available via the UNAVCO web site ([72]) or from the USGS. Processing raw GPS data requires a software tool capable of understanding the RINEX data format. Several such tools are freely available and only require the submission of a licensing agreement to obtain. Mr. Junek was denied a license request made to the NASA Jet Propulsion Laboratory for use of their GIPSY-OASIS II GPS data processing application. However, he was granted a license request for use of the GAMIT GLOBK processing application, which was developed and is distributed by the Massachusetts Institute of Technology (MIT). Preprocessed GPS data for Yellowstone National Park and Mount Saint Helens was acquired from the USGS.

- DEM information was obtained from the NASA shuttle radar tomography mission (SRTM) ftp site[12][13].

CHAPTER 4: FORECASTING ALGORITHM

4.1 Event Tree Analysis System

An event tree is an analytical tool that estimates the outcome of a set of pre-defined events using a branching decision-making process. Each branch or node of the tree represents a set of possible outcomes for a particular event, which increase in specificity with each step. Progression to the next branch is accomplished when the probability estimate for the preceding node exceeds a pre-defined threshold. Here, the event tree is initiated upon the detection of unrest and grows to forecast volcanic activity in increasing detail, such as the probability of eruption and intensity.

The event tree utilized in this research is shown in Figure 4.1. Each node estimates the conditional probability for a specific event via Bayes theorem, which is defined as

$$P(n|n-1) = \frac{P(n, n-1)}{P(n-1)} = \frac{P(n-1|n)P(n)}{P(n-1|n)P(n) + P(n-1|n')P(n')} \tag{4.1}$$

where $P(n-1|n)$ is the likelihood, $P(n)$ is the prior probability, $P(n-1)$ is the marginal probability, $P(n|n-1)$ is the posterior probability, the prime symbol represents the complement, and n is the event tree node in question. This event tree implementation is comprised of the following nodes:

- Node 1. *Unrest: Does the geophysical activity at the selected volcano exceed a predetermined threshold?* Geophysical activity includes heightened seismicity or surface deformation. If the amount of unrest exceeds a predefined threshold, the decision making process

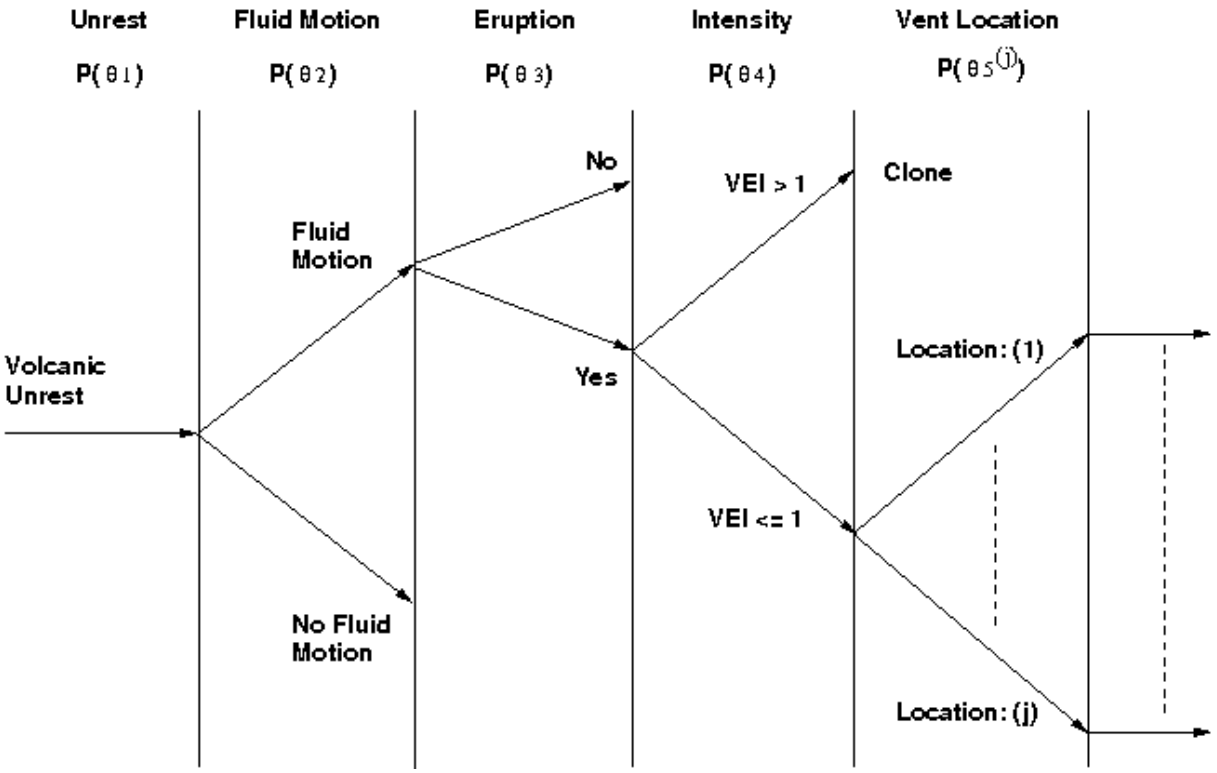

Figure 4.1: Schematic representation of the event tree implementation, where the clone label indicates the tree structure at that point is identical to that below.

progresses to the next branch, otherwise it terminates and restarts when new data is available. If the predefined threshold is exceeded the probability that unrest is occurring equals one, which is given by

$$P(\Theta_1) = P(1) = \begin{cases} 0 & \text{if } \nu_1 = 0 \\ \\ 1 & \text{if } \nu_1 > 0 \end{cases} \tag{4.2}$$

where ν_1 is the summation of several explanatory variables that are defined in Section 4.2.5.

- Node 2. *Fluid Motion: Is the observed unrest the result of a magmatic intrusion?* Fluid motion can be detected from the presence of heightened levels of seismicity having specific spectral characteristics or continuous, or rapidly varying, surface deformation (see Section 3.4). Possible causes of unrest that are not related to fluid motion include tectonic and geothermal activity. If the unrest is related to fluid motion, the process progresses to the next branch, otherwise it terminates and restarts when new data is available. The probability that an intrusive event is occurring is given by

$$P(\Theta_2) = P(2|1) = \frac{P(1|2)P(2)}{P(1|2)P(2) + P(1|2')P(2')} \tag{4.3}$$

where $P(2)$ is defined as

$$P(2) = P(Intrusion|X_2) \tag{4.4}$$

and X_2 is a set of independent explanatory variables described in Section 4.2.6.

- Node 3. *Eruption: Does the detected fluid motion have the potential to reach the surface and cause an eruption?* If the source of the unrest is a magmatic intrusion with associated

seismicity, the probability that the fluid will reach the surface may be high if that particular volcano has a historically high eruption frequency. If the observed, modeled, and historic information support this hypothesis the algorithm moves to the next branch, otherwise it terminates and restarts when new data is available. The probability that an eruption will occur is given by

$$P(\Theta_3) = P(3|2) = \frac{P(2|3)P(3)}{P(2|3)P(3) + P(2|3')P(3')} \tag{4.5}$$

where $P(3)$ is defined as

$$P(3) = P(Eruption|X_3) \tag{4.6}$$

and X_3 is a set of independent explanatory variables described in Section 4.2.7.

- Node 4. *Intensity: What is the eruption intensity?* The determination of the intensity will be driven by the training dataset defined in Table 4.2. The probability of the eruption's intensity exceeding a VEI of 1.0 is given by

$$P(\Theta_4) = P(4|3) = \frac{P(3|4)P(4)}{P(3|4)P(4) + P(3|4')P(4')} \tag{4.7}$$

where $P(4)$ is defined as

$$P(4) = P(Intensity > 1|X_4) \tag{4.8}$$

and X_4 is a set of independent explanatory variables described in Section 4.2.8.

- Node 5. *Vent Location: Where is the eruption likely to occur?* A vent location probability map is generated and the area with the highest probability of occurrence is identified as the likely eruption location. Given previous conditions are satisfied, the most probable vent location may be those with collocated surface deformation and seismicity. The probability of an eruption occurring at any location in a specified area is given by

$$P(\Theta_5^{(j)}) = P(5^{(j)}|4) = \sum_{j=1}^{(j)} \frac{P(4|5^{(j)})P(5^{(j)})}{P(4|5^{(j)})P(5^{(j)}) + P(4|5'^{(j)})P(5'^{(j)})} \tag{4.9}$$

where j is the vent location under consideration and $P(5)$ is defined in Section 4.2.9.

The probability of an event occurring at a particular event tree node is defined as

$$P(\Theta) = \prod_{1}^{l} P(\Theta_l) \tag{4.10}$$

where l is the event tree node for which the probability is being estimated. For example, the probability of an eruption occurring at the j^{th} location is estimated from the product, $P(\Theta_1)\ P(\Theta_2)\ P(\Theta_3)\ P(\Theta_4)\ P(\Theta_5^j)$. Whereas the probability of an eruption occurring at a given volcano is estimated by $P(\Theta_1)\ P(\Theta_2)\ P(\Theta_3)$.

4.1.1 Quantification of USGS Color Code

The event tree was adapted to issue warnings according to the USGS hazard program ground-based color code system shown in Figure 3.1. This method assigns colors ranging from

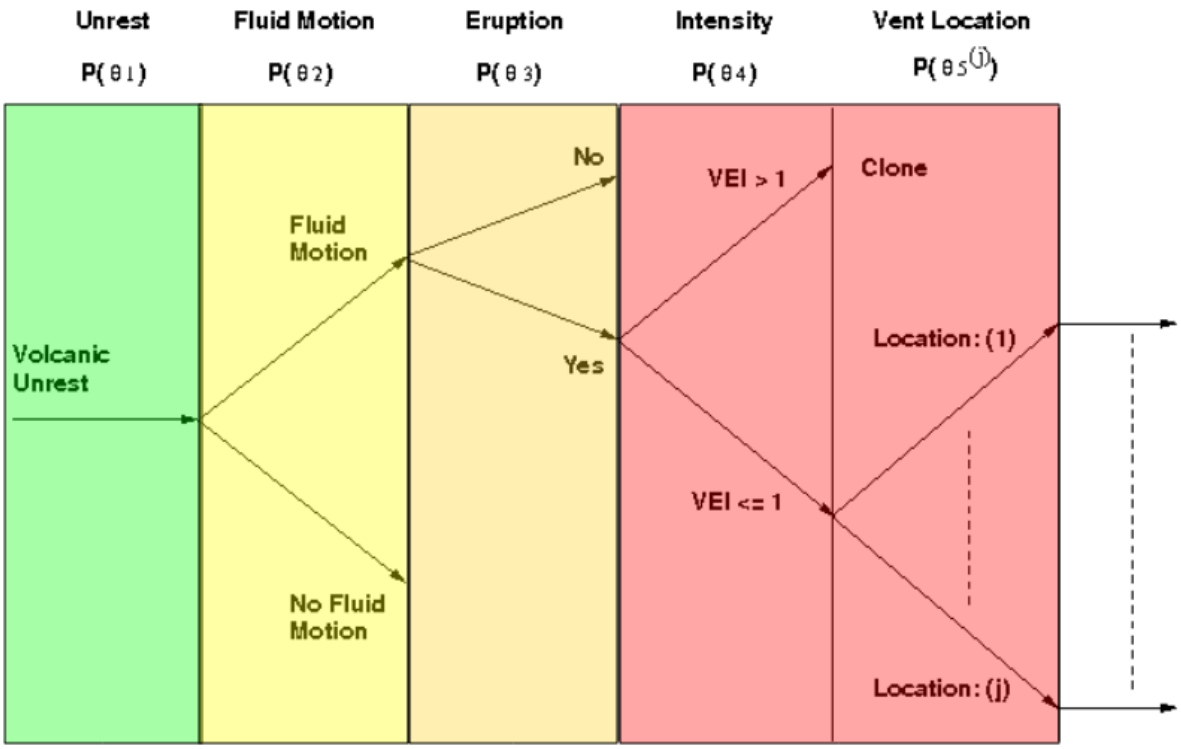

Figure 4.2: Event Tree algorithm with USGS color code superimposed over respective stages.

green to red to a particular volcano according to its current eruption hazard condition. Figure 4.2 shows the color code assignments relative to each stage of the event tree. As with the USGS system, colors range from green to red and increase in brightness with each event tree node. The final color designation is set according to the point in the algorithm where processing is terminated. For example, if the algorithm is activated by a new unrest episode and is not allowed to progress past the eruption node, because the probability of occurrence does not exceed a predefined detection threshold, then the final hazard level is set to orange. However, if the algorithm were to progress to the intensity node the hazard level is set to red. Linking the color code designation to a predefined detection threshold allows for quantification of the USGS warning scheme, which is one of the principle contributions of this research.

4.2 Estimation of Nodal Probabilities

4.2.1 Previously Published Implementations

Previous event tree implementations for forecasting volcanic activity have utilized a variety of methodologies to estimate nodal probabilities. A description of these strategies is provided below.

- *Newhall and Hoblitt 2002:* Probabilities for short term forecasts are based on expert assessment of historic behavior and monitoring data. Conditional probabilities are computed using Equation 4.1, where $P(n)$, $P(n-1|n)$, $P(n')$, and $P(n-1|n')$ are set by the user on a case by case basis. Estimates of $P(n|n-1)$ are revised as new information about the evolution of the unrest event is acquired. Event tree forecasts are computed using Equation 4.10. The results are used to assess various risk factors associated to the volcano in question (e.g., exposure or vulnerability to a lahar or pyroclastic flow).

- *Marzocchi et al. 2004:* Improved upon Newhall and Hoblitt's approach by computing and assigning a probability density function (PDF) to each node as apposed to discrete values. The procedure for deriving the PDFs consists of three parts. First, an initial PDF, $p_a(\theta_k)$, is estimated based on any available a priori knowledge (e.g. theoretical models, expert judgment, or beliefs). If no a priori information is available, a uniform distribution (complete ignorance) must be assumed. Second, $p_a(\theta_k)$ is combined with any available historic data

using Bayes Theorem, which is given by

$$p_b(\theta_k|n) = \frac{P_a(n|\theta_k)P(\theta_k)}{P(n)} \tag{4.11}$$

where a Bernoulli trial scheme is employed to derive the likelihood function using past data. If $p_a(\theta_k)$ has a uniform distribution, then the modified PDF, $p_b(\theta_k)$, takes the form of a beta function

$$p_b(\theta_k) = Beta(\alpha_b = n + 1, \beta_b = N - n + 1) \tag{4.12}$$

where n and N are the number of successes and trials. Finally, the mean of $p_b(\theta_k)$ is modified based on the results of recently acquired monitoring data using

$$E_c[\Theta_k] = \begin{cases} \frac{E_b[\Theta_k]}{\Psi} & \text{if } Z_k = 0 \\ 1 - e^{-z} & \text{if } Z_k > 0 \end{cases} \tag{4.13}$$

where Ψ is a subjectively assigned value that is based on expert judgment and Z_k is an anomalous parameter value computed from monitoring data. This produces the nodal PDF $p_c(\theta_k)$. Unique nodal PDFs must be derived for each volcano being monitored. Nodal probability estimates are generated from the 10^{th}, 50^{th}, and 90^{th} percentiles of the derived PDFs.

- *Marzocchi et al. 2008:* Builds upon the procedure defined in Marzocchi et al. 2004 by combining a fuzzy approach and Bayesian inference. The resulting nodal PDFs are based on the weighted sum between two different types of knowledge. This methodology assigns a degree of belief, ζ, to represent the state of volcanic unrest in lieu of simply setting the

probability to one upon detection. The value of ζ is assigned using the fuzzy approach defined in [73]. Its value ranges from 0 to 1 and is used to weight the linear combination of monitoring and non-monitoring information. The PDF at the k^{th} node is then defined as

$$[\Theta_k^{(j)}] = \zeta[\Theta_k^{(j)[M]}] + (1-\zeta)[\Theta_k^{(j)[\bar{M}]}] \tag{4.14}$$

where M and $\bar{M}$ represent information defined by monitoring and non-monitoring information. The monitoring ($\Theta_k^{(j)[M]}$) an non-monitoring ($\Theta_k^{(j)[\bar{M}]}$) PDFs are estimated using Bayes theorem, which is defined as

$$[\Theta_k^{j|.|}] = [\Theta_k^{j|.|}|y] = \frac{[\Theta_k^{j|.|}]prior[y|\Theta_k^{j|.|}]}{[y]} \tag{4.15}$$

where the $j|.|$ represents the j^{th} monitoring or non-monitoring information. The remaining steps in the PDF design process are similar to that outlined in Marzocchi et al. 2004. One exception is the modification to the nodal PDFs mean based on monitoring data, which is adjusted using

$$E_c[\Theta_k] = 1 - qe^{-pz} \tag{4.16}$$

where the values of q and p are estimated using past monitoring data from the site in question.

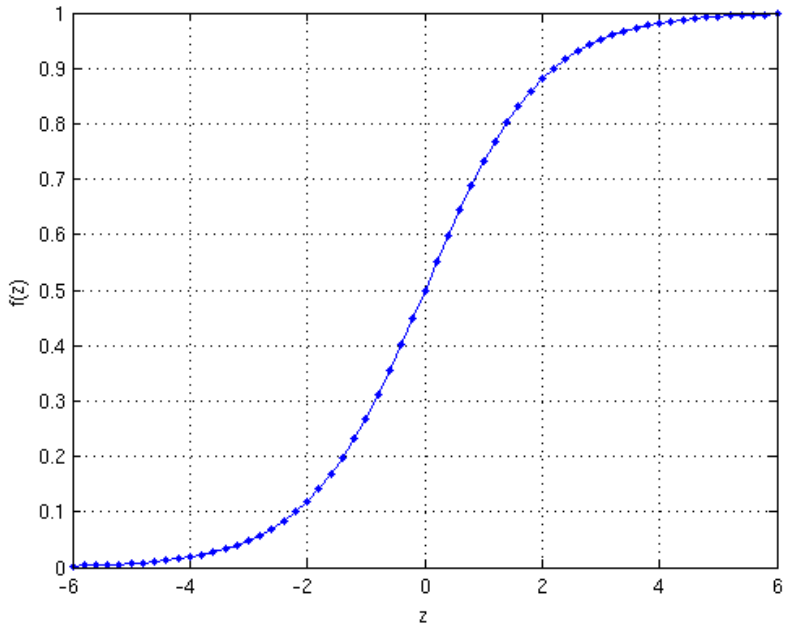

Figure 4.3: Logistic function variation as a function of z.

4.2.2 Logistic Regression

Logistic regression is a statistical modeling technique used to analyze multivariate problems [74], [9], [75]. It attempts to describe the complex relationship between a set of independent explanatory variables and a response variable. This popular modeling approach is used extensively in medical research, bioinformatics, and marketing analysis [76]. It has also found use in geophysical applications, such as the prediction of landslides and rain rate [77], [78]. To the best of the author's knowledge, this is the first study to use logistic regression to forecast volcanic processes.

The logistic function, $f(z)$, is given by

$$f(z) = \frac{1}{1 + e^{-z}} \tag{4.17}$$

where z is a value computed from a logistic model. Figure 4.3 shows the relationship between z and $f(z)$. The range of $f(z)$ is bound between 0 and 1 over -∞ and +∞. Unlike other modeling techniques, a probability between 0 and 1 is guaranteed with logistic regression regardless of the value of z.

The logistic model is the weighted summation of a set of explanatory variables, which is defined as

$$z = \beta_0 + \sum_{n=1}^{N} \beta_n X_n \tag{4.18}$$

where X_n is a collection of n explanatory variables, β_0 is a constant (intercept), and β_n is a collection of n weighting (regression) coefficients. The value of the weighting coefficients represents the relative influence that variable has on the outcome. Therefore, variables with large coefficients significantly influence the outcome of the event and those with small values have an insignificant effect. The values of β_0 and β_n are determined through maximum likelihood estimation. This requires a training dataset consisting of a collection of observations that relate the outcome of a particular event (response variable) to the explanatory variables. The process of deriving the β values is performed using a GLMR, which is explained in Section 4.2.3.

The probability of the event in question occurring is defined as the conditional probability

$$P(\theta = 1|X_1...X_N) = \frac{1}{1 + e^{-z}} \tag{4.19}$$

where $P(\theta_n)$ is the prior probability estimate for the n^{th} event tree node and X_N are the explanatory variables. The complement is computed as

$$P(\theta = 0|X_1...X_N) = 1 - P(\theta = 1|X_1...X_N) \tag{4.20}$$

Logistic regression is employed to relate various types of volcanic activity to a collection of independent variables to provide occurrence probabilities for event tree nodes 2 - 4. The independent variables are source modeling results, historic eruption frequency, and monitoring data acquired from a variety of sources. The training dataset used to derive the logistic model coefficients is discussed in Section 4.2.4. A description of each explanatory variable and their possible range of values is listed in Table 4.1, where the normalization factors for X_{CSM} and X_{ERH} are $1e20$ and 211, respectively.

Table 4.1: Logistic model explanatory variable names, descriptions, and possible range of values.

Explanatory Variable	Description	Value
X_{MM}	Unrest consistent with intrusion model	0 or 1
X_{NE}	Average Number of Earthquakes Per Day	$0 - \infty$
X_{CSM}	Average Normalized Cumulative Seismic Moment Per Day	$0 - \infty$
X_{DAYS}	Episode Duration in Days	$0 - \infty$
X_{ERH}	Average Eruption History	$0 - \infty$

4.2.3 Generalized Linear Model

A generalized linear model (GLM) is an algorithm that uses ordinary least squares regression to fit data to a distribution belonging to the exponential family. These distributions include:

Gaussian, Bernoulli, Binominal, Multinominal, Exponential, Poisson, Dirichlet. The general form of these distributions are defined as

$$f_Y(y|\theta,\tau) = h(y,\tau)exp\left(\frac{b(\theta)T(y) - A(\theta)}{d(\tau)}\right) \tag{4.21}$$

where θ is related to the mean, $d(\tau)$ is a known function, $b(\theta)$ is the natural parameter, τ is the dispersion parameter, $T(y)$ is the sufficient statistic, $A(\theta)$ is a normalization factor, and $h(y,\tau)$ is the base measure [79]. Information acquired by a set of independent variables is incorporated into the model via a linear predictor, η, using the expression

$$\eta = X\beta \tag{4.22}$$

where the matrices X and β represent a set of independent (i.e., explanatory) variables and a set of unknown coefficients. A linking function, g, establishes the connection between the mean of the response variables, Y, and the linear predictor, which is written as

$$E[Y] = \mu = g^{-1}(\eta) \tag{4.23}$$

where the linking function is defined by the user. Applications assuming a binominal distribution (logistic regression) typically employ a logit linking function which is defined as

$$X\beta = ln\left(\frac{\mu}{1-\mu}\right) \tag{4.24}$$

Using a Logit or other type of canonical linking function (e.g., Normal, Multinominal, Poisson, etc.) implies $b(\mu) = \theta = X\beta$ and allows $X'Y$ to serve as a sufficient statistic for β [79].

The values of β are determined through maximum likelihood estimation, which is performed by an iterative reweighted least squares algorithm. All β coefficients derived for this research were computed using the GLM function in the R statistical analysis package or $Matlab$. These software packages also provided the supporting statistical information for each of the logistic model coefficients, where the null hypothesis for all p value estimates is $\beta = 0$ and the alternate hypothesis is $\beta \neq 0$. More information regarding the maximum likelihood and iterative reweighted least squares algorithms can be found in [80].

The goodness-of-fit (G) of a logistic model is often assessed using a likelihood ratio test [9]. This test statistic is derived from the difference between the deviance, $-2ln(L_n)$, of the null (intercept only) and complete (full) logistic models. The deviance is similar to the residual sums of squares metric used in ordinary least squares regression in the sense that it attempts to estimate the discrepancy between the modeled and observed data. Thus, the quality of the regression model decreases with increasing deviance. Here G is estimated via the ratio

$$G = \chi^2 = -2ln\left(\frac{L_{null}}{L_{full}}\right) \tag{4.25}$$

where L_{null} and L_{full} are the likelihoods of the null and full models. The test statistic is χ^2 distributed, where its degrees of freedom, df, is equivalent to the number of constrained predictors (explanatory variables) in the logistic model. Statistical significance of the difference is estimated using a p value test, where the null hypothesis states the null model fits the data better than the full

model. If the difference is statistically significant ($p < 0.05$), then the null hypothesis is rejected and the full model is said to fit the data better than the null model.

4.2.4 Training Data

A database comprised of monitoring data acquired from multidisciplinary techniques, source modeling results, and historic eruption information from a series of volcanic unrest episodes is required for deriving the logistic model coefficients. Unfortunately no such database base currently exists in the public domain. Therefore, one had to be constructed for this research. Ideally, a large and diversified set of data is desired for identifying the set of explanatory variables that will produce the most robust logistic model. Moreover, it is also desirable to identify a large number of events that both culminate and fail to culminate to an eruption. However, published accounts of volcanic unrest events vary in detail and do not contain a consistent set of observations. This problem is exacerbated by the fact that events which eventually result in an eruption are published, while those that fail typically are not. This fact has artificially biased the open literature toward eruptive events as opposed to those that eventually fail [81]. As a result, only a small set of unrest events with known sources and a consistent set of explanatory variables could be identified for this research. This fact is unfortunate, since the majority of unrest events fail to culminate into an eruption [81].

The database constructed for this research is listed in Table 4.2. It is comprised of a collection of unrest events with a consistent set of observations whose causes were identified through source modeling exercises. The 41 events were gathered from various volcanoes in Northern

America, Iceland, and Italy. In order for an event to be included in the database, a high resolution seismic catalog and modeling results that identify the source of the unrest must be publicly available. These data were acquired from a combination of journal articles, technical reports, conference papers, and open seismic catalogs that are made freely available to the public by a number of organizations (e.g. USGS, ANSS, Icelandic Meteorological Institute) via the internet. It is assumed that this collection of events represents a random sample of volcanic activity in the northern hemisphere and is representative of this population.

Table 4.2 consists of eleven columns. The first two columns list the episode year and volcano of origin. Column three is the event's Volcanic Explosivity Index, (VEI) (see Section 2.3). The fourth column, (Er), specifies whether the event culminated in an eruption, where true (eruption) and false (no eruption) outcomes are represented by a 1 or 0. The cause of the unrest is listed in column five, (In), where the a value of 0 or 1 states whether the source is a magmatic intrusion. Source modeling results are listed in column six, (MM), where the a value of 0 or 1 states if the source of the unrest can be modeled as a magmatic intrusion. The total number of earthquakes occurring over the course of the episode is listed in column seven, (TNE). An estimate of the total cumulative seismic moment generated throughout the episode, $(TCSM)$, is listed in column eight. The duration of each episode in terms of days is listed in column nine, $(Days)$. The total number of eruptions at a particular site over the last 211 years is listed in column ten, (TEH). Finally the source of the information listed in each row is referenced in column eleven. Superscripts above the volcano name represent that sample's participation in the derivation of logistic coefficients for each node. The dagger represents samples excluded from the logistic regression but used to calculate $(Pn-1|n)$ and $(Pn-1|n')$, which is listed in Section 4.4.

Note that the logistic regression is performed after the TNE and $TCSM$ columns are transformed to average values per day and the normalization factors defined in section 4.2.2 are applied to the appropriate variables.

4.2.5 Node 1: Detection of Volcanic Unrest

Geologic activity in the vicinity of a volcano typically varies from site to site and episode to episode. Thus, each unrest event at a particular volcano may be unique and could be caused by a different set of circumstances than previous episodes. Therefore, it is difficult, if not impossible, to quantify the exact type of activity that may arise during an unrest event or prior to an eruption. One way to recognize the onset of anomalous activity is to search for behavior that deviates from normal activity. If an archive of historic observations is available, it can be used to establish a baseline that describes typical background behavior. Therefore, the identification of measurements that markedly deviate from historic behavior (outliers) can be treated as the onset of an unrest event [124], [125].

Outliers are observations that are significantly different from other members of a sample distribution. They are defined here as measurements greater than a value given by

$$Outlier\ Threshold = Q_3 + c(Q_3 - Q_1) \tag{4.26}$$

where c is a constant, Q_1 and Q_3 are the 25^{th} and 75^{th} percentiles of the sample distribution, and $(Q_3 - Q_1)$ is the interquartile range [126]. The sample distribution is typically visualized using a

Table 4.2: Raw logistic regression training data

Episode		Response Var.			Independent Variable					
Year	Volcano	VEI	Er	In	MM	TNE	TCSM	Days	TEH	Ref.
1993	Medicine Lake[2,3,4]	0	0	0	0	115	6.0e+21	2492	1	[82]
1993	Makushin[3,4]	0	0	1	1	0	0	365	12	[83]
1994	Hengill[2,3,4]	0	0	1	1	63450	7.7e+23	1607	0	[84]
1995	Trident[2,3,4]	0	0	1	1	69	3.2e+19	137	13	[85]
1996	Lassen Peak[2,3,4]	0	0	0	0	110	3.4e+21	1460	1	[86]
1996	Eyjafjallajökull[2,3,4]	0	0	1	1	144	5.2e+19	114	2	[87]
1996	Akutan[2]	0	0	1	1	1194	7.6e+22	32	34	[88]
1996	Iliamna[2,3,4]	0	0	1	1	1477	2.1e+21	382	2	[89]
1996	Peulik[2,3,4]	0	0	1	1	0	0	365	2	[90], [91]
1997	Kilauea[2,3]	1	1	1	0	1869	1.9e+22	20	63	[92]
1998	Kiska[2,3,4]	0	0	0	0	0	0	365	3	[93]
1998	Grimsvötn[2,3,4]	3	1	1	1	31	9.4e+20	10	29	[94]
1999	Shishaldin[2,3,4]	3	1	1	0	688	9.0e+22	42	34	[95]
1999	Fisher[2,3,4]	0	0	0	1	0	0	365	1	[96]
2000	Katla[2,3,4]	0	0	1	1	12460	1.2e+23	2190	4	[97]
2000	Kilauea[2,3,4]	0	0	0	0	48	5.8e+20	13	63	[98]
2000	Three Sisters[2,3,4]	0	0	1	1	0	0	1460	1	[91]
2000	Hekla[2,3,4]	3	1	1	1	196	3.4e+20	15	9	[99],[100]
2000	Eyjafjallajökull[2,3,4]	0	0	1	1	170	4.1e+20	365	2	[101]
2001	Etna[2,3,4]	2	1	1	1	414	1.0e+23	28	115	[102]
2001	Okmok[4]	0	0	0	1	19	8.1e+21	2	16	[103]
2001	Aniakchak[2,3,4]	0	0	0	1	13	5.8e+20	64	1	[104]
2002	Hood[2,3,4]	0	0	0	0	86	7.8e+22	60	2	[105]
2002	Etna[2,3,4]	3	1	1	1	353	2.1e+23	94	115	[106]
2003	Veniaminof[2]	2	1	1	1	103	6.2e+20	1050	22	[107]
2004	Grimsvötn[2,3,4]	3	1	0	0	920	6.3e+21.9	490	29	[108]
2004	Spurr[3,4]	0	0	0	0	2743	5.1e+20	239	2	[109], [110]
2004	Etna[2,3,4]	1	1	1	1	156	4.8e+21	186	115	[111]
2004	Saint Helens[2,3,4]	2	1	1	1	1094	1.5e+23	21	14	[112]
2005	Augustine[2,3,4]	3	1	1	1	2007	3.1e+20	80	9	[113]
2006	Korovin[2,3,4]	1	1	0	1	377	1.4e+21	329	7	[114], [115]
2007	Pavlof[2]	2	1	1	0	2	8.8e+18	30	39	[116]
2007	Upptyppingar[2,3,4]	0	0	1	0	3124	6.5e+20	133	0	[117]
2008	Yellowstone[2,3]	0	0	1	1	2594	6.9e+22	49	0	[118]
2008	Paricutin[2,3,4]	0	0	0	0	0	0	21900	1	[119]
2008	Hengill	0	0	0	0	3309	1.1e+24	10	0	[120]
2008	Okmok[2,3,4]	4	1	1	1	464	4.9e+21	100	16	[121], [103]
2008	Kasatochi[2,3,4]	4	1	1	0	1489	7.4e+24	22	1	[122]
2009	Redoubt[2,3,4]	3	1	1	1	4219	3.9e+21	365	6	[100]
2010	Eyjafjallajökull[2,3,4]	4	1	1	1	4019	1.1e+22	100	2	[123]
2010	Yellowstone†	0	0	1	1	4674	7.3e+22	28	0	[118]

boxplot, where the lower and upper bounds of the box represent the 25^{th} and 75^{th} percentiles, the line inside the box is the 50^{th} percentile (Q_2), and samples falling outside the whiskers are labeled as outliers.

Unique unrest detection thresholds are derived empirically on a volcano-by-volcano and monitoring discipline basis using historic observations. Outlier thresholds are determined from Equation 4.26, where c is set empirically for each monitoring discipline. After thresholds are established, outlier detection processing commences on each data type independently. Unrest severity is estimated by

$$\nu_1 = \sum_{n=1}^{N} \beta_n X_n \tag{4.27}$$

where β_n are weighting coefficients and X_n are binary variables that are toggled from 0 to 1 when measurements from its respective monitoring discipline exceeds its outlier detection threshold. The functional form of Equation 4.27 is given by

$$\nu_1 = 0.25(X_{sr} + X_{df} + X_{lm} + X_{md}) \tag{4.28}$$

where each term is defined in Table 4.3. All variables are weighted equally (β_n = 0.25) to allow activation of the forecasting algorithm upon the detection of unrest by one or more monitoring techniques. This triggering mechanism is similar to those used in previously published event tree implementations [23]. Severity declarations are based on the number simultaneous cross-disciplinary detections, which are defined in Table 4.4.

Table 4.3: Explanatory variable names, descriptions, and possible values for node 1.

Explanatory Variable	Description	Value
X_{sr}	Seismicity Rate	0/1
X_{df}	Surface Deformation	0/1
X_{lm}	Large Magnitude	0/1
X_{md}	Model Indicates Intrusion	0/1

Table 4.4: Unrest severity declarations.

z_1	Severity
0.25	Low
0.50	Moderate
0.75	Heightened
1.00	Extreme

4.2.6 Node 2: Fluid Motion

A logistic regression for node 2 was performed using a subset of the data listed in Table 4.2 and the In field as the response variable. The resulting model is written as

$$z_2 = -2.2187 + 3.1495(X_{MM}) + 0.3791(X_{NE}) + 0.0047(X_{CSM}) - 0.0001(X_{DAYS}) \quad (4.29)$$

where each explanatory variable is defined in Table 4.1. The influence of the binary variable (X_{MM}) and the weighting coefficients on the cumulative distribution function (CDF) is studied by setting the other variables equal to each other and plotting the model response between ± 20. In this example negative values have no physical meaning and are only shown so the full range of the CDF is plotted. Equation 4.29 and Figure 4.4 indicate the regression placed a heavy emphasis on the modeling results, moderate emphasis on the average number of earthquakes per day, and limited importance on the average seismic moment and episode duration. Figure 4.4 shows that

even in the absence of positive modeling results, episodes producing large numbers of earthquakes and or releasing large amounts of seismic energy have a high probability of being generated by a magma intrusion. In addition, the probability of an eruption is non-zero even if the values of all the explanatory variables are equal to zero. This is a realistic and reassuring result, since eruptions have been known to occur without any precursory geologic activity or warning.

A statistical summary of the logistic coefficients is shown in Table 4.5 and Table 4.6. The coefficients's p-values show that only the intercept and X_{MM} values meet the generally accepted statistical significance bar. However, the remaining coefficients have a large practical significance, despite their high p-value, since they are necessary to account for episodes exhibiting high seismicity and no measurable surface deformation. Table 4.6 shows that only the intercept and X_{MM} are somewhat correlated and the remaining variables are essentially uncorrelated. A goodness of fit estimate for the complete model was performed using the likelihood ratio test and resulted in a χ^2 value of 22.5247, a df of 4, and a p-value of 0.0002. Therefore, the full set of explanatory variables fits the data better than the null model.

Table 4.5: Statistical summary of logistic model coefficients for intrusion node.

Explanatory Variable	Standard Error	p Value
Intercept	1.2827	0.0837
X_{MM}	1.3124	0.0164
X_{NE}	0.3169	0.2316
X_{CSM}	0.1375	0.9725
X_{DAYS}	0.0004	0.8017

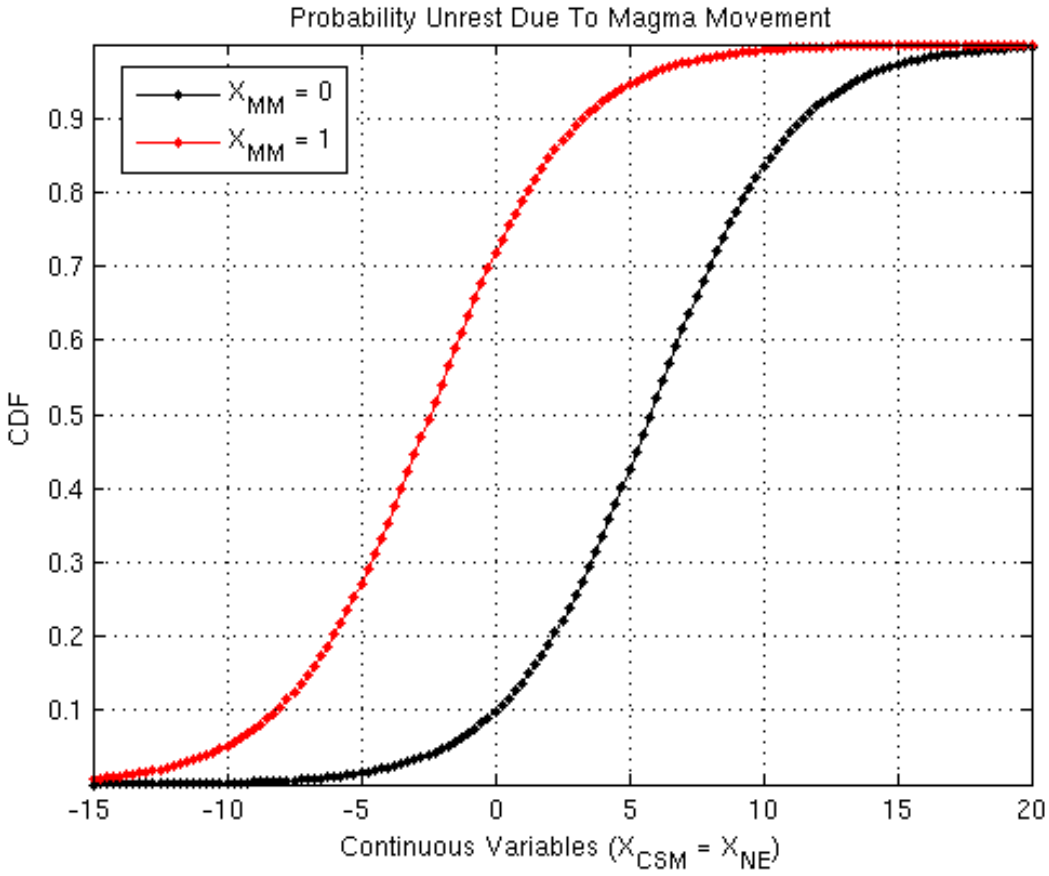

Figure 4.4: Cumulative density functions illustrating the influence of each of the explanatory variables on the probability estimate, where the black and red curves represents $X_{MM} = 0$ and $X_{MM} = 1$, respectively.

Table 4.6: Logistic model coefficients correlation matrix for intrusion node.

Explanatory Variable	Intercept	X_{MM}	X_{NE}	X_{CSM}	X_{DAYS}
Intercept	1.0	-0.83	-0.37	-0.14	-0.31
X_{MM}	-0.83	1.0	0.13	0.13	0.13
X_{NE}	-0.37	0.13	1.0	-0.36	0.09
X_{CSM}	-0.14	0.13	-0.36	1.0	0.07
X_{DAYS}	-0.31	0.13	0.09	0.07	1.0

4.2.7 Node 3: Eruption Occurrence

The logistic model developed for node 3 required an additional explanatory variable to account for the complex relationship between historic eruption activity and monitoring data. It is meant to prevent overestimation of the probability of eruption at sites that typically display high and fluctuating levels of geologic activity, but rarely erupt. The ERH parameter in Table 4.2 is the number of eruptions that have occurred at a particular site over the last 211 years. This time span represents the extent of the Smithsonian Institute (SI) global volcanism database of eruptions that are known to have occurred in modern history (post 1800) [127]. The Yellowstone caldera is a prime example of where such a term is necessary. If historic eruption activity is not accounted for at Yellowstone, forecasts would show that an eruption is imminent (probability of eruption = 1.0) inside the caldera on an almost continuous basis. When historic eruptive activity is taken into account, the probability of eruption is adjusted to account for long periods of non-eruptive behavior.

The logistic model for the eruption occurrence node is defined as

$$z_3 = -2.6577 + 1.8377(X_{MM}) + 0.0326(X_{NE}) + 0.0168(X_{CSM}) - 0.0016(X_{DAYS}) + 14.5305(X_{ERH}) \quad (4.30)$$

where the regression was performed using a subset of data listed in Table 4.2 and the Er field as the response variable. A description of each explanatory variable is listed in Table 4.1. In this case, the regression place high importance on the modeling results, moderate importance on seismic information, low importance of episode duration, and extreme importance on historic activity. The response of this CDF to the variation of the X_{MM} variable is assessed by setting the remaining variables equal to each other and computing a range of probabilities between ± 20. Again, negative values have no physical meaning in this example and are only shown to visualize the complete CDF. Figure 4.5 shows the effect of the modeling results on the probability is not as dramatic as that produced by Equation 4.29. However, the incorporation of positive modeling results increases the probability of eruption by approximately 0.25. In addition, the probability of eruption is non-zero in the absence of positive modeling results and increases with increasing seismic activity. In the absence of positive modeling results, episodes displaying high seismicity have the potential to result in an eruption. This scenario occurred prior to Shishaldin's 1999 eruption (line 13 of Table 4.2). In this case, pre-eruption surface deformation could not be modeled as a magmatic intrusion and was determined to be the result of earthquake activity. These are the situations where the value of the other explanatory variables becomes apparent.

A statistical summary of the logistic coefficients is shown in Table 4.7 and Table 4.8. P-values for all coefficients exceed the generally accepted definition of statistical significance. However, the majority of the p-values are below 0.40 and the intercept and ERH variables are in the 0.11-0.12 range. These variables possess a high practical significance, despite their relatively high p-values, since they are necessary to produce eruption forecasts for volcanoes that display precursory surface deformation that can not be explained by an intrusive source model or have not erupted in recorded history. Table 4.8 shows that X_{MM} and X_{ER} coefficients are somewhat correlated to the intercept, while the remaining variables are essentially uncorrelated. A goodness of fit estimate for the complete model was performed using the likelihood ratio test and resulted in a χ^2 value of 21.0747, a df of 5, and a p-value of 0.0008. Therefore, the full set of explanatory variables fits the training data better than the null model.

Table 4.7: Statistical summary of logistic model coefficients for eruption node.

Explanatory Variable	Standard Error	p Value
Intercept	1.7256	0.1235
X_{MM}	1.4817	0.2149
X_{NE}	0.0357	0.3609
X_{CSM}	0.0641	0.7931
X_{DAYS}	0.0015	0.2975
X_{ER}	9.2369	0.1157

Table 4.8: Logistic model coefficients correlation matrix for eruption node.

Explanatory Variable	Intercept	X_{MM}	X_{NE}	X_{CSM}	X_{DAYS}	X_{ER}
Intercept	1.00	-0.86	-0.20	-0.11	-0.35	-0.70
X_{MM}	-0.86	1.00	-0.05	0.18	0.08	0.50
X_{NE}	-0.20	-0.45	1.00	-0.50	0.21	0.19
X_{CSM}	-0.11	0.18	-0.50	1.00	0.10	0.12
X_{DAYS}	-0.35	0.08	0.02	0.10	1.00	0.22
X_{ER}	-0.70	0.50	0.19	0.12	0.23	1.00

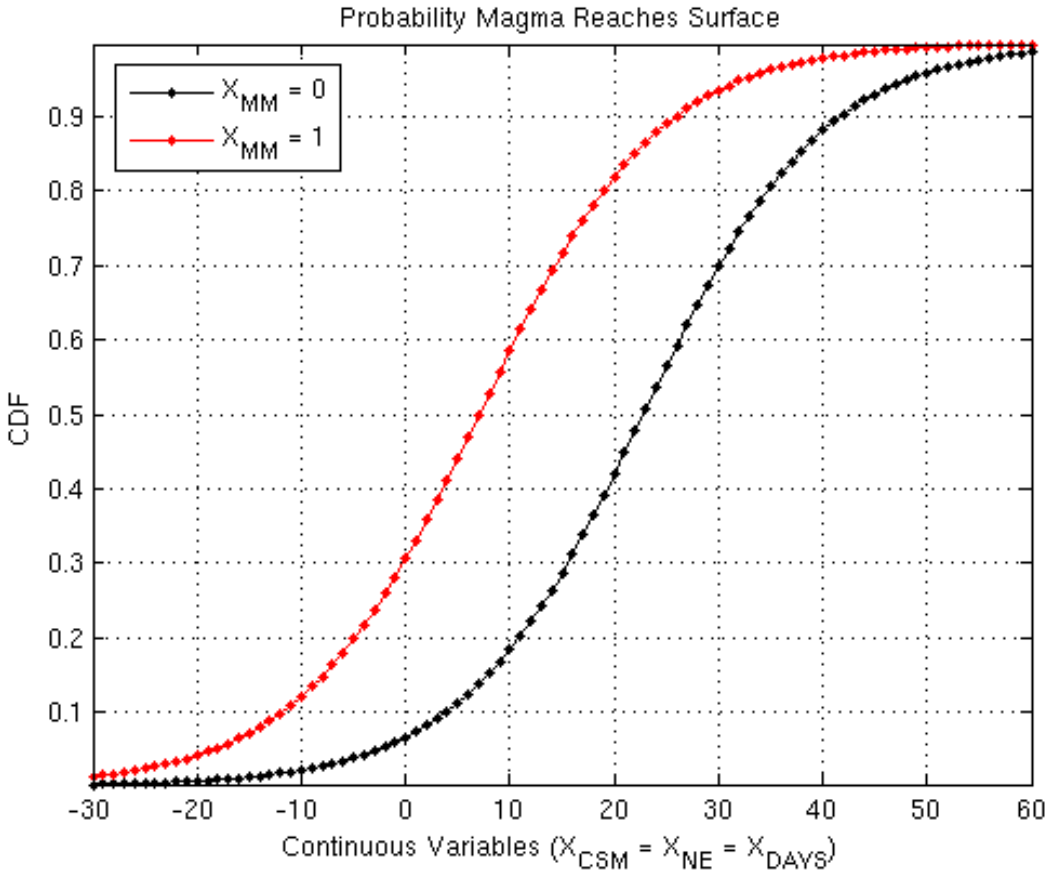

Figure 4.5: Cumulative density functions illustrating the influence of each of the explanatory variables on the probability estimate, where the black and red curves represents $X_{MM} = 0$ and $X_{MM} = 1$, respectively.

4.2.8 Node 4: Eruption Intensity

The regression for eruption intensity is performed using a subset of data listed in Table 4.2 and the VEI field as the response variable. The resulting logistic model is defined as

$$z_4 = -1.5279 + 1.0662(X_{MM}) + 0.1159(X_{NE}) + 0.0043(X_{CSM}) - 0.0038(X_{DAYS}) \quad (4.31)$$

where a description of the explanatory variables is listed in Table 4.1. Since there are only a limited number of samples that culminate to an eruption, the model is designed to estimate the probability that an eruption's intensity will be greater than a VEI of 1.0. The regression place high importance on the modeling results, moderate importance on average daily seismicity, and de-emphasized average seismic moment and episode duration. The response of the intensity CDF to changes in X_{MM} is examined by again setting all other variables equal to each other and computing a range of probabilities between ± 20 (see Figure 4.6). As before, negative values of X have no physical meaning in this example and are only included to visualize the complete CDF. The incorporation of positive modeling results increased the probability that the eruption will exceed a VEI of 1.0 by approximately 20 percent. Moreover, the probability of a large intensity eruption occurring is non-zero in the absence of positive modeling results and increases with increasing seismic activity.

A statistical summary of the logistic coefficients is shown in Table 4.9 and Table 4.10. The p-values for X_{NE} and X_{DAYS} appear to be statistically significant, while the results for the remaining coefficients exceed 0.18. As with Nodes 2 and 3, even though the p-values for the remaining coefficients are not statistically significant, they have a high practical significance due

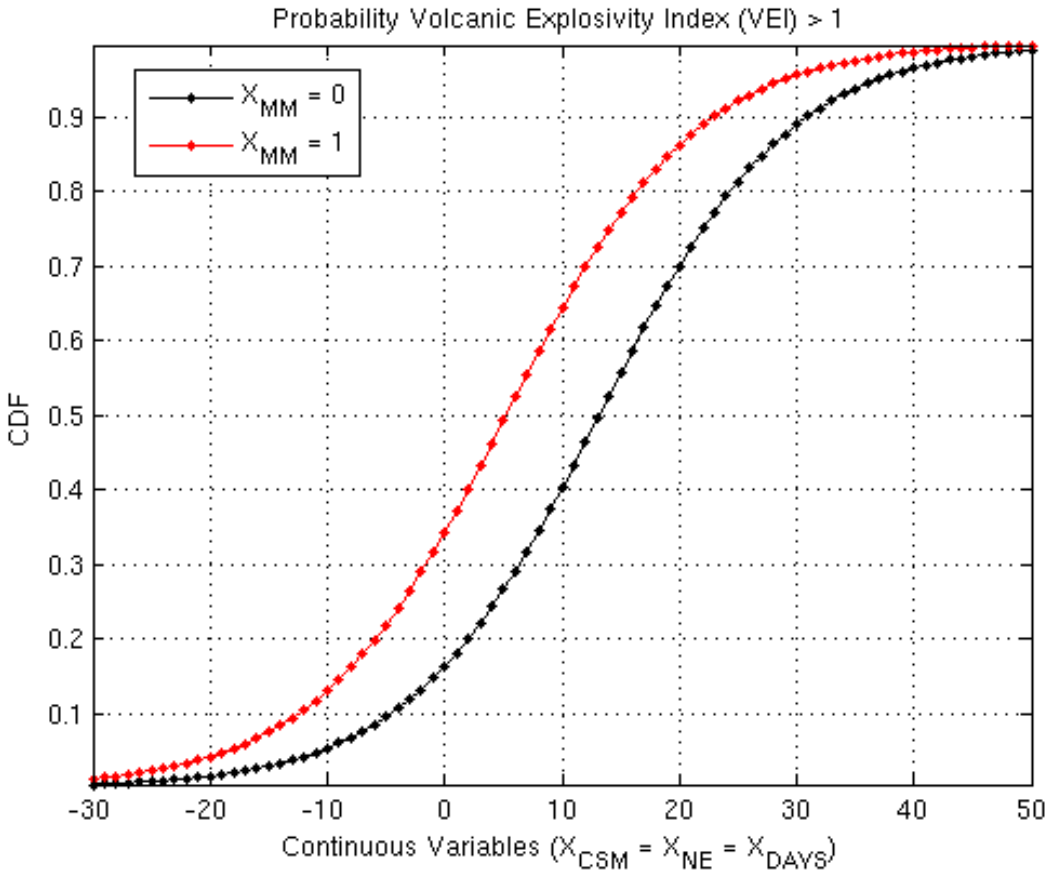

Figure 4.6: Cumulative density functions illustrating the influence of each of the explanatory variables on the probability estimate, where the black and red curves represents $X_{MM} = 0$ and $X_{MM} = 1$, respectively.

to their ability to estimate the intensity probability in the presence of negative modeling results. Table 4.10 shows that X_{MM} is somewhat correlated to the intercept, while the remaining variables are essentially uncorrelated. A goodness of fit estimate for the complete model was performed using the likelihood ratio test and resulted in a χ^2 value of 17.0901, a df of 4, and a p-value of 0.0019. Therefore, the full set of explanatory variables fits the training data better than the null model.

Table 4.9: Statistical summary of logistic model coefficients for intensity node.

Explanatory Variable	Standard Error	p Value
Intercept	1.1603	0.1879
X_{MM}	1.1916	0.3709
X_{NE}	0.0633	0.0671
X_{CSM}	0.0425	0.9181
X_{DAYS}	0.0021	0.0759

Table 4.10: Logistic model coefficients correlation matrix for intensity node.

Explanatory Variable	Intercept	X_{MM}	X_{NE}	X_{CSM}	X_{DAYS}
Intercept	1.00	-0.79	-0.43	-0.12	-0.02
X_{MM}	-0.79	1.00	0.34	-0.14	-0.28
X_{NE}	-0.43	0.34	1.00	-0.34	-0.48
X_{CSM}	-0.12	-0.14	-0.34	1.00	0.37
X_{DAYS}	-0.02	-0.28	-0.48	0.37	1.00

4.2.9 Node 5: Volcanic Vent Location

The vent location process is initiated by discretizing the area of concern into J cells of arbitrary shape and size. Rectangular or hexagonal tessellations could be chosen, as could more irregular Delaunay triangles, but cell size should reflect the inherent resolution of the data sets being examined. In this dissertation, a regular rectangular tessellation is employed on which a DEM has been imposed.

The spatial PDF for estimating the probability of vent formation (VF) at the j^{th} location is a function of the data used for monitoring a particular volcanic center. Its construction can be generalized as

$$P(VF^j|X_n^j) = \frac{X_n^j}{\sum_{i=1}^{J}(X_n^i)} \tag{4.32}$$

where X_n^j is a collection of observations (both empirical and simulated) from the j^{th} location acquired by n different disciplines (e.g., seismic, deformation, thermal, geochemical, modeling, etc.). By displaying the PDFs for the J cells as an image, the location of the most likely sites for a volcanic vent can then be identified. The following procedure outlines the PDF's construction using deformation data (X_{def}) and the spatiotemporal distribution of seismic epicenters (X_{seis}).

The first step is to restrict the area of computation to regions where the available data indicate the hightest likelihood of eruption. Here the power of InSAR is exploited to illuminate areas being deformed by magma ascent. The resulting interferograms, however, highlight deformation in areas where the correlation between individual SAR images is high. Therefore, no information regarding the deformation process is ascertained in areas where the correlation between individual SAR images is poor. Gaps in the observation can be filled by modeling the theoretical extend of the deformation field and generating a synthetic interferogram.

Next, each location within the area of interest is assigned a X_{def} and X_{seis} value. X_{def}^j is set to 1 if deformation is detected in the j_{th} location and 0 in its absence. X_{seis}^j is the summation of monitoring samples (e.g., earthquakes) originating in the j^{th} location. For example, if 10 earthquakes occur at the j^{th} location residing in the theoretical deformation field, X_{seis}^j = 10 and X_{def}^j = 1.

X_{seis} values derived from earthquake epicenter locations must be modified to account for location uncertainties. Here the uncertainty estimate is the average location error of the employed seismic network, which can often be obtained from the organization operating the sites. It is used by setting all X_{seis}^j samples within a distance equal to half the average location error to 1. This produces a cloud of possible locations around the epicenter that represents the uncertainty.

Finally, Equation (4.32) is rewritten in terms of X^j_{def} and X^j_{seis} as

$$P(VF^j|X^j_{seis}, X^j_{def}) = \frac{X^j_{seis} + X^j_{def}}{\sum_{i=1}^{J}(X^i_{seis} + X^i_{def})} \tag{4.33}$$

and updated upon the acquisition of new data. As a result, regions with a higher probability of vent formation become more apparent as the episode evolves and more information is acquired. This method differs from Marzocchi's approach through its use of source modeling information to spatially constrain the process [128].

4.2.10 Bootstrapping Analysis

The logistic model coefficients and associated statistical parameters discussed in Sections 4.2.6 - 4.2.8 were derived using selected subsets of the sample data listed in Table 4.2. Ideally, it is desirable to perform the regression analysis over many combinations of random samples from the population we are attempting to model. After many iterations a distribution of parameter estimates, such as the sample mean or regression coefficients, can be produced and their true value estimated. In this case, however, there is no additional data available. Therefore, a bootstrapping approach is invoked to estimate the distribution of logistic model coefficients and associated statistical parameters for Nodes 2, 3 and 4.

Bootstrapping is a resampling technique that produces M datasets from a single set of random samples taken from a specific population. Each of the newly constructed datasets contain a random combination of samples that were drawn from the original dataset. Since a sample with

replacement (Monte Carlo sampling) process is used, it is possible for each new dataset to contain multiple or no copies of any particular sample. Thus, the probability that a particular sample is selected for inclusion in a bootstrapped dataset each time a drawing is made is $1/N$, where N is the number of samples in the original dataset.

Sections 4.2.11 - 4.2.13 discuss the results of a bootstrapping analysis of each of the logistic models after 50,000 iterations. The bootstrapping process for each model used the same subsets of training data employed to compute the models shown in Sections 4.2.6 - 4.2.8. Distributions for each of the logistic model coefficients appears to be bimodal. The two distributions represent cases where the regression process was either properly or ill constrained. Situations where the regression is ill constrained caused the GLMR to fail after exhausting its maximum number of iterations, which results in a bogus set of model coefficients. Conversely, properly constrained cases represent runs where the GLMR converges to a solution within its maximum number of iterations. Therefore, the ill constrained results are rejected as outliers and the properly constrained distributions were retained and used to estimate logistic model information. In Sections 4.2.11 - 4.2.13, the complete and truncated logistic model coefficient distributions are shown in the top and bottom panels of each figure. The median value of the truncated distributions are used to estimate the model coefficients for each node.

Distributions for each model coefficient's standard error, p-value, and correlation matrix are also shown in Sections 4.2.11 - 4.2.13. Standard error estimates and cross correlation values for each coefficient are estimated as the median of their respective distributions. Resulting p-value distributions, in general, are not as well defined as the other estimators. Therefore, p-values for individual model coefficients were estimated using the median and mode of their distributions to

gauge which calculation is the more robust estimate. The results indicate that the mode of the p-value distribution is a better indicator of its true value as opposed to the median. This result is most likely due to the large kurtosis of the p-value distributions, which cause the median values to be inflated. Please note that values derived through bootstrapping are denoted with a hat, so they are not confused with those shown in Sections 4.2.6 - 4.2.8.

4.2.11 Node 2: Fluid Motion Model Via Bootstrapping

Distributions for each of the bootstrapped intrusion model coefficients, standard errors, and p-values are shown in Figure 4.7 - Figure 4.16. The revised intrusion model is shown in Equation 4.34. The relative weighting between each of the coefficients remains essentially unchanged, where values for $\hat{X}_{NE}$, $\hat{X}_{CSM}$, and $\hat{X}_{DAYS}$ are nearly identical to those shown in Equation 4.29. The intercept and $\hat{X}_{MM}$ values are now somewhat smaller. This difference causes the curves shown in Figure 4.19 to shift to the left and spread further apart relative to those shown in Figure 4.4. As a result, a larger probability of occurrence is produced when $\hat{X}_{MM}$ varies between 0 and 1 and all other input values are 0. The difference between the CDFs is now approximately 0.60.

Each coefficient's associated standard error and p-value is listed in Table 4.11. The standard error and median p-value estimates for $\hat{X}_{NE}$, $\hat{X}_{CSM}$, and $\hat{X}_{DAYS}$ are nearly identical to the non-bootstrapped results. However, median p-value estimates for the intercept and $\hat{X}_{MM}$ are slightly larger, where the intercept value is now in the 0.19 range. The mode p-value estimates are lower than the median values, with the exception of the $\hat{X}_{CSM}$ value which is approaching 1.0. Mode p-value estimates for the intercept and X_{MM} node are in the generally accepted range of statistical

significance. The remaining values are all above 0.05, but it is clear from Figure 4.19 that these explanatory variables have an effect on the probability estimate when $\hat{X}_{MM}$ equals 0. Therefore, their practical significance is high.

Statistics for the complete model likelihood-ratio test are shown in Figure 4.18, where the top panel is the distribution of χ^2 values and the bottom panel is the corresponding p-value distribution. Complete model p-value distribution is fairly well defined. The median p-value for the complete intrusion model is approximately 0.001, which suggests the resulting model has approximately a 99.9 percent chance of outperforming the null model (intercept only).

The lower, off-diagonal, correlation matrix components are shown in Figure 4.17 and their median values are listed in Table 4.12. Bootstrapped correlation coefficients are also similar to those shown in Table 4.5. There appears to be significant correlation between the intercept and $\hat{X}_{MM}$. This relationship could explain the large difference in probability estimates when $\hat{X}_{MM}$ varied between 0 and 1.

$$\hat{z}_2 = -1.5618 + 2.6869(\hat{X}_{MM}) + 0.3465(\hat{X}_{NE}) - 0.0041(\hat{X}_{CSM}) - 0.0001(\hat{X}_{DAYS}) \quad (4.34)$$

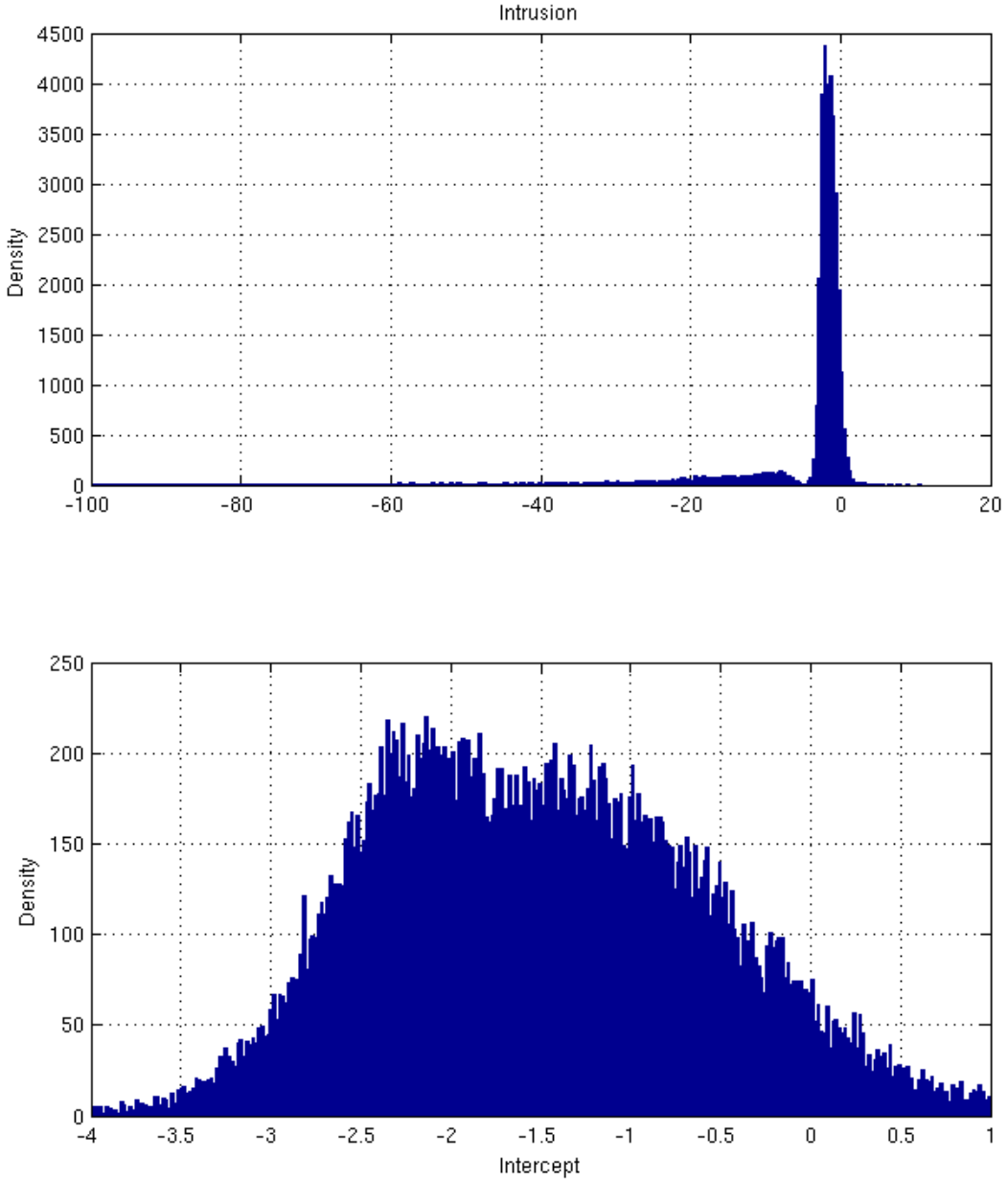

Figure 4.7: Bootstrapping analysis results for the intrusion model intercept, where the top panel is the complete distribution and the bottom panel shows the portion used to derive the intercept value.

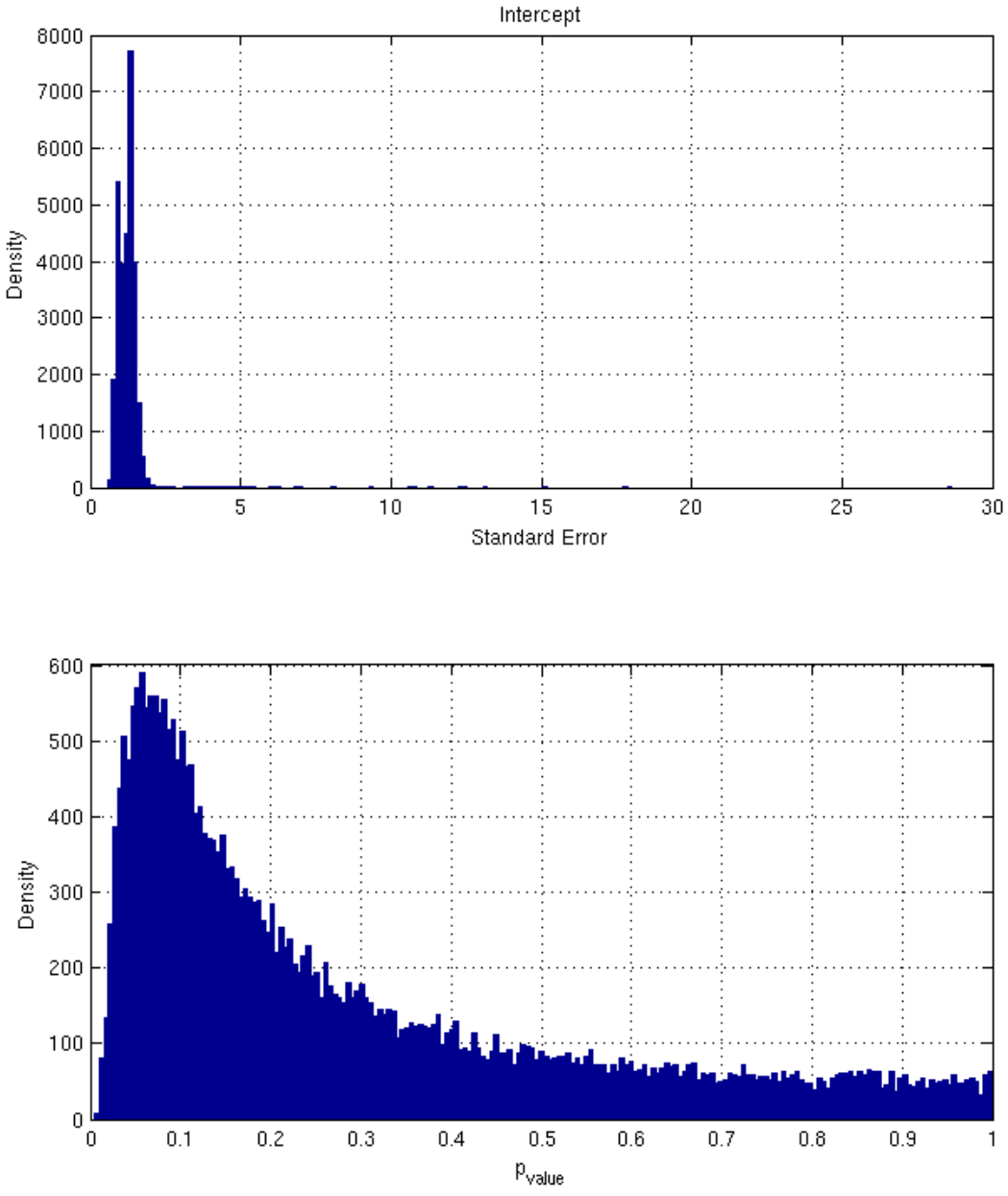

Figure 4.8: P-value distribution for intrusion model intercept parameter.

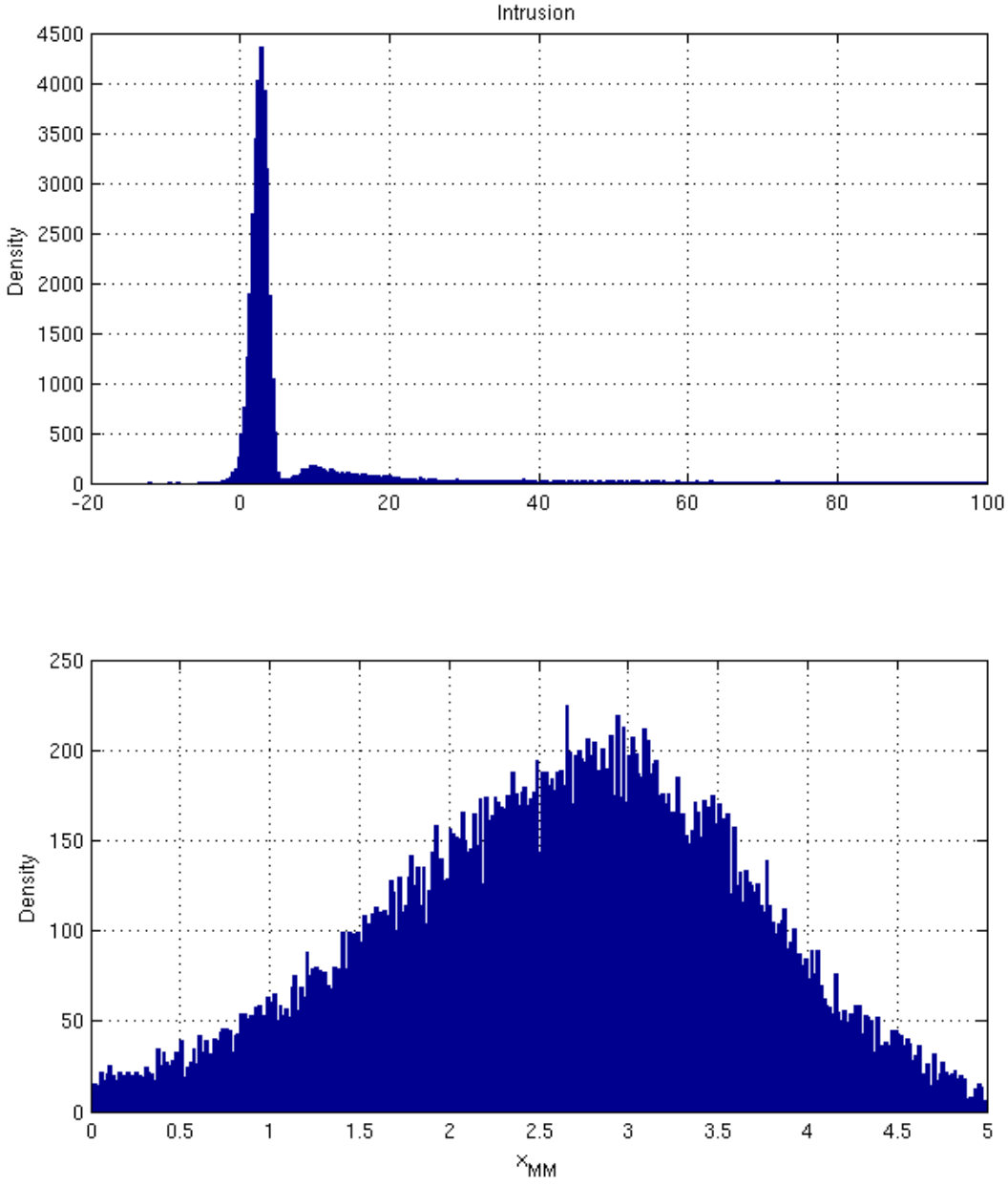

Figure 4.9: Bootstrapping analysis results for the intrusion model $\hat{X}_{MM}$ term, where the top panel is the complete distribution and the bottom panel shows the portion used to derive the $\hat{X}_{MM}$ value.

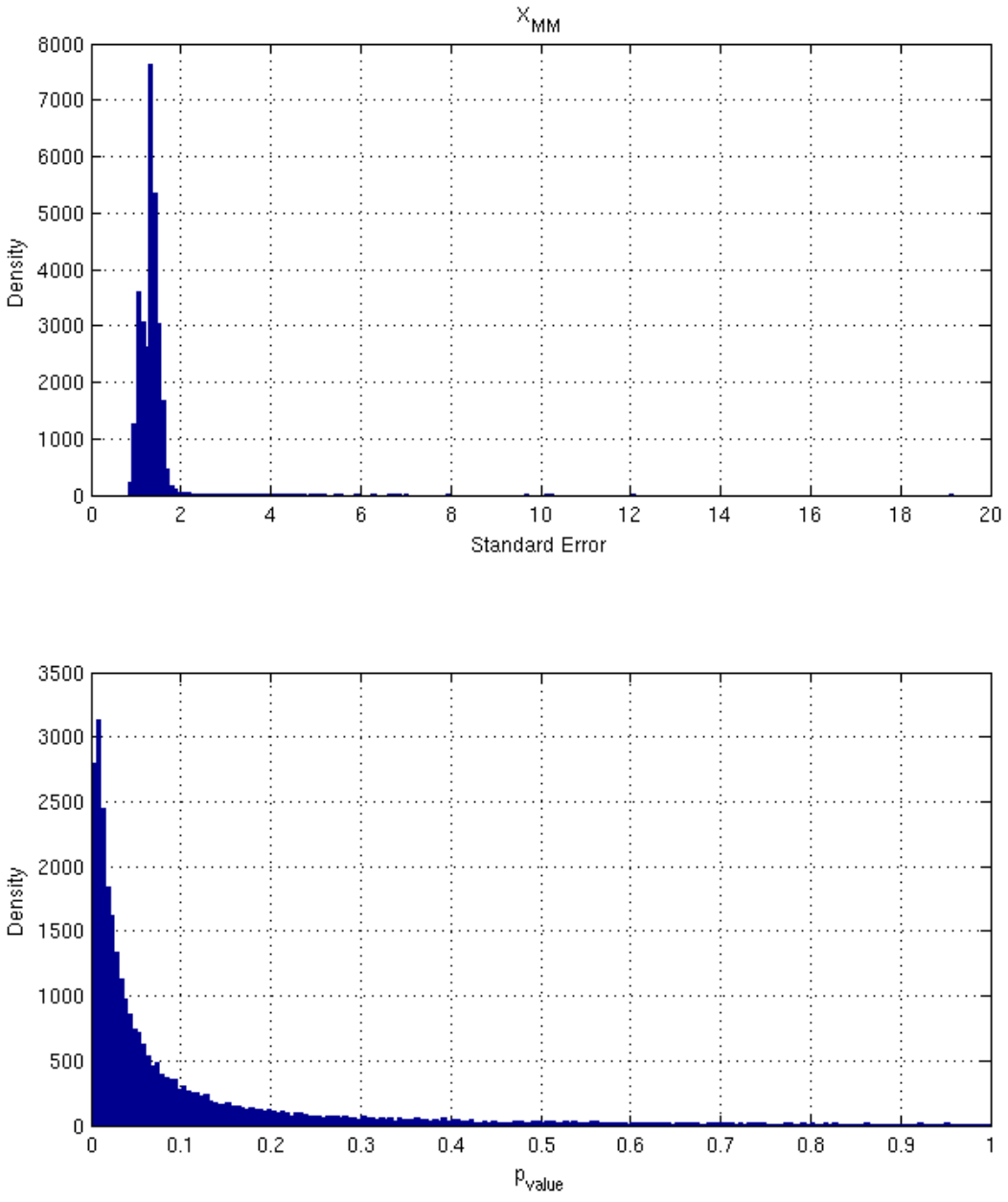

Figure 4.10: P-value distribution for intrusion model $\hat{X}_{MM}$ parameter.

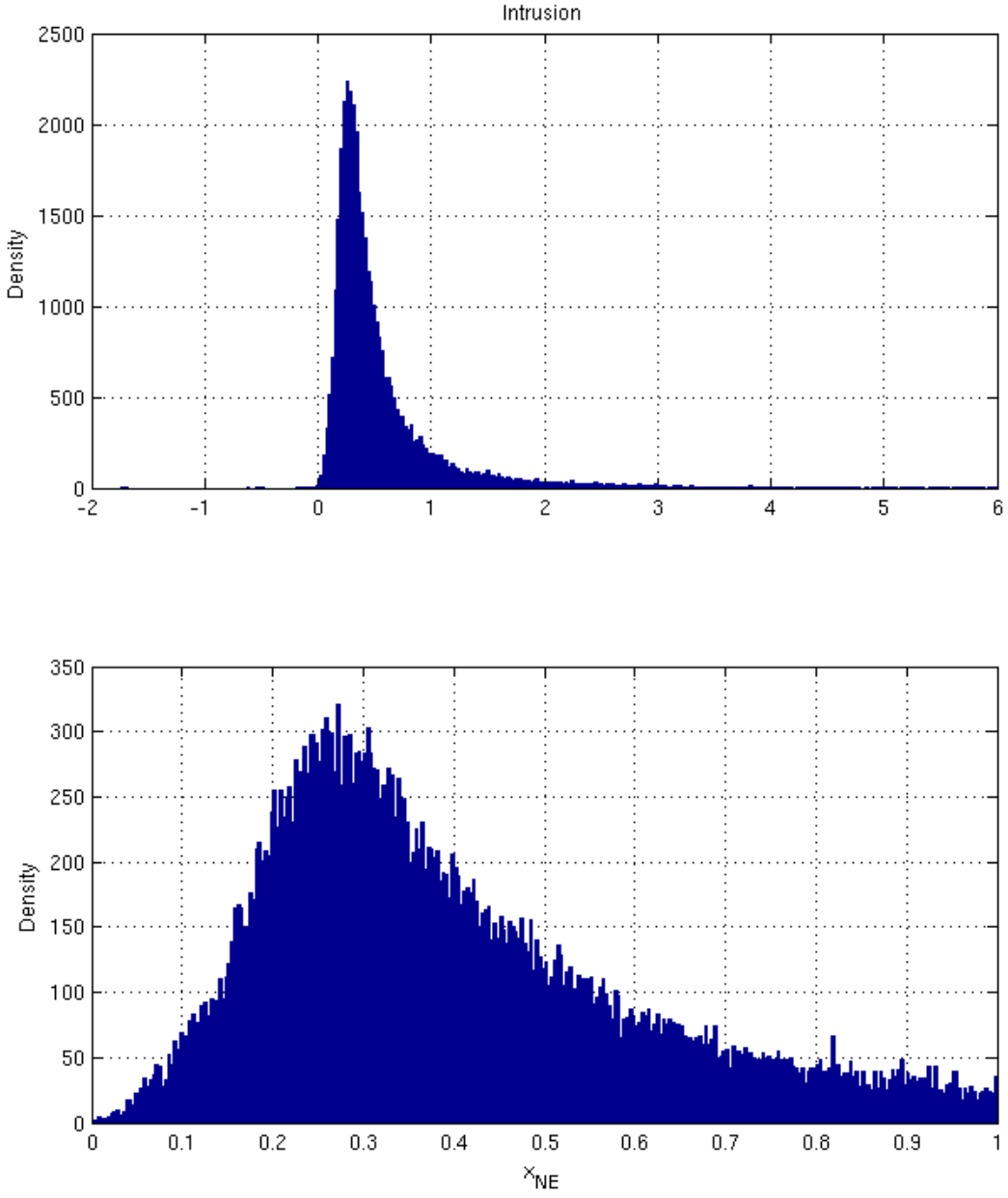

Figure 4.11: Bootstrapping analysis results for the intrusion model $\hat{X}_{NE}$ term, where the top panel is the complete distribution and the bottom panel shows the portion used to derive the $\hat{X}_{NE}$ value.

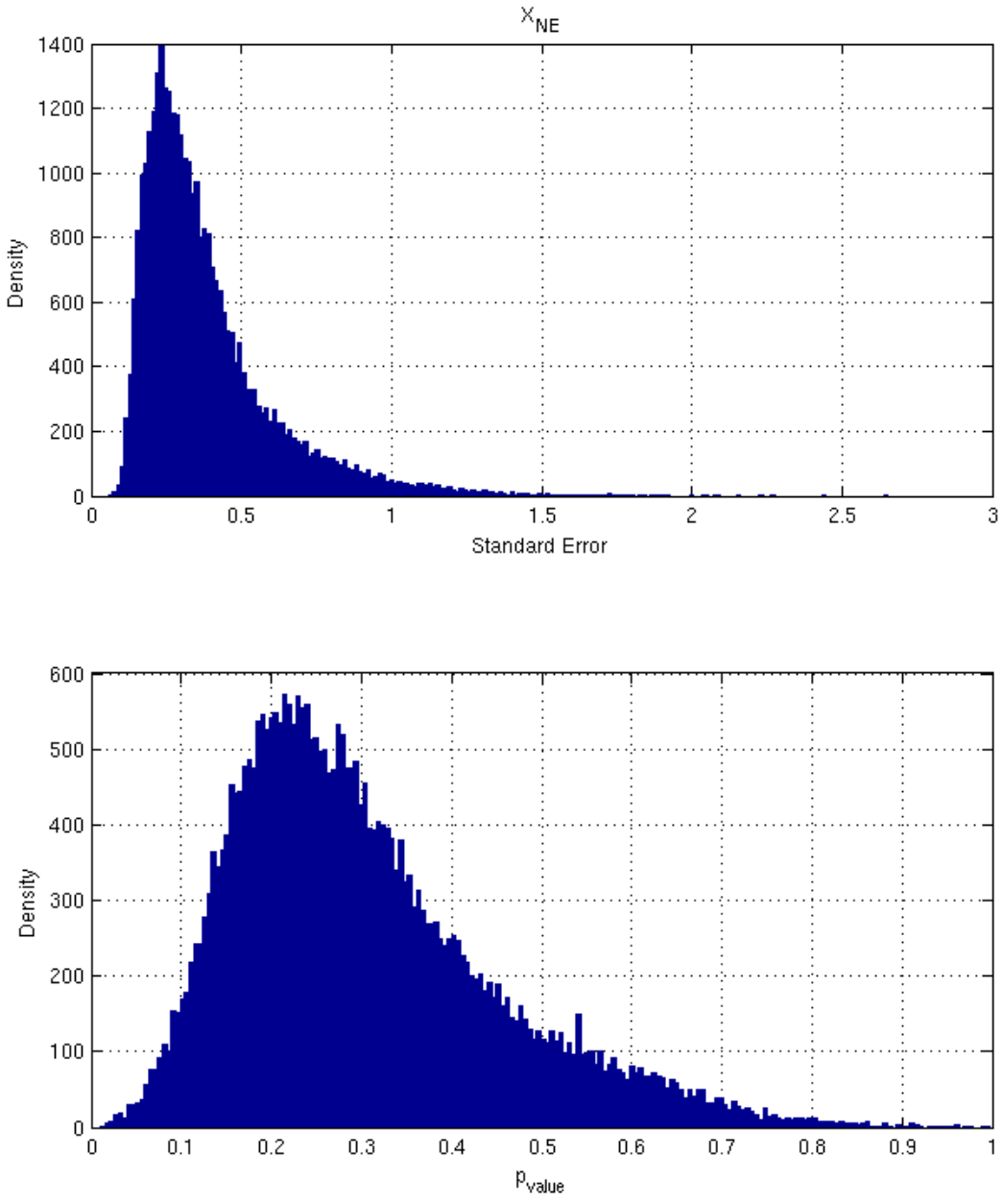

Figure 4.12: P-value distribution for intrusion model $\hat{X}_{NE}$ parameter.

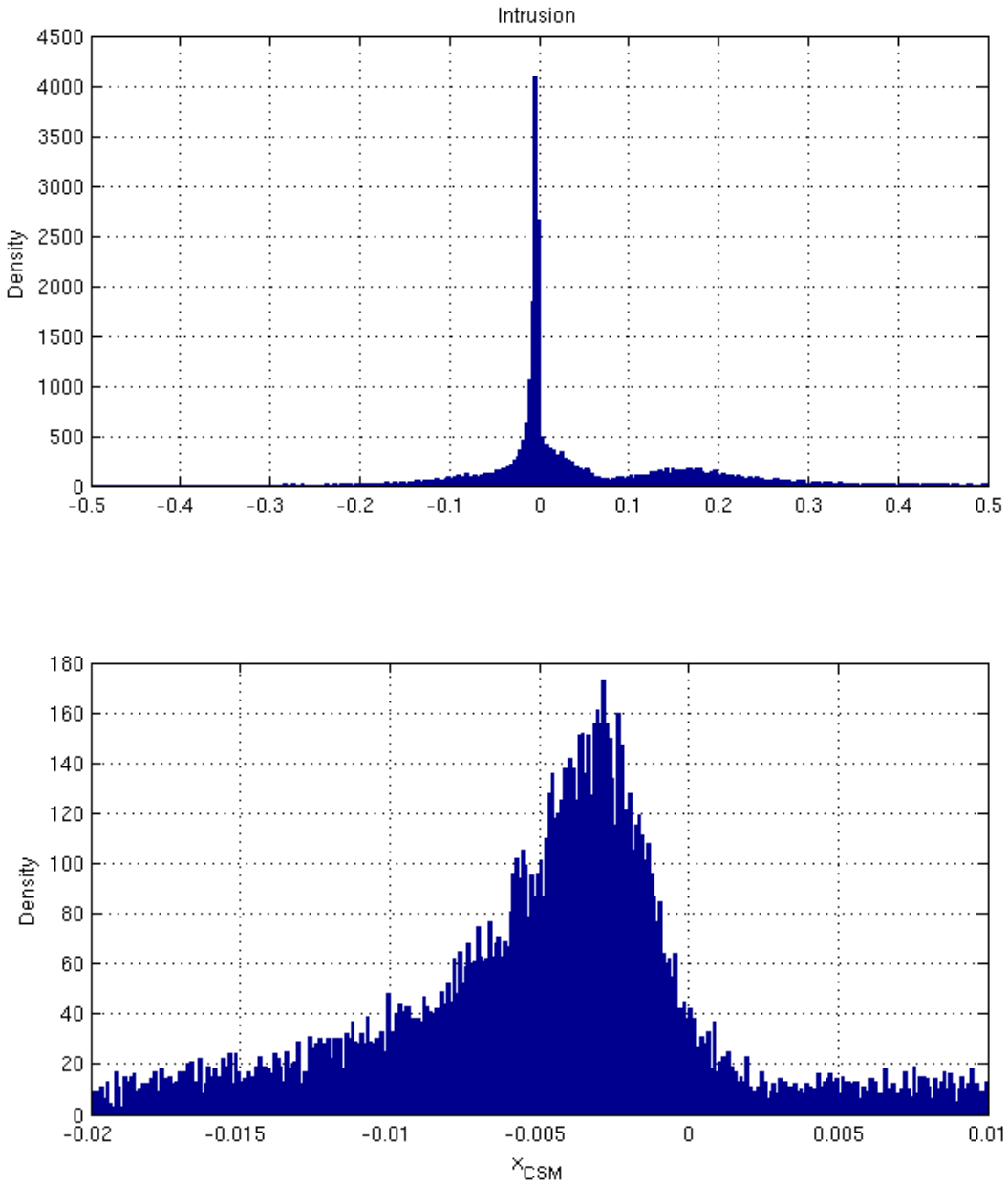

Figure 4.13: Bootstrapping analysis results for the intrusion model $\hat{X}_{CSM}$ term, where the top panel is the complete distribution and the bottom panel shows the portion used to derive the $\hat{X}_{CSM}$ value.

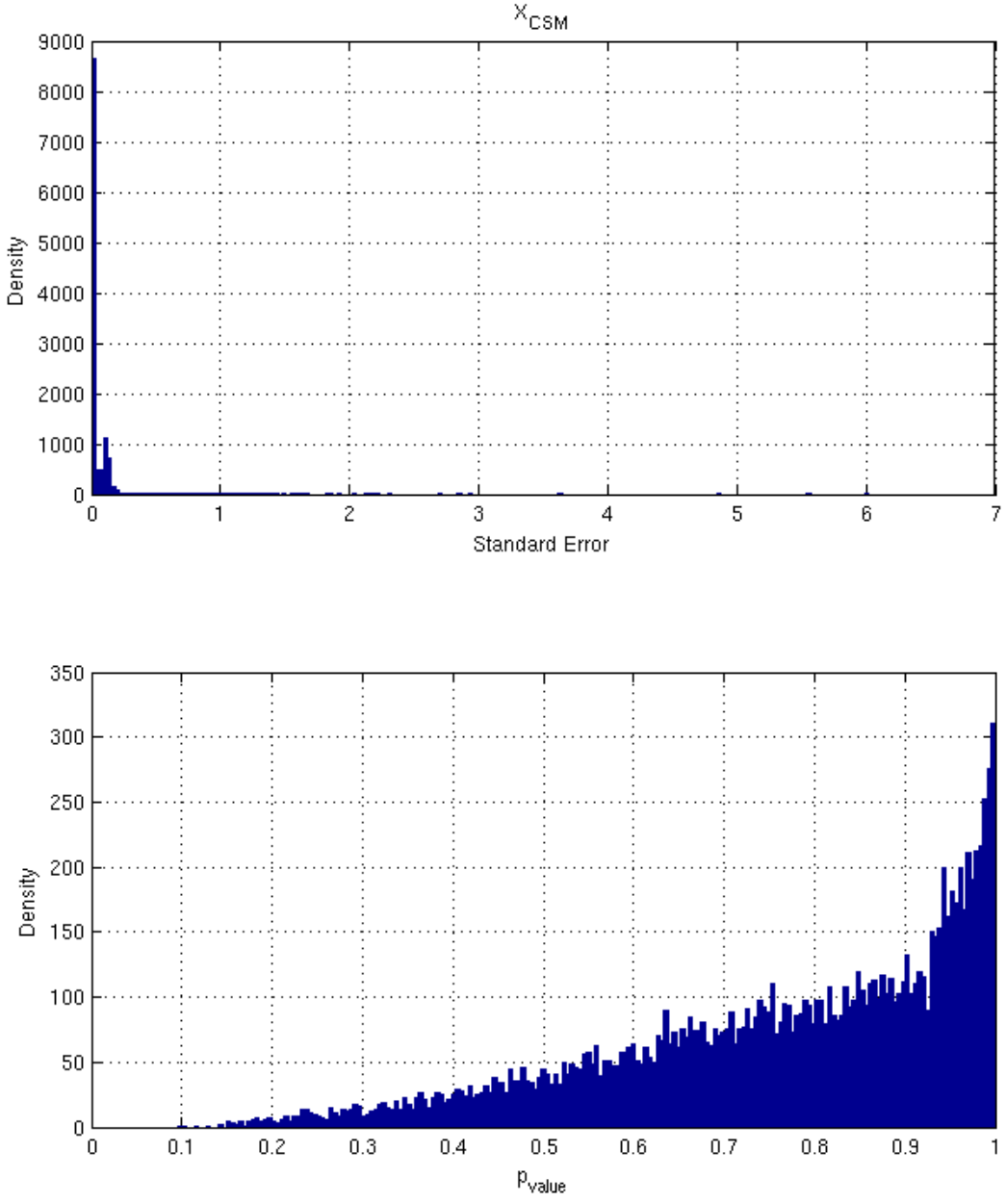

Figure 4.14: P-value distribution for intrusion model $\hat{X}_{CSM}$ parameter.

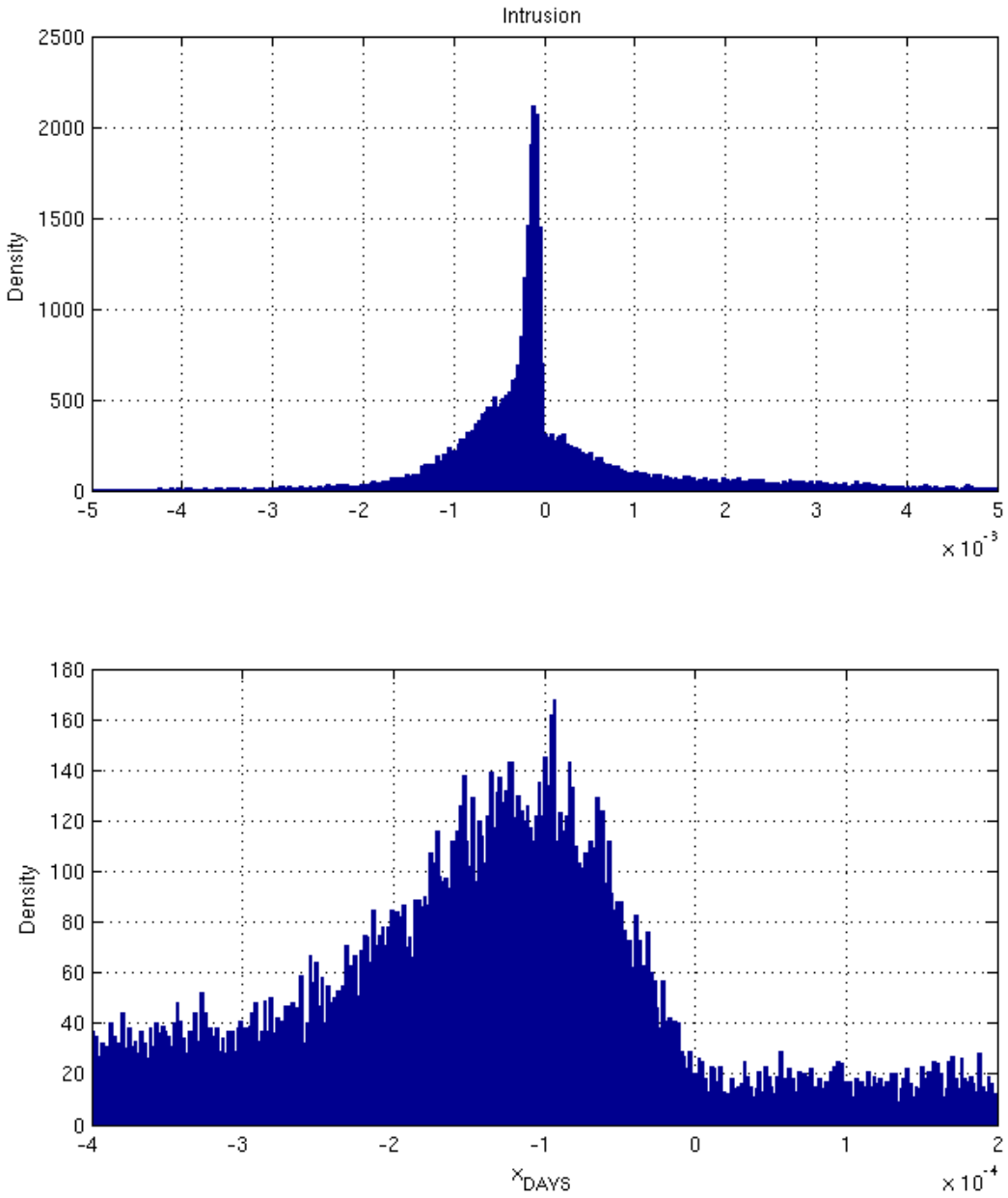

Figure 4.15: Bootstrapping analysis results for the intrusion model $\hat{X}_{DAYS}$ term, where the top panel is the complete distribution and the bottom panel shows the portion used to derive the $\hat{X}_{DAYS}$ value.

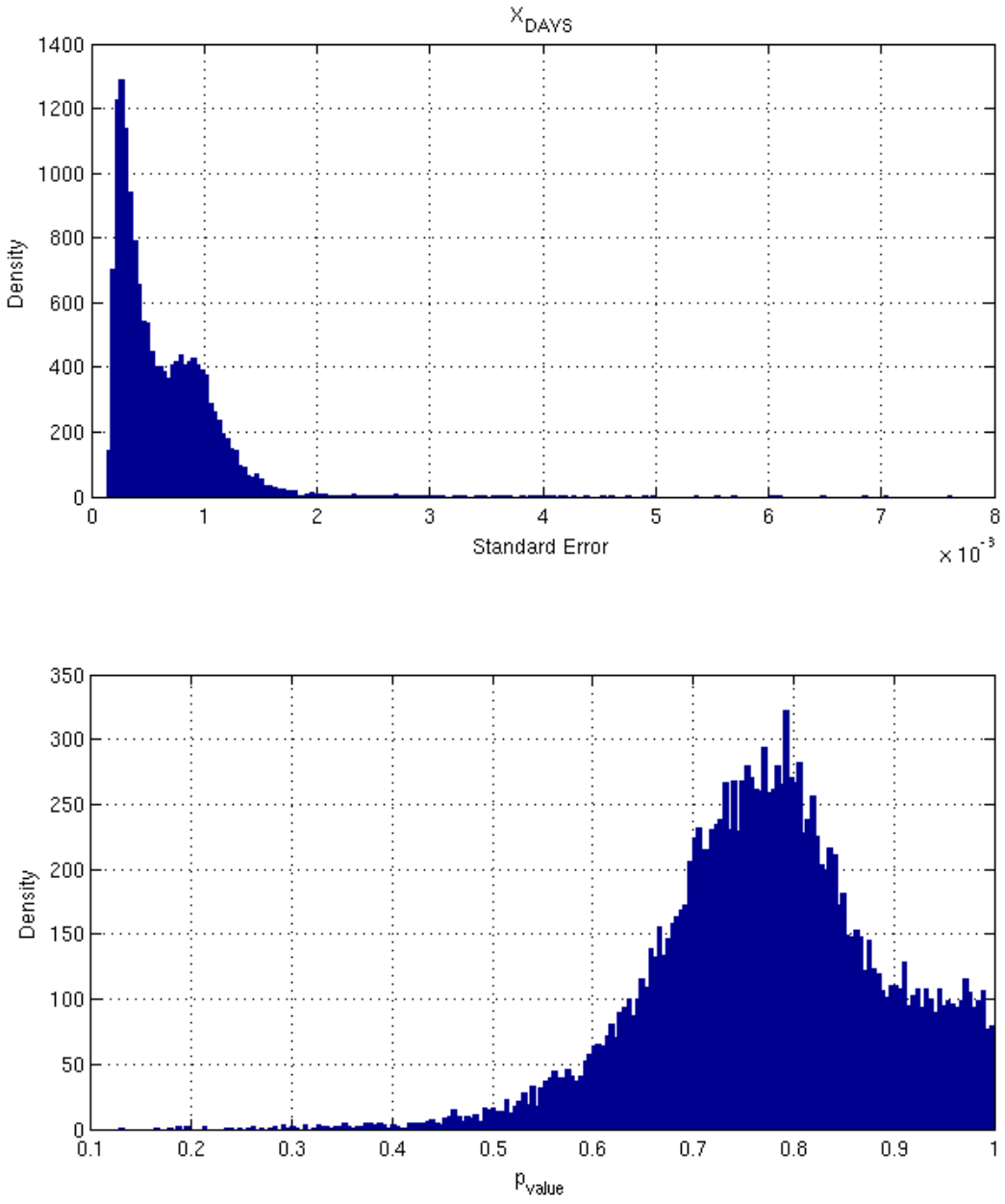

Figure 4.16: P-value distribution for intrusion model $\hat{X}_{DAYS}$ parameter.

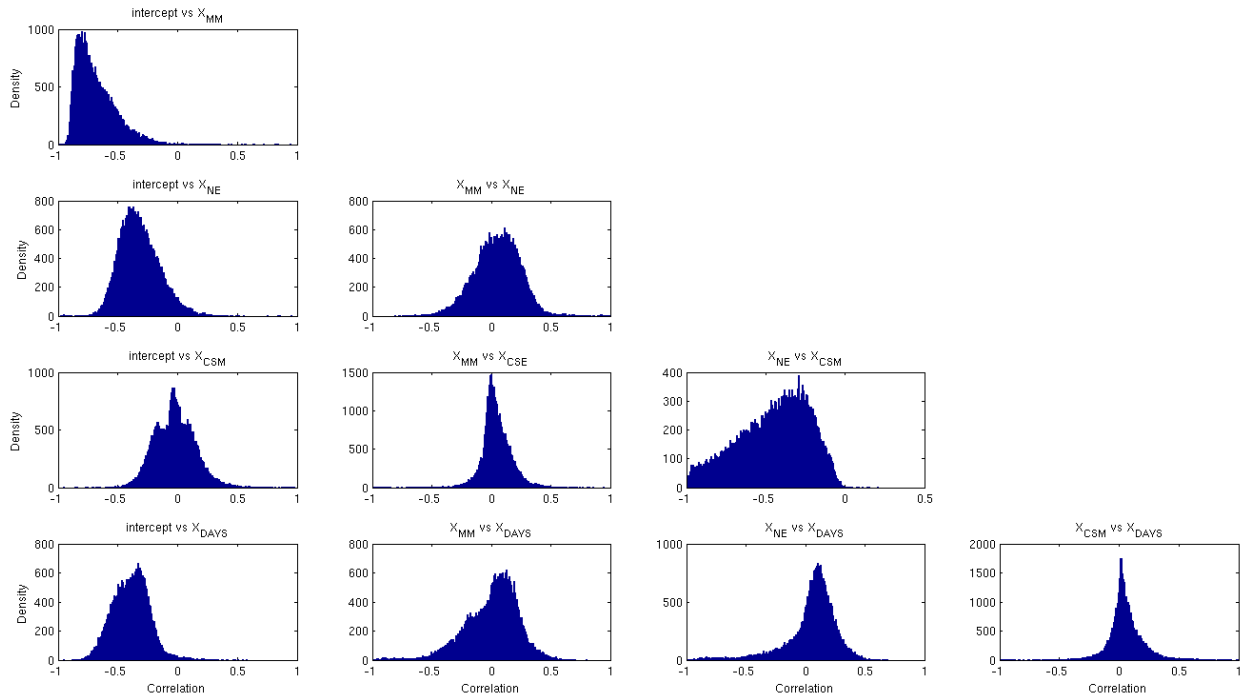

Figure 4.17: Intrusion node correlation matrix.

Table 4.11: Statistical summary of logistic model coefficients for intrusion node derived from bootstrapping analysis.

Explanatory Variable	Standard Error	p Value (Median)	p Value (Mode)
Intercept	1.2611	0.1920	0.0573
$\hat{X}_{MM}$	1.3350	0.0379	0.0082
$\hat{X}_{NE}$	0.3226	0.2733	0.2149
$\hat{X}_{CSM}$	0.0151	0.8061	0.9977
$\hat{X}_{DAYS}$	0.0005	0.7754	0.7929

Table 4.12: Logistic model coefficients correlation matrix for intrusion node derived from bootstrapping analysis.

Explanatory Variable	Intercept	$\hat{X}_{MM}$	$\hat{X}_{NE}$	$\hat{X}_{CSM}$	$\hat{X}_{DAYS}$
Intercept	1.00	-0.77	-0.36	-0.04	-0.40
$\hat{X}_{MM}$	-0.77	1.00	0.09	0.04	0.07
$\hat{X}_{NE}$	-0.36	0.09	1.00	-0.37	-0.12
$\hat{X}_{CSM}$	-0.04	0.04	-0.37	1.00	0.05
$\hat{X}_{DAYS}$	-0.40	0.07	-0.12	0.05	1.00

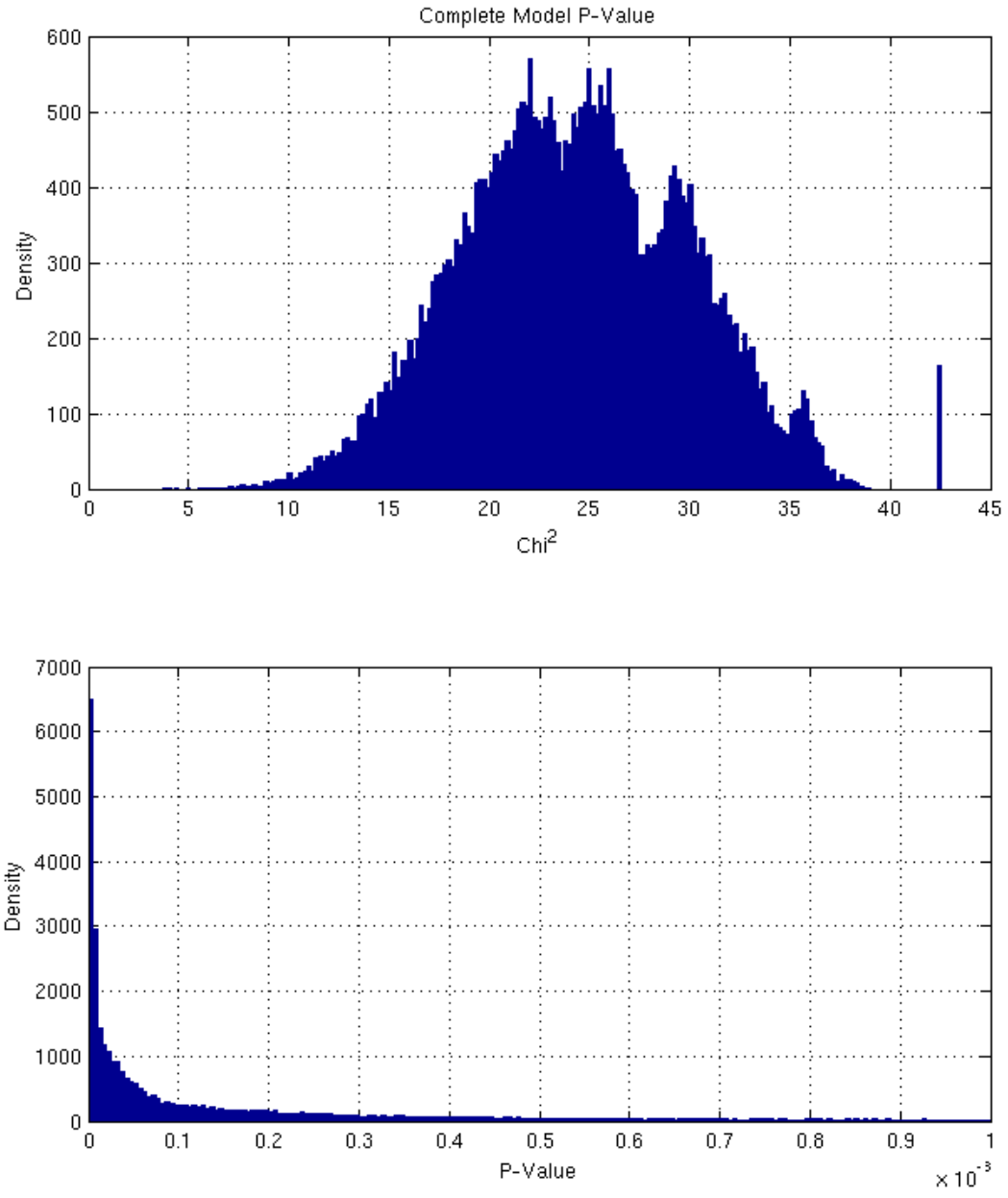

Figure 4.18: Chi squared and P-value distribution for complete intrusion model, where the median p-value is approximately 0.001.

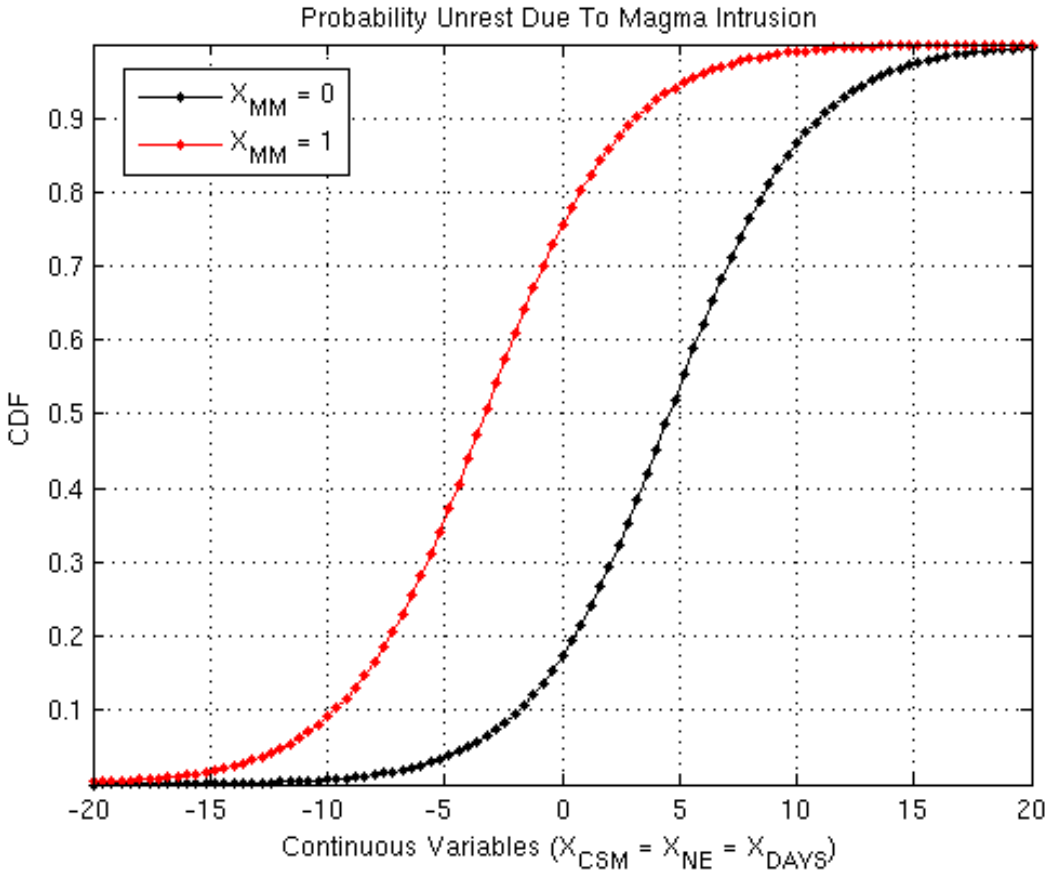

Figure 4.19: Cumulative density functions derived from bootstrapping process illustrating the influence of each of the explanatory variables on the probability estimate, where the black and red curves represents $\hat{X}_{MM} = 0$ and $\hat{X}_{MM} = 1$, respectively.

4.2.12 Node 3: Eruption Occurrence Model Via Bootstrapping

Distributions for each of the bootstrapped eruption model coefficients, standard errors, and p-values are shown in Figure 4.20 - Figure 4.31. The revised logistic model is shown by Equation 4.35 and is significantly different from the model shown by Equation 4.30. The bootstrapping analysis reduced the weight of $\hat{X}_{NE}$ and $\hat{X}_{CSM}$ coefficients by an order of magnitude relative to those derived for X_{NE} and X_{CSM}. This substantial reduction in weight suggests the true contribution of $\hat{X}_{NE}$ and $\hat{X}_{CSM}$ on the probability of occurrence estimate is not as significant as previously thought. In addition, the weight of the intercept and the $\hat{X}_{MM}$ coefficients have also changed, where the difference between these values is larger than the non-bootstrapped versions. This change is evident in Figure 4.34, where the curves are now shifted to the right relative to those shown in Figure 4.5. The difference between the CDFs when $\hat{X}_{MM}$ varies between 0 and 1 is now approximately 0.18 when all other input values are 0.

The median standard error, p-value, and correlation values are shown in Table 4.13. There is a substantial difference in p-value estimates generated from the median and mode of their respective distributions. In general, the median values are larger than the mode values, which is due to large kurtosis of the p-value distributions. In this case, all of the mode p-value estimates are above 0.05. However, the intercept, $\hat{X}_{MM}$, and $\hat{X}_{ERH}$ values are small enough to suggest they possess some statistical significance. As stated earlier, explanatory variables with large p-values still have an effect on the probability estimate when $\hat{X}_{MM}$ equals 0, as shown in Figure 4.34. Therefore, they have a substantial practical significance in the probability estimate.

Statistics for the complete model likelihood-ratio test are shown in Figure 4.34. Again, the complete model median p-value has increased by an order of magnitude. However, the median p-value is approximately 0.014, which suggests the resulting model has approximately a 98.6 percent chance of outperforming the null model (intercept only).

The lower, off-diagonal, correlation matrix components are shown in Figure 4.32 and listed in Table 4.14. The bootstrapping results have not significantly changed the relationships between the coefficients. However, the unusual bimodal structure observed in the C_{34} matrix component may be an artifact of the ill constrained GLMR runs.

$$\hat{z}_3 = -3.4589 + 2.1401(\hat{X}_{MM}) + 0.0056(\hat{X}_{NE}) + 0.0023(\hat{X}_{CSM}) - 0.0014(\hat{X}_{DAYS}) + 12.8714(\hat{X}_{EH}) \quad (4.35)$$

Table 4.13: Statistical summary of logistic model coefficients for eruption node derived from bootstrapping analysis.

Explanatory Variable	Standard Error	p Value (Median)	p Value (Mode)
Intercept	2.2786	0.1756	0.0657
$\hat{X}_{MM}$	1.9030	0.6525	0.1699
$\hat{X}_{NE}$	0.0332	0.7675	0.9378
$\hat{X}_{CSM}$	0.0079	0.7723	0.7181
$\hat{X}_{DAYS}$	0.0017	0.4478	0.4046
$\hat{X}_{ERH}$	9.1931	0.1533	0.1151

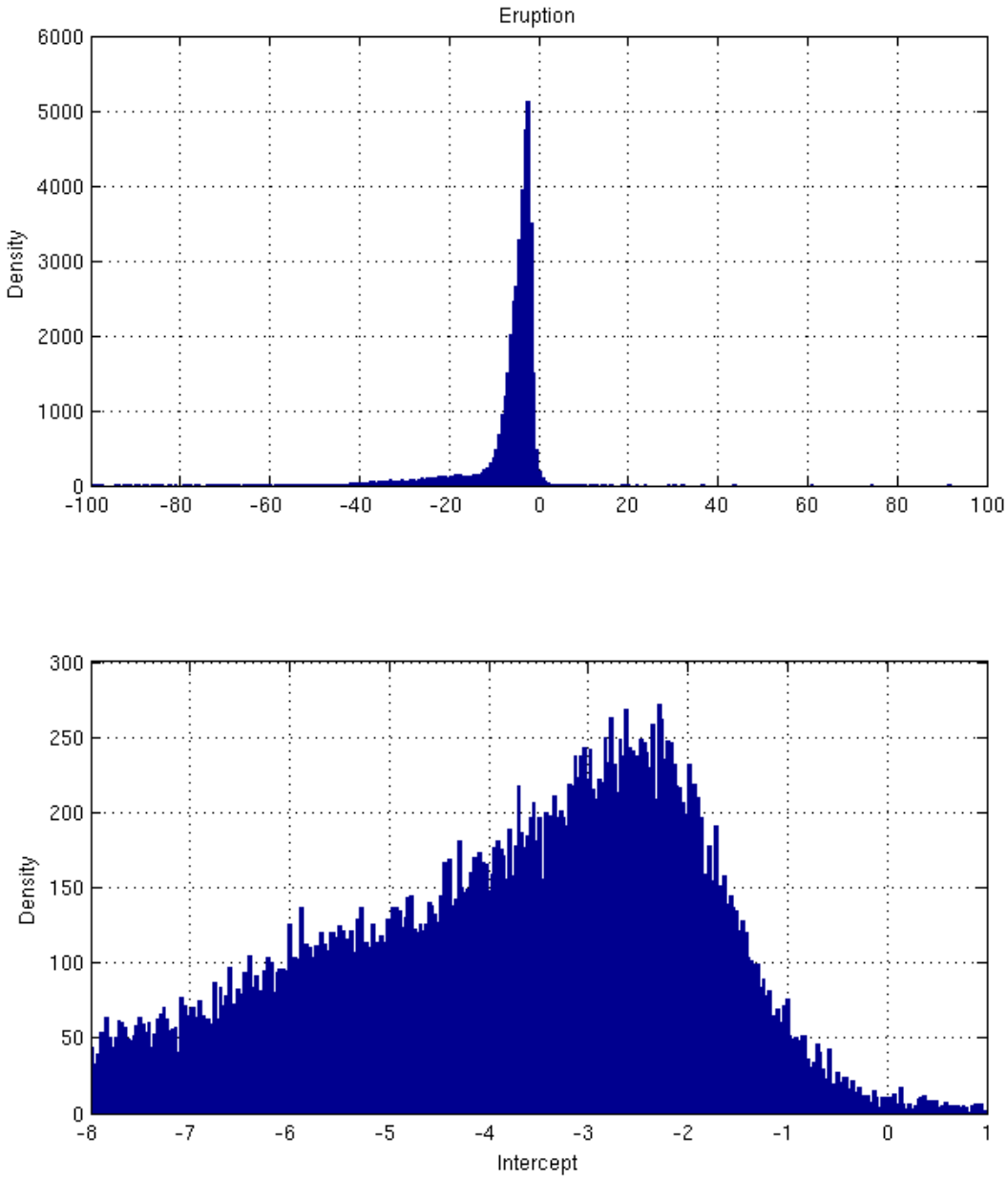

Figure 4.20: Bootstrapping analysis results for the eruption model intercept term, where the top panel is the complete distribution and the bottom panel shows the portion used to derive the intercept value.

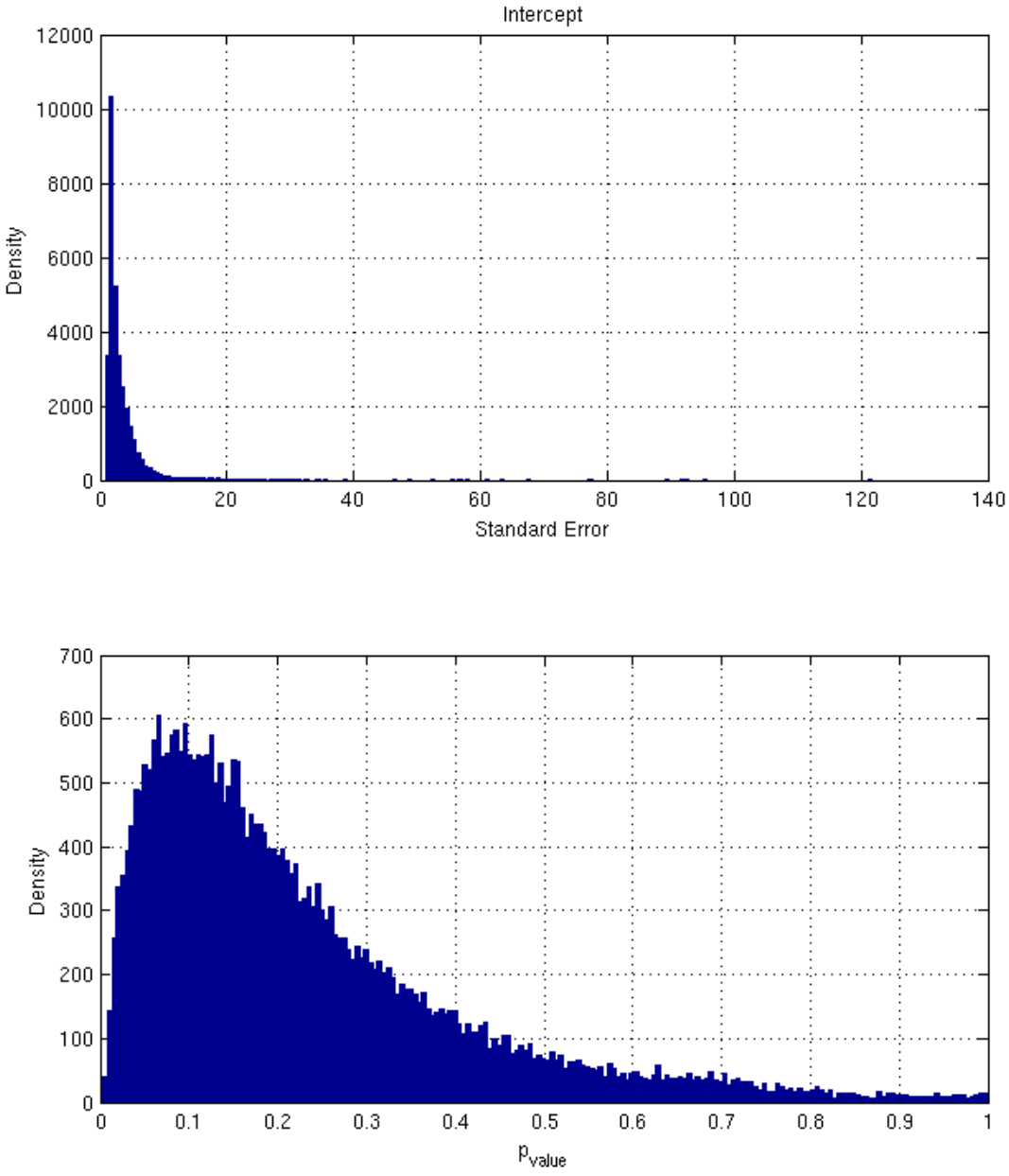

Figure 4.21: P-value distribution for eruption model intercept parameter.

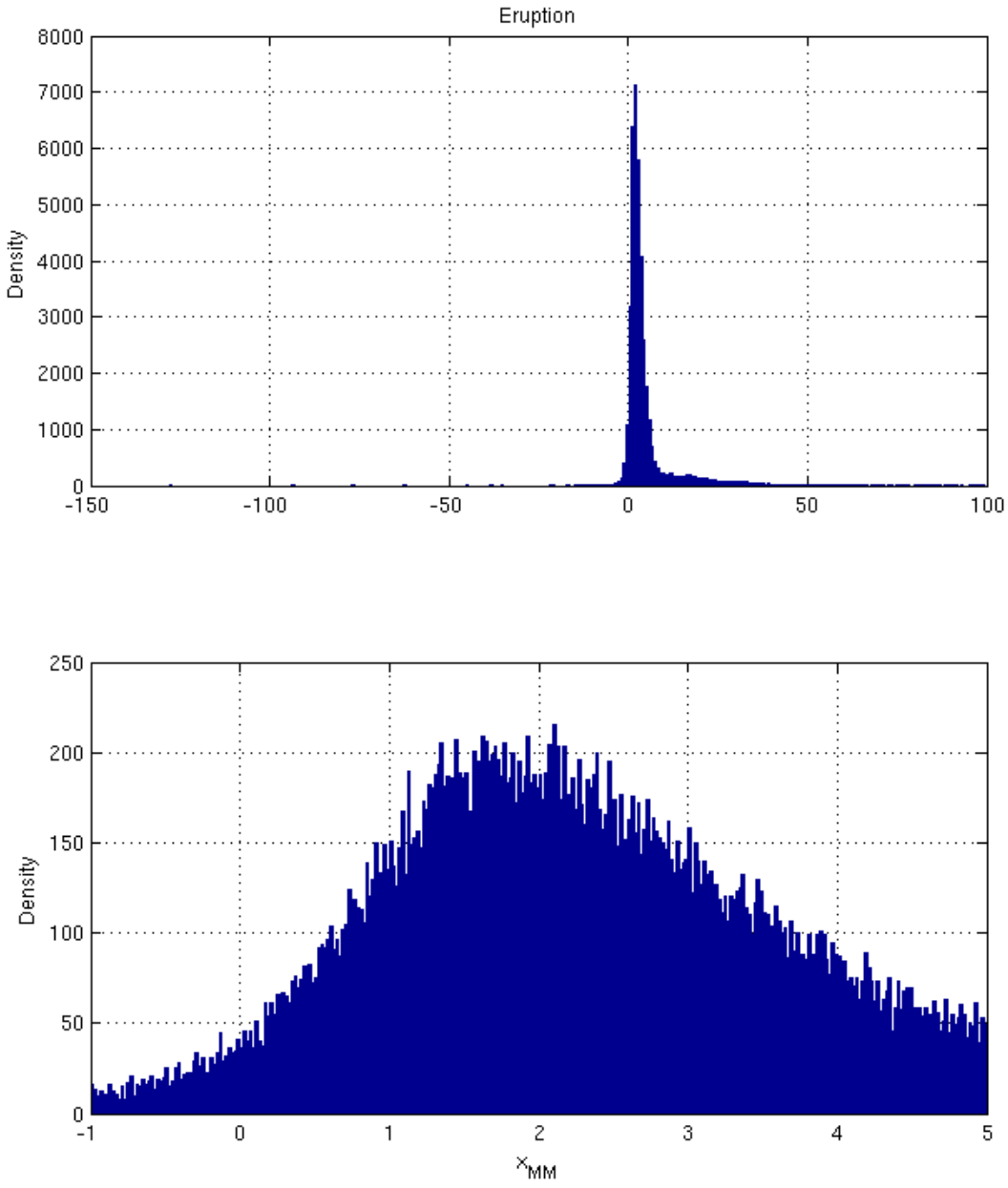

Figure 4.22: Bootstrapping analysis results for the eruption model $\hat{X}_{MM}$ term, where the top panel is the complete distribution and the bottom panel shows the portion used to derive the $\hat{X}_{MM}$ value.

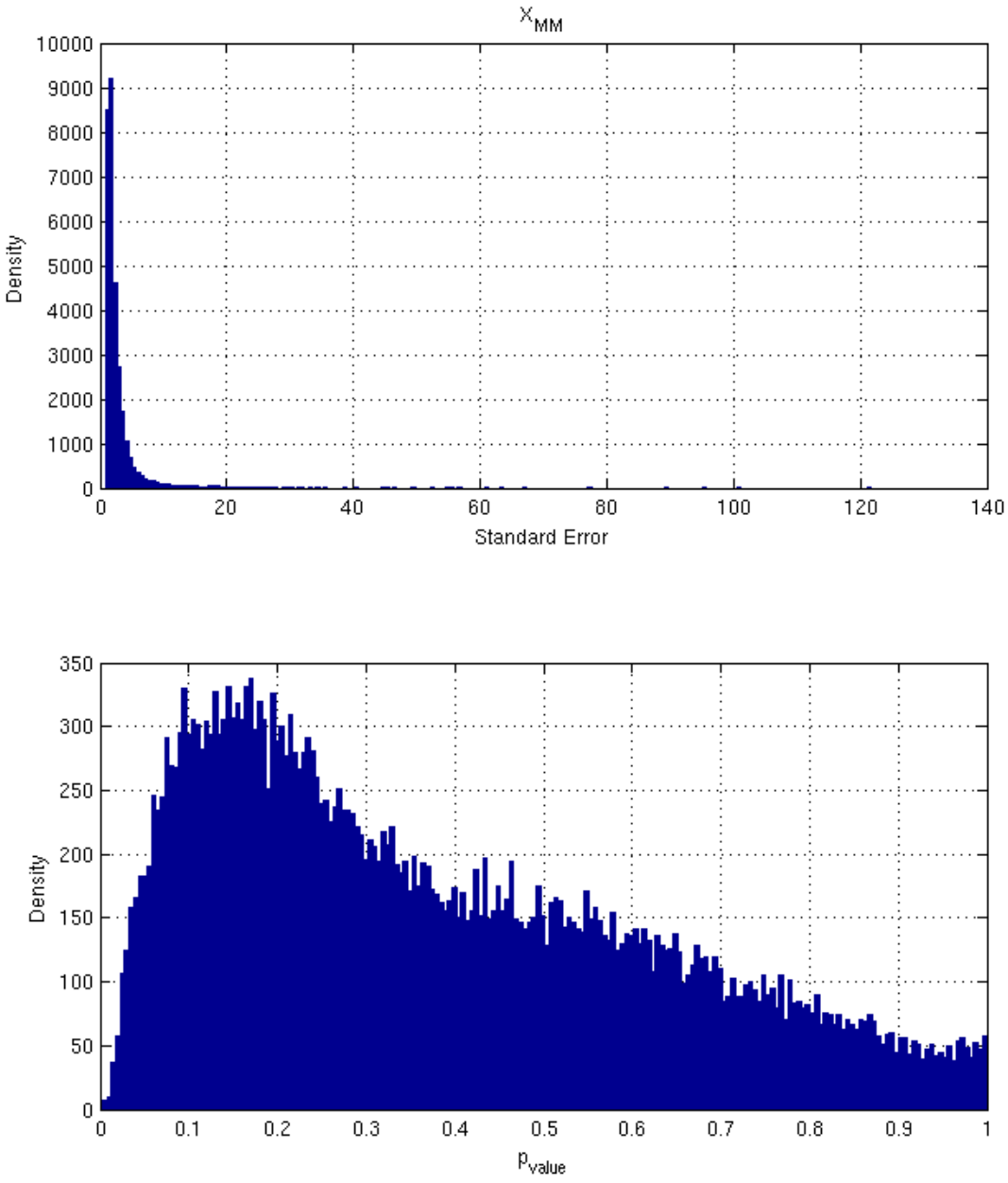

Figure 4.23: P-value distribution for eruption model $\hat{X}_{MM}$ parameter.

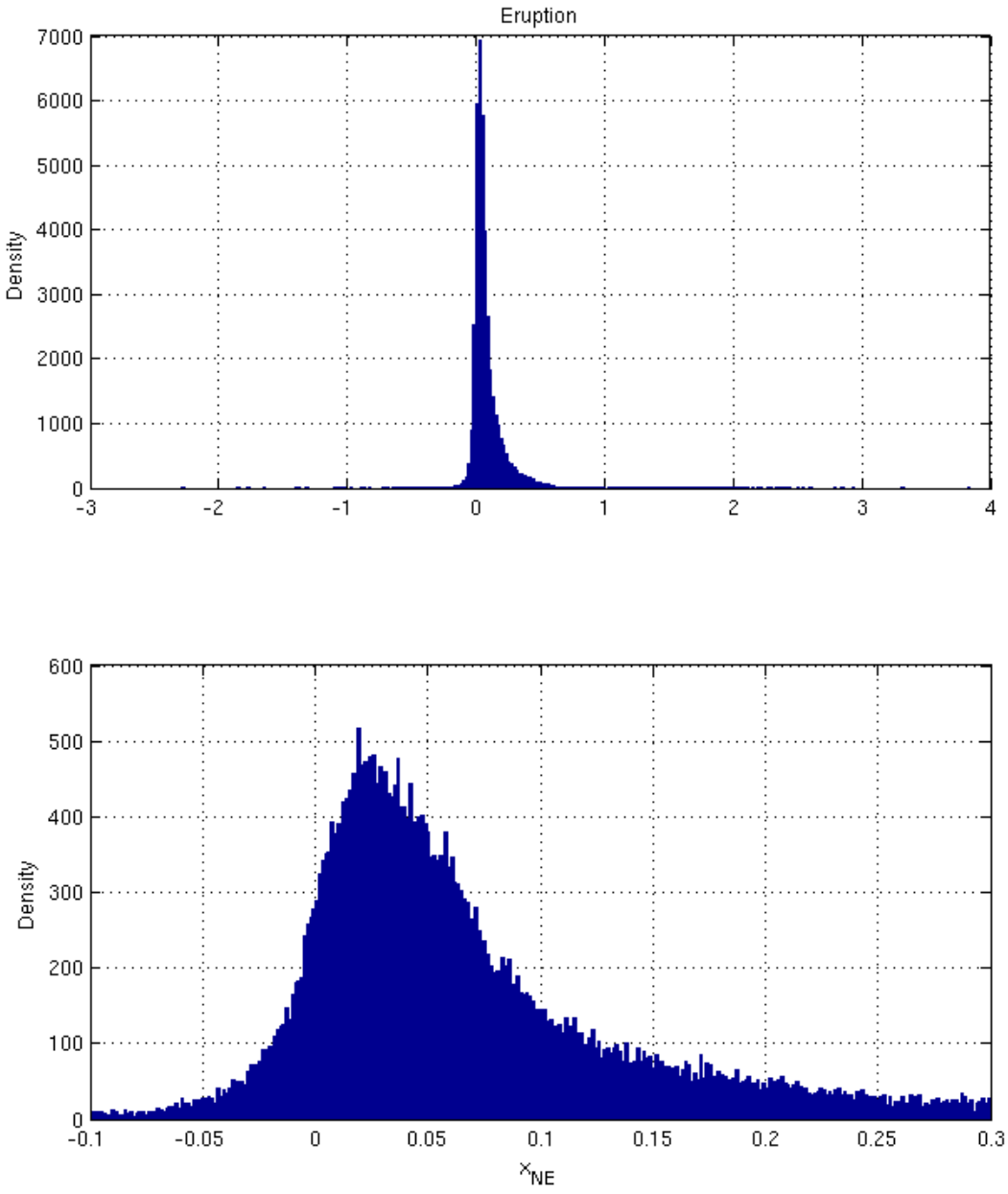

Figure 4.24: Bootstrapping analysis results for the eruption model $\hat{X}_{NE}$ term, where the top panel is the complete distribution and the bottom panel shows the portion used to derive the $\hat{X}_{NE}$ value.

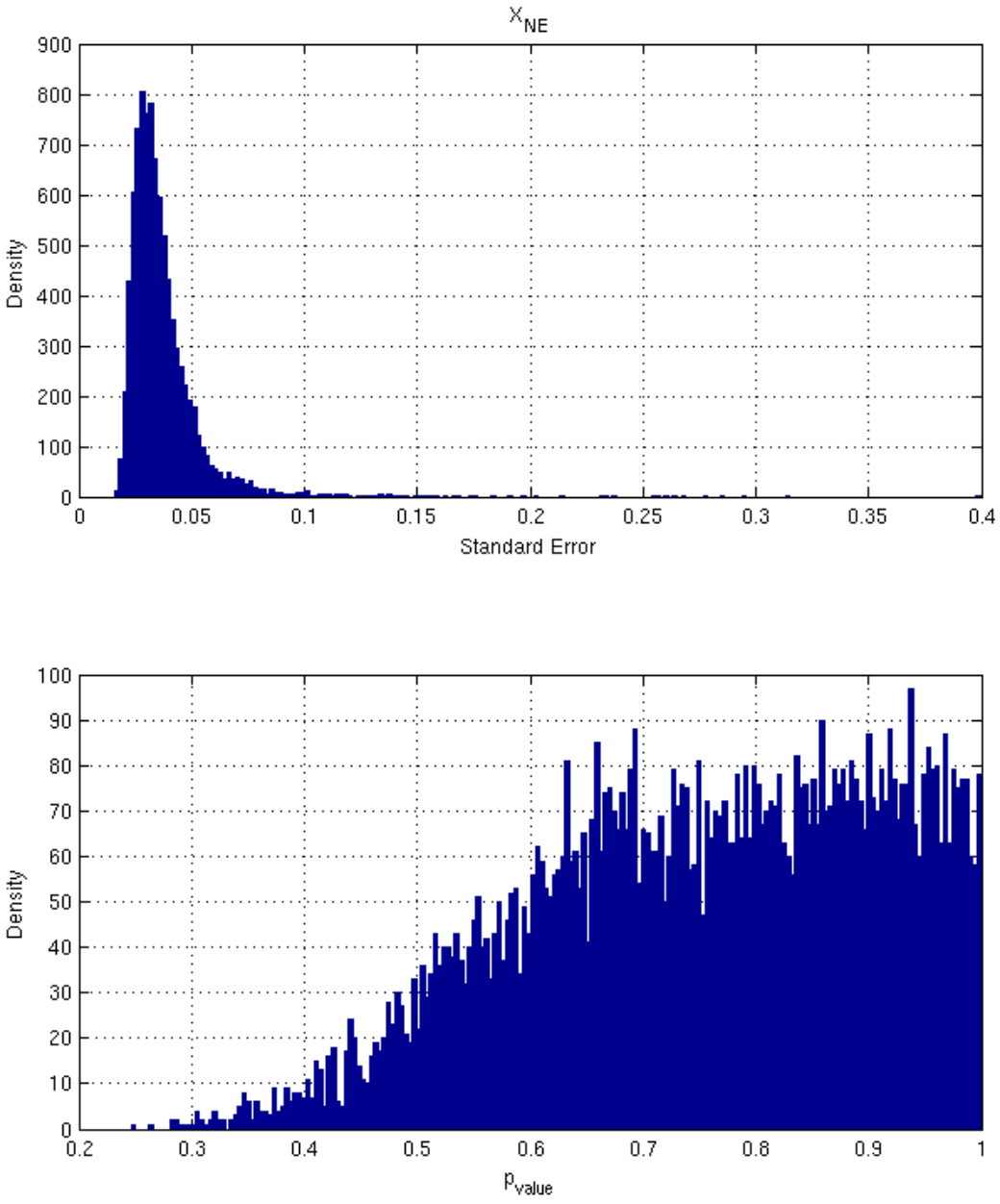

Figure 4.25: P-value distribution for eruption model $\hat{X}_{NE}$ parameter.

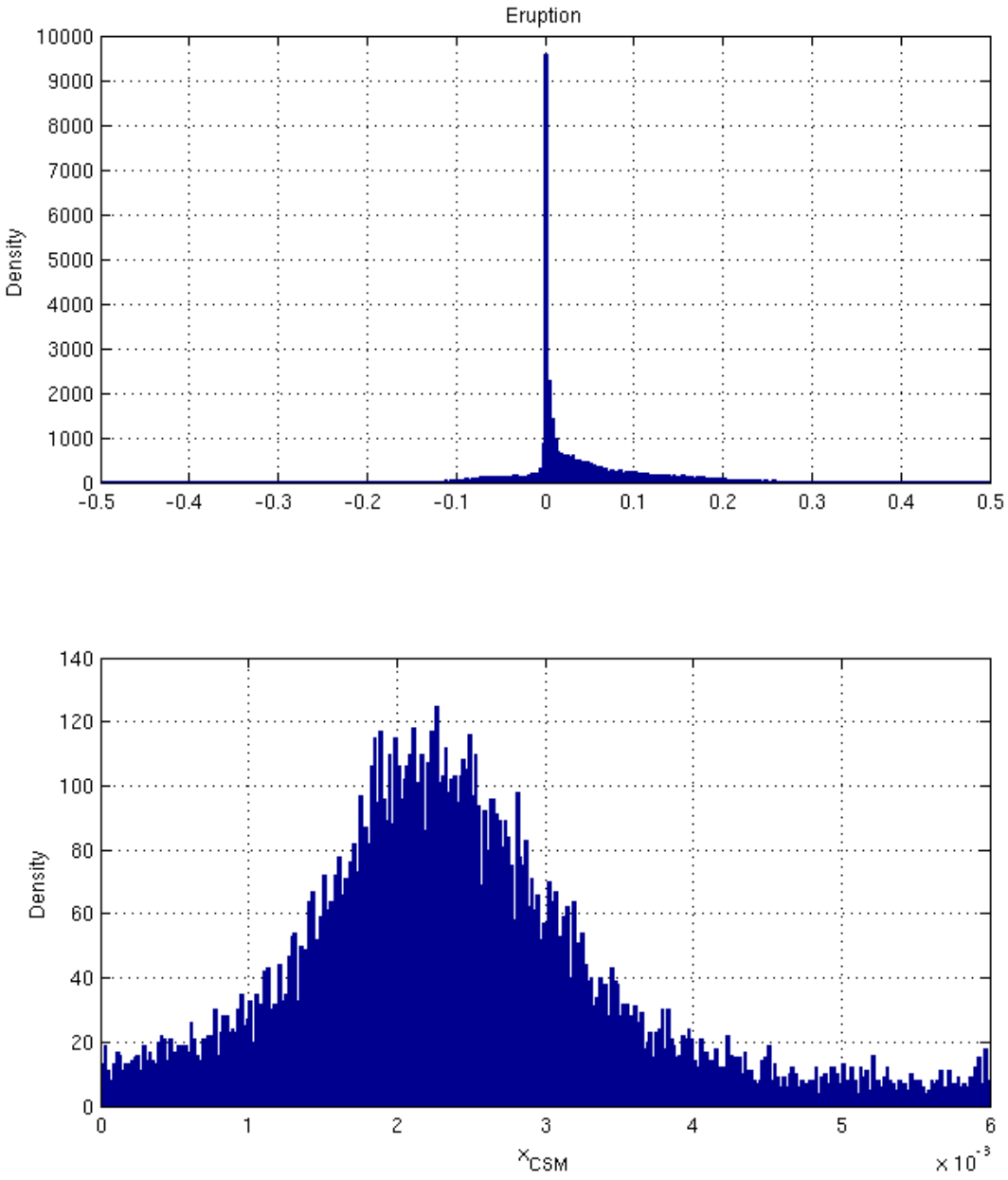

Figure 4.26: Bootstrapping analysis results for the eruption model $\hat{X}_{CSM}$ term, where the top panel is the complete distribution and the bottom panel shows the portion used to derive the $\hat{X}_{CSM}$ value.

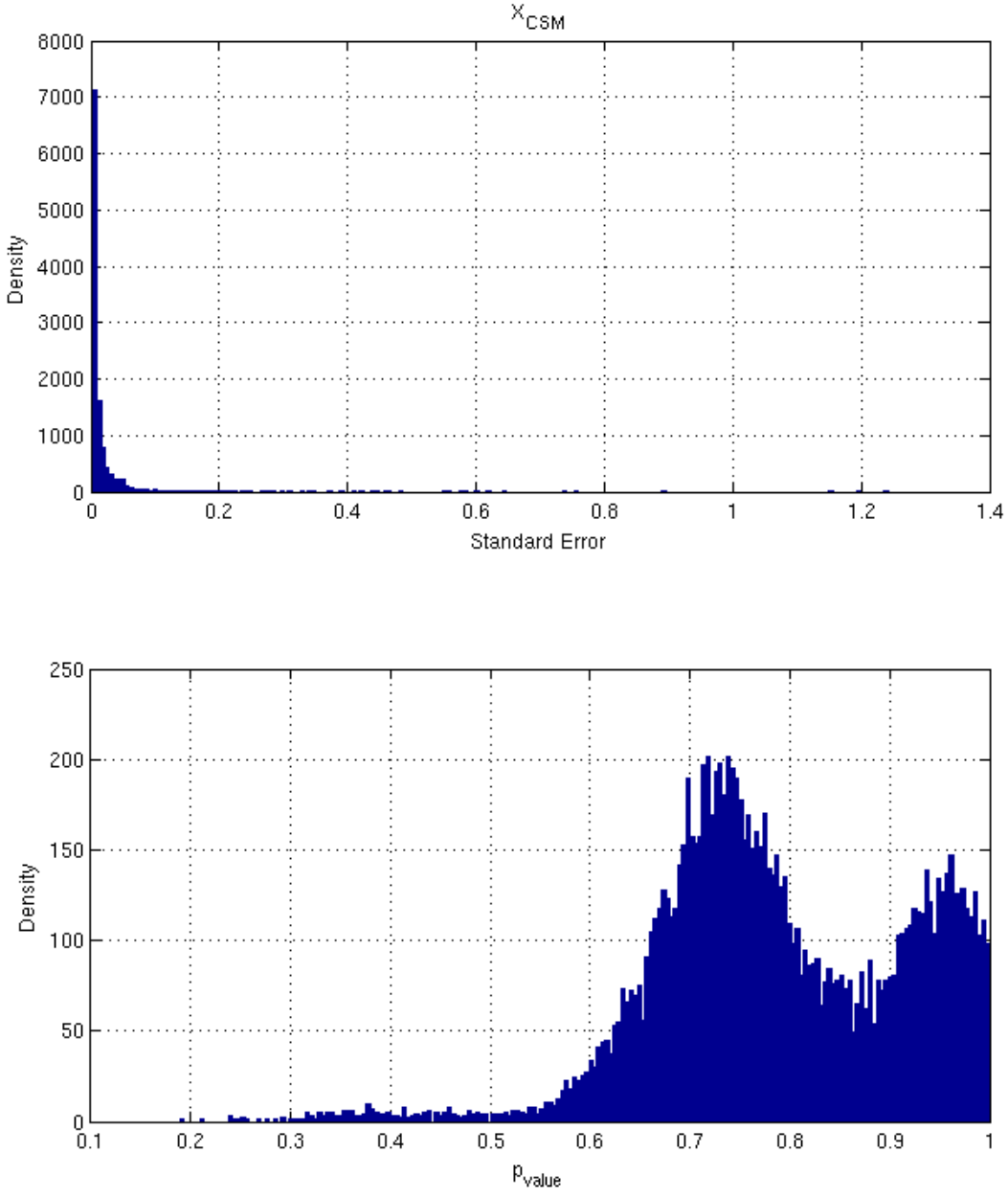

Figure 4.27: P-value distribution for eruption model $\hat{X}_{CSM}$ parameter.

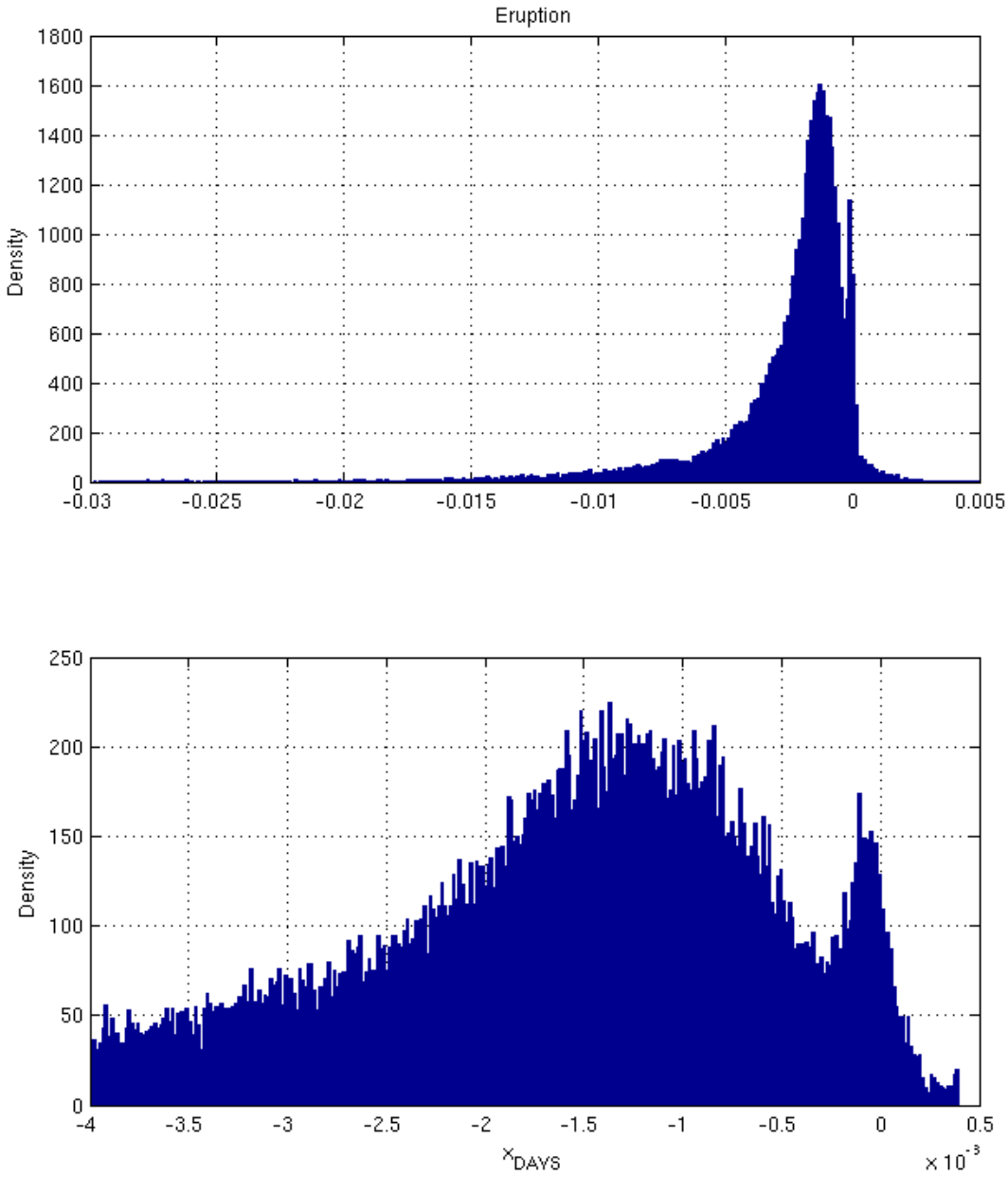

Figure 4.28: Bootstrapping analysis results for the eruption model $\hat{X}_{DAYS}$ term, where the top panel is the complete distribution and the bottom panel shows the portion used to derive the $\hat{X}_{DAYS}$ value.

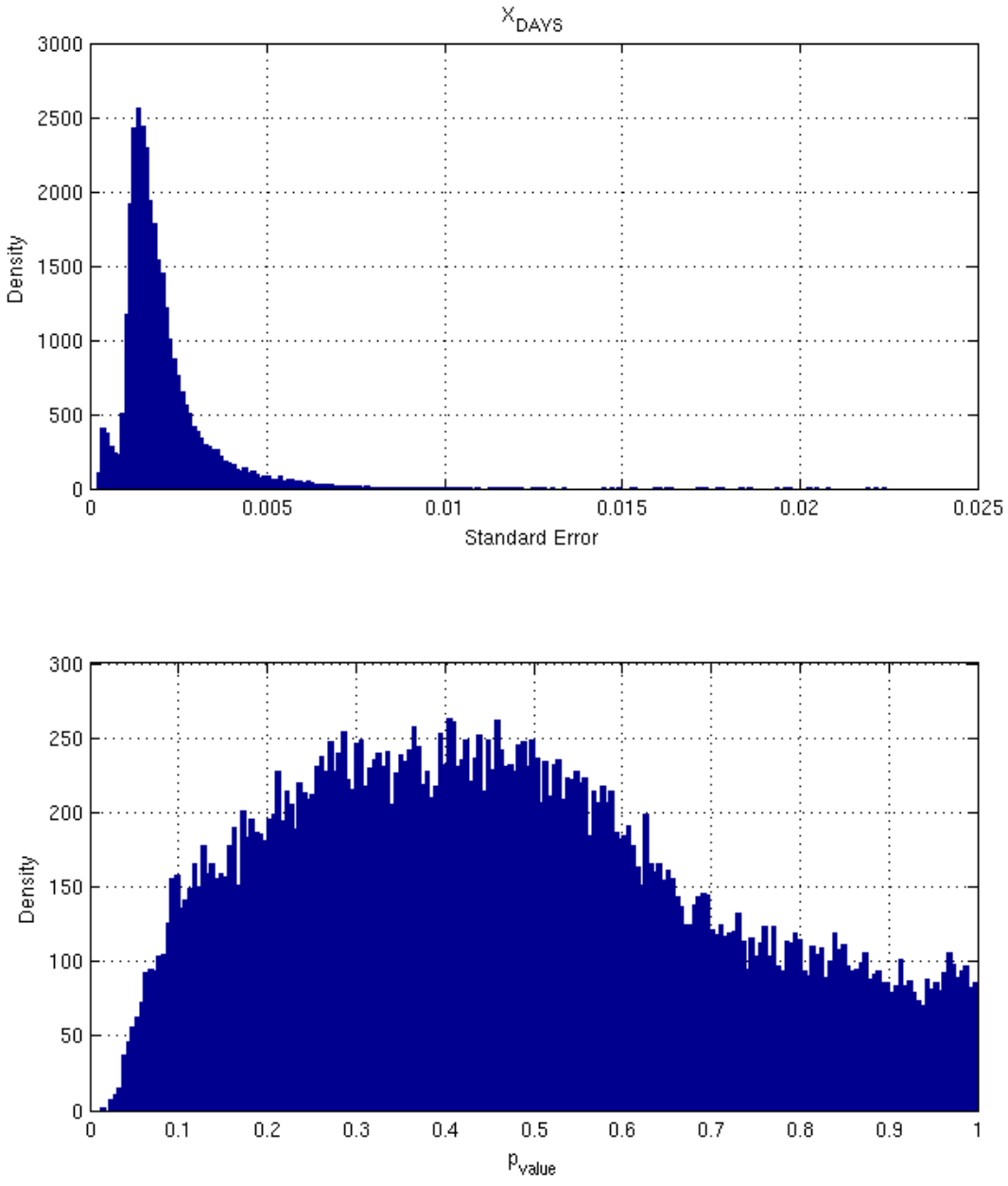

Figure 4.29: P-value distribution for eruption model $\hat{X}_{DAYS}$ parameter.

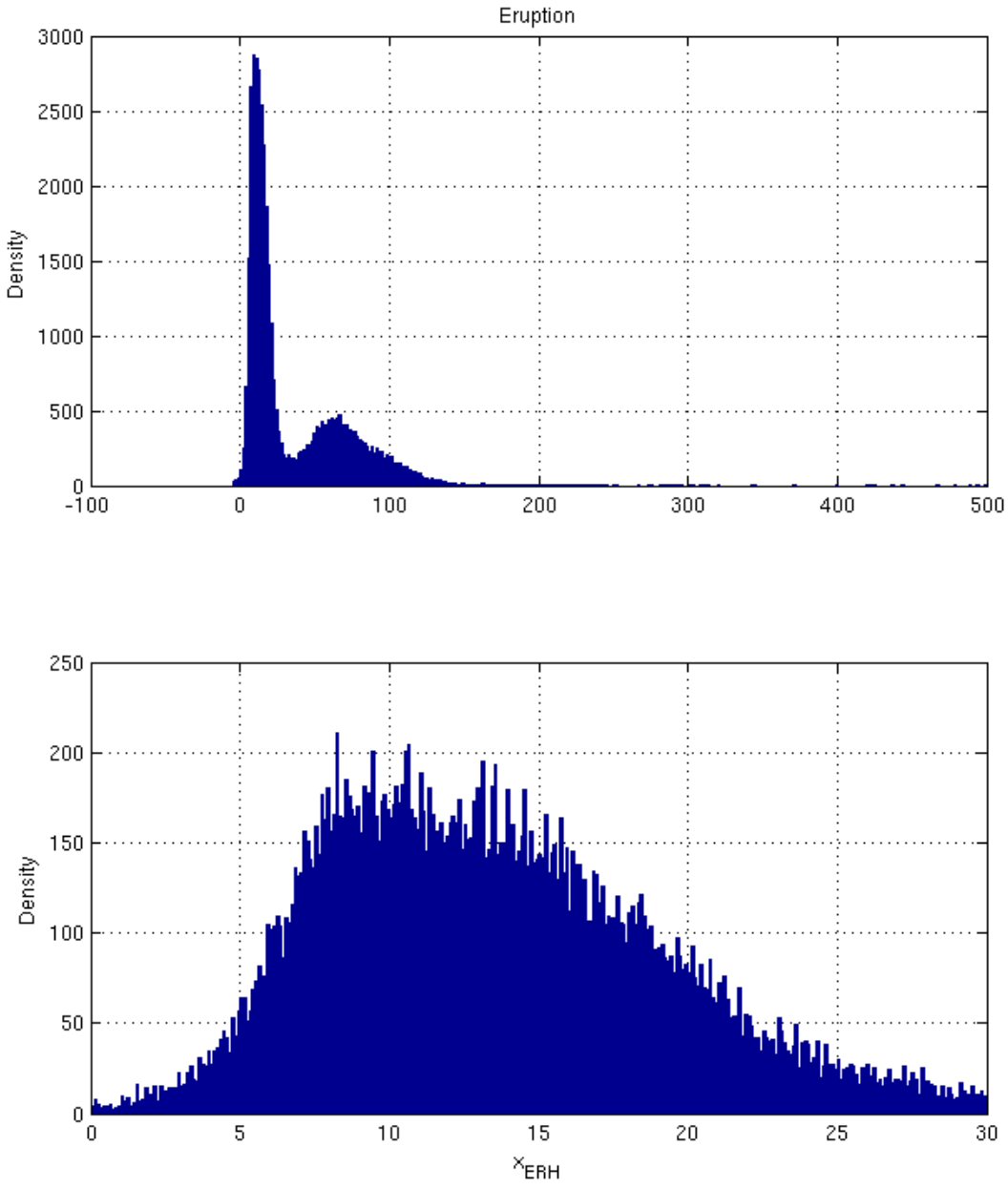

Figure 4.30: Bootstrapping analysis results for the eruption model $\hat{X}_{ERH}$ term, where the top panel is the complete distribution and the bottom panel shows the portion used to derive the $\hat{X}_{ERH}$ value.

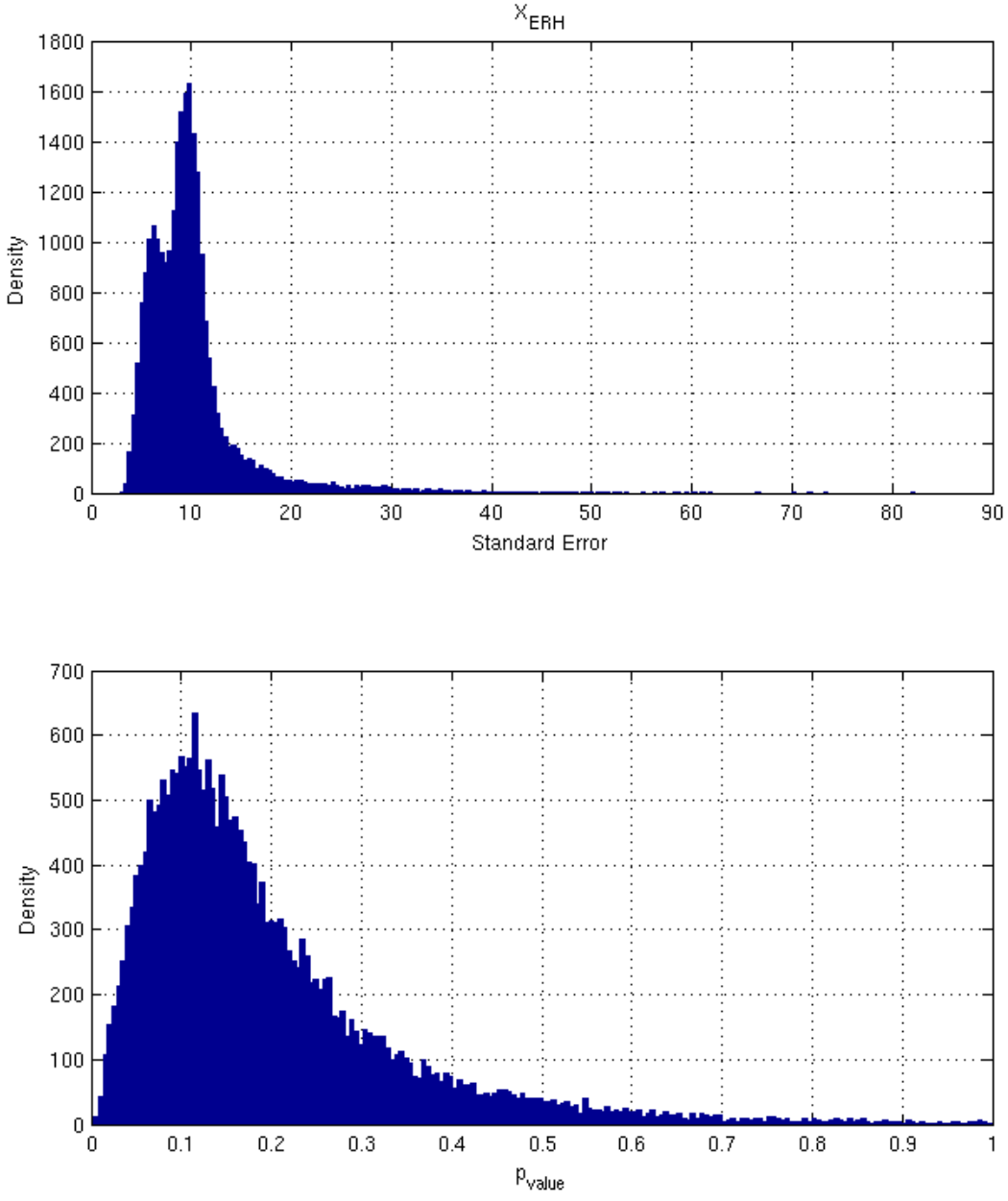

Figure 4.31: P-value distribution for eruption model $\hat{X}_{ERH}$ parameter.

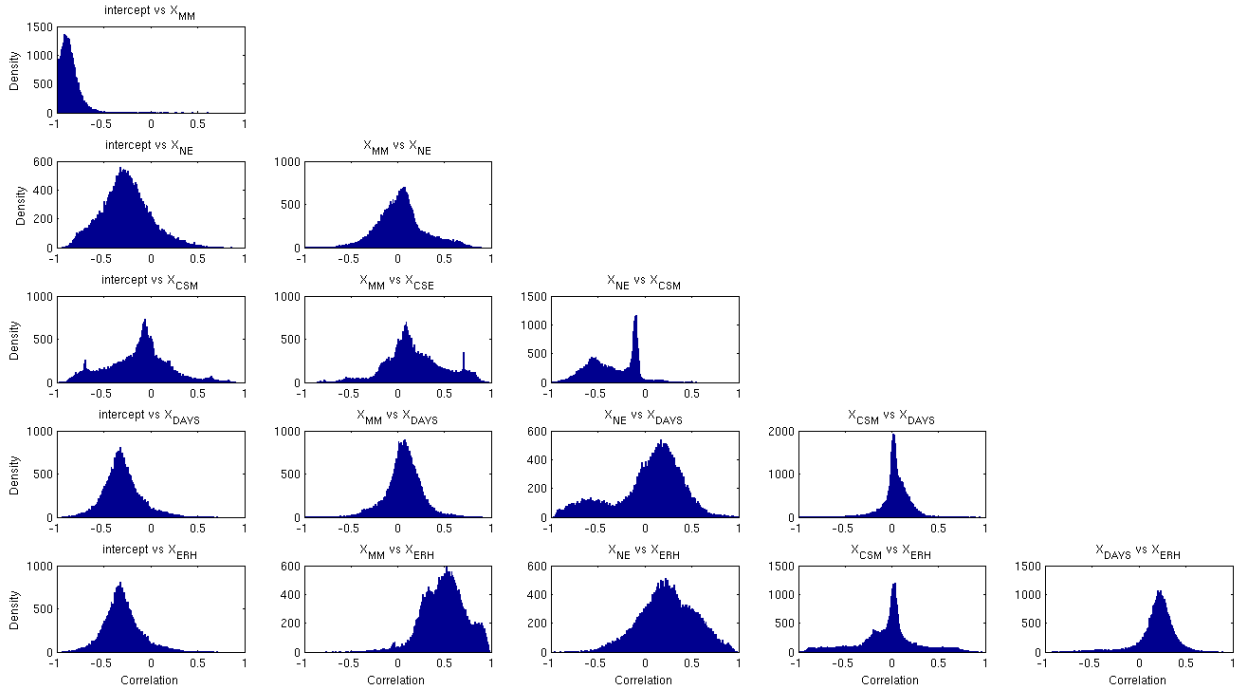

Figure 4.32: Eruption node correlation matrix.

Table 4.14: Logistic model coefficients correlation matrix for eruption node derived from bootstrapping analysis.

Explanatory Variable	Intercept	$\hat{X}_{MM}$	$\hat{X}_{NE}$	$\hat{X}_{CSM}$	$\hat{X}_{DAYS}$	$\hat{X}_{ER}$
Intercept	1.00	-0.89	-0.26	-0.13	-0.29	-0.71
$\hat{X}_{MM}$	-0.89	1.00	-0.04	0.17	0.06	0.51
$\hat{X}_{NE}$	-0.26	-0.04	1.00	-0.33	0.11	0.26
$\hat{X}_{CSM}$	-0.13	0.17	-0.33	1.00	0.04	0.01
$\hat{X}_{DAYS}$	-0.29	0.06	0.11	0.04	1.00	0.21
$\hat{X}_{ER}$	-0.71	0.51	0.26	0.01	0.21	1.00

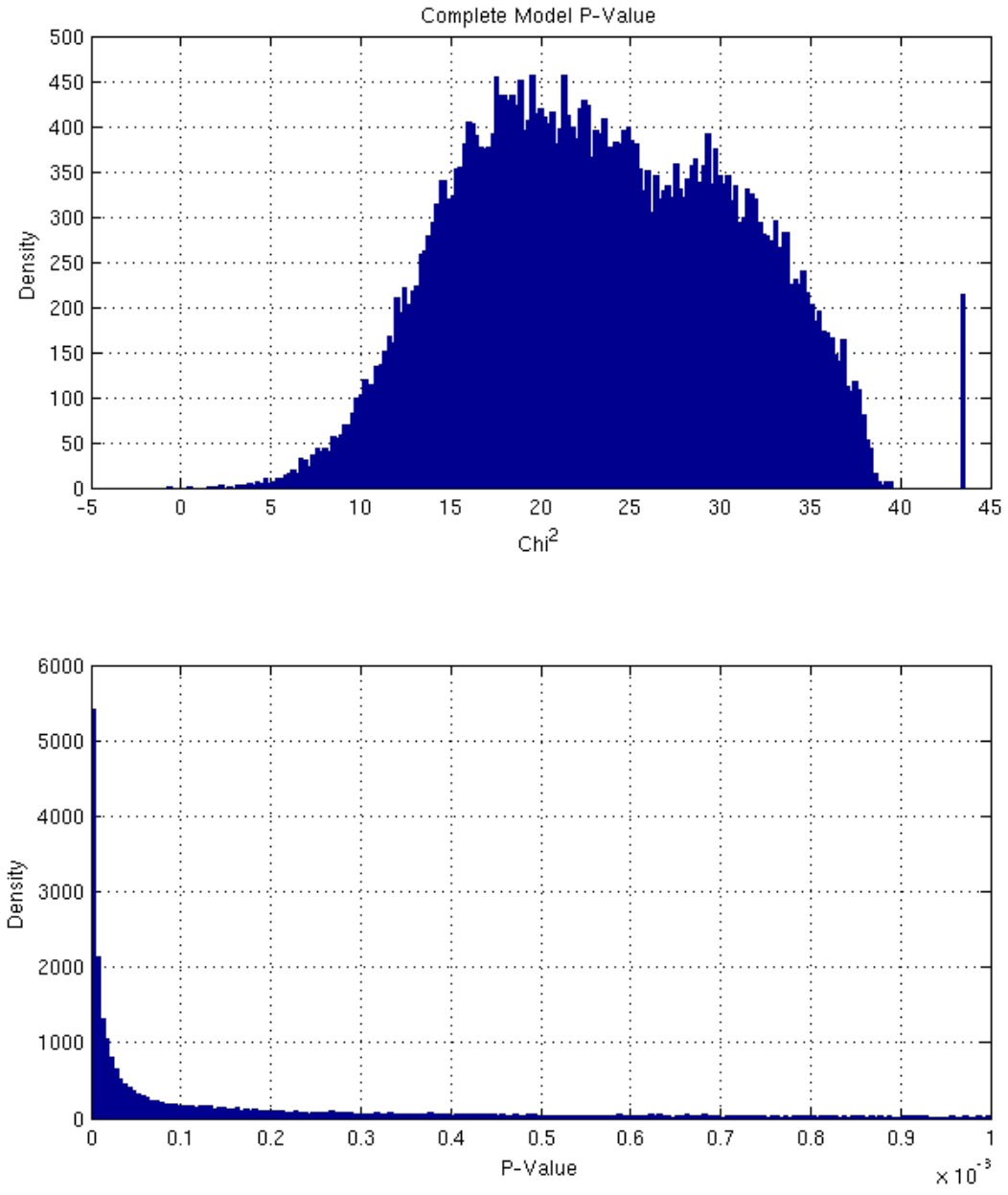

Figure 4.33: Chi squared and P-value distribution for complete eruption model, where the median p-value is approximately 0.014.

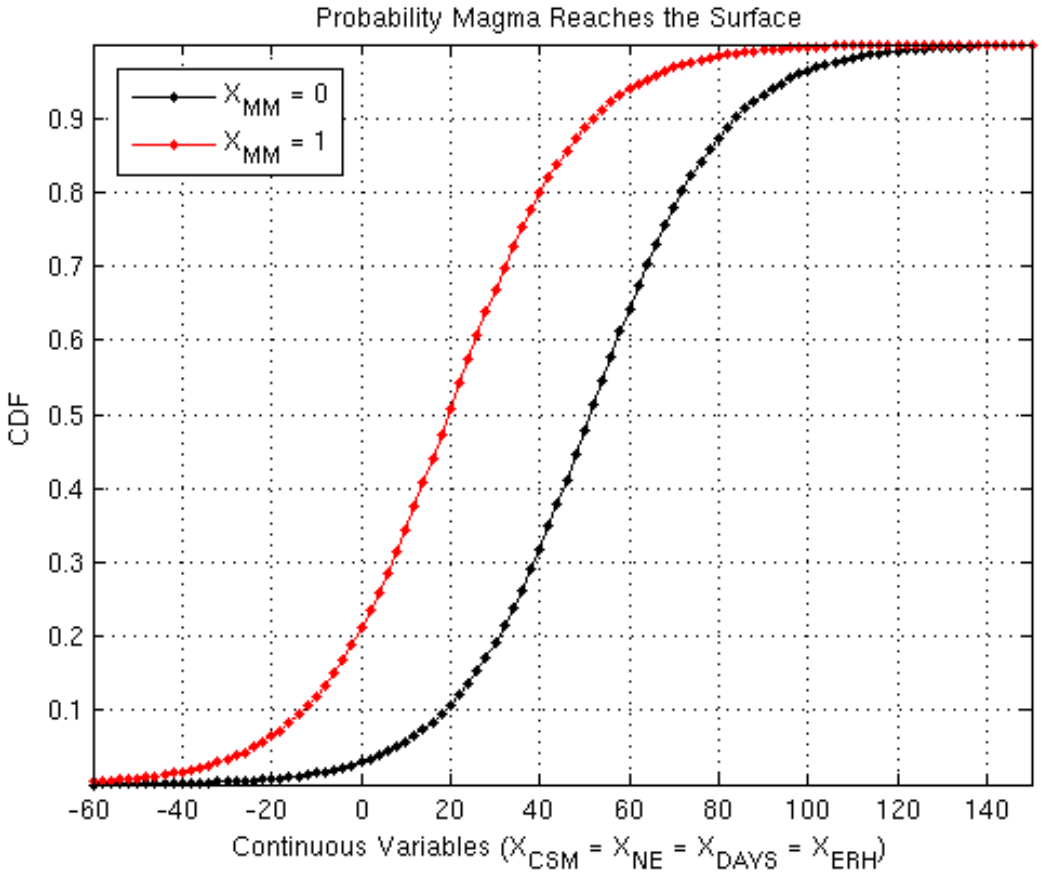

Figure 4.34: Cumulative density functions derived from bootstrapping process illustrating the influence of each of the explanatory variables on the probability estimate, where the black and red curves represents $\hat{X}_{MM} = 0$ and $\hat{X}_{MM} = 1$, respectively.

4.2.13 Node 4: Eruption Intensity Model Via Bootstrapping

Distributions for each of the intensity logistic model coefficients, standard errors, and p-values are shown in Figure 4.35 - Figure 4.44. The revised intensity model is shown in Equation 4.36. Relative weighting of the bootstrapped coefficients is similar to those observed for the non-bootstrapped version. In this case, the $\hat{X}_{CSM}$ coefficient has also been reduced by an order of magnitude. This substantial reduction in weight again suggests the true contribution $\hat{X}_{CSM}$ on the probability of occurrence estimate is not as significant as that proposed by Equation 4.31. Again, the intercept and $\hat{X}_{MM}$ coefficient values have also been modified. The curves shown in Figure 4.47 have remained in the same position, but the difference between them has been reduced by approximately 0.05 as a result of the changes made to the intercept and $\hat{X}_{MM}$ coefficient values. The difference between these curves is now approximately 0.14 when $\hat{X}_{MM}$ changes from 0 to 1 and all other input values are 0.

The median standard error, p-value, and correlation values for each coefficient is shown in Table 4.15. Median P values for the intercept, $\hat{X}_{MM}$, and $\hat{X}_{NE}$ have remained relatively unchanged. However, the median p-values for $\hat{X}_{CSM}$ (increased) and $\hat{X}_{CSM}$ (decreased) have changed slightly. All median p-values are greater than 0.05. Mode p-value estimates are significantly smaller, with the exception of $\hat{X}_{CSM}$ which is again approaching 1.0. Each of the other mode p-value estimates are near the generally accepted statistical significance value. However, the practical significance of $\hat{X}_{CSM}$ is evident in Figure 4.47.

Statistics for the complete model drawn from the likelihood-ratio test are shown in Figure 4.46. The complete model p-value is similar (.007 versus .002) to that shown in Section 4.2.8. This

result suggests the bootstrapped model has approximately a 99.3 percent chance of outperforming the null model (intercept only).

The lower, off-diagonal, correlation matrix components are shown in Figure 4.45 and listed in Table 4.16. The bootstrapping results have not significantly changed the relationships between the coefficients. There is still a strong relationship between the intercept and the $\hat{X}_{MM}$ and $\hat{X}_{NE}$ parameters. It also appears that the relationship between $\hat{X}_{MM}$ and $\hat{X}_{NE}$ has been slightly de-emphasized.

$$\hat{z}_4 = -1.7369 + 0.7924(\hat{X}_{MM}) + 0.1293(\hat{X}_{NE}) - 0.0006(\hat{X}_{CSM}) - 0.0033(\hat{X}_{DAYS}) \quad (4.36)$$

Table 4.15: Statistical summary of logistic model coefficients for intensity node derived from bootstrapping analysis.

Explanatory Variable	Standard Error	p Value (median)	p Value (Mode)
Intercept	1.3550	0.1977	0.0605
$\hat{X}_{MM}$	1.3594	0.3889	0.1118
$\hat{X}_{NE}$	0.0761	0.0835	0.0438
$\hat{X}_{CSM}$	0.0050	0.8719	0.9803
$\hat{X}_{DAYS}$	0.0022	0.1296	0.0352

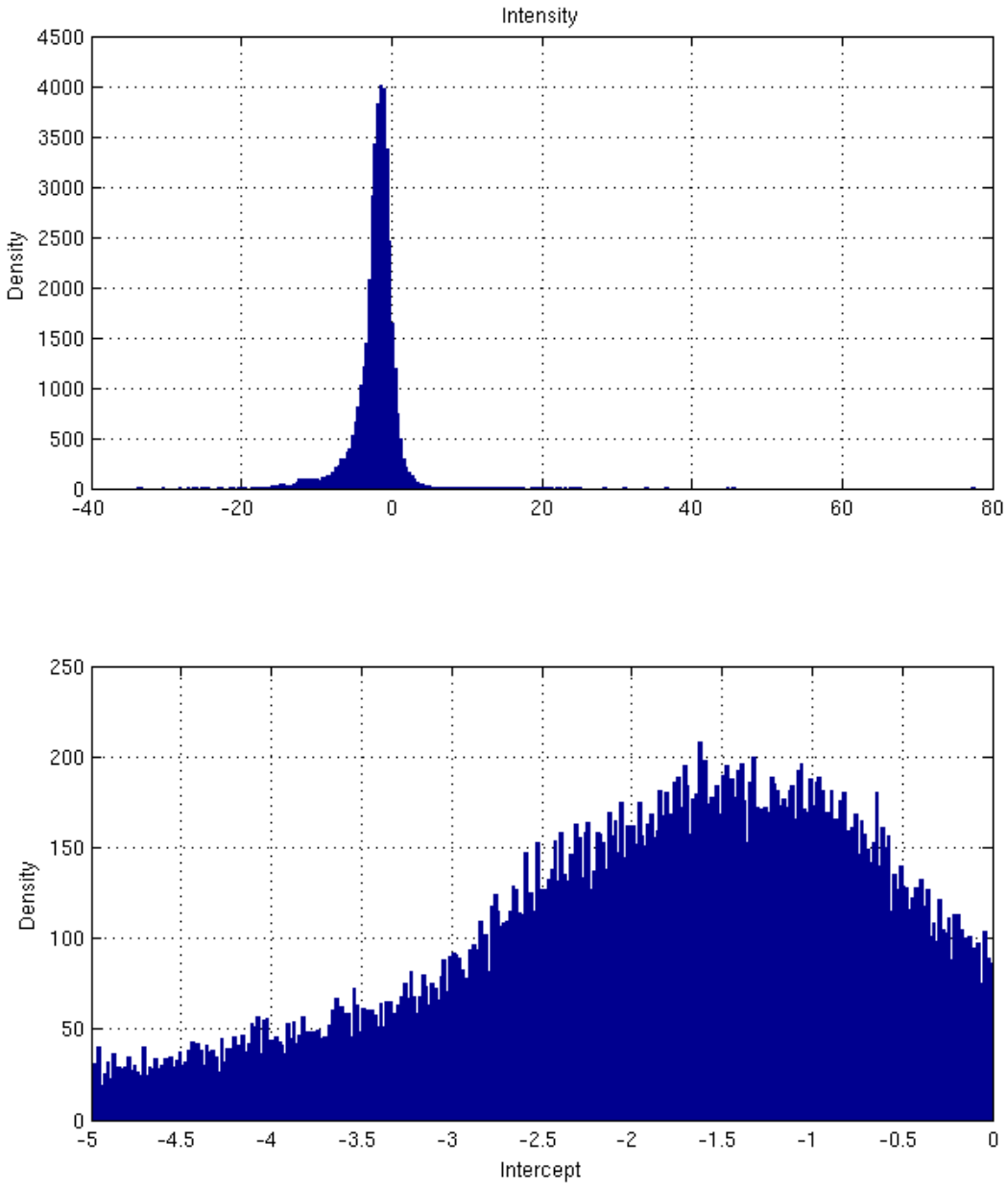

Figure 4.35: Bootstrapping analysis results for the intensity model intercept term, where the top panel is the complete distribution and the bottom panel shows the portion used to derive the intercept value.

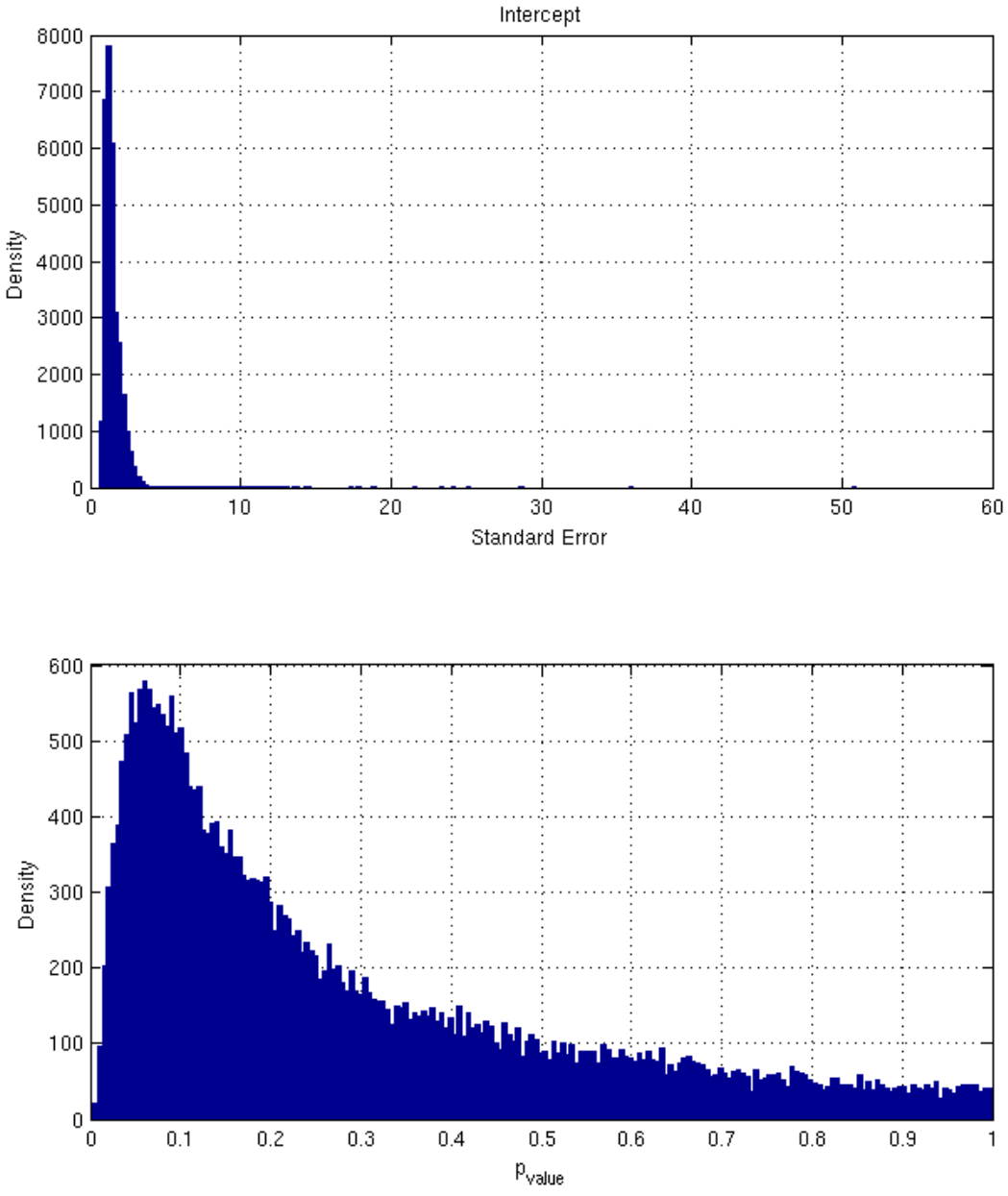

Figure 4.36: P-value distribution for intensity model intrusion parameter.

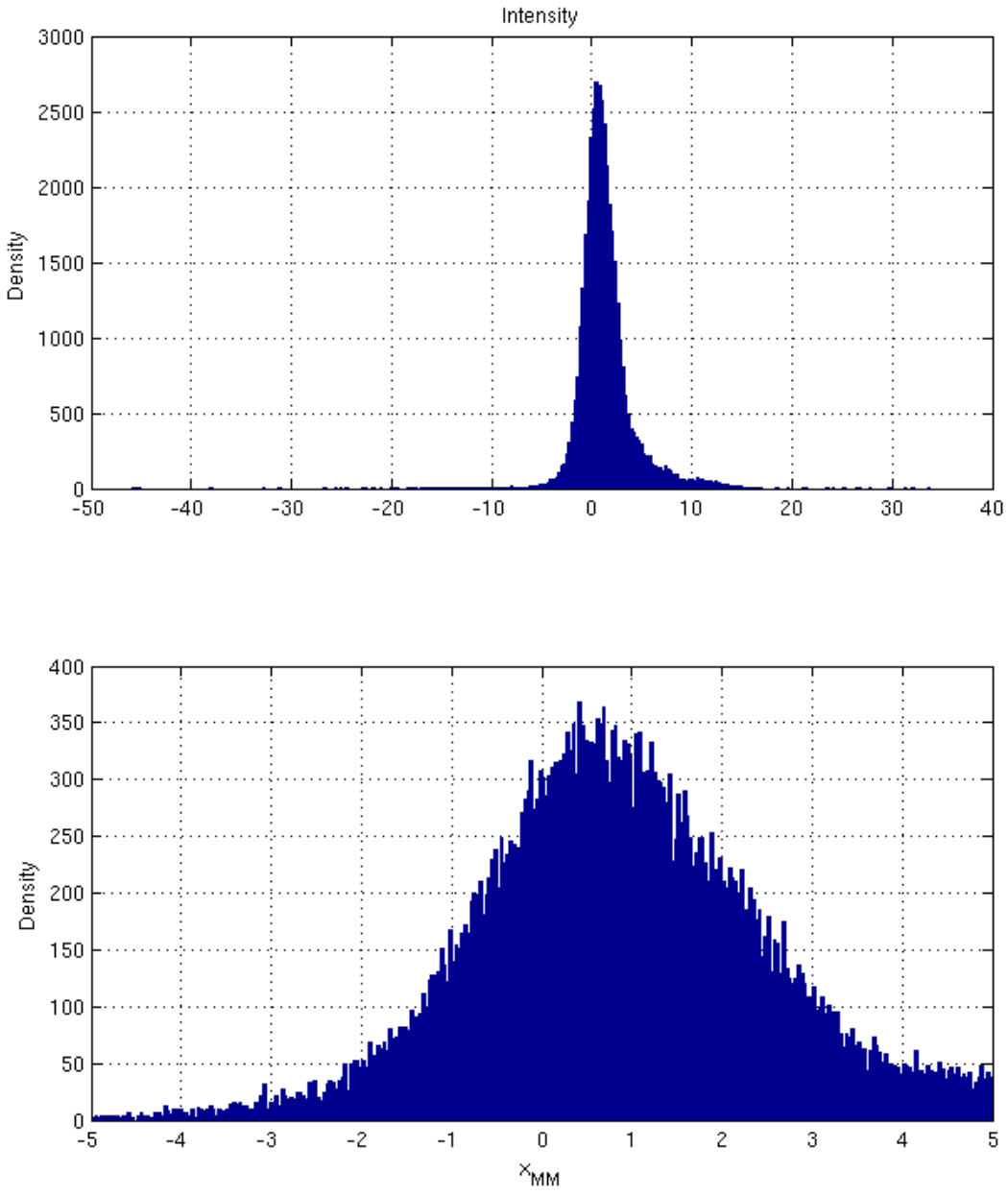

Figure 4.37: Bootstrapping analysis results for the intensity model $\hat{X}_{MM}$ term, where the top panel is the complete distribution and the bottom panel shows the portion used to derive the $\hat{X}_{MM}$ value.

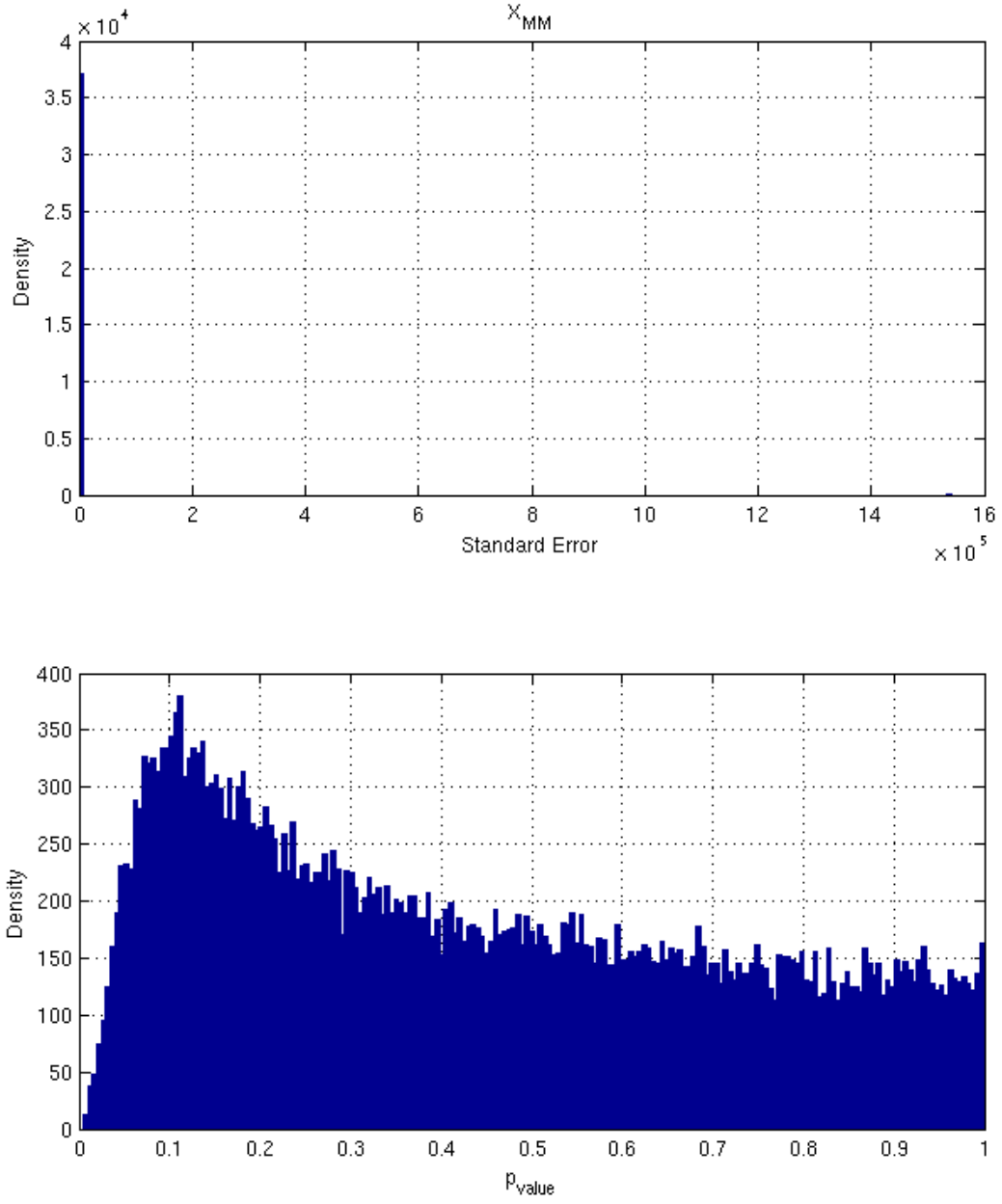

Figure 4.38: P-value distribution for intensity model $\hat{X}_{MM}$ parameter.

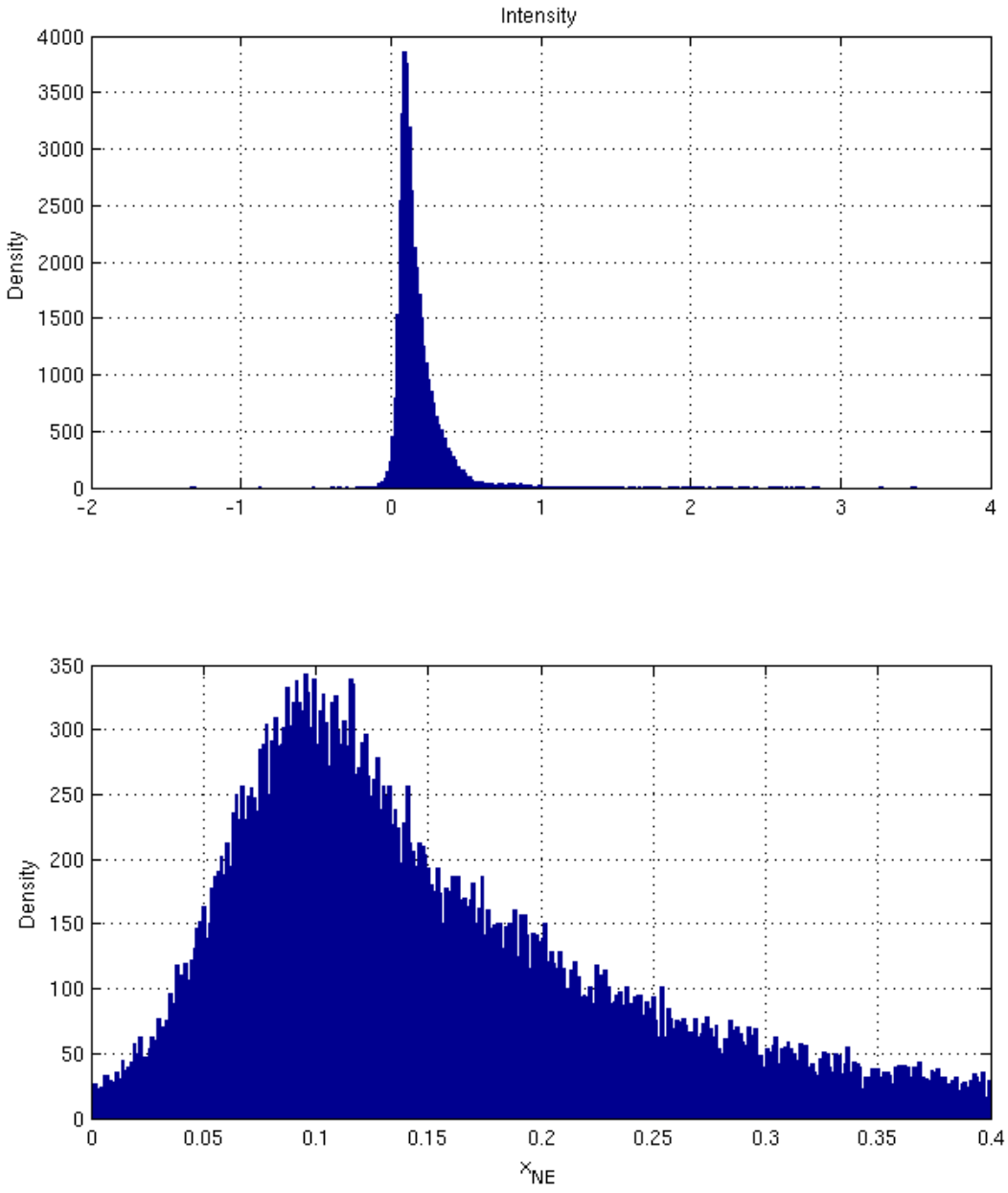

Figure 4.39: Bootstrapping analysis results for the intensity model $\hat{X}_{NE}$ term, where the top panel is the complete distribution and the bottom panel shows the portion used to derive the $\hat{X}_{NE}$ value.

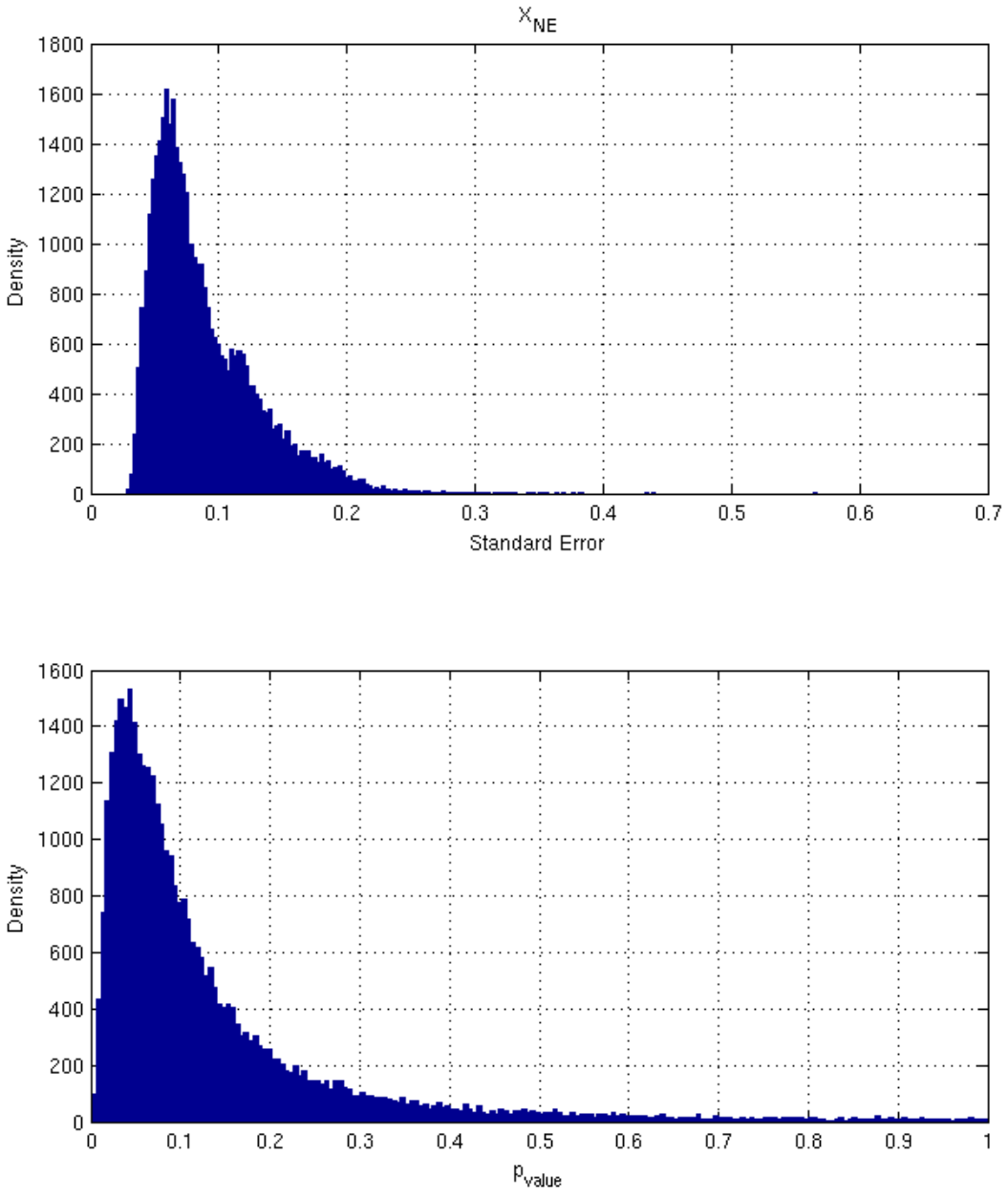

Figure 4.40: P-value distribution for intensity model $\hat{X}_{NE}$ parameter.

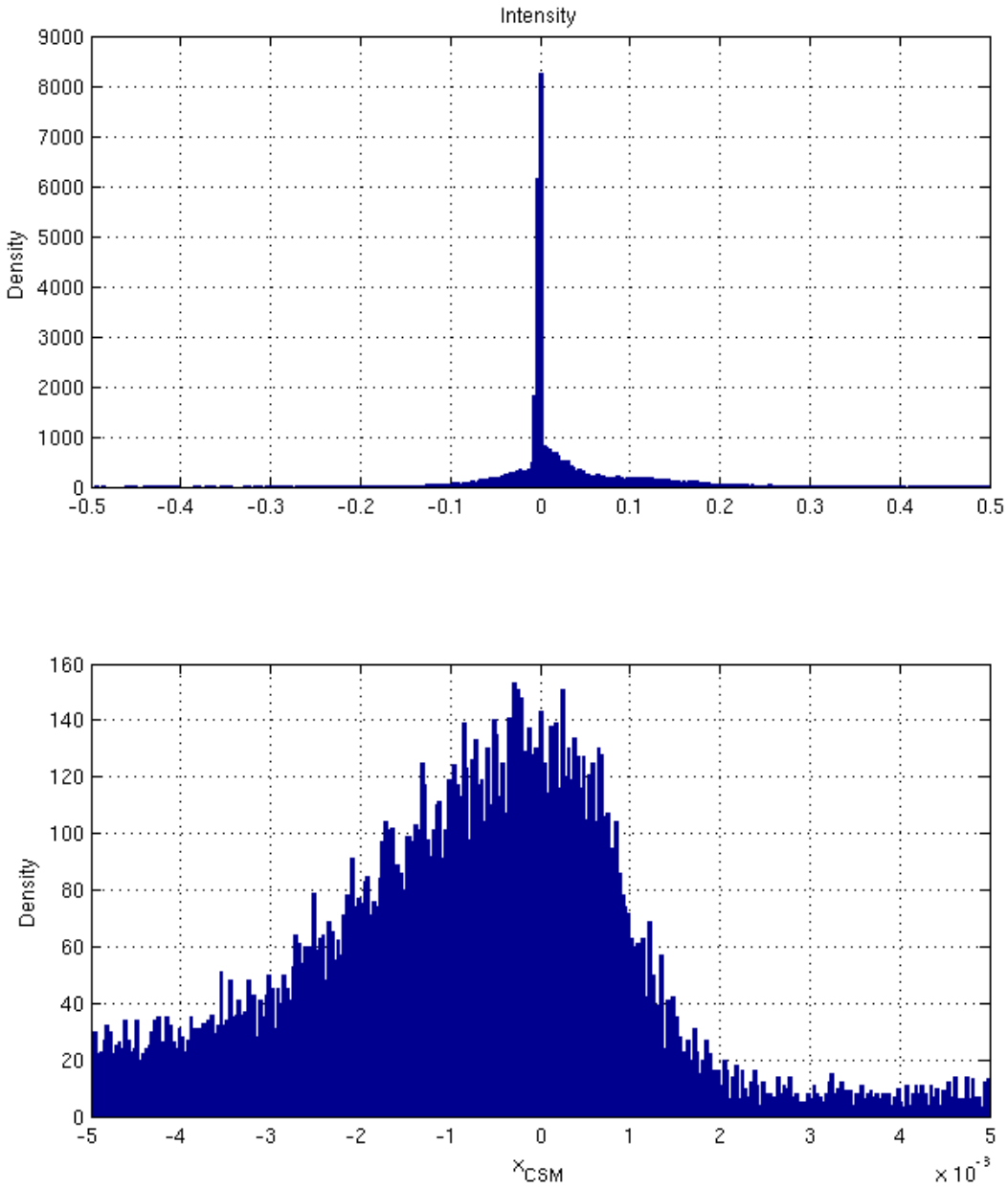

Figure 4.41: Bootstrapping analysis results for the intensity model $\hat{X}_{CSM}$ term, where the top panel is the complete distribution and the bottom panel shows the portion used to derive the $\hat{X}_{CSM}$ value.

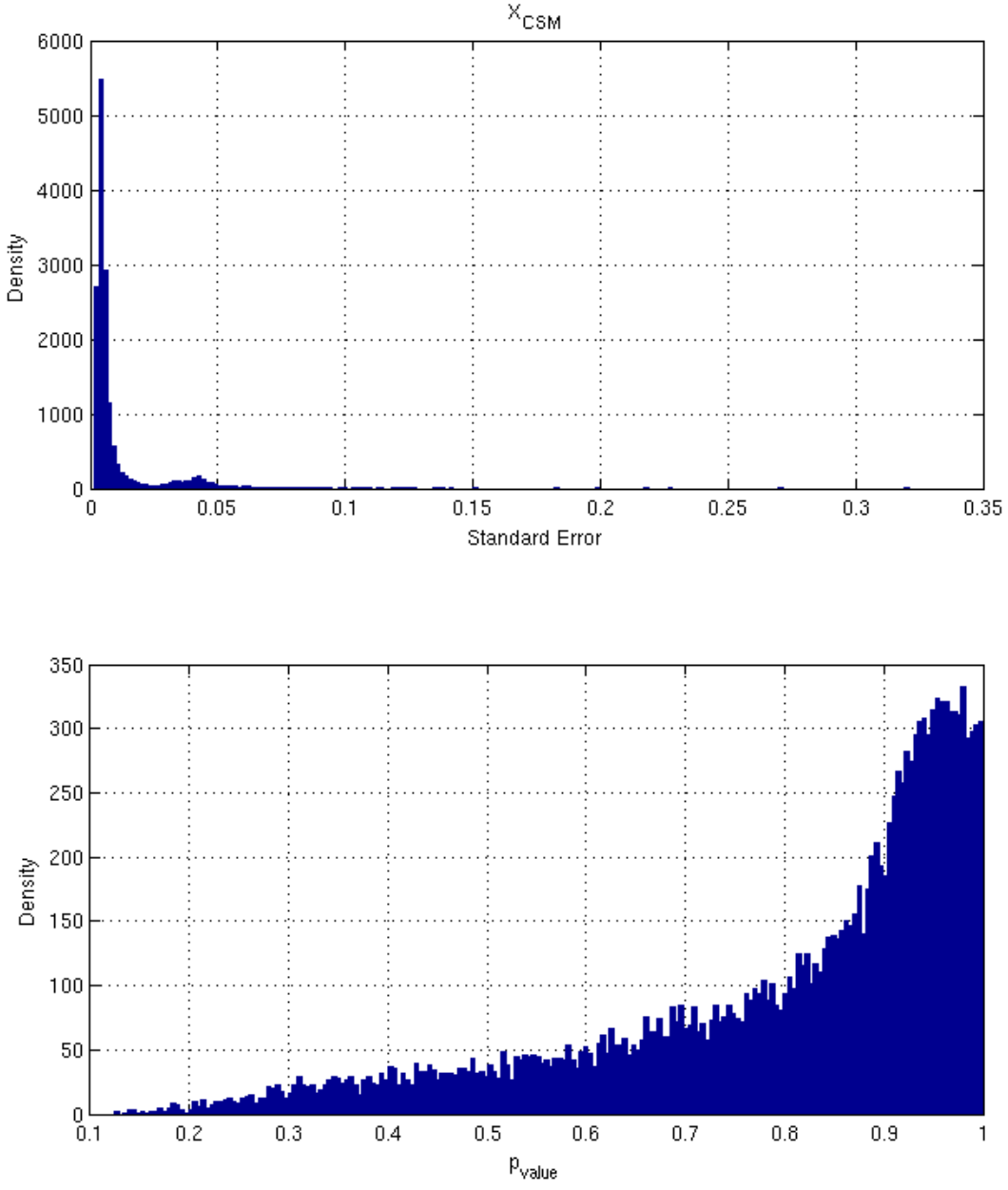

Figure 4.42: P-value distribution for intensity model $\hat{X}_{CSM}$ parameter.

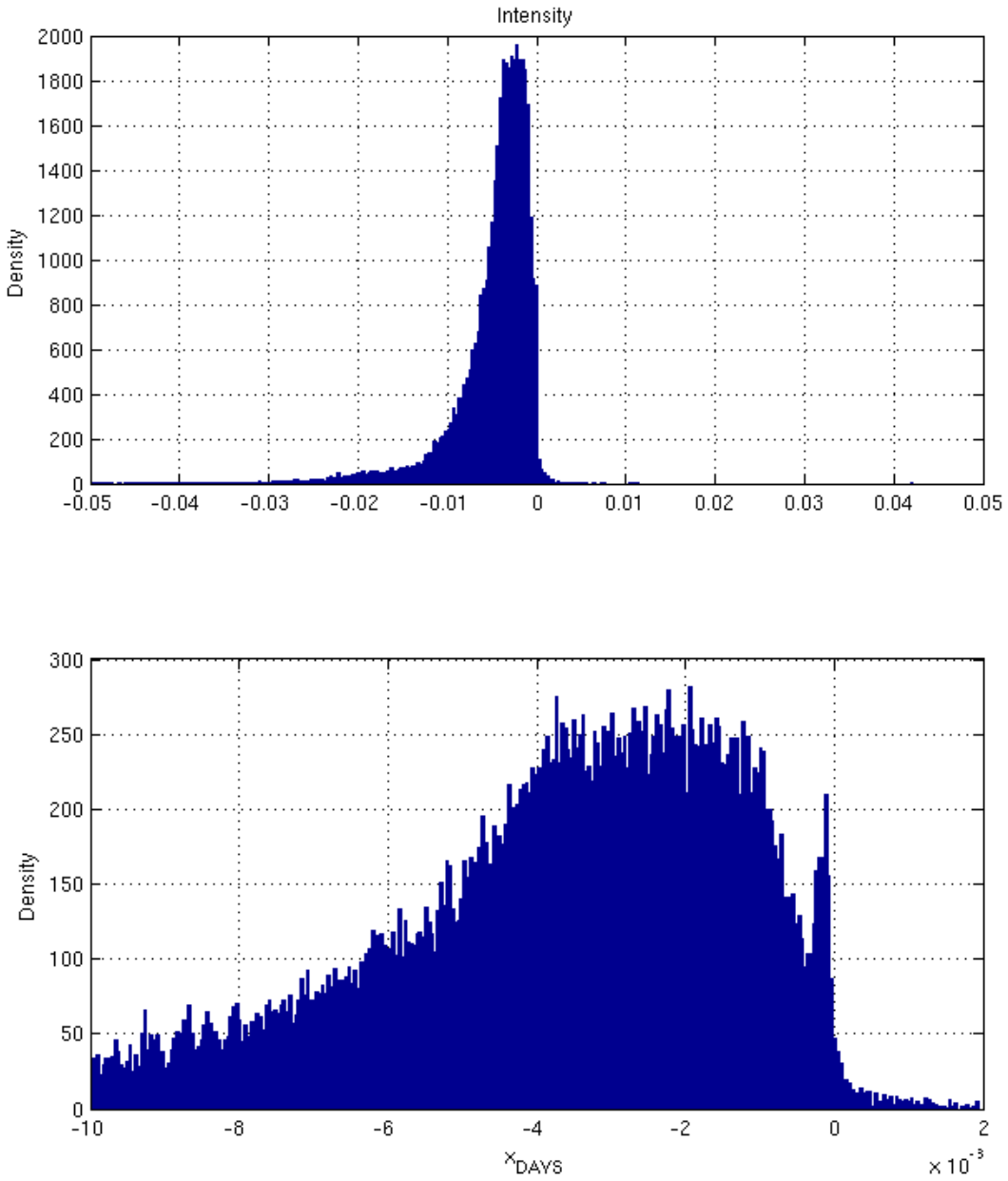

Figure 4.43: Bootstrapping analysis results for the intensity model $\hat{X}_{DAYS}$ term, where the top panel is the complete distribution and the bottom panel shows the portion used to derive the $\hat{X}_{DAYS}$ value.

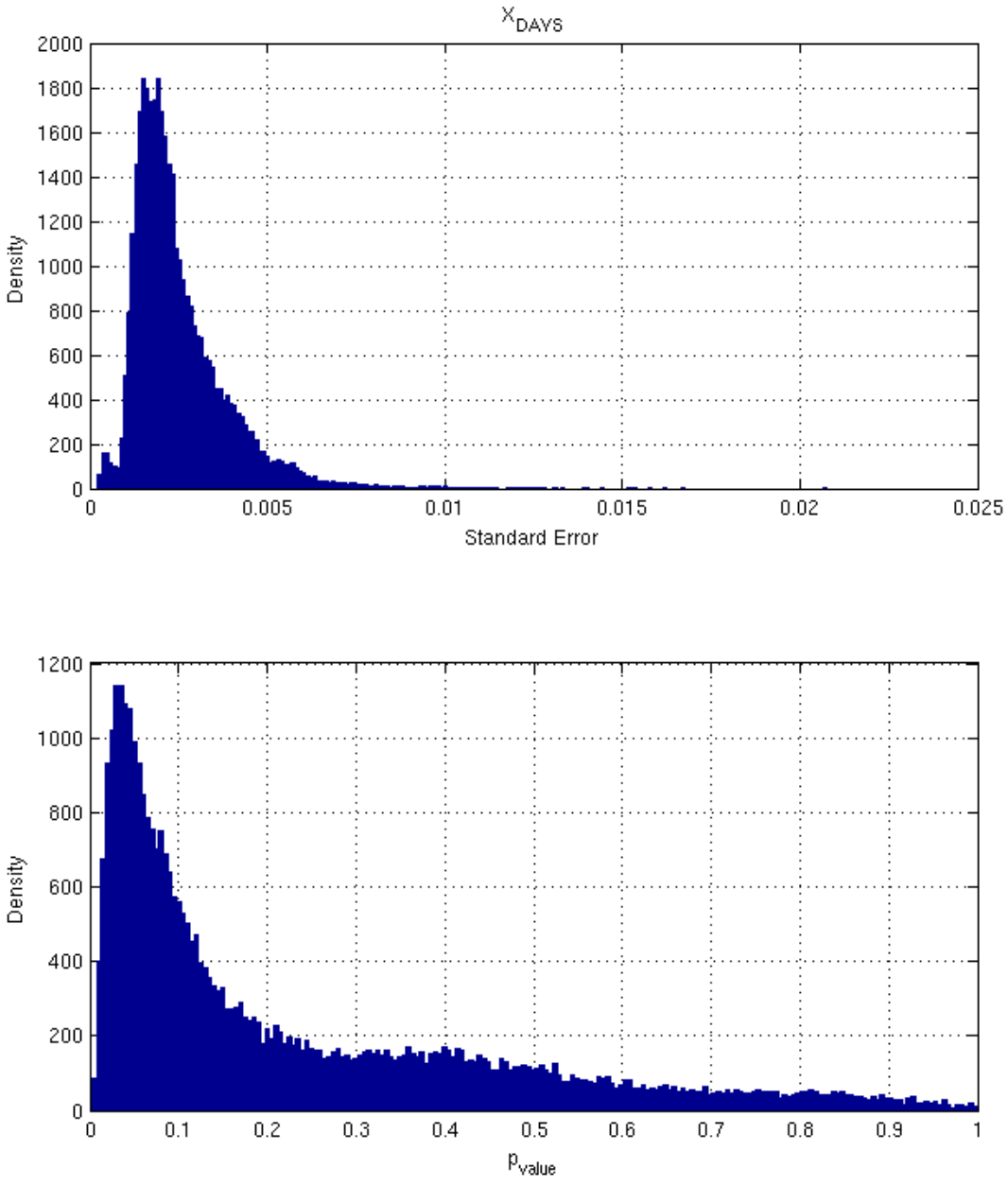

Figure 4.44: P-value distribution for intensity model $\hat{X}_{DAYS}$ parameter.

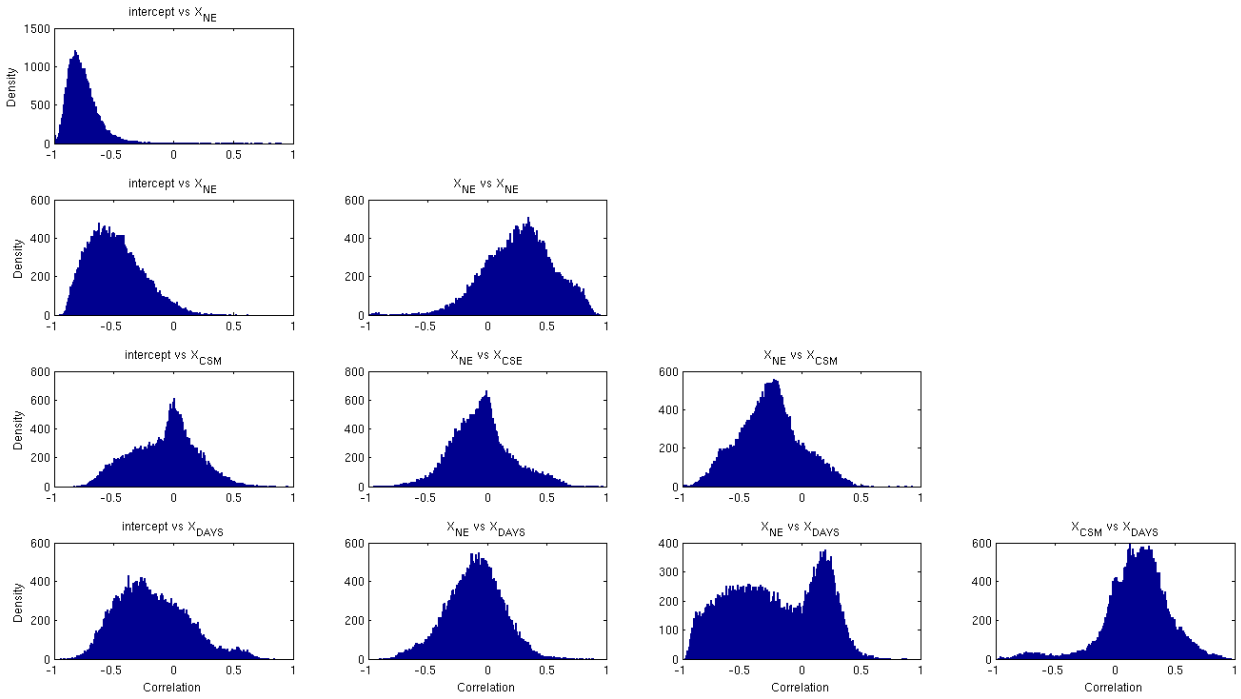

Figure 4.45: Intensity node correlation matrix.

Table 4.16: Logistic model coefficients correlation matrix for intensity node derived from bootstrapping analysis.

Explanatory Variable	Intercept	$\hat{X}_{MM}$	$\hat{X}_{NE}$	$\hat{X}_{CSM}$	$\hat{X}_{DAYS}$
Intercept	1.0	-0.78	-0.51	-0.04	-0.21
$\hat{X}_{MM}$	-0.78	1.0	0.29	0.06	0.10
$\hat{X}_{NE}$	-0.51	0.29	1.0	-0.27	-0.23
$\hat{X}_{CSM}$	-0.04	0.06	-0.27	1.0	0.20
$\hat{X}_{DAYS}$	-0.21	0.10	-0.23	0.20	1.0

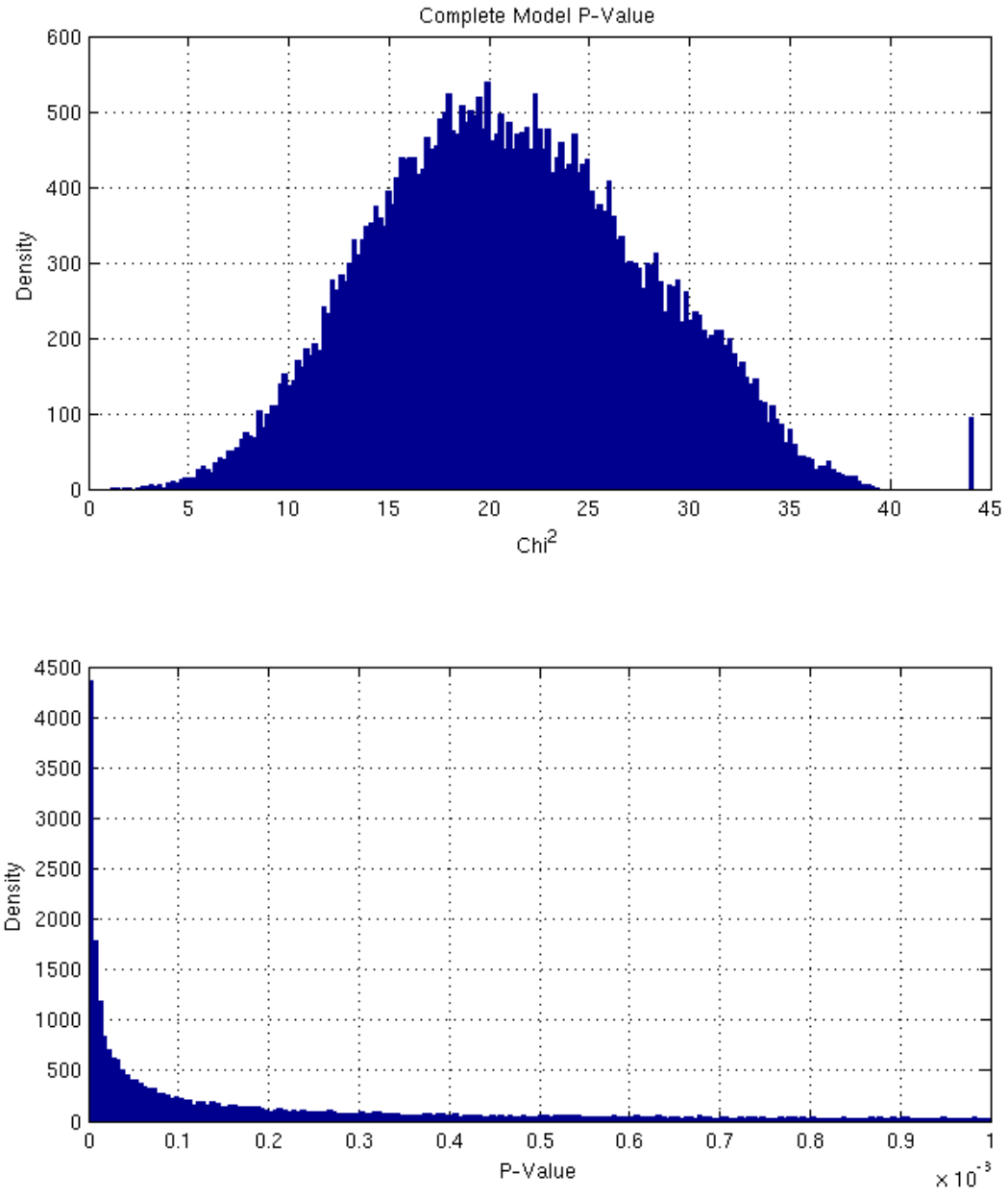

Figure 4.46: Chi squared and P-value distribution for complete intensity model, where the median p-value is approximately 0.007.

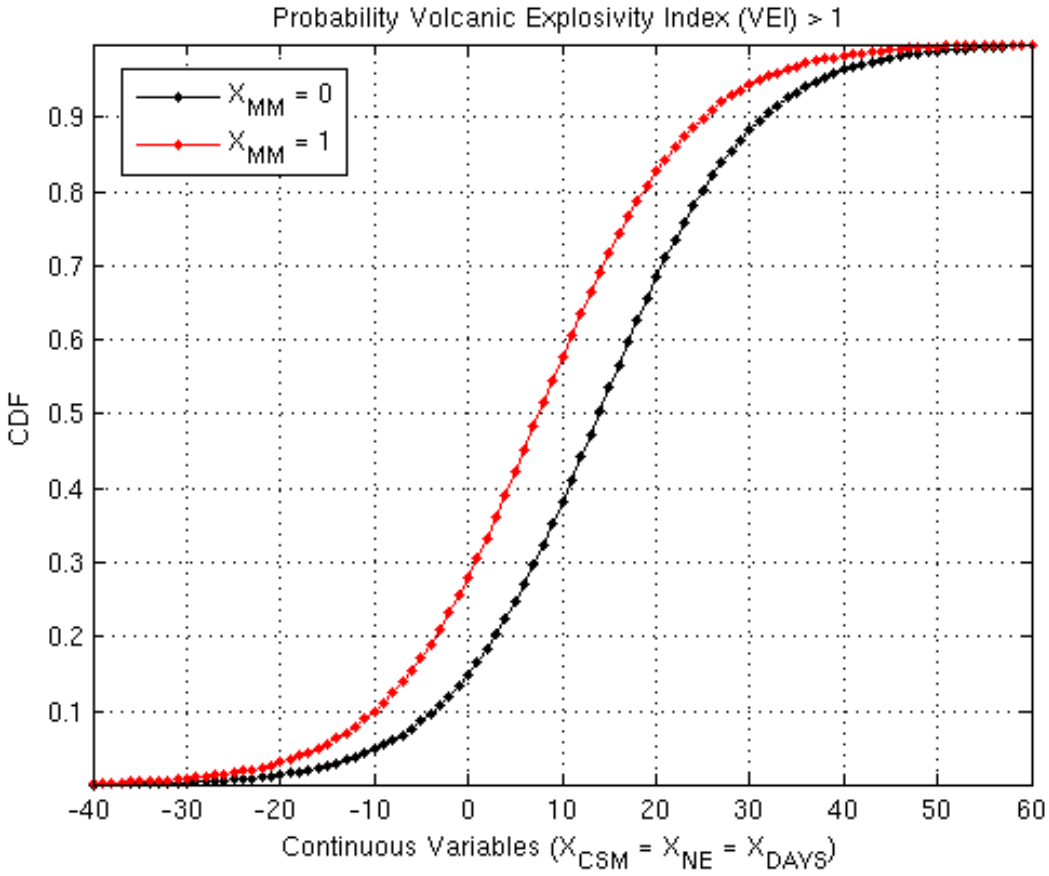

Figure 4.47: Cumulative density functions derived from bootstrapping process illustrating the influence of each of the explanatory variables on the probability estimate, where the black and red curves represents $\hat{X}_{MM} = 0$ and $\hat{X}_{MM} = 1$, respectively.

4.3 Cross Validation

Binary classification problems attempt to categorize the outcome of an event into one of two categories (true or false). This process can result in one of four possible outcomes that are defined as follows:

- *True Positive (TP)*: Predicted outcome matches actual outcome.
- *False Positive (FP)*: Predicted result is true, but the actual result is false (i.e., type I error: valid null hypothesis incorrectly rejected).
- *False Negative (FN)*: Predicted result is false, but the actual result is true (i.e., type II error: invalid null hypothesis not rejected).
- *True Negative (TN)*: Predicted and actual result is false

These classification declarations are typically quantified in a structure known as a confusion matrix which is defined in Table 4.17.

Table 4.17: Confusion matrix for a binary classification algorithm.

Category	Prediction True	Prediction False
Known True	TP	FN
Known False	TF	TN

The quality of a binary classifier is assessed through a receiver operating characteristic (ROC) analysis. A ROC curve is generated by plotting the prediction algorithm's true positive rate (TPR or sensitivity) versus its false positive rate (FPR or 1-specificity). These parameters are

defined as

$$TPR(t) = \frac{TP(t)}{TP(t) + FN(t)} = Sensitivity(t) \tag{4.37}$$

$$FPR(t) = \frac{FP(t)}{TN(t) + FP(t)} = 1 - Specificity(t) \tag{4.38}$$

where the values of TP, FP, FN, and TN are the number of occurrences for a given decision (detection) threshold, t. The algorithms predictive capability is quantified by computing the area under the ROC (AUROC) curve [129], [9]. Its predictive power increases as the AUROC approaches 1.0 and decreases as its approaches 0.0. An AUROC of 0.5 is equivalent to randomly selecting an outcome. The objective of any classification algorithm is to maximum the AUROC. General guidelines for grading the performance of a classification algorithm as a function of AUROC are listed in Table 4.18. The accuracy and precision of the algorithm represent a measure of its ability to consistently estimate the true outcome of an event. These metrics are defined as

$$Accuracy(t) = \frac{TP(t) + TN(t)}{TP(t) + TN(t) + FP(t) + FN(t)} \tag{4.39}$$

$$Precision(t) = \frac{TP(t)}{TP(t) + FP(t)} \tag{4.40}$$

where both expressions are a function of t.

The prediction power of the forecasting algorithm is characterized using a bootstrapped, leave one out (LOO), cross validation approach. This process requires the removal of one sample from the training data, regeneration of the statistical model using the remaining data, and prediction of the outcome of the removed sample via the new model. Cross validation for each forecasting

Table 4.18: ROC assessment guidelines for a binary prediction algorithm utilizing logistic regression [9].

AUROC	Predictive Capability
0.90 - 1.00	Excellent Predictive Power
0.80 - 0.90	Good Predictive Power
0.70 - 0.80	Fair Predictive Power
0.60 - 0.70	Poor Predictive Power
0.00 - 0.60	No Predictive Power

stage was conducted using 50,000 bootstrapped datasets. Before each iteration one event is removed from the bootstrapped dataset selection process for validation purposes. This is repeated for each sample in the training set for a collection of detection thresholds that range between 0.0 and 1.0. If the resulting probability is greater than or equal to the threshold, the outcome of the event is declared to be true. If the probability is less than the threshold, the outcome of the event is declared to be false. Since the outcome of each of the training events is known, the number of TP, TN, FP, and FN detections can be determined as a function of the detection threshold, and plotted in ROC space.

An optimum decision line (detection threshold) for each stage of the algorithm is determined from the point on the ROC curve that is closest to the point of perfect classification (0,1). This threshold represents the best trade off between the TPR and FPR. Optimum detection thresholds are also used to derive accuracy and precision metrics for each stage of the algorithm.

4.3.1 Logistic Models

The bootstrapped LOO cross validation for each logistic model was conducted using a set of unique datasets. This allows for an independent and robust assessment of each model. ROC curves and AUROC estimates for the intrusion, eruption, and intensity logistic models are shown in Figure 4.48, Figure 4.50, and Figure 4.52. The results suggest the models have good predictive capabilities.

The number of TP, TN, FP, and FN detections at the optimized thresholds for each node are listed in Table 4.19 - Table 4.21. The validation results show the optimum decision threshold decreases across the nodes. In addition, values of TP and FN are decreasing, while the values of FP and TN are increasing across the nodes. The FPR estimates tend to increase, while the TPR estimates are fluctuating from node to node. Figure 4.49, Figure 4.51, and Figure 4.53 illustrate the accuracy and precision calculations for each of the ROC runs. These plots show accuracy estimates are fluctuating and precision values are decreasing at the optimized decision threshold across each node.

Table 4.19: Confusion matrix for the intrusion node with a decision threshold of 0.83, where the number of properly constrained GLMR run is 37649.

Category	Prediction True	Prediction False
Known True	18896	8401
Known False	2718	7634

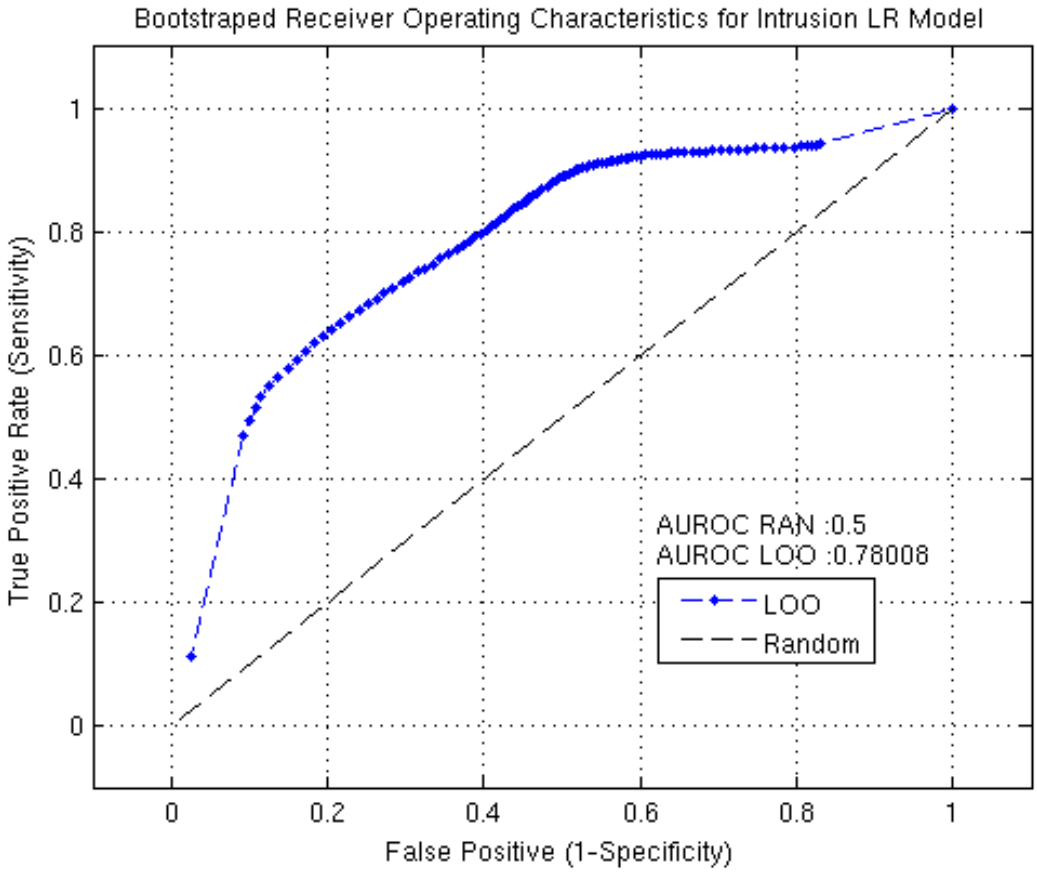

Figure 4.48: Receiver Operating Characteristics for Equation 4.34. The AUROC value of approximately 0.78 suggests this node will have fair to good predictive capabilities. A TPR and FPR of 69% and 26% are obtained at the optimized decision threshold (0.83)

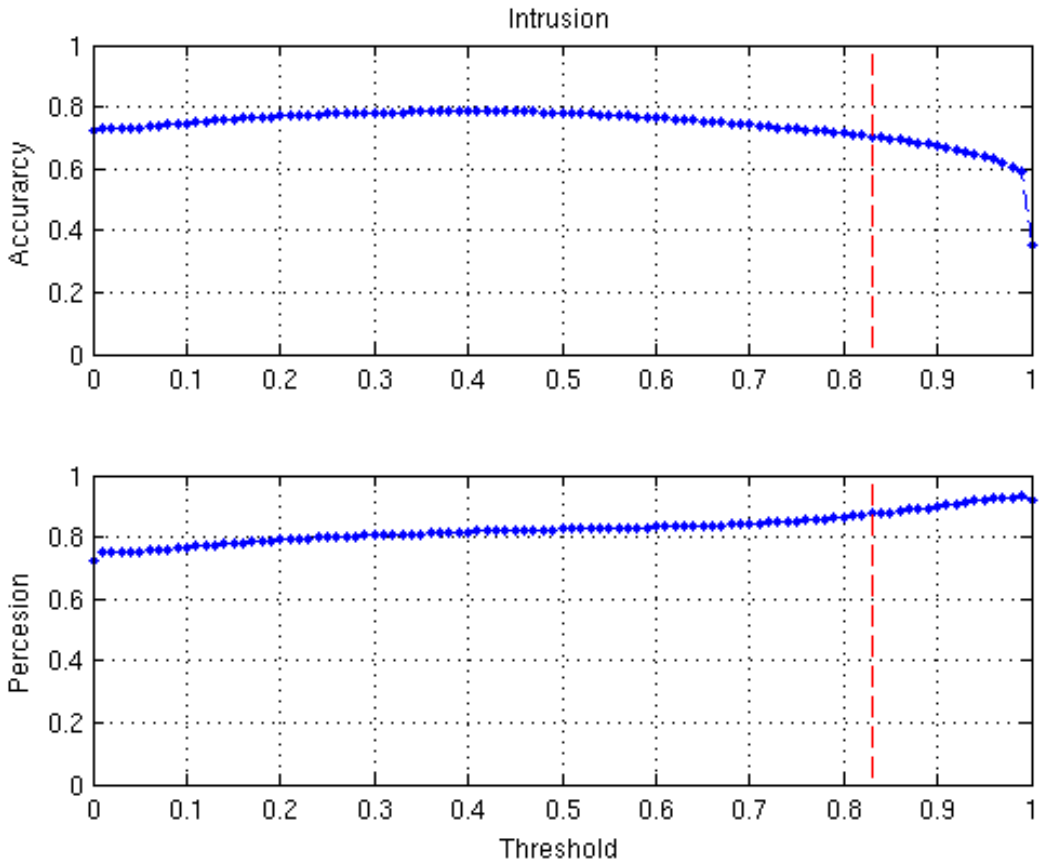

Figure 4.49: Accuracy and precision estimates for the intrusion logistic model, where an accuracy and precision of approximately 70% and 87% are obtained at the optimized decision threshold of 0.83 (shown in red).

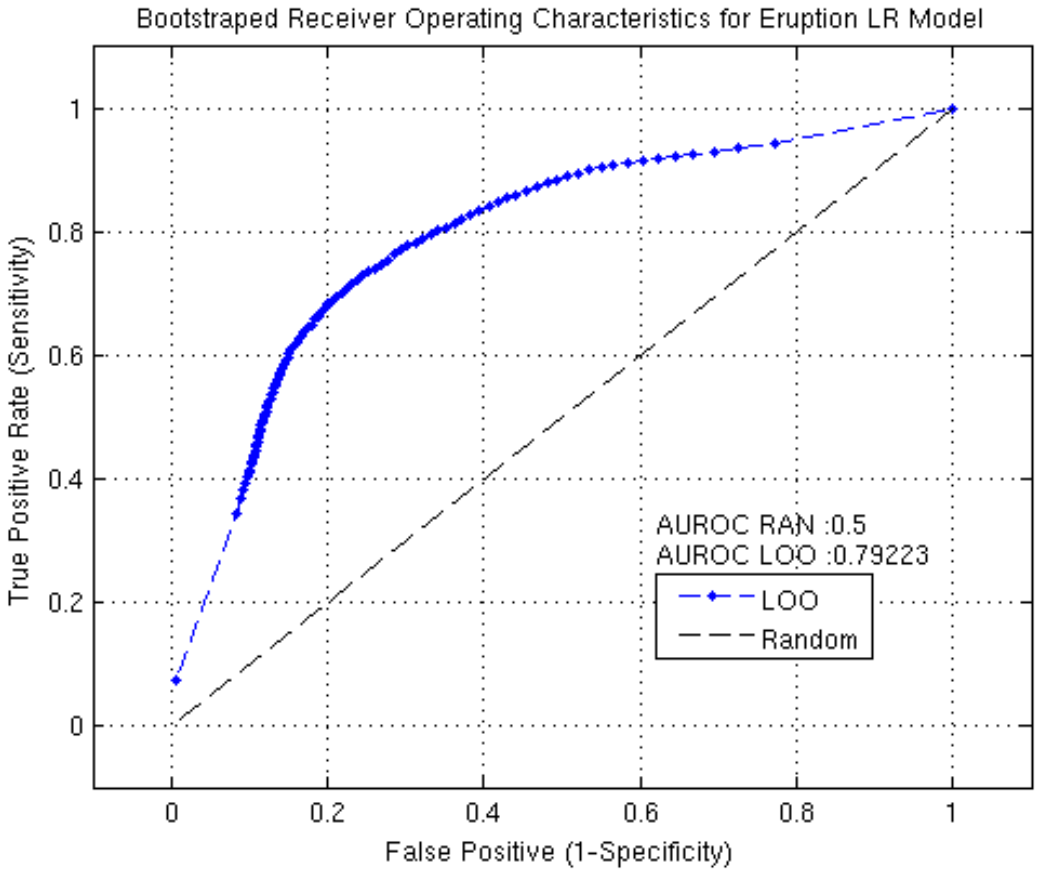

Figure 4.50: Receiver Operating Characteristics for Equation 4.35. The AUROC value of approximately 0.79 suggests this node will have fair to good predictive capabilities. A TPR and FPR of 73% and 25% are obtained at the optimized decision threshold (0.38)

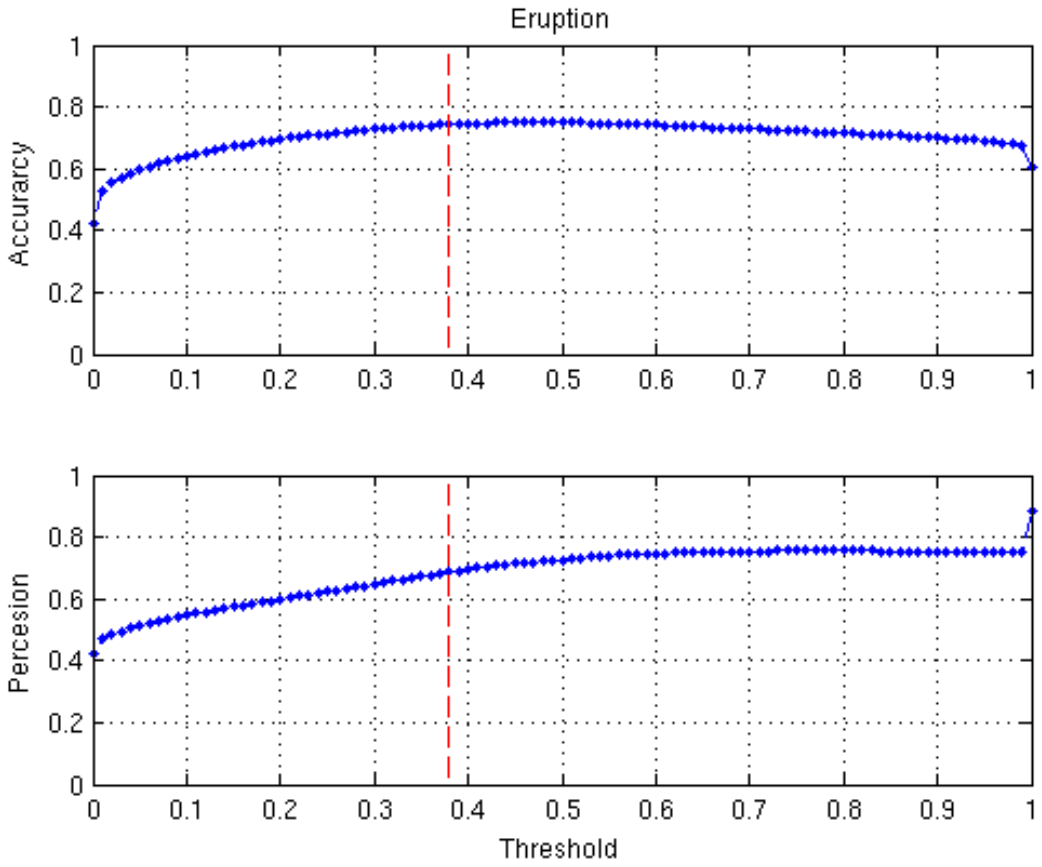

Figure 4.51: Accuracy and precision estimates for the eruption logistic model, where an accuracy and precision of approximately 74% and 69% are obtained at the optimized decision threshold of 0.38 (shown in red).

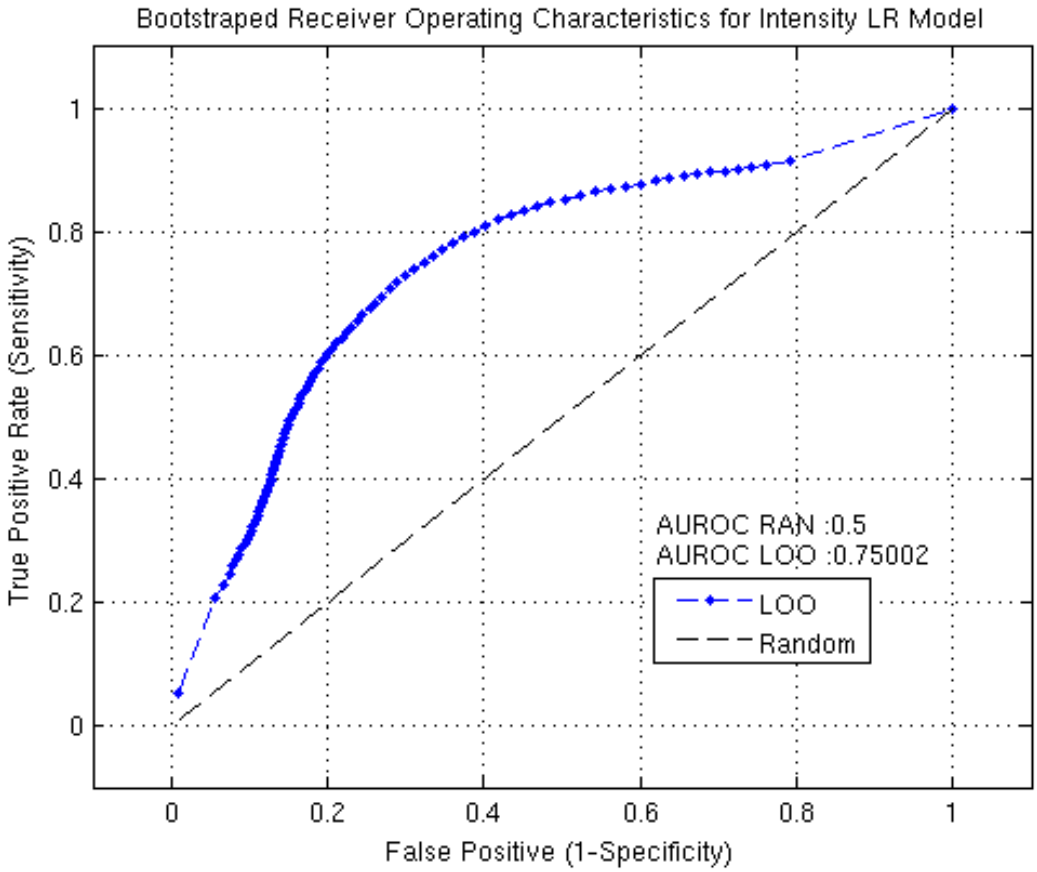

Figure 4.52: Receiver Operating Characteristics for Equation 4.36. The AUROC value of approximately 0.75 suggests this node will have fair to good predictive capabilities. A TPR and FPR of 72% and 29% are obtained at the optimized decision threshold (0.31)

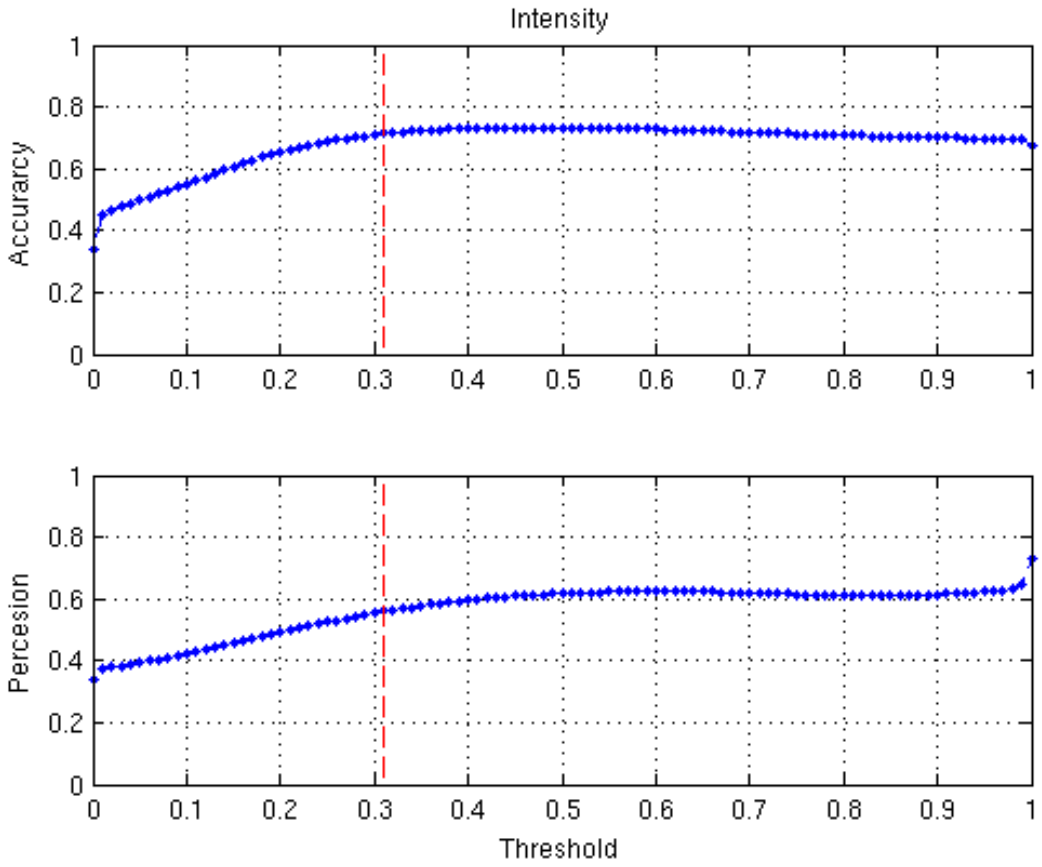

Figure 4.53: Accuracy and precision estimates for the intensity logistic model, where an accuracy and precision of approximately 71% and 56% are obtained at the optimized decision threshold of 0.31 (shown in red).

Table 4.20: Confusion matrix for the eruption node with a decision threshold of 0.38, where the number of properly constrained GLMR run is 32476.

Category	Prediction True	Prediction False
Known True	10025	3732
Known False	4589	14130

Table 4.21: Confusion matrix for the intensity node with a decision threshold of 0.31, where the number of properly constrained GLMR run is 35340.

Category	Prediction True	Prediction False
Known True	8614	3342
Known False	6759	16625

4.3.2 Event Tree Conditional Probabilities: Nodes 2-4

Cross validation of the conditional probability estimates for each node was conducted using the same bootstrapped LOO dataset. This was done to insure the assessment assumes statistical dependence across all nodes. Therefore, only the logistic models resulting from properly constrained GLMR's runs, across all nodes, are used in the validation. ROC curves and AUROC estimates for the intrusion, eruption, and intensity conditional probabilities are shown in Figure 4.54, Figure 4.56, and Figure 4.58. AUROC estimates for the intrusion, eruption, and intensity nodes are 0.78, 0.80, and 0.77, which suggest the conditional probabilities have good prediction capability. In this case, the shape of each curve is similar to those derived from the individual logistic models.

The number of TP, TN, FP, and FN detections at the optimized thresholds for each node are listed in Table 4.22 - Table 4.24. Several interesting trends are observed across the nodes. First, the optimized detection thresholds are also decreasing across the nodes. Next, the number of TP and FN detections are decreasing, while the FP and TN detections are increasing at each node. Finally,

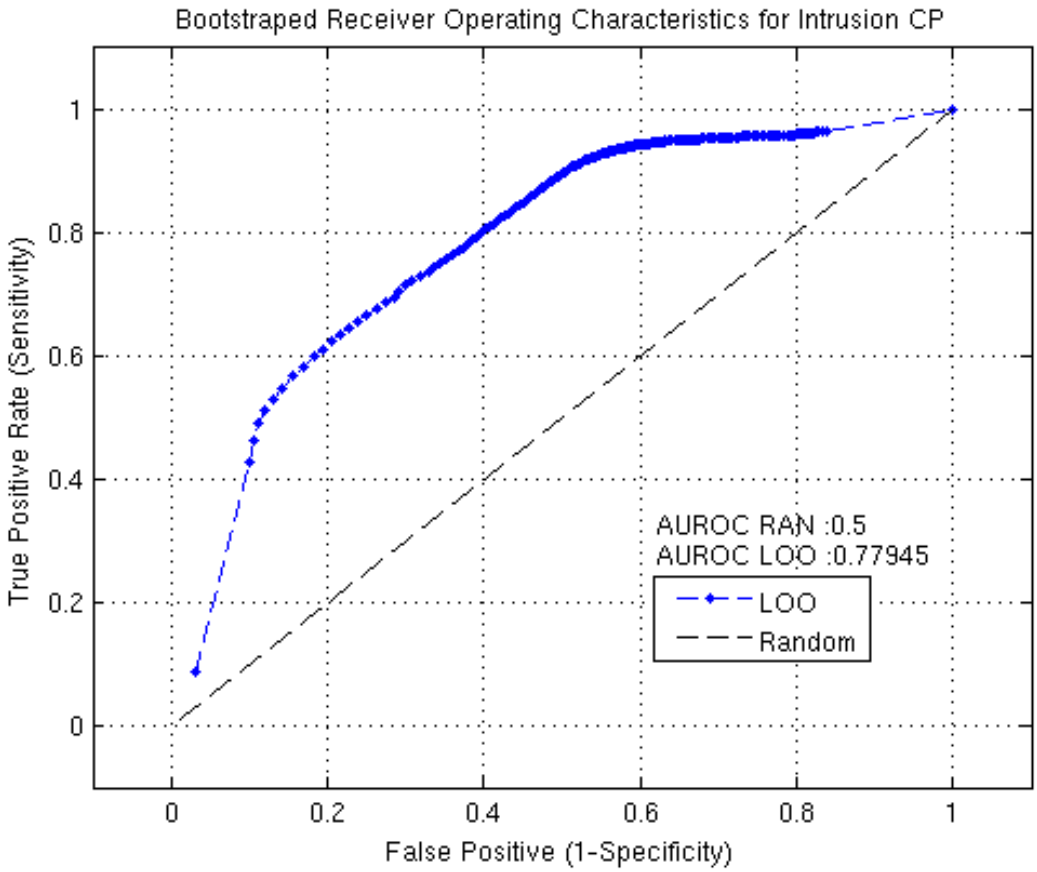

Figure 4.54: Receiver Operating Characteristics for the intrusion conditional probability. The AUROC value of approximately 0.78 suggests this node will have fair to good predictive capabilities. A TPR and FPR of 70% and 29% are obtained at the optimized decision threshold (0.91)

the FPR and TPR are increasing and decreasing, respectively. Figure 4.55, Figure 4.57, and Figure 4.59 illustrate the accuracy and precision calculations for each of the ROC runs. These plots also show accuracy estimates are fluctuating, while the precision values are decreasing at the optimized decision threshold across each node.

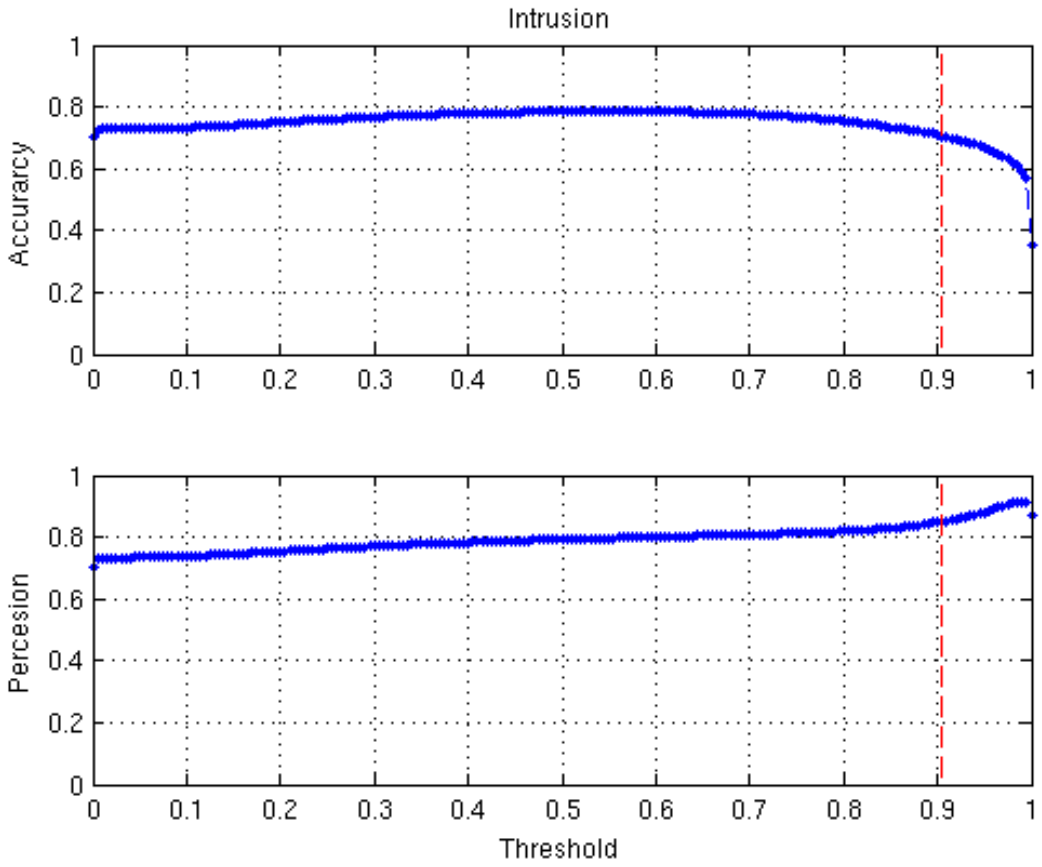

Figure 4.55: Accuracy and precision estimates for the intrusion logistic model, where an accuracy and precision of approximately 71% and 85% are obtained at the optimized decision threshold of 0.91 (shown in red).

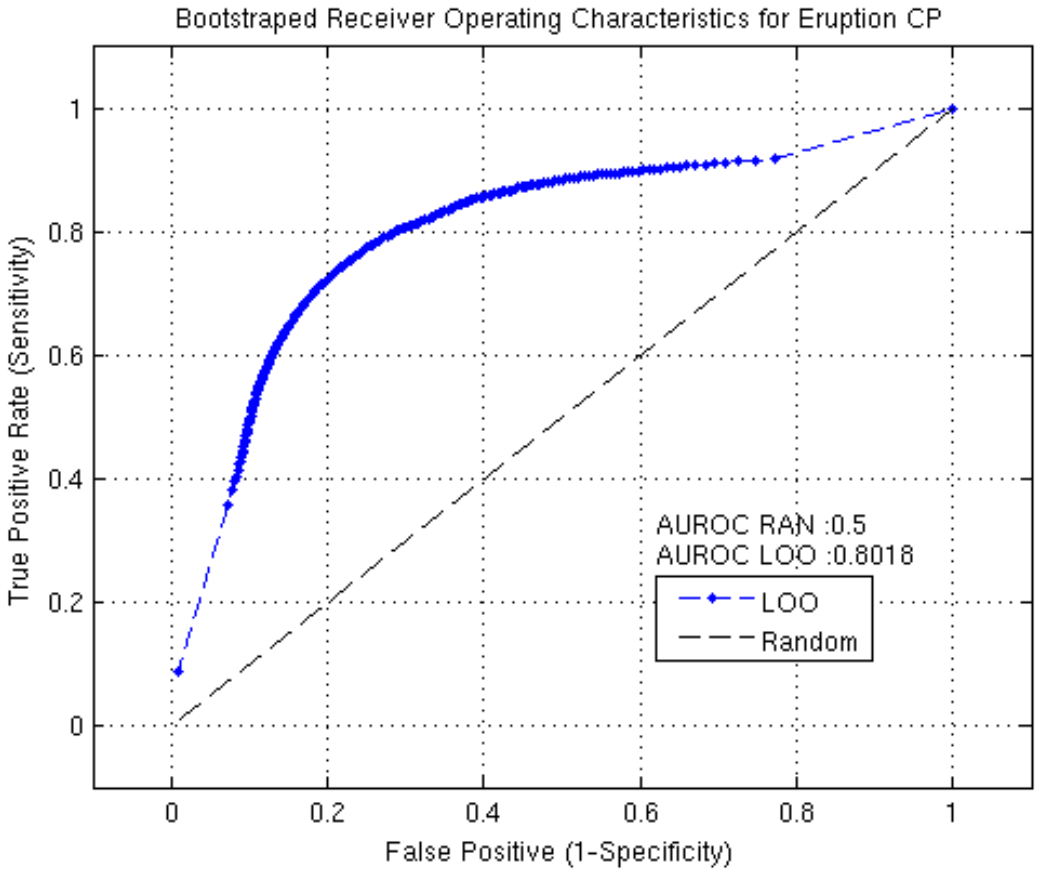

Figure 4.56: Receiver Operating Characteristics for the eruption conditional probability. The AUROC value of approximately 0.80 suggests this node will have fair to good predictive capabilities. A TPR and FPR of 76% and 24% are obtained at the optimized decision threshold (0.52)

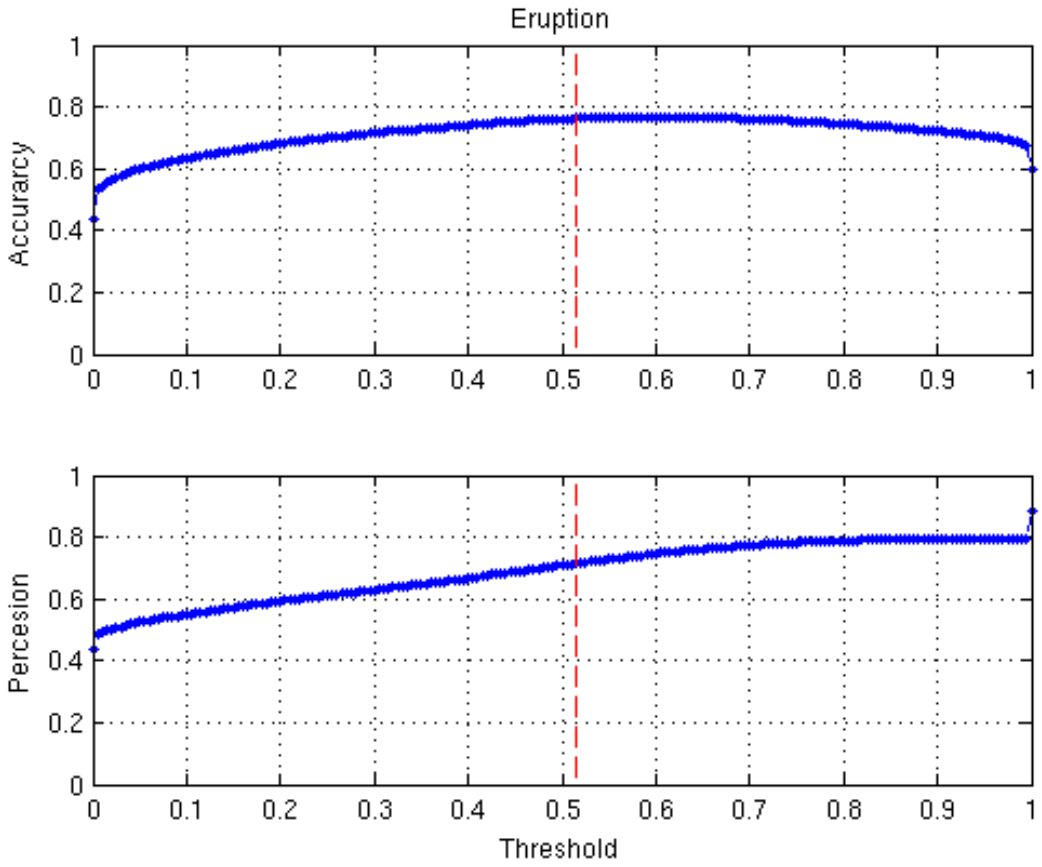

Figure 4.57: Accuracy and precision estimates for the eruption logistic model, where an accuracy and precision of approximately 76% and 72% are obtained at the optimized decision threshold of 0.52 (shown in red).

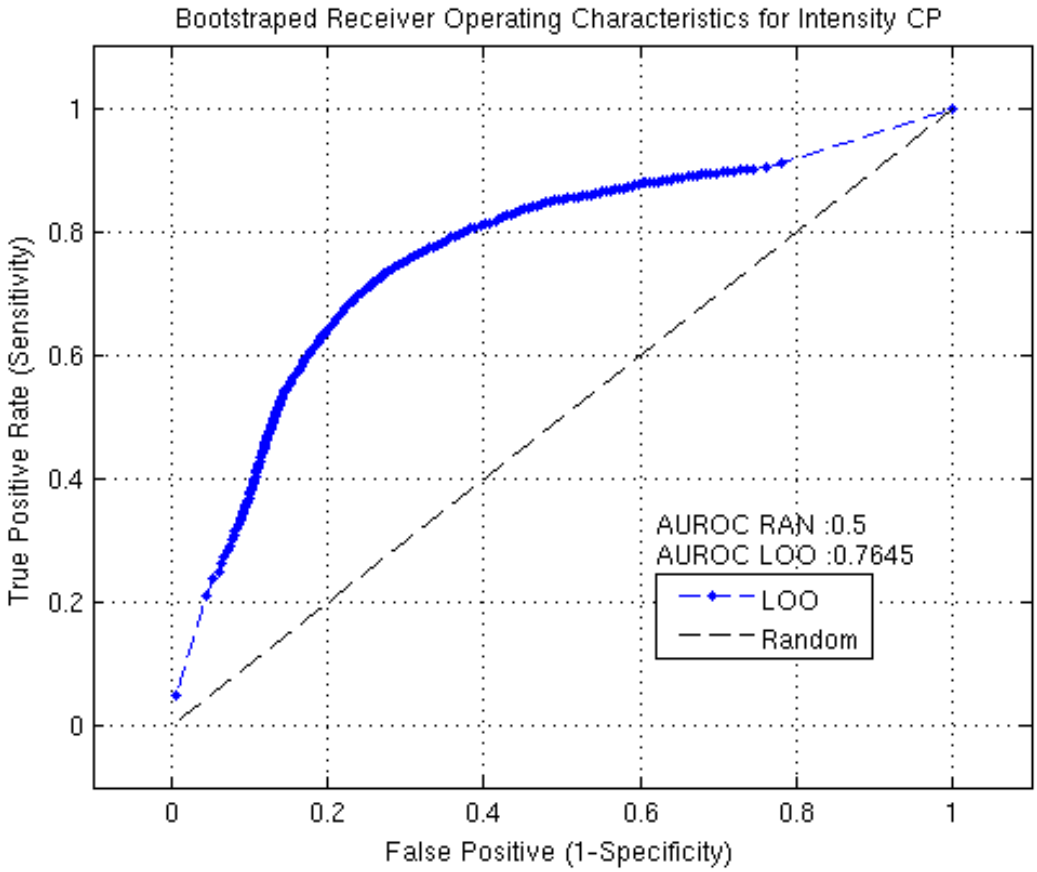

Figure 4.58: Receiver Operating Characteristics for intensity conditional probability. The AUROC value of approximately 0.77 suggests this node will have fair predictive capabilities. A TPR and FPR of 73% and 27% are obtained at the optimized decision threshold (0.44)

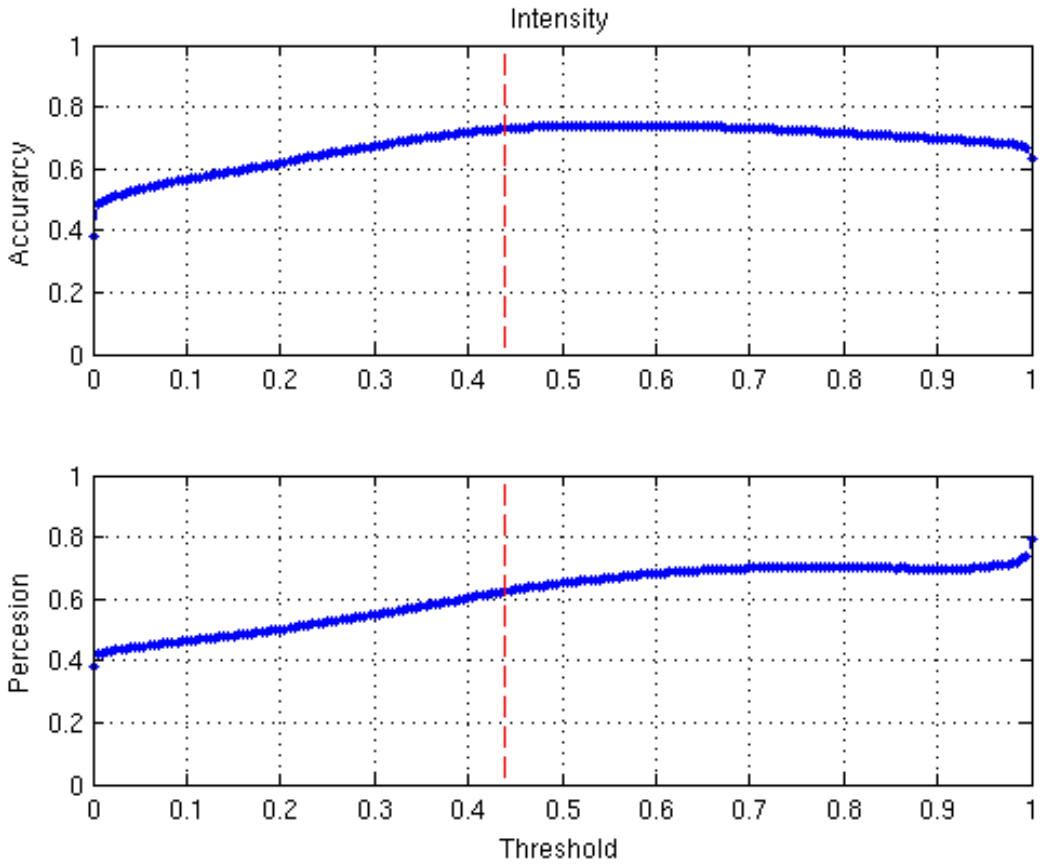

Figure 4.59: Accuracy and precision estimates for the intensity logistic model, where an accuracy and precision of approximately 73% and 62% are obtained at the optimized decision threshold of 0.44 (shown in red).

Table 4.22: Confusion matrix for the event tree intrusion node conditional probability with a decision threshold of 0.91, where the number of properly constrained GLMR run is 23559.

Category	Prediction True	Prediction False
Known True	11653	4877
Known False	2045	4984

Table 4.23: Confusion matrix for the event tree eruption node conditional probability with a decision threshold of 0.52, where the number of properly constrained GLMR run is 23559.

Category	Prediction True	Prediction False
Known True	7887	2455
Known False	3136	10081

Table 4.24: Confusion matrix for the event tree intensity node conditional probability with a decision threshold of 0.44, where the number of properly constrained GLMR run is 23559.

Category	Prediction True	Prediction False
Known True	6605	2405
Known False	3965	10584

4.3.3 Event Tree Probabilities: Node 2-4

Cross validation of the event tree nodes is conducted in a manner similar to that performed in the previous section. ROC curves and AUROC estimates for the intrusion, eruption, and intensity event tree nodes are shown in Figure 4.60, Figure 4.62, and Figure 4.64. AUROC estimates are similar to those shown in Sections 4.3.1 and 4.3.2 and suggest the algorithm will have good forecasting capabilities.

The number of TP, TN, FP, and FN detections at the optimized thresholds for each node are listed in Table 4.25 - Table 4.27. Similar performance trends are observed. The optimized decision thresholds are decreasing across the nodes. The number of TP and FN detections are decreasing, while the FP and TN detections are increasing at each node. FPR and TPR values are decreasing

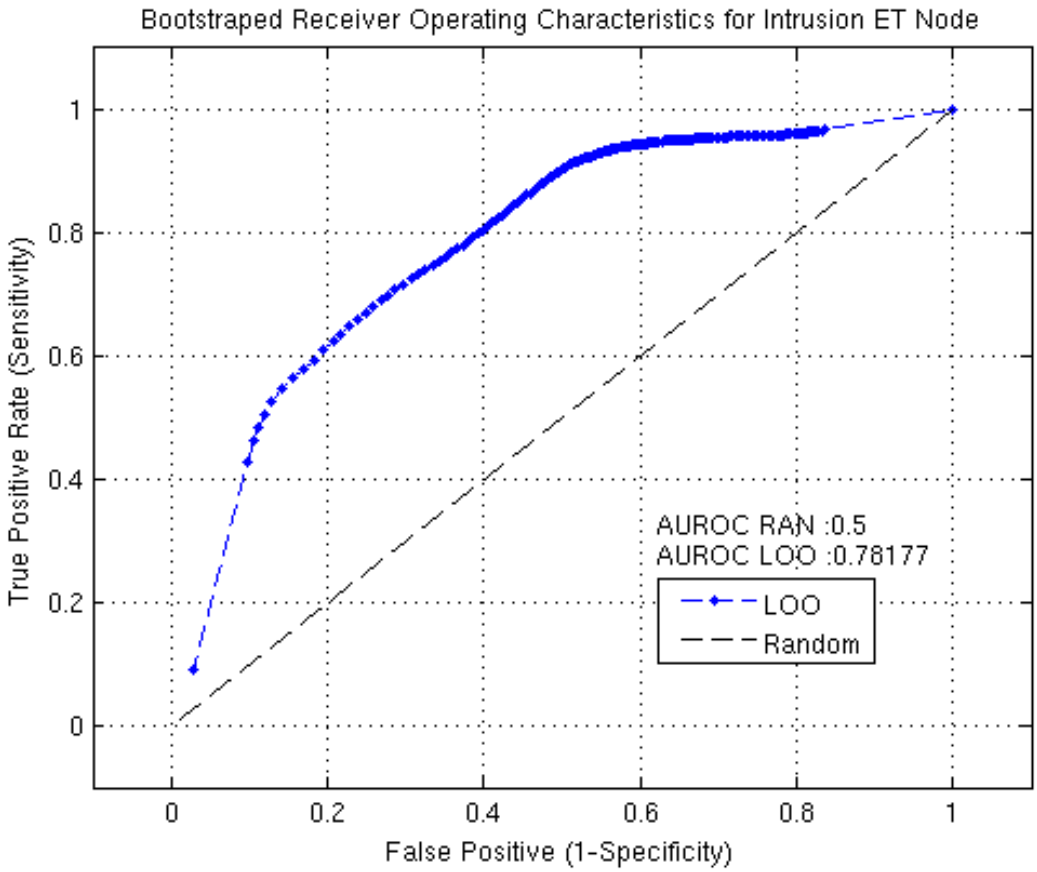

Figure 4.60: Receiver Operating Characteristics for the intrusion event tree node. The AUROC value of approximately 0.78 suggests this node will have fair to good predictive capabilities. A TPR and FPR of 71% and 29% are obtained at the optimized decision threshold (0.91)

and fluctuating, respectively. Figure 4.61, Figure 4.63, and Figure 4.65 illustrate the accuracy and precision calculations for each of the ROC runs. The figures show accuracy and precision values are increasing and decreasing, respectively, at the optimum decision threshold across the nodes.

Table 4.25: Confusion matrix for the event tree intrusion node with a decision threshold of 0.91, where the number of properly constrained GLMR run is 23481.

Category	Prediction True	Prediction False
Known True	11629	4801
Known False	2020	5031

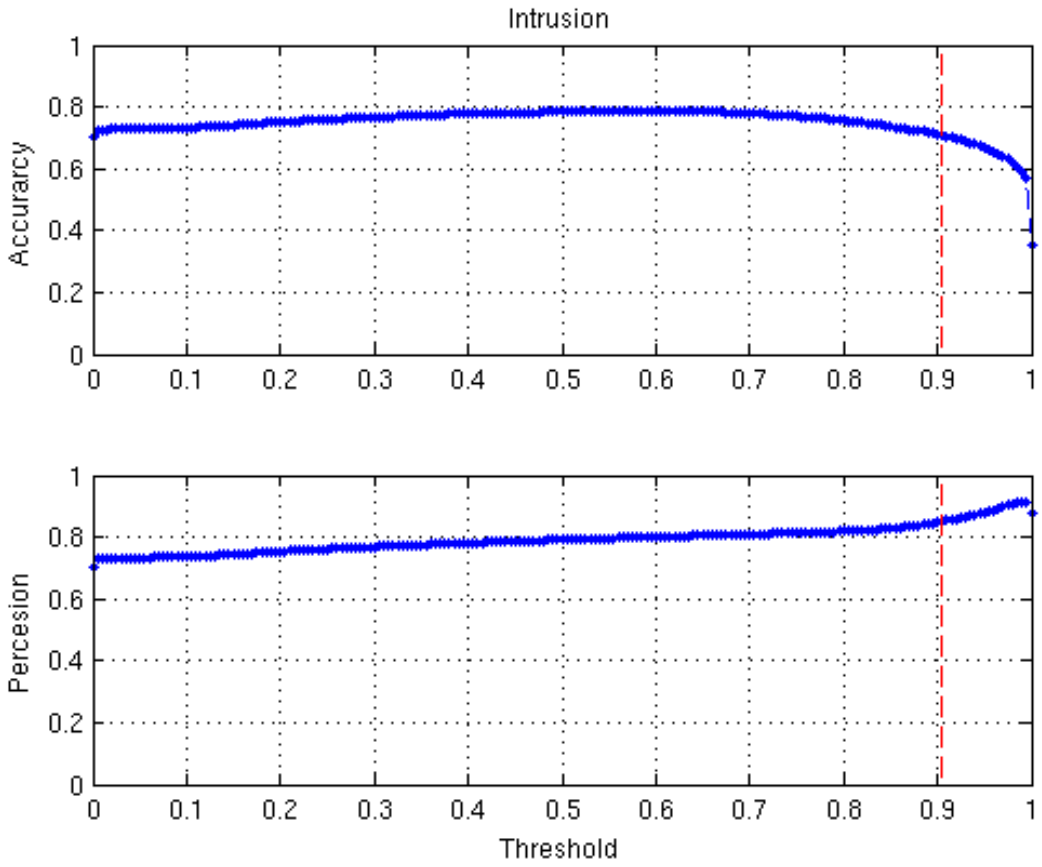

Figure 4.61: Accuracy and precision estimates for the intrusion logistic model, where an accuracy and precision of approximately 71% and 85% are obtained at the optimized decision threshold of 0.91 (shown in red).

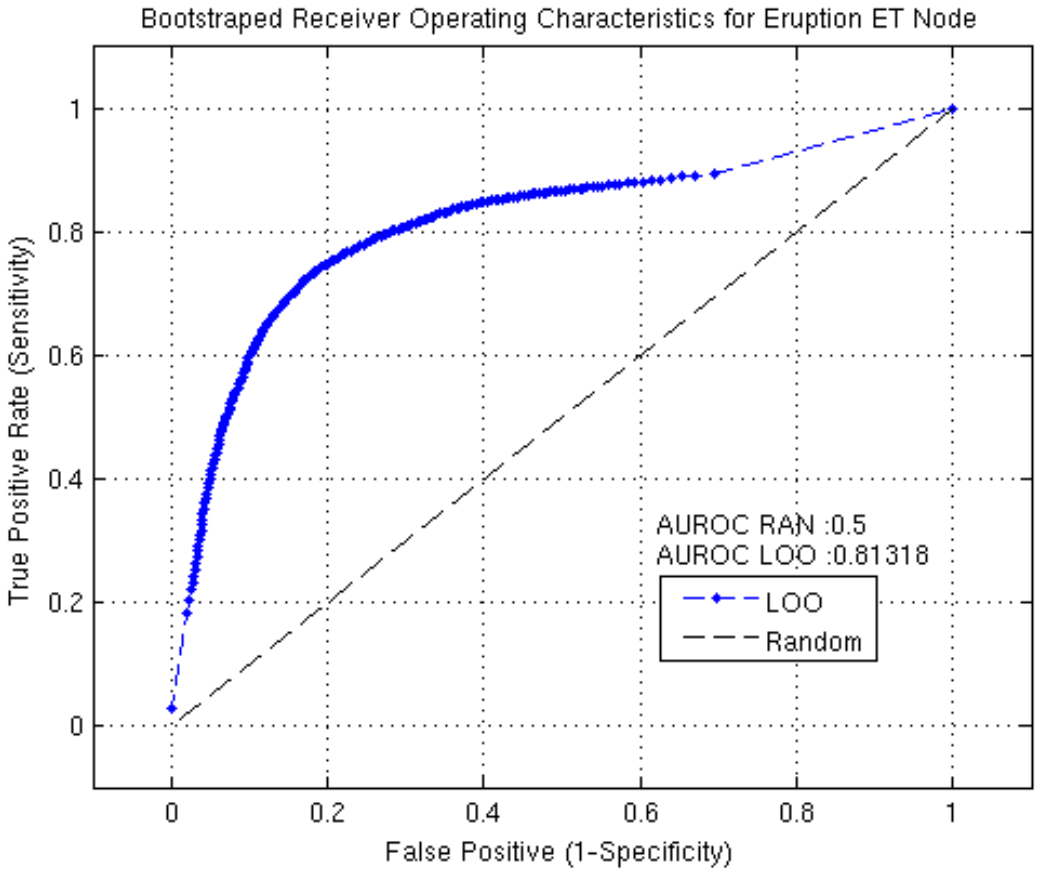

Figure 4.62: Receiver Operating Characteristics for the eruption event tree node. The AUROC value of approximately 0.81 suggests this node will have fair to good predictive capabilities. A TPR and FPR of 75% and 21% are obtained at the optimized decision threshold (0.47)

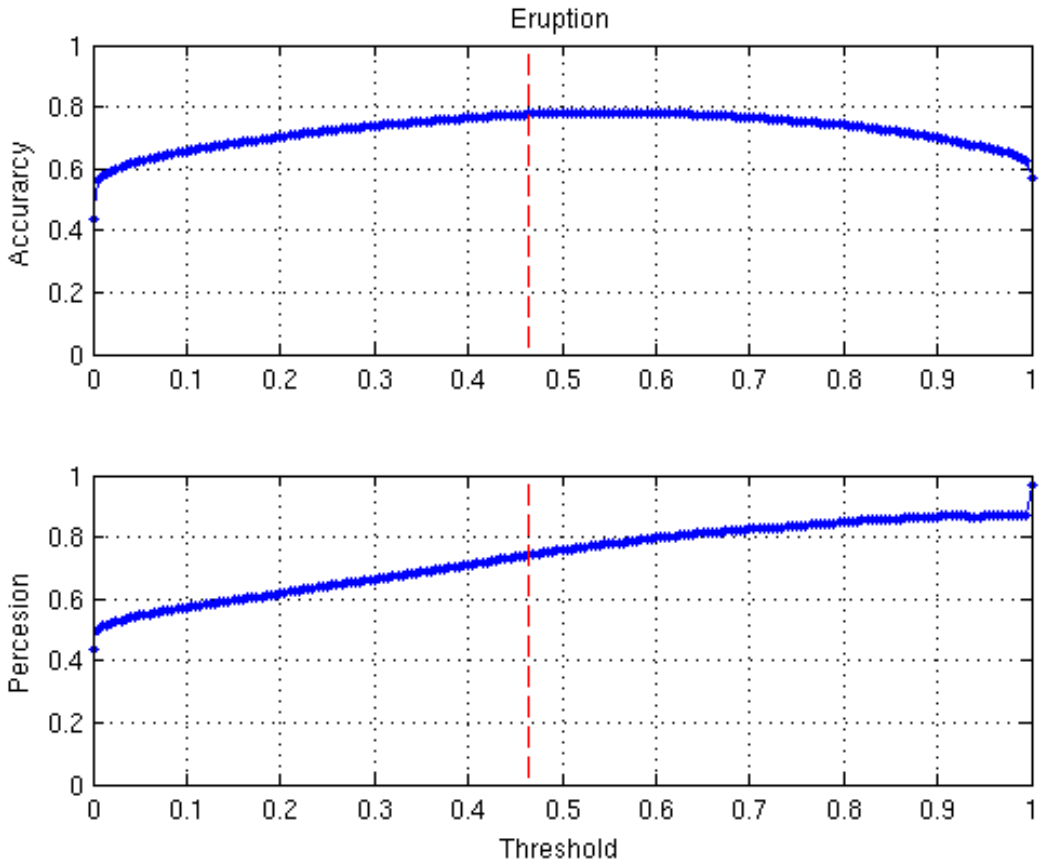

Figure 4.63: Accuracy and precision estimates for the eruption logistic model, where an accuracy and precision of approximately 78% and 74% are obtained at the optimized decision threshold of 0.47 (shown in red).

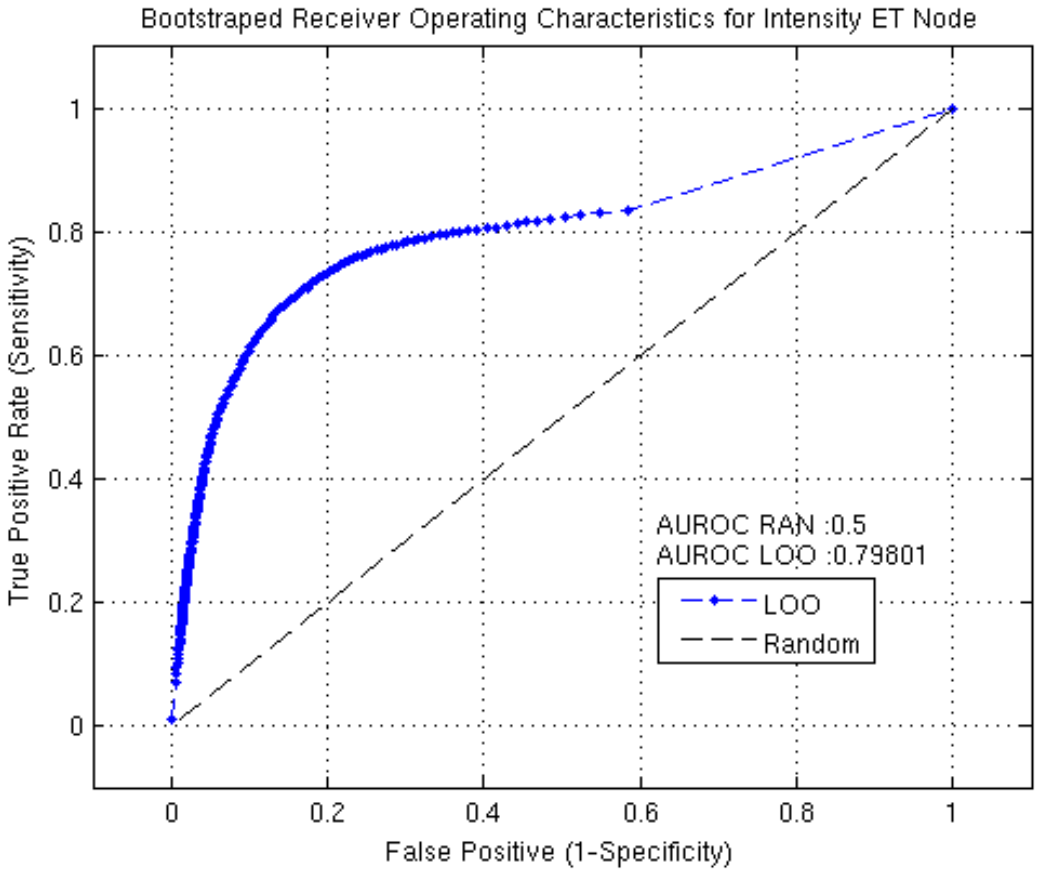

Figure 4.64: Receiver Operating Characteristics for the intensity event tree node. The AUROC value of approximately 0.80 suggests this node will have fair to good predictive capabilities. A TPR and FPR of 73% and 19% are obtained at the optimized decision threshold (0.21)

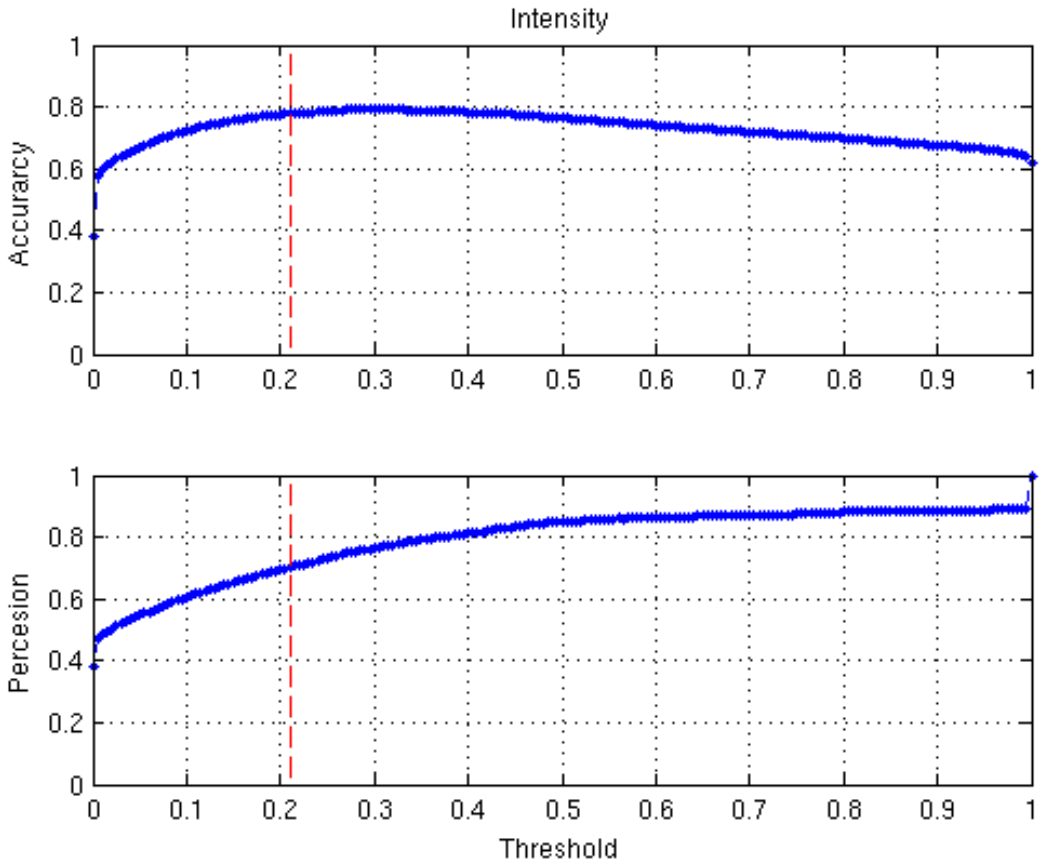

Figure 4.65: Accuracy and precision estimates for the intensity logistic model, where an accuracy and precision of approximately 78% and 70% are obtained at the optimized decision threshold of 0.21 (shown in red).

Table 4.26: Confusion matrix for the event tree eruption node with a decision threshold of 0.47, where the number of properly constrained GLMR run is 23481.

Category	Prediction True	Prediction False
Known True	7796	2541
Known False	2706	10438

Table 4.27: Confusion matrix for the event tree intensity node with a decision threshold of 0.21, where the number of properly constrained GLMR run is 23481.

Category	Prediction True	Prediction False
Known True	6520	2449
Known False	2740	11772

4.4 Algorithm Implementation

Results generated form the bootstrapping and cross validation analysis were used to select the model formulations and detection thresholds for the final implementation of the forecasting algorithm. The selected models and corresponding thresholds are listed in Table 4.28. No detection threshold is required for the vent location nodes, since the most likely location is represented by the area showing the largest probability of occurrence relative to other areas within the deformed area. The values used for the $P(n-1|n)$ and $P(n-1|n')$ components of the conditional probability estimate for each node are given by Equations 4.41 - 4.46. Each of the values were derived from Table 4.2, with the exception of Equation 4.43 which was taken from [21].

$$P(1|2) = \frac{28}{41} \tag{4.41}$$

$$P(1|2') = \frac{13}{41} \tag{4.42}$$

$$P(2|3) = 0.95 \tag{4.43}$$

$$P(2|3') = \frac{17}{41} \tag{4.44}$$

$$P(3|4) = \frac{27}{41} \tag{4.45}$$

$$P(3|4') = \frac{14}{41} \tag{4.46}$$

Table 4.28: Logistic models and corresponding decision thresholds used in final algorithm implementation, where SSOT stands for site specific outlier threshold and NA means not applicable.

Node	Model Definition	Decision Threshold
Unrest	Equation 4.28	SSOT
Intrusion	Equation 4.34	0.91
Eruption	Equation 4.35	0.47
Intensity	Equation 4.36	0.21
Vent Location	Equation 4.33	NA

Block diagrams highlighting the functionality of the forecasting algorithm are shown in Figure 4.66 and Figure 4.67. Once process is initiated at a selected volcano, it searches all available monitoring and modeling data for outliers on a day-by-day basis. As data is fed into the algorithm,

the user has the option to use the information to model the source of an event. Once the source has been determined, the modeling input parameter (X_{MM}) is set to 1 if the unrest is the result of a magmatic intrusion or 0 otherwise. In addition, the algorithm provides a mechanism for a human analyst to override any of the automated results. This allows the analyst to introduce information that may not have been accounted for in the algorithm's decision making process (e.g., personal experience or information not included in the training data).

Upon the detection of unrest, the algorithm's trigger state vector transitions from 0 to 1. While in the trigger state, data corresponding to the appropriate explanatory variables are routed directly to nodes 2-5 for a user specified number of days. During this time the algorithm produces probability estimates for each node, a daily color coded hazard declaration, an unrest severity estimate (as described in Table 4.4), and a vent location probability map. Once the specified number of days has been reached, the trigger states returns to 0, and outlier detection is reinitialized.

Recalibration of the logistic models can be performed automatically upon the introduction of new samples into the training dataset. Once the models have been redefined and validated, the old models are replaced, and the new functionality is instantly available at all sites being monitored. This guarantees that all forecasting results are derived from the most current logistic models.

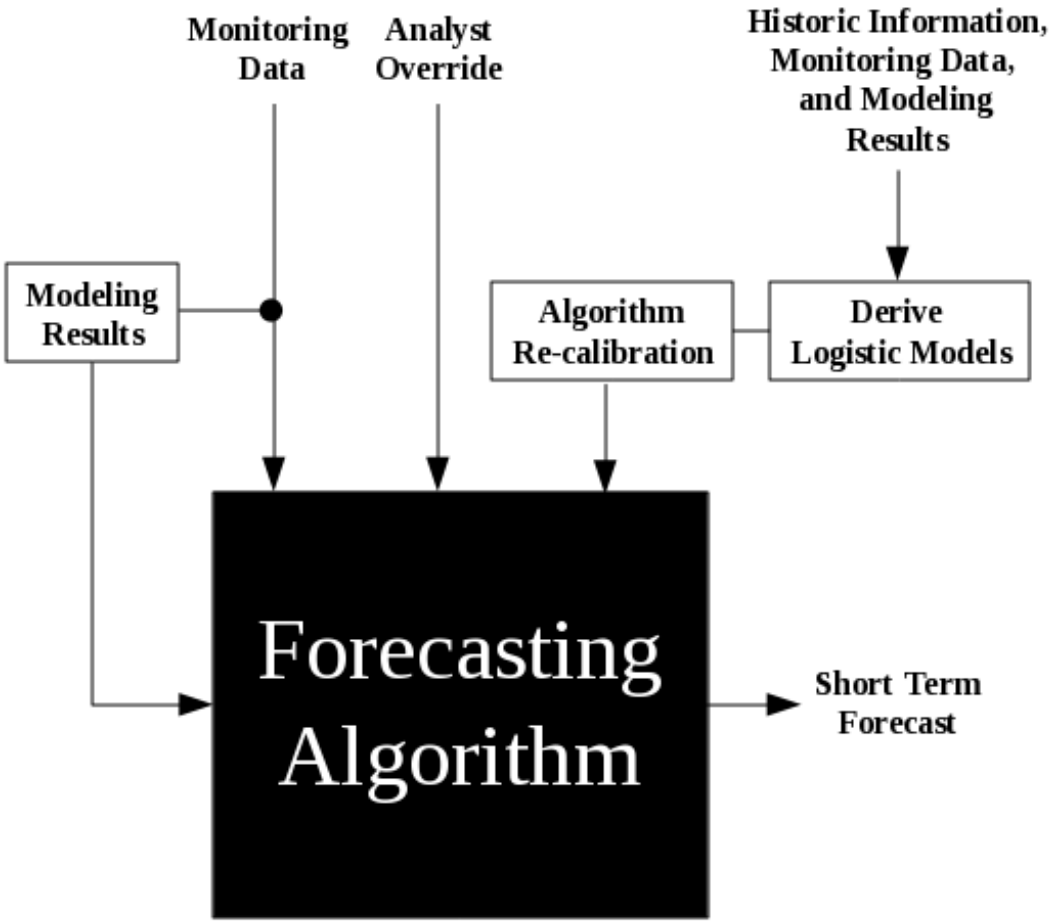

Figure 4.66: Schematic diagram showing the data flow to and from the forecasting algorithm.

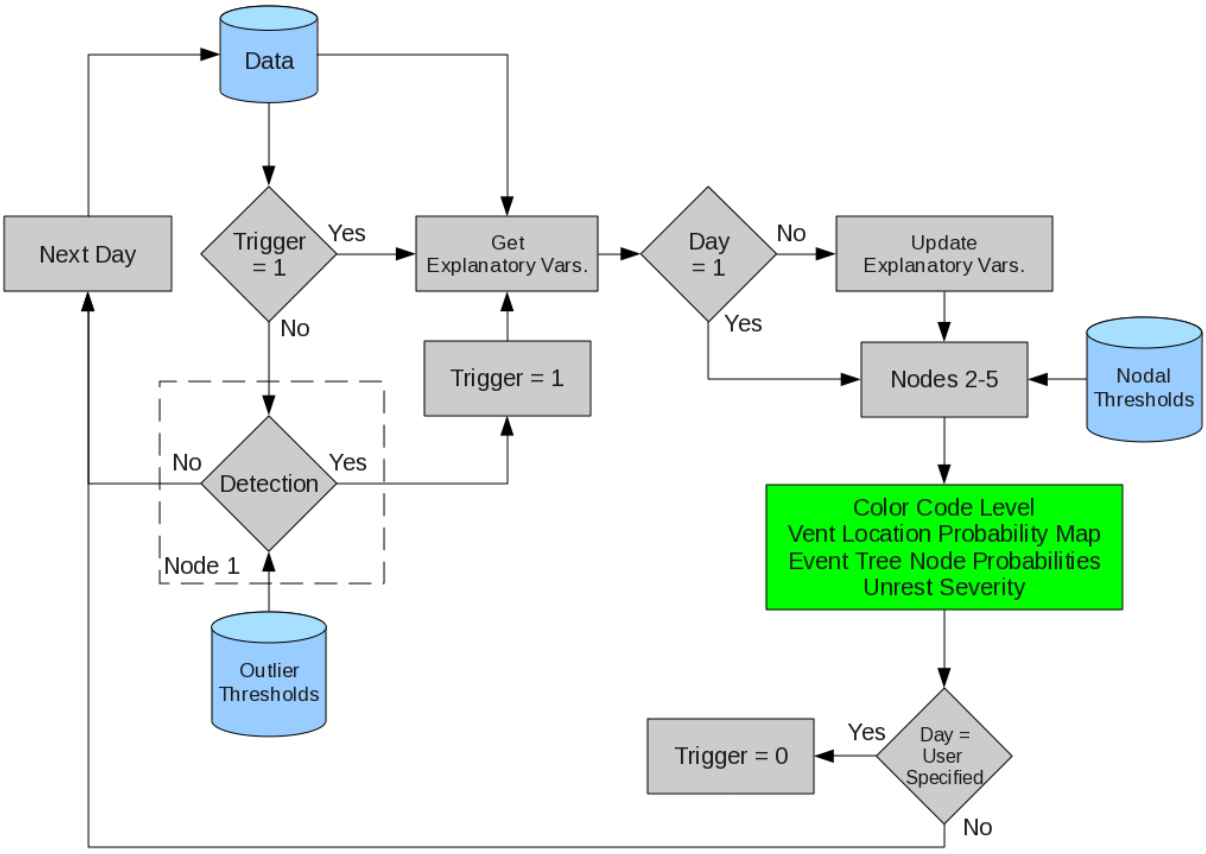

Figure 4.67: Block diagram showing the internal functionality of the forecasting algorithm, where gray indicates processes internal to the algorithm, blue represents external data sources (e.g., monitoring data, analyst override), and green identifies products.

CHAPTER 5: DISCUSSION OF RESULTS

The volcanic eruption forecasting algorithm (VEFA) was tested on four unrest episodes occurring at volcanoes located in the Aleutian Islands, Iceland, Yellowstone National Park, and the Cascade Mountain range. Only the Aleutian example is part of the training data set. All other examples were not used in the logistic regression. A detailed discussion of each example is presented, which includes an overview of the volcanic setting, a discussion of the unrest episode's evolution, applicable source modeling results, and a time series of volcanic activity forecasts. Results are also compared to comparable forecasts generated by the Bayesian Event Tree Eruption Forecasting (BETEF) 2.0 application, which is publicly available via the internet [25]. It should be noted that in each of the examples below, algorithm and episode day represent the number of days since the algorithms activation and the transition of the trigger state from 0 to 1, respectively.

5.1 Okmok Volcano

Okmok is an active shield volcano that comprises the northeastern portion of Umnak Island, which is located off Alaska's west coast near the center of the Aleutian Arc (Figure 5.1). It has a large caldera complex that spans approximately 10 km in diameter, which was most likely formed 65 to 100 million years ago [11]. Okmok has a rich eruption history, where approximately 16 documented events have occurred since 1805 [127]. A list of observed events is shown in Table 5.1. The record shows there was considerable activity during the 1930s, a quiescent period throughout

Table 5.1: Okmok Eruption History [10], [11]

Year	Event Type
1805	Not an Eruption
1817	Explosive Eruption
1824	Explosive Eruption
1878	Explosive Eruption
1899	Explosive Eruption
1931	Explosive Eruption
1935	Explosive Eruption
1936	Unknown Eruption Type
1938	Unknown Eruption Type
1943	Explosive Eruption
1945	Explosive Eruption
1953	Not an Eruption
1958	Explosive Eruption
1960	Explosive Eruption
1981	Explosive Eruption
1983	Explosive Eruption
1986	Explosive Eruption
1997	Explosive Eruption
2001	Not an Eruption (Significant Seismic Activity)
2008	Explosive Eruption

the 1970s, and period of sparse activity in late 1980s, mid 1990s and early 2000s. The most recent eruption took place on July 12, 2008.

Seismic activity on Umnak Island is monitored continuously by the AVO to detect precursors that may signal the onset of an eruption at this highly active volcano. The AVO seismic catalog (Figure 5.1) offers an abundance of information regarding the geophysical processes occurring within Okmok's interior. The figure shows the location of the Okmok seismic network, blue triangles, which offers a good degree of coverage around the volcanic edifice, and the distribution of seismicity (red squares) across the island.

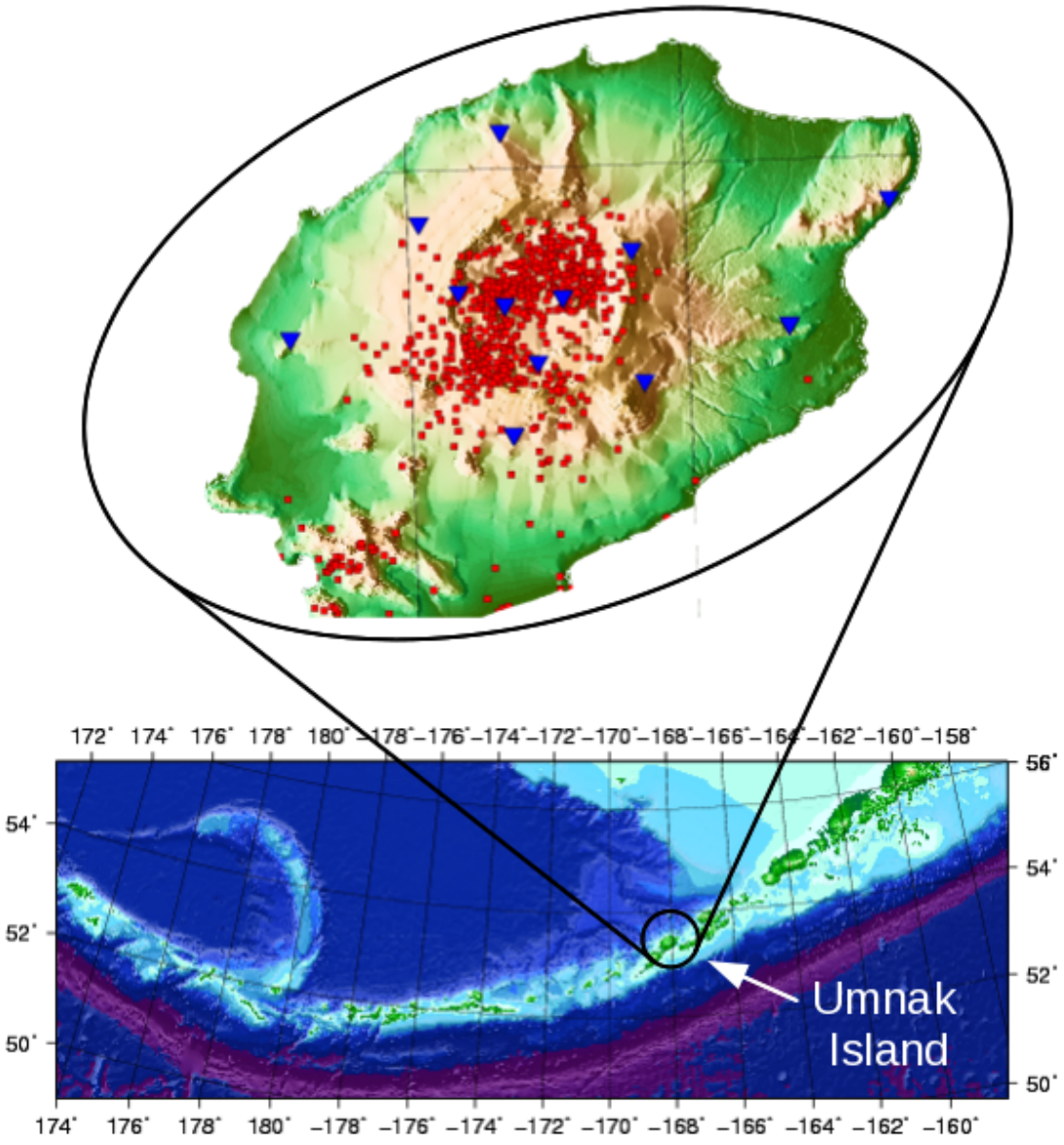

Figure 5.1: Location of Umnak Island within the Aleutian Arc, where triangles illustrate the island's seismic network and red squares show the distribution of seismicity between 2002 and 2009. The seismic catalog is used in the statistical analysis discussed in Section 3.4.1.

5.1.1 Magma Supply Dynamics

The spatial variation of b-values across Umnak Island is shown in Figure 5.2 a, b, and, c. A large b-value anomaly is detected near the southwest flank of the caldera which extends approximately 8.0 km below its floor. The spatial extent of the anomaly grows with depth and becomes uniform at depths greater than 8.0 km. In addition, there is a region of low seismicity between the volumes of high and low b-values at a depth of approximately 4.0 km. The proximity of the b-value anomaly centroid and low seismicity zone signal the presence of a magma chamber approximately 4.0 km below the caldera floor.

Multi-year Interferograms spanning 1995-2008 were computed using the ROI PAC. Figure 5.3 shows a collection of selected inteferograms, where the first and second columns are the actual and modeled images. Each of the modeled interferograms are computed using a source depth of 4.0 km (derived from the results shown in Section 3.4.1) and empirically derived values of C. Over this time period both co- and post-1997 eruption deflation and inflation are captured. The results show continuous inflation has occurred beneath the caldera between 1997 and 2008 [7], [103], [130].

The temporal evolution of C and ΔV between 1995 and 2008 is shown in Figure 5.4. The large deflation event occurring between 1995 and 1997 is attributed to Okmok's 1997 eruption. Cumulative volumetric change in magma between 1995 and 2008, highlighted in red, is relative to the ΔV computed for the 1995-1997 time frame. The figure shows magma replenishment occurring at a rate of approximately 7.0x10^{-3} km^3/year between 1997 and 2008 [7], [103], [130].

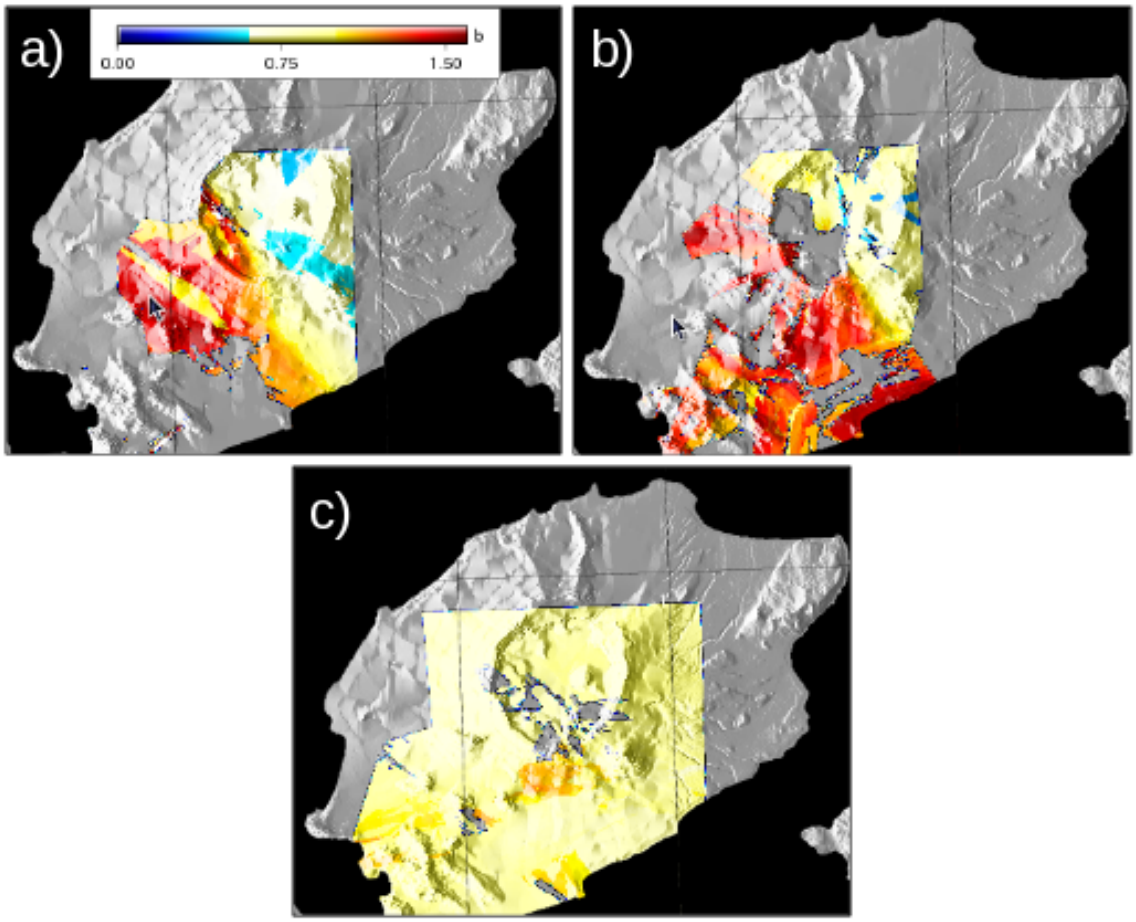

Figure 5.2: Spatial variation of b-values across Umnak Island. a) 0.0 to 3.0 km depth range, where 0 represents the caldera floor. b) 3.0 to 8.0 km depth range. c) 8.0 to 43.0 km depth range [7].

In addition, the estimated volume within the chamber returns to the pre-1997 eruption state by June 2008, which is approximately one month prior to the 2008 eruption.

5.1.2 Forecasts Preceding Okmok's 2008 Eruption

Figure 5.5 shows the outlier analysis results for the Okmok volcano based on data acquired between 2003 and 2008. Box plots show the distribution of seismicity rate per day, M_L, and vertical surface deformation measurements acquired by USGS GPS sensors, where points residing above the whiskers are outliers. The value separating each of the outliers from the typically observed values will serve as the unrest decision lines for each monitoring discipline, where thresholds of approximately 3.0 earthquakes events per day, M_L of 2.6, and vertical surface deformation of 44.3 mm (at GPS site OKCE) are employed.

A time series plot of monitoring data versus the outlier thresholds is shown in Figure 5.6. The plots show several instances where the unrest thresholds are exceeded on one or more of the monitoring channels. In addition, continuous deformation is observed between 2000 and 2008. The forecasting algorithm is triggered when any monitoring measurement exceeds the detection threshold or positive modeling results are found. Moreover, the severity of the unrest episode will be determined by the number of triggers that occur simultaneously across different monitoring channels (see Section 4.2.5).

The forecasting algorithm was initiated on 2008-05-17 and triggered on the presence of positive modeling results on 2008-06-29. The unrest severity and trigger state vectors are shown in Figure 5.7 A and B. Since the algorithm triggered on positive modeling generated from InSAR

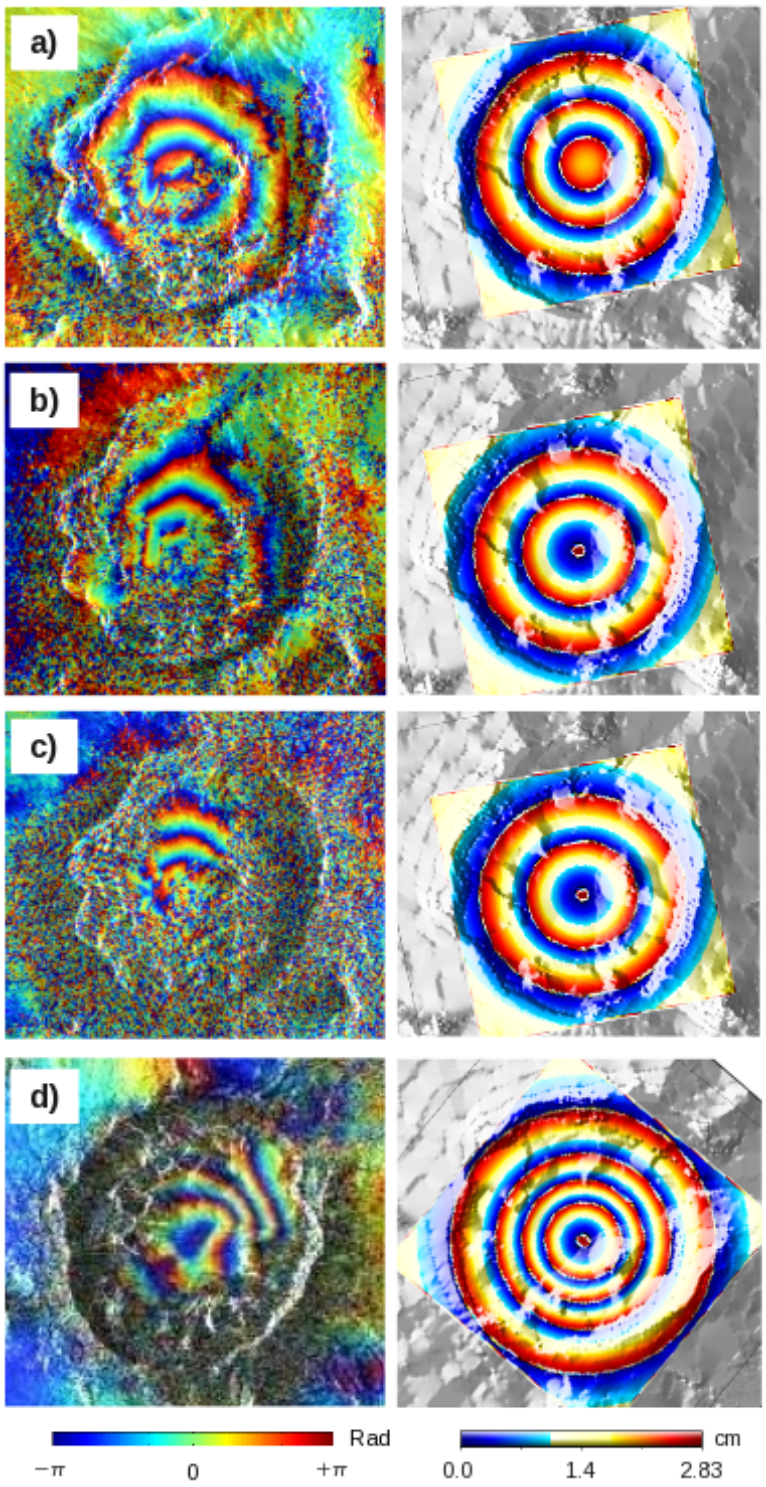

Figure 5.3: Multi-year interferograms highlighting deformation within the Okmok caldera [7]. Color scale for images shown in columns one and two highlight phase wrapping intervals which span $\pm\pi$ and $0 - 2.83$ cm for the actual and modeled interferograms. a) 1997-1998 b) 1998-1999 c)2000-2002 d) 2007-2008.

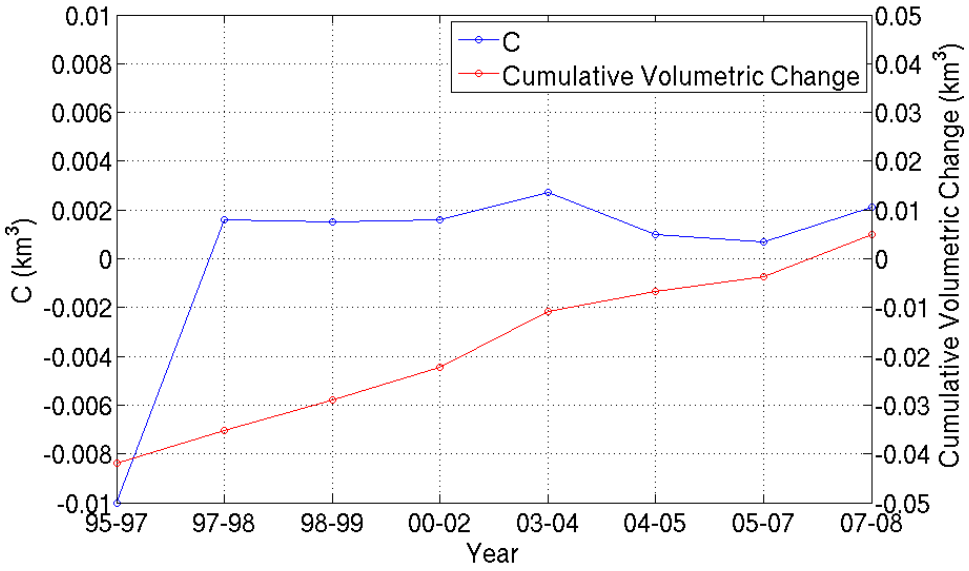

Figure 5.4: The scale factor C (blue) and cumulative volumetric change in magma (red) between 1995 and 2008.

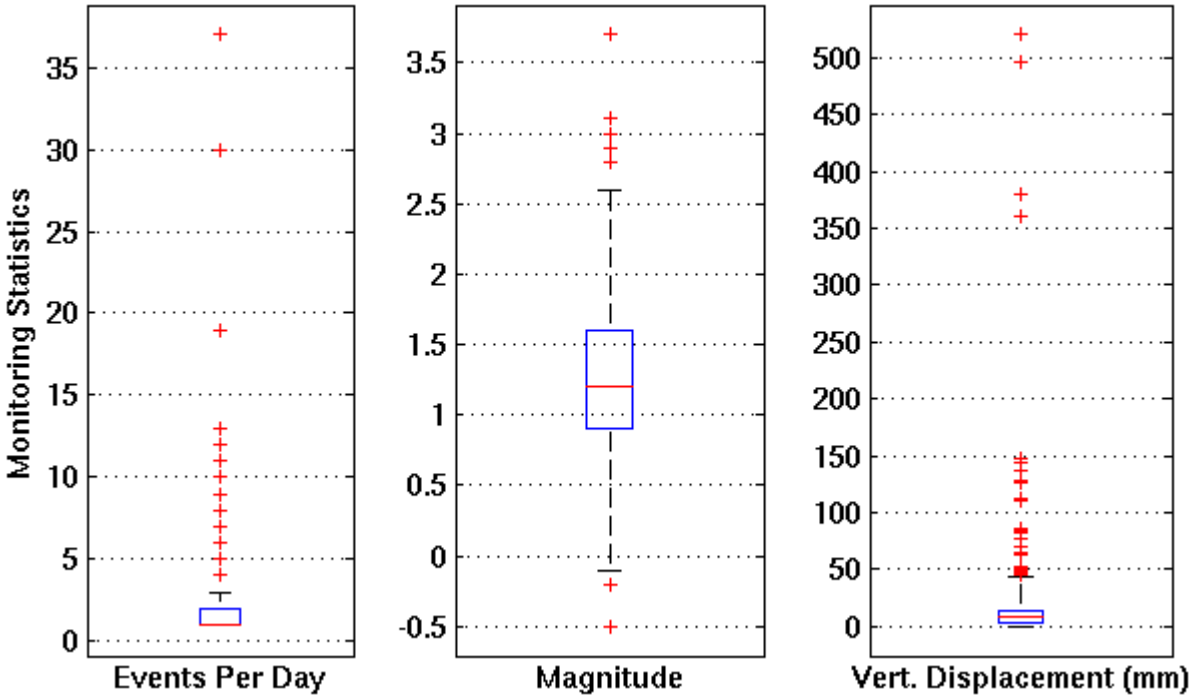

Figure 5.5: Boxplots highlighting the distribution of seismicity and deformation on Umnak island between 2003 and 2008, where the events per day and magnitude whiskers are set to 1.5 and the vertical GPS deformation measurements are 3 times the inter quartile range. Monitoring thresholds are 3.0 events per day, m_l of 2.6, and 44.3 mm of deformation.

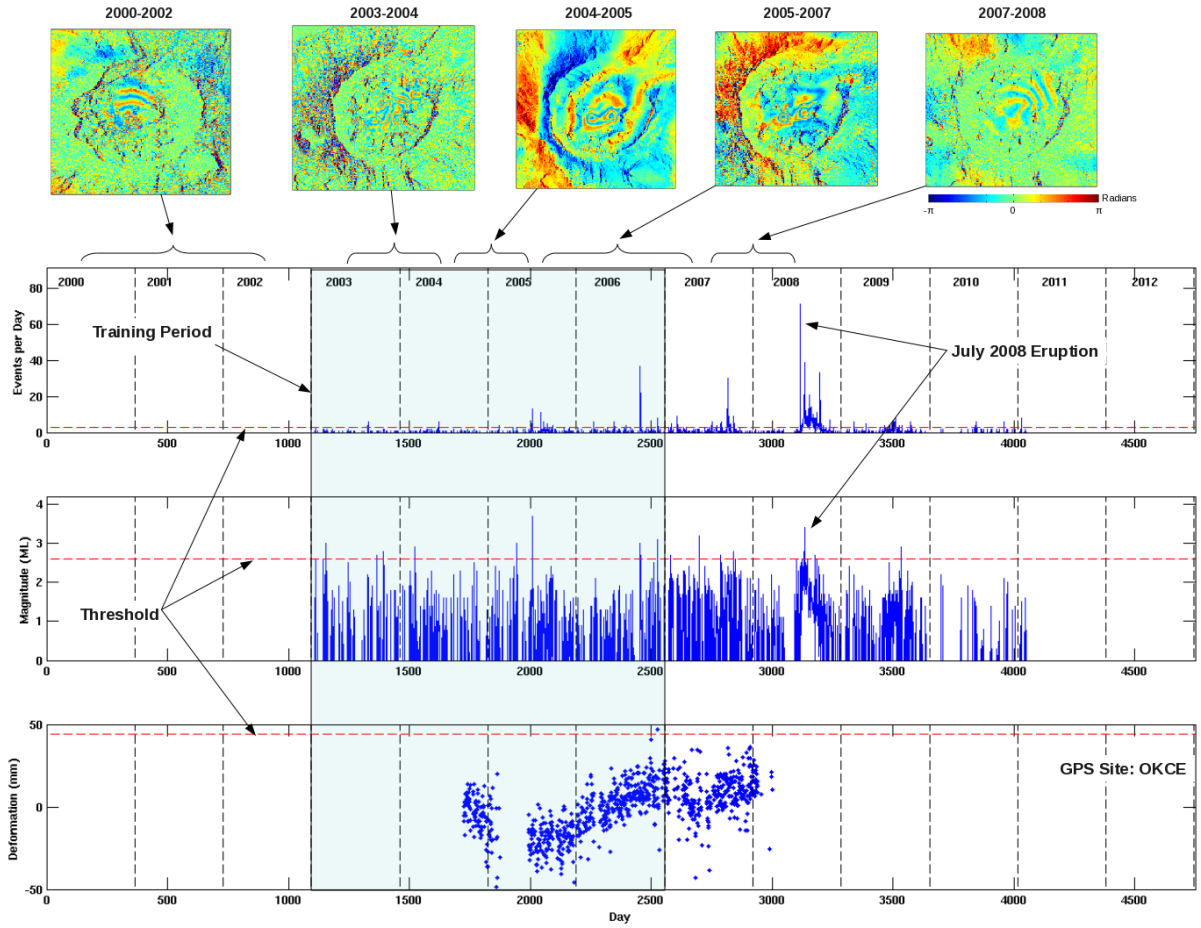

Figure 5.6: Time series of monitoring data acquired from the Okmok volcano between 2000 and 2011, where the red dotted lines are the outlier thresholds that are based on data in the blue window. Top panel: Interferograms highlighting surface deformation within the Okmok Caldera. Panel Two: Seismicity rate per day. Panel Three: Maximum magnitude per day. Panel Four: GPS data showing vertical displacement between late 2004 and early 2008. Data shown in panels two through four were acquired from the Alaska Volcano Observatory and the United States Geologic Survey.

data the unrest severity level is set to moderate (0.50). The severity declaration remains stable throughout the episode due to the lack of anomalous precursory seismicity (see Figure 5.8 A and B).

Figure 5.9 A shows a time series of intrusion, eruption, and intensity forecasts over the 13 days preceding Okmok's 2008 eruption for each logistic model. The plot shows that the detected unrest has a high probability (approximately 0.77) of being the result of a magmatic intrusion. This estimate is essentially driven by source modeling results that show the surface deformation field is consistent with the expansion of a spherical magma chamber (see Figure 5.3). The eruption node forecasts are in the 0.41 to 0.42 range over the length of the time series. This result is driven, in part, by the positive modeling results and the historic eruption frequency at this site. Relatively low levels of seismicity are preventing the probability from exceeding 0.41 (see Figure 5.8 A and B). The probability that a potential eruption's intensity will exceed a VEI of 1.0 is approximately 0.28, which is also low due to the lack of significant seismicity.

Figure 5.9 B shows a time series of the conditional probability estimates for the intrusion, eruption, and intensity nodes. The likelihood of a magmatic intrusion occurring, given the detection of unrest, is now approximately 0.88. The increase in the probability is driven by the fact that magmatic unrest is highly unlikely in the absence of fluid motion. This is reflected in the value of $P(1|2)$ in Equation 4.41, which was set to approximately 0.70 based on the number of unrest events that were confirmed to be the result of a magmatic intrusion in Table 4.2. The eruption and intensity conditional probabilities have also increased and are now in the 0.61 and 0.43 range over the course of the episode.

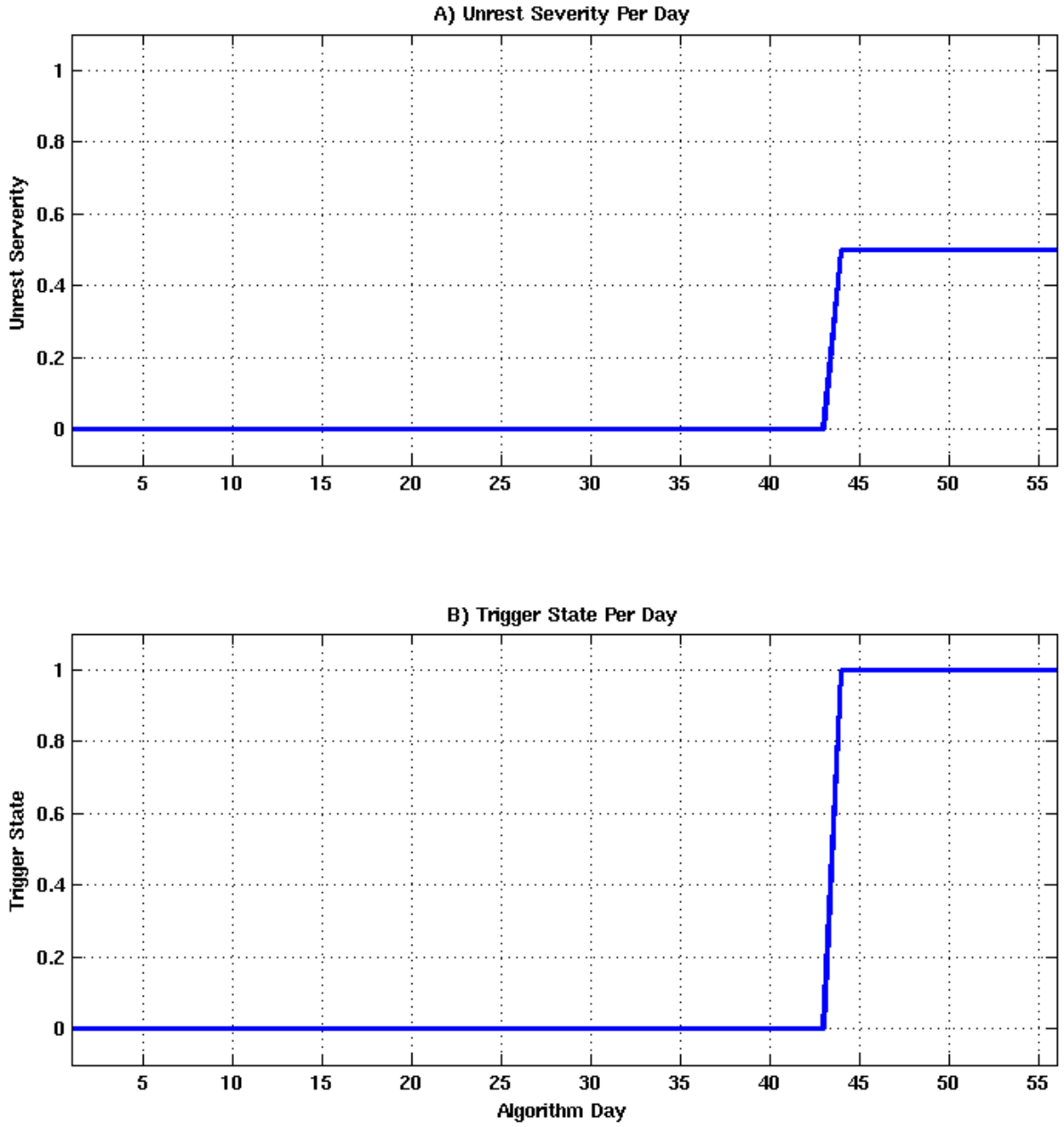

Figure 5.7: Algorithm state as a function of processing day. A) Unrest severity estimates per day, where a description of the states is listed in Table 4.4. B) Trigger state of the forecasting algorithm, where the trigger state transitioned from 0 to 1 on algorithm day 43.

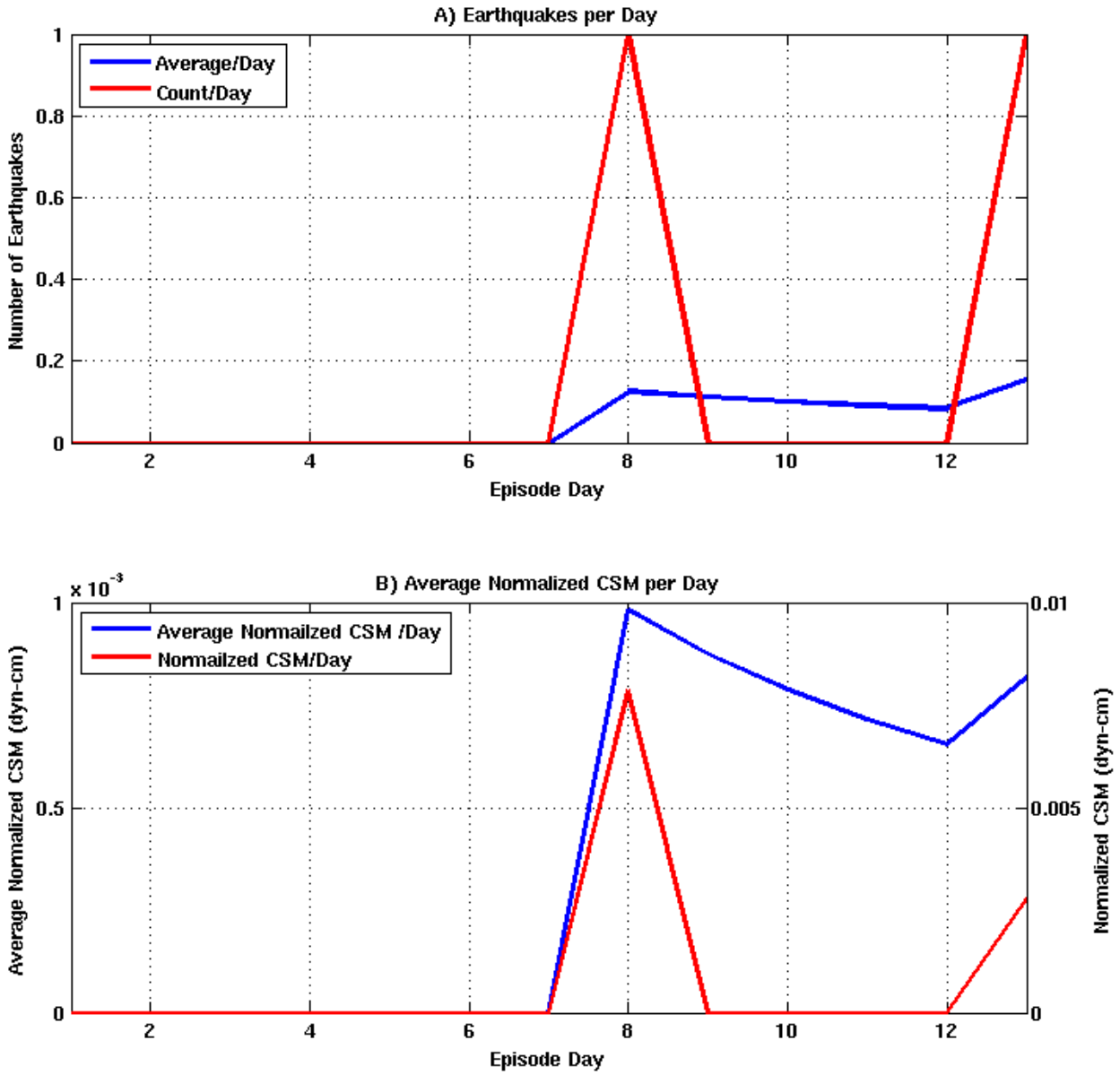

Figure 5.8: Volcano monitoring data preceding Okmok's 2008 eruption. A) Count and average (X_{NE}) number of earthquakes per episode day (X_{DAYS}), shown in blue and red. B) Count and average (X_{CSM}) seismic moment per episode day (X_{DAYS}), shown in blue and red.

Figure 5.9 C shows a time series of the event tree forecasts for the intrusion, eruption, and intensity nodes. Since the unrest node probability is always equal to 1.0 after its triggered, the intrusion probabilities are equal to the $P(2|1)$ values which remain relatively constant at 0.88. Eruption probability is slightly reduced, since the values of $P(2|1)$ are approximately 0.88, and is now in the 0.55 range. The probability that Okmok will erupt with an intensity greater than VEI 1.0 is approximately 0.23.

Figure 5.9 D shows a time series of the equivalent USGS ground-based hazard color code. The hazard declaration remains green throughout the evaluation period since the intrusion forecast never crosses the detection threshold. This result is consistent with the published USGS hazard level for Okmok over this time period. Intrusion probability estimates remain relatively constant at 0.88 over the course of the episode, which is just below the detection threshold. In addition, the eruption and intensity probabilities are both above their respective decision thresholds.

A time series of selected spatial PDFs highlighting probable volcanic vent locations are shown in Figure 5.10. The value of J in Equation (4.33) is determined by the size and spatial resolution of the forecast area. Here the spatial resolution of each PDF is dictated by the DEM used for Umnak Island, which is 2 arc-seconds (5.56e-4°). InSAR imagery and modeling results suggest the deformation source is located 4.0 km below the caldera center and has an isotropic radiation pattern that is approximately 11 km in diameter (see Figure 5.3). A square search area is used to simplify earthquake database queries within the deformed area. As a result, the PDF is quantitatively constrained to a 121 km^2 area. Since modeling results show deformation is occurring within the caldera, earthquakes located outside this area are ignored and the PDF is shaped by seismicity originating within the deformed region. The average epicenter uncertainty for the AVO

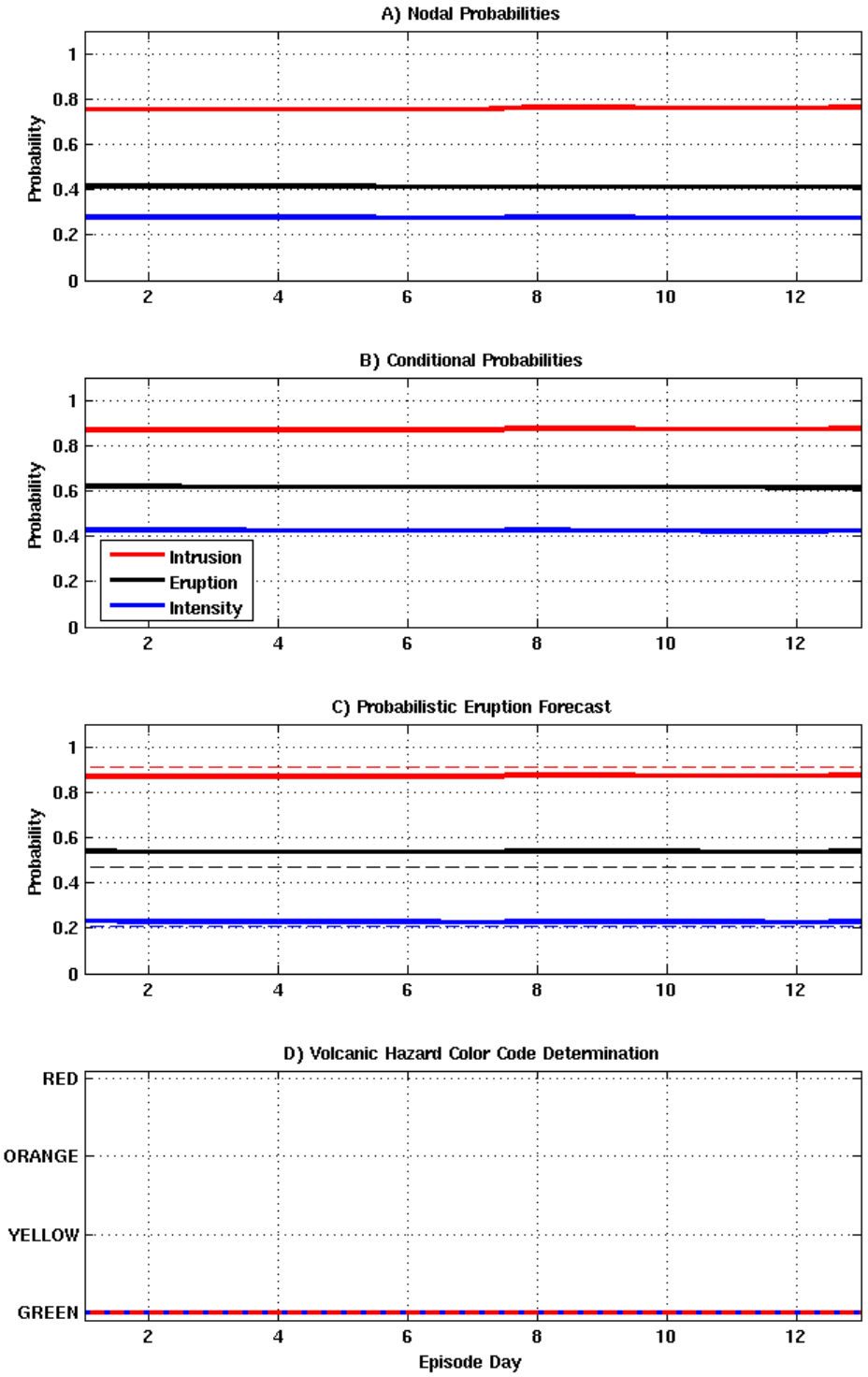

Figure 5.9: Forecasts of volcanic activity preceding Okmok's 2008 eruption, where the intrusion, eruption, and intensity probabilities and thresholds are shown by the red, black, and blue, solid and dotted lines. A) Evolution of prior probability estimates as a function of episode day. B) Variation of conditional probability estimates. C) Probability of occurrence for event tree node. D) Equivalent USGS volcanic ground-hazard color code declaration.

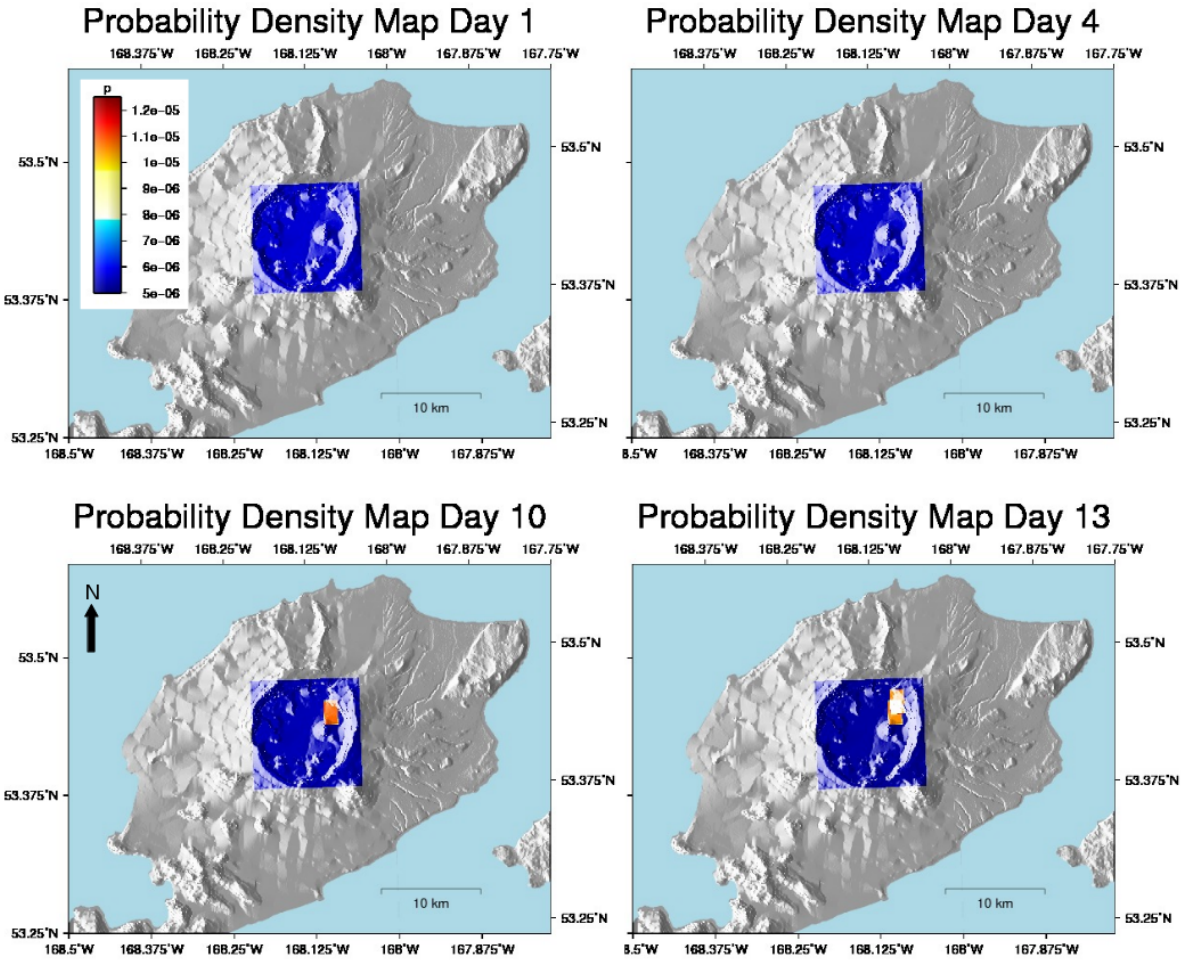

Figure 5.10: Spatial Probability Density Maps for the selected days preceding Okmok's 2008 eruption.

network in 2008 is approximately 2.30 km [131]. Therefore, all X^j_{seis} samples within 1.15 km of each epicenter are set to 1. In all cases, day numbers represent the time span used to constrain earthquake database queries, J = 53,044 probable locations, and all X^j_{def} = 1. Since no seismicity is detected inside the caldera on days 1 and 4, a uniform distribution covers the extent of the theoretical deformation field, which indicates the vent is equally likely to form anywhere within the deformed region. Over the next thirteen days, seismic activity accumulates and the spatial PDF begins to highlight a preferred vent location in the northeast section of the caldera.

On episode day 14 (2008-07-12) an explosive eruption of intensity (VEI) 4 occurred in the northeast corner of the caldera. In this case the algorithm provided probability estimates of 0.88, 0.55, and 0.23 that an intrusive unrest event would culminate to an eruption that will exceed a VEI of 1. It also correctly identified the caldera's northeast corner as the most likely vent location. The color code level was set to green throughout the episode. Hazard level upgrades can only occur when the event tree decision thresholds are exceeded in order of increasing specificity. Since the intrusion estimate remains below the decision threshold, the color code estimate remains at green for the duration of the episode. If additional seismicity had occurred, the hazard level would have been elevated to red. This episode is as example where the volcano broke its historic eruption trend [132]. This event was significantly different from previous eruptions, due to its hydrovolcanic nature, lack of lava flows, and absence of precursory seismicity [133]. The anomalous nature of this event lead to the under estimation of its potential hazard. However, the proximity of the intrusion probability to the detection threshold may have compelled a human analyst to elevate the hazard level.

5.2 Yellowstone Caldera, Wyoming

The Yellowstone Caldera and Snake River valley are well known for displaying elevated signs of magmatic and tectonic activity [134], [135]. Between 2005 and 2010 an unprecedented episode of magmatic unrest took place within the Yellowstone caldera. Through extensive source modeling, this episode was determined to be the result a complex magmatic intrusion occurring beneath the park [118]. Figure 5.11 shows the location of two earthquake sequences that occurred

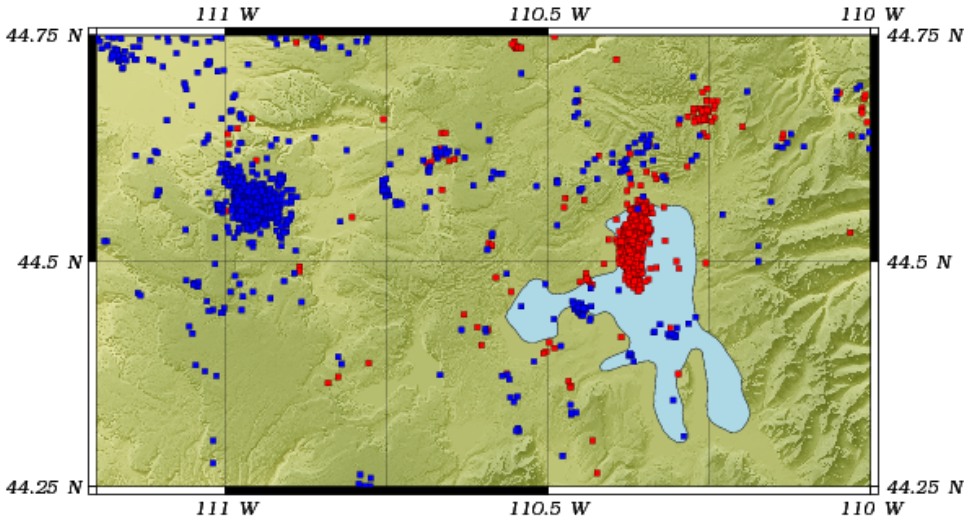

Figure 5.11: Earthquake sequences within the Yellowstone caldera cataloged by the USGS, where the 12/2008-1/2009 Lake Yellowstone sequence is shown in red and the 2010 sequence is shown in blue.

within the caldera in 2008 (red) and 2010 (blue) as a result of the intrusion episode. Figure 5.12 and Figure 5.13 highlight the collocation of each earthquake sequence with regions having large surface deformation gradients. In each case, deformation surfaces, shown as contours, are computed from measurements acquired by a suite of GPS sensor located throughout Yellowstone National Park. GPS data used to derived surface deformation fields are shown in Appendix F.

The 2010 Yellowstone sequence was selected for computing the expressions shown in Section 4.4 and was not used to train the logistic models. The incorporation of this episode into the training dataset resulted in an unnatural decrease in the probability of eruption in the presence of elevated levels of seismicity. Since this behavior contradicts reality, it was removed from the logistic training dataset and used as a test case for the VEFA.

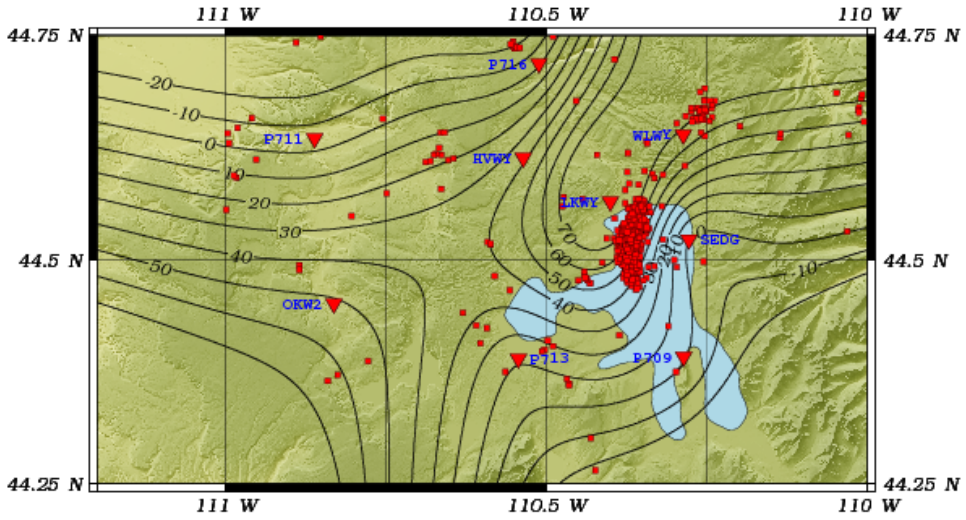

Figure 5.12: Correlation between the 12/2008-1/2009 Lake Yellowstone sequence and surface deformation derived from continuous GPS measurements, where the red triangles show the location of the USGS GPS sensors, the red squares show the USGS Yellowstone earthquake catalog between 11/2008 and 03/2009, and the contours represent surface deformation in millimeters.

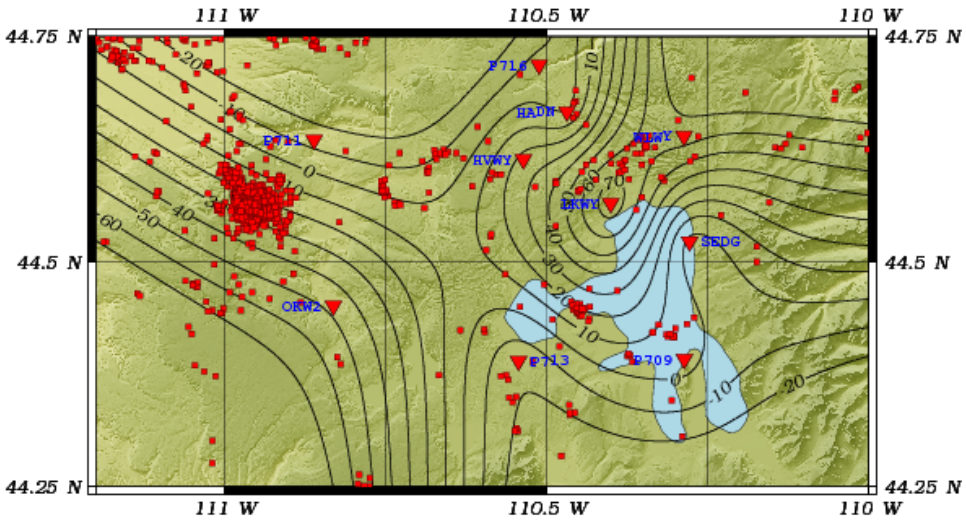

Figure 5.13: Correlation between the 2010 Yellowstone earthquake sequence and surface deformation derived from continuous GPS measurements, where the red triangles show the location of the USGS GPS sensors, the red squares show the USGS Yellowstone earthquake catalog between 12/2010 and 09/2011, and the contours represent surface deformation in millimeters.

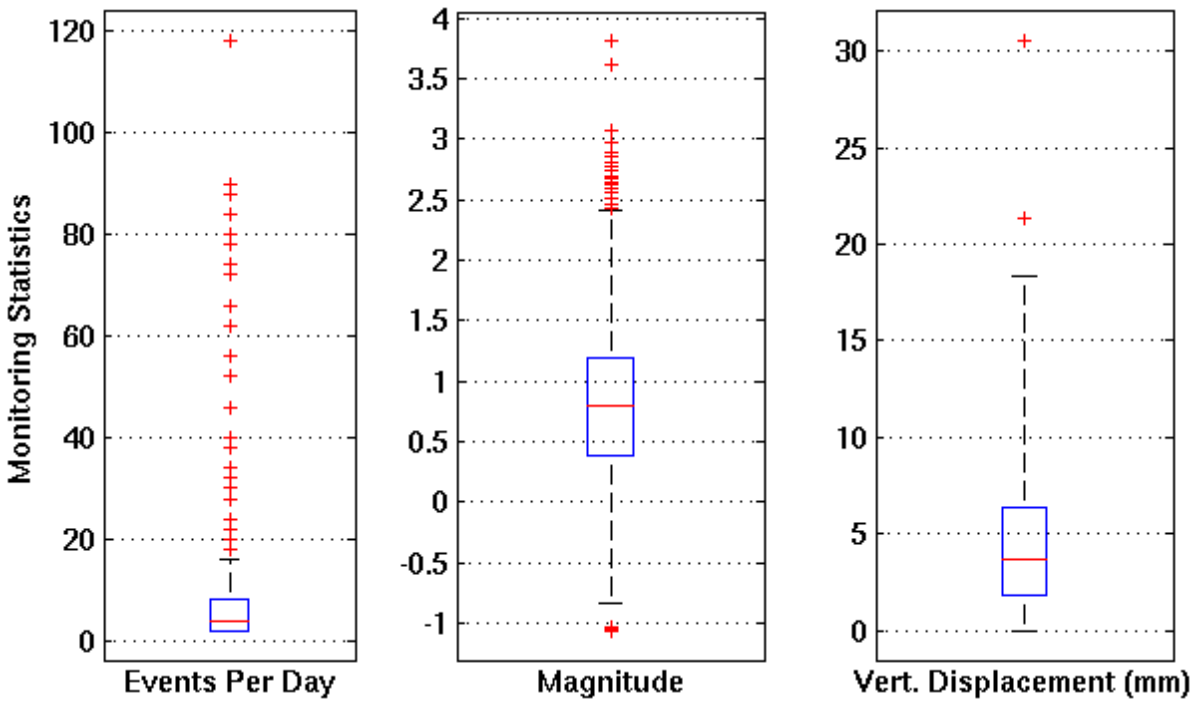

Figure 5.14: Boxplots highlighting the distribution of seismicity and deformation within the Yellowstone caldera between 2005 and 2008, where the events per day and magnitude whiskers are set to 1.5 and the vertical GPS deformation measurements are 3 times the inter quartile range. Monitoring thresholds are 16.0 events per day, m_l of 2.42, and 18.3 mm of deformation.

5.2.1 Eruption Forecasts for the 2010 Yellowstone Earthquake Sequence

Figure 5.14 shows the outlier analysis results for the Yellowstone caldera based on data acquired between 2005 and 2008. In this case, the unrest detection thresholds for each monitoring discipline are 16.0 earthquakes events per day, M_L of 2.42, and vertical surface deformation of 18.3 mm (at GPS site P711). GPS station P711 was selected for this example due to its proximity to the 2010 sequence.

Forecasts of volcanic activity are initiated 90 days before the conclusion of the episode. On 2009-12-18 the algorithm was initiated and triggered on anomalous seismic activity on 2009-

12-26. The unrest severity and trigger state vectors are shown in Figure 5.15 A and B. Positive modeling results were injected into the algorithm 3 days after its initial detection of unrest. This was done to simulate the potential delay associated with a rapid modeling study that may be conducted upon the surprise detection of unrest at a monitored volcano. Severity declarations fluctuate throughout the episode due to the elevated periods of anomalous seismicity (see Figure 5.16 A and B). Estimates begin low, elevate to moderate upon the injection of positive modeling results, and reach extreme during elevated periods of seismicity between episode days 31 and 48.

Figure 5.17 A shows a time series of intrusion, eruption, and intensity forecasts for each of the logistic models. The plot shows the unrest event has an extremely high probability of being the result of a magmatic intrusion. This estimate is the result of the positive modeling results and the extraordinarily high levels of seismic activity within the caldera (see Figure 5.16 A and B). However, the probability of eruption is extremely low and ranges between 0.05 at the episode onset, rises to 0.34, and eventually settles near 0.25. This result is not surprising since Yellowstone has not erupted in over a millennium. This is an example of the ERH value preventing the eruption forecast from being over inflated and not reflecting reality. Intensity estimates are also extremely high. Given the amount of activity and positive modeling results, if the volcano were to erupt it would be a cataclysmic event.

Figure 5.17 B shows a time series of intrusion, eruption, and intensity conditional probability estimates for event tree nodes 2, 3, and 4. Since the initial estimates for the intrusion and intensity nodes were essentially 1.0, there is little change in the probabilities of these events. The eruption probability has been elevated slightly due to the high intrusion probability.

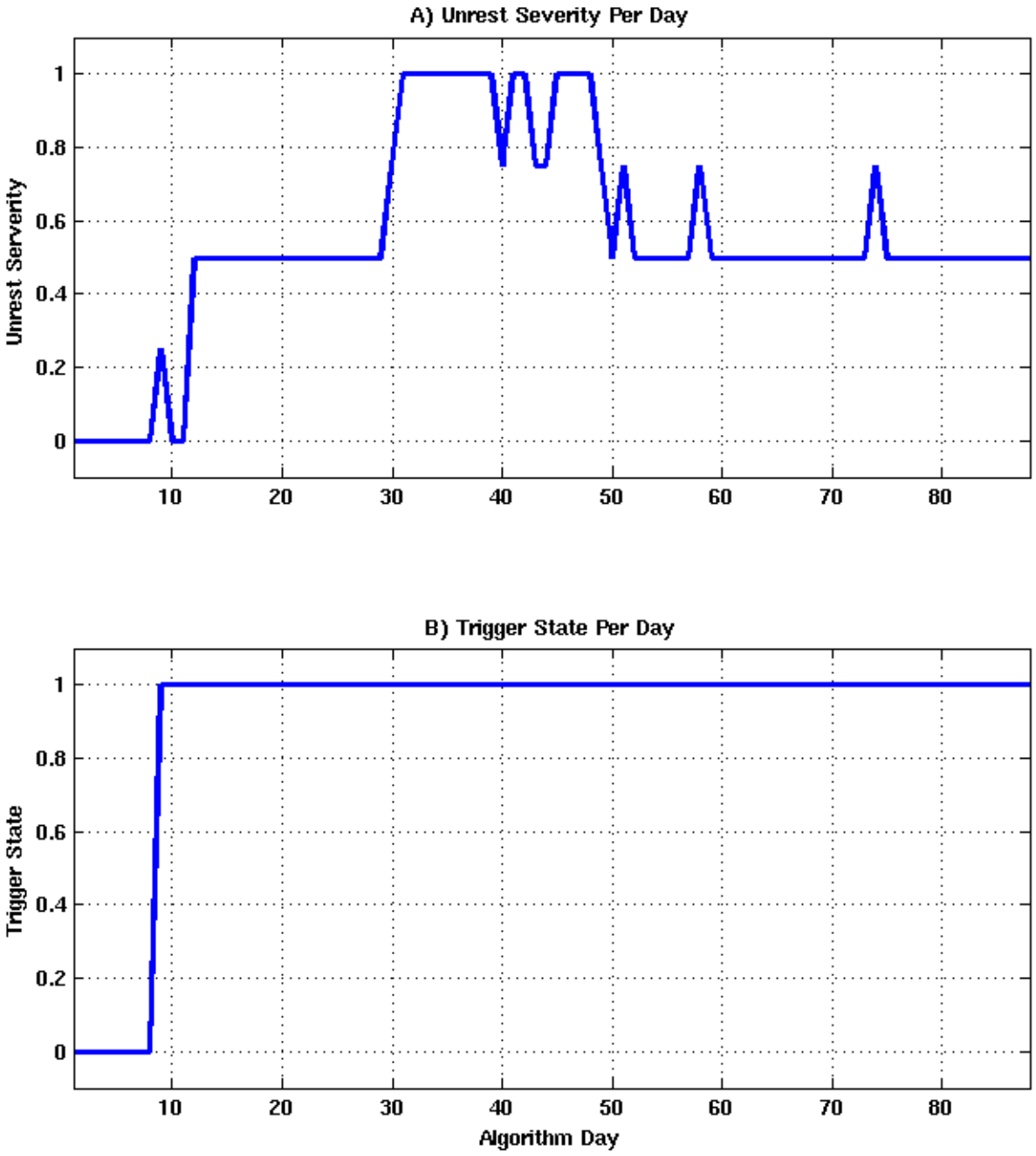

Figure 5.15: Algorithm state as a function of processing day. A) Unrest severity estimates per day, where a description of the states is listed in Table 4.4. B) Trigger state of the forecasting algorithm, where the trigger state transitioned from 0 to 1 on algorithm day 8.

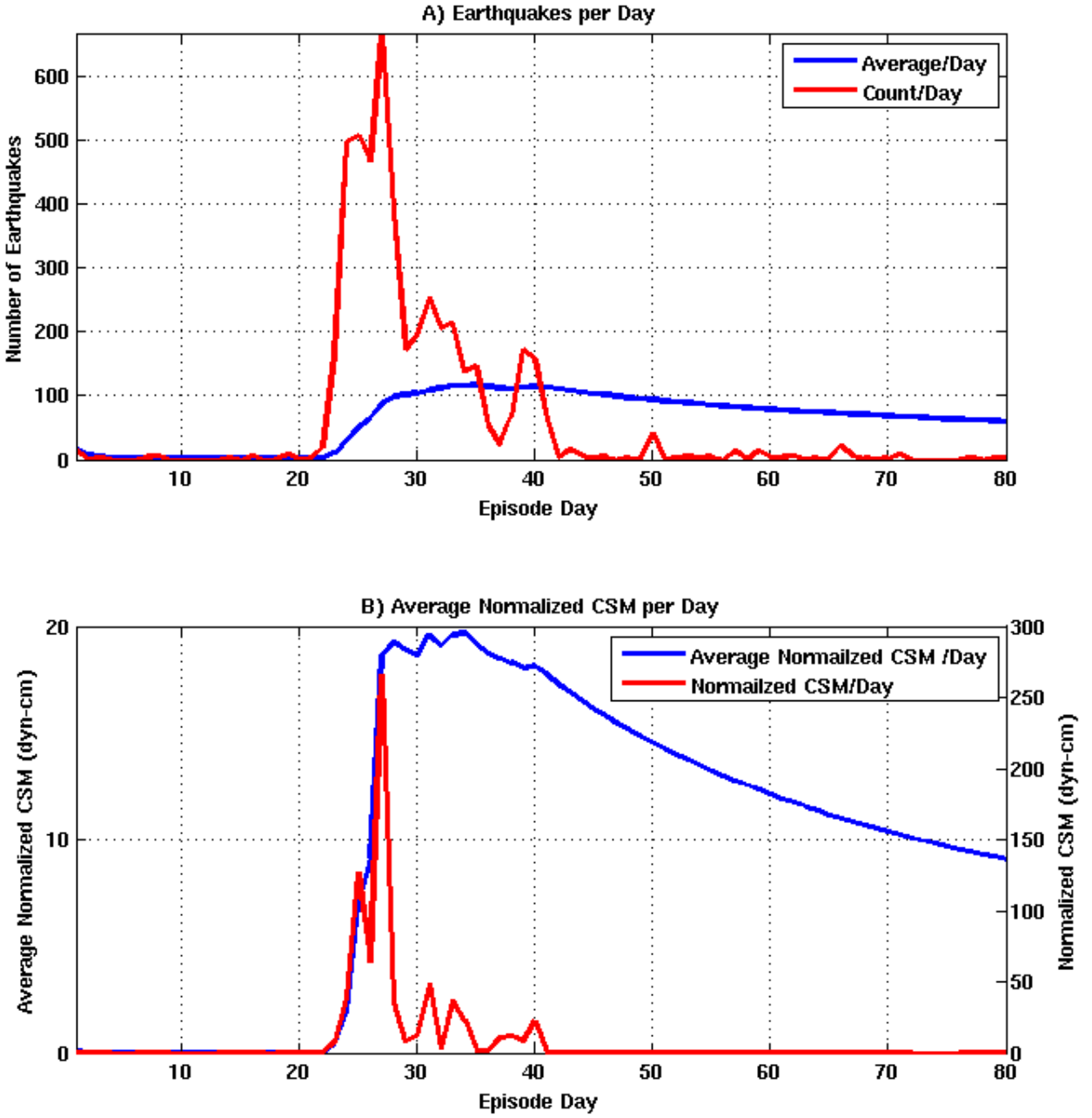

Figure 5.16: Volcano monitoring data preceding the 2010 Yellowstone earthquake sequence. A) Count and average (X_{NE}) number of earthquakes per episode day (X_{DAYS}), shown in blue and red. B) Count and average (X_{CSM}) seismic moment per episode day (X_{DAYS}), shown in blue and red.

Figure 5.17 C shows a time series of intrusion, eruption, and intensity forecasts generated by the event tree framework. There is no change in the intrusion estimate, since the probability of unrest is equal to 1.0. The eruption probability also remains unchanged since the unrest and intrusion probabilities are essentially equal to 1.0. Eruption probability estimates range between 0.05 on day 1, peaks at 0.54 on day 35, and settles to approximately 0.44 on day 88. Given the intensity estimate was set to 1.0 by the previous processes, the new estimate is now in lock step with the eruption forecast. Therefore, the chance of a violent eruption at Yellowstone resulting from this unrest event is, on average, approximately 0.45 over the course of the episode.

A time series of the USGS color code declarations are shown in Figure 5.17 D. This episode begins as a yellow event, drops to green for one day and increases to yellow for 22 days. During the rapid onset of high levels of seismicity, the algorithm elevates the episode to red for 34 days. Several days after the conclusion of the earthquake sequence, the episode is downgraded to yellow and remains there for its duration.

A time series of selected spatial PDFs highlighting probable volcanic vent locations within the Yellowstone Caldera are shown in Figure 5.18. In this case, the spatial resolution of the DEM is 1 arc-seconds (2.78e-4°). Since the average epicenter uncertainty for the Yellowstone seismic network is unknown, a value of 2.3 km is assumed for demonstration purposes. As a result of this assumption, all X^j_{seis} samples within 1.15 km of each epicenter are set to 1. Due to the initial absence of modeling information, the map for Day 1 shows probable vent locations scatter over the Snake River Valley. Initially, the search area spans 14140 km^2, J=20,744,274, and all X^j_{def} = 0. Published modeling results and deformation maps shown in Figure 5.12 and Figure 5.13 indicate the uplift is caused by a large sill (magmatic intrusion with a horizontal orientation) beneath the

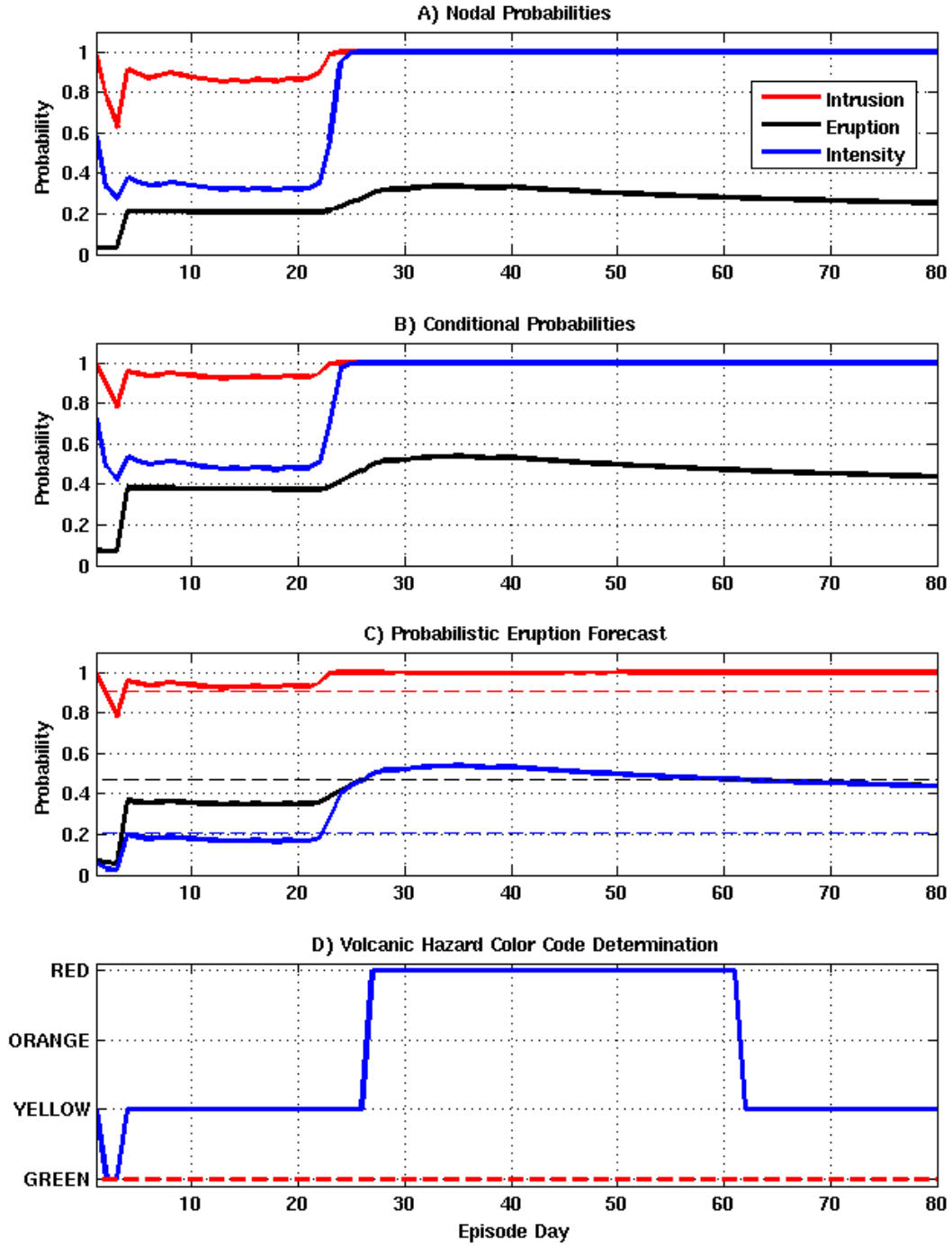

Figure 5.17: Forecasts of volcanic activity preceding the 2010 Yellowstone earthquake sequence, where the intrusion, eruption, and intensity probabilities and thresholds are shown by the red, black, and blue, solid and dotted lines. A) Evolution of prior probability estimates as a function of episode day. B) Variation of conditional probability estimates. C) Probability of occurrence for event tree node. D) Volcanic ground hazard color code declaration.

caldera [118]. This information is injected into the algorithm seven days after initiation. As a result, the forecast area is constrained to a 81 km by 55 km rectangular, which reduces the search area to 4455 km^2 area, J= 6,534,594 probable locations, and all X^j_{def} = 1. Over the next 80 days, seismic activity accumulates and the spatial PDF begins to highlight a preferred vent location which resides in the western corner of the park. On day 80 activity subsided without the onset of an eruption.

5.3 Grimsvötn Volcano, Iceland

Grimsvötn is located approximately 200m below the northwestern portion of the Vatnajökull icecap in southeastern Iceland (see Figure 5.19). This volcano is among the most active Iceland. It has erupted approximately 29 times over the last 211 years, where five have occurred within the last 100 years (e.g., 1938, 1983, 1998, 2004, and 2011) [127]. Its 2011 eruption began on 21 May, 2011, which is approximately 13 months after the now infamous 2010 Eyjafjallajökull eruption. Like its predecessor, it produced large ash clouds that extended approximately 20km into the atmosphere which disrupted European air traffic for several days [136].

Since Grimsvötn is a subglacial volcano, InSAR techniques cannot be used to search for surface deformation. Therefore, GPS data is required to identify deformation consistent with a magmatic intrusion. GPS data acquired by Icelandic Meteorological Office stations posted on the Icelandic Institute of Earth Science (IES) website was used to estimate the Mogi source parameters for this episode [137], [138]. The GPS stations (GRIM and GFUM) are located approximately 3km from the caldera center. Ground motion measurements acquired by these instruments appear

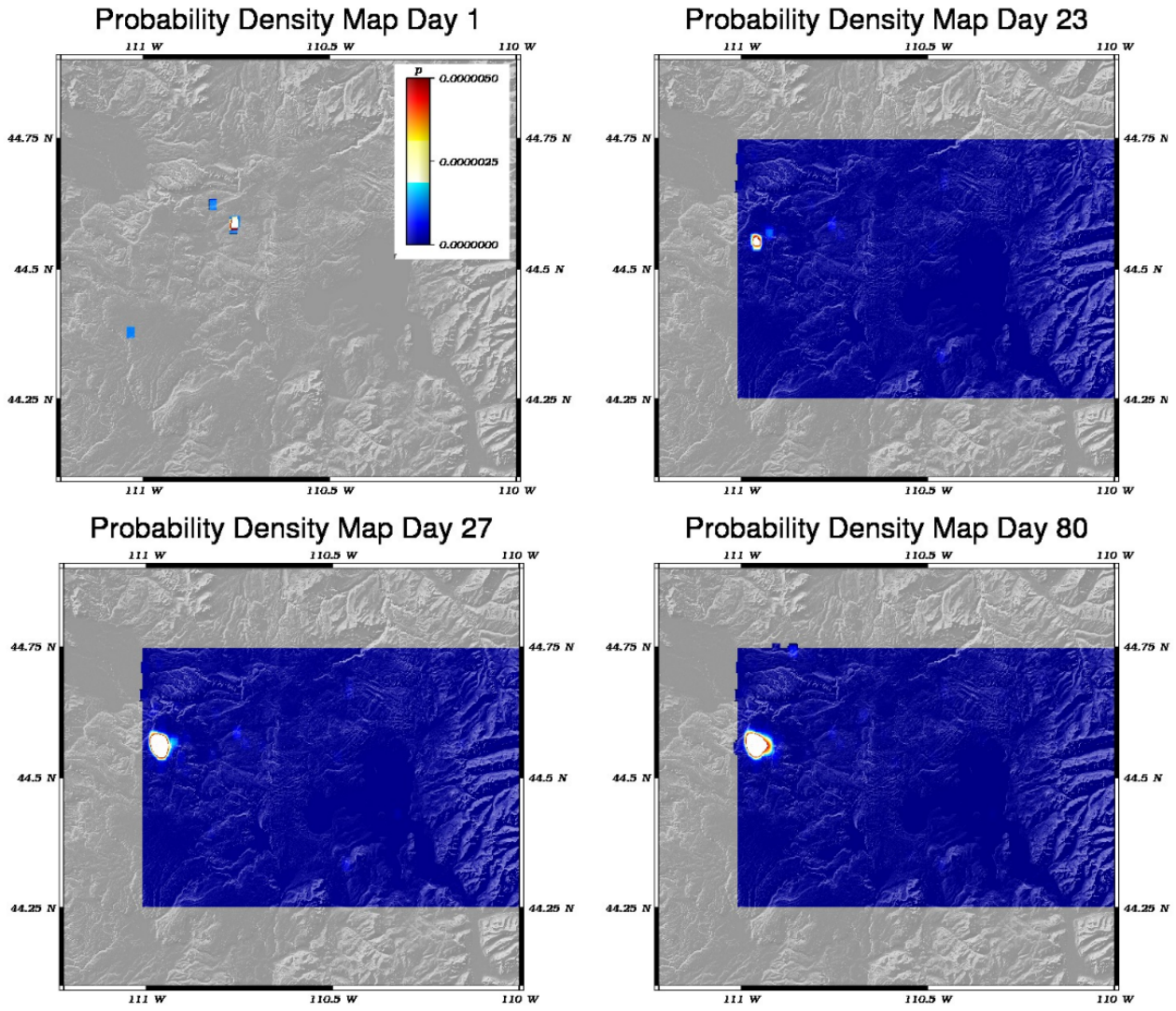

Figure 5.18: Spatial Probability Density Maps for Yellowstone Caldera.

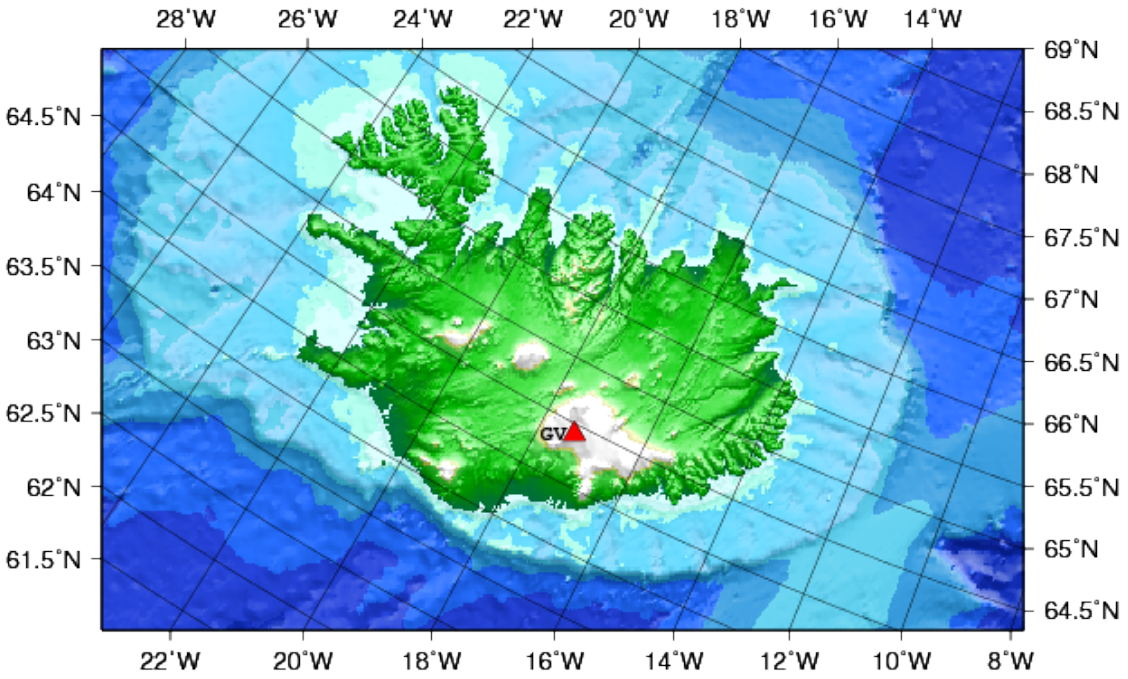

Figure 5.19: Location of the Grimsvötn Volcano (red triangle) relative to the Vatnajökull icecap in southeastern Iceland.

to be identical. There is, however, a substantial difference in the sampling frequency between the stations, where GRIM is approximately one sample per 30 days and GFUM is approximately 1 sample per day. Both sensors show continuous uplift at the site following the 2004 eruption, which increases at almost linear rate between 2005 and 2011. This same pattern of activity was also observed for the five years prior to the 2004 eruption.

Mogi source model parameters were derived using vertical and horizontal ground motion measurements from GFUM. The analysis technique and assumptions used to determined the source parameters for this episode are similar to those used to study the 1998 eruption [94]. The intrusion source depth was estimated by taking the ratio of Equations 2.1 and 2.2 and solving for d, which is estimated by $(\Delta h(r)/\Delta r(r))r = d$. Vertical and horizontal displacements are measured directly from the GPS records and the location of the intrusion is assumed to reside beneath the caldera

center ($r = 3.0km$). Resulting source parameters derived eight months before and approximately 30 days after the 2011 eruption are shown in Table 5.2. The results of this analysis are similar to those from the 1998 eruption, where the estimated source depth was 1.62 km [94].

Table 5.2: Estimated Mogi source parameters derived from GFUM approximately 240 before and 30 days after the 2011 Grimsvötn Eruption, where positive and negative values of C indicate uplift or subsidence occurred and positive and negative values of Δ V mean material was acquired or expelled.

Sample	Δ h	Δ r	d	C	Δ V
Pre-eruption	40 mm	36 mm	3.00 km	0.0011 km^3	0.0068 km^3
Post-eruption	250 mm	468 mm	1.60 km	-0.0061 km^3	-0.0383 km^3

The vent location search area is estimated using Equation 2.1 and the pre-eruption source parameters shown in Table 5.2. Resulting deformation profiles are shown in Figure 5.20. Based on the modeling results a search radius of 17km is used to constrain the vent location process.

5.3.1 Forecasts Preceding Grimsvötn's 2011 Eruption

The VEFA was used to assess the possibility of volcanic activity at Grimsvötn preceding its 2011 eruption. Since the raw GPS data from GFUM is not available and InSAR techniques will not work in this situation, only seismic data was used for unrest detection. The boxplots shown in Figure 5.21 represent the distributions of the number or earthquakes per day and earthquake magnitudes between 2005 and 2011. The seismic unrest thresholds used for this volcano are 8.0 events per day and a magnitude of 2.27.

Monitoring was initiated on 2010-11-24 and triggered on an anomalously large seismic event (M_L 3.54) on 2010-11-25. Unrest severity estimates and trigger state vector are shown

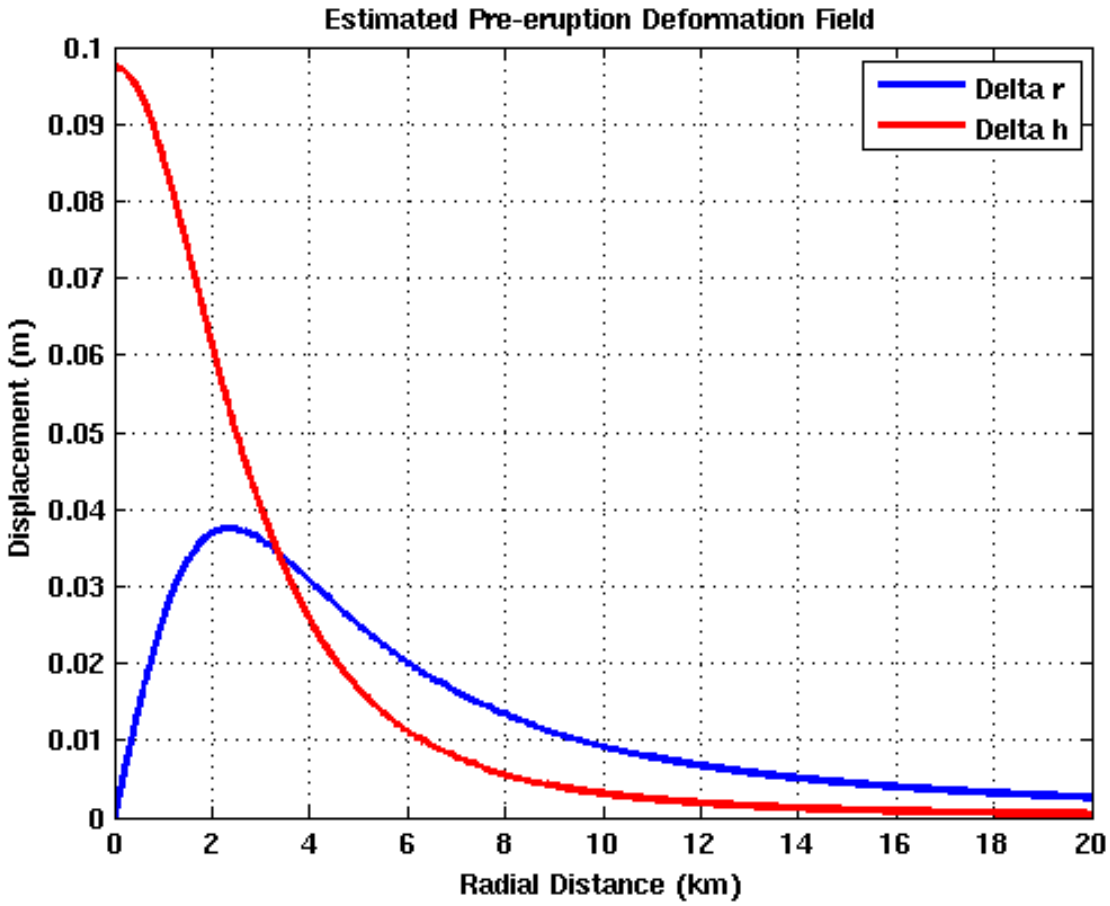

Figure 5.20: Estimated extent of the deformation field preceding Grimsvötn 2011 eruption.

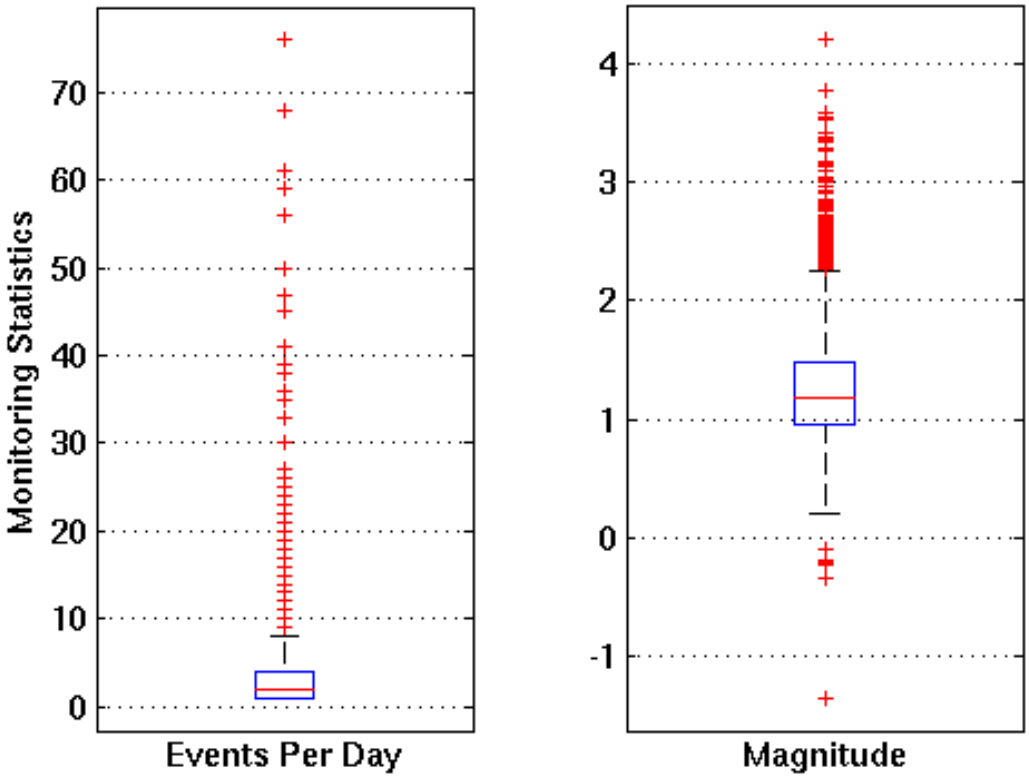

Figure 5.21: Boxplots highlighting the distribution of seismicity and deformation beneath the Grimsvötn caldera between 2005 and 2011, where the events per day and magnitude whiskers are set to 1.5 time the inter quartile range. Monitoring thresholds are 8.0 events per day and a m_l of 2.27

in Figure 5.22 A and B. The rapidly fluctuating unrest severity is caused by elevated periods of anomalous seismicity throughout the episode (See Figure 5.23 A and B). On algorithm day 136, positive modeling results were injected into the algorithm. This is meant to simulate potential delays associated with manual source modeling exercises that may be initiated upon the detection of unrest.

Figure 5.24 A, B, and C show a time series of intrusion, eruption, and intensity forecasts for each stage of the algorithm. Initially, activity forecasts shown in Figure 5.24 C fluctuate between 0.60 - 0.79, 0.18 - 0.20, and 0.04 - 0.09 for the intrusion, eruption, and intensity estimates. The large variation in forecasts are due to the rapidly changing seismic conditions at the site. Forecast probabilities increase dramatically upon the injection of positive modeling results into the algorithm. Revised forecasts suggest this event has a 0.91 probability of being caused by a magmatic intrusion, a 0.68 probability of culminating to an eruption, and a 0.24 of probability exceeding an intensity of 1.0.

The color code declarations shown in Figure 5.24 D change dramatically over the course of the episode. Initial results place the hazard level as green. Upon the determination that the event is the result of a magmatic intrusion, the hazard level immediately jumps to red. This declaration suggests that an eruption of greater than VEI 1.0 may be imminent.

A time series of selected spatial PDFs highlighting probable volcanic vent locations at Grimsvötn are shown in Figure 5.25. Here the spatial resolution of the grid is also 1 arc-seconds (2.78e-4°). Since the average epicenter uncertainty for the Icelandic seismic network is unknown a value of 2.3km is assumed for demonstration purposes. Thus, all X^j_{seis} samples within 1.15 km of each epicenter are set to 1. Due to the absence of modeling information, maps for days 1 and

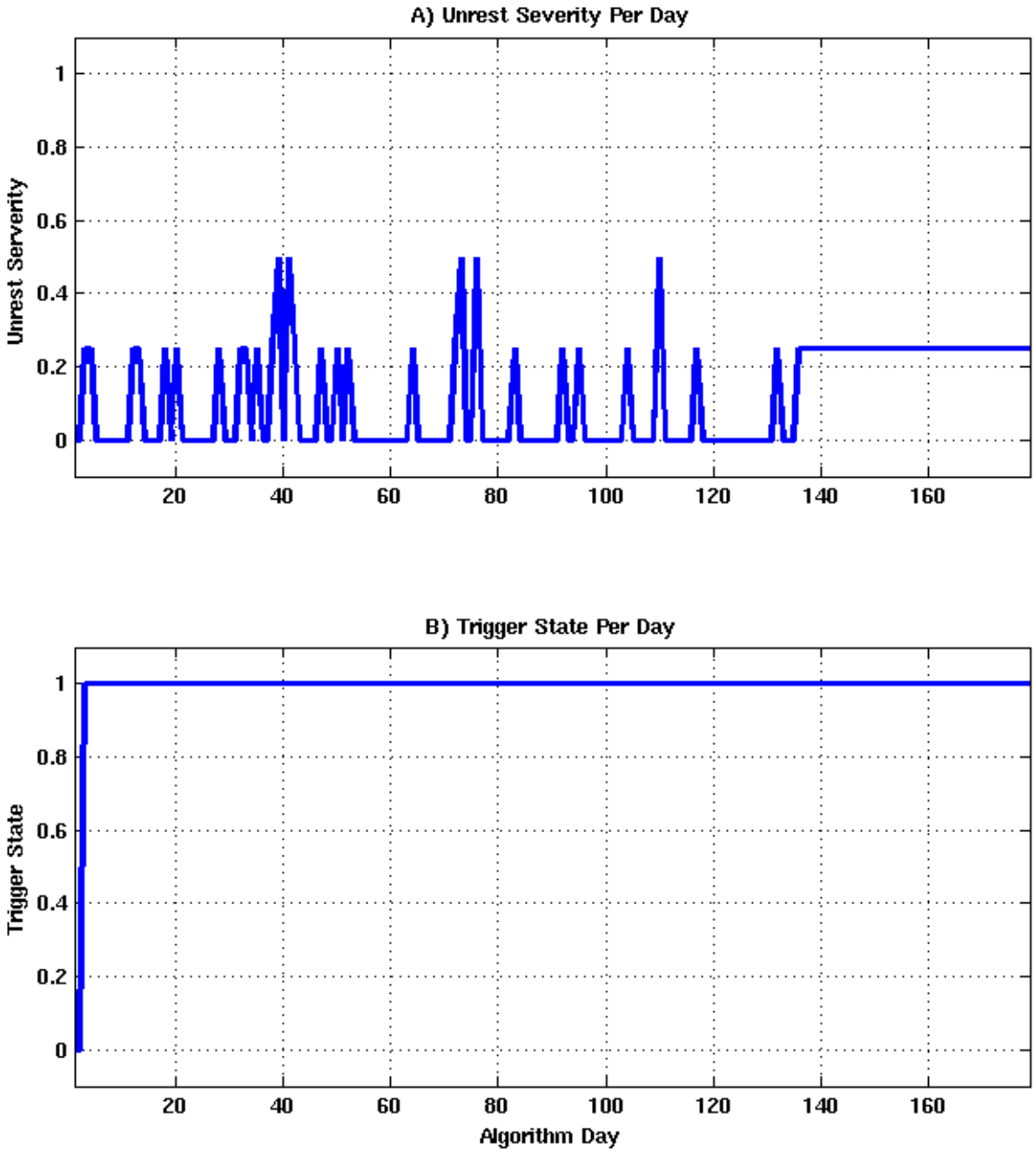

Figure 5.22: Algorithm state as a function of processing day. A) Unrest severity estimates per day, where a description of the states is listed in Table 4.4. B) Trigger state of the forecasting algorithm, where the trigger state transitioned from 0 to 1 on algorithm day 2.

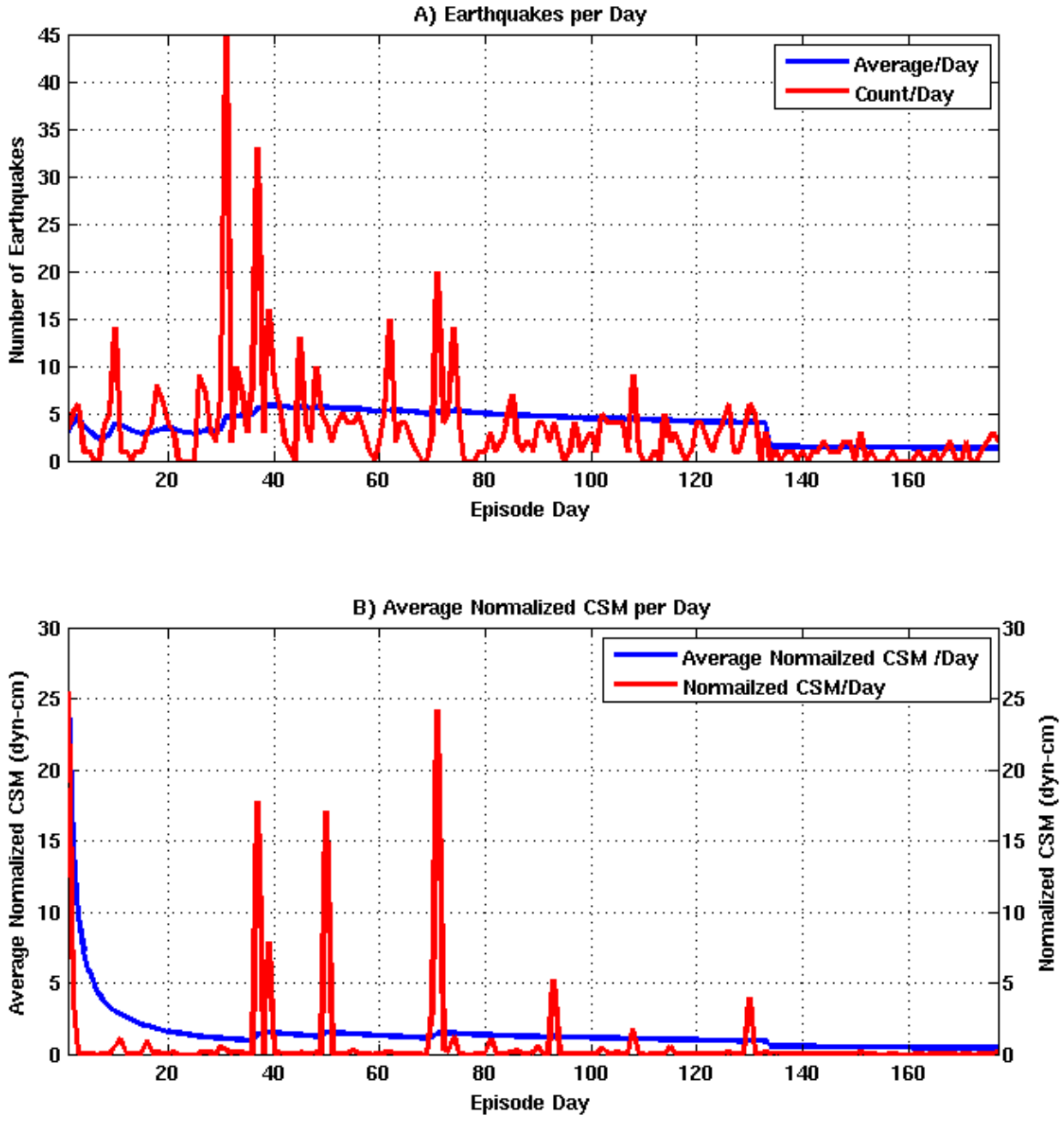

Figure 5.23: Volcano monitoring data preceding Grimsvötn 2011 eruption. A) Count and average (X_{NE}) number of earthquakes per episode day (X_{DAYS}), shown in blue and red. B) Count and average (X_{CSM}) seismic moment per episode day (X_{DAYS}), shown in blue and red.

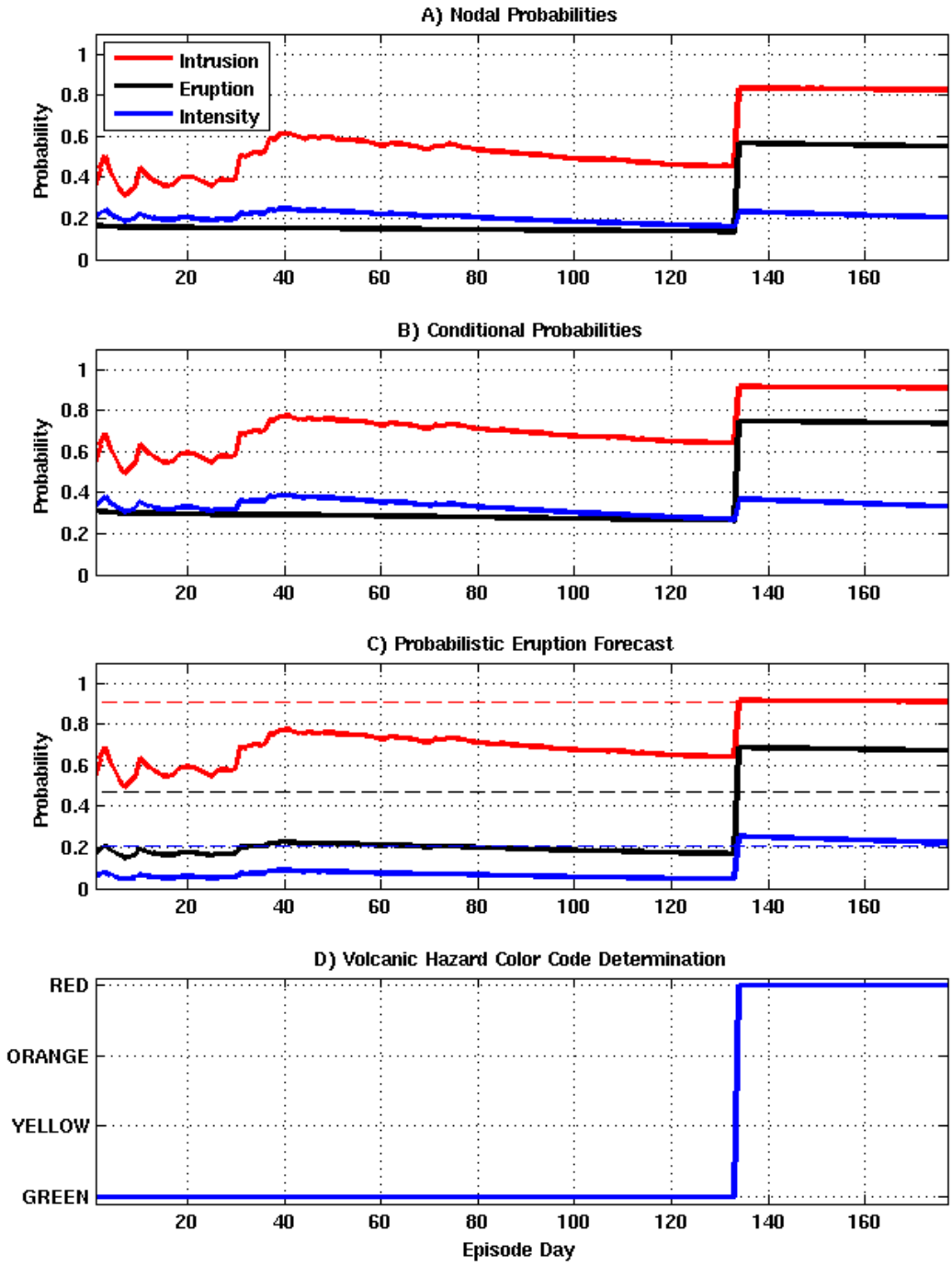

Figure 5.24: Forecasts of volcanic activity preceding Grimsvötn 2011 eruption, where the intrusion, eruption, and intensity probabilities and thresholds are shown by the red, black, and blue, solid and dotted lines. A) Evolution of prior probability estimates as a function of episode day. B) Variation of conditional probability estimates. C) Probability of occurrence for event tree node. D) Volcanic ground hazard color code declaration.

37 show probable vent locations are scatter over the Vatnajökull icecap. Initially, the search area spans 2979 km^2, J=7,094,495, and all X^j_{def} = 0. Modeling results shown in Figure 5.20 suggest the deformation source is located approximately 3.33 km below the caldera center and has an isotropic radiation pattern that is approximately 34 km in diameter. This information provides the justification to quantitatively constrain the PDF to a square search area spanning 1156 km^2, reduce J to 2,788,920 probable locations, and set all X^j_{def} = 1. As seismic activity accumulates over time, the spatial PDF begins to highlight a preferred vent location. Maps computed for Days 134, and 177 show the most likely area for vent formation is in the eastern portion of the caldera.

Grimsvötn erupted on algorithm day 179. Much like the Eyjafjallajökull eruption of 2010, this event disrupted transatlantic and European air traffic for several days. Due to the recent nature of this event, official source modeling results, vent location, and eruption intensity estimates have not been published.

5.4 Mount Saint Helens

Mount Saint Helens is an active stratovolcano that is part of the Cascade Mountain Range and is located in the southwestern region of Washington state. It has erupted approximately fourteen times since 1800, which includes four in the last 30 years. The most recent eruption began in 2004 and subsided in 2008[127]. Its most notable eruption occurred in 1980. This episode was initiated by a large earthquake caused by a rapid magmatic intrusion. The earthquake triggered a slope collapse that resulted in explosive decompression of volatiles contained within the mountain. The ensuing explosion and VEI 5 eruption destroyed the top section of the mountain (reducing

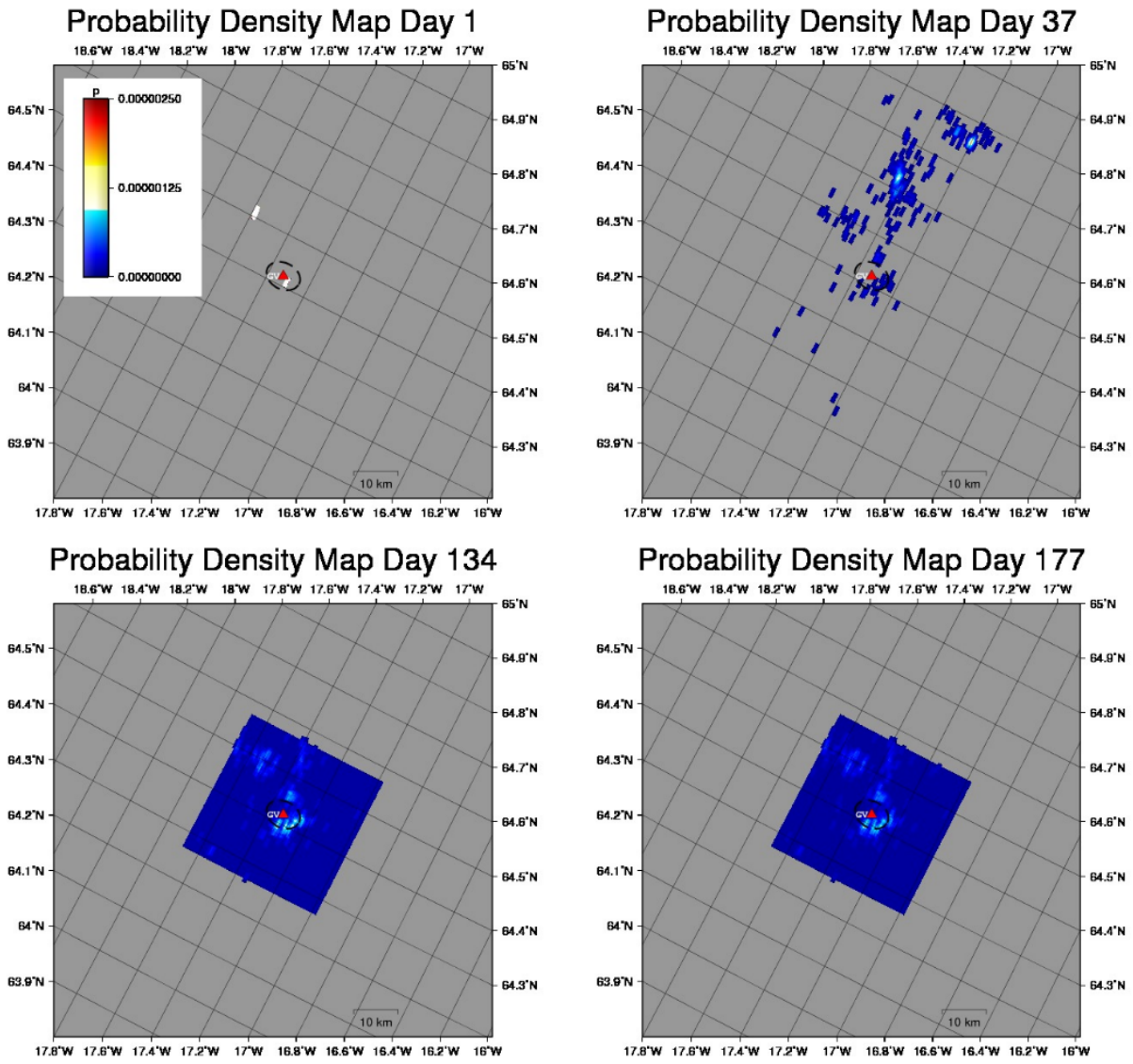

Figure 5.25: Spatial Probability Density Maps for volcanic activity preceding Grimsvötn 2011 eruption, where the black ellipse outlines the approximate area of the caldera.

its elevation by approximately 1000 feet), inflicted massive damage on the surrendering area, and resulted in the death of some local residents and a USGS volcanologist.

In mid February 2011 a magnitude 4.3 earthquake occurred approximately 15 km north of the 1980 eruption crater. A map highlighting the location of the earthquake and its associated aftershock sequence is shown in Figure 5.26. Examination of the available data for this sequence indicates its origin is tectonic in nature and not the result of a new magmatic intrusion. Moment tensor solutions published by the University of Washington using the Pacific Northwest Seismic Network (PNSN) show the main shock having a strike slip faulting mechanism which is typical for tectonic earthquakes. Moreover, examination of GPS data acquired by the three nearest stations show not appreciable surface deformation associated with this event (See Appendix G). Since there is no indication that a magmatic intrusion is taking place, the X_{MM} parameter is set to negative (0) for the duration of the episode.

5.4.1 Eruption Forecasts for the 2011 Earthquake Sequence

Figure 5.27 shows the outlier analysis results for the Mount Saint Helens area based on data acquired between 2007 and 2011. Estimated unrest thresholds for each monitoring discipline are 3.0 earthquakes events per day, M_L of 3.1, and vertical surface deformation of 23.3 mm per day (at GPS site JRO1). GPS station JRO1 was selected for this example due to its proximity to the sequence.

The algorithm was initiated on 2010-12-31 and triggered on elevated levels of seismicity on 2011-01-27. A time series of unrest severity estimates and the trigger state vector are shown

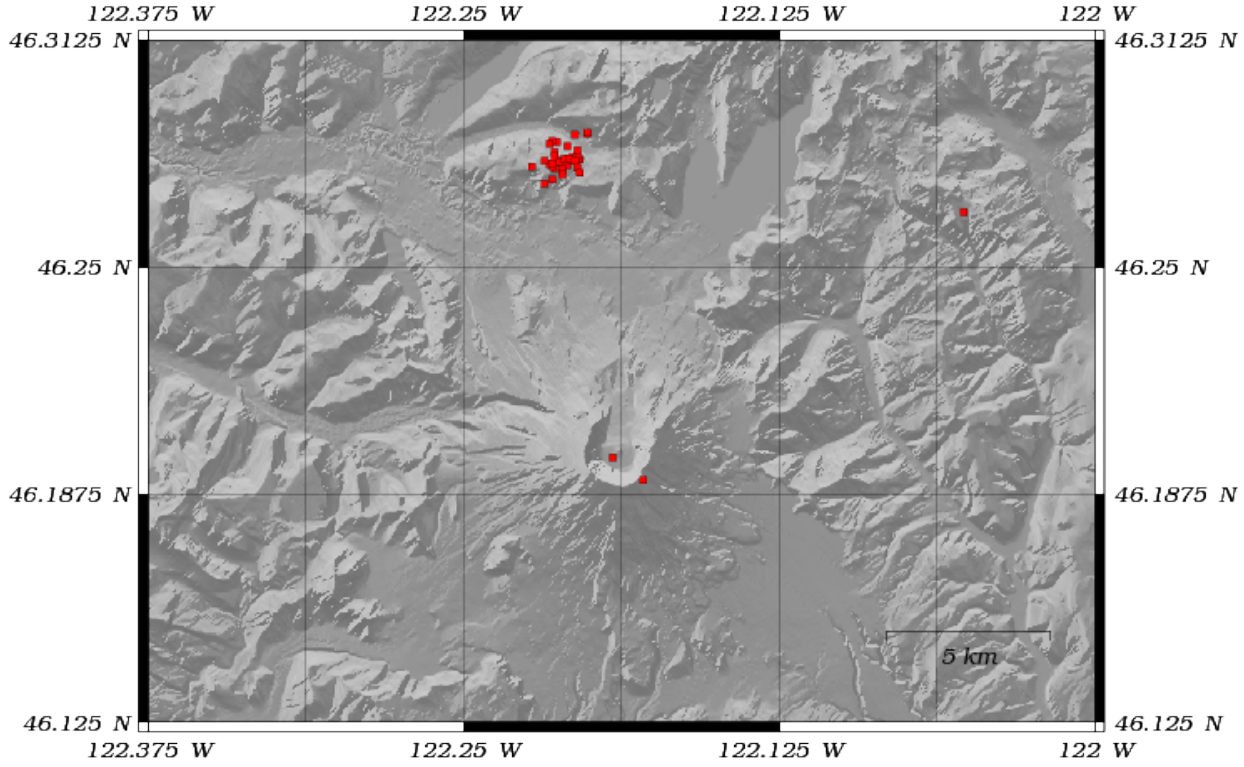

Figure 5.26: Location of a small earthquake sequence that occurred between January and March of 2011 relative to Mount Saint Helens, where earthquake epicenters are shown by red squares.

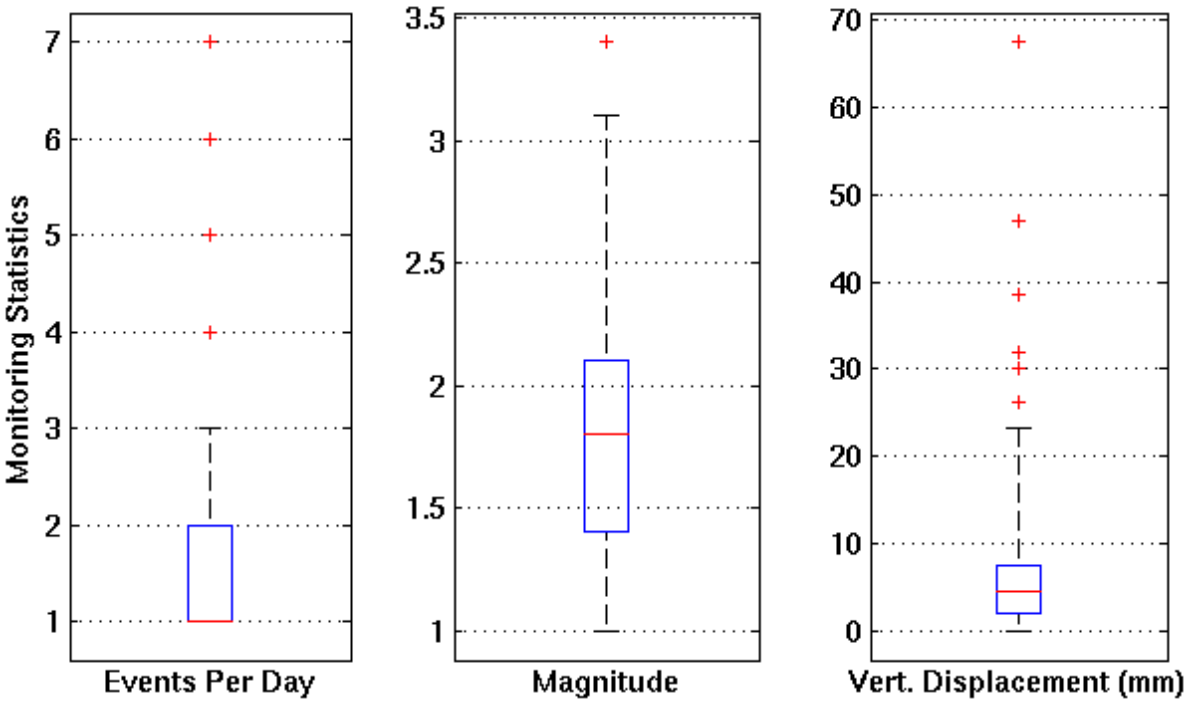

Figure 5.27: Boxplots highlighting the distribution of at Mount Saint Helens between 2007 and 2011, where the events per day and magnitude whiskers are set to 1.5 and the vertical GPS deformation measurements are 3 time the inter quartile range. Monitoring thresholds are 3.0 events per day, m_l of 3.1, and 23.3 mm of deformation.

in Figure 5.28 A and B. The figures show the processing triggering on algorithm day 26. Unrest severity estimates are essentially flat with the exception of several spikes occurring on algorithm day 27, 29, 30, 45, and 46, where the last two bursts of activity are associated to the February 2011 sequence.

Volcanic activity forecasts shown in Figure 5.30 A, B, and C illustrate intrusion, eruption, and intensity estimates from nodes 2, 3, and 4. Figure C shows all event tree forecasts fall below their respective detection thresholds. Intrusion probabilities are initially in the 0.60 range and drop to the 0.37 range as the level of average seismicity per day decreases (see Figure 5.29). On algorithm day 14 all forecast models stabilize and remain relatively constant for the duration of the episode. Final activity forecasts for this episode range between 0.37 - 0.60, 0.05 - 0.09, and 0.01 - 0.03 that a magmatic intrusion is occurring and will result in an eruption that will exceed a VEI of 1.0. The color code declarations shown in Figure 5.30 D remain at green for the entire episode, which is consistent with the hazard level published by the USGS.

A time series of selected spatial PDFs highlighting probable volcanic vent locations near Mount Saint Helens are shown in Figure 5.31. The spatial resolution of the DEM used in this example is 1 arc-seconds (2.78e-4°). Since no notable deformation can be attributed to this event, no quantitative constraint on the forecast area is available. As a result, a 20 km square search area is used and the resulting PDF spans a 400 km^2 area. Since, the average epicenter uncertainty for the Pacific North West Seismic Network is also unknown, a value of 2.3 km is assumed for demonstration purposes. As a result of the assumptions, all X^j_{seis} samples within 1.15 km of each epicenter are set to 1, J = 1,360,800 probable locations, and all X^j_{def} = 0. Over the course of the 33 day episode, seismic activity accumulates and the spatial PDF highlights a preferred vent location

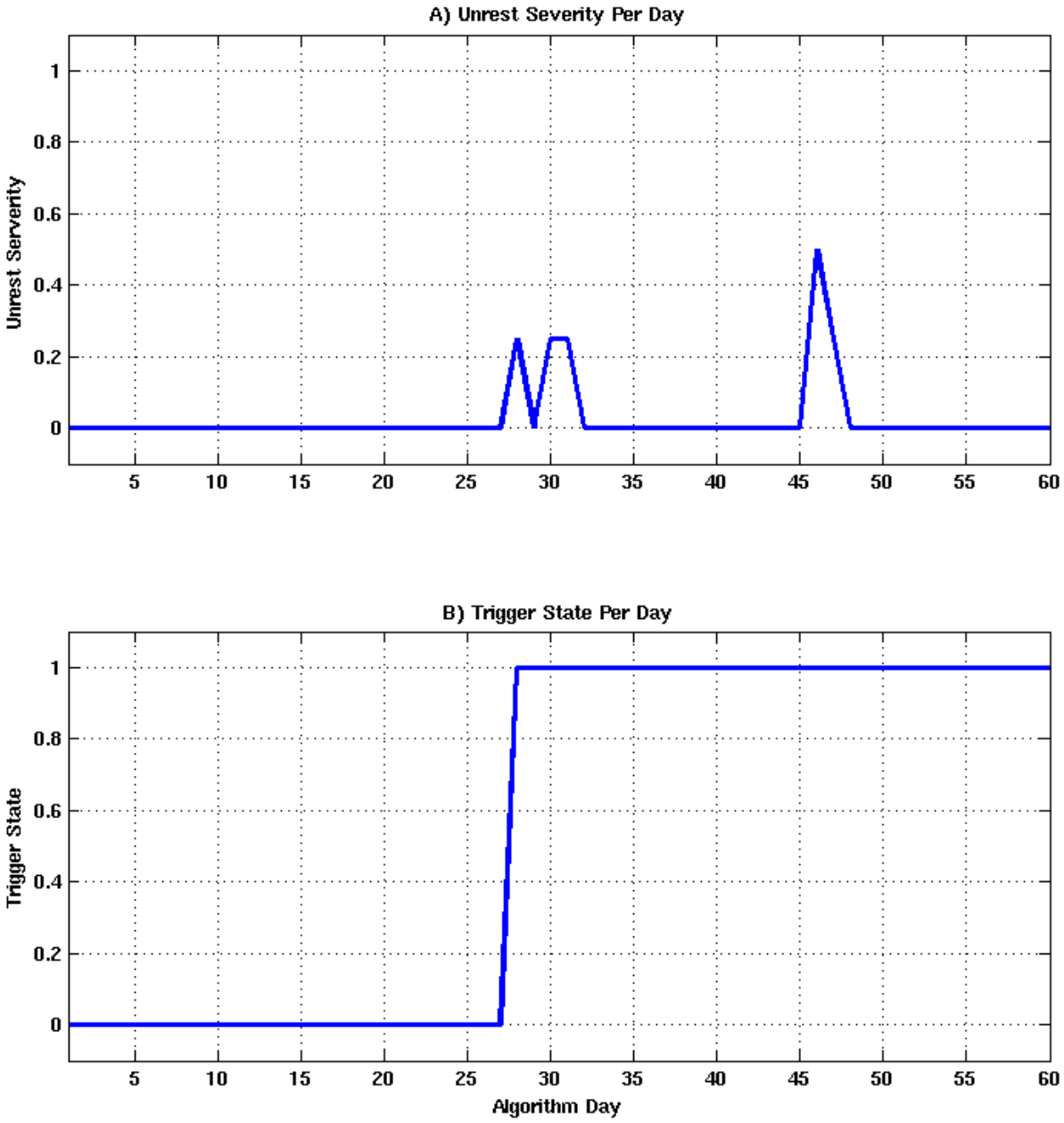

Figure 5.28: Algorithm state as a function of processing day. A) Unrest severity estimates per day, where a description of the states is listed in Table 4.4. B) Trigger state of the forecasting algorithm, where the trigger state transitioned from 0 to 1 on algorithm day 28.

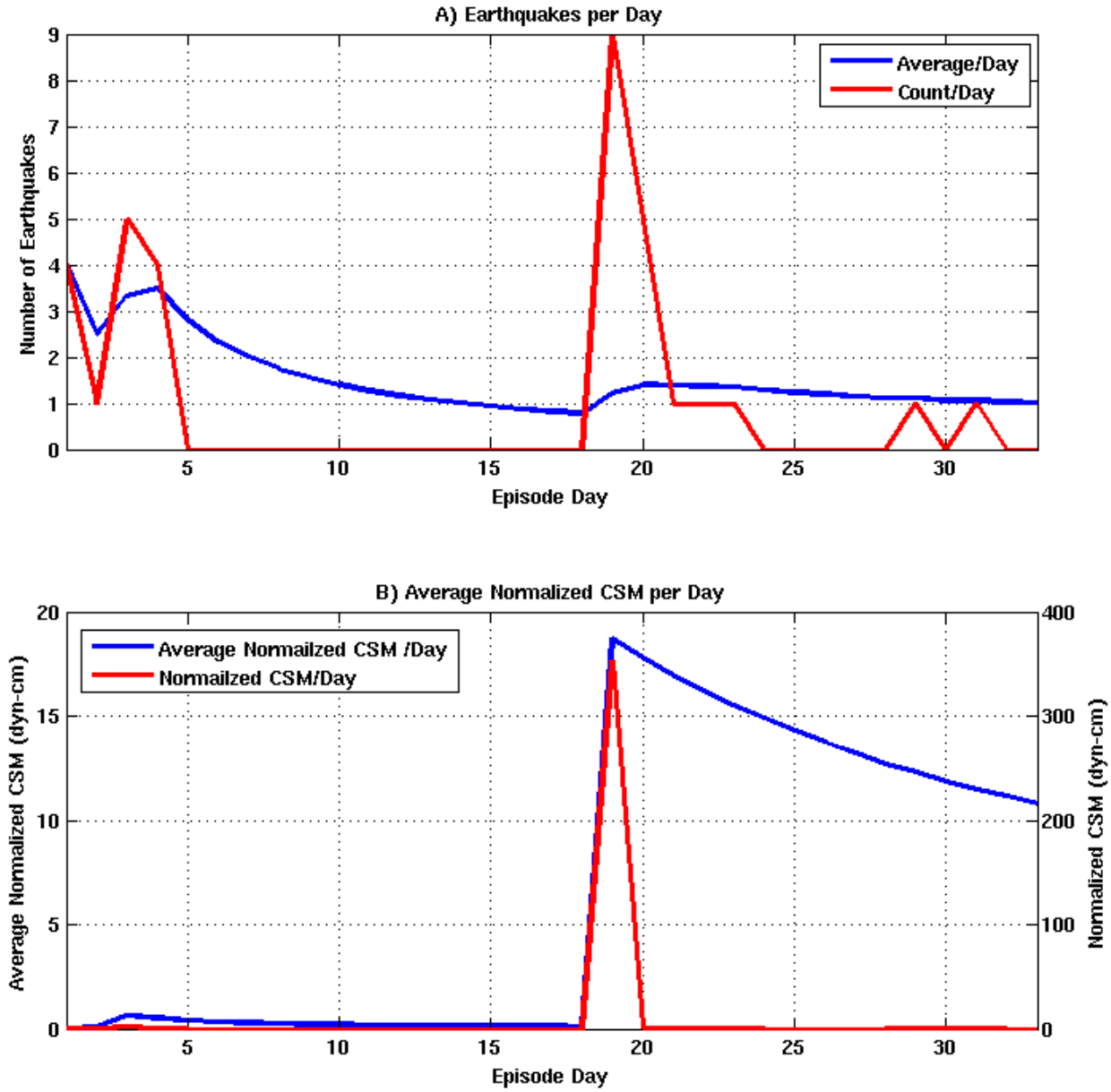

Figure 5.29: Volcano monitoring data preceding the 2011 Mount Saint Helens earthquake sequence. A) Count and average (X_{NE}) number of earthquakes per episode day (X_{DAYS}), shown in blue and red. B) Count and average (X_{CSM}) seismic moment per episode day (X_{DAYS}), shown in blue and red.

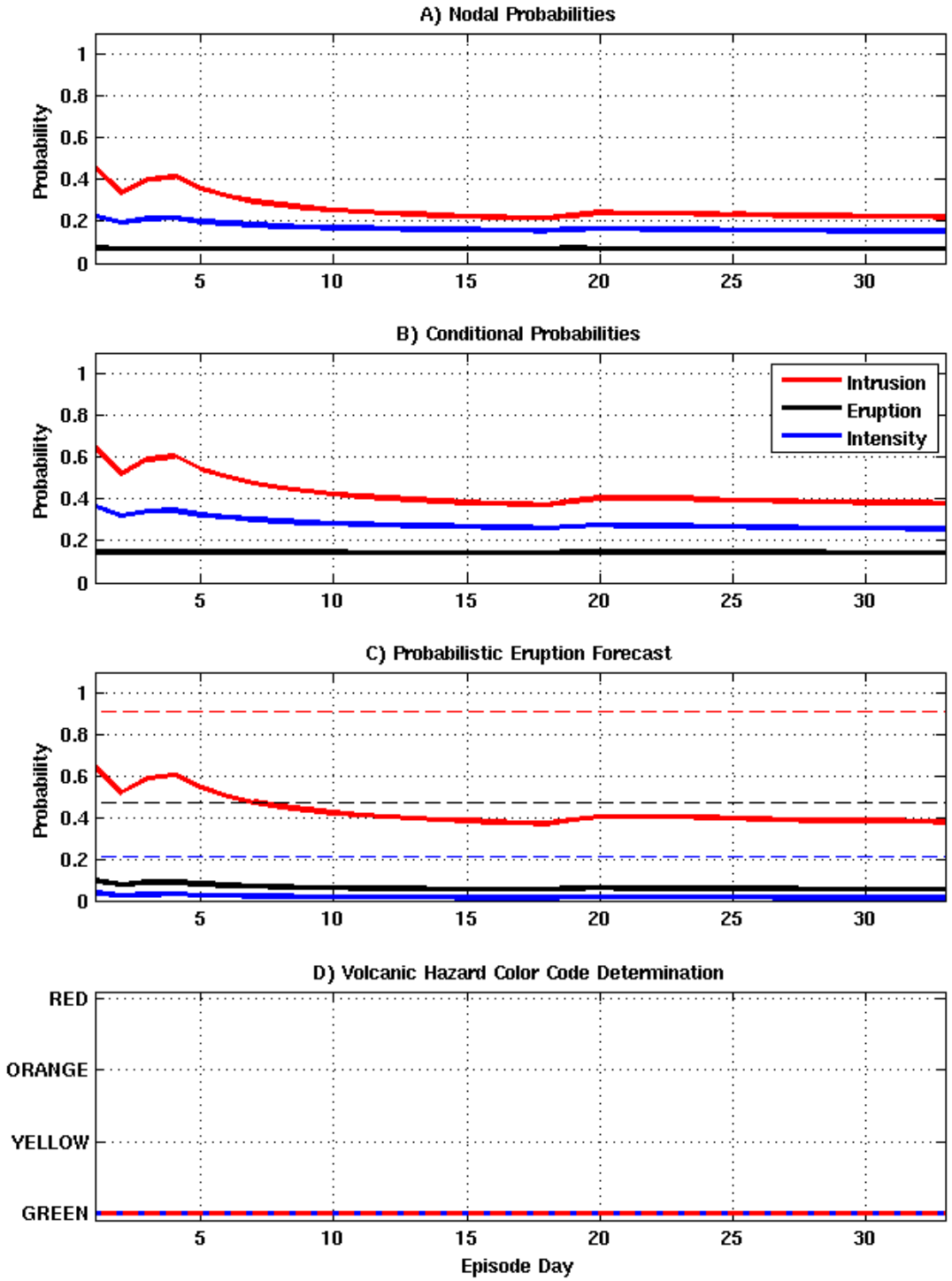

Figure 5.30: Forecasts of volcanic activity preceding the 2011 Mount Saint Helens earthquake sequence, where the intrusion, eruption, and intensity probabilities and thresholds are shown by the red, black, and blue, solid and dotted lines. A) Evolution of prior probability estimates as a function of episode day. B) Variation of conditional probability estimates. C) Probability of occurrence for event tree node. D) Volcanic ground hazard color code declaration.

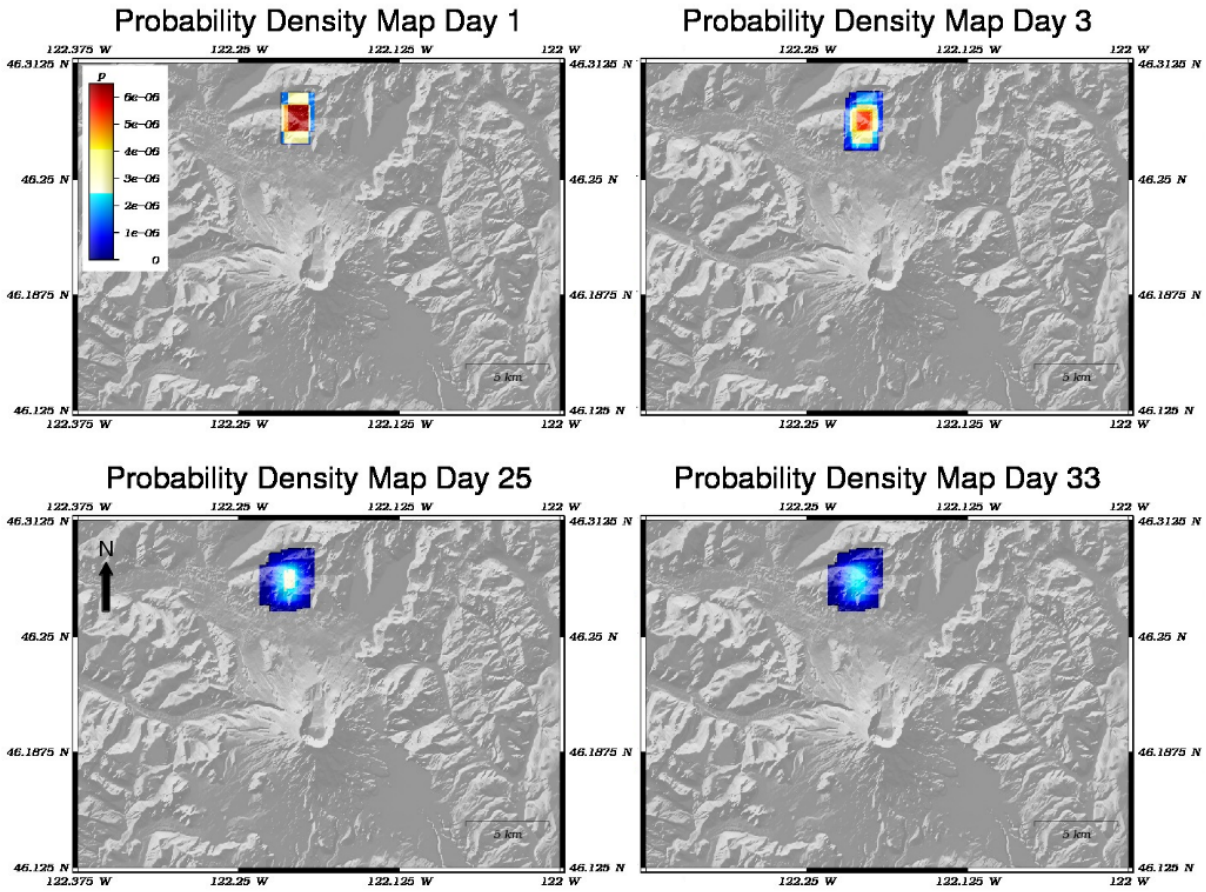

Figure 5.31: Spatial Probability Density Maps for the Mount Saint Helens 2011 earthquake sequence.

to the north of the 1980 eruption crater. Maps computed for days 1, 3, 25, and 33 show the most likely area for vent formation is north of the mountain near Sprit Lake. The large distance between the potential vent and the location of previous activity at Mount Saint Helens show how different this episode is from previous events, which reinforces the low probabilities produced by the VEFA.

5.5 Algorithm Comparisons

The results generated by the VEFA are compared to those derived from the BETEF v2.0 application. The BETEF tool was developed by Warner Marzocchi, Laura Sandri, and Jacopo Selva of the INGV and is freely available via the internet. It employs the statistical processing methodology described in Section 4.2.1 (bullets two and three) and several peer reviewed publications (e.g., [23], [25]). In order to use the tool, unique statistical models must be developed for each volcano being monitored. This means each instance of the application uses a set of assumptions and statistical models that are only valid for a specific volcano. These models are non-transportable and have no defined false positive rate or optimized detection threshold. All model weighting coefficients and detection thresholds used by this application are selected subjectively by the user at the time of their development.

The models used for each example were trained using monitoring and modeling data acquired from the most recent unrest episode preceding the event under test. Modeling results (X_{MM}) were included in the BETEF training set to determine their influence on its forecasting capability. Since eruption history is built directly into the BETEF model during the design process, the ERH parameter is not required as a real time input. Weighting coefficients for each of the BETEF input parameters (X_{NE}, X_{CSM}, X_{MM}, and X_{DAYS}) were set to 1. All VEFA and BETEF forecasts are based on the same input data to ensure the comparability of results. The median value of the BETEF forecast is used for comparison purposes in all examples shown below. Detailed information regarding each BETEF forecast and its associated input parameters are shown in Appendix H.

Intrusion forecast comparisons for each of the previous examples are shown in Figure 5.32 A, B, C, and D. There are substantial differences between the forecasts for Okmok and Mount Saint Helens. In both cases, the results provided by the VEFA are driven by source modeling results since there is little seismicity associated with these episodes. The BETEF does not appear to use the supplied modeling information to effectively predict the outcome of the episode. Intrusion probability estimates for the Yellowstone and Grimsvötn episodes are in very good agreement with one another. However, both of these episodes have a substantial amount of associated seismicity which is likely driving the BETEF's predictions.

Eruption forecast comparisons are shown in Figure 5.33 A, B, C, and D. The large difference between the Okmok and Mount Saint Helens forecasts is still observed, where the results differ on average by 0.6 and 0.7, respectively. This discrepancy is likely due to the lack of seismicity associate with these episodes and the VEFA's ability to properly assimilate source modeling information. Forecasts generated for the Yellowstone and Grimsvötn episodes are fairly similar. However, this agreement is again most likely due to the high levels of seismicity produced by these episodes.

A comparison of eruption intensity estimates are shown in Figure 5.34 A, B, C, and D. Forecasts for the Yellowstone episode are significantly different, while the results for Okmok, Grimsvötn and Mount Saint Helens are fairly consistent. The discrepancy in the Yellowstone forecasts further highlight the influence the modeling results have on the VEFA's forecasts. This is most apparent in the Yellowstone example, where the VEFA's knowledge of the source and the extreme levels of associated seismicity are driving its intensity predictions significantly higher than the BETEF's.

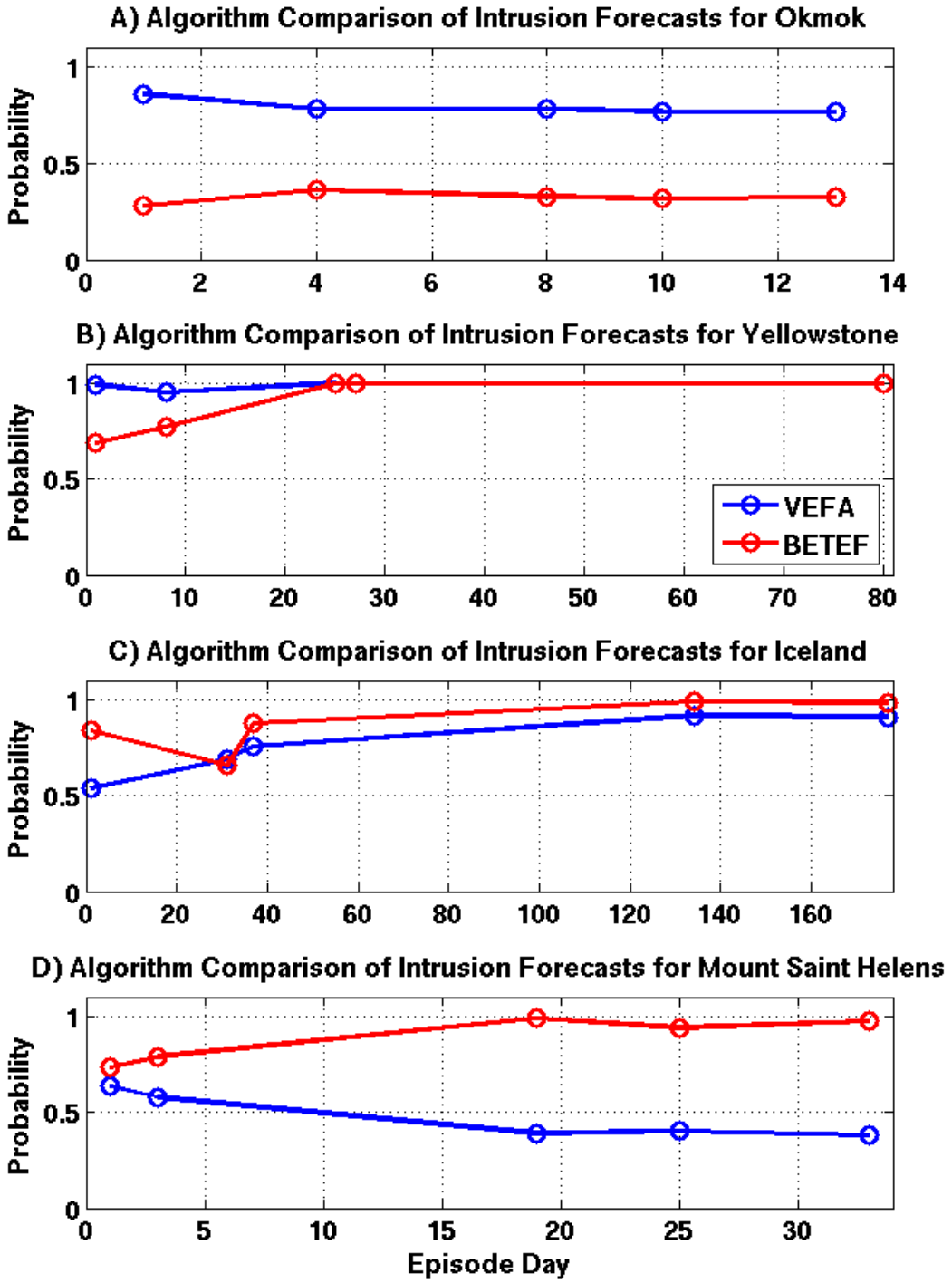

Figure 5.32: Intrusion probability comparisons for selected episode days, where each time sample is highlighted with a circle and the VEFA and BETEF results are shown in blue and red. The VEFA outperforms or produces results comparable to the BETEF in all cases. A) Okmok 2008. B) Yellowstone 2010. C) Grimsvötn 2011. D) Mount Saint Helens 2011.

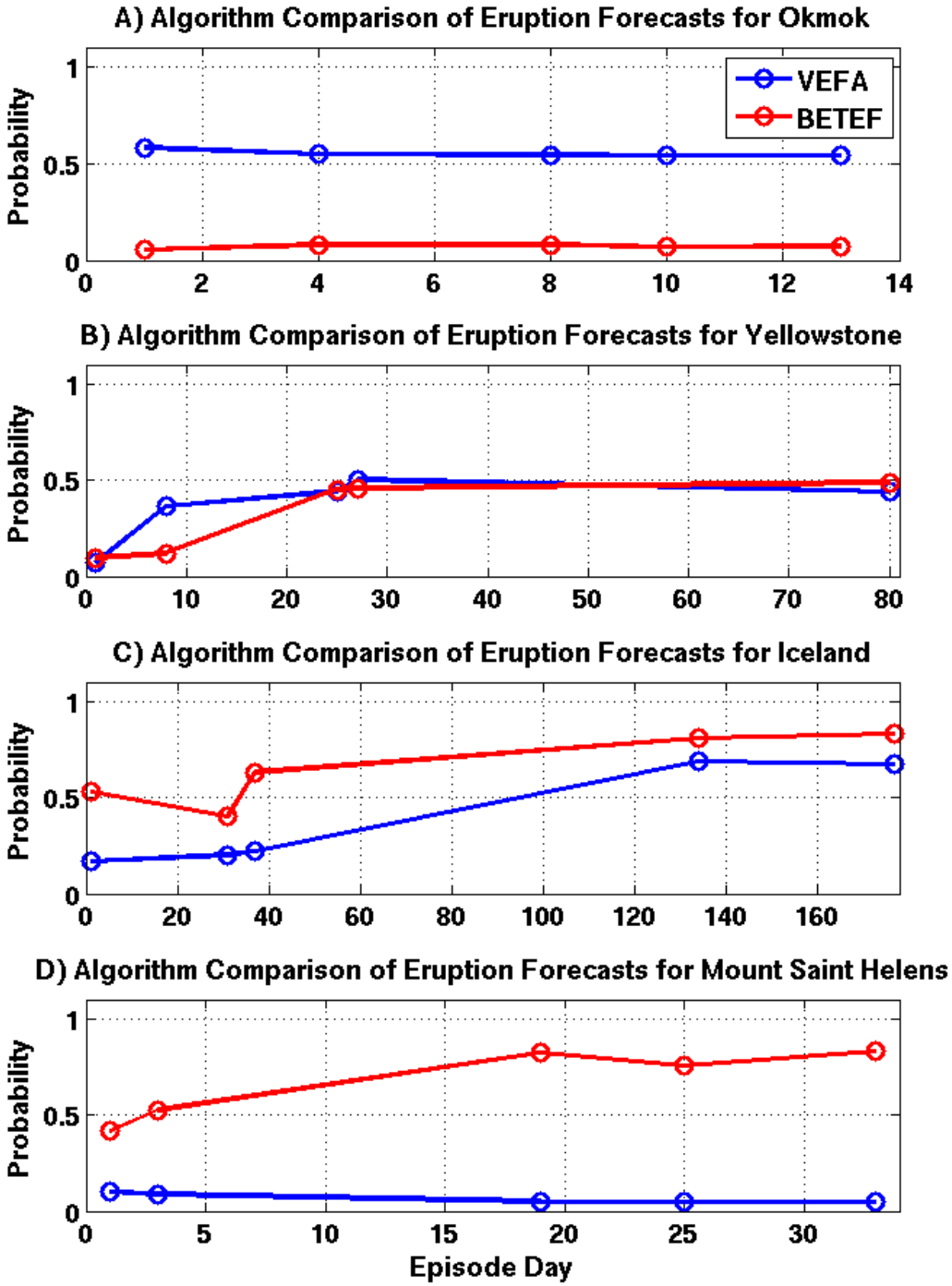

Figure 5.33: Eruption probability comparisons for selected episode days, where each time sample is highlighted with a circle and the VEFA and BETEF results are shown in blue and red. The VEFA outperforms or produces results comparable to the BETEF in all cases. A) Okmok 2008. B) Yellowstone 2010. C) Grimsvötn 2011. D) Mount Saint Helens 2011.

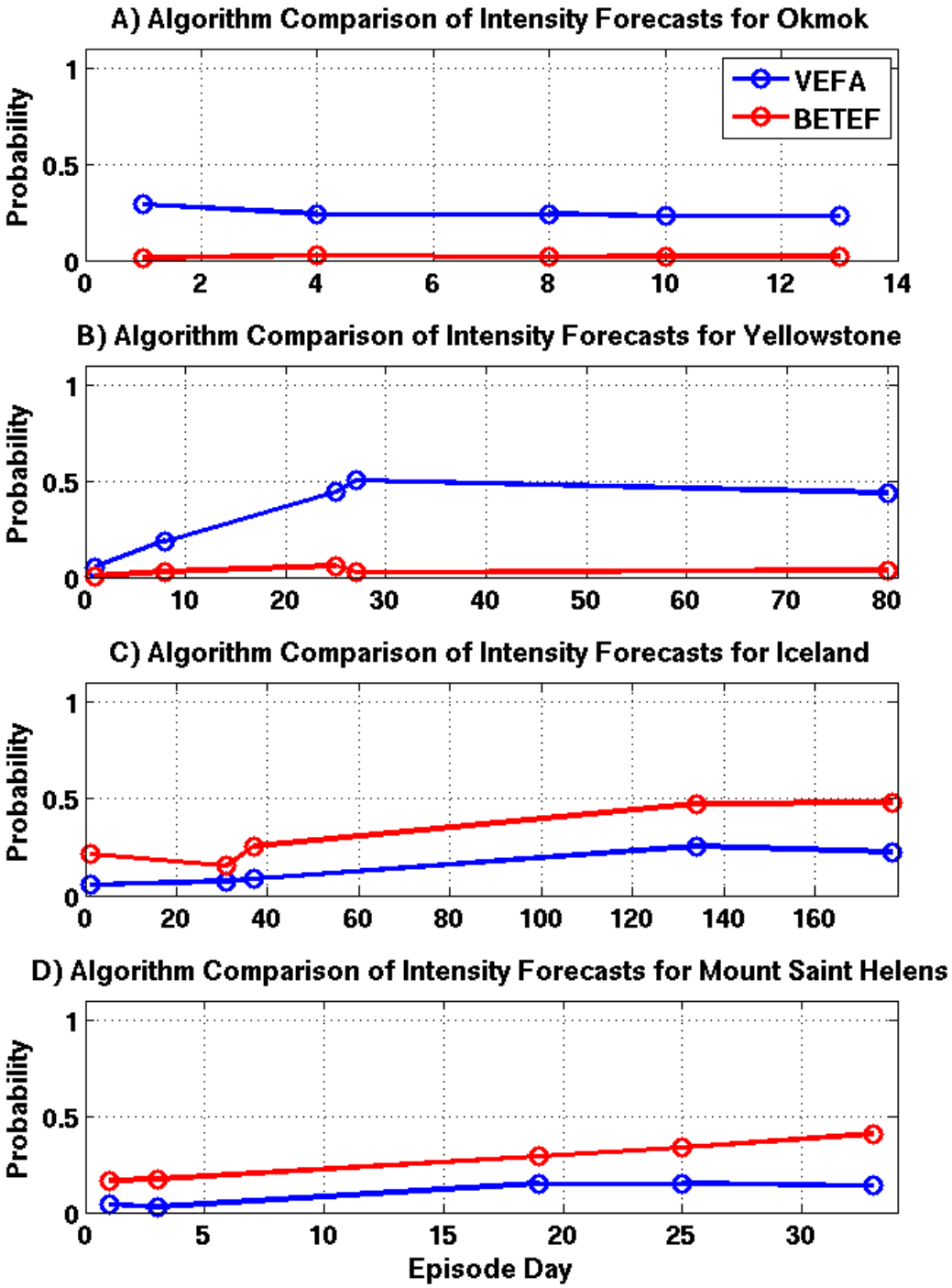

Figure 5.34: Intensity probability comparisons for selected episode days, where each time sample is highlighted with a circle and the VEFA and BETEF results are shown in blue and red. The VEFA outperforms or produces results comparable to the BETEF in all cases. A) Okmok 2008. B) Yellowstone 2010. C) Grimsvötn 2011. D) Mount Saint Helens 2011.

CHAPTER 6: CONCLUSIONS

An algorithm that forecasts volcanic activity using an established event tree analysis system and logistic regression has been developed, characterized, and validated. The suite of empirical logistic models that drive the system were derived from a geographically diverse dataset comprised of source modeling results, monitoring data, and the historic behavior of analog volcanoes. This allows the algorithm to simultaneously utilize this information in its decision making process. A bootstrapping analysis of the training dataset allowed for the estimation of robust logistic model coefficients. Probabilities generated from the logistic models increase with positive modeling results, escalating seismicity, and high eruption frequency and decrease with increasing episode length. The cross validation analysis produced a series of ROC curves with AUROC values in the 0.78 - 0.81 range, which indicate the algorithm has good predictive capabilities. In addition, ROC curves also allowed for the determination of the false positive rate and optimum detection threshold for each stage of the algorithm.

This dissertation has demonstrated the utility of employing logistic regression to derive a viable suite of empirical statistical models from a sparse and geographically diverse dataset for forecasting the outcome of complex volcanic unrest episodes. Probabilities and ground based hazard estimates for the Yellowstone, Grimsvötn, and Mount Saint Helens episodes are consistent with the actual outcome of these episodes. The green hazard declaration for the Okmok episode is not unreasonable given the absence of precursory seismicity and the sudden onset of the eruption. Probabilities generated by each stage of the VEFA for the Okmok either exceed or were just below their respective detection thresholds. This highlights a situation where a human analyst may decide

to override the automatic VEFA result and manually elevate the intrusion probability to force the hazard declaration to go red.

Modeling results had a significant influence on the probability estimates for each node. This is reflected in the relatively large logistic coefficients assigned to X_{MM}, which carried the largest value in two out of three cases. The CDFs shown in Figure 4.19, Figure 4.34, and Figure 4.47 indicate its influence on the probability degrades between nodes 2, 3, and 4. This result make sense, because the presence of fluid motion alone does not guarantee escalating volcanic activity. Probability estimates for node 2 should be significantly higher with positive modeling result, since its function is to forecast the presence of fluid motion. However, there is no guarantee an eruption will occur in the presence of fluid motion. Furthermore, the intensity of an eruption is a not function of the presence moving fluids. Rather, it is the fluid's chemical composition, accumulate rate, and the amount pressure exerted on its storage vessel that dictates intensity. Thus degradation of the modeling results influence on the probability estimates generated by later nodes is consistent with eruption mechanics.

Results show the quality of vent location estimates varies as a function of the information used in its construction. PDFs generated exclusively from seismic data were spread over a broad area, are highly fragmented, and do not convey any information about probable vent locations in regions exhibiting no seismicity (see Appendix B). This can lead to false conclusions regarding potential vent locations and adversely effect a response to a developing volcanic crisis. The deformation signal and modeling information improved PDF quality by providing a quantitative spatial constraint that cannot be obtained from seismic data alone. The spatial PDFs produced for Okmok, Yellowstone, and Grimsvötn were confined to areas known to be experiencing the effects of magma

ascent and shaped by monitoring data originating within the deformed area. As a result, forecasts are focused on areas that are directly affected by magma ascent and not those exhibiting unrelated forms of geologic activity. The lack of a deformation signal at Mount Saint Helens forced the consideration of a large search area, where the likely vent is estimated to be approximately 15 from the 1980 eruption crater.

The ability of this process to adapt to the dynamic conditions typically observed during a developing volcanic crisis was demonstrated by the spatial PDF time series examples shown in Sections 5.1.2, 5.2.1, 5.3.1, and 5.4.1. PDFs were modified as a function of the spatiotemporal distribution of seismicity and the availability of deformation data over the evaluation period. The time varying forecasts highlight areas within the deformed region where magma ascent may be causing multiple forms of collocated volcanic unrest due to sudden changes in fluid motion, pressure regimes, and or thermal alteration of country rock.

A comparison of the performance between the VEFA and BETEF further illustrates the power of using source modeling information to produce short-term forecasts. Source modeling data significantly enhanced the VEFA's forecasting capabilities, especially in situations where little or no associated seismicity exists. This point is confirmed by the differences in the BETEF and VEFA intrusion and eruption forecasts for Okmok and Mount Saint Helens. In both cases, the VEFA leveraged source modeling information to confirm or deny the observed unrest was the result of fluid motion. While the BETEF was also given this information during the development and evaluation of its statistical models, it was unable to make the physical connection between the input data and the source of the unrest. Therefore, the BETEF was unable to produce realistic forecasts in situations where little or no precursory seismicity was present. Comparison results

suggest that a static suite of empirical statistical models derived from a geographically diverse and sparse dataset are transportable and can compete with, and in some cases outperform, non-transportable empirical models trained exclusively from site specific information.

To the best of the authors knowledge, this is the first time logistic regression is used to forecast volcanic activity. Furthermore, the derivation of optimized detection thresholds allowed for the quantification of the USGS color code and the determination of an associated false positive rate. This was made possible by the data contained in the volcanic unrest database constructed exclusively for this research. The incorporation of source modeling data into the event tree's decision making process has begun the transition of volcano monitoring applications from simple mechanized pattern recognition algorithms to a physical model based system. This dissertation shows the VEFA has potential for forecasting volcanic activity at various locations throughout the world. Moreover, it can potentially aid civil authorities in determining the proper response to an impending eruption and can be easily implemented by a NVEWS. It should be stressed, however, that this algorithm is meant to assist and not replace the volcanologist in assessing the potential hazard associated with volcanic unrest episodes. Its results should be weighed carefully against a scientist's personnel experience and all other available information. It must also be stressed that low probability of occurrence means the event is unlikely, but not impossible. There will be situations where an unlikely event will occur.

6.1 Future Work

Future work will focus on expanding the training dataset. Emphasis will be placed on identifying additional dependent variables that can further enhance the predictive power of the algorithm. The Earth Observatory of Singapore, Nanyang Technological University, is leading a research initiative to develop a global volcanic unrest database referred to as WOVOdat [139]. This database will contain observations from various monitoring technologies and source modeling results from volcanoes all over the world. However, this database is still under construction and not open to the public. Once available, each of the logistic models will be redefined to exploit this diverse and comprehensive database.

APPENDIX A: SAR PROCESSOR OVERVIEW

A.1 Introduction

The goal of evaluation is to identify the SAR processing tools necessary to conduct the work outlined in this dissertation. Since the subject of InSAR signal processing has been studied extensively over the last twenty years and is not the primary focus of this research, one of the many freely available processing packages were considered for producing the interferograms necessary to achieve Mr. Junek's scientific goals [36][37][4][38][39][40][34][41][42]. Therefore, an evaluation of the available processing packages was required to identify the one best suited for this research.

A.1.1 ROI PAC

The ROI PAC is an open source InSAR processing application that was developed by Caltech and the Jet Propulsion Laboratory (JPL) [43]. ROI PAC is freely available for downloaded from the Open Channel Foundation website [44]. The download tar file contained source code and a collection of test data to determine if the compilation was successful. One major compilation problem was encountered and solved by upgrading the workstation RAM from 512 MB to 1.5 GB. Successful processing of the ROI PAC test data set confirmed the software was installed correctly and functioning properly.

ROI PAC is essentially a collection of PERL scripts that call a series of C and FORTRAN functions that perform all of the computationally intense processing. It handles all aspect of InSAR processing from the initial data formatting to the creation of geocoded differential InSAR images.

Table A.1: ROI PAC Image File Format

File Extension	Type	File Type
.slc	Single Look Complex	Interlaced Real and Imaginary Pixels
.int	Interferogram	Interlaced Real and Imaginary Pixels
.cor	Correlation	Interlaced Amplitude and Phase Pixels
.unw	Unwrapped Phase	Interlaced Amplitude and Phase Pixels
.hgt	Height	Interlaced Amplitude and Phase Pixels
.amp	Amplitude	Interlaced Real and Imaginary Pixels

The software is controlled by a simple parameter file that points to two SAR images of the same scene, a DEM, and specifies the processing options the user wishes to invoke. A high level block diagram of the ROI PAC processing algorithm is shown in Figure A.1. First, two raw data (level 0) files and precision orbit information are read, and two SLC images are created. Next, the two SLC images are co-registered using a set of common points existing in each scene. An initial interferogram is computed and the coherence between images is estimated. Then the interferometric baseline is re-estimated, the DEM is read, the topography of the scene is simulated, and removed from the interferogram. Next, the phase is unwrapped and the coordinate system of the image is converted to a true geographic coordinate system. The tool produces a series of images in one of two possible image formats that are denoted by a series of file extensions, which are described in Table A.1 . The interlaced images are read and displayed using the "Multibandread" function in Matlab.

A.1.2 Okmok Digital Elevation Model

DEM information for Okmok was obtained from the NASA SRTM ftp site[12][13]. The 1-arc-second data is segmented into one degree by one degree tiles, whose names correspond to

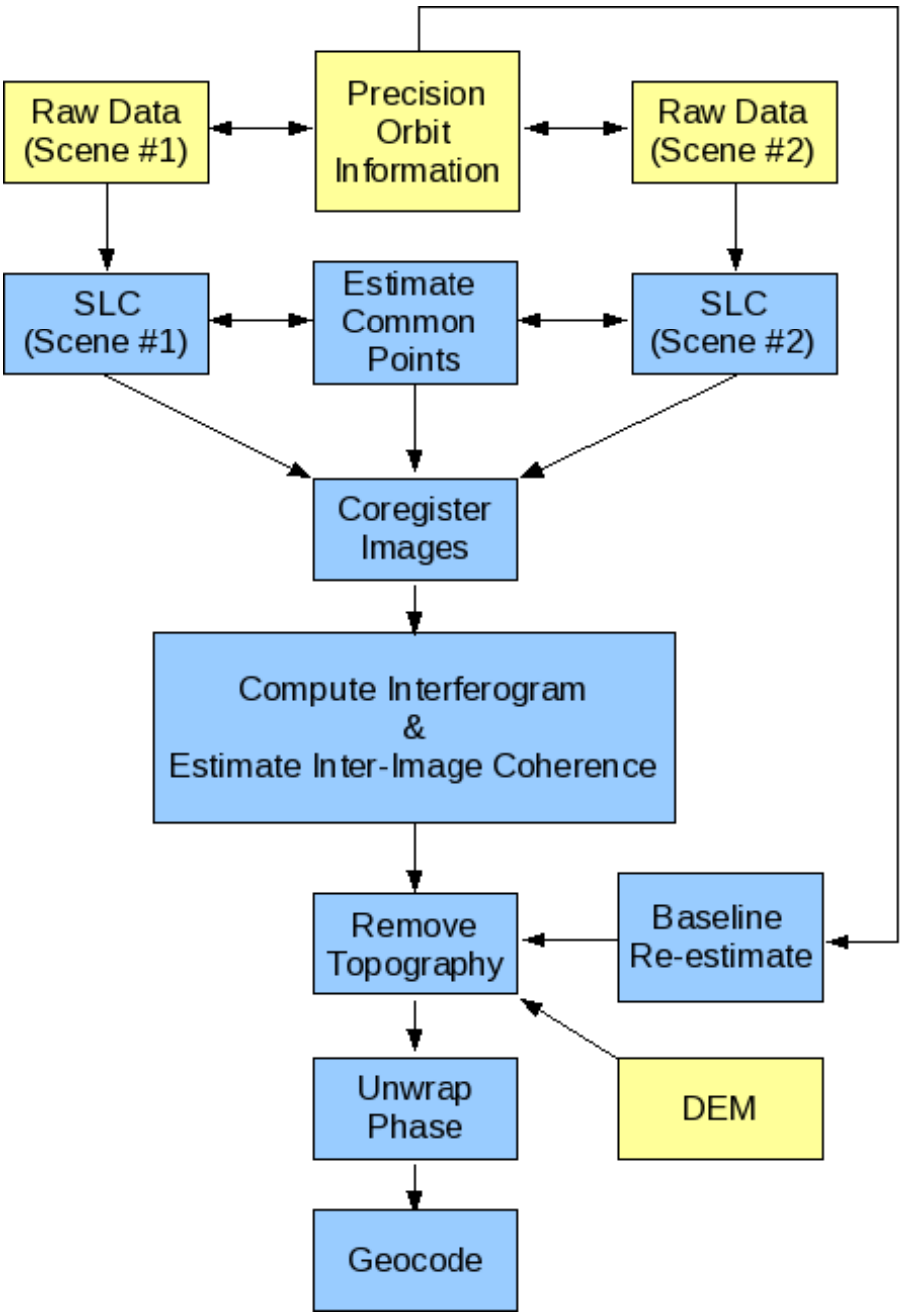

Figure A.1: Block Diagram of ROI PAC Processing Algorithm, where the blue and yellow boxes represent computed results and external data, respectively.

the upper left corner latitude and longitude coordinates. The binary height (.hgt) files are stored in compressed, big-endian, format. Since the InSAR processors require a DEM whose area is larger

Table A.2: Latitude and longitude of the SRTM tiles used in this study[12][13]

Latitude	Longitude
53^oN	167^oW
53^oN	168^oW
53^oN	169^oW
53^oN	170^oW
52^oN	169^oW
52^oN	170^oW

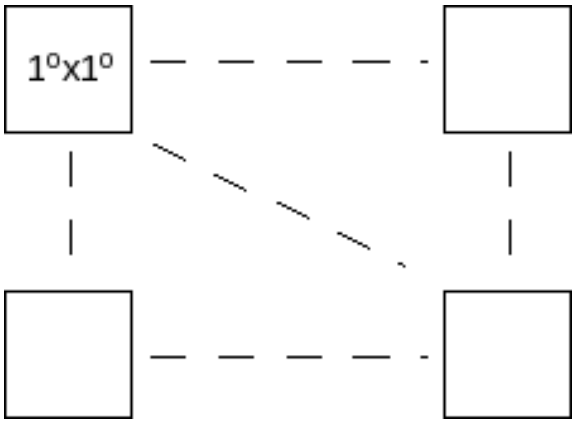

Figure A.2: A broad area DEM was constructed from eight, 1^ox1^o, 1 arc-second tiles, from data collected by the NASA SRTM [8]

then the scene being studied and the SRTM data is stored in one degree tiles, a broad area DEM was constructed manually. A series of tiles, corresponding to the North Pacific and Bering Sea that contain Umnak island and some of the surrounding islands, were downloaded and assembled into one large DEM. A list of the tiles used in this study is shown in Table A.2. The broad area DEM construction process is illustrated in Figure A.2. Since broad ocean areas were not studied by the SRTM mission, two tiles consisting of zeros were assembled and placed into the area where no data was available. This was necessary to produce a rectangular DEM mosaic. The broad area DEM was stored in binary format and used in all subsequent InSAR processing. A section of the DEM mosaic containing Umnak island is shown in Figure A.3.

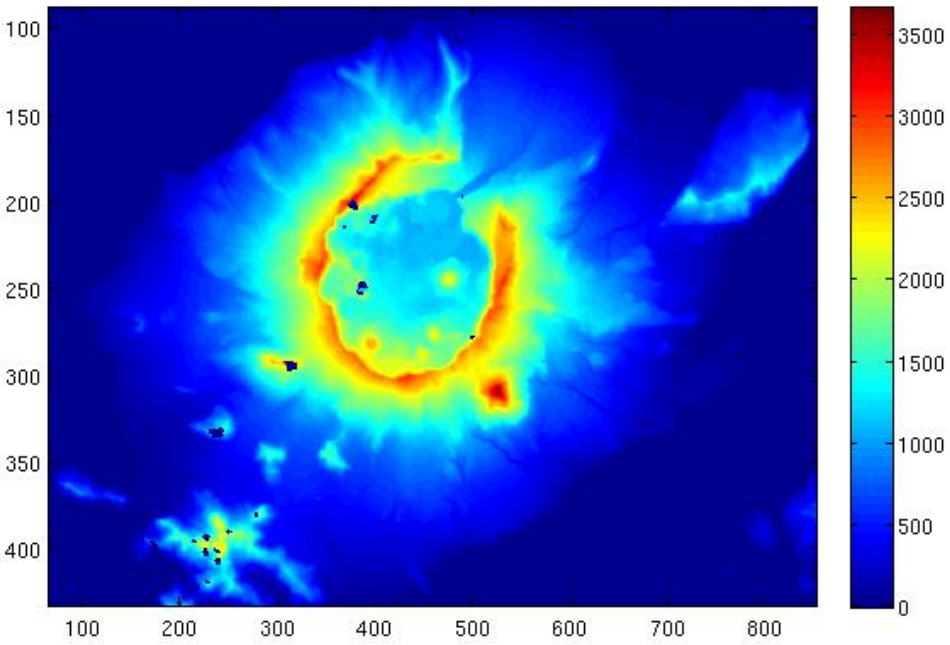

Figure A.3: Digital Elevation model of Umnak Island, where the color scale is in meters and the x and y axis are pixels

A.1.3 ROI PAC Results

The series of figures shown below were generated from two sets of complex SAR images. These results were taken from key points in the InSAR processing algorithm, which were described in detail in Sections 3.2 and 3.2.1. Each image was cropped to emphasize the area around Umnak Island and the Okmok caldera. The ROI PAC results are shown in the radar coordinate system. As a result, Figure A.4 through Figure A.16 are flipped in the East-West direction, relative to the true orientation of the Island. Note that transformation back to a geographic coordinate system is not performed until the geocoding portion of the processing chain.

Figure A.4 through Figure A.10 were generated between the October 25, 1995 and October 26, 1995 data set, which is denoted as image pair 1/2 in Table A.3. This image pair is spaced approximately 24 hours apart and was used by Lu et al 2000 to derive a custom DEM for Umnak Island. Figure A.4 shows the co-registered InSAR image. Since the ghosting effect that highlights areas of poor co-registration is not observed in this case, we can conclude the alignment between images is excellent. Figure A.5 shows the raw interferogram of the total interferometric phase defined in Equation 3.7. The flat earth effect is evident by the parallel fringe pattern around the island, which is highlighted by Figure A.6. Figure A.7 shows the coherence estimate between the co-registered image pair, where high and low coherence values are represented by bright and dark colors, respectively. The interferometric fringe pattern typically breaks down in regions with low coherence. Therefore, a high degree of coherence is critical for high quality interferograms. Figure A.8 shows the interferogram after the flat earth term is removed. The resulting fringe pattern is dominated by the topography of the island. Figure A.9 shows the simulated topographic image

derived from the mosaic DEM. The simulated DEM is used to compute the result shown in Figure A.10. Since the time between images is approximately 24 hours, it is assumed that no ground deformation has occurred between images [31]. Therefore, the difference between images should be approximately constant. Notice there is some variation in the results across the image that is most likely caused by atmospheric effects, which are not accounted for in this report.

Figure A.11 through Figure A.16 were generated from the September 25, 1997 and September 10, 1998 data set, which is denoted as image pair 4/5 in Table A.3. This image pair is spaced approximately one year apart and was used by Lu to highlight the deformation caused by post eruption inflation of a spherical magma chamber beneath the center of the caldera [31]. Figure A.11 is the co-registered SLC image pair that shows a good degree of alignment between images. Figure A.12 shows the raw interferogram of the total interferometric phase, where the parallel fringe pattern is only clear in the upper right corner of the caldera. Figure A.13 shows the coherence estimate between the co-registered image pair. In this case, the degree of coherence around the island is low, with the exception of the bright area in the upper right corner of the caldera. This area of high coherence is producing the bright fringe pattern in the upper right corner of the caldera in Figure A.12. Since the majority of the island exhibits a low degree of coherence, the resulting interferograms will be poor for the majority of the landmass. Figure A.14 shows the interferogram with the flat earth term removed. The resulting fringe pattern is dominated by the topography of the Island. Figure A.15 shows the simulated topographic image derived from the DEM mosaic, which was used to produce the differential interferogram shown in Figure A.16. Once the topographic component of the interferometric phase is removed, a large spherical deformation pattern originating in the center of the caldera is easily observed. Recall that the time span between im-

Table A.3: Interferometer geometry parameters, where T_s is the time separation between images

Image Pair	B (m)	T_S	H_a (m)	θ (deg)	α (deg)	δp_{disp} (cm)	ρ (km)
1/2	86.6	24 hours	123.8	23.8	43.7	2.83	876
4/5	125.4	1 Year	85.8	23.8	43.7	2.83	876

ages is approximately one year, so the fringe pattern observed in the center of the caldera is due to ground deformation that has occurred between image acquisitions.

ROI PAC computes all of the geometric parameters for the RPI and stores them in a series of ACSII text files. These files are referred to as resource files (.rsc), which also list an abundance of additional information regarding the radar operational parameters. The geometric parameters for each RPI is shown in Table A.3.

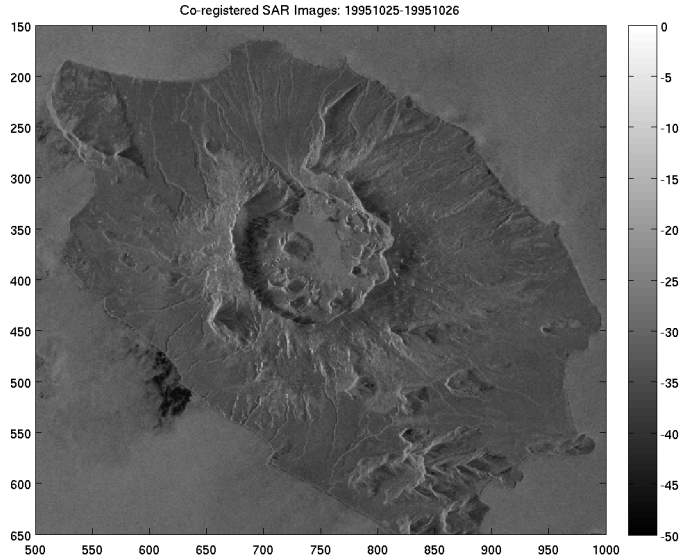

Figure A.4: Co-registered image pair:19951025 - 19951026, where the color scale is power in dB

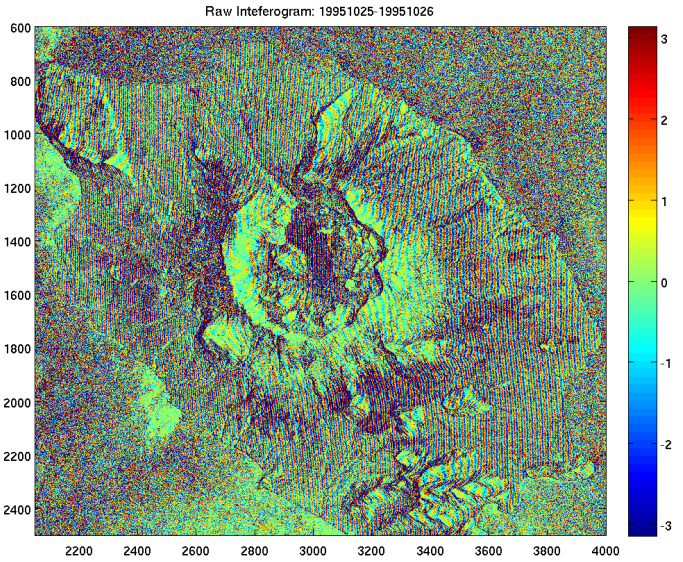

Figure A.5: Raw Interferogram:19951025 - 19951026, where the color scale represents phase values between $\pm\pi$

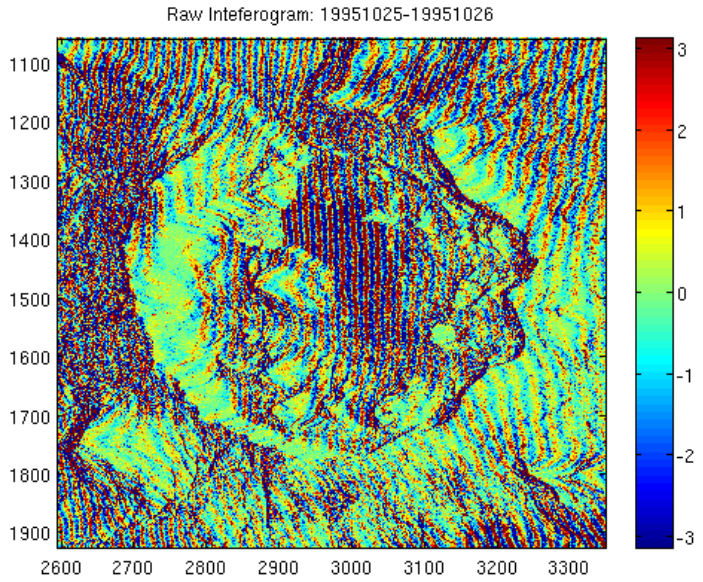

Figure A.6: Raw Interferogram around Okmok Caldera:19951025 - 19951026, where the color scale represents phase values between $\pm\pi$

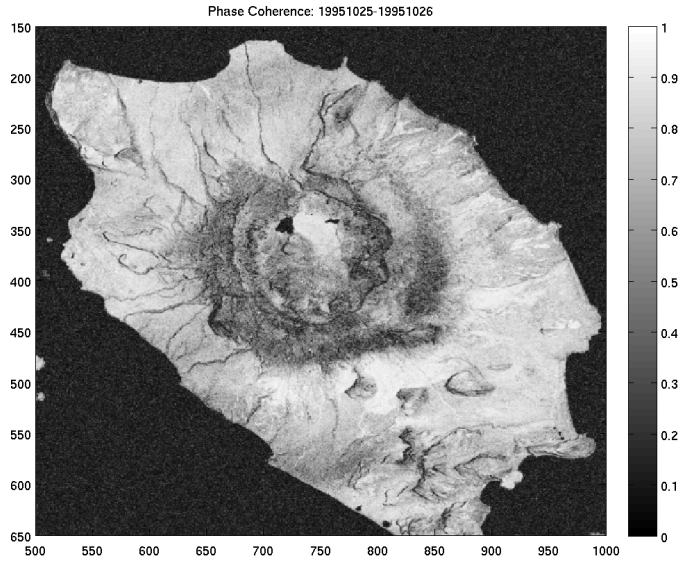

Figure A.7: Phase Correlation:19951025 - 19951026, where the color scale represents the coherence values between 0 and 1.

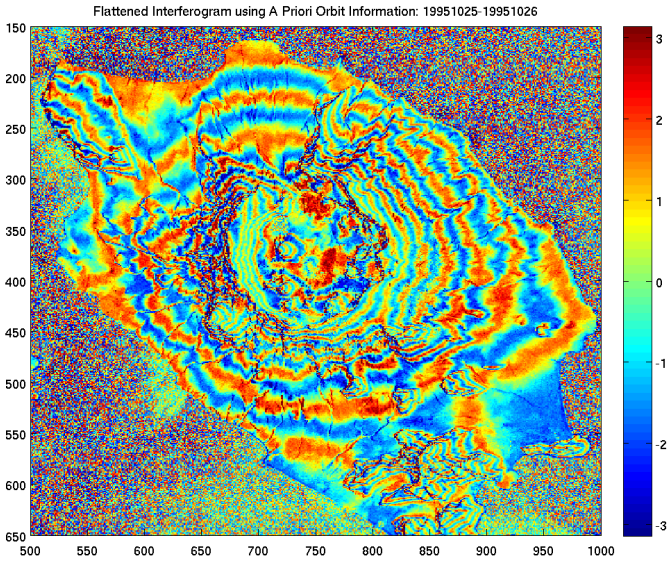

Figure A.8: Flattened Interferogram:19951025 - 19951026, where the color scale represents phase values between $\pm\pi$ and the displacement associated with one complete phase revolution is 124m

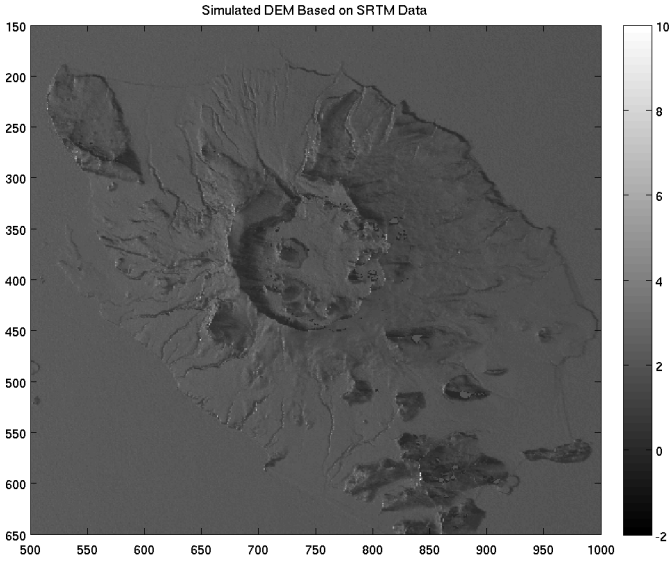

Figure A.9: Simulated Digital Elevation Model:19951025 - 19951026, where the color scale is power in dB

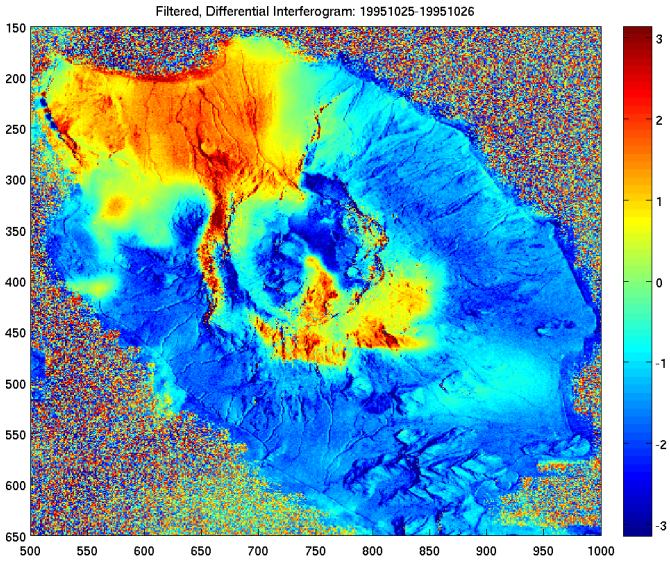

Figure A.10: Differential Interferogram with Topography Removed:19951025 - 19951026, where the color scale represents phase values between $\pm\pi$ and the displacement associated with one complete phase revolution is 2.83cm

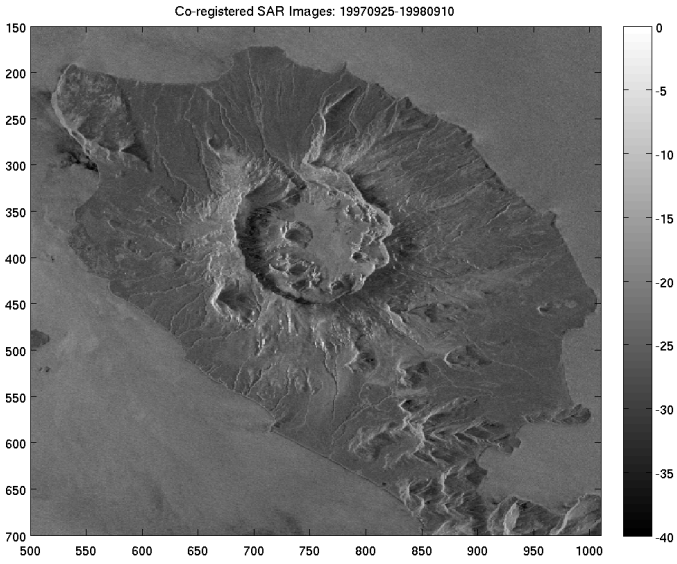

Figure A.11: Co-registered image pair:19970925 - 19980910, where the color scale is power in dB

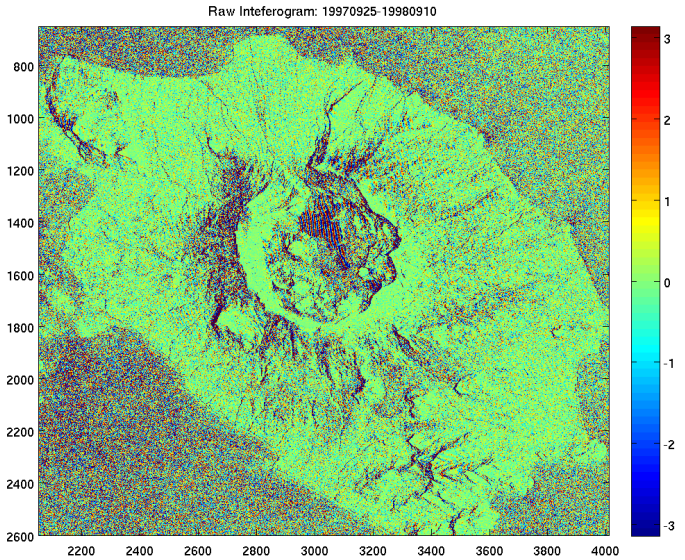

Figure A.12: Raw Interferogram:19970925 - 19980910, where the color scale represents phase values between $\pm\pi$

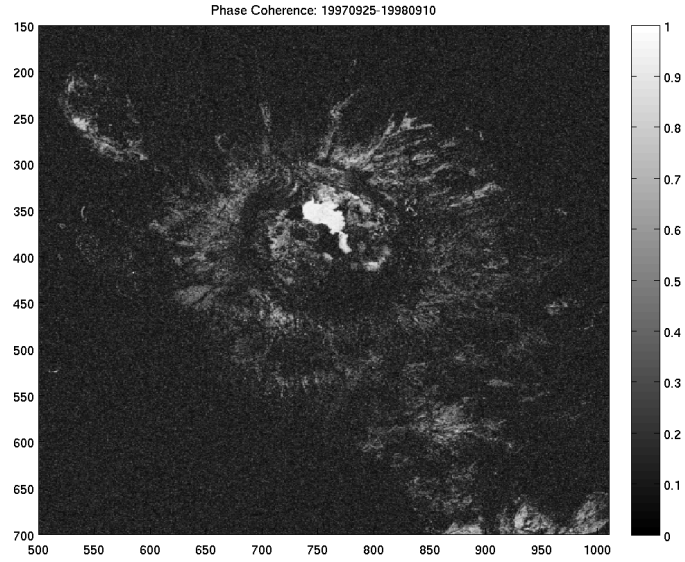

Figure A.13: Phase Correlation:19970925 - 19980910, where the color scale represents the coherence values between 0 and 1.

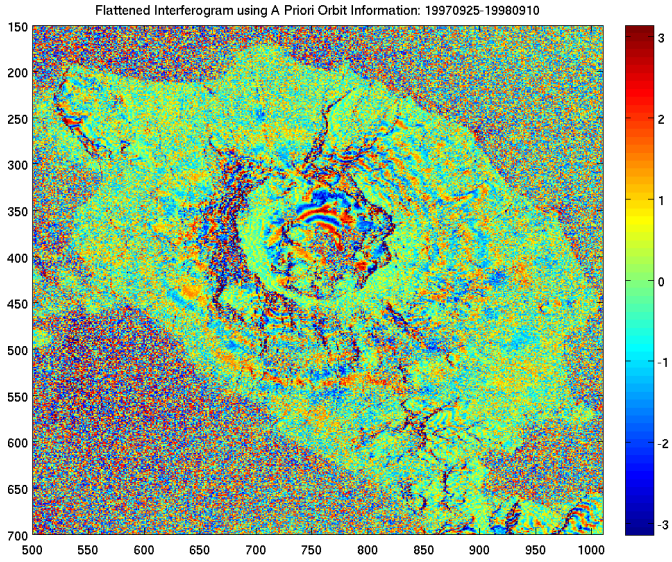

Figure A.14: Flattened Interferogram:19970925 - 19980910, where the color scale represents phase values between $\pm\pi$ and the displacement associated with one complete phase revolution is 86m.

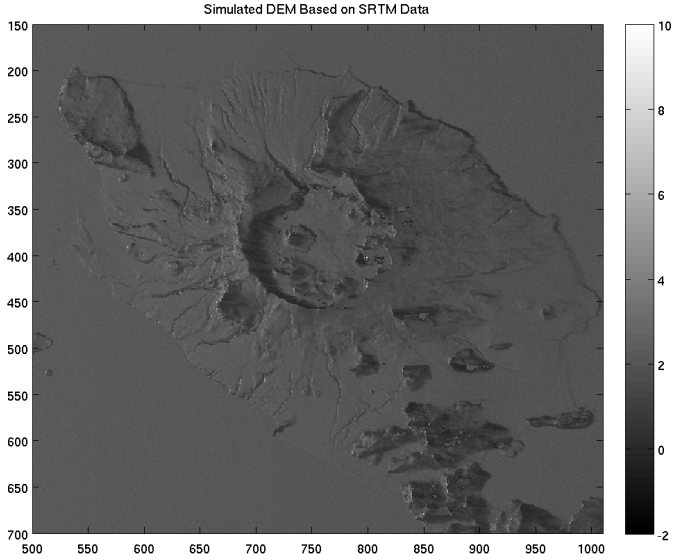

Figure A.15: Simulated Digital Elevation Model:19970925 - 19980910, where the color scale is power in dB

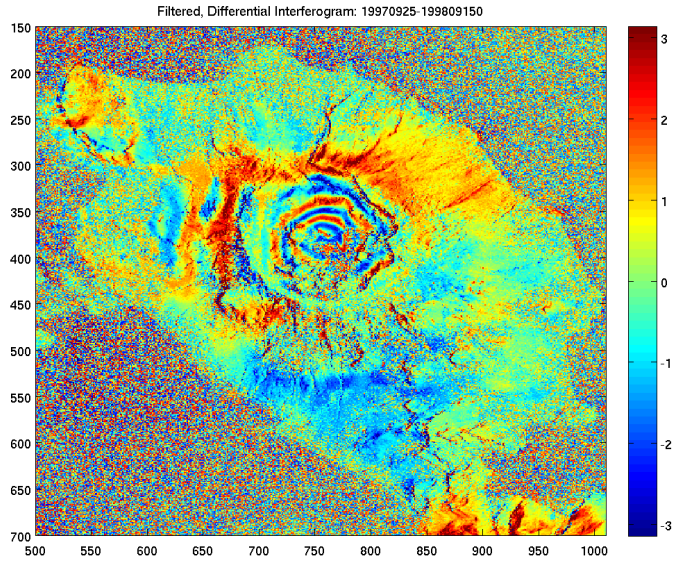

Figure A.16: Differential Interferogram with Topography Removed:19970925 - 19980910, where the color scale represents phase values between $\pm\pi$ and the displacement associated with one complete phase revolution is 2.83cm

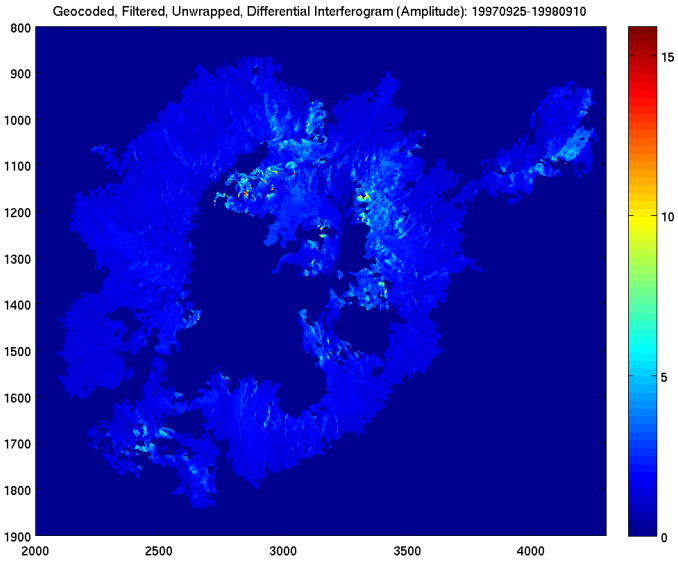

Figure A.17: Geocoded, Unwrapped, Interferogram (Amplitude):19970925 - 19980910

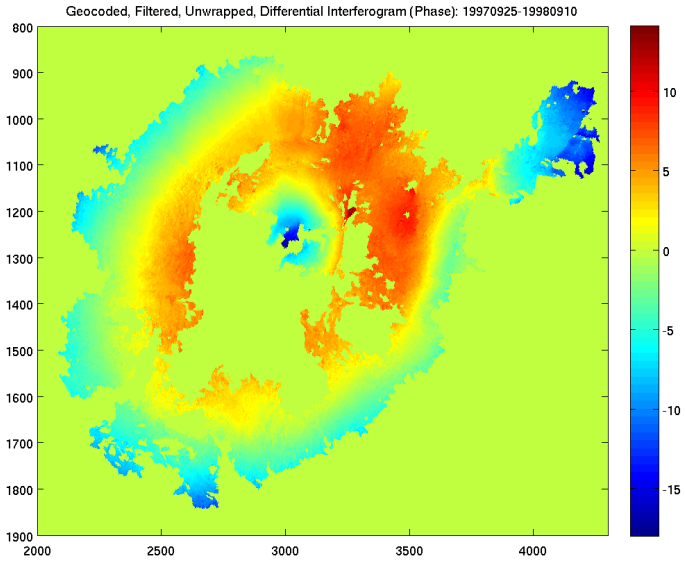

Figure A.18: Geocoded, Unwrapped, Interferogram (Phase):19970925 - 19980910

A.1.4 RAT

The Radar Tools (RAT) application is an open source InSAR processing application that was developed by the Berlin University of Technology in Germany. RAT is freely available for download from the Computer Vision and Remote Sensing Group website [140]. The application is downloaded in the form of a compiled .sav file that can be run using a fully licensed version of IDL or an IDL virtual machine (VM). An IDL VM can be downloaded from the ITT, Visual Information Solutions, website free of charge [141]. RAT can then be initiated using a simple command, $(idl - vm = rat.sav)$, that pipes the .sav file through the IDL VM and displays the RAT GUI shown in Figure A.19.

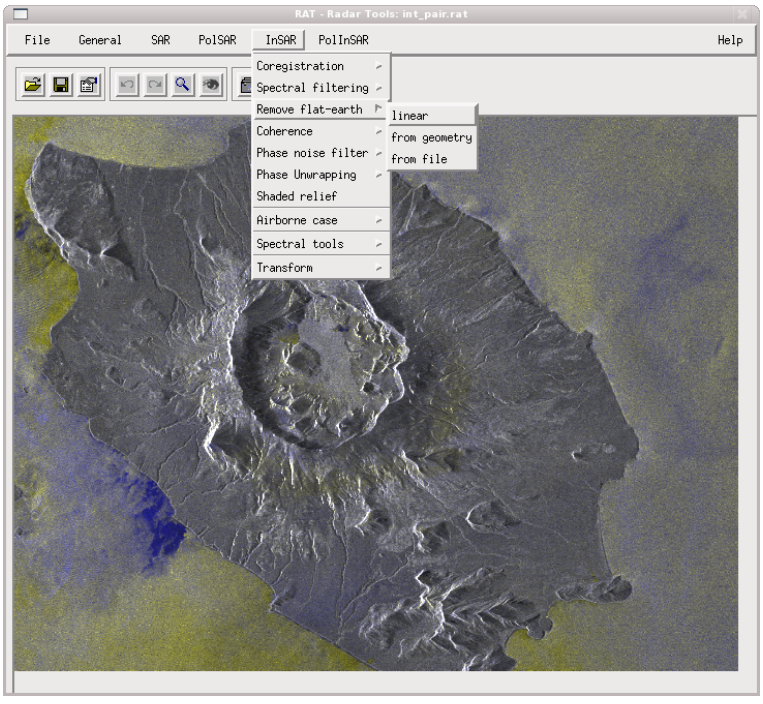

Figure A.19: Screenshot of the RAT graphical user interface

RAT is an interactive tool that is controlled through a menu driven graphical user interface (GUI). Unlike ROI PAC, this tool is not capable of automated processing and requires SLC SAR data as input. The user must manually initiate each step of the InSAR processing chain. RAT is not capable of incorporating DEM information for topography simulation and removal. As a result, it is not capable of producing differential InSAR images that highlight ground deformation. There is also no mechanism for retrieving the RTI geometric information for H_a estimation for interferograms dominated by topographic fringe patterns. In addition, the phase unwrapping algorithm failed to execute, which makes it incapable of computing unwrapped interferograms.

A.1.4.1 RAT Results

The ASF dataset was processed with RAT and the results were compared to those of Zhong Lu et al 2000[31]. Figure A.20 is the co-registered image pair for the October 25, 1995 and October 26, 1995 data set. The images, as with the ROI PAC example, actually encompass a must larger area, but were cropped to emphasize Umnak Island. The areas exhibiting yellow and blue tints are areas of poor co-registration. This will degrade the interferogram quality in these areas. Figure A.21 shows the inter-image coherence, where high and low coherence areas are highlighted in bright and dark colors, respectively. The majority of the landmass is highly coherent, which should result in a well defined fringe pattern over most of the island. Note that the dark regions correlate to the areas of poor co-registration. Figure A.22 shows the interferogram using the total interferometric phase. The resulting fringe pattern is dominated by the flat earth component, which is evident by the parallel fringe pattern. RAT has several option for removing

the flat earth component. For this study, the linear option was used and the resulting interferogram is shown in Figure A.23. The fringe pattern is dominated by the topography of the island and is very similar to the interferogram shown in Figure A.8. Due to RAT's inability to utilize DEM information or successfully unwrap the interferometric phase, no additional work was performed with this tool and the evaluation was halted.

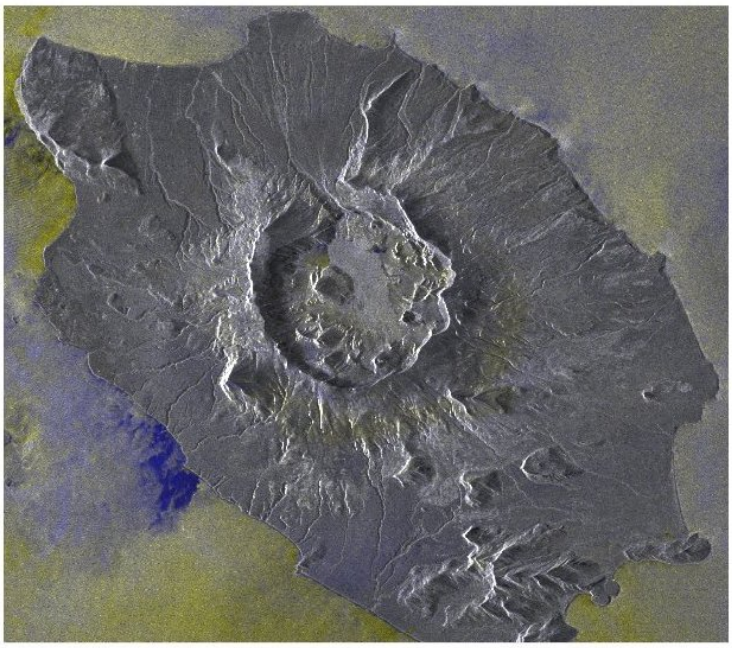

Figure A.20: RAT generated co-registered SAR image of Okmok

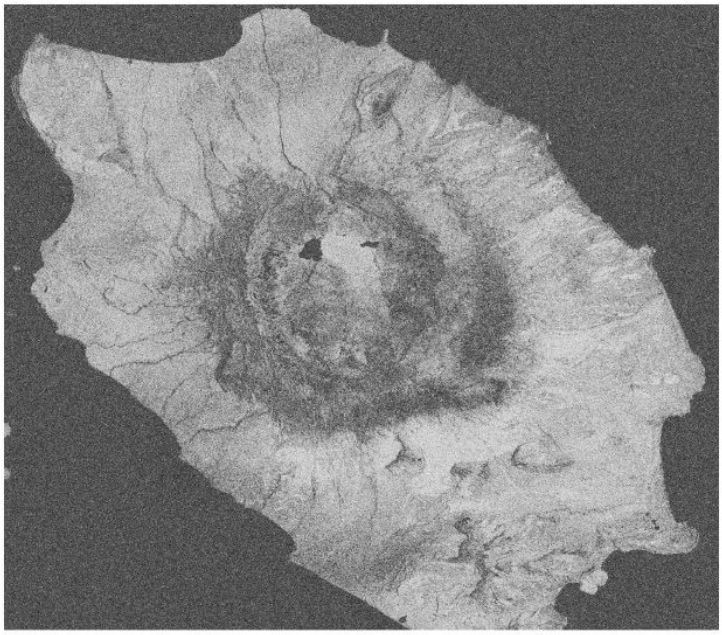

Figure A.21: RAT generated coherence Image of Okmok

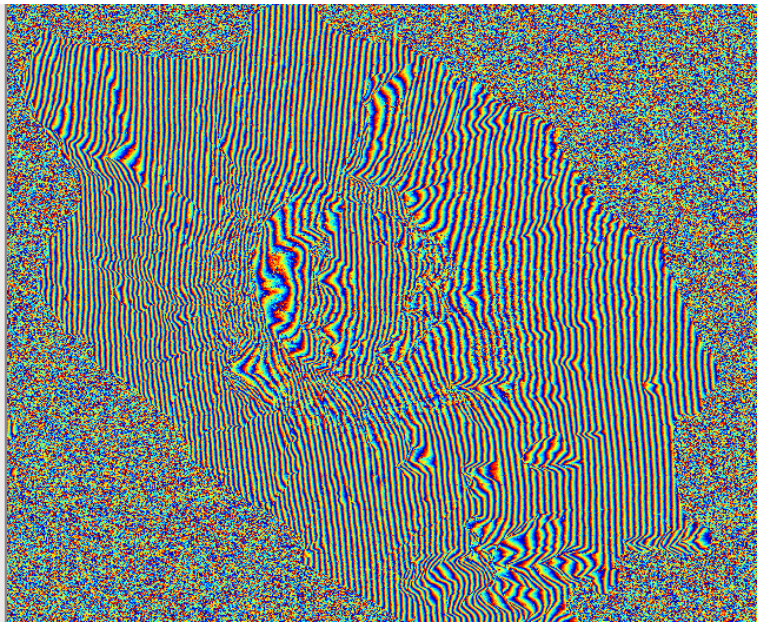

Figure A.22: RAT generated interferogram dominated by Flat Earth contribution to the total Interferometric phase

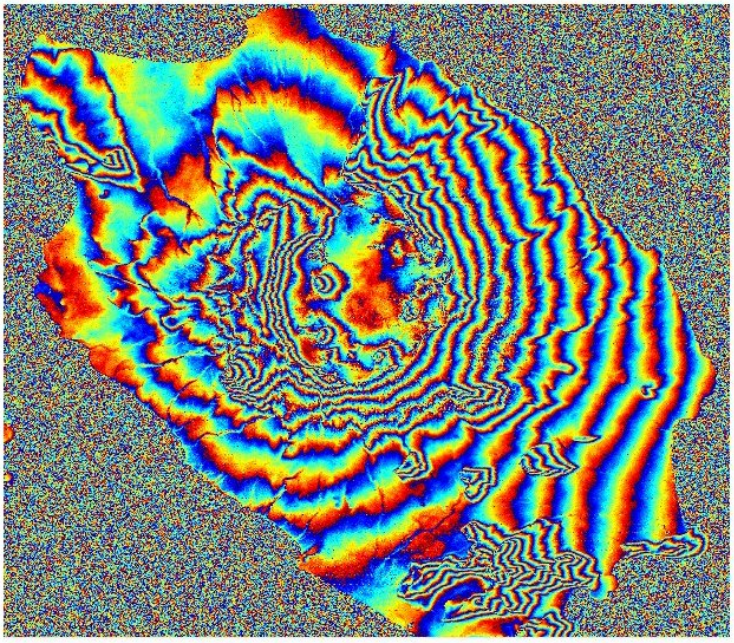

Figure A.23: RAT generated interferogram illustrating Umnak Island topography

A.1.5 DORIS

The Delft Object-Oriented Radar Interferometric Software (DORIS) was developed by the Delft Institute of Earth Observation and Space Systems at the Delft University of Technology in the Netherlands. Like RAT and ROI PAC, DORIS is an open source InSAR processor that is freely available for download from the Delft website. Like RAT, DORIS requires SLC data as its input[142]. However, it appears that the ASF SLC data was incompatible with DORIS. As a result, none of the ASF data could be processed and the tool was immediately declared to be unusable for this research project.

A.2 Summary

The goal of this short term study was to acquire the InSAR processing tools necessary to achieve the research goals of this dissertation. Three freely available InSAR processing tools were evaluated in this study: ROI PAC, RAT, and DORIS. ROI PAC was the only tool able to produce the required DInSAR images of a deformation field around a volcano. The reproduction of two key results published by Lu et al 2000 confirms that the tool is being used properly, input data (raw ERS-1/2 and SRTM DEM data) is being read correctly, and the correct results are being generated. As a result, Mr. Junek selected the ROI PAC InSAR processing tool to perform this dissertation research.

APPENDIX B: SPATIAL PDF ASSESSMENT

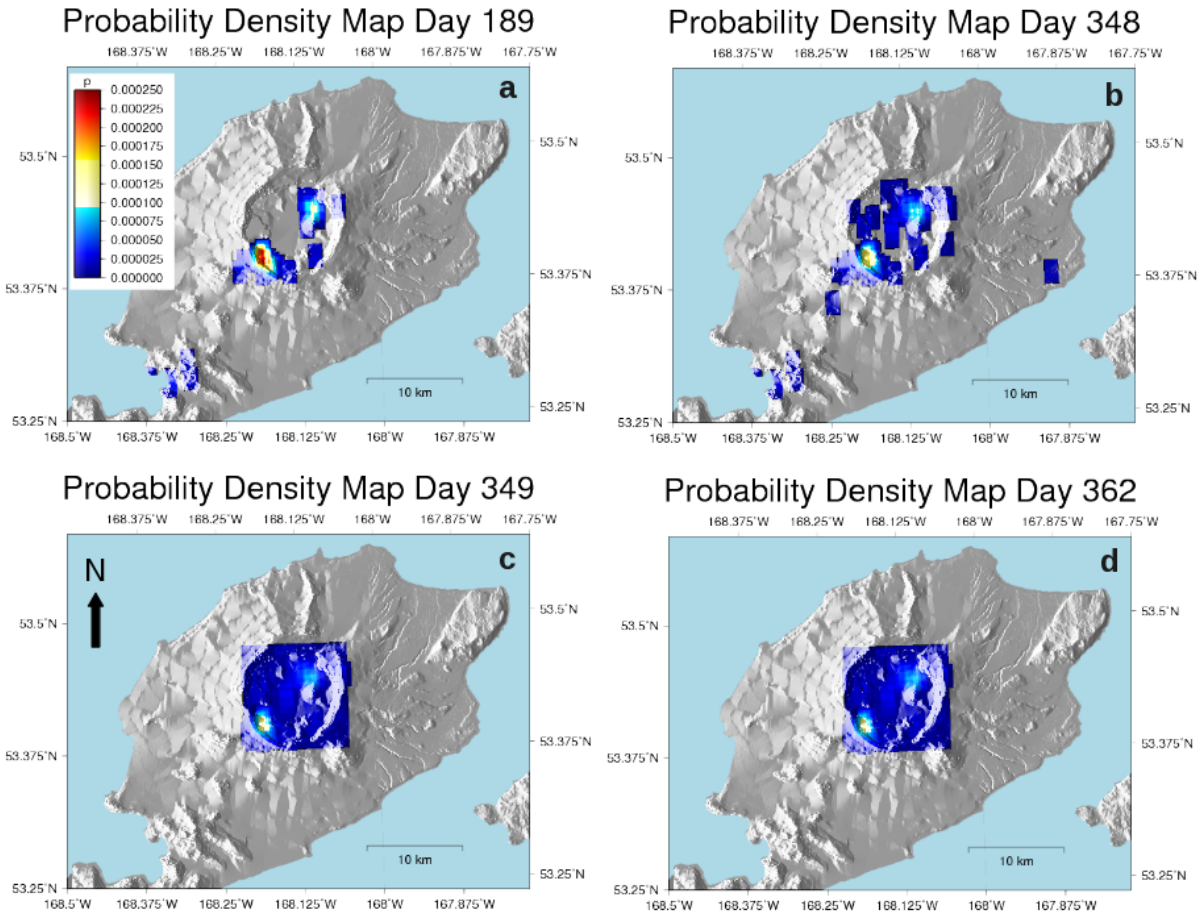

Figure B.1: Time series of selected PDFs. a) Day 189. b) Day 348, c) Day 349 (acquisition date of second SAR image used to construct interferogram). d) Day 362 (day before 2008 eruption).

The influence of modeling information on PDF quality is evaluated by comparing results generated before and after the detection of the deformation signal. The evaluation period for the examples shown in Figure B.1 begins on July 13, 2007 and spans 362 days, where detection of the deformation signal occurs on day 349. All results are plotted on the same probability scale to allow for meaningful comparisons. The value of J in Equation (4.33) is determined by the size and spatial resolution of the forecast area. Here the spatial resolution of each PDF is dictated by the DEM used for Umnak Island, which is 2 arc-seconds (5.56e-4°). The space-time window

for each example is determined by the available modeling information and spans the number of days relative to the start of the evaluation period (day number). If no modeling information is available, total ignorance of deformation processes is assumed and earthquake database queries encompass the entire landmass. On the other hand, if the extent of the deformation field is known then earthquake database queries are restricted to the deformed area.

In the absence of modeling information, the non-spatially constrained PDFs shown in Figure B.1(a) and Figure B.1(b) are fragmented and scattered over a broad area. These PDFs precede the acquisition of the second SAR image and the availability of modeling information. The lack of a quantitative spatial constraint on the forecast requires the PDF be constructed over the entire landmass. As a result, the rectangular forecast area spans 831 km^2, J = 673,920 probable locations, and all X^j_{def} = 0. Evolving seismicity between days 189 and 348 causes the PDF to change over time. Initially, seismicity occurs in isolated areas of the caldera and in areas to the southwest. Eventually seismicity migrates to other regions of the caldera and the southeastern section of the island. Values of X^j_{seis} are modified according to the cumulative spatiotemporal distribution of seismicity over the landmass.

On day 349, the second SAR image is acquired and a theoretical deformation field is available to constrain the forecast area. The PDFs shown in Figure B.1(c) and Figure B.1(d) are confined to the caldera and shaped by seismicity occurring within the deformed region. The availability of modeling information changes the search area to 121 km^2, J = 53,044 probable locations, and all X^j_{def} = 1. Modeling information reduced the search area by 710 km^2 and J by 620,876 points. In this case, values of X^j_{seis} reflect the cumulative spatiotemporal distribution of seismicity within the deformed area. Therefore, seismicity primarily triggered by the magma ascent process is incorpo-

rated into the PDFs. The similarity between PDFs for day 349 and 362 (day before the eruption) is due to the low seismicity rate between days. As a result, the PDF is not altered significantly and the forecast remains relatively unchanged between these days.

APPENDIX C: FIRST SAR DATA REQUEST

To Whom It May Concern

I am a graduate student at the University of Central Florida, pursuing a Ph.D in Electrical Engineering under the guidance of Dr. Linwood Jones, Director of the Central Florida Remote Sensing Laboratory. I would like to request the ERS-1/2 datasets listed in Table C.1 to perform proof of concept work related to my dissertation research, which are both briefly described below. Upon the successful completion of this work, I plan to submit a formal proposal requesting access to the data I need to conduct my dissertation research. This proposal will thoroughly outline the research I intend to perform and the results I am planning to obtain. This request in being submitted in the fashion described to me by Alaska Satellite Facility (ASF) personnel at the 2007 and 2008 Fall American Geophysical Union conferences, where I was informed that a limited amount of data is routinely released to graduate students for proof of concept research via an email request.

Table C.1: Requested Data Sets (Level Zero and Single Look Complex Formats are required)

Date	Orbit Number	Frames
October 25, 1995	E1 22376	317, 316
October 26, 1995	E2 2703	317, 316
June 7, 1995	E1 20372	316
September 25, 1997	E2 12723	317, 316
September 10, 1998	E2 17733	317, 316

Dissertation Research Summary

My dissertation research focuses on the determination and interpretation of the geophysical processes occurring within a volcano using space-based microwave remote sensing techniques. Surface deformation measurements in and around a volcano will be made using Interferometric Synthetic Aperture Radar (InSAR) techniques. Deformation estimates will be related to the activity of a magma chamber via a model obtained from previously published studies. A series of

deformation maps will be computed and fed into a Kalman filter to estimate the future state of the parameters that define the magma chamber model.

Proof of Concept Research

Since the subject of InSAR data processing has been studied extensively, I intend to use an established processing package to produce interferograms. Currently, I am evaluating three InSAR processors that are freely available over the Internet (ROI PAC, RAT, and DORIS) to identify the application that is best suited for this research. To date, I have successfully downloaded and compiled each software package. In the cases of ROI PAC and RAT, I have been able to process the preconditioned test data they supplied. In addition, I have also obtained and read precision orbit data for ERS-1/2 from the Delft University of Technology, Department of Earth Observation and Space Systems. In order to verify that I am using these tools correctly, I would like to recreate the Digital Elevation Model (DEM) and several key interferograms shown in Zhong Lu 2000 study of the 1997 eruption of Okmok [**?**]. The data being requested in this letter will be used for this purpose.

Thank you for your time and attention. If you have any questions or comments regarding this request or my dissertation research, please do not hesitate to contact me.

Regards,

William Junek

Central Florida Remote Sensing Laboratory, University of Central Florida

APPENDIX D: SECOND SAR DATA REQUEST

To Whom It May Concern

I am a graduate student at the University of Central Florida, pursuing a Ph.D in Electrical Engineering under the guidance of Dr. Linwood Jones, Director of the Central Florida Remote Sensing Laboratory. I would like to request the ERS-2, level zero, datasets listed in Table D.1 to perform proof of concept work related to my dissertation research, which are both briefly described below. Upon the successful completion of this work, I plan to submit a formal proposal requesting access to the data I need to conduct my dissertation research. This proposal will thoroughly outline the research I intend to perform and the results I am planning to obtain. This request is being submitted in the fashion described to me by Alaska Satellite Facility (ASF) personnel at the 2007 and 2008 Fall American Geophysical Union conferences and in recent telephone conversations, where I was informed that a limited amount of data is routinely released to graduate students for proof of concept research via an email request.

Table D.1: Requested Data Sets (Level Zero and Single Look Complex Formats are required)

Date	Orbit Number	Track
05/08/1997	10719	344
07/17/1997	11721	344
09/30/1999	23244	344
07/06/2000	27252	344
09/14/2000	28254	344
07/11/2002	37773	344
08/15/2002	38274	344
09/19/2002	38775	344
05/15/2008	68334	344
06/04/2009	73845	344
07/24/2008	69336	344
08/28/2008	69837	344
08/13/2009	74847	344
07/05/2007	63825	344
08/09/2007	64326	344
09/17/2009	75348	344

Dissertation Research Summary

The goal of my dissertation research is to develop an automated process that estimates the Mogi source model parameters for a spherical magma chamber (e.g. radius, pressure, depth, and position) through time series analysis of surface and subsurface measurements. The surface component will focus on the temporal evolution of deformation measurements, which will be derived from a combination of InSAR images and GPS records. The subsurface portion will focus on the temporal evolution of the seismic velocity structure within the volcano using Rayleigh wave group velocity dispersion measurements, acquired through ambient noise cross correlation techniques. The parameter estimation algorithm and the mechanism for combining the geophysical measurements will be the major focus of my research. Parameter estimation methodologies under consideration include both Kalman and Bootstrap Particle filters. I am planning to use the Okmok volcano as a test bed due its rich eruption history and vast amount of pre-existing studies. I plan to examine other volcanoes, once I demonstrate the process works properly.

Proof of Concept Research

I am preparing my dissertation proposal which is scheduled for December 14, 2009. As part of my proposal, I need to produce a time series of interferograms and model them using a Mogi source to demonstrate I understand the technical challenges associated with my proposed

research. Since the subject of InSAR data processing has been studied extensively, I am an using an established processing package to produce interferograms (ROI PAC). In order to prove that I am producing credible results, four of the eight interferometric scenes I plan to create are identical to those shown in [1], which I will use to verify my results. The remaining scenes span 2007-2009 and will be original work associated with my dissertation research.

Thank you for your time and attention. If you have any questions or comments regarding this request or my dissertation research or this request, please do not hesitate to contact me.

Regards,

William Junek

Central Florida Remote Sensing Laboratory, University of Central Florida

APPENDIX E: OKMOK GPS RECORDS: 2004-2008

GPS data processing was performed using the GAMIT GLOBK application developed by the Massachusetts Institute of Technology (MIT) [143].

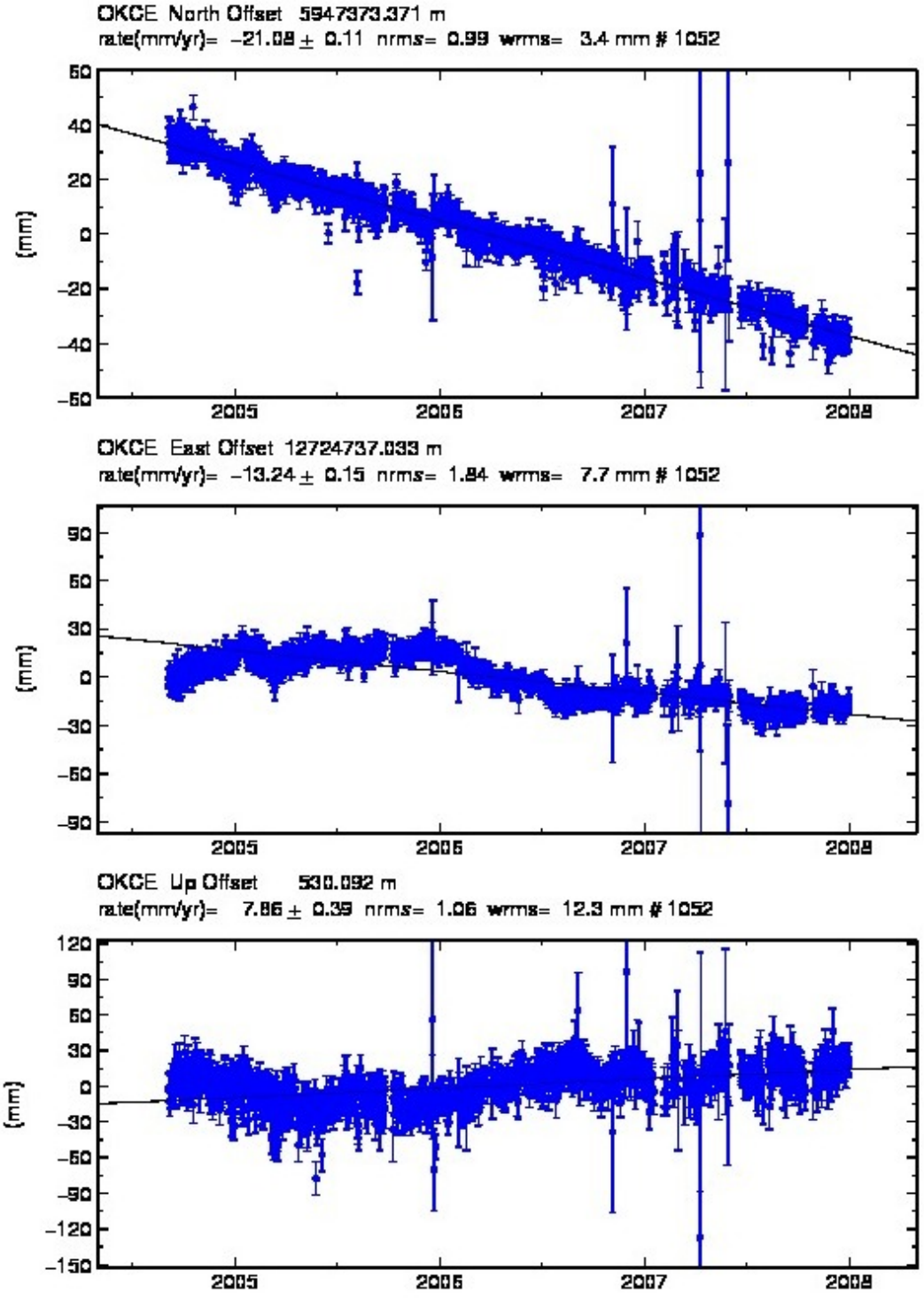

Figure E.1: Station: OKCE. Raw displacement measurements produced by the GAMIT / GLOBK processing package.

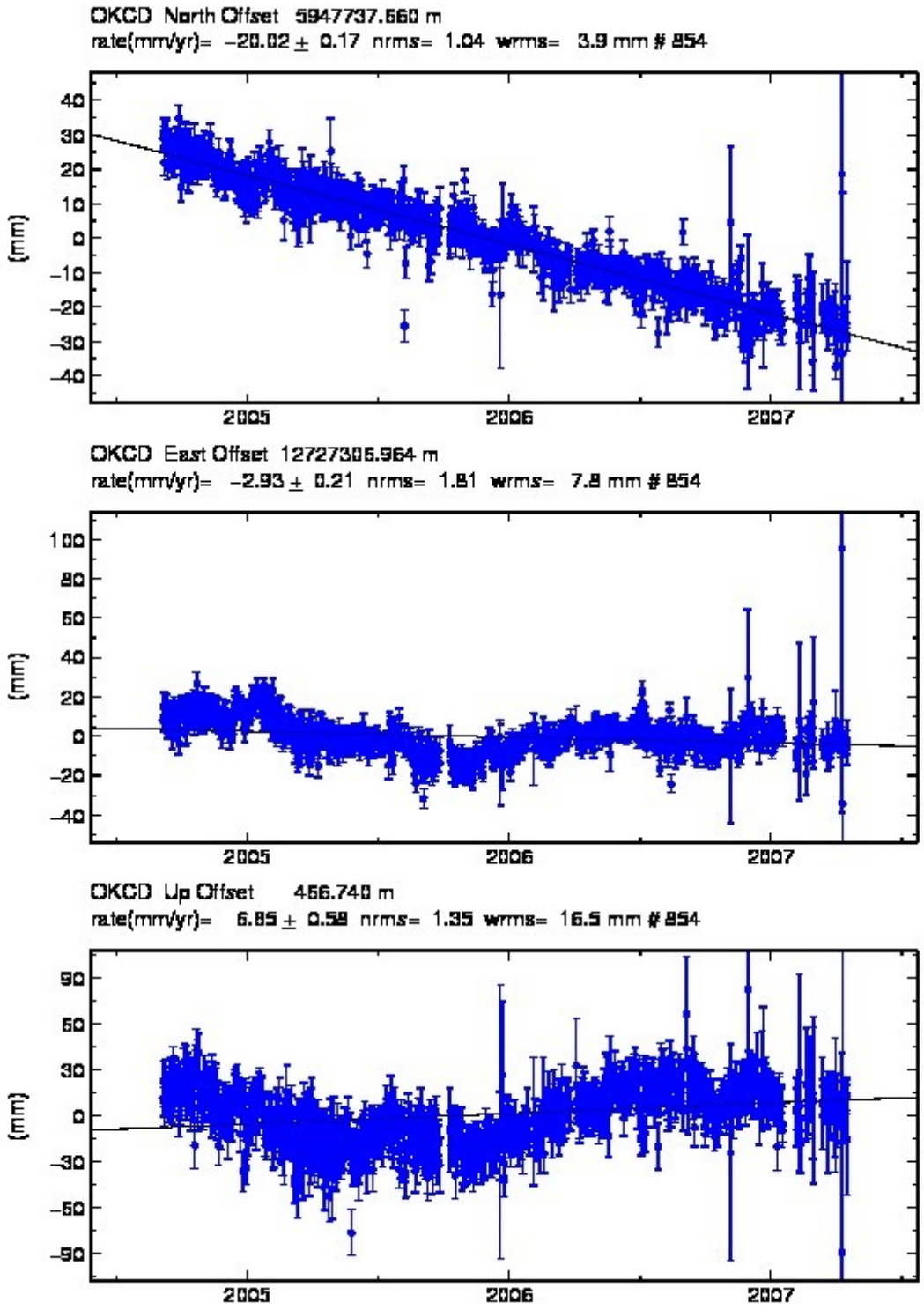

Figure E.2: Station: OKCD. Raw displacement measurements produced by the GAMIT / GLOBK processing package.

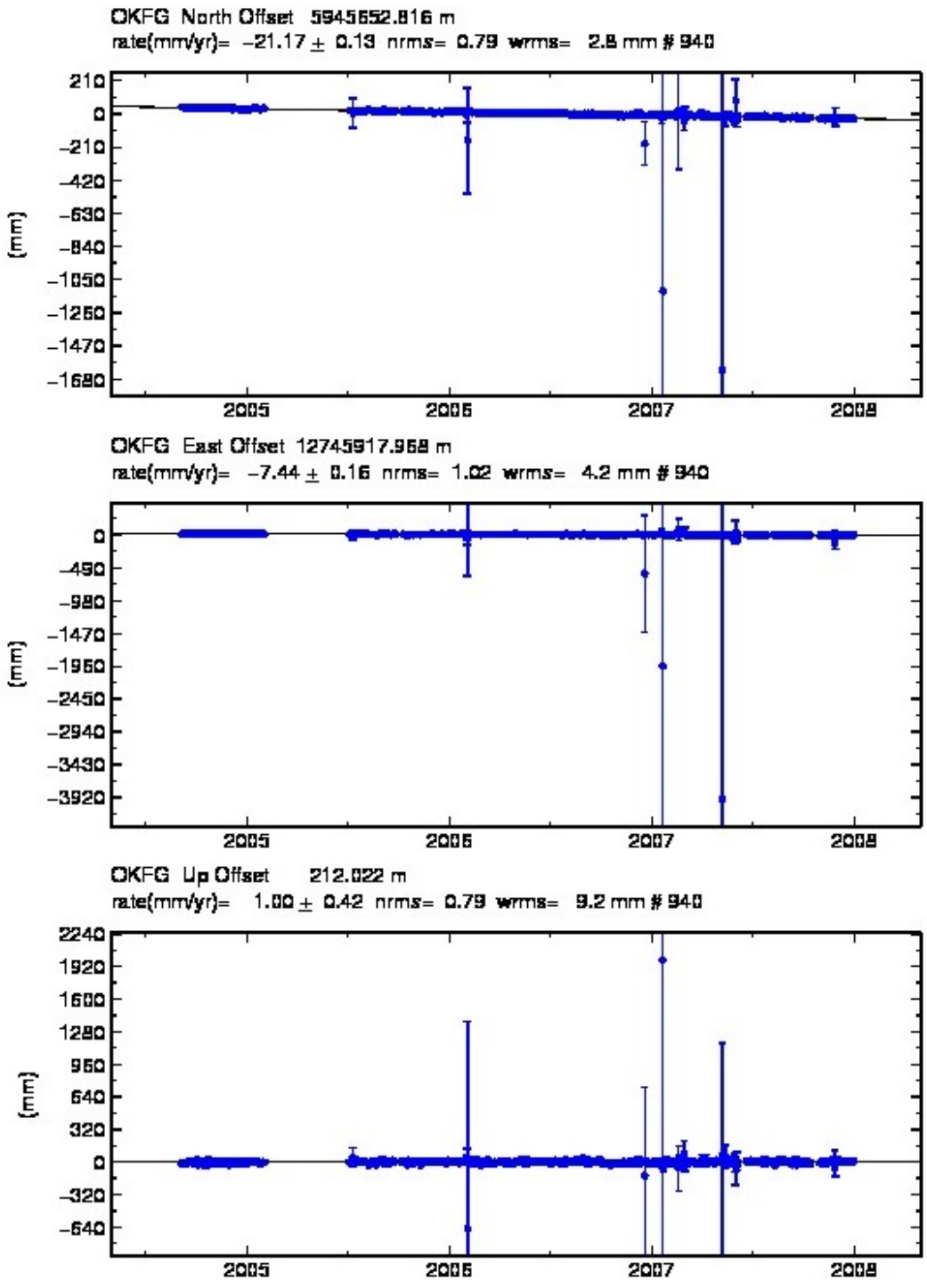

Figure E.3: Station: OKFG. Raw displacement measurements produced by the GAMIT / GLOBK processing package.

APPENDIX F: YELLOWSTONE GPS RECORDS: 2005-2011

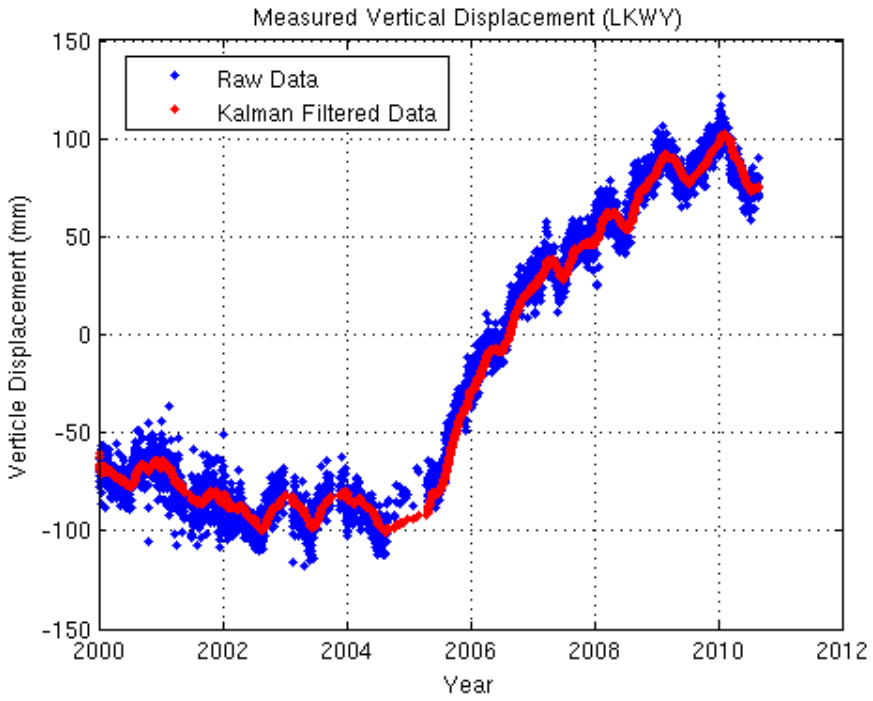

Figure F.1: USGS GPS Station LKWY

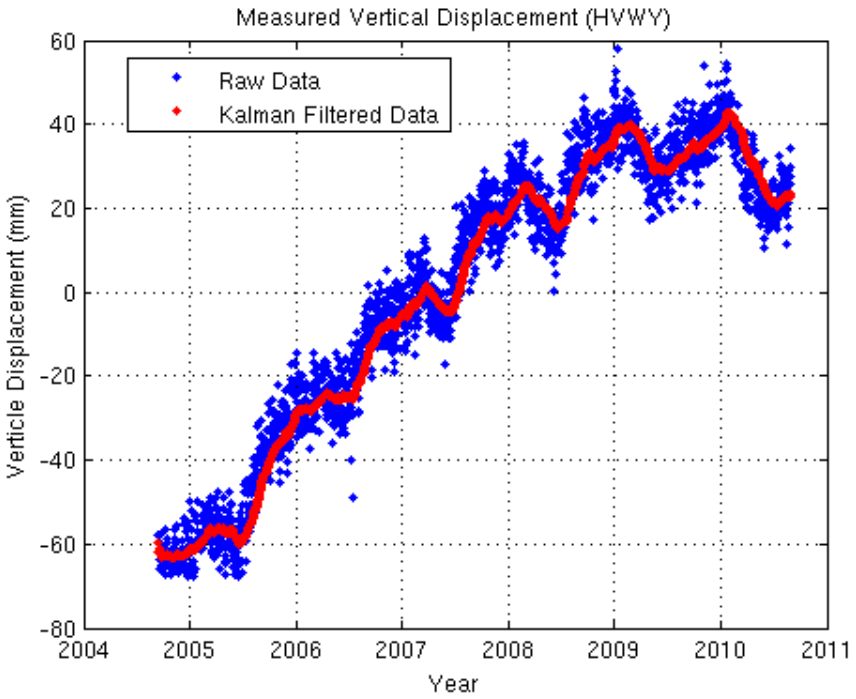

Figure F.2: USGS GPS Station HVWY

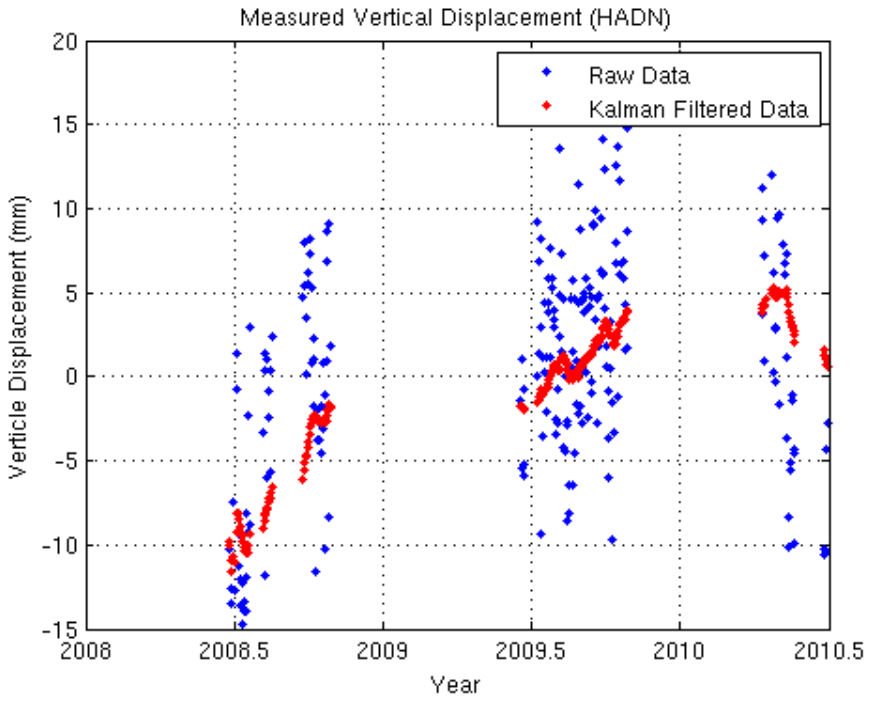

Figure F.3: USGS GPS Station HADN

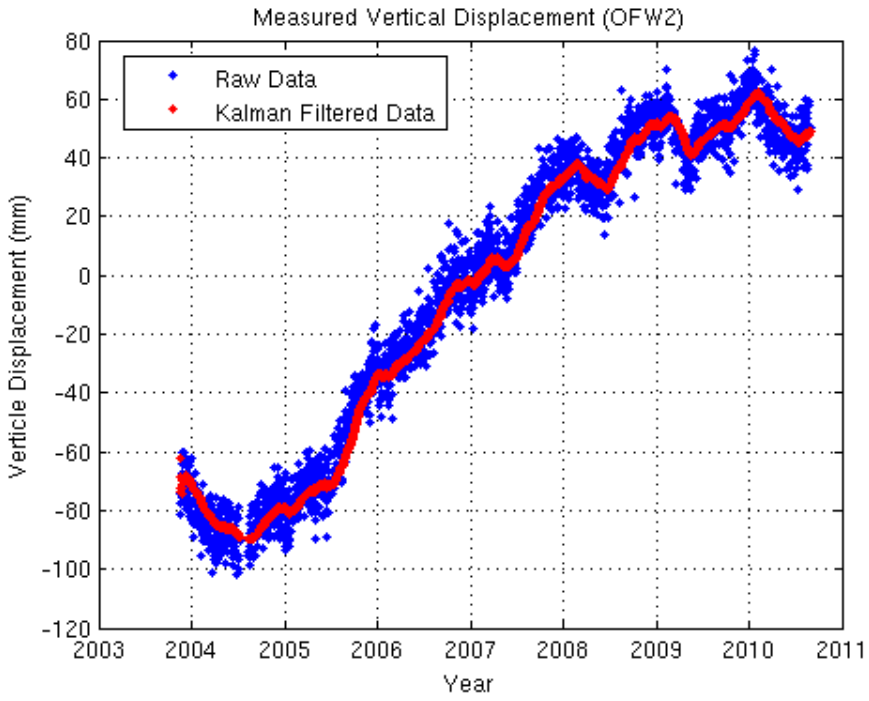

Figure F.4: USGS GPS Station OFW2

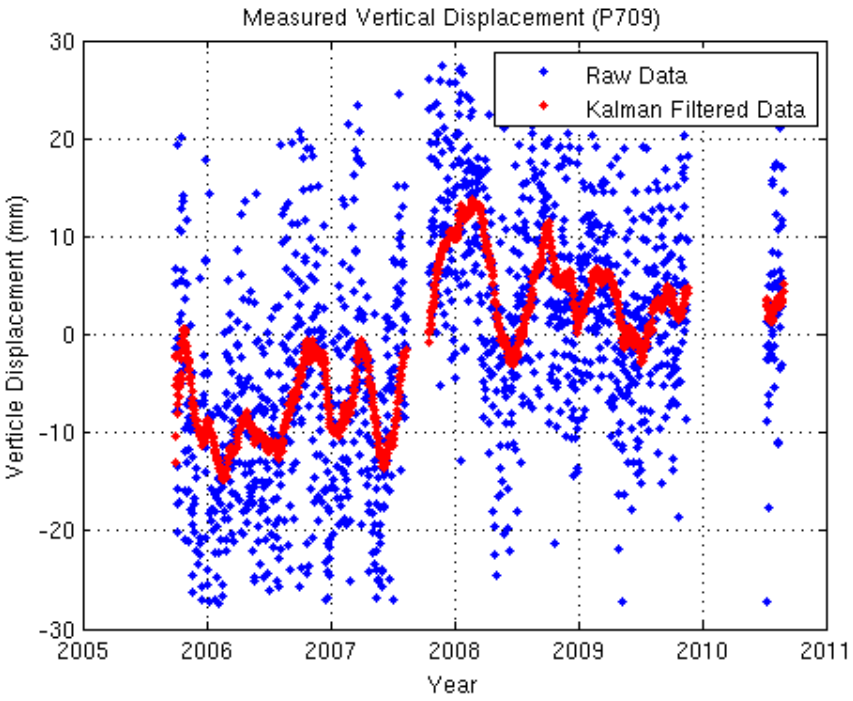

Figure F.5: USGS GPS Station P709

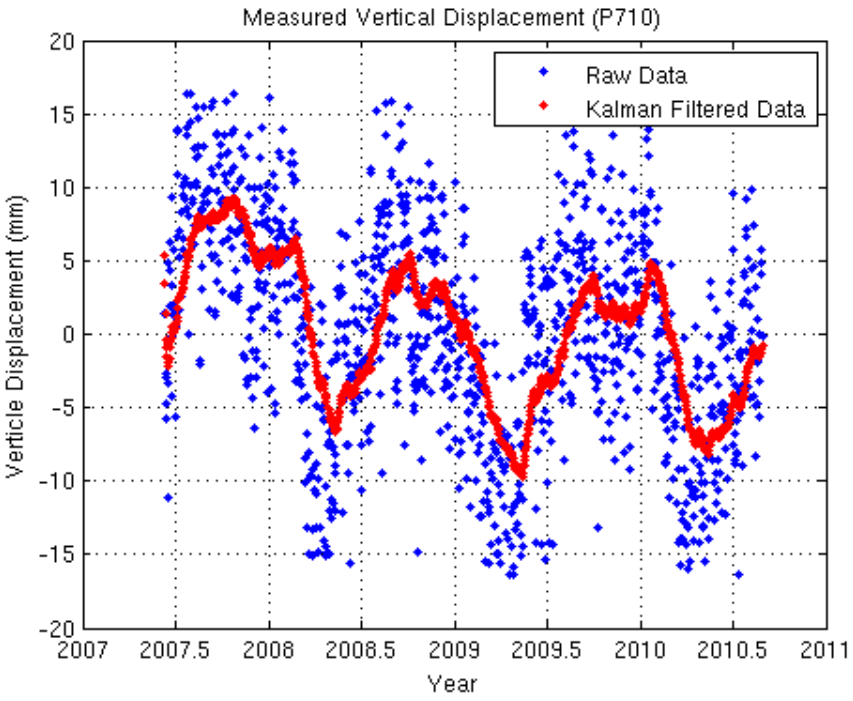

Figure F.6: USGS GPS Station P710

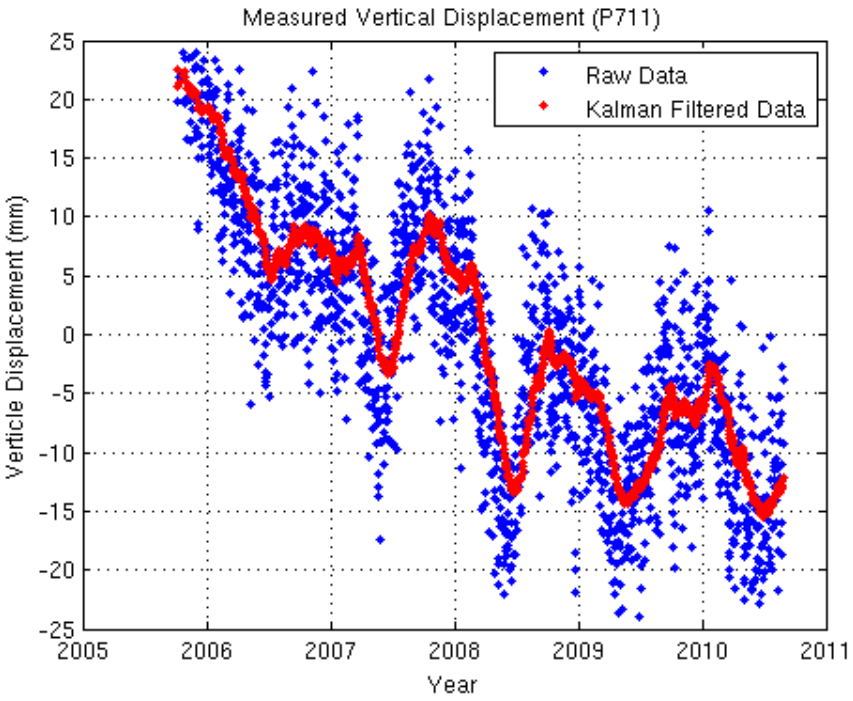

Figure F.7: USGS GPS Station P711

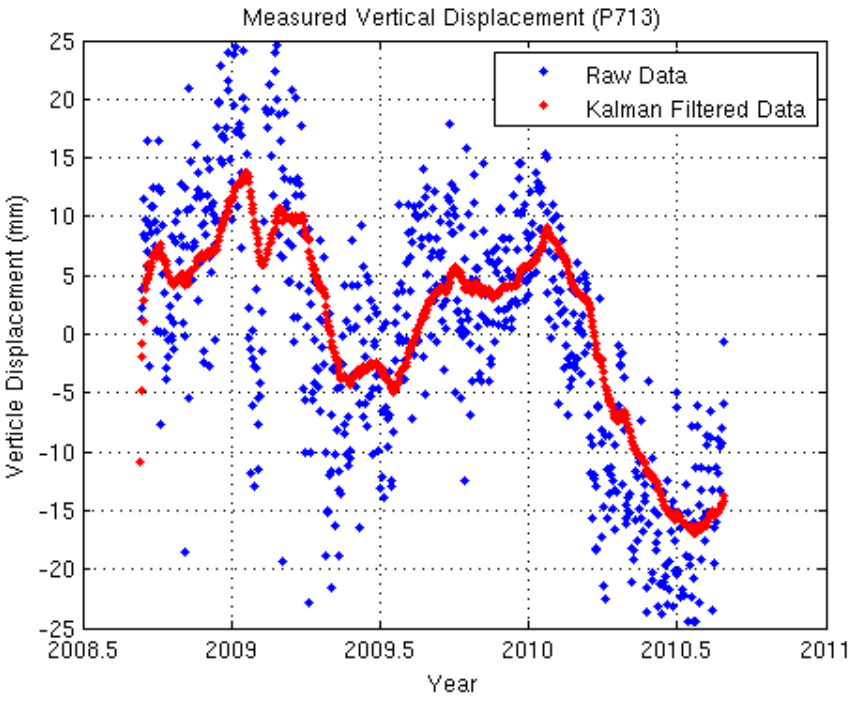

Figure F.8: USGS GPS Station P713

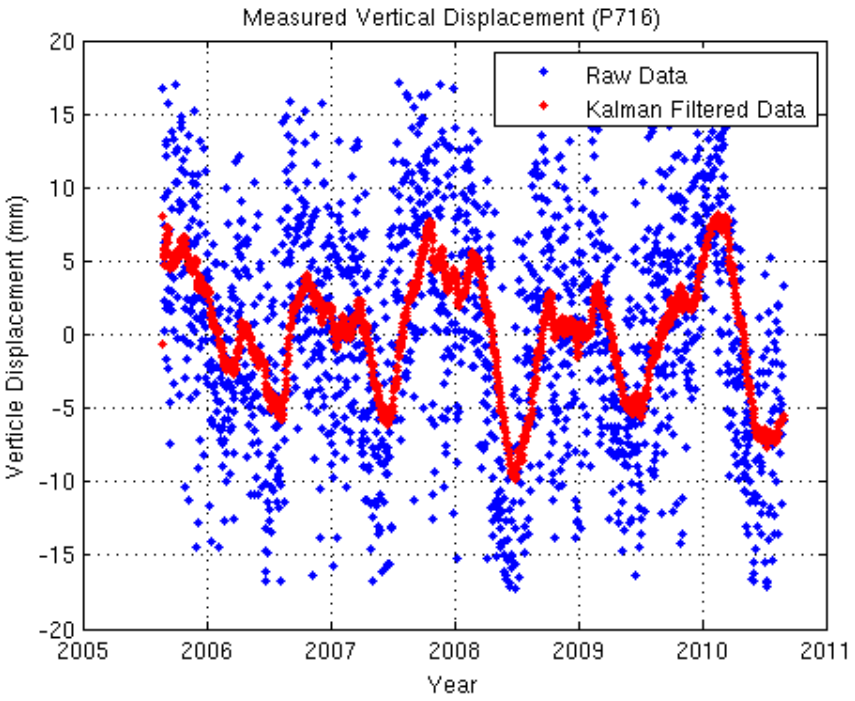

Figure F.9: USGS GPS Station P716

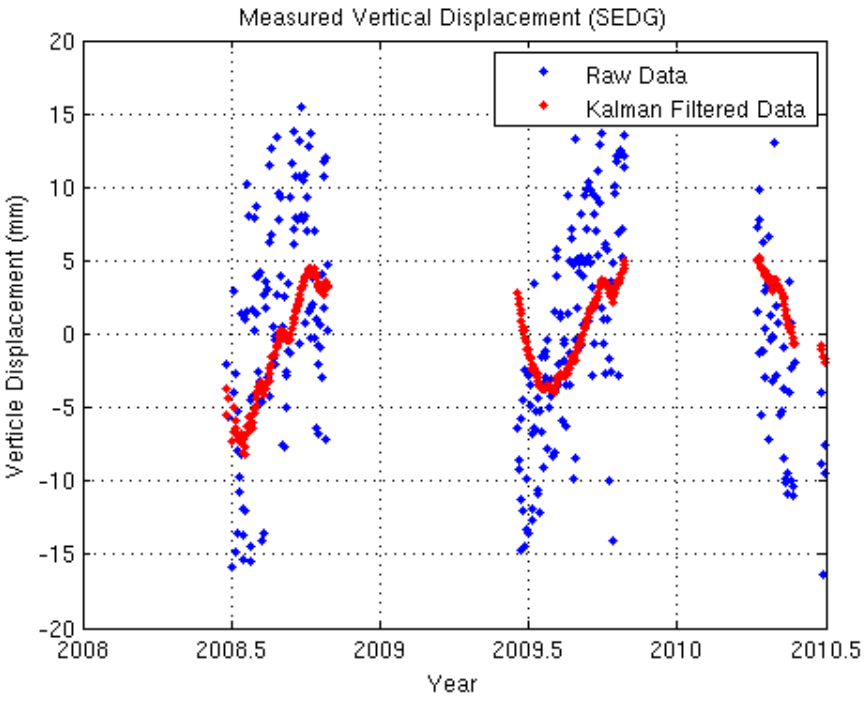

Figure F.10: USGS GPS Station SEDG

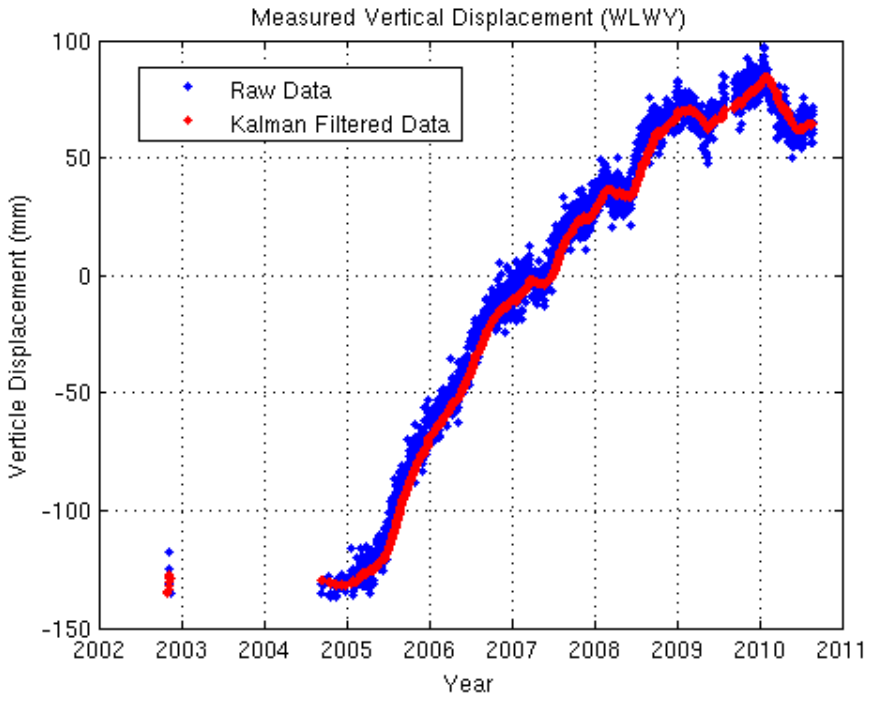

Figure F.11: USGS GPS Station WLYW

APPENDIX G: SELECTED MOUNT SAINT HELENS GPS RECORDS: 2005-2011

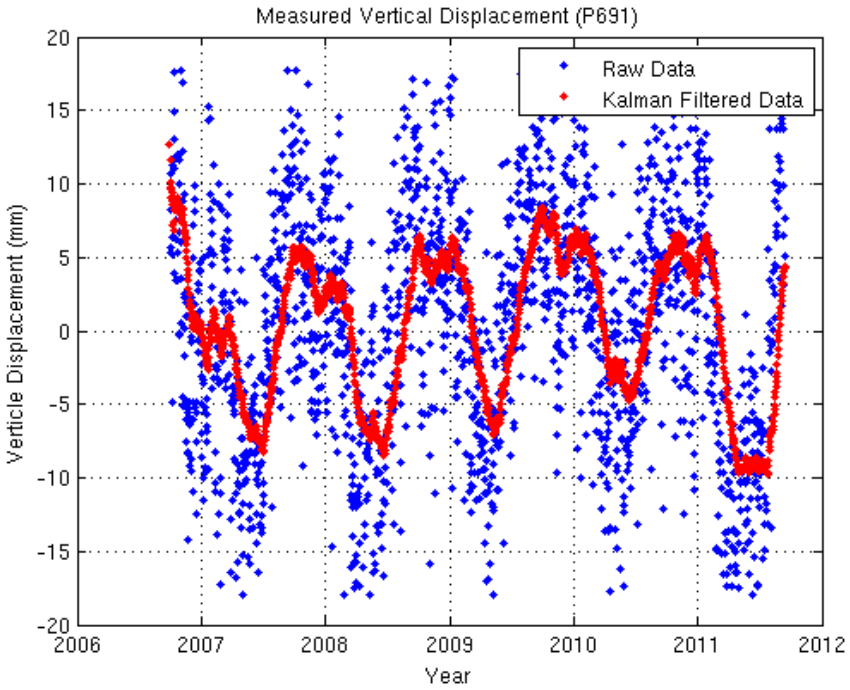

Figure G.1: USGS GPS Station P691

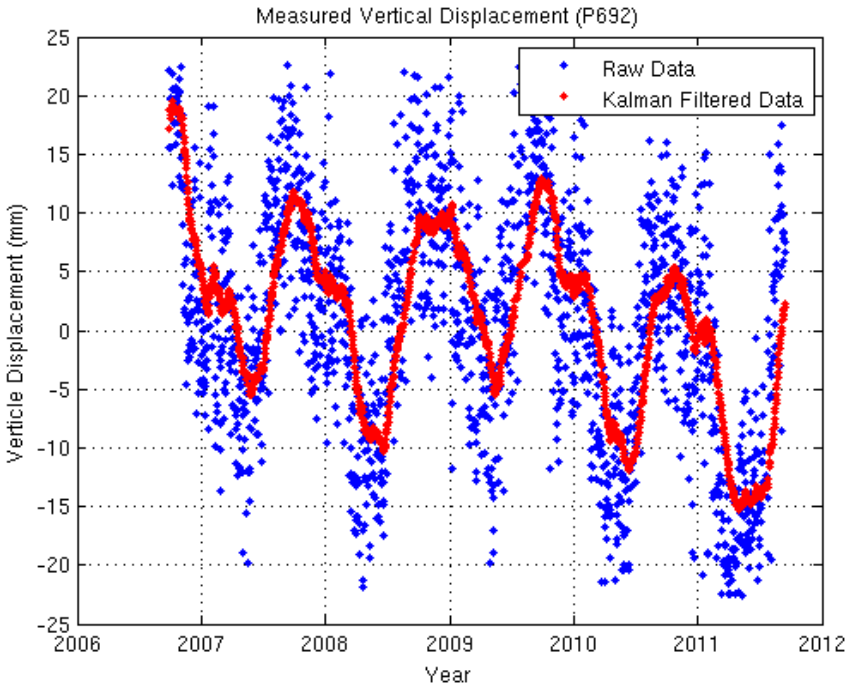

Figure G.2: USGS GPS Station P692

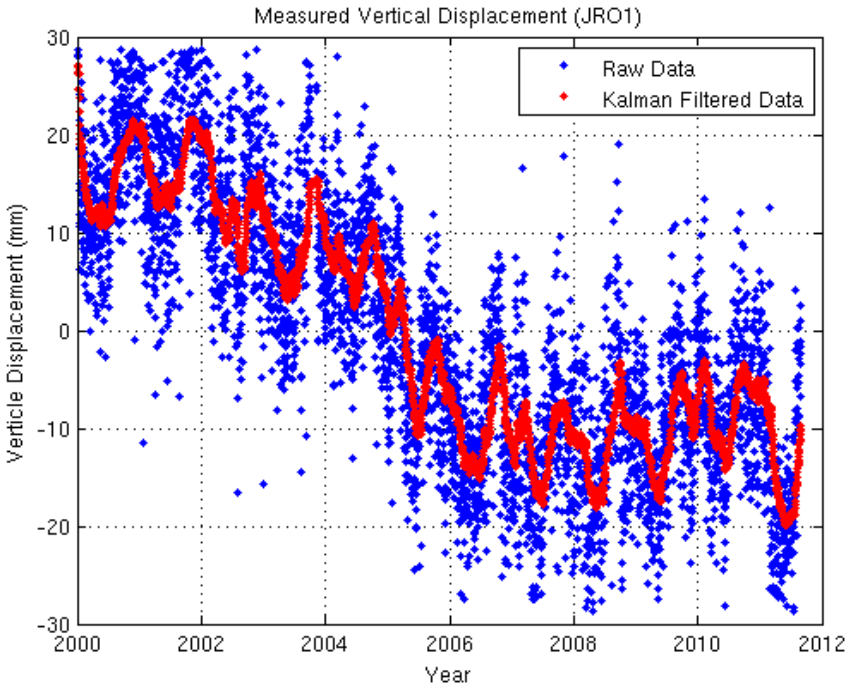

Figure G.3: USGS GPS Station JRO1

APPENDIX H: BETEF RESULTS

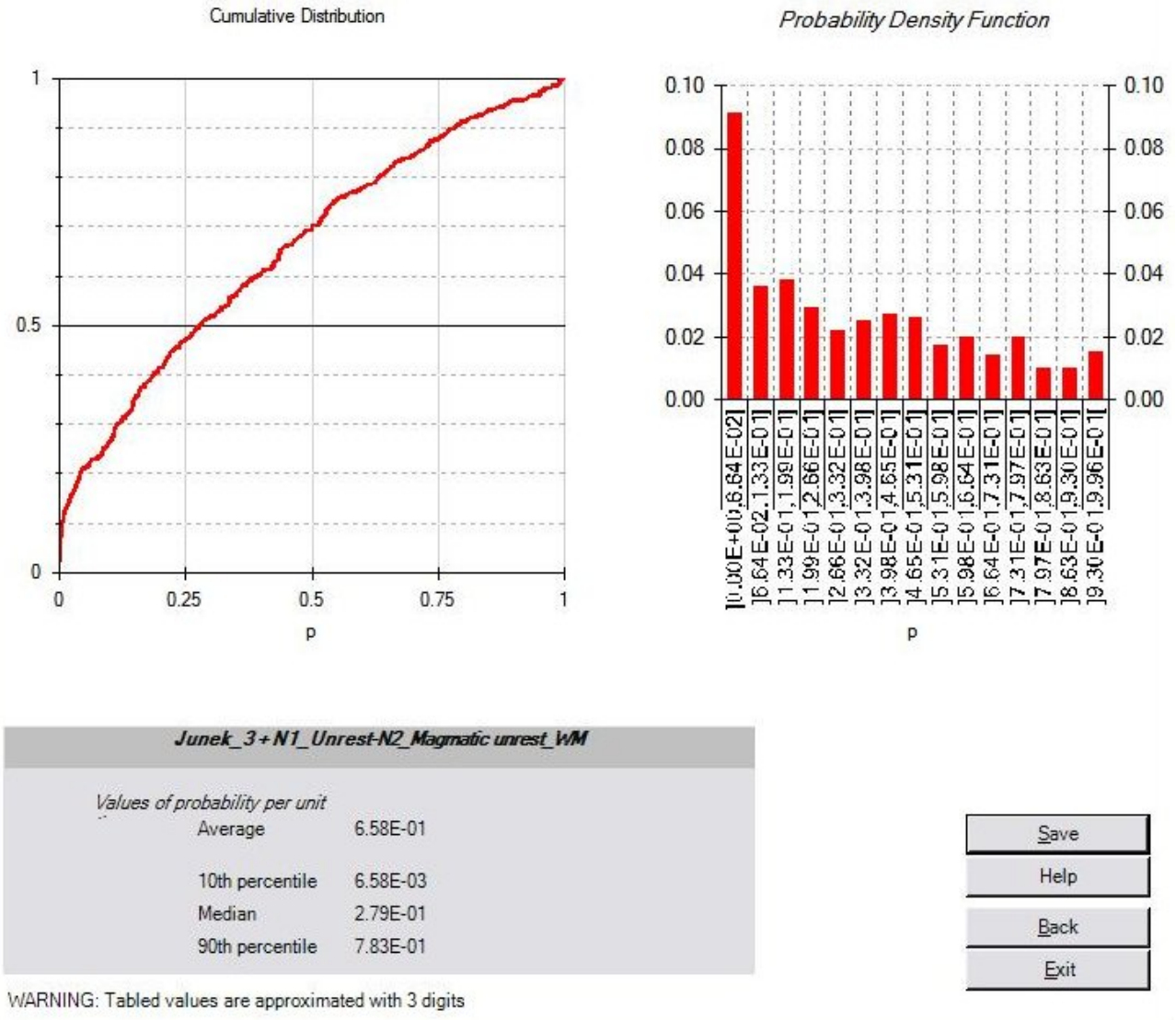

Figure H.1: Results generated using BETEF V2.0 for Okmok episode day 1, where $X_{NE} = 0.000$, $X_{CSM} = 0.0000$, and $X_{MM} = 1$ which are the same values used by the logistic models.

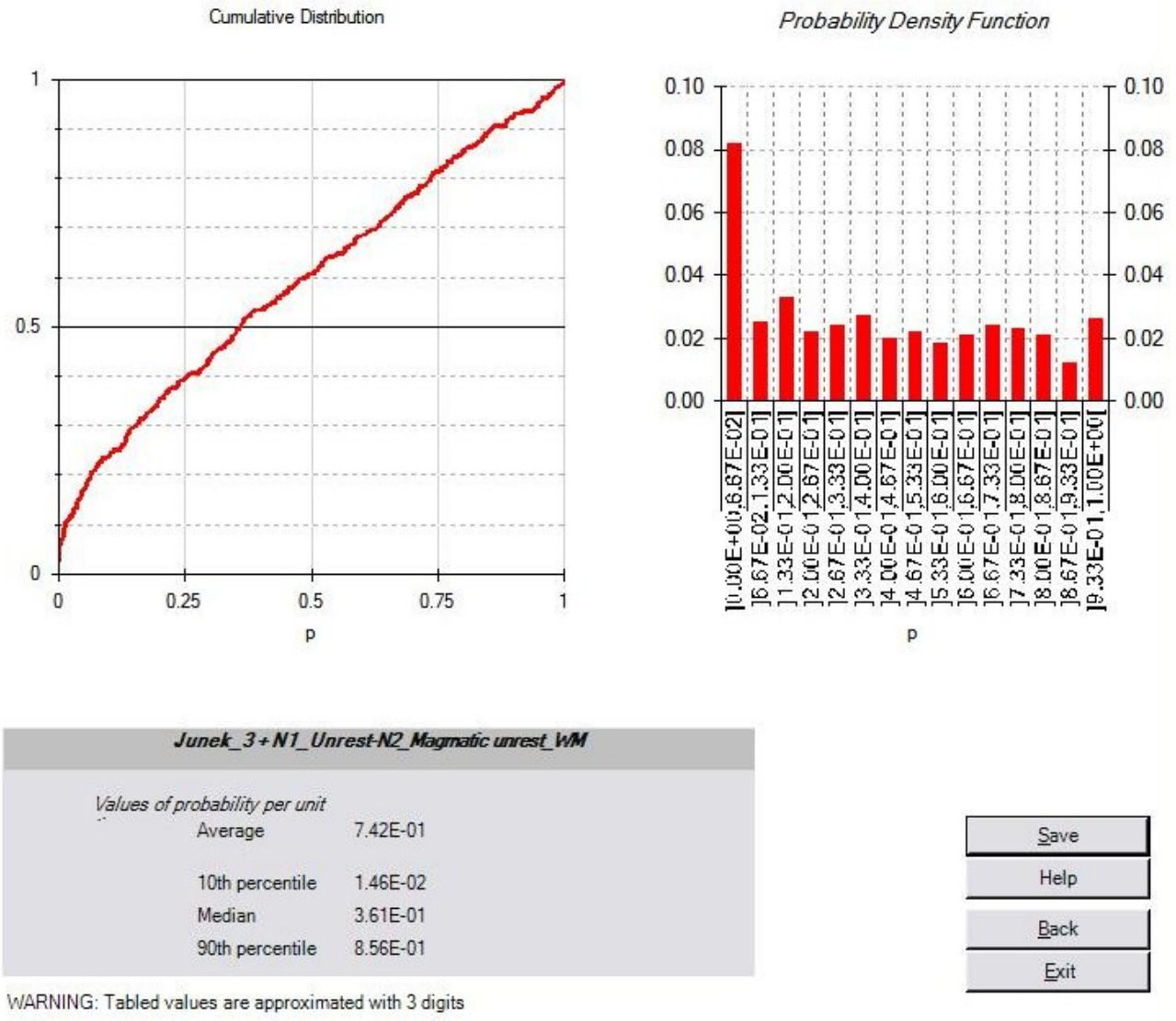

Figure H.2: Results generated using BETEF V2.0 for Okmok episode day 4, where $X_{NE} = 0.000$, $X_{CSM} = 0.0000$, and $X_{MM} = 1$ which are the same values used by the logistic models.

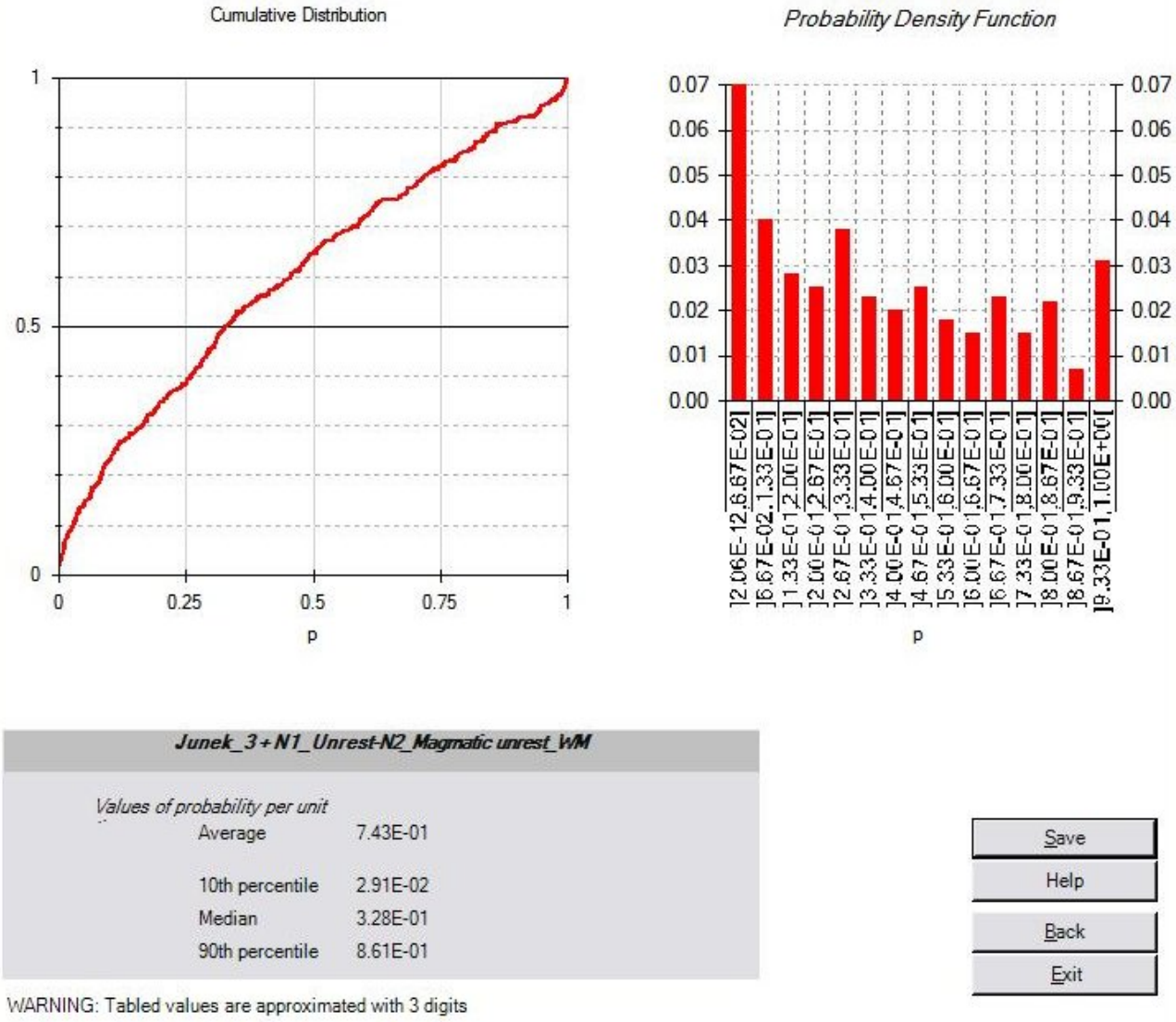

Figure H.3: Results generated using BETEF V2.0 for Okmok episode day 8, where $X_{NE} = 0.125$, $X_{CSM} = 0.0009$, and $X_{MM} = 1$ which are the same values used by the logistic models.

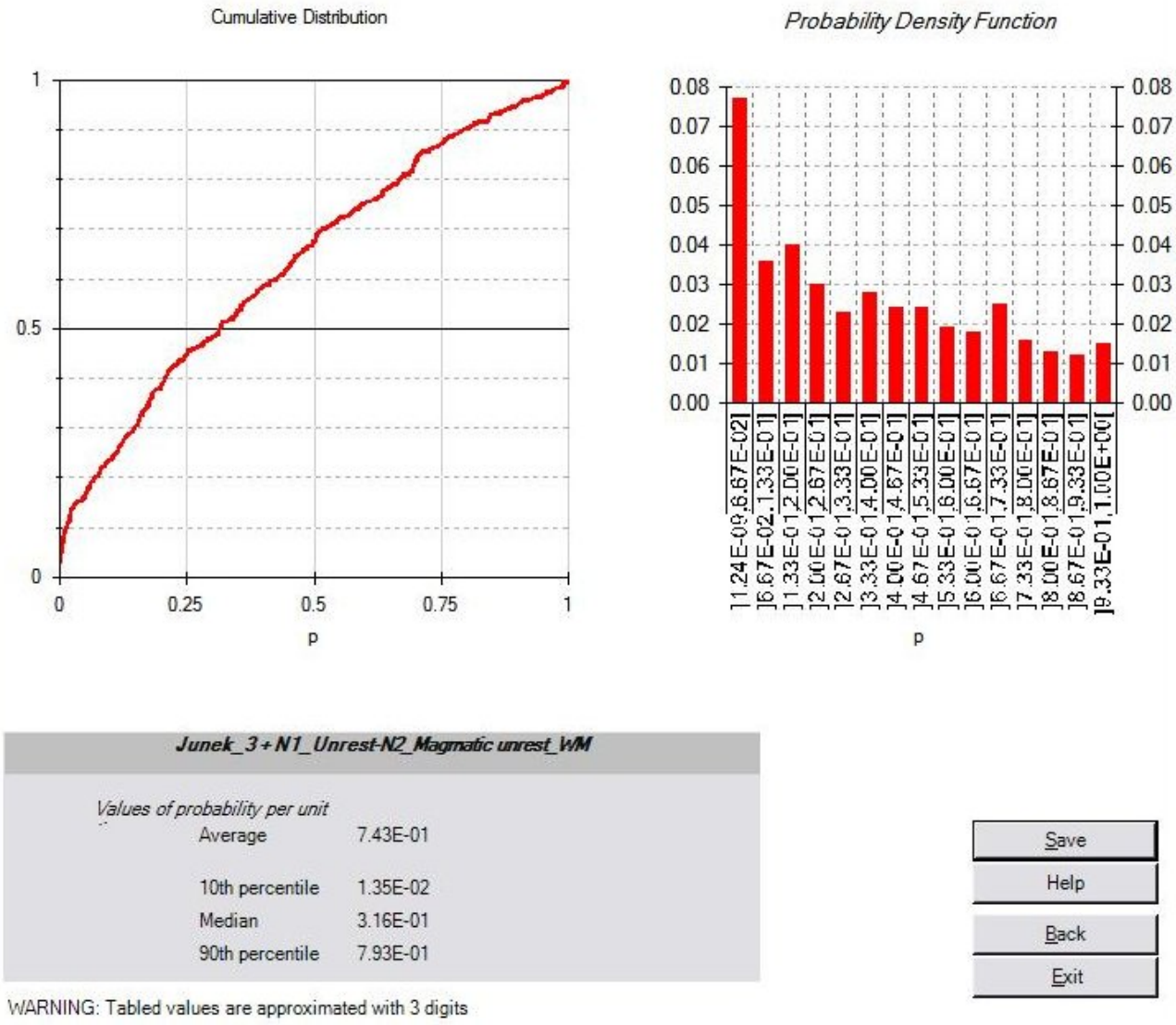

Figure H.4: Results generated using BETEF V2.0 for Okmok episode day 10, where $X_{NE} = 0.100$, $X_{CSM} = 0.0008$, and $X_{MM} = 1$ which are the same values used by the logistic models.

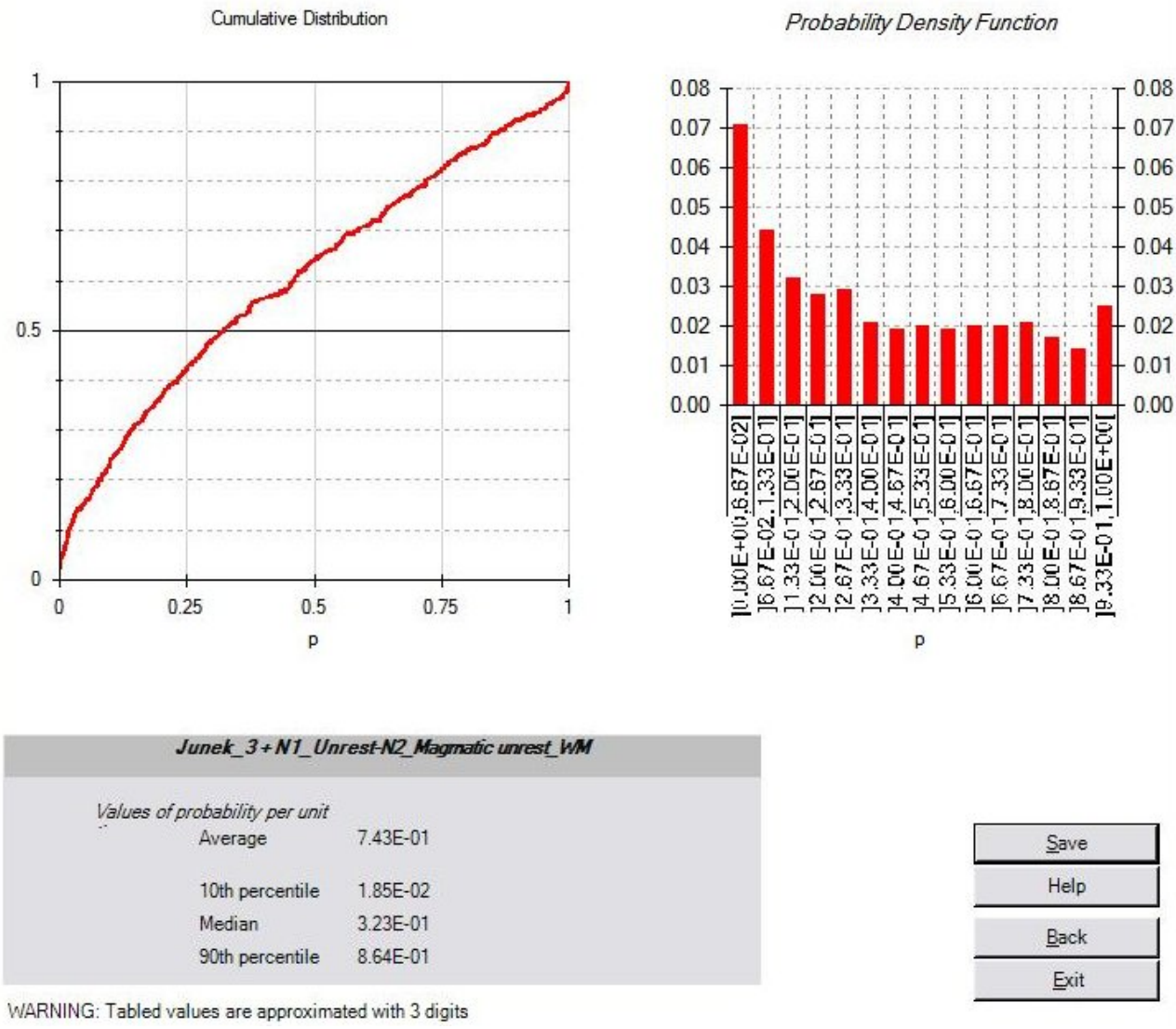

Figure H.5: Results generated using BETEF V2.0 for Okmok episode day 13, where $X_{NE} = 0.154$, $X_{CSM} = 0.0008$, and $X_{MM} = 1$ which are the same values used by the logistic models.

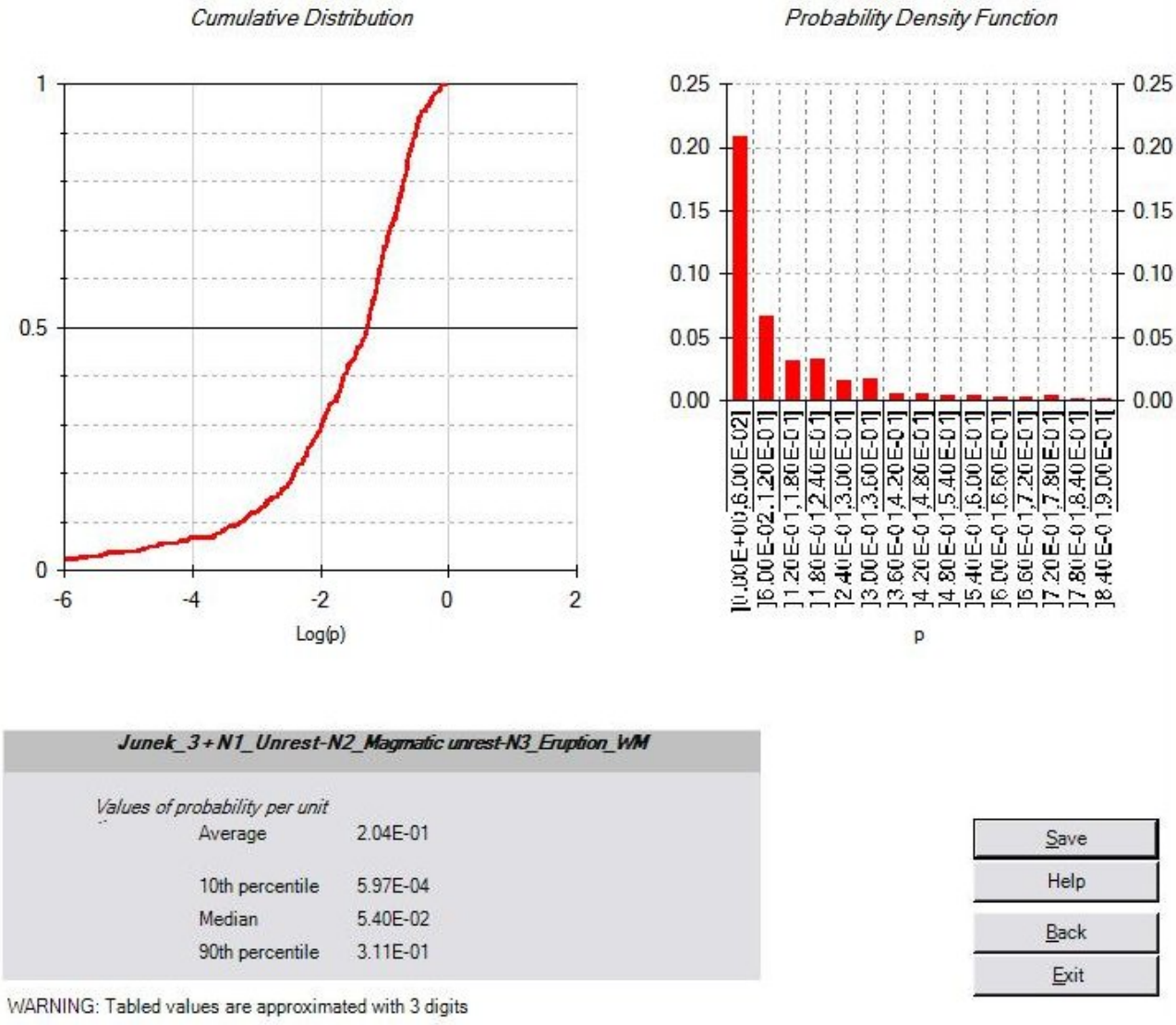

Figure H.6: Results generated using BETEF V2.0 for Okmok episode day 1, where $X_{NE} = 0.000$, $X_{CSM} = 0.0000$, and $X_{MM} = 1$ which are the same values used by the logistic models.

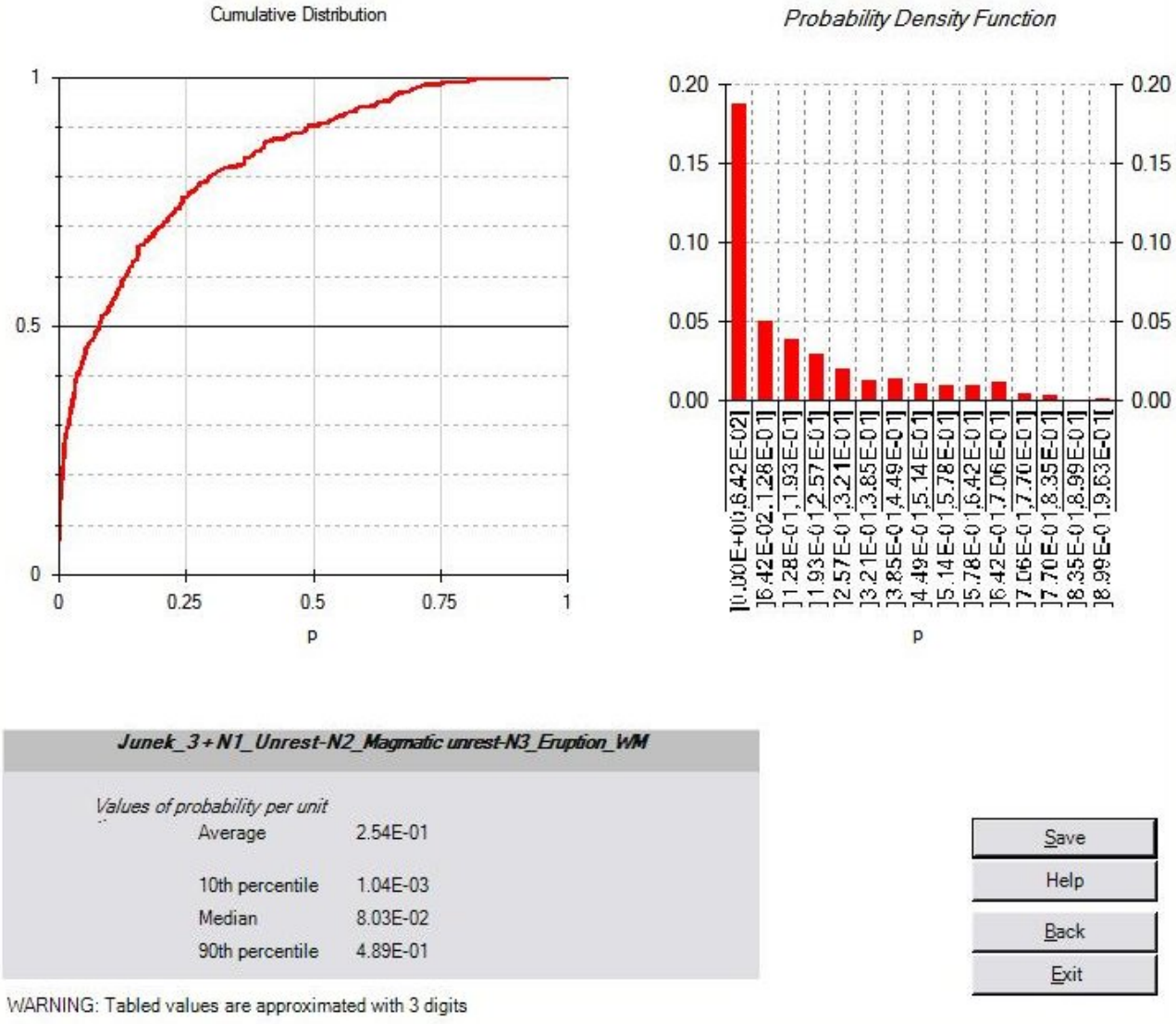

Figure H.7: Results generated using BETEF V2.0 for Okmok episode day 4, where $X_{NE} = 0.000$, $X_{CSM} = 0.0000$, and $X_{MM} = 1$ which are the same values used by the logistic models.

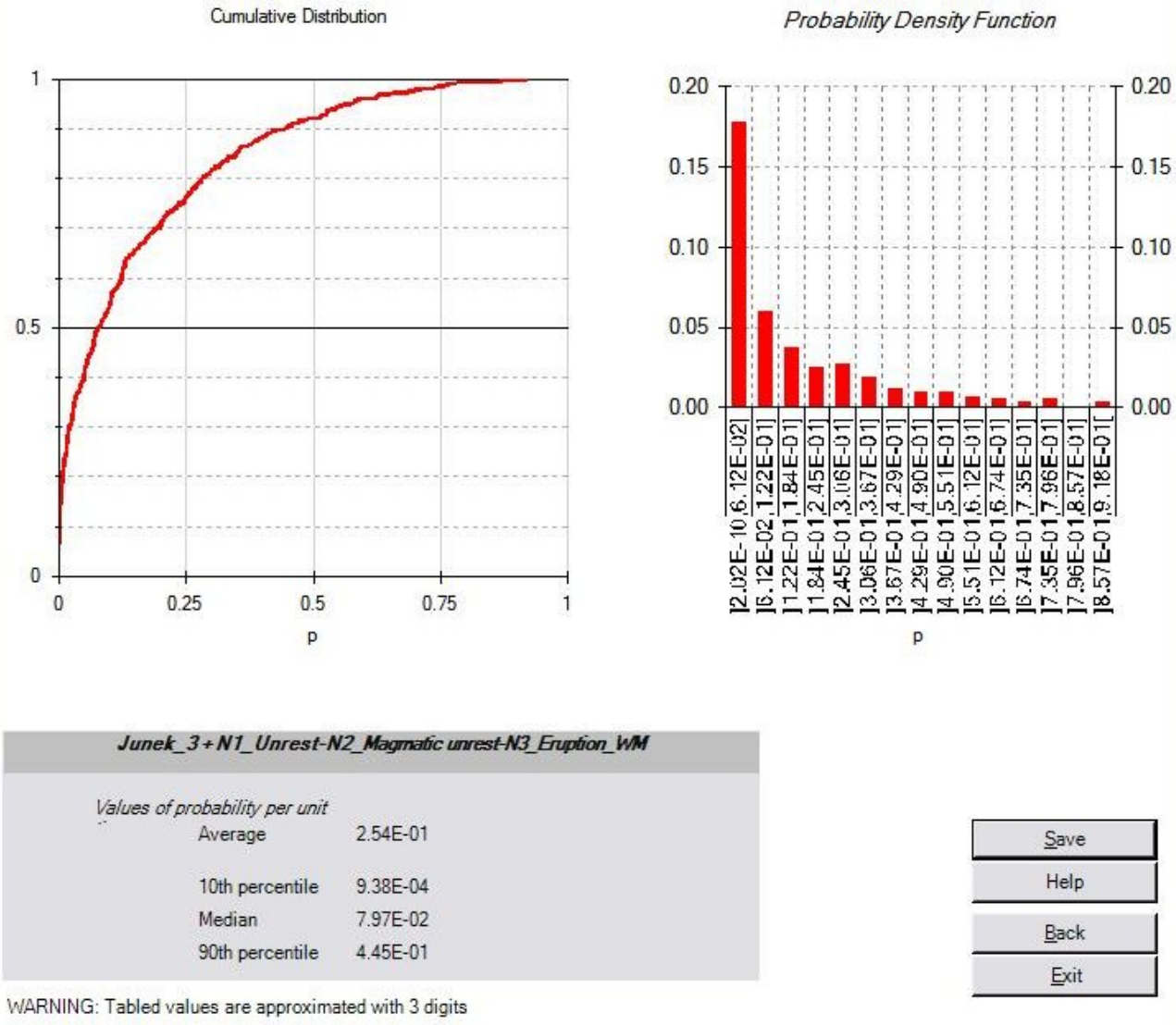

Figure H.8: Results generated using BETEF V2.0 for Okmok episode day 8, where $X_{NE} = 0.125$, $X_{CSM} = 0.0009$, and $X_{MM} = 1$ which are the same values used by the logistic models.

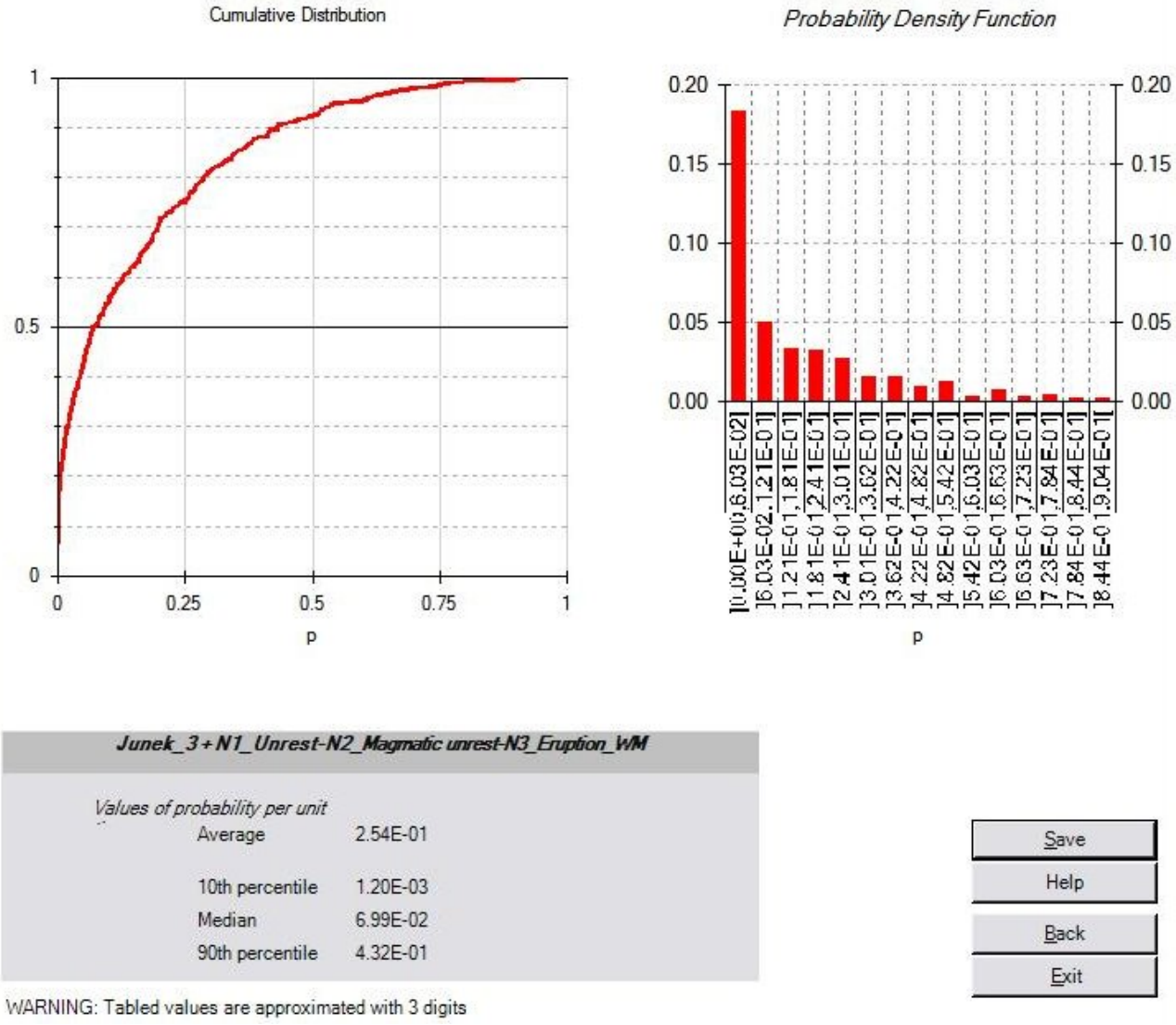

Figure H.9: Results generated using BETEF V2.0 for Okmok episode day 10, where $X_{NE} = 0.100$, $X_{CSM} = 0.0008$, and $X_{MM} = 1$ which are the same values used by the logistic models.

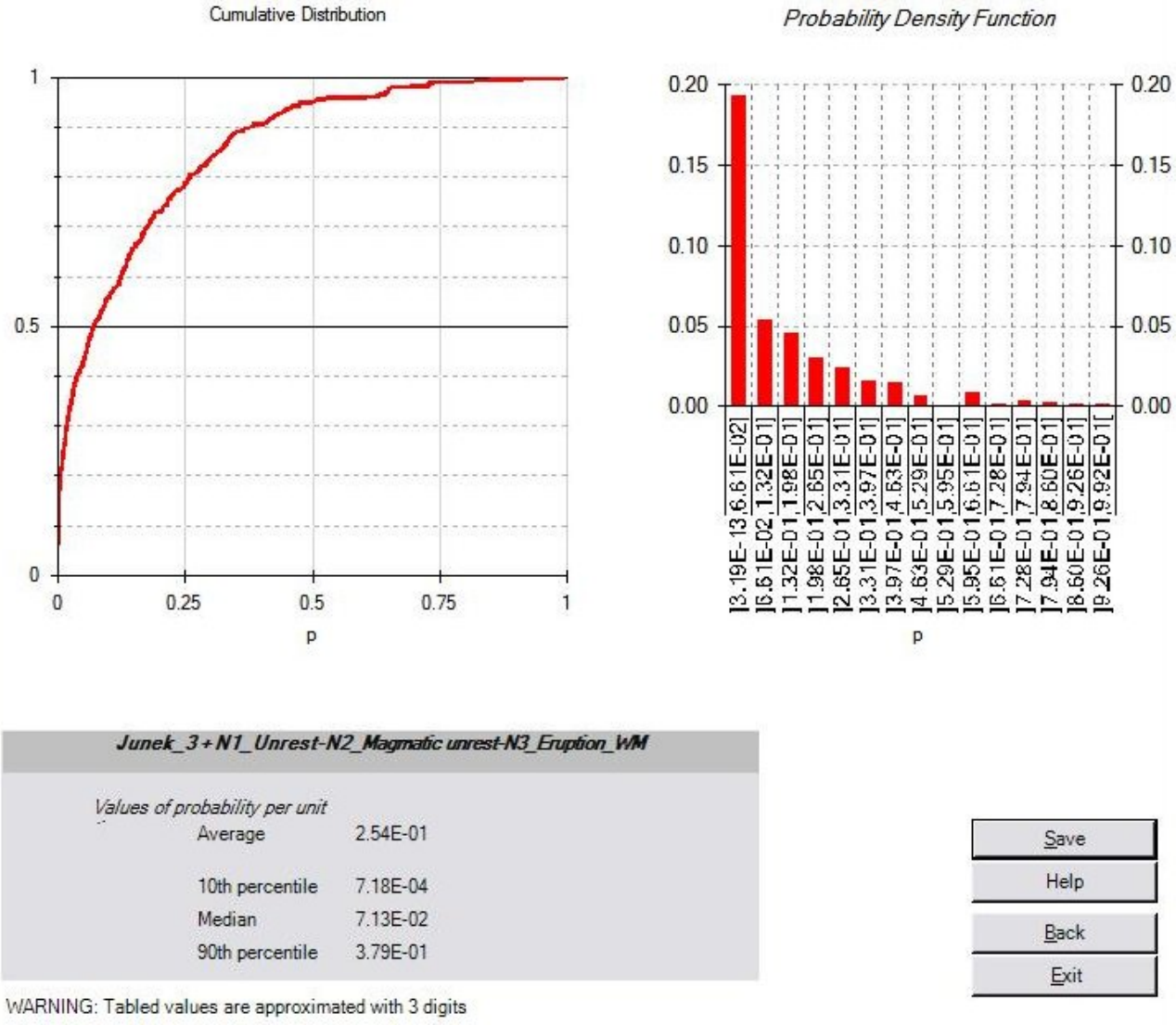

Figure H.10: Results generated using BETEF V2.0 for Okmok episode day 13, where $X_{NE} = 0.154$, $X_{CSM} = 0.0008$, and $X_{MM} = 1$ which are the same values used by the logistic models.

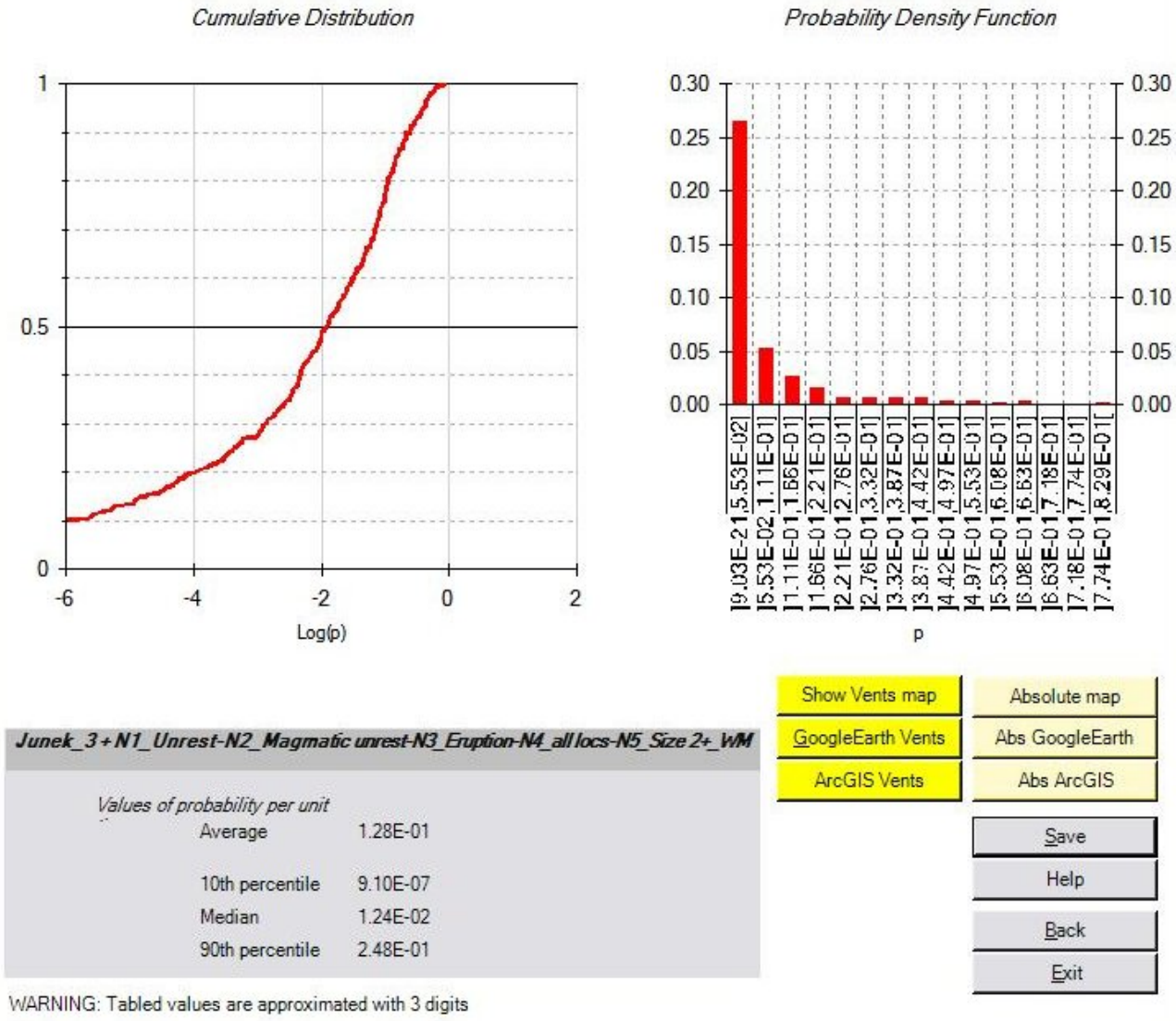

Figure H.11: Results generated using BETEF V2.0 for Okmok episode day 1, where $X_{NE} = 0.000$, $X_{CSM} = 0.0000$, and $X_{MM} = 1$ which are the same values used by the logistic models.

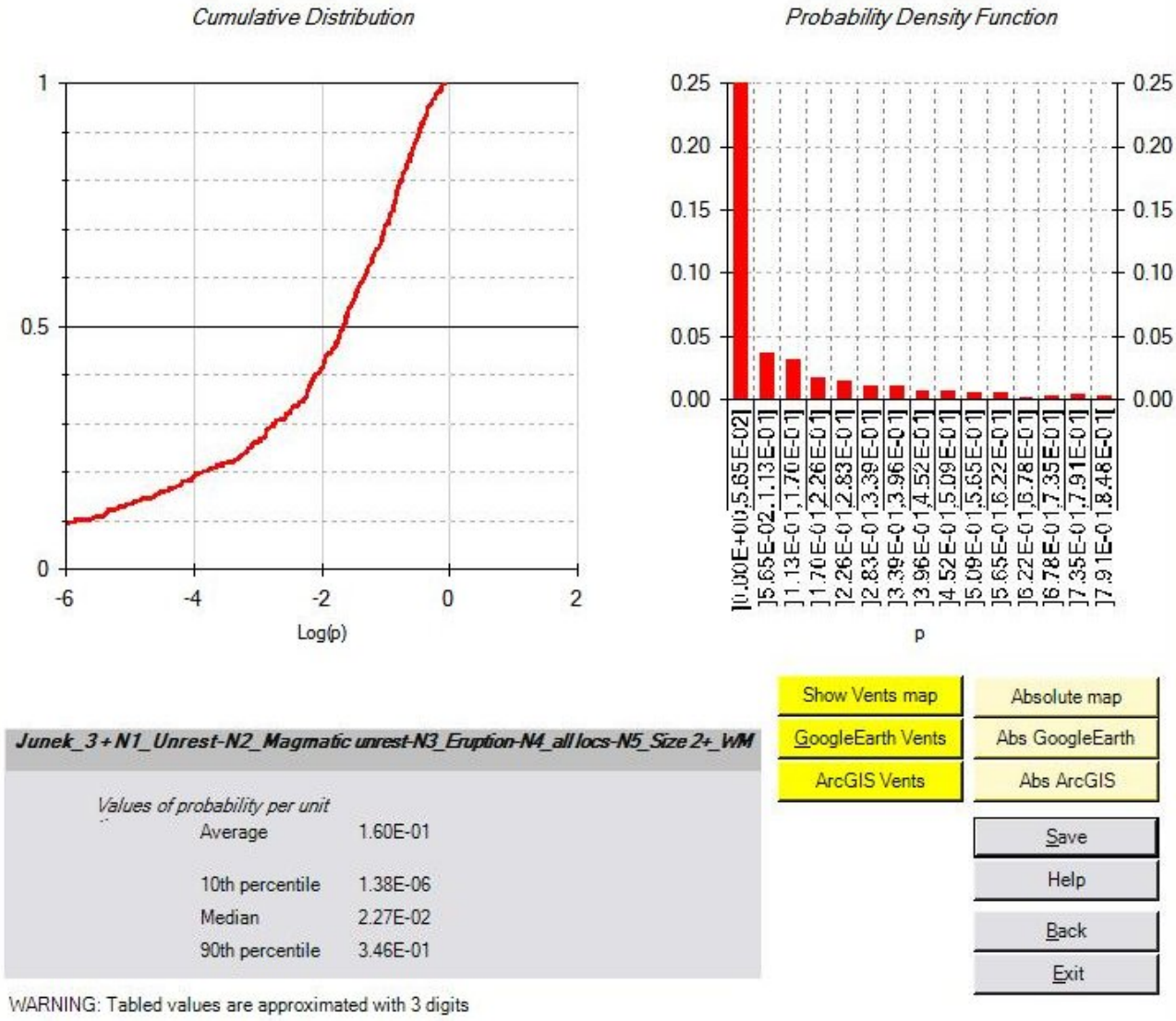

Figure H.12: Results generated using BETEF V2.0 for Okmok episode day 4, where $X_{NE} = 0.000$, $X_{CSM} = 0.0000$, and $X_{MM} = 1$ which are the same values used by the logistic models.

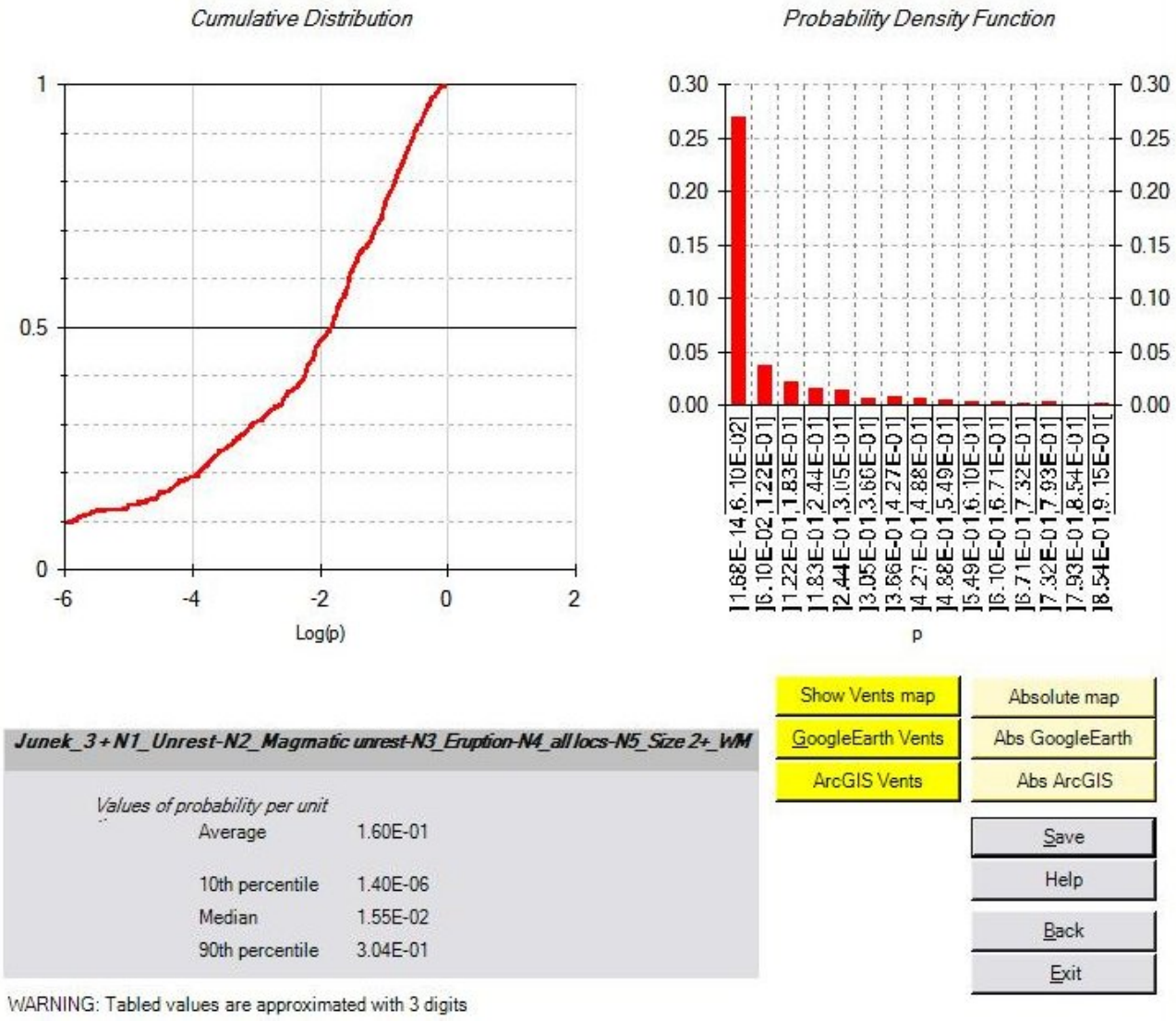

Figure H.13: Results generated using BETEF V2.0 for Okmok episode day 8, where $X_{NE} = 0.125$, $X_{CSM} = 0.0009$, and $X_{MM} = 1$ which are the same values used by the logistic models.

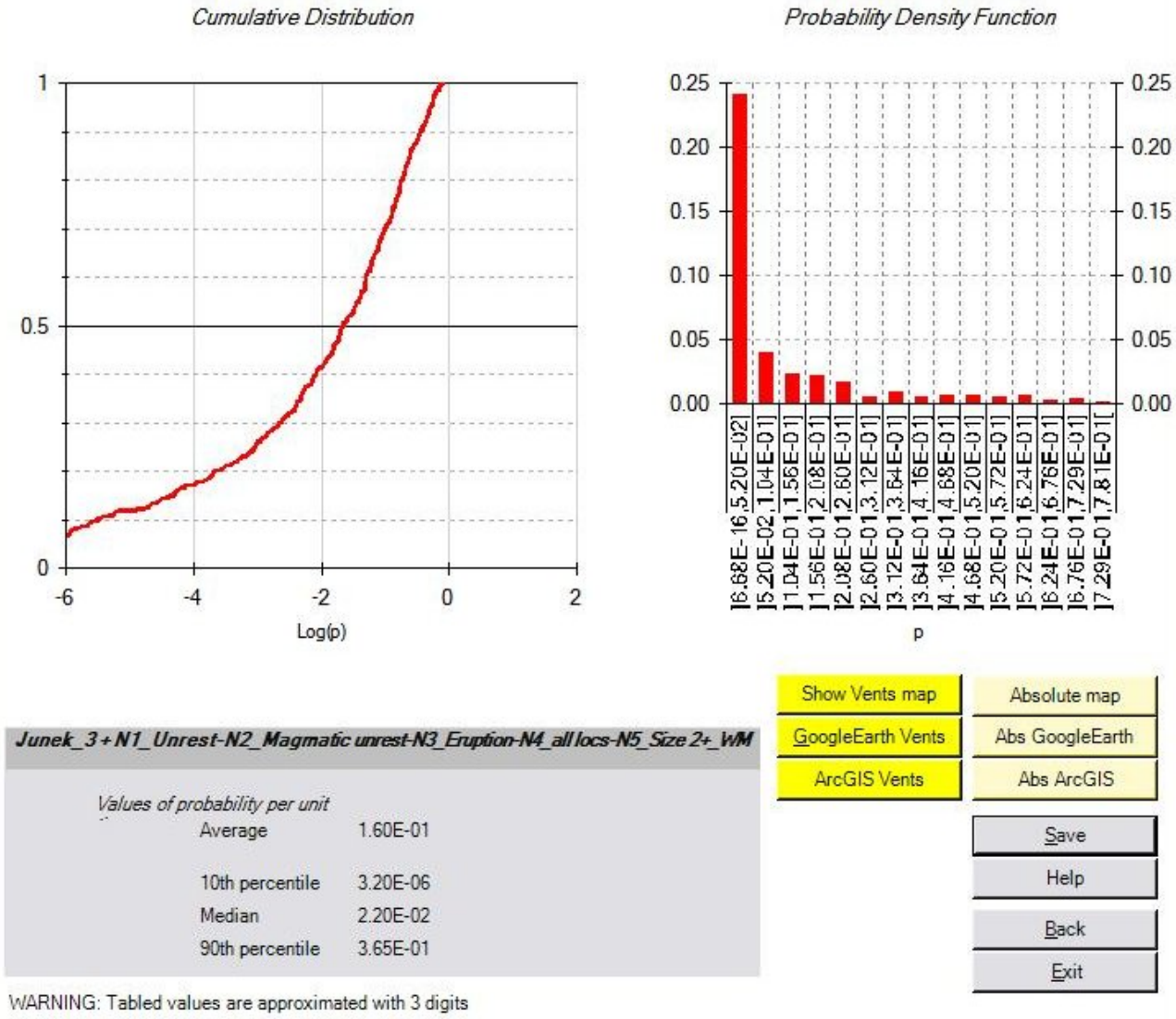

Figure H.14: Results generated using BETEF V2.0 for Okmok episode day 10, where $X_{NE} = 0.100$, $X_{CSM} = 0.0008$, and $X_{MM} = 1$ which are the same values used by the logistic models.

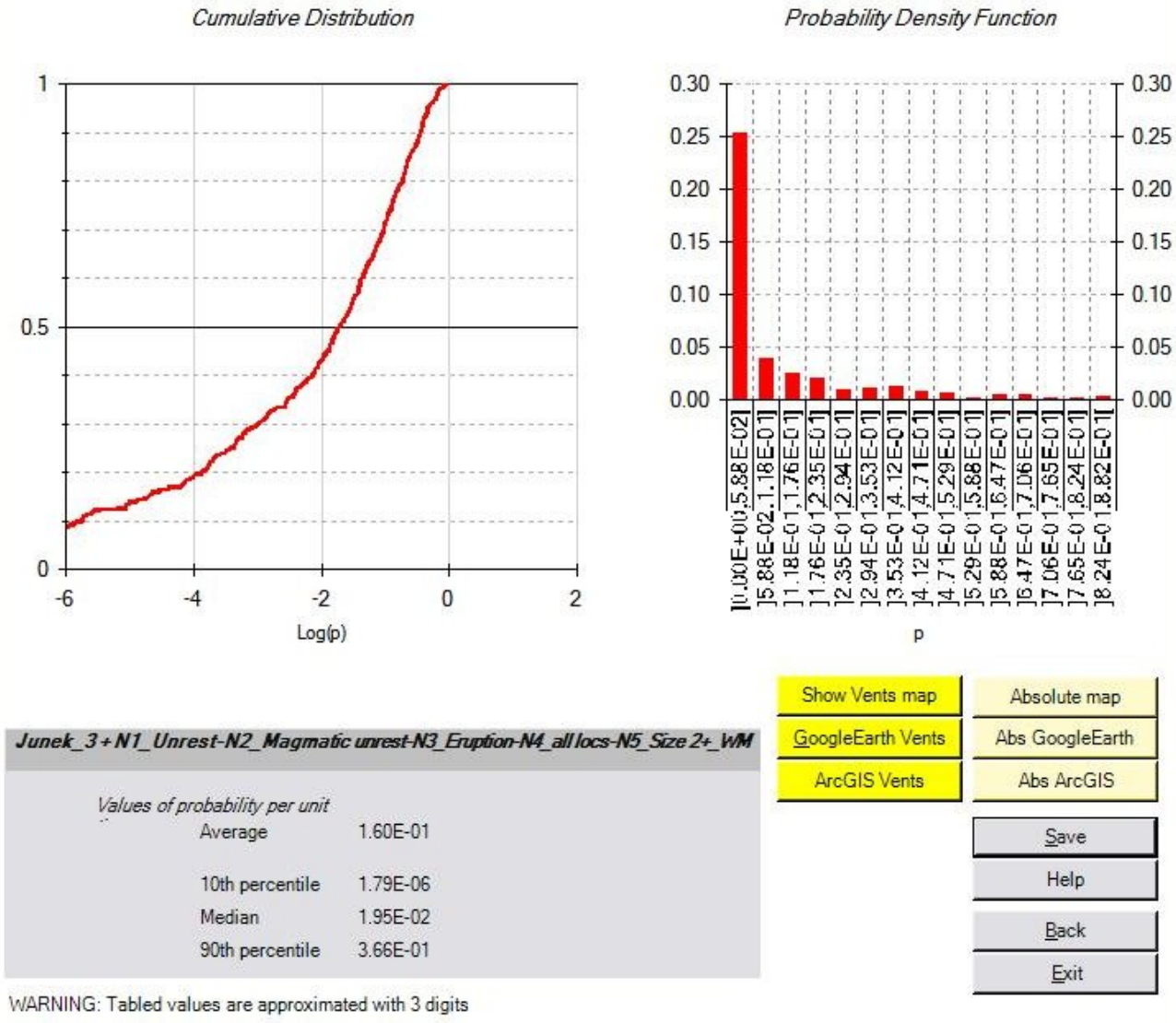

Figure H.15: Results generated using BETEF V2.0 for Okmok episode day 13, where $X_{NE} = 0.154$, $X_{CSM} = 0.0008$, and $X_{MM} = 1$ which are the same values used by the logistic models.

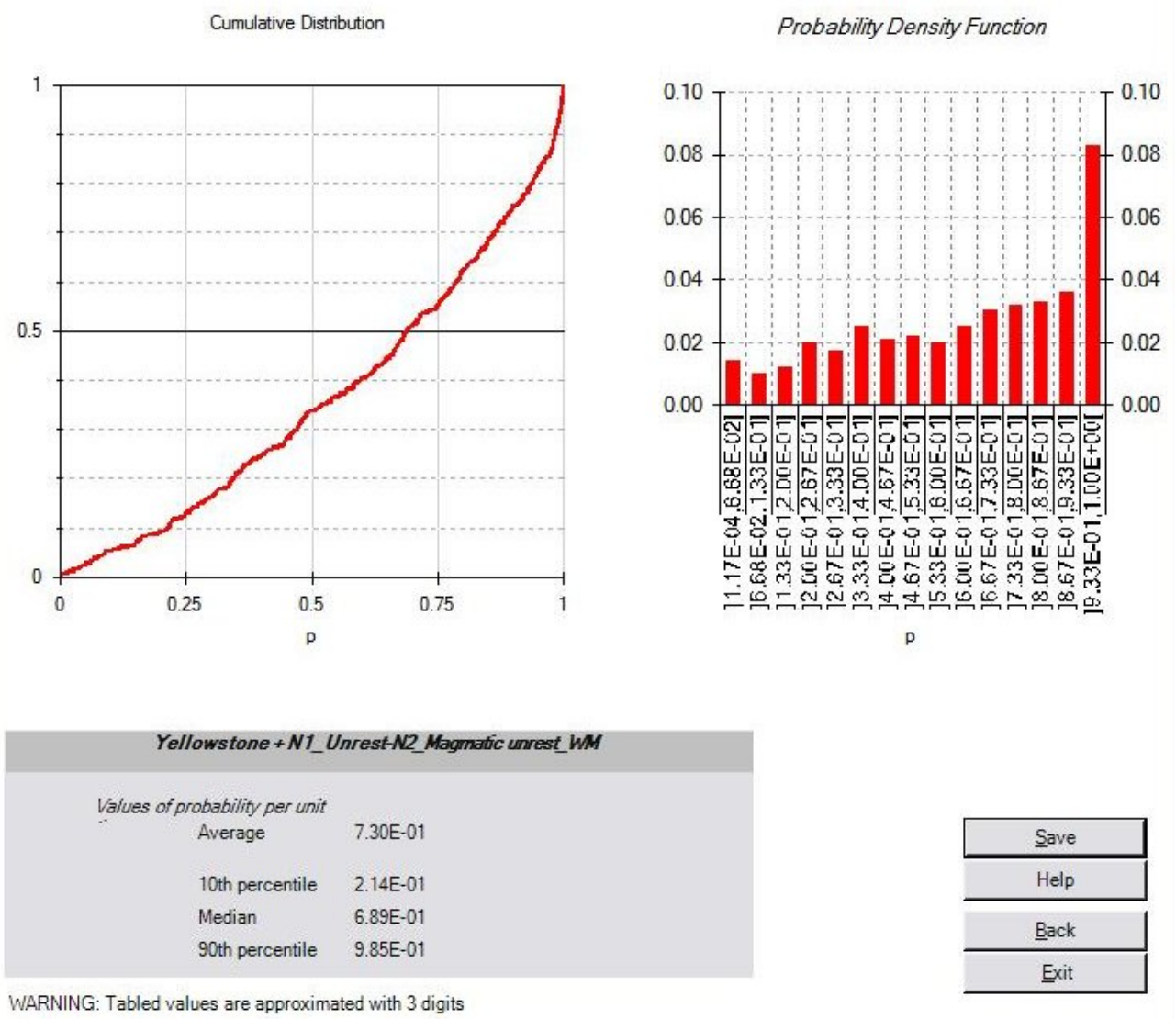

Figure H.16: Results generated using BETEF V2.0 for Yellowstone episode day 1, where $X_{NE} = 16$, $X_{CSM} = 0.065$, and $X_{MM} = 0$ which are the same values used by the logistic models.

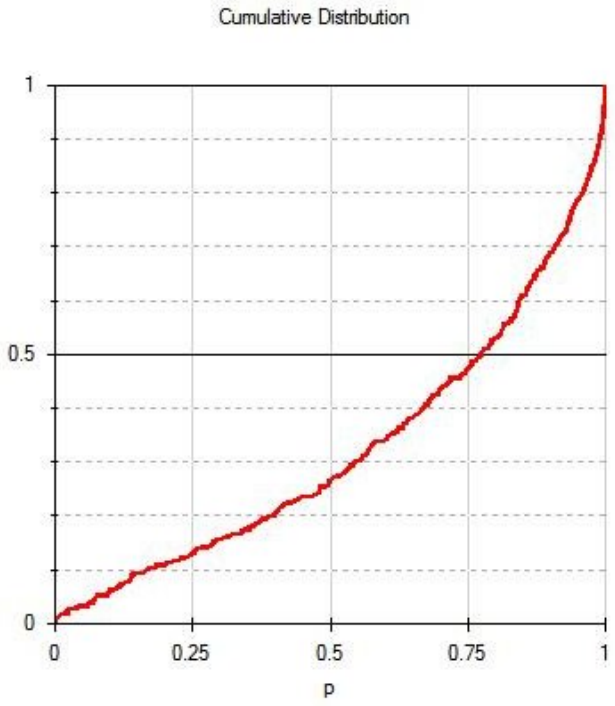

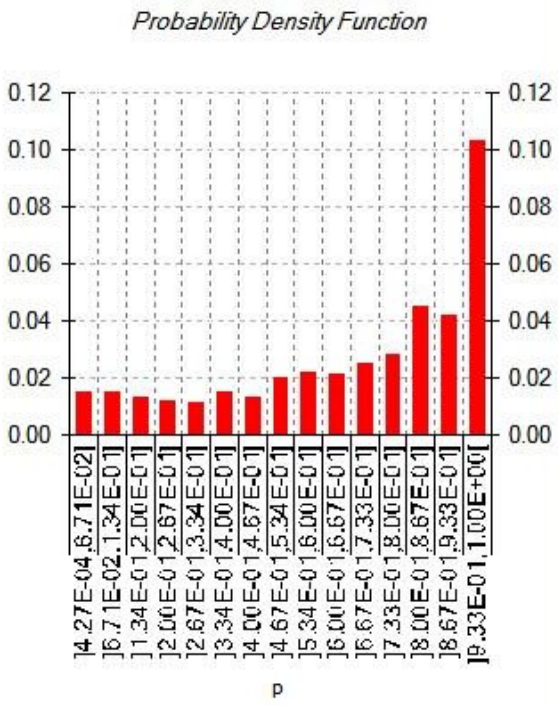

Yellowstone + N1_Unrest-N2_Magmatic unrest_WM

Values of probability per unit

Average	9.02E-01
10th percentile	1.71E-01
Median	7.75E-01
90th percentile	9.91E-01

WARNING: Tabled values are approximated with 3 digits

Save
Help
Back
Exit

Figure H.17: Results generated using BETEF V2.0 for Yellowstone episode day 8, where $X_{NE} = 3$, $X_{CSM} = 0.0085$, and $X_{MM} = 1$ which are the same values used by the logistic models.

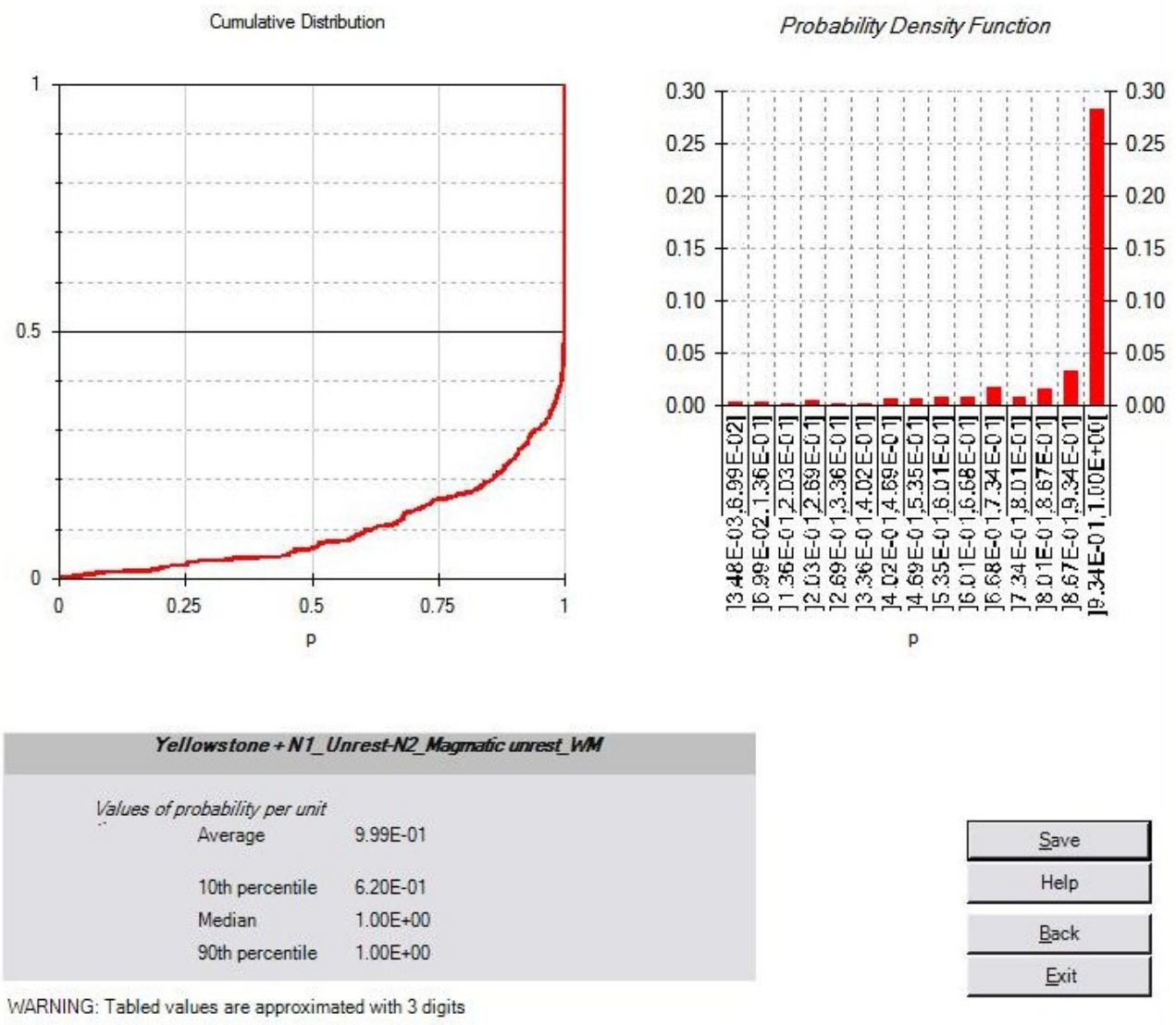

Figure H.18: Results generated using BETEF V2.0 for Yellowstone episode day 25, where $X_{NE} = 49.4$, $X_{CSM} = 6.94$, and $X_{MM} = 1$ which are the same values used by the logistic models.

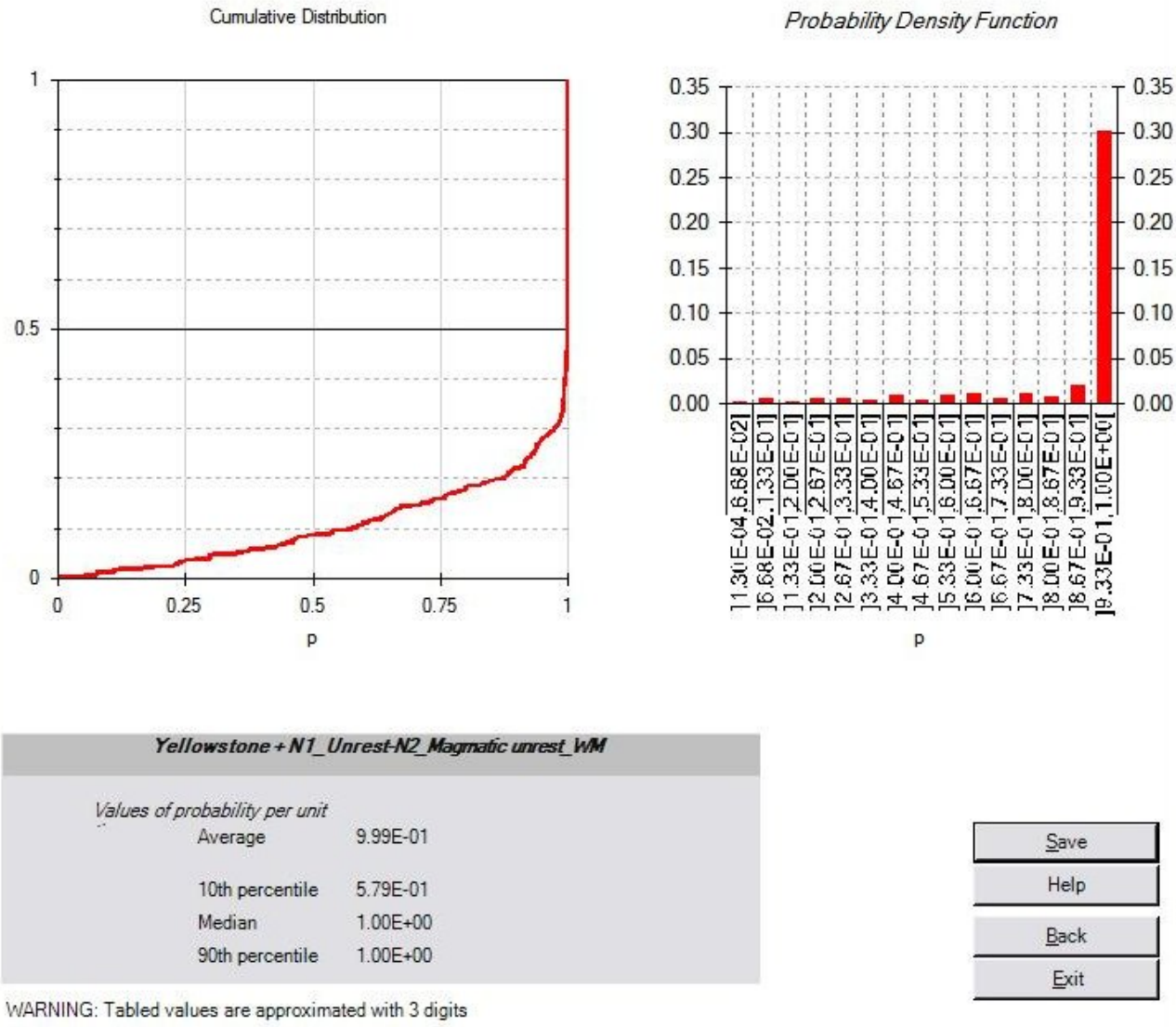

Figure H.19: Results generated using BETEF V2.0 for Yellowstone episode day 27, where $X_{NE} = 87.9$, $X_{CSM} = 18.65$, and $X_{MM} = 1$ which are the same values used by the logistic models.

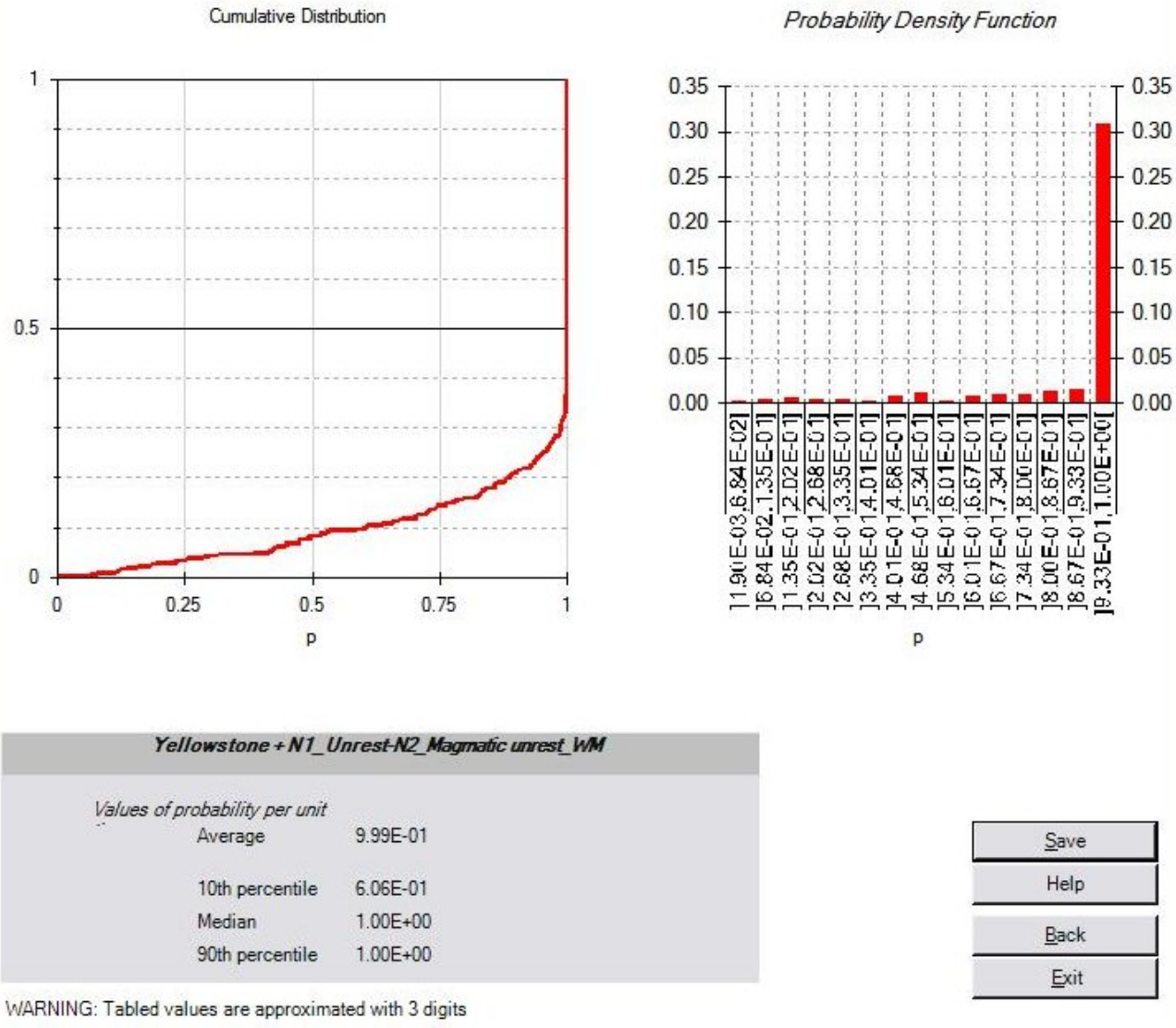

Figure H.20: Results generated using BETEF V2.0 for Yellowstone episode day 80, where $X_{NE} = 60.1$, $X_{CSM} = 9.09$, and $X_{MM} = 1$ which are the same values used by the logistic models.

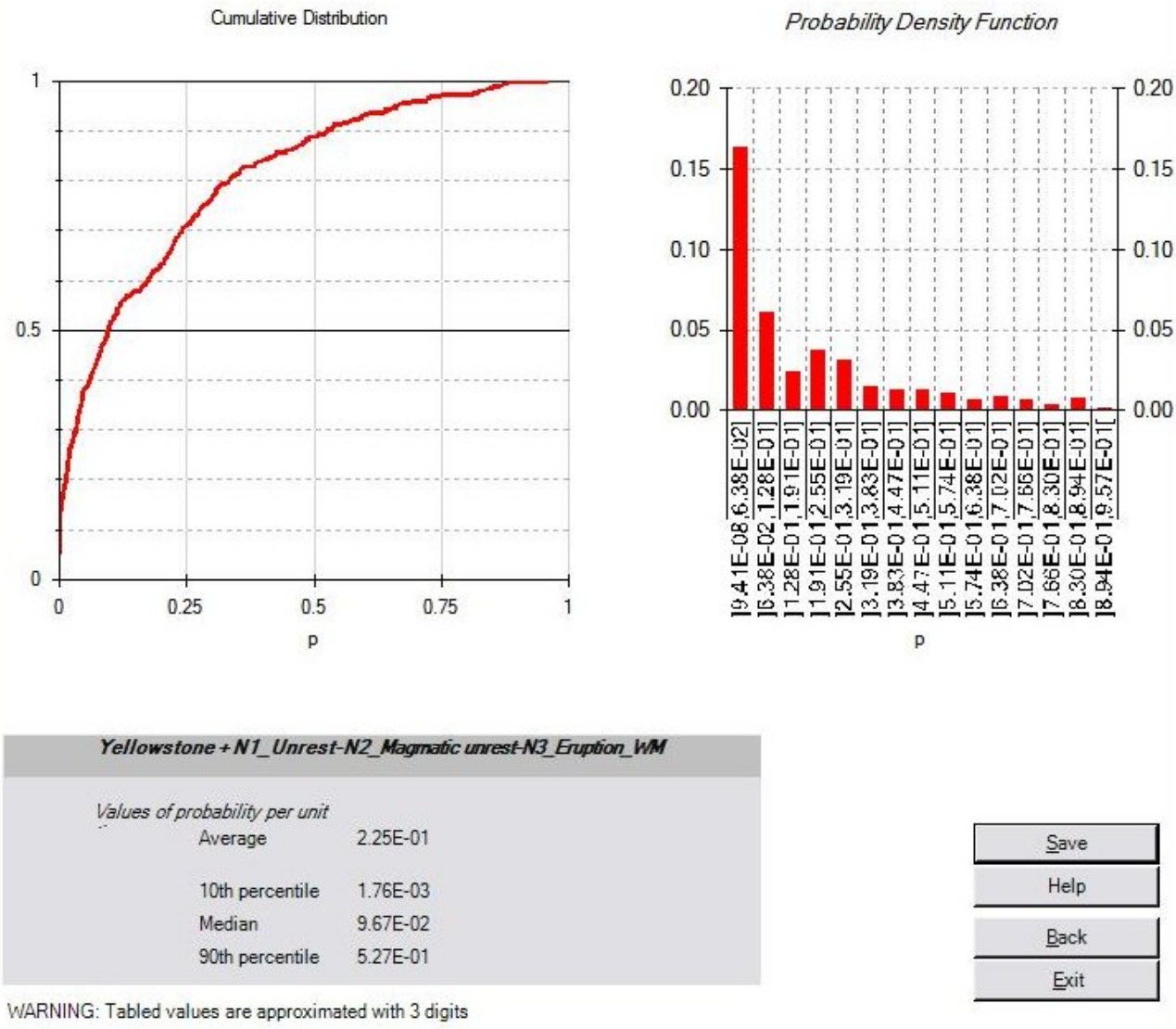

Figure H.21: Results generated using BETEF V2.0 for Yellowstone episode day 1, where $X_{NE} = 16$, $X_{CSM} = 0.065$, and $X_{MM} = 0$ which are the same values used by the logistic models.

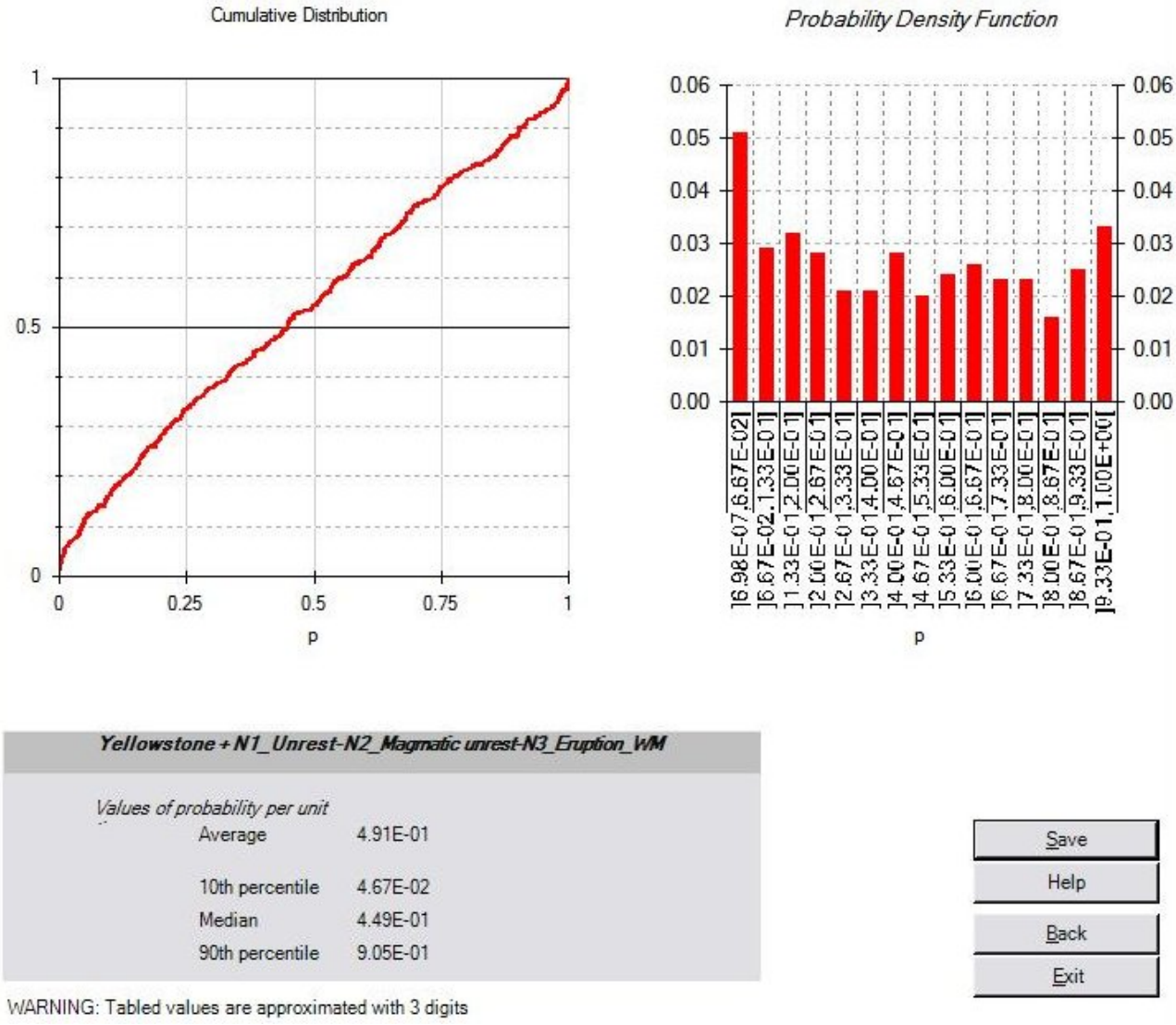

Figure H.22: Results generated using BETEF V2.0 for Yellowstone episode day 8, where $X_{NE} = 3$, $X_{CSM} = 0.0085$, and $X_{MM} = 1$ which are the same values used by the logistic models.

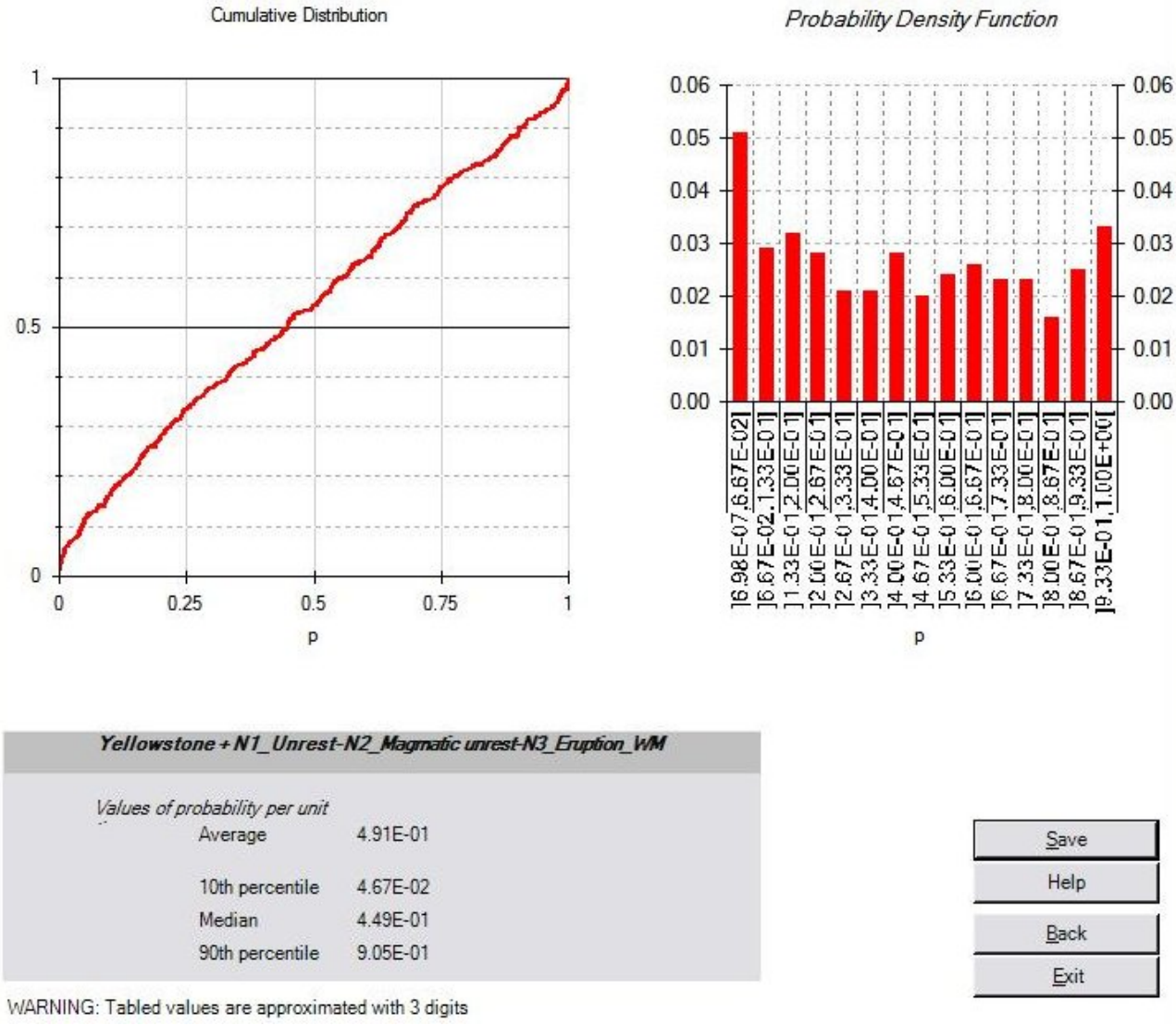

Figure H.23: Results generated using BETEF V2.0 for Yellowstone episode day 25, where $X_{NE} = 49.9$, $X_{CSM} = 6.94$, and $X_{MM} = 1$ which are the same values used by the logistic models.

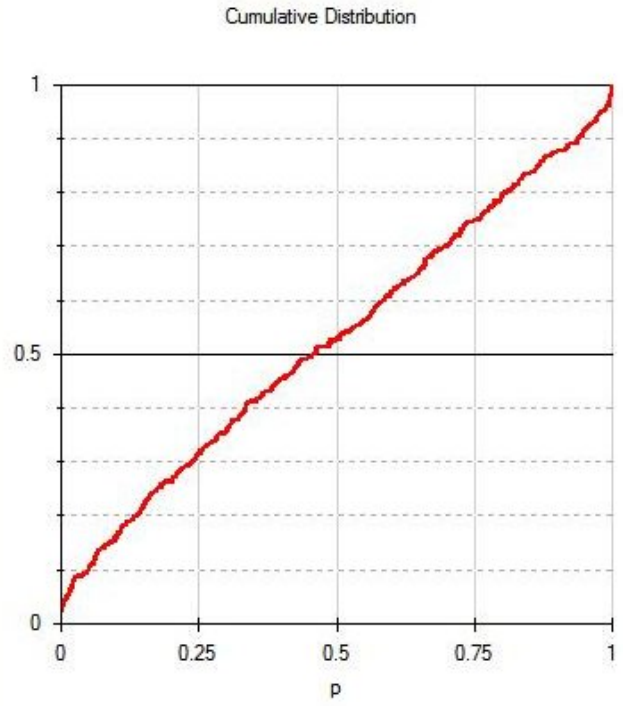

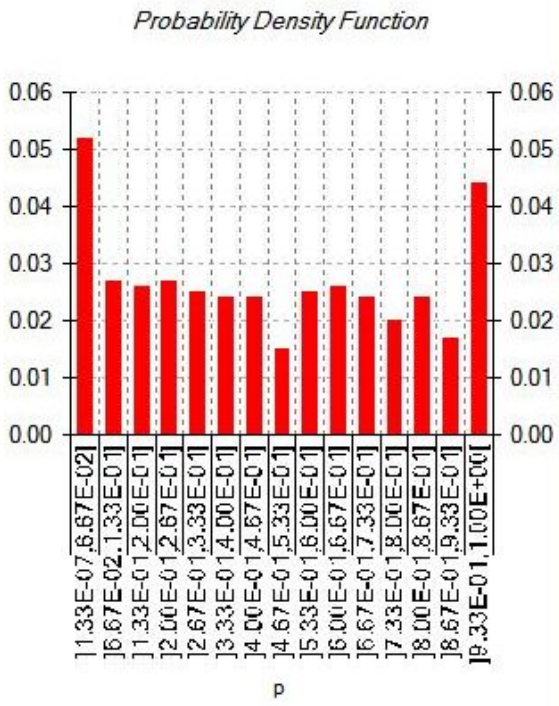

Yellowstone + N1_Unrest-N2_Magmatic unrest-N3_Eruption_WM

Values of probability per unit

Average	4.95E-01
10th percentile	5.10E-02
Median	4.58E-01
90th percentile	9.39E-01

WARNING: Tabled values are approximated with 3 digits

Save
Help
Back
Exit

Figure H.24: Results generated using BETEF V2.0 for Yellowstone episode day 27, where $X_{NE} = 87.9$, $X_{CSM} = 18.65$, and $X_{MM} = 1$ which are the same values used by the logistic models.

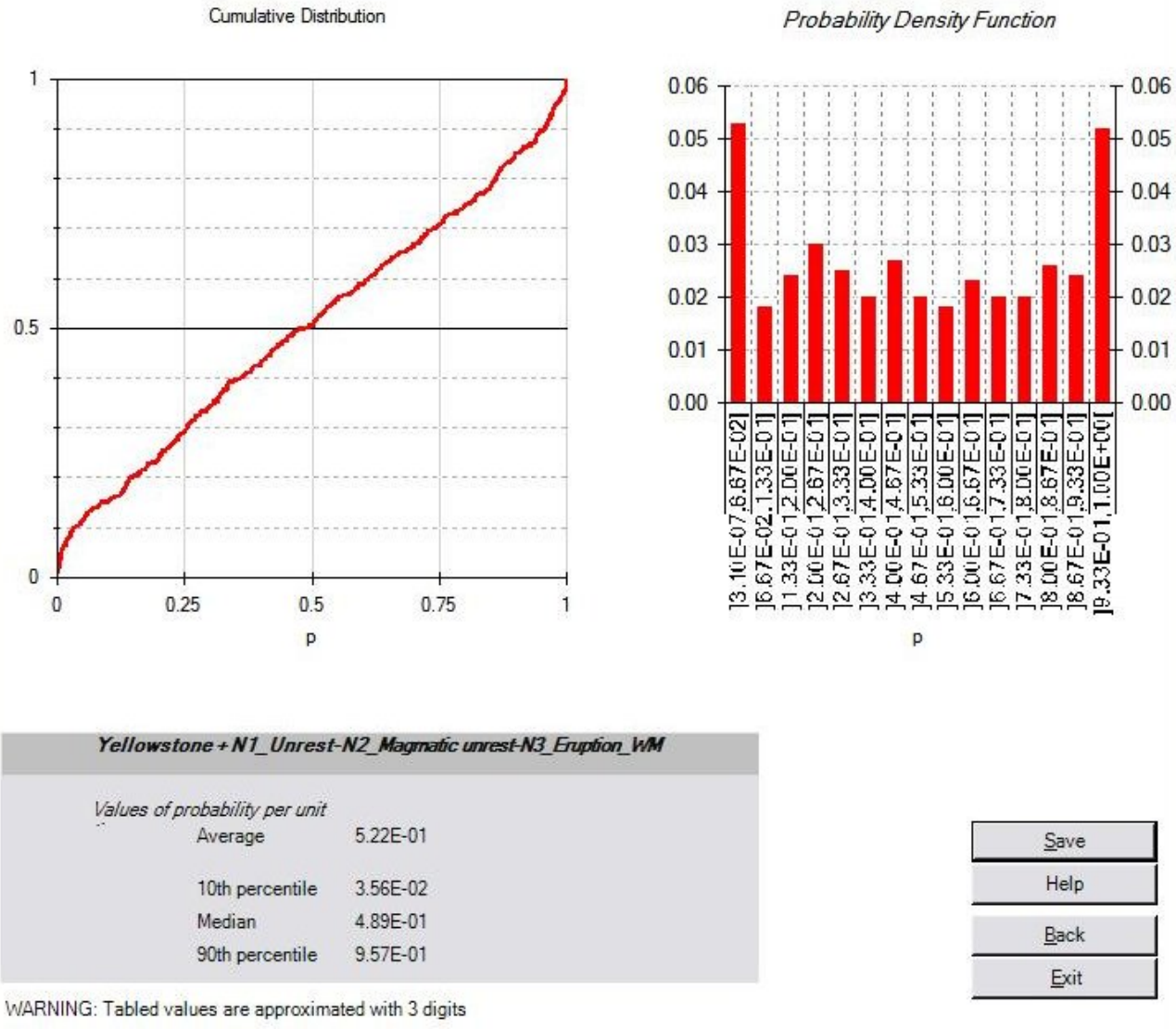

Figure H.25: Results generated using BETEF V2.0 for Yellowstone episode day 80, where $X_{NE} = 60.1$, $X_{CSM} = 9.09$, and $X_{MM} = 1$ which are the same values used by the logistic models.

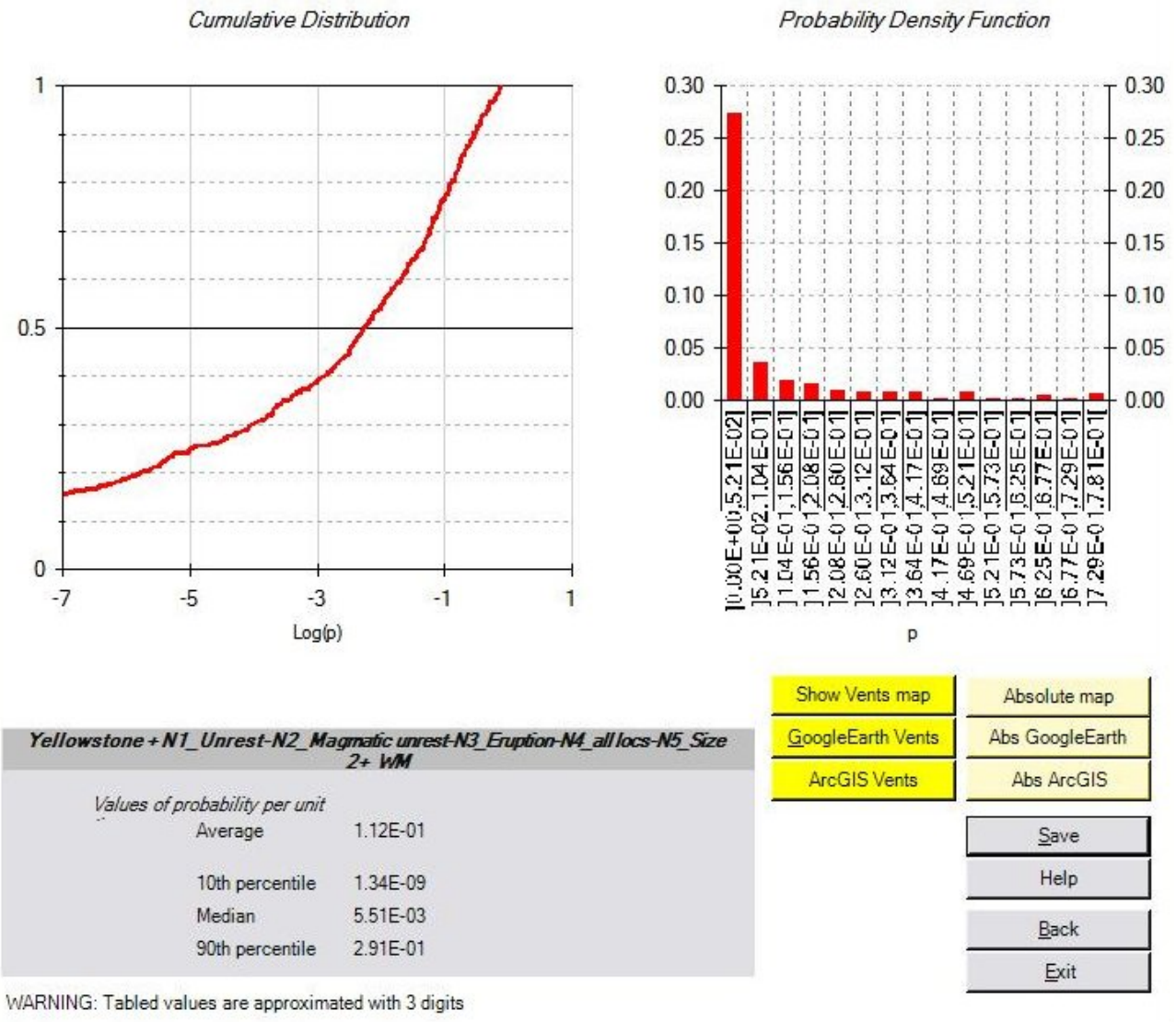

Figure H.26: Results generated using BETEF V2.0 for Yellowstone episode day 1, where $X_{NE} = 16$, $X_{CSM} = 0.065$, and $X_{MM} = 0$ which are the same values used by the logistic models.

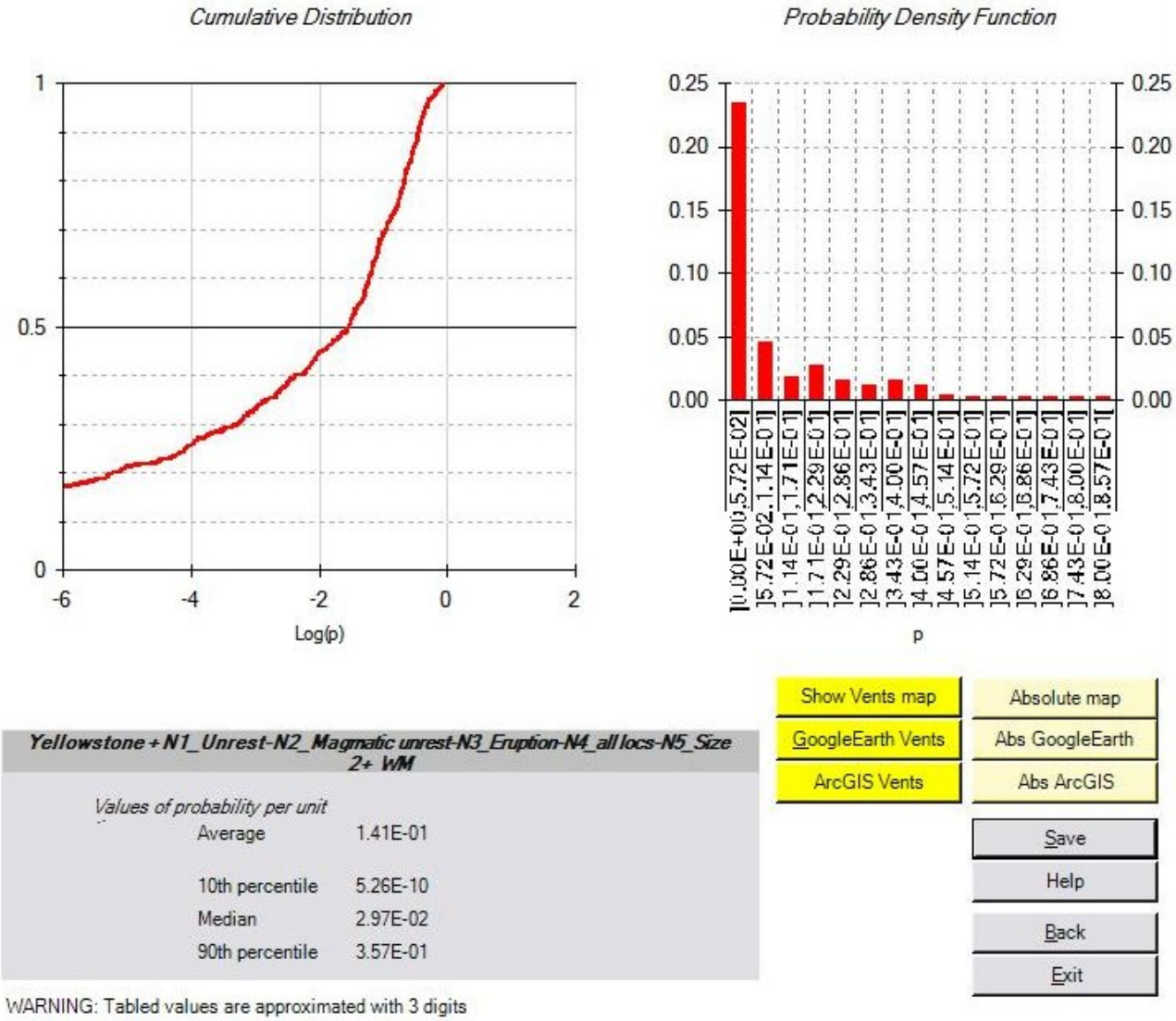

Figure H.27: Results generated using BETEF V2.0 for Yellowstone episode day 8, where $X_{NE} = 3$, $X_{CSM} = 0.0085$, and $X_{MM} = 1$ which are the same values used by the logistic models.

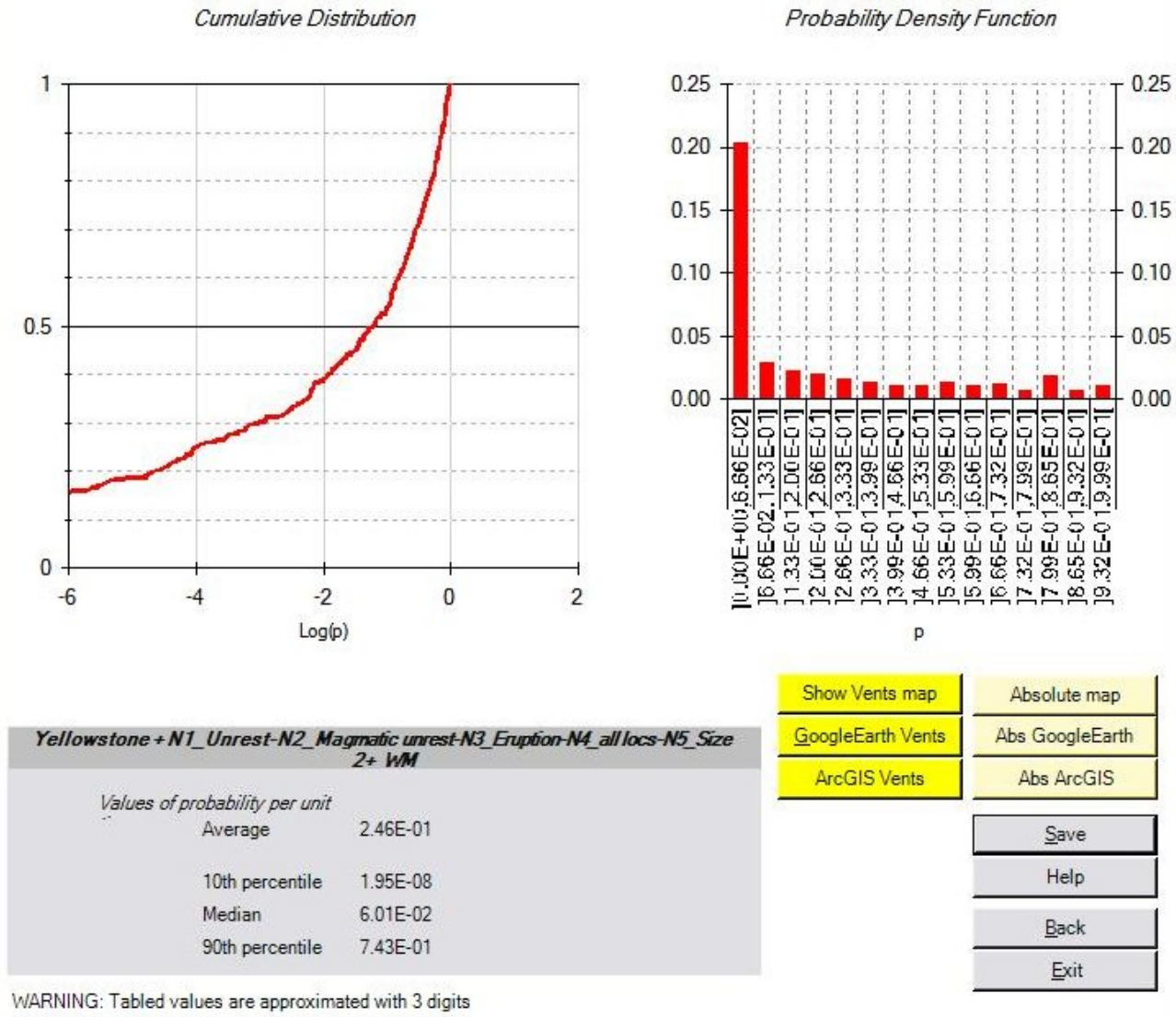

Figure H.28: Results generated using BETEF V2.0 for Yellowstone episode day 25, where $X_{NE} = 49.4$, $X_{CSM} = 6.94$, and $X_{MM} = 1$ which are the same values used by the logistic models.

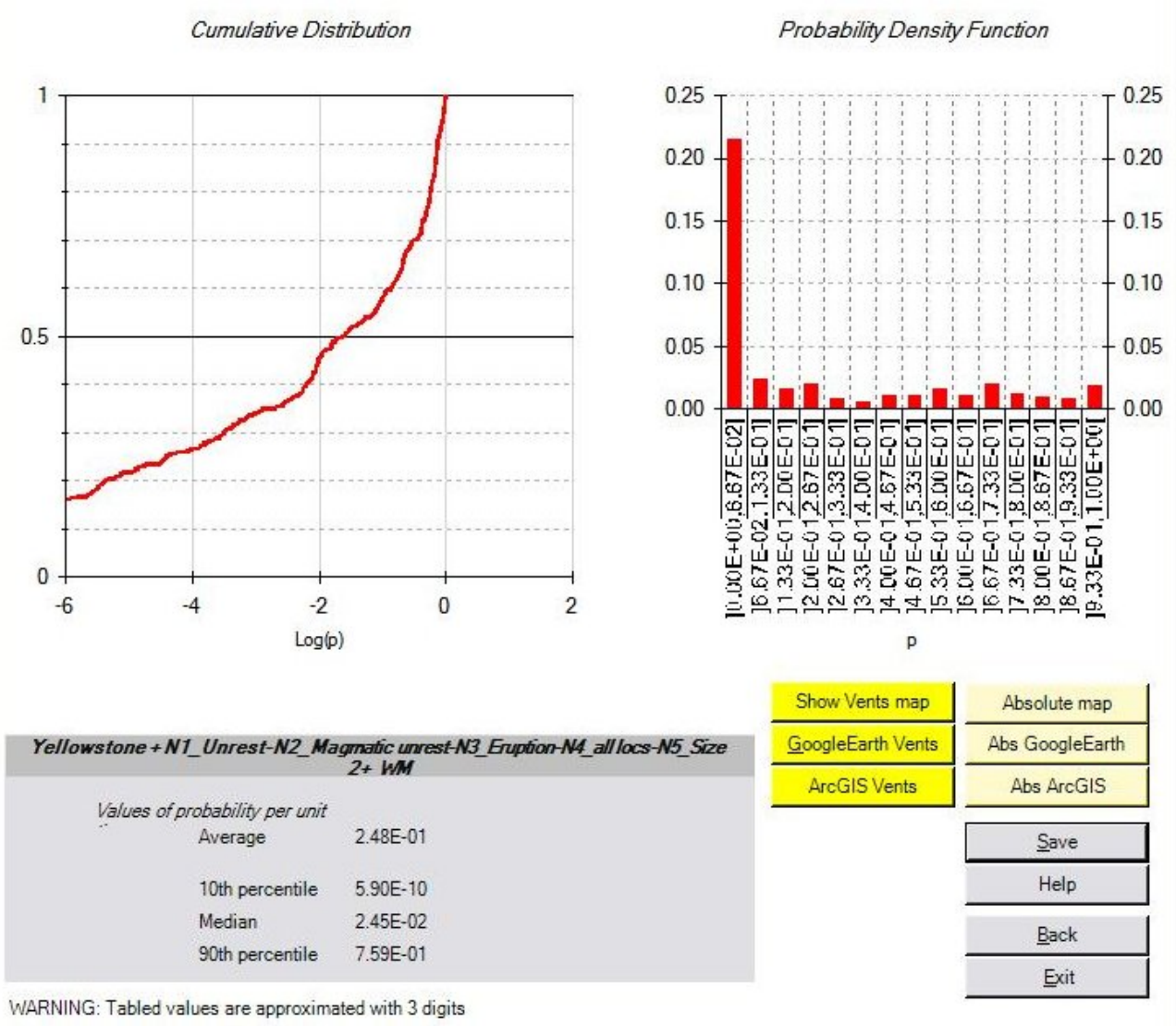

Figure H.29: Results generated using BETEF V2.0 for Yellowstone episode day 27, where $X_{NE} = 87.9$, $X_{CSM} = 18.65$, and $X_{MM} = 1$ which are the same values used by the logistic models.

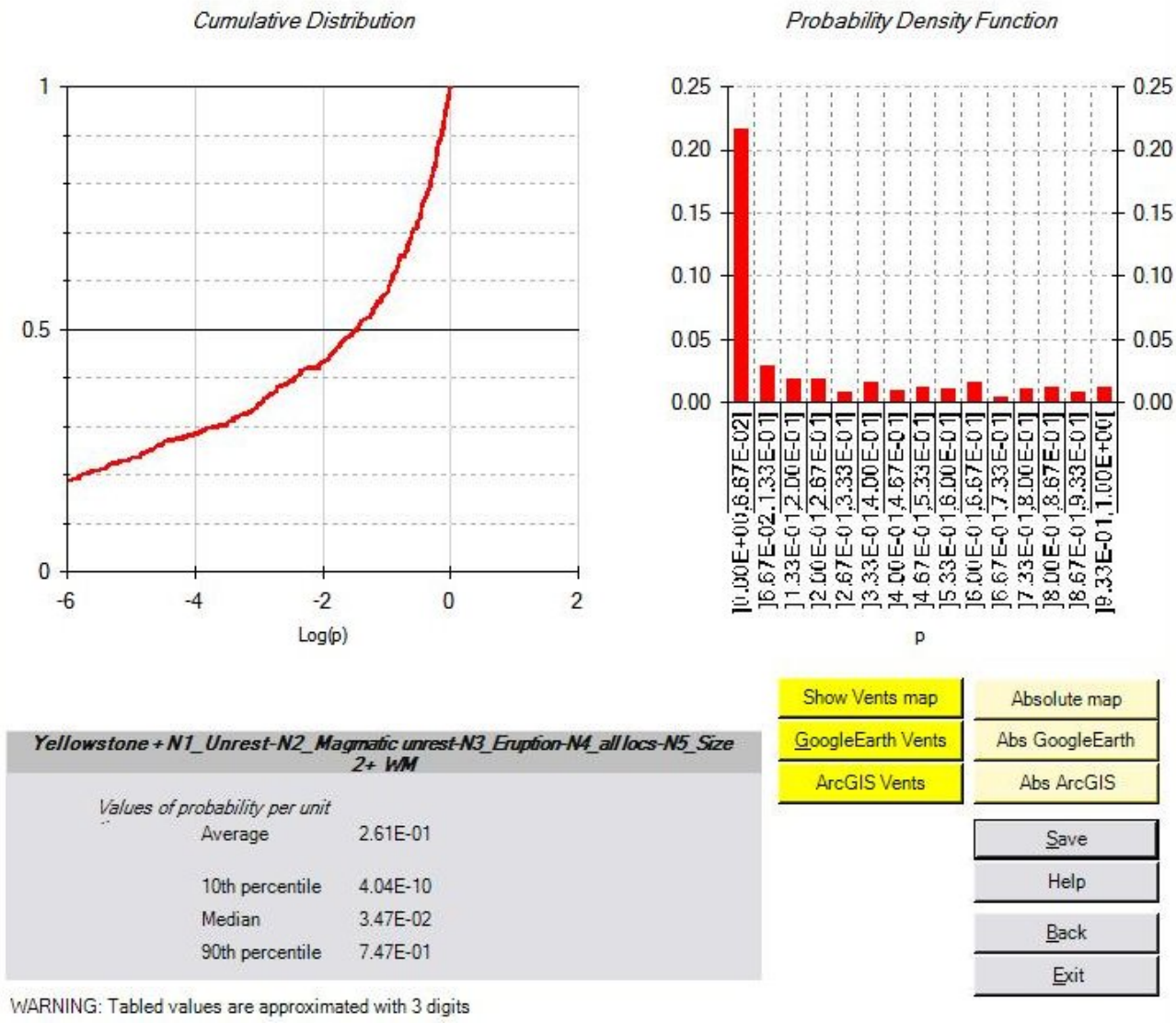

Figure H.30: Results generated using BETEF V2.0 for Yellowstone episode day 80, where $X_{NE} = 60.1$, $X_{CSM} = 9.09$, and $X_{MM} = 1$ which are the same values used by the logistic models.

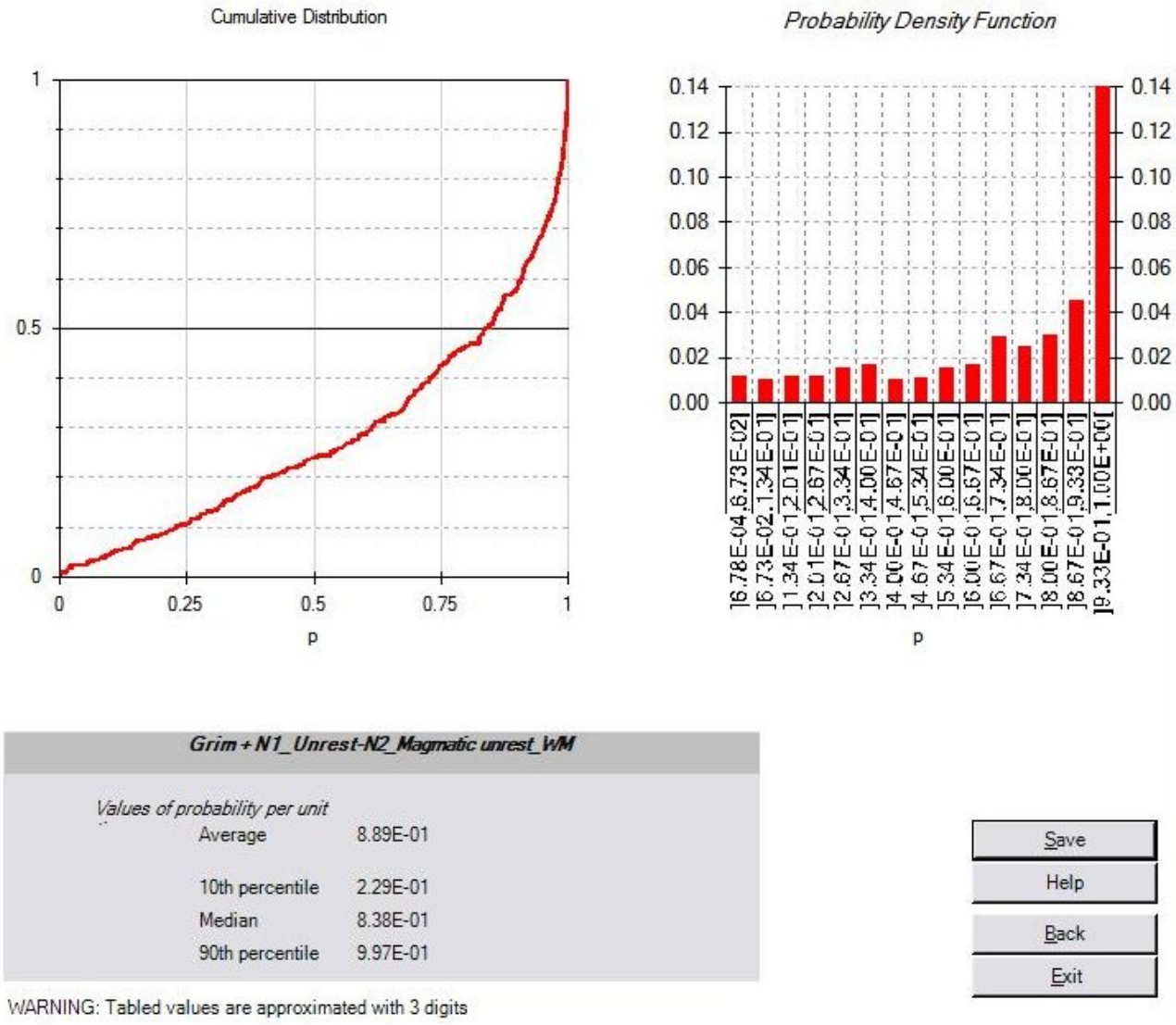

Figure H.31: Results generated using BETEF V2.0 for Grimsvötn episode day 1, where $X_{NE} = 3$, $X_{CSM} = 25$, and $X_{MM} = 0$ which are the same values used by the logistic models.

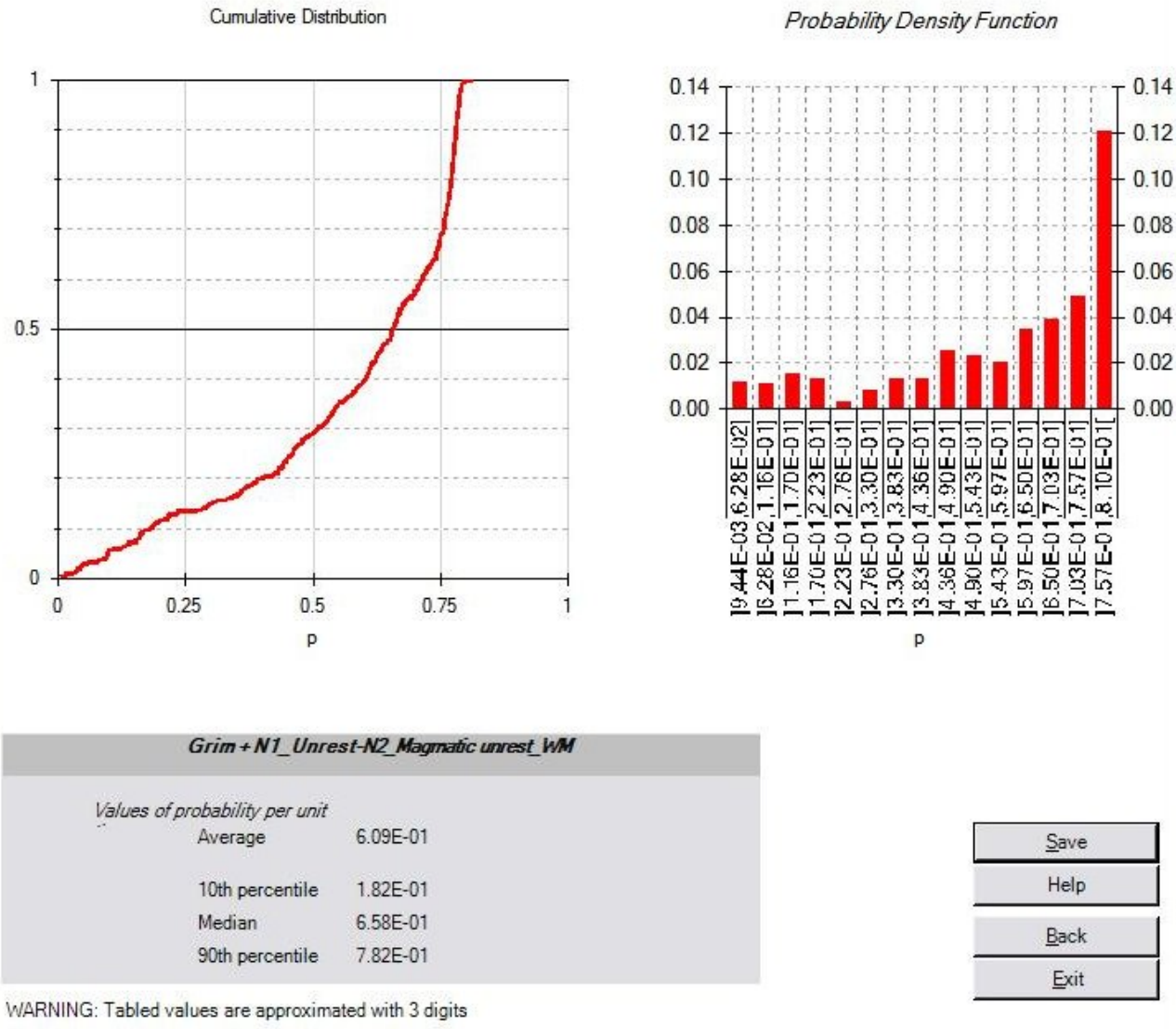

Figure H.32: Results generated using BETEF V2.0 for Grimsvötn episode day 31, where $X_{NE} = 4.6$, $X_{CSM} = 1.08$, and $X_{MM} = 0$ which are the same values used by the logistic models.

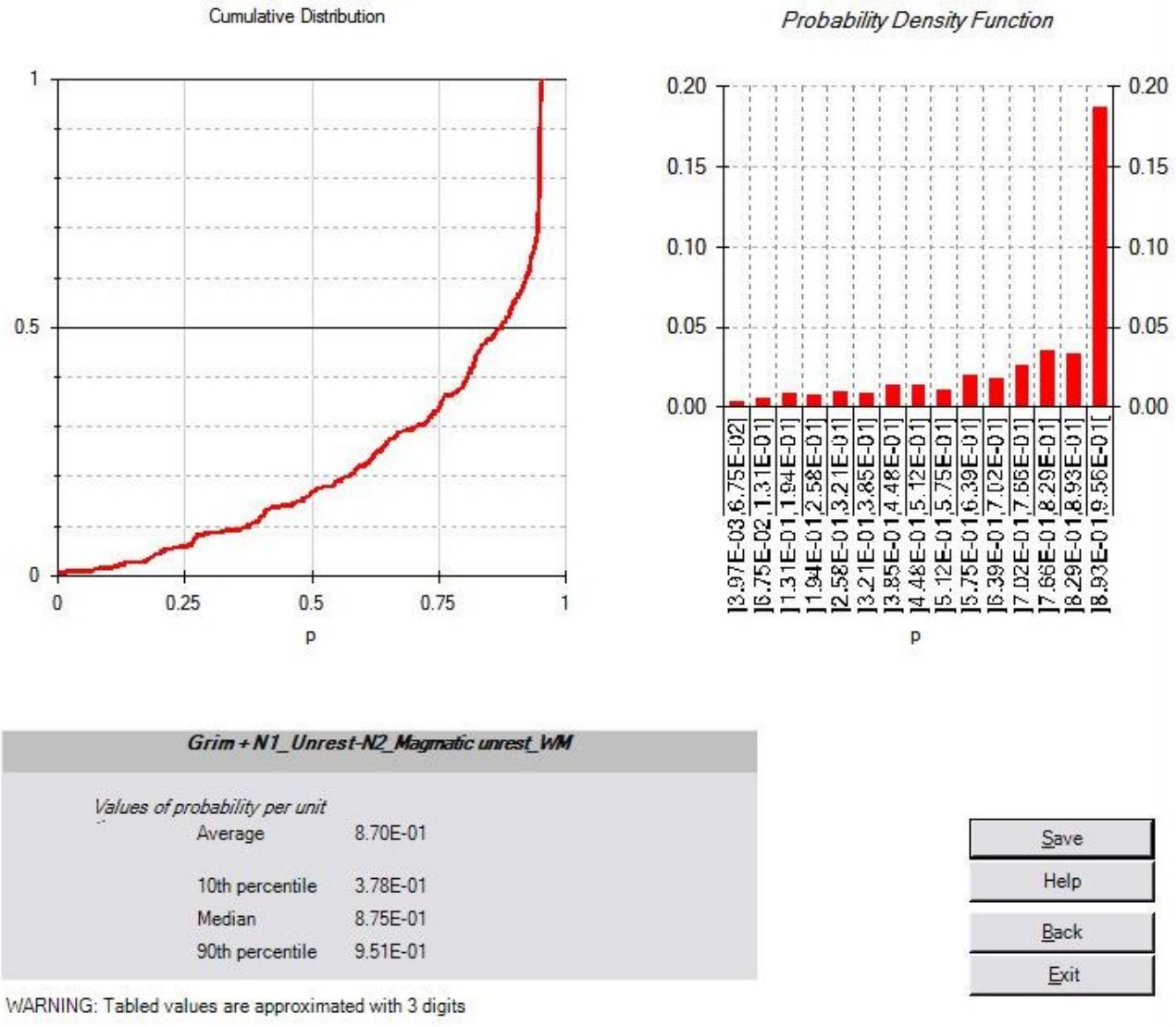

Figure H.33: Results generated using BETEF V2.0 for Grimsvötn episode day 37, where $X_{NE} = 5.6$, $X_{CSM} = 1.39$, and $X_{MM} = 0$ which are the same values used by the logistic models.

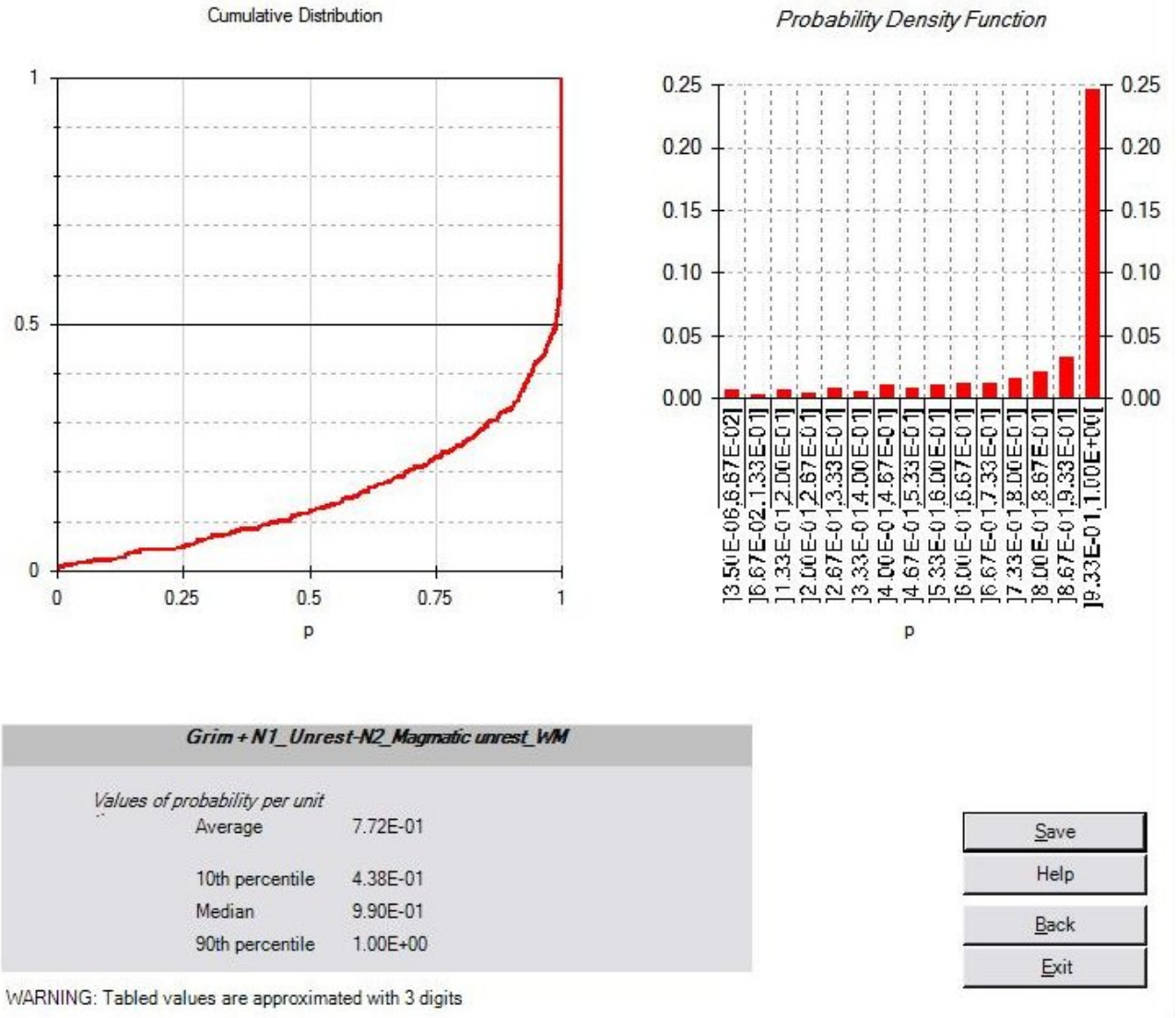

Figure H.34: Results generated using BETEF V2.0 for Grimsvötn episode day 134, where $X_{NE} = 1.5$, $X_{CSM} = 0.54$, and $X_{MM} = 1$ which are the same values used by the logistic models.

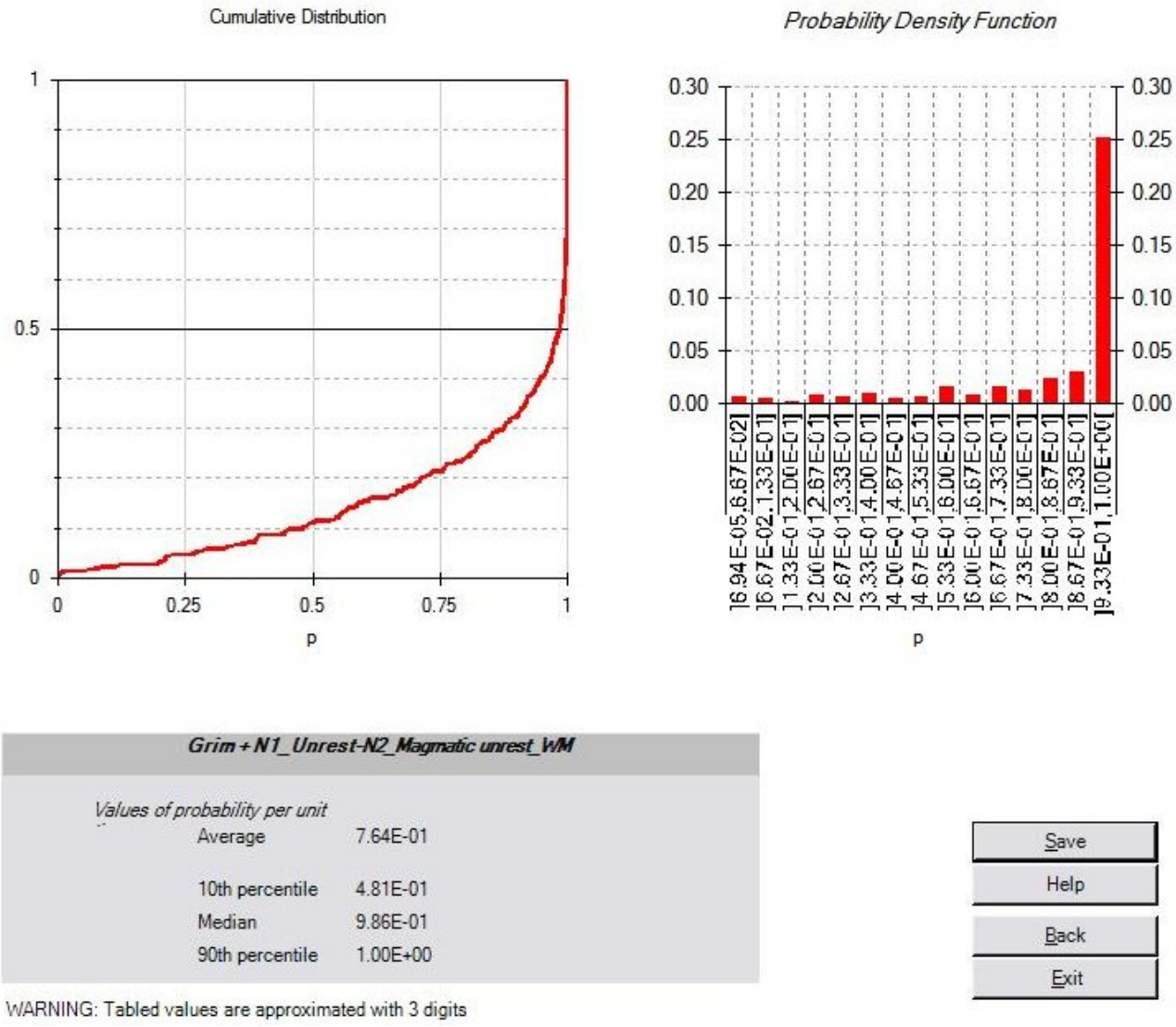

Figure H.35: Results generated using BETEF V2.0 for Grimsvötn episode day 177, where $X_{NE} = 1.3$, $X_{CSM} = 0.42$, and $X_{MM} = 1$ which are the same values used by the logistic models.

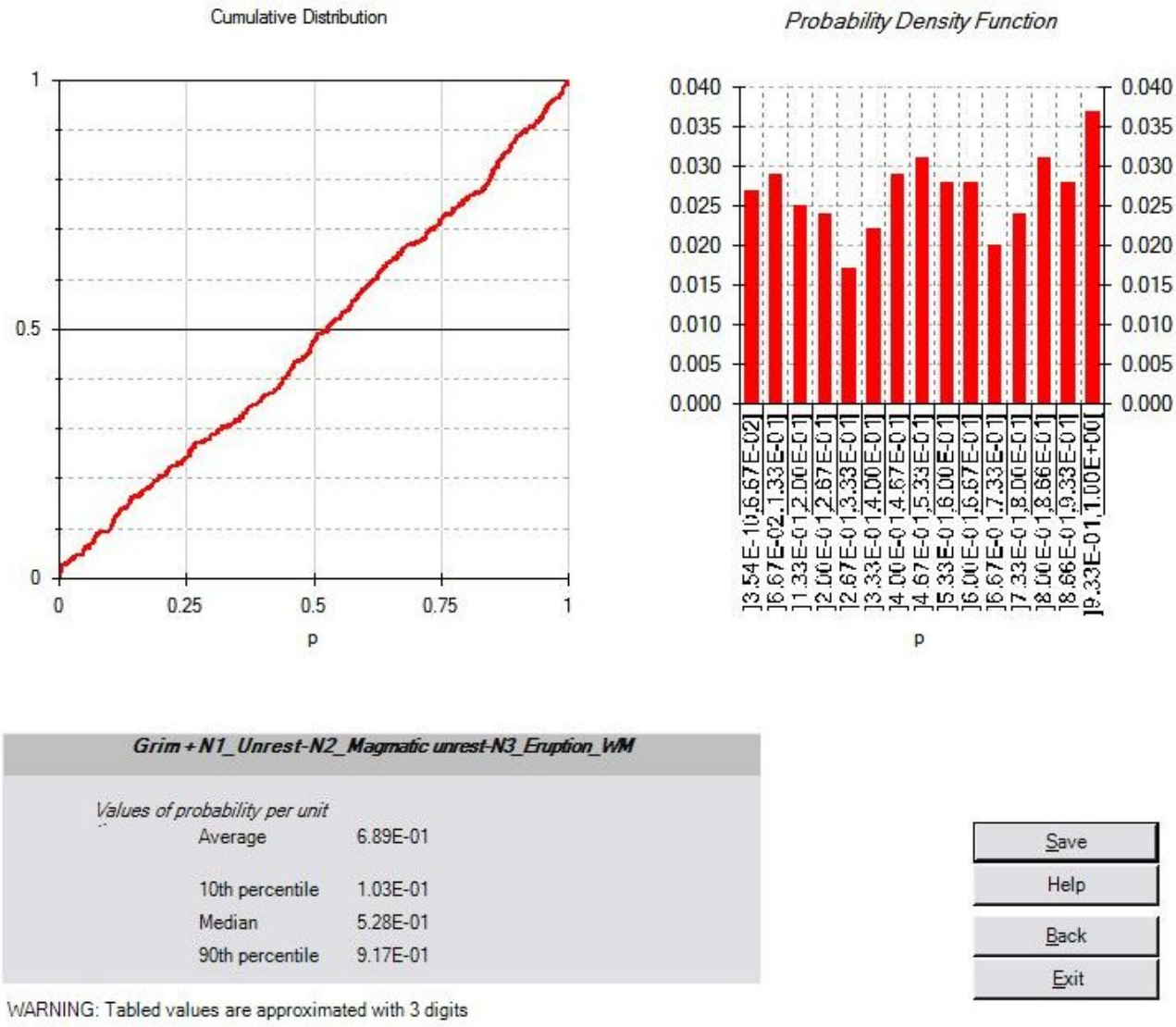

Figure H.36: Results generated using BETEF V2.0 for Grimsvötn episode day 1, where $X_{NE} = 3$, $X_{CSM} = 25$, and $X_{MM} = 0$ which are the same values used by the logistic models.

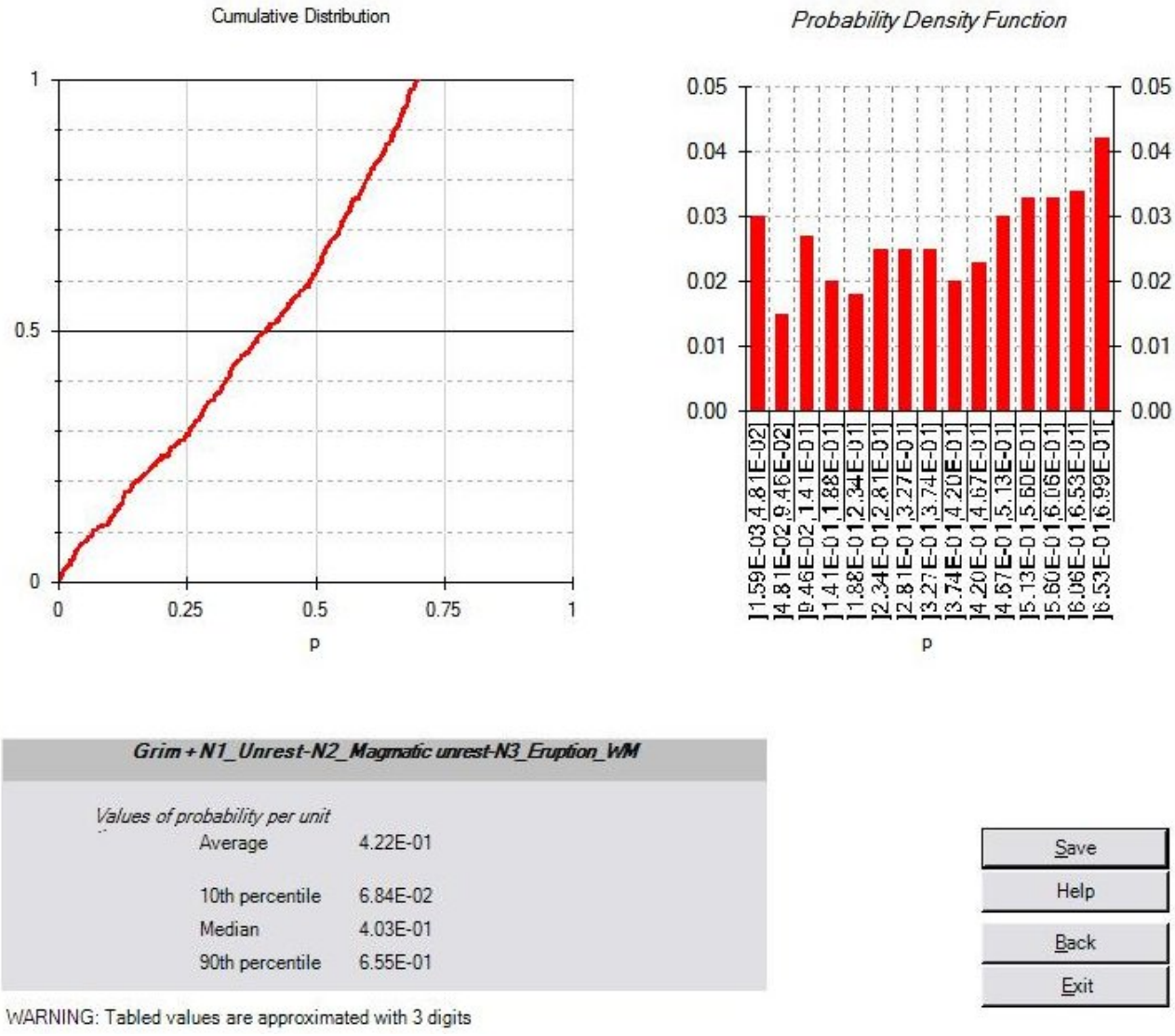

Figure H.37: Results generated using BETEF V2.0 for Grimsvötn episode day 31, where $X_{NE} = 4.6$, $X_{CSM} = 1.08$, and $X_{MM} = 0$ which are the same values used by the logistic models.

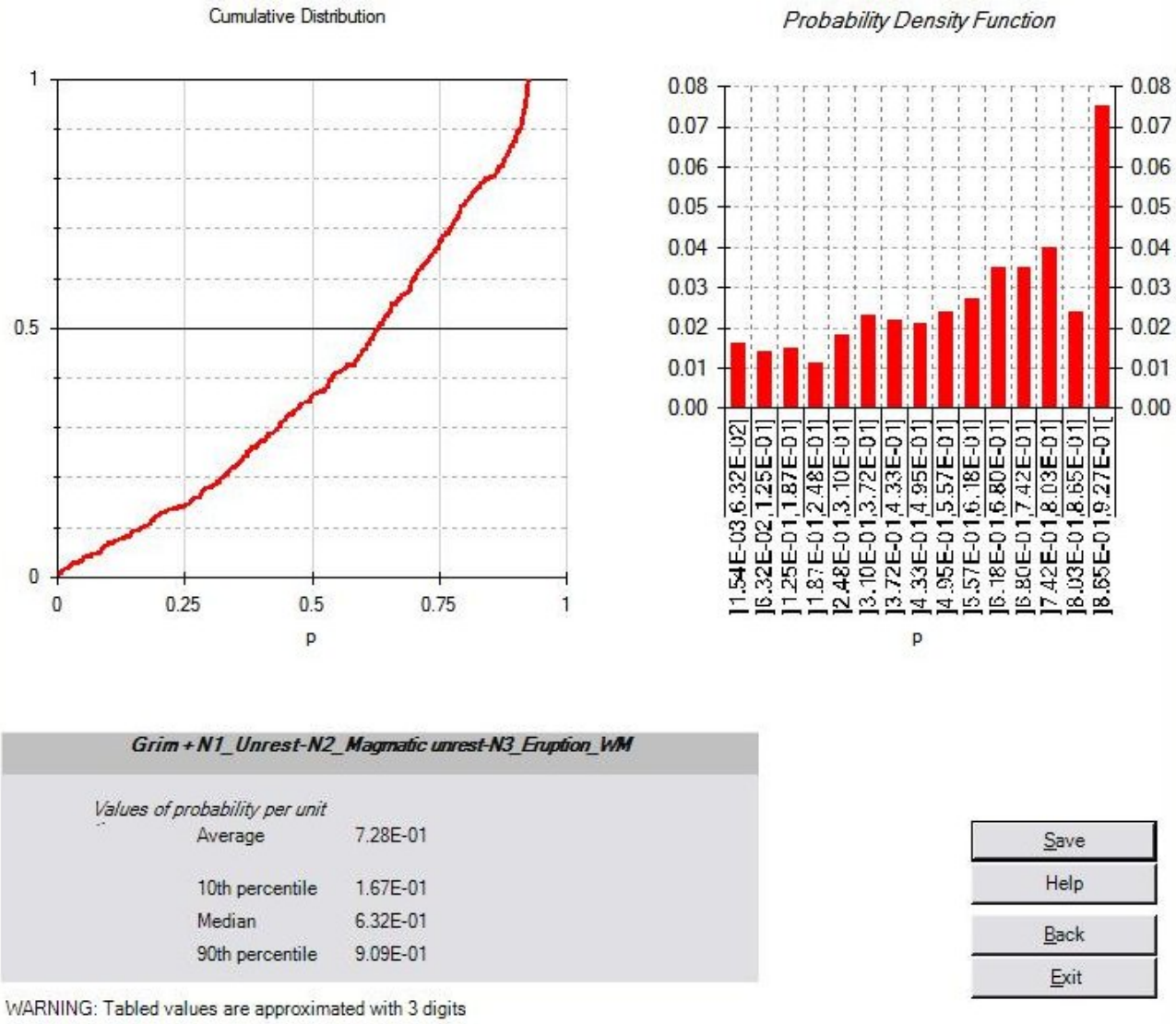

Figure H.38: Results generated using BETEF V2.0 for Grimsvötn episode day 37, where $X_{NE} = 5.6$, $X_{CSM} = 1.39$, and $X_{MM} = 0$ which are the same values used by the logistic models.

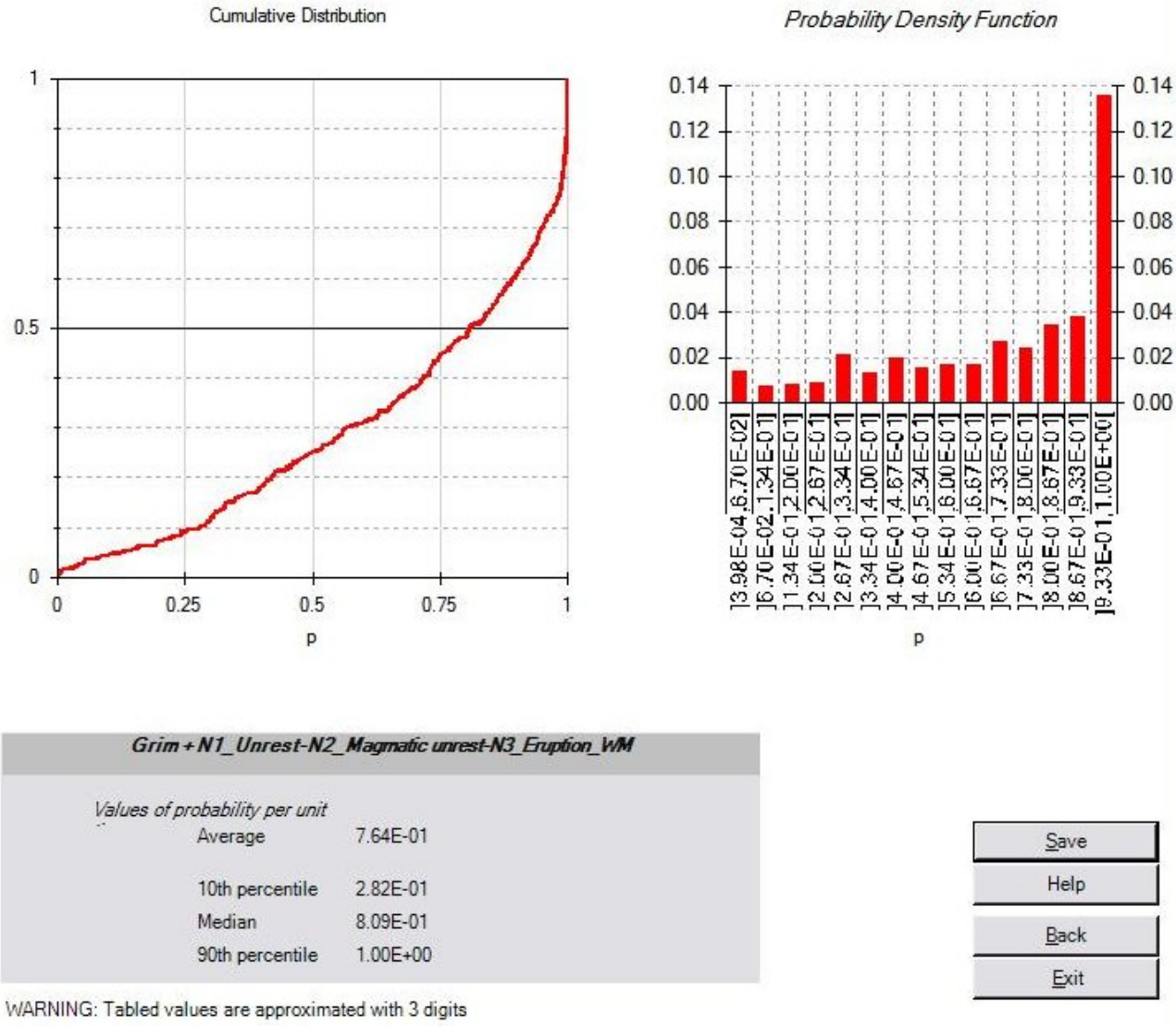

Figure H.39: Results generated using BETEF V2.0 for Grimsvötn episode day 134, where $X_{NE} = 1.5$, $X_{CSM} = 0.54$, and $X_{MM} = 1$ which are the same values used by the logistic models.

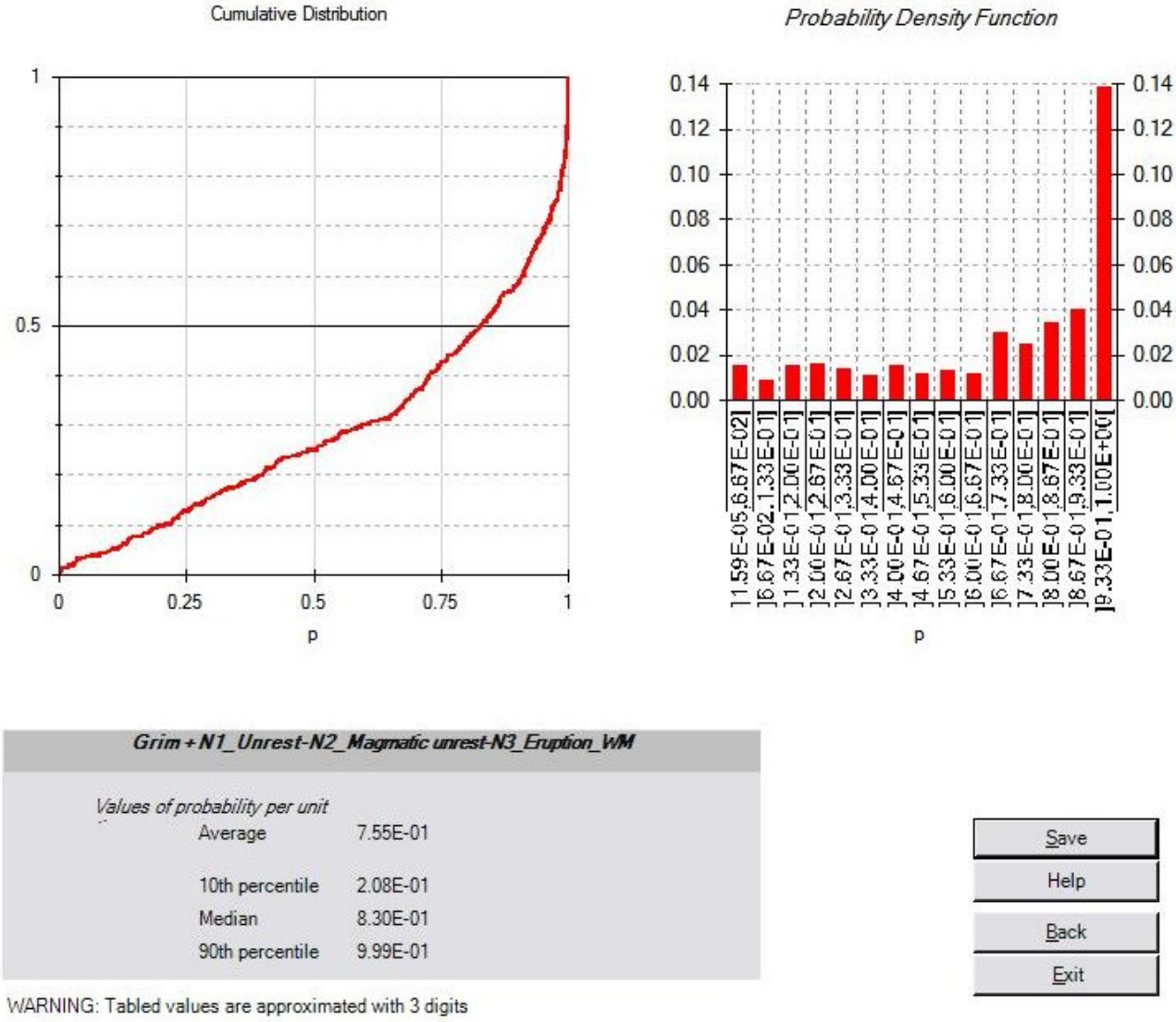

Figure H.40: Results generated using BETEF V2.0 for Grimsvötn episode day 177, where $X_{NE} = 1.3$, $X_{CSM} = 0.42$, and $X_{MM} = 1$ which are the same values used by the logistic models.

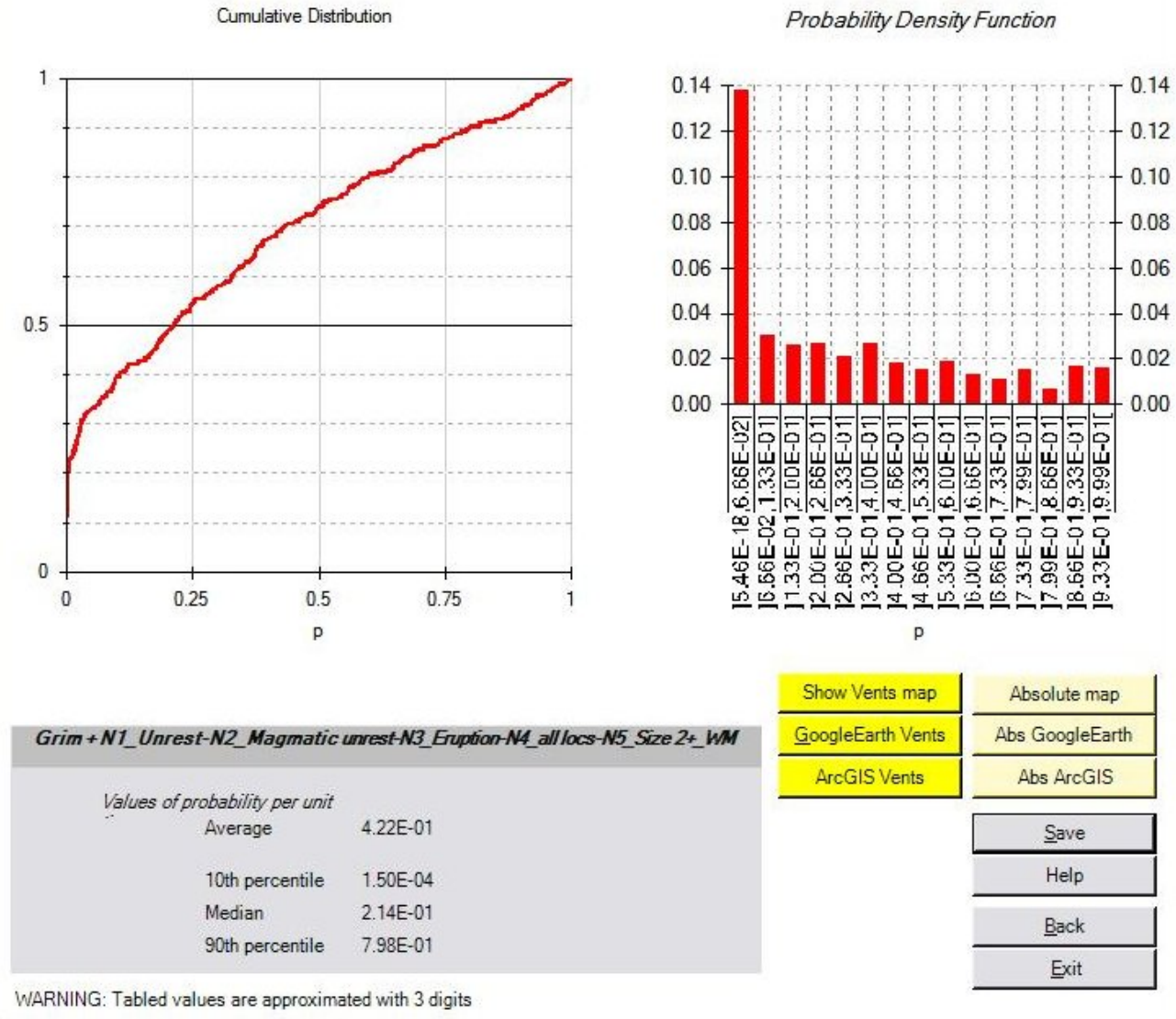

Figure H.41: Results generated using BETEF V2.0 for Grimsvötn episode day 1, where $X_{NE} = 3$, $X_{CSM} = 25$, and $X_{MM} = 0$ which are the same values used by the logistic models.

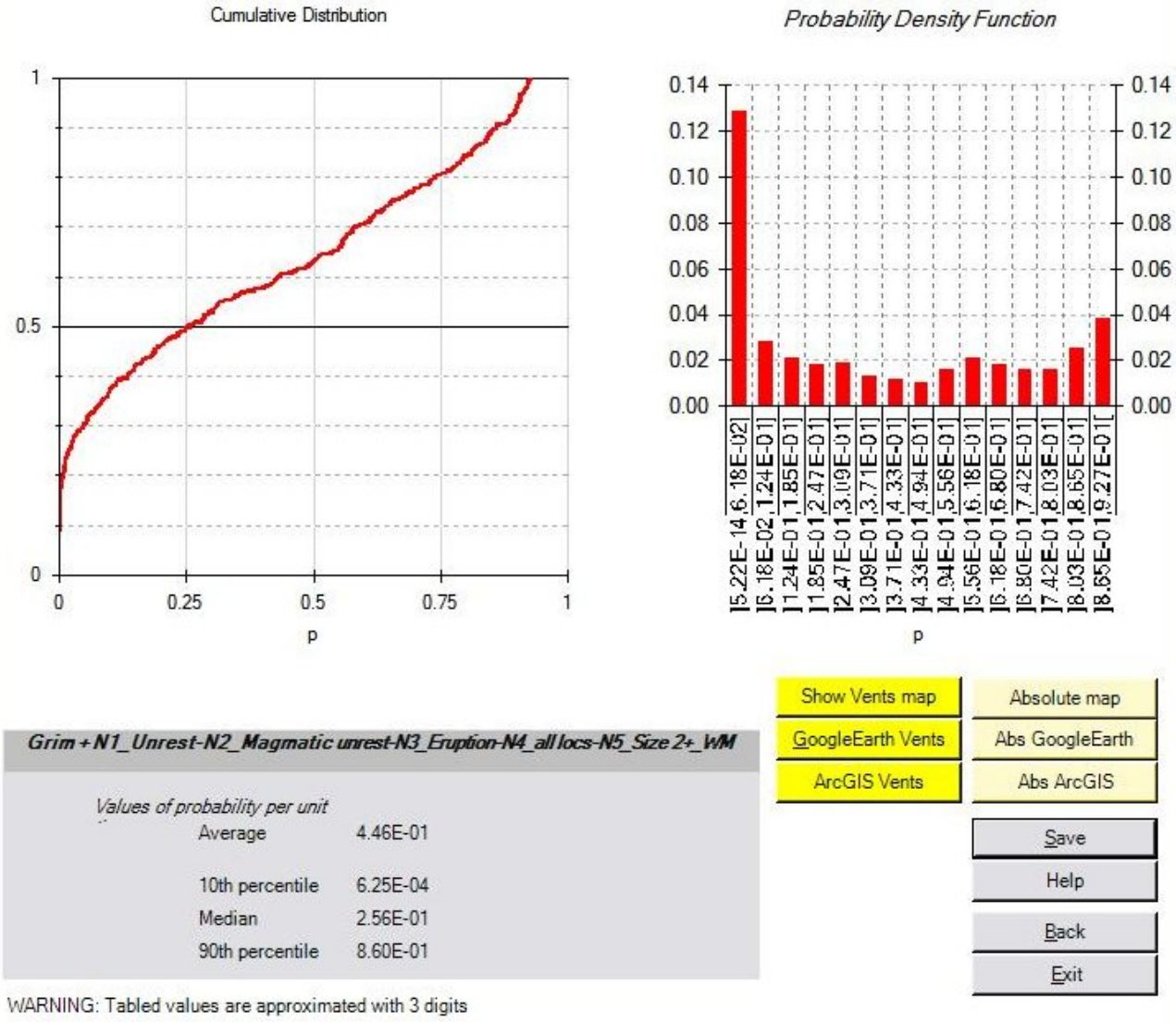

Figure H.42: Results generated using BETEF V2.0 for Grimsvötn episode day 31, where $X_{NE} = 4.6$, $X_{CSM} = 1.08$, and $X_{MM} = 0$ which are the same values used by the logistic models.

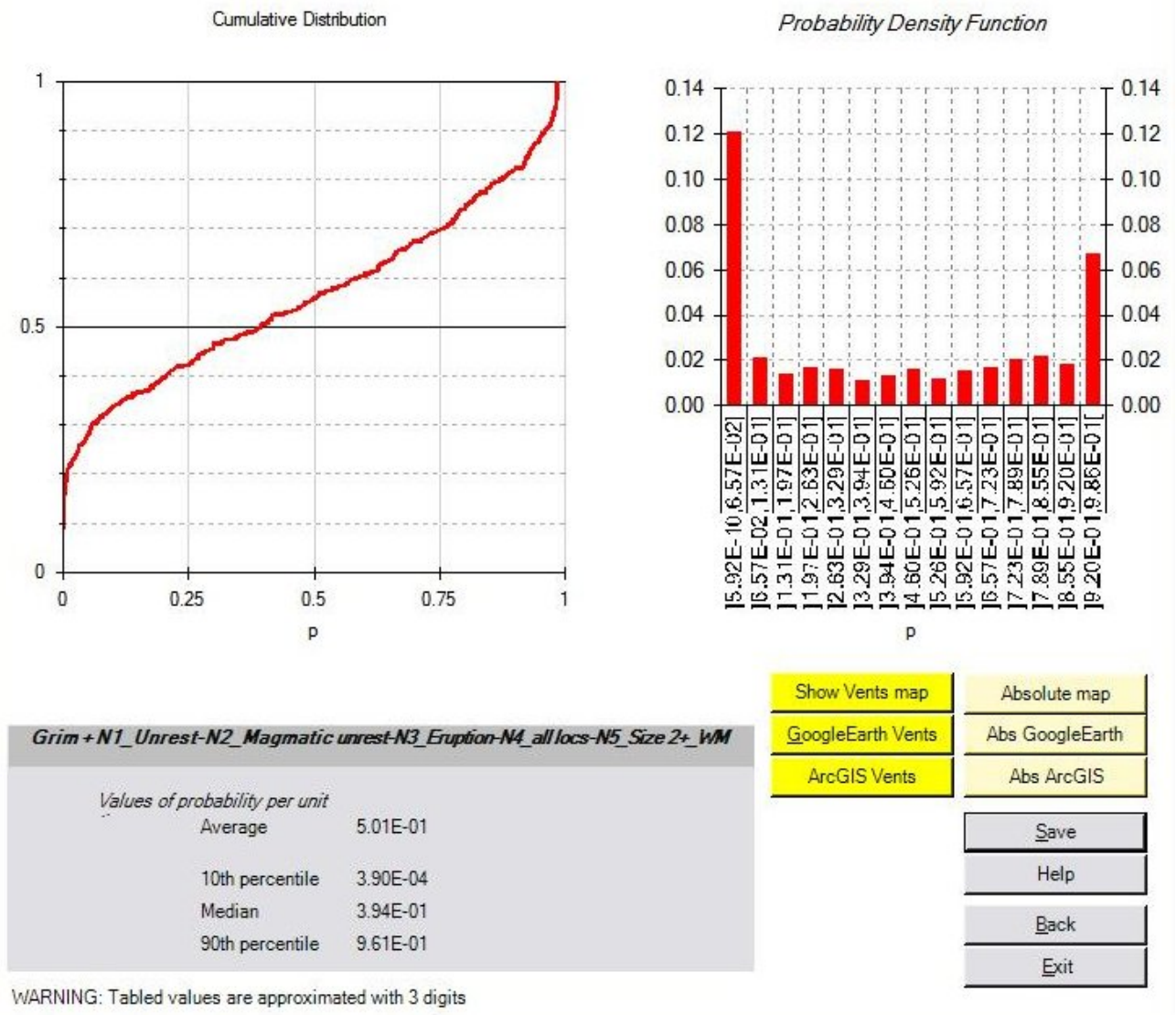

Figure H.43: Results generated using BETEF V2.0 for Grimsvötn episode day 37, where $X_{NE} = 5.6$, $X_{CSM} = 1.39$, and $X_{MM} = 0$ which are the same values used by the logistic models.

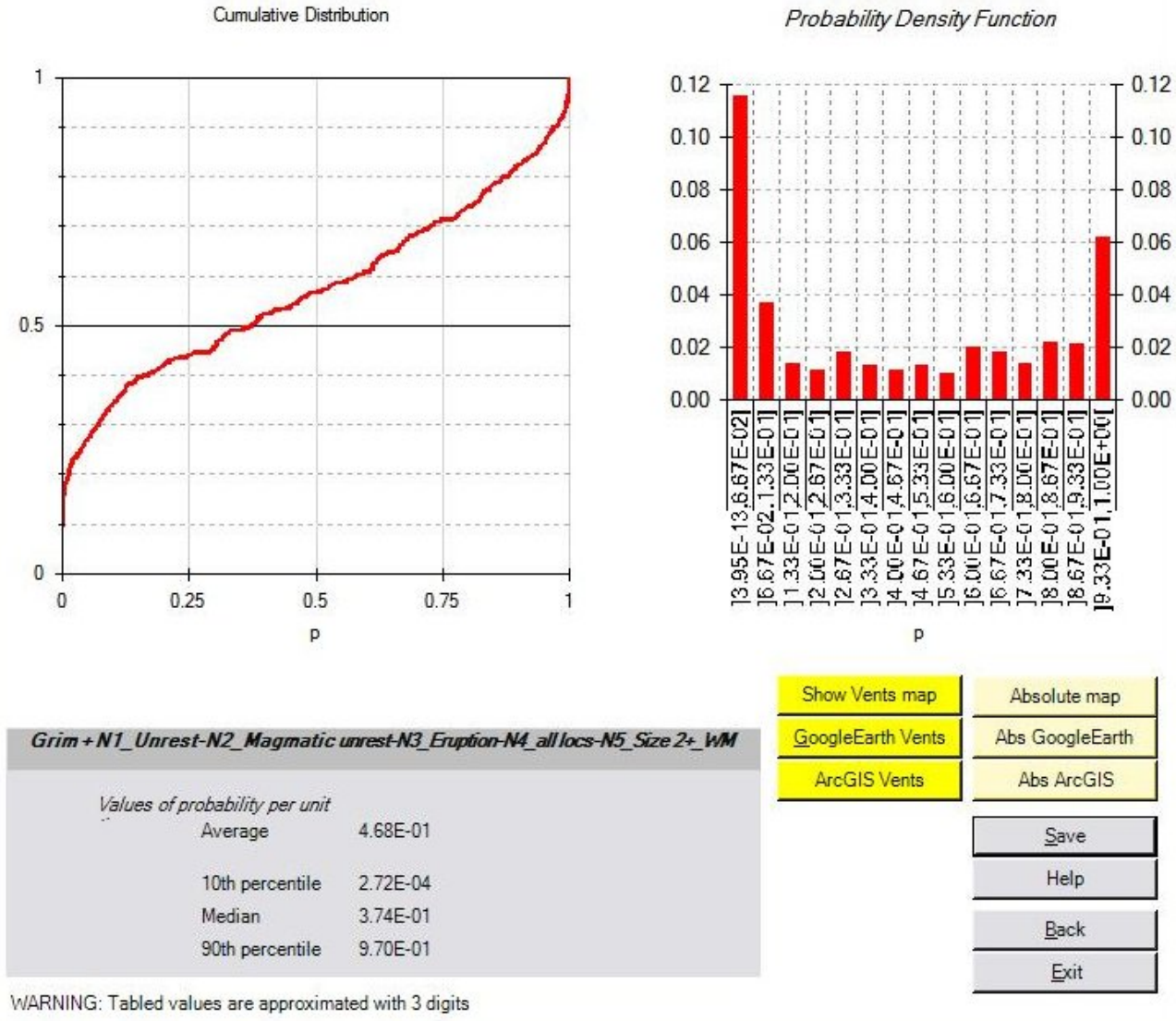

Figure H.44: Results generated using BETEF V2.0 for Grimsvötn episode day 134, where $X_{NE} = 1.5$, $X_{CSM} = 0.54$, and $X_{MM} = 1$ which are the same values used by the logistic models.

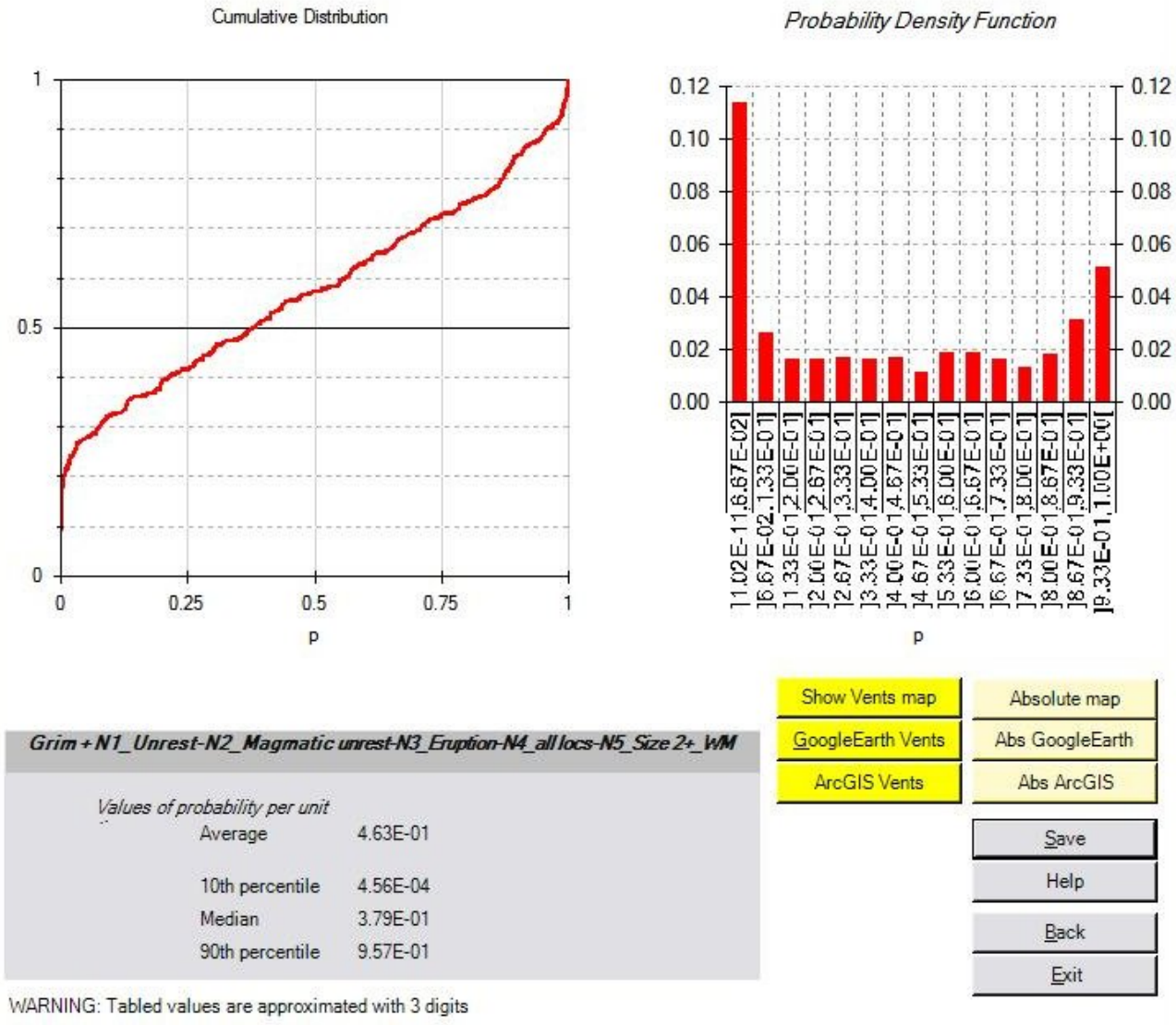

Figure H.45: Results generated using BETEF V2.0 for Grimsvötn episode day 177, where $X_{NE} = 1.3$, $X_{CSM} = 0.42$, and $X_{MM} = 1$ which are the same values used by the logistic models.

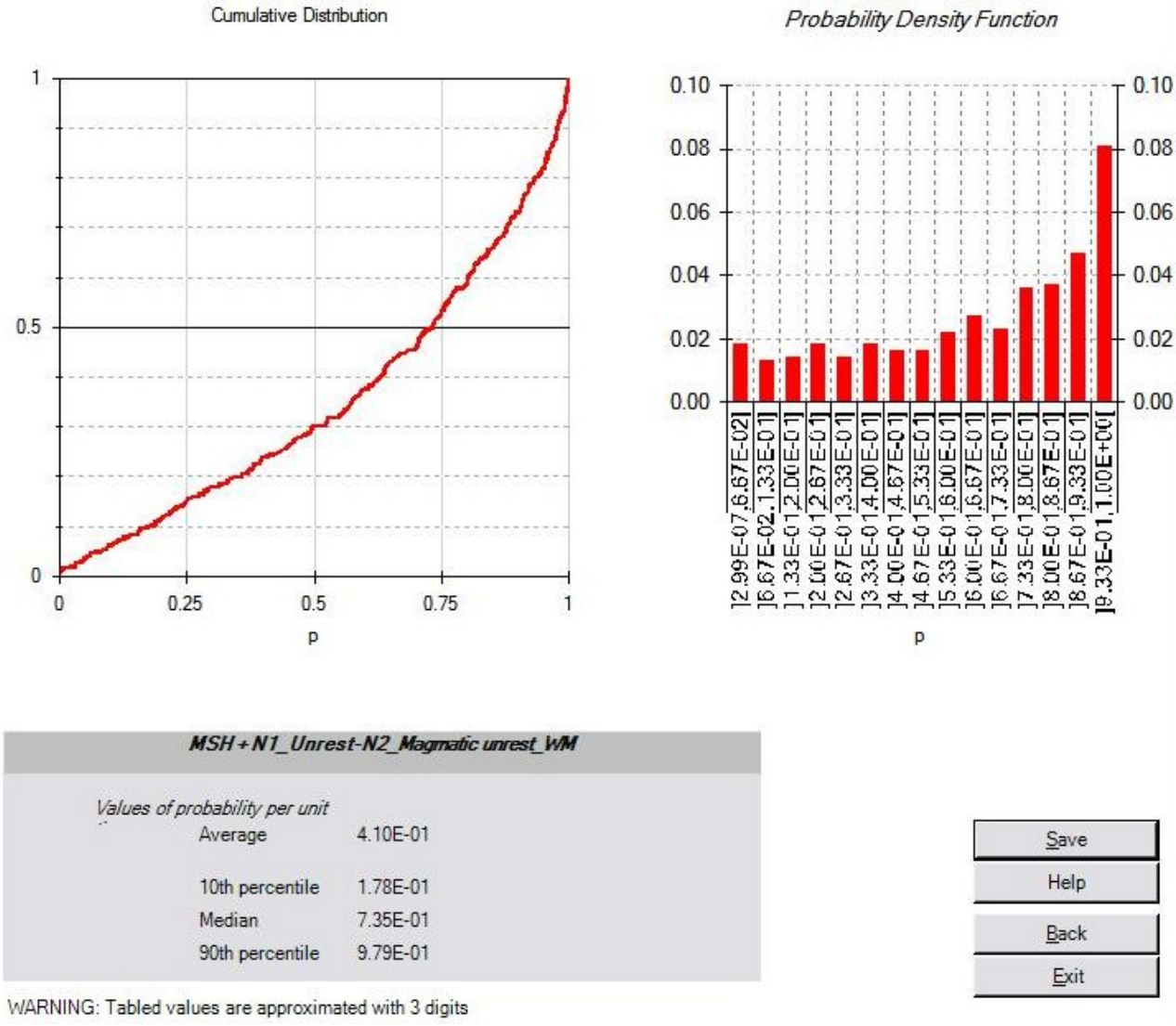

Figure H.46: Results generated using BETEF V2.0 for Mount Saint Helens episode day 1, where $X_{NE} = 4$, $X_{CSM} = 0.03$, and $X_{MM} = 0$ which are the same values used by the logistic models.

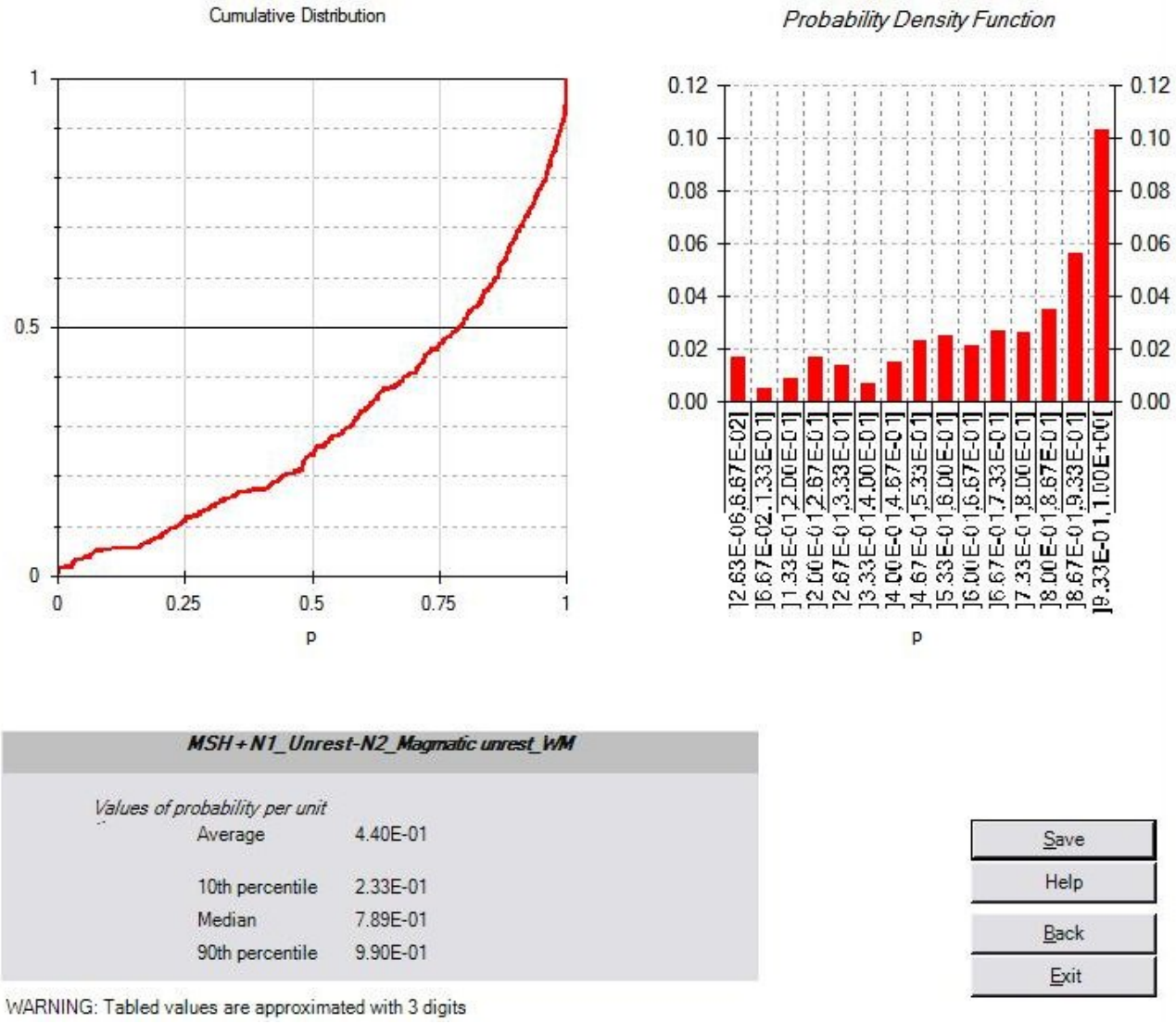

Figure H.47: Results generated using BETEF V2.0 for Mount Saint Helens episode day 3, where $X_{NE} = 3.35$, $X_{CSM} = 0.65$, and $X_{MM} = 0$ which are the same values used by the logistic models.

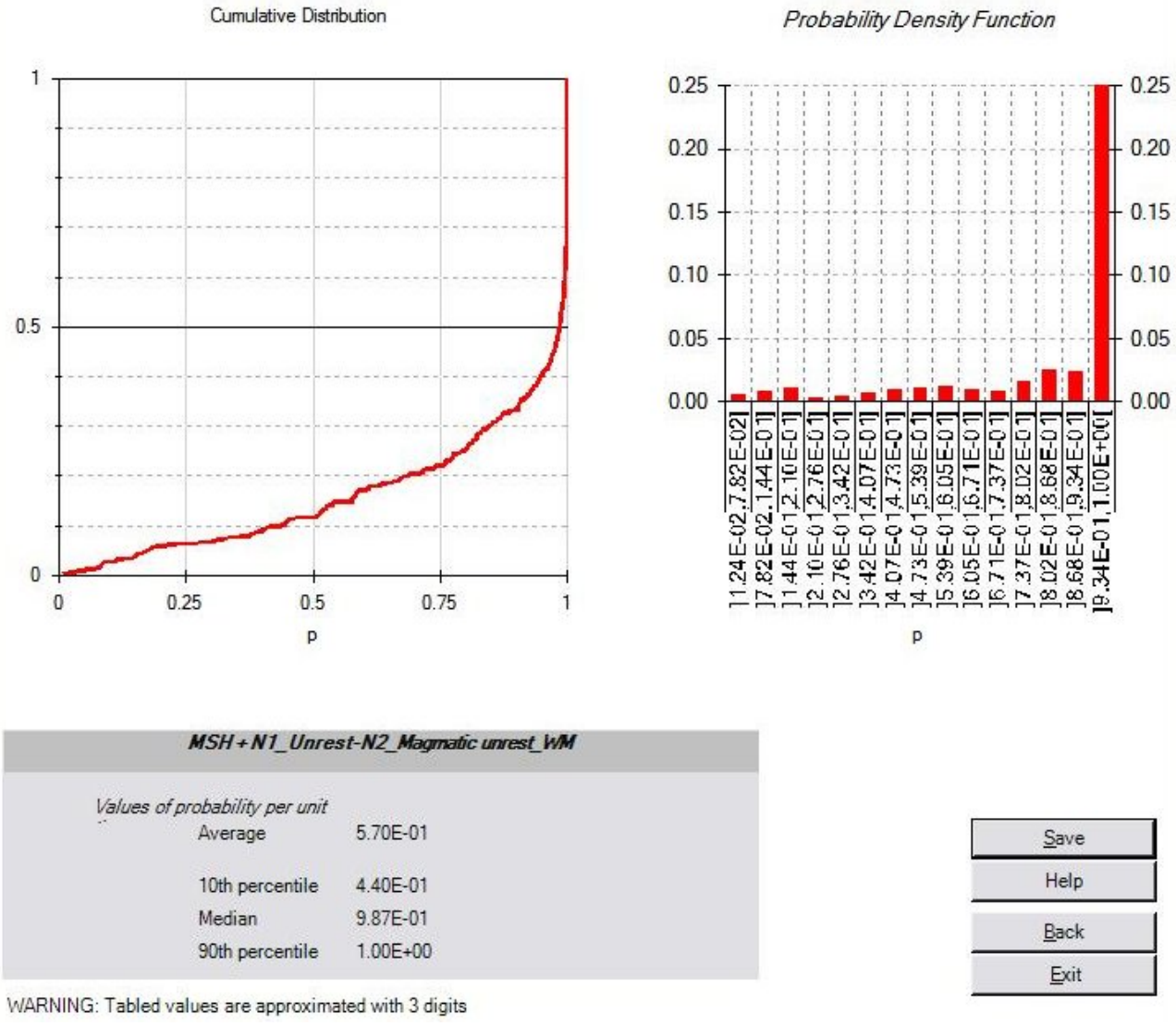

Figure H.48: Results generated using BETEF V2.0 for Mount Saint Helens episode day 19, where $X_{NE} = 1.2$, $X_{CSM} = 18.71$, and $X_{MM} = 0$ which are the same values used by the logistic models.

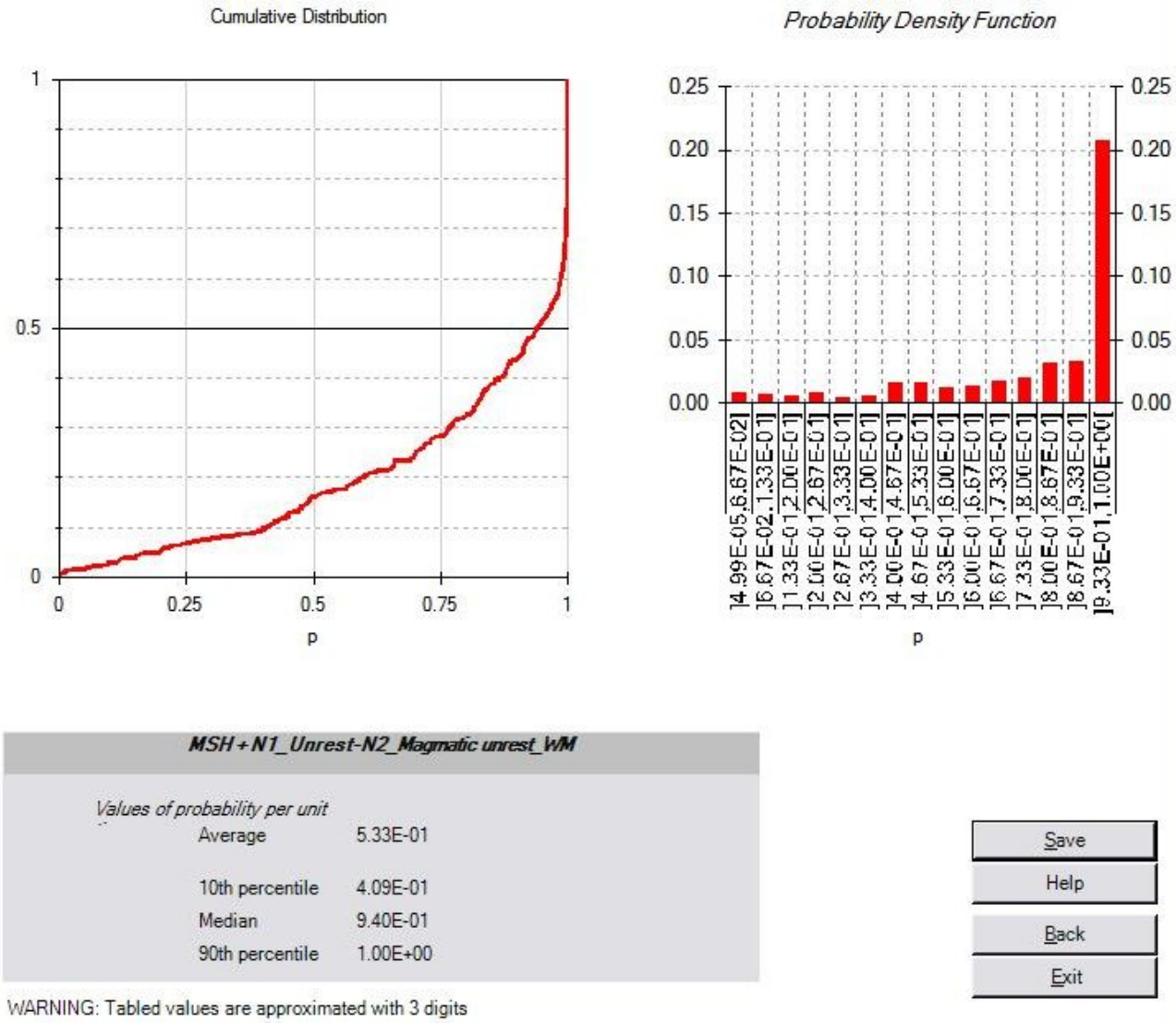

Figure H.49: Results generated using BETEF V2.0 for Mount Saint Helens episode day 25, where $X_{NE} = 0$, $X_{CSM} = 14.25$, and $X_{MM} = 0$ which are the same values used by the logistic models.

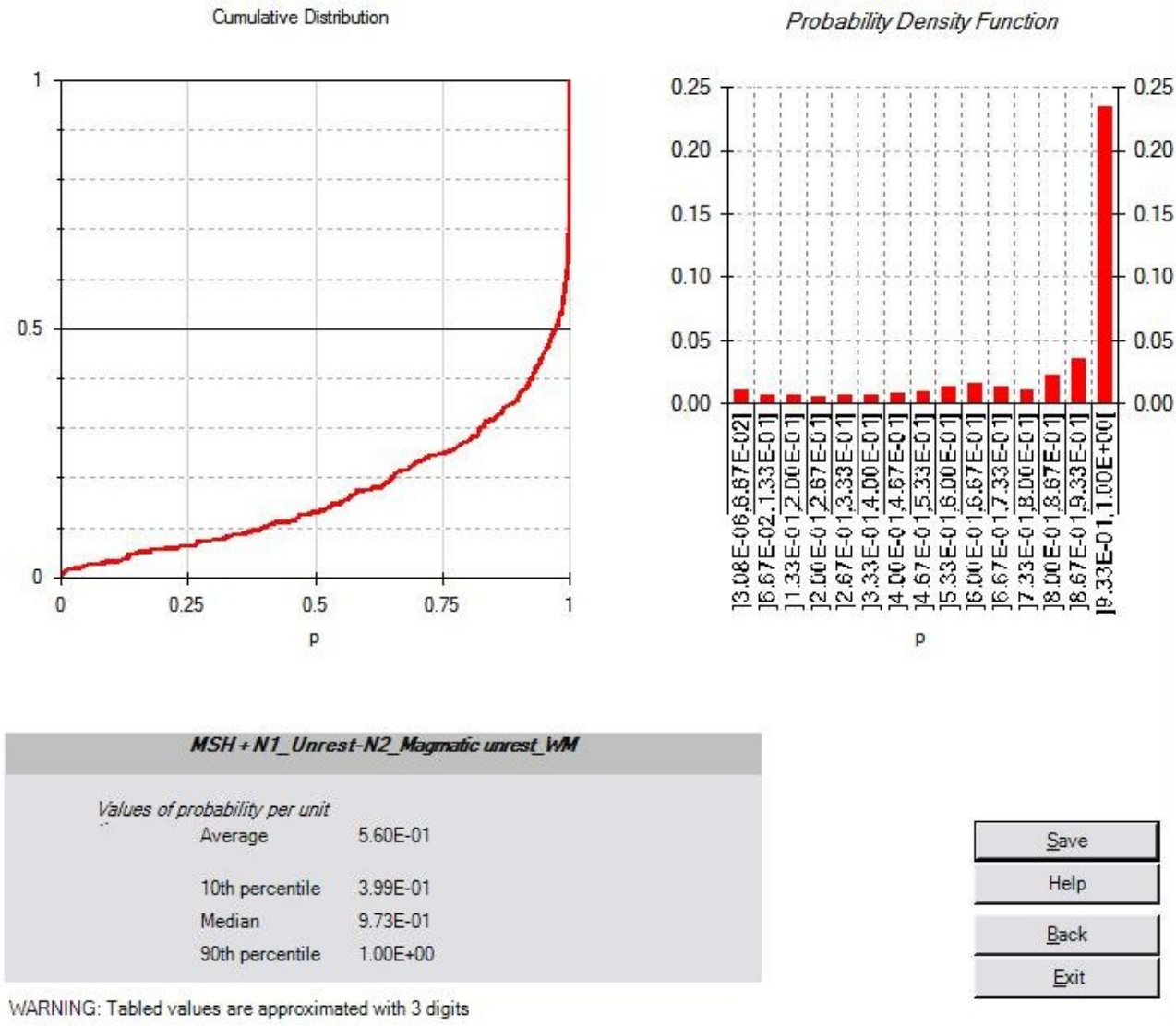

Figure H.50: Results generated using BETEF V2.0 for Mount Saint Helens episode day 33, where $X_{NE} = 1$, $X_{CSM} = 10.8$, and $X_{MM} = 0$ which are the same values used by the logistic models.

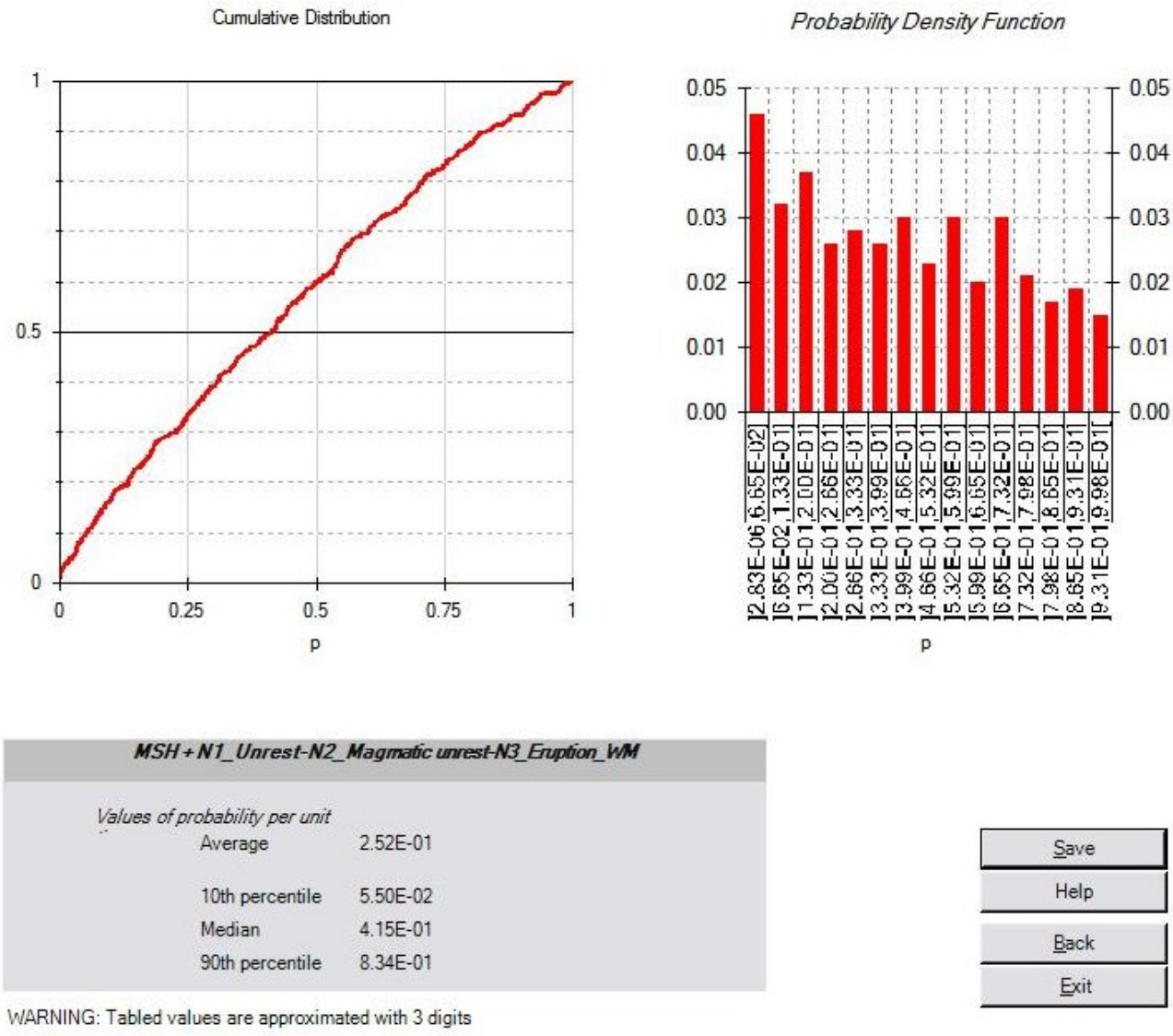

Figure H.51: Results generated using BETEF V2.0 for Mount Saint Helens episode day 1, where $X_{NE} = 4$, $X_{CSM} = 0.03$, and $X_{MM} = 0$ which are the same values used by the logistic models.

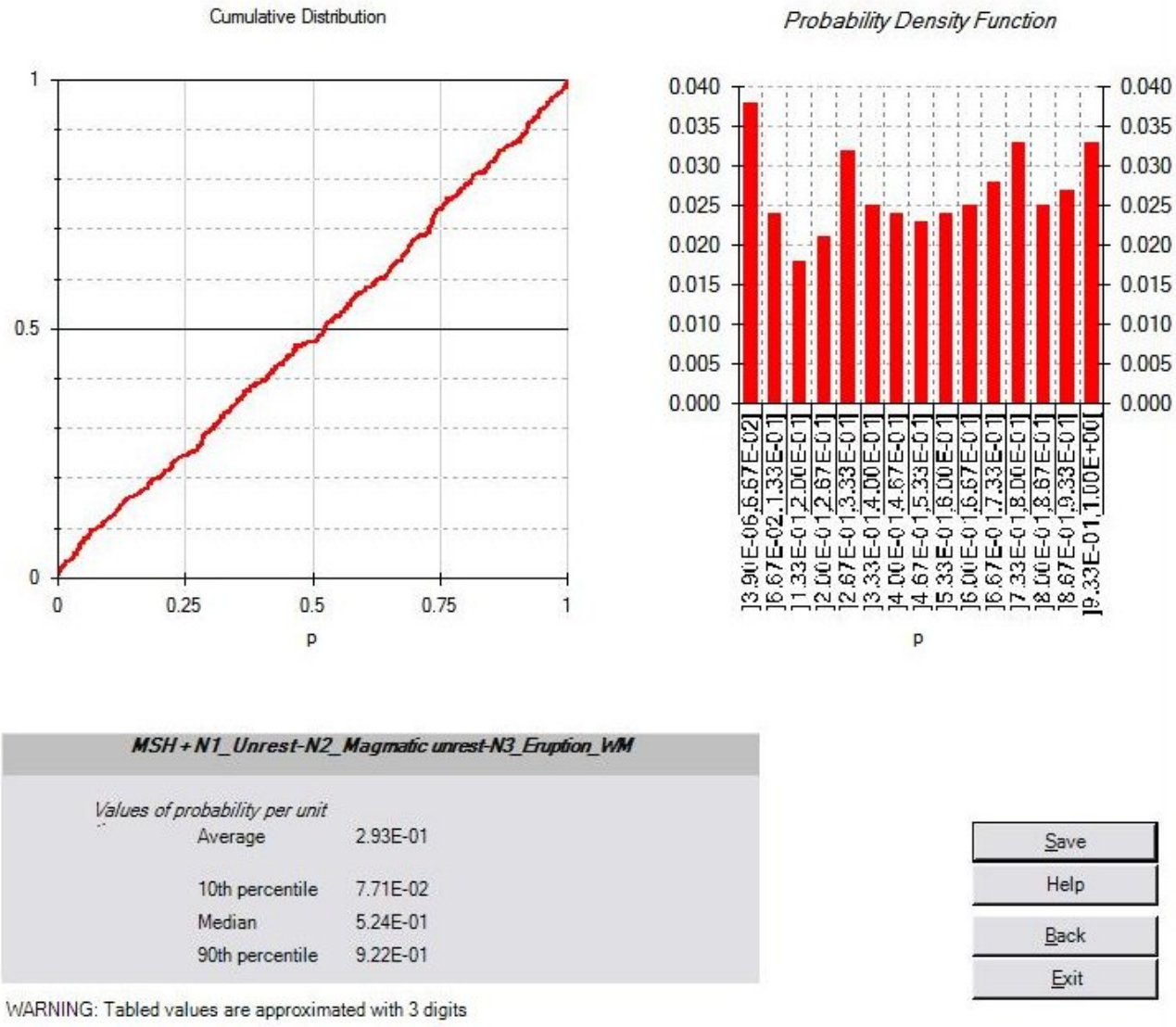

Figure H.52: Results generated using BETEF V2.0 for Mount Saint Helens episode day 3, where $X_{NE} = 3.35$, $X_{CSM} = 0.65$, and $X_{MM} = 0$ which are the same values used by the logistic models.

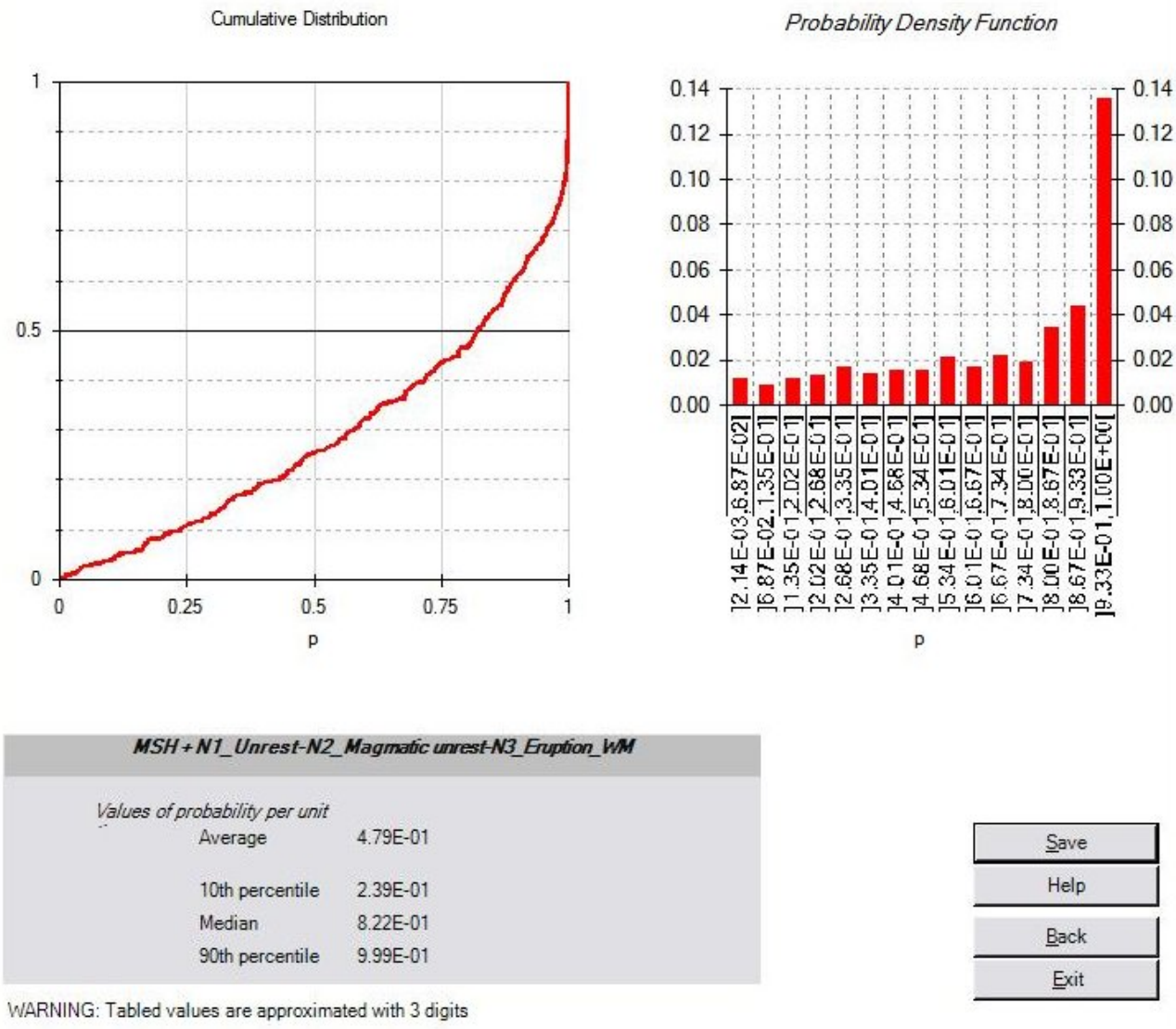

Figure H.53: Results generated using BETEF V2.0 for Mount Saint Helens episode day 19, where $X_{NE} = 1.2$, $X_{CSM} = 18.71$, and $X_{MM} = 0$ which are the same values used by the logistic models.

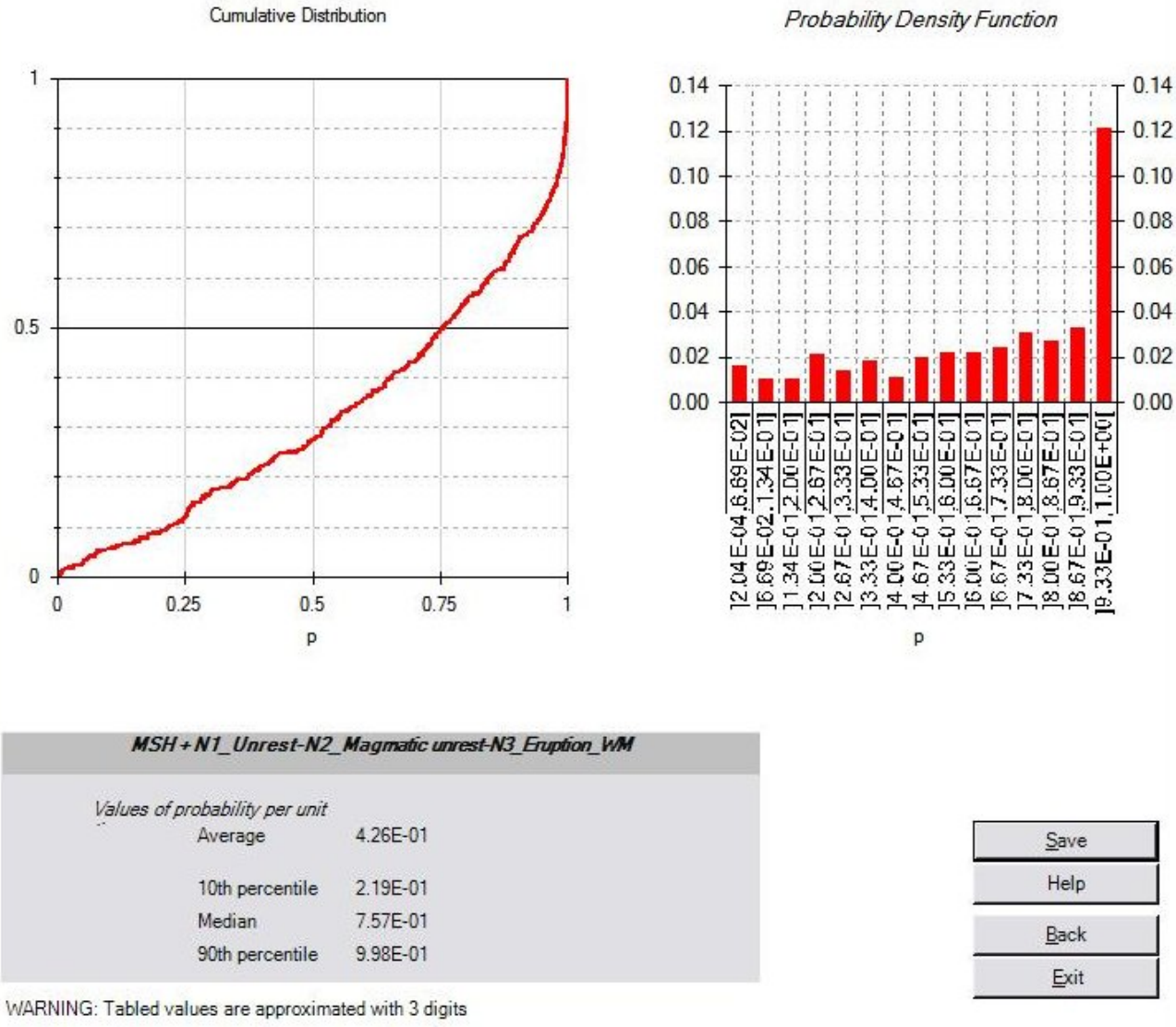

Figure H.54: Results generated using BETEF V2.0 for Mount Saint Helens episode day 25, where $X_{NE} = 0$, $X_{CSM} = 14.25$, and $X_{MM} = 0$ which are the same values used by the logistic models.

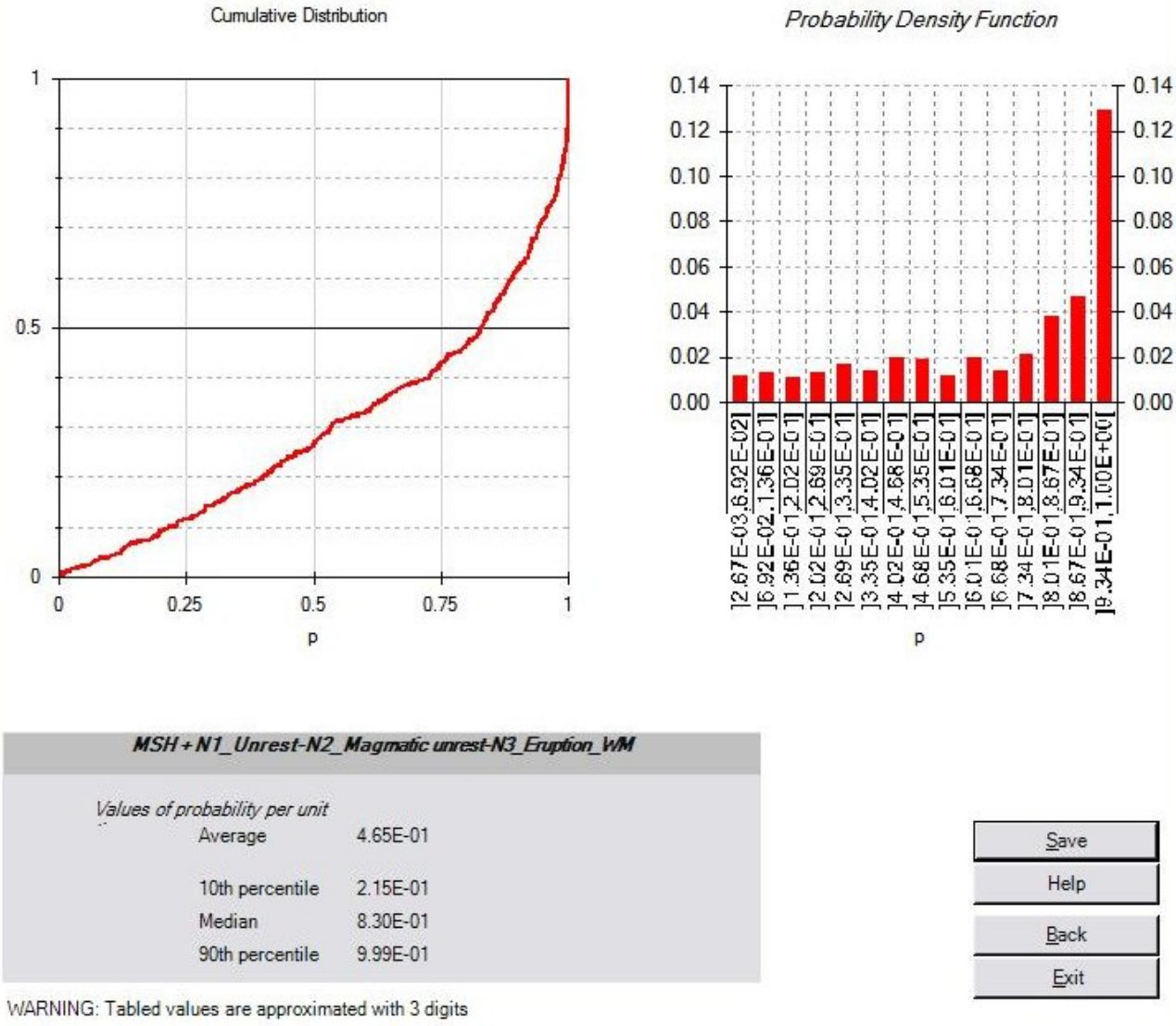

Figure H.55: Results generated using BETEF V2.0 for Mount Saint Helens episode day 33, where $X_{NE} = 1$, $X_{CSM} = 10.8$, and $X_{MM} = 0$ which are the same values used by the logistic models.

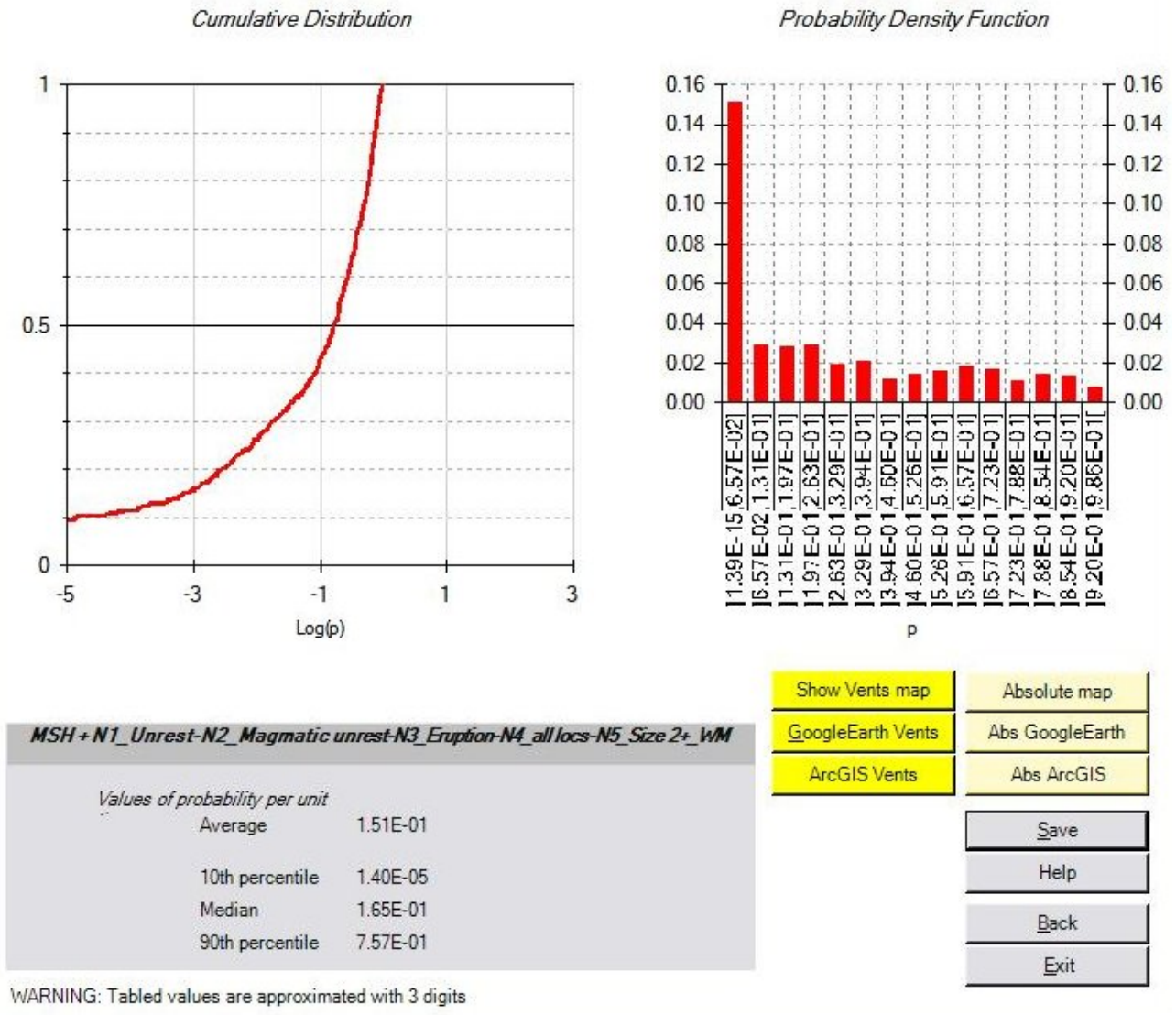

Figure H.56: Results generated using BETEF V2.0 for Mount Saint Helens episode day 1, where $X_{NE} = 4$, $X_{CSM} = 0.03$, and $X_{MM} = 0$ which are the same values used by the logistic models.

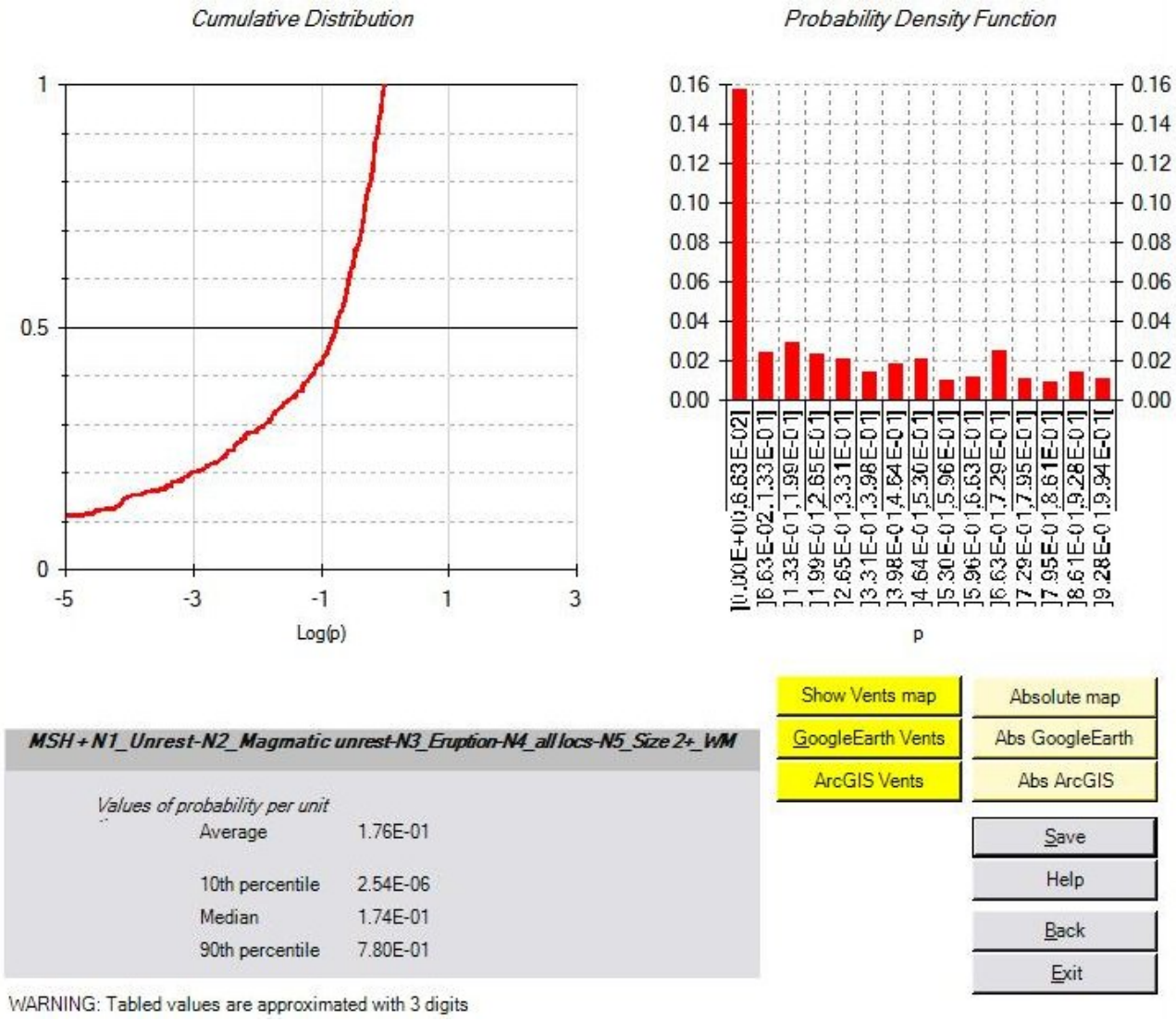

Figure H.57: Results generated using BETEF V2.0 for Mount Saint Helens episode day 3, where $X_{NE} = 3.35$, $X_{CSM} = 0.65$, and $X_{MM} = 0$ which are the same values used by the logistic models.

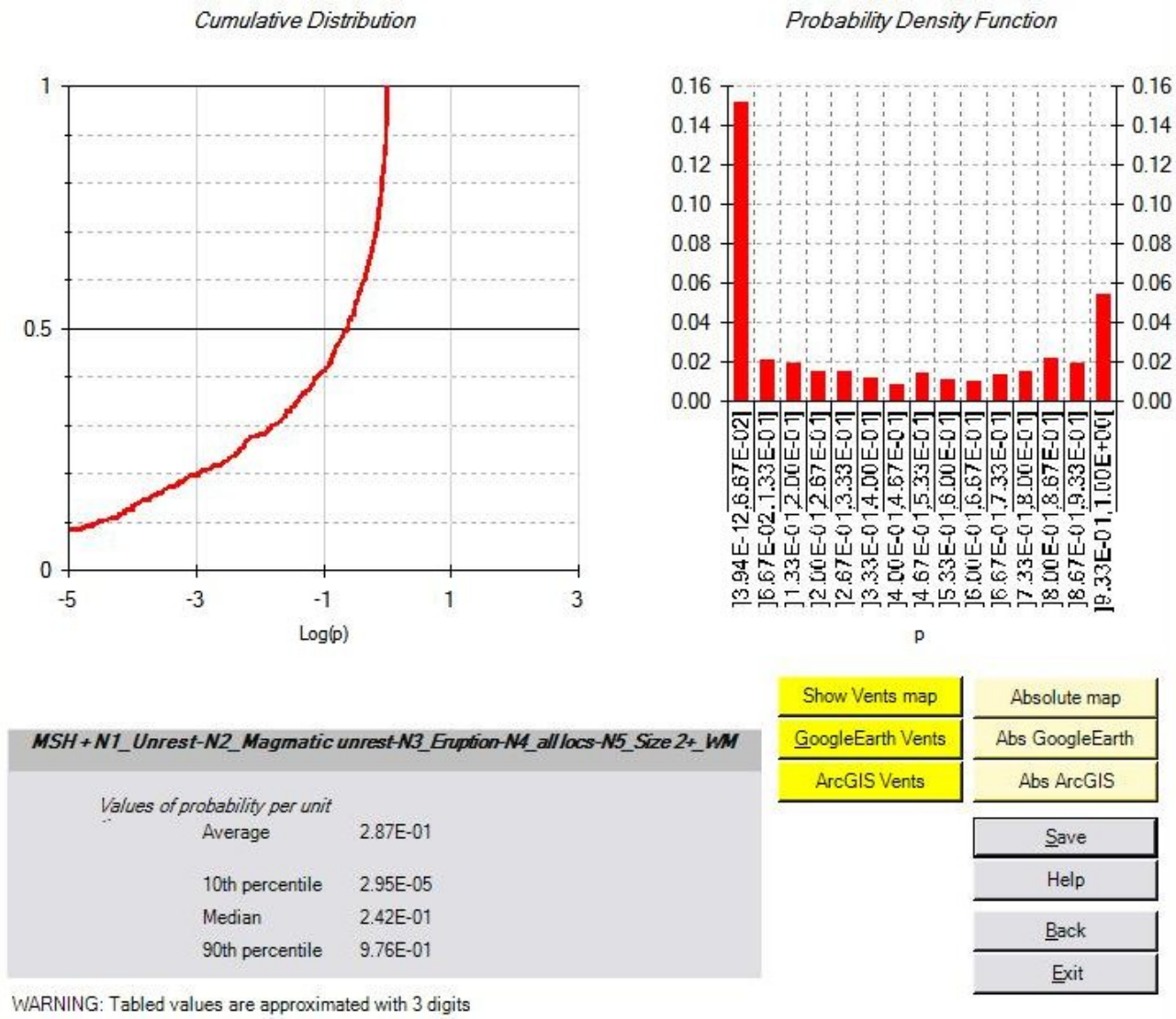

Figure H.58: Results generated using BETEF V2.0 for Mount Saint Helens episode day 19, where $X_{NE} = 1.2$, $X_{CSM} = 18.71$, and $X_{MM} = 0$ which are the same values used by the logistic models.

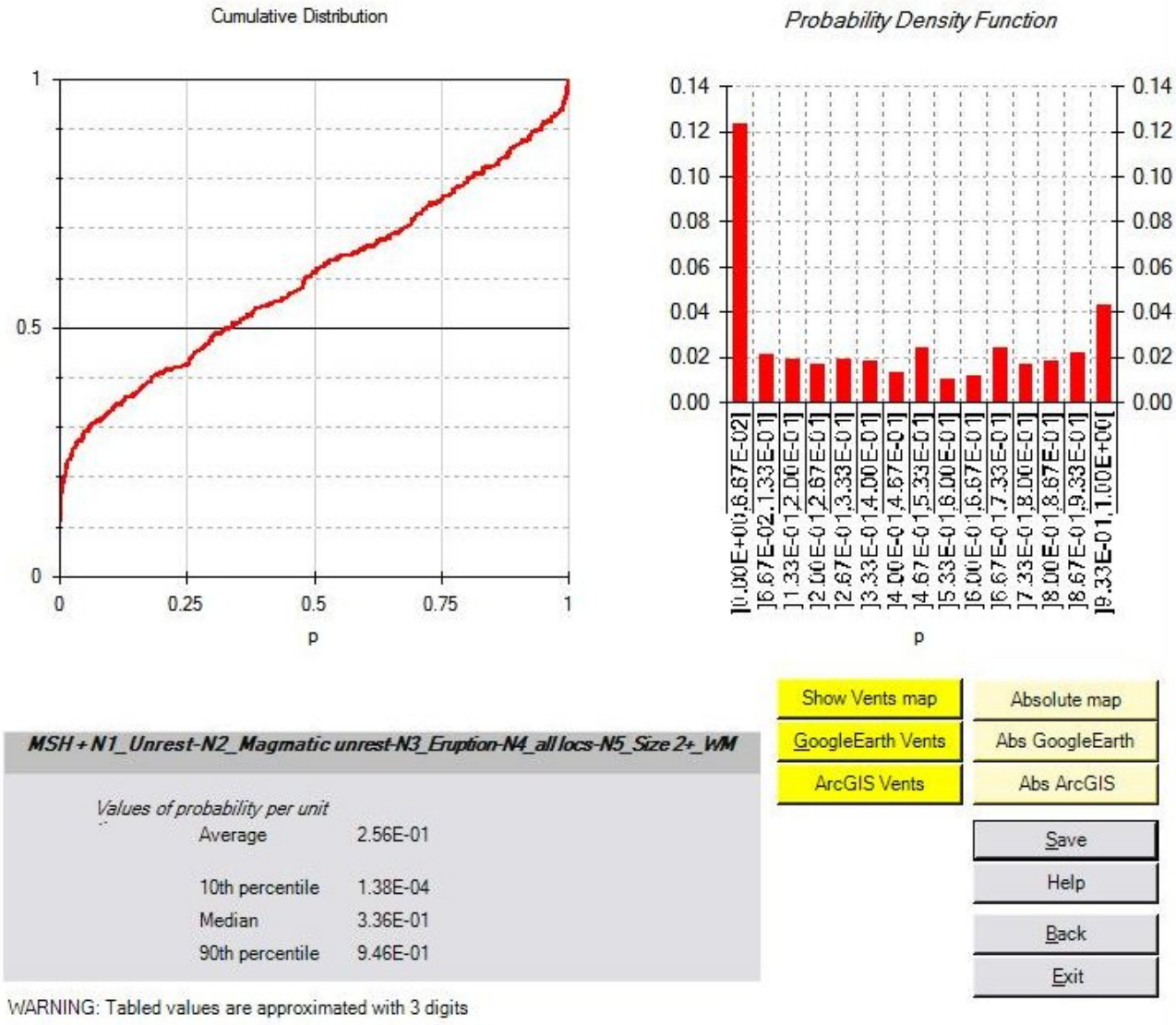

Figure H.59: Results generated using BETEF V2.0 for Mount Saint Helens episode day 25, where $X_{NE} = 0$, $X_{CSM} = 14.25$, and $X_{MM} = 0$ which are the same values used by the logistic models.

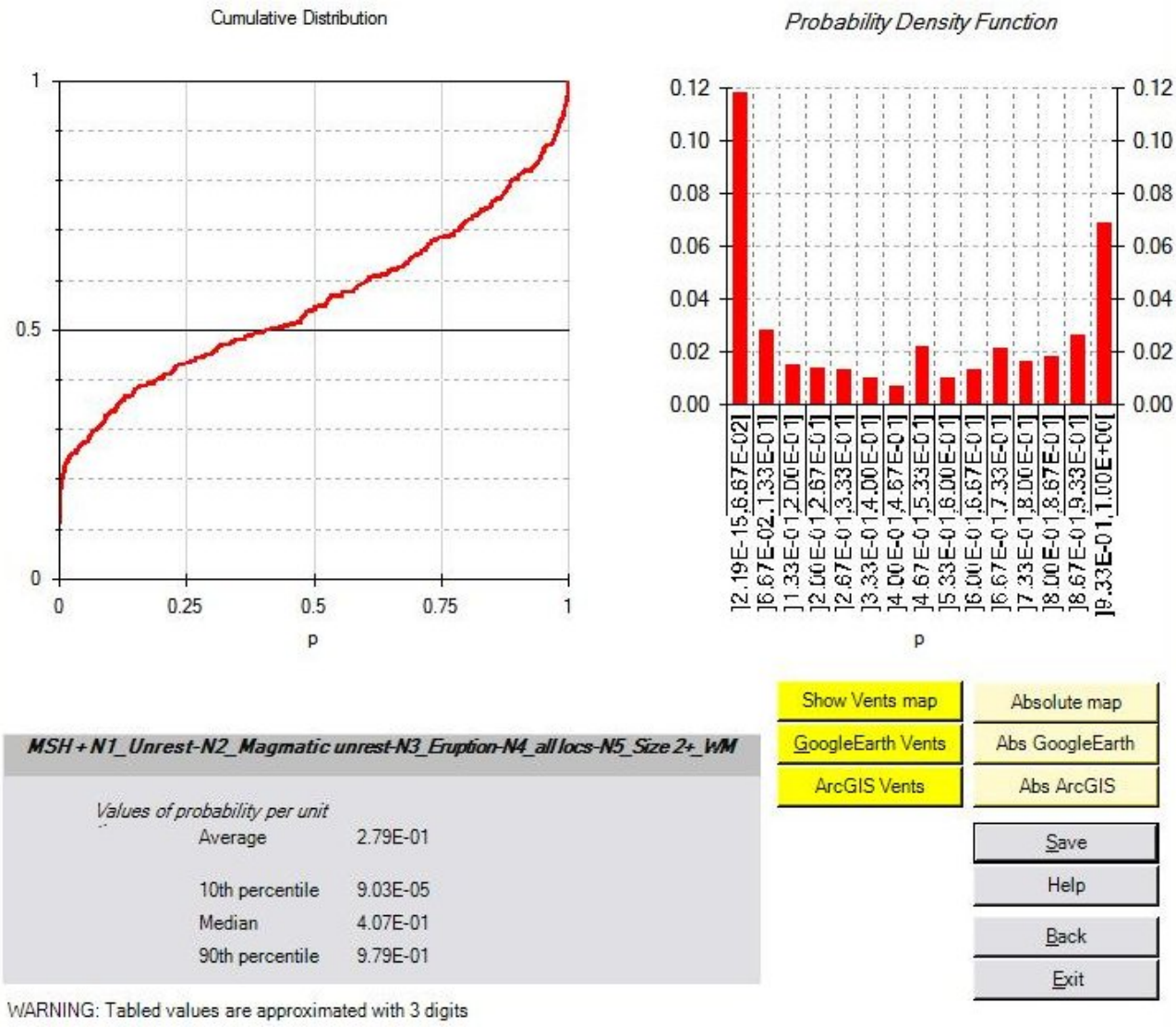

Figure H.60: Results generated using BETEF V2.0 for Mount Saint Helens episode day 33, where $X_{NE} = 1$, $X_{CSM} = 10.8$, and $X_{MM} = 0$ which are the same values used by the logistic models.

LIST OF REFERENCES

[1] S. Wessel and W. Smith, "New, improved version of the generic mapping tool released," *EOS Transactions AGU*, vol. 79, p. 579, 1998.

[2] U. S. G. Survey, "Volcano Hazards Program," 2009. `http://http://volcanoes.usgs.gov`.

[3] E. Parfitt and L. Wilson, *Fundamentals of Physical Volcanology*. Blackwell Publishing, 2008.

[4] P. Rosen, S. Hensley, I. Joughin, F. Lin, S. Madsen, E. Rodríguez, and R. Goldstein, "Synthetic aperture radar interferometry," *Proceedings of the IEEE*, vol. vol. 88, no. no. 3, pp. 333–380, 2000.

[5] G. Stimpson, *Introduction to Airborne Radar*. SciTech Publishing, INC, 1998.

[6] T. R. Lauknes, "Long-term surface deformation mapping using small-baseline differential SAR interferograms," Master's thesis, University of Tromsø, 2004.

[7] W. N. Junek, W. L. Jones, and M. T. Woods, "Temporal analysis of the magma supply system beneath the Okmok Caldera by interferometric synthetic aperture radar and statistical seismology," in *IEEE International Geoscience and Remote Sensing Symposium Proceedings*, pp. 1545–1548, 2010.

[8] "Shuttle radar tomography mission." `http://www2.jpl.nasa.gov/srtm/`.

[9] D. G. Kleinbaum and M. Klein, *Logistic Regression: A Self Learning Text*. Springer, 2010.

[10] J. E. Beget, J. Larsen, C. Neal, C. J. Nye, and J. R. Schafer, "Preliminary volcano-hazard assessment for Okmok volcano, Umnak Island Alaska," report of investigations 2004-3, Alaska Department of Natural Resources, Division of Geological and Geophysical Surveys, 2005.

[11] U. of Alaska, "Alaska Volcano Observatory, Okmok." `http://www.avo.alaska.edu/volcanoes/volcinfo.php?volcname=Okmok`.

[12] "Nasa shuttle radar topography mission," Feburary 2006. `http://www2.jpl.nasa.gov/srtm`.

[13] "Nasa shuttle radar topography mission," October 2004. `ftp://e0srp01u.ecs.nasa.gov`.

[14] T. Simkin and L. Siebert, *Volcanoes of the World*. Geoscience Press, Tucson, 1994.

[15] H. Mader, S. Coles, C. Connor, and L. Connor, *Statistics in Volcanology*. Geological Society for IAVCEI, 2006.

[16] J. W. Ewert, M. Guffanti, and T. L. Murray, "An assessment of volcanic threat and monitoring capabilities in the United States: Framework for a national volcano early warning system," Open File Report 2005-1164, United States Geologic Survey, 2005.

[17] C. G. Newhall, "Volcanology 101 for seismologists," *Teatise on Geophysics*, vol. 4, pp. 351–388, 2007.

[18] C. Newhall, "A method for estimating intermediate and long-term risks from volcanic activity, with an example from Mount St. Helens, Washington," Open File Report 82-396, United States Geologic Survey, 1982.

[19] C. Newhall, "Semiquantitative assessment of changing volcanic risk at Mount St. Helens, Washington," Open File Report 84-272, United States Geologic Survey, 1984.

[20] W. P. Aspinall and R. m. Cooke, "Expert judgement and the Montserrat Volcano eruption," in *Proceedings of the 4th International Conference on Probabilistic Safety Assessment and Management PSAM4*, vol. 3, pp. 2113–2118, 1998.

[21] C. Newhall and R. P. Hoblitt, "Constructing events trees for volcanic crises," *Bulletin of Volcanology*, vol. 64, pp. 3–20, 2002.

[22] W. Aspinall, G. Woo, B. Voight, and P. Baxter, "Evidence-based volcanology: Application to eruption crises," *Journal of Volcanology and Geothermal Research*, vol. 128, pp. 273 – 285, 2003.

[23] W. Marzocchi, L. Sandri, P. Gasparini, C. Newhall, and E. Boschi, "Quantifying probabilities of volcanic events: The example of volcanic hazard at Mount Vesuvius," *Journal of Geophysical Research*, vol. 109, p. 18, 2004.

[24] W. Marzocchi, L. Sandri, and J. Selva, *A quantitative model for volcanic hazard assessment, in Statistics in Volcanology*, vol. 1. London: Geological Society for IAVCEI, 2006.

[25] W. Marzocchi, L. Sandri, and J. Selva, "BET EF: A probabilistic tool for long and short term eruption forecasting," *Bulletin of Volcanology*, vol. 70, pp. 623 – 632, 2008.

[26] W. Marzocchi, L. Sandri, and J. Selva, "BET VH: A probabilistic tool for long term volcanic hazard assessment," *Bulletin of Volcanology*, vol. 72, pp. 705 – 716, 2010.

[27] R. Sobradelo and J. Marti, "Bayesian event tree for long term volcanic hazard assessment: Application to teide-pico viejo stratovolcanoes, tenerife, canary islands," vol. 115, p. 12, 2010.

[28] J. Lindsay, W. Marzocchi, G. Jolly, R. Constantinescu, J. Selva, and L. Sandri, "Towards real-time eruption forecasting in the Auckland Volcanic Field: Application of BETEF during the New Zealand national disaster exercise Ruaumoko," *Bulletin of Volcanology*, vol. 72, pp. 185–204, 2010.

[29] C. G. Newhall and S. Self, "The volcanic explosivity index (VEI): An estimate of the explosive magnitude for historic eruptions," *Journal of Geophysical Research*, vol. 87, pp. 1231 – 1238, 1982.

[30] K. Mogi, "Relationships between the eruptions of various volcanoes and the deformations of the ground surfaces around them," *Bulletin of the Earthquake Research Institute*, vol. 36, pp. 99–134, 1958.

[31] Z. Lu, D. Mann, J. Freymueller, and D. Meyer, "Synthetic aperture radar interferometry of Okmok Volcano, Alaska: Radar observations," *Journal of Geophysical Research*, vol. 105, pp. 10791–10806, 2000.

[32] F. Sigmundsson, P. Einarsson, and R. Bilham, "Magma chamber deflation recorded by the global positioning system: The Hekla 1991 eruption," *Geophysical Research Letters*, vol. 19, no. 14, pp. 1483–1486, 1992.

[33] H. Griffiths, "Interferometric synthetic aperture radar," *Electronics and Communications Engineering Journal*, pp. 247–256, 1995.

[34] J. Fitch, *Synthetic Aperture Radar*. Springer-Verlag, 1988.

[35] W. N. Junek, "Implementation and test of a dual beam interferometric synthetic aperture radar for ocean current estimates," Master's thesis, University of Massachusetts, 2003.

[36] L.C.Graham, "Synthetic interferometric radar for topographic mapping," *Proceedings of the IEEE*, 1974.

[37] A. Gabriel, R. M. Goldstein, and H. A. Zebker, "Mapping small elevation changes over large area: Differential radar interferometry," *Journal of Geophysical Research*, 1989.

[38] H. Zebker and R. Goldstein, "Topographic mapping from interferometric SAR observations," *Journal of Geophysical Research*, 1986.

[39] R. Goldstein, H. Zebker, and C. Werner, "Satellite radar interferometry: Two dimensional phase unwrapping," *Radio Science*, 1988.

[40] R. F. Hanssen, *Radar Interferometry*. Kluwer Academic Publishers, 2001.

[41] J. C. Curlander and R. N. McDonough, *Synthetic Aperture Radar: Systems and Signal Processing*. Wiley, 1991.

[42] W. G. Carrara, R. S. Goodman, and R. M. Majewski, *Spotlight Synthetic Aperture Radar: Signal Processing Algorithms*. Artech House, 1995.

[43] P. A. Rosen, S. Henley, G. Peltzer, and M. Simons, "Updated repeat orbit interferometry package released," *EOS Transactions AGU*, vol. 85, no. 5, p. 47, 2004.

[44] "Open channel foundation." `http://www.openchannelfoundation.org`.

[45] "Delft precision orbit information." http://www.deos.tudelft.nl/ers/operorbs/.

[46] "European space agancy." http://earth.esa.int/ers/.

[47] D. R. Sherrod, W. E. Scott, and P. H. Stauffer, "A volcano rekindled; the renewed eruption of Mount St. Helens, 2004-2006," Professional Paper 1750, United States Geologic Survey, 2008.

[48] B. A. Chouet, "Long period volcano seismicity: Its source and use in eruption forecasting," *Nature*, vol. 380, pp. 309–316, 1996.

[49] A. D. Miller, R. C. Stewart, R. A. White, R. Luckett, B. J. Baptie, W. P. Aspinall, J. L. Latchman, L. L. Lynch, and B. Voight, "Seismicity associated with dome growth and collapse at the Soufriere Hills Volcano, Montserrat," *Geophysical Research Letters*, vol. 25, no. 18, pp. 3401 – 3404, 1998.

[50] R. S. J. Sparks, "Forecasting volcanic eruptions," *Earth and Planetary Science Letters*, vol. 210, pp. 1–15, 2003.

[51] G. Curilem, J. Vergara, G. Fuentealba, G. Acuna, and M. Chacon, "Classification of seismic signals at Villarrica volcano (Chile) using neural networks and genetic algorithms," *Journal of Volcanology and Geothermal Research*, vol. 180, pp. 1–8, 2009.

[52] S. Scarpetta, F. Giudicepietro, E. C. Ezin, S. Petrosino, E. D. Pezzo, M. Martini, and M. Marinaro, "Automatic classification of seismic signals at Mt. Vesuvius Volcano, Italy, using neural networks," *Bulletin of the Seismological Society of America*, vol. 95, no. 1, pp. 185–196, 2005.

[53] C. G. Newhall and D. Dzurisin, "Historic unrest at large calderas of the world: Volume 1," Bulletin 1855, United States Geologic Survey, 1988.

[54] C. G. Newhall and D. Dzurisin, "Historic unrest at large calderas of the world: Volume 2," Bulletin 1855, United States Geologic Survey, 1988.

[55] M. Ishimoto and K. Iida, "Observations of earthquakes registered with microseismograph constructed recently," *Bull. Earthq. Res. Inst.*, vol. 17, pp. 443–478, 1939.

[56] R. Gutenberg and C. F. Richter, "Frequency of earthquakes in California," *Bulletin of the Seismological Society of America*, vol. 34, pp. 185–188, 1944.

[57] S. Wiemer and S. R. McNutt, "Variation of the frequency-magnitude distribution with depth in two volcanic areas: Mount St. Helens, Washington, and Mount Spurr, Alaska," *Geophysical Research Letters*, vol. 24, no. 2, pp. 189–192, 1997.

[58] S. Wiemer and J. P. Benoit, "Mapping the b-value anomaly at 100 km depth in the Alaska and New Zealand subduction zones," *Geophysical Research Letters*, vol. 13, no. 23, pp. 1557–1560, 1996.

[59] M. Wyss, K. Shimazaki, and S. Wiemer, "Mapping active magma chambers by b values beneath the Off-Ito Volcano, Japan," *Journal of Geophysical Research*, vol. 102, no. B9, pp. 20,413–20,422, 1997.

[60] M. Murru, C. Montuori, R. Console, and A. Lisi, "Mapping of the b value anomalies beneath Mount Etna, Italy, during the July-August 2001 lateral eruption," *Geophysical Research Letters*, vol. 32, 2005.

[61] W. N. Junek, "Statistical analysis of seismicity beneath Alaskan volcanoes," *Seismological Research Letters*, vol. 81, no. 2, p. 381, 2010.

[62] N. W. Warren and G. V. Latham, "An experimental study of thermally induced microfracturing and its relation to volcanic seismicity," *Journal of Geophysical Research*, vol. 75, pp. 4455–4464, 1970.

[63] C. H. Scholz, "The frequency-magnitude relation of microfracturing in rock and its relation to earthquakes," *Bulletin of the Seismological Society of America*, vol. 58, pp. 399–415, 1958.

[64] T. I. Urbancic, C. I. Trifu, J. M. Long, and R. P. Young, "Young space-time correlations of b-values with stress release," *Pure and Applied Geophysics*, vol. 130, pp. 449–462, 1992.

[65] R. Dmowska and B. Saltzman, *Advances in Geophysics, Vol. 45*. Academic Press, 2002.

[66] S. Stein and M. Wysession, *An Introduction to Seismology, Earthquakes, and Earth Structure*. Blackwell Publishing, 2003.

[67] W. A. Thelen, S. D. Malone, and M. E. West, "Response time and cumulative seismic moment: A new tool for forecasting eruptions," *Geophysical Research Letters*, vol. 37, 2010.

[68] A. S. Facility, "SAR data request guidelines." `http://www.asf.alaska.edu/reference/daac_proposal_guidelines`.

[69] "Delft precision orbit information tool." `http://www.deos.tudelft.nl/ers/precorbs/tools/getorb/docs/odrfmt.txt`.

[70] "Delft precision orbit information derivation." `http://www.deos.tudelft.nl/ers/precorbs/tools/getorb/docs/odrfmt.txt`.

[71] IRIS, "About the Incorporated Research Institutions for Seismology." `http://www.iris.edu/hq/about_iris`.

[72] UNAVCO, "Corporation web site," 2009. `http://www.unavco.org`.

[73] L. A. Zadeh, "Fuzzt sets," *Information and Control*, vol. 8, pp. 338–353, 1965.

[74] S. J. Press and S. Wilson, "Choosing between logistic regression and discriminant analysis," *Journal of the American Statistical Association*, vol. 73, no. 364, pp. 699–705, 1978.

[75] J. Neter, W. Wasserman, and M. K. Kutner, *Applied Linear Regression Models*. Richard D. Irwin, INC., 1989.

[76] B. Samanta, G. L. Bird, M. Kuijpers, R. A. Zimmerman, G. P. Jarvik, G. Wernovsky, R. R. Clancy, D. J. Licht, J. W. Gaynor, and C. Nataraj, "Prediction of preiventricular leukomalacia part 1: Selection of hemodynamic features using logistic regression and decision tree algorithms," *Artificial Intelligence in Medicine*, vol. 46, pp. 201–215, 2009.

[77] L. S. Chiu, "Estimating the exceedance probability of rain rate by logistic regression," *Journal of Geophysical Research*, vol. 95, no. B3, pp. 2217–2227, 1990.

[78] S. Lee, "Application of logistic regression model and its validation for landslide susceptibility mapping using GIS and remote sensing data," *International Journal of Remote Sensing*, vol. 26, no. 7, pp. 1477–1491, 2005.

[79] Wikipedia, "Generalized linear model — wikipedia, the free encyclopedia," 2011. `http://en.wikipedia.org/w/index.php?title=Generalized_linear_model&oldid=467124760`.

[80] J. Verzani, *Using R for Introductory Statistics*. Chapman and Hall/CRC, 2005.

[81] S. C. Moran, C. Newhall, and D. C. Roman, "Failed magmatic eruptions: last-stage cessation of magma," *Bulletin of Volcanology*, vol. 73, pp. 115–122, 2011.

[82] M. Poland, R. Burgmann, D. Dzurisin, M. Lisowski, T. Masterlark, S. Owen, and J. Fink, "Constraints on the mechanism of long-term, steady subsidence at Medicine Lake volcano, northern California, from GPS, leveling, and InSAR," *Journal of Volcanology and Geothermal Research*, vol. 150, pp. 55–78, 2006.

[83] D. L. Bridges and S. S. Gao, "Spatial variation of seismic b-values beneath Makushin Volcano, Unalaska Island, Alaska," *Earth and Planetary Science Letters*, vol. 245, pp. 408–415, 2002.

[84] K. L. Feigl, J. Gasperi, F. Sigmundsson, and A. Rigo, "Crustal deformation near Hengill volcano, Iceland 1993-1998: Coupling between magmatic activity and faulting inferred from elastic modeling of satellite radar interferograms," *Journal of Geophysical Research*, vol. 105, no. B11, pp. 25,655–25,670, 2000.

[85] Z. Lu, R. Fatland, M. Wyss, S. Li, J. Eichelberger, K. Dean, and J. Freymueller, "Deformation of New Trident volcano measured by ERS-1 SAR interferometry, Katmai National Park, Alaska," *Geophysical Research Letters*, vol. 24, no. 6, pp. 695–698, 1997.

[86] M. Poland, G. Bawden, M. Lisowski, and D. Dzurisin, "Newly discovered subsidence at Lassen Peak, southern Cascade Range, California, from InSAR and GPS," in *EOS transaction, 2004 Fall Meeting Supplement*, 2004.

[87] S. Hjaltadottir, K. S. Vogfjord, and R. Slunga, "Seismic signs of magma pathways through the crust in the Eyjafjallajokull volcano, South Iceland," Tech. Rep. VI 2009-013, Icelandic Meteorological Office, 2009.

[88] Z. Lu, C. Wicks, J. A. Power, and D. Dzurisin, "Ground deformation associated with the March 1996 earthquake swarm at Akutan volcano, Alaska, revealed by satellite radar interferometry," *Journal of Geophysical Research*, vol. 105, no. B9, pp. 21,483–21,495, 2000.

[89] D. C. Roman and J. A. Power, "Mechanism of the 1996 97 non-eruptive volcano-tectonic earthquake swarm at Iliamna Volcano, Alaska," *Bulletin of Volcanology*, vol. 73, pp. 143–153, 2011.

[90] Z. Lu, C. Wicks, J. Power, D. Dzurisin, W. Thatcher, and T. Masterlark, "Interferometric synthetic aperture radar studies of Alaska volcanoes," in *IEEE International Geoscience and Remote Sensing Symposium Proceedings*, pp. 191–194, 2002.

[91] C. W. Wicks, D. Dzurisin, S. Ingebritsen, W. Thatcher, Z. Lu, and J. Iverson, "Magmatic activity beneath the quiescent Three Sisters volcanic center, central Oregon Cascade Range, USA," *Geophysical Research Letters*, vol. 29, no. 7, 2002.

[92] S. Owen, P. Segall, M. Lisowski, A. Miklius, M. Murray, M. Bevis, and J. Foster, "January 30, 1997 eruptive event on Kilauea Volcano, Hawaii as monitored by continuous GPS," *Geophysical Research Letters*, vol. 27, no. 17, pp. 2757–2760, 2000.

[93] Z. Lu, T. Masterlark, J. Power, D. Dzurisin, and C. Wicks, "Subsidence at Kiska Volcano, Western Aleutians, detected by satellite radar interferometry," *Geophysical Research Letters*, vol. 29, no. 18, 2002.

[94] E. Strukell, P. Einarsson, F. Sigmundsson, S. Hreinsdóttir, and H. Geirsson, "Deformation of Grimsvotn volcano, Iceland: 1998 eruption and subsequent inflation," *Geophysical Research Letters*, vol. 30, no. 4, 2003.

[95] S. C. Moran, O. Kwoun, T. Masterlark, and Z. Lu, "On the absence of InSAR-detected volcano deformation spanning the 1995-1996 and 1999 eruptions of Shishaldin Volcano, Alaska," *Journal of Volcanology and Geothermal Research*, vol. 150, pp. 119–131, 2006.

[96] D. Mann and J. Freymueller, "Volcanic and tectonic deformation on Unimak Island in the Aleutian Arc, Alaska," *Journal of Geophysical Research*, vol. 108, no. B2, 2003.

[97] E. Sturkell1, P. Einarsson, F. Sigmundsson, A. Hooper, B. G. Ofeigsson, H. Geirsson, and H. O. lafsson, "Katla and Eyjafjallajokull Volcanoes," *Developments in Quaternary Sciences*, vol. 13, pp. 5–21, 2010.

[98] P. Cervelli, P. Segall, K. Johnson, M. Lisowski, and A. Miklius, "Sudden aseismic fault slip on the south flank of Kilauea volcano," *Letters to Nature*, vol. 415, pp. 1014–1018, 2002.

[99] B. G. Ofeigsson, A. Hooper, F. Sigmundsson, E. Sturkell, and R. Grapenthin, "Deep magma storage at Hekla volcano, Iceland, revealed by InSAR time series analysis," *Journal of Geophysical Research*, vol. 116, 2011.

[100] R. Grapenthin, B. G. feigsson, F. Sigmundsson, E. Sturkell, and A. Hooper, "Pressure sources versus surface loads: Analyzing volcano deformation signal composition with an application to Hekla volcano, Iceland," *Geophysical Research Letters*, vol. 37, no. L20310, 2010.

[101] R. Pedersen and F. Sigmundsson, "Temporal development of the 1999 intrusive episode in the Eyjafjallajokull volcano, iceland, derived from InSAR images," *Bulletin of Volcanology*, vol. 68, pp. 377–393, 2006.

[102] A. Bonaccorso, M. Aloisi, and M. Mattia, "Dike emplacement forerunning the Etna July 2001 eruption modeled through continuous tilt and gps data," *Geophysical Research Letters*, vol. 29, no. 13, 2002.

[103] Z. Lu, D. Dzurisin, J. Biggs, C. Wicks, and S. McNutt, "Ground surface deformation patterns, magma supply, and magma storage at Okmok volcano, Alaska, from InSAR analysis: 1. intereruption deformation, 1997-2008," *Journal of Geophysical Research*, vol. 115, no. B00B02, 2010.

[104] O. lg Kwoun, Z. Lu, C. Neal, and C. Wicks, "Quiescent deformation of the Aniakchak Caldera, Alaska, mapped by IaSAR," *Geology*, vol. 34, no. 1, pp. 5–8, 2005.

[105] J. Jones and S. D. Malone, "Mount Hood earthquake activity: Volcanic or tectonic origins?," *Bulletin of the Seismological Society of America*, vol. 95, no. 3, pp. 818–832, 2005.

[106] D. Patane, M. Mattia, and M. Aloisi, "Shallow intrusive process during 2002-2004 and current volcanic activity on Mt.Etna," *Geophysical Research Letters*, vol. 32, 2005.

[107] T. Fournier and J. Freymueller, "Inflation detected at Mount Veniaminof, Alaska, with campaign GPS," *Geophysical Research Letters*, vol. 35, no. L20306, 2008.

[108] F. Albino, V. Pinel, and F. Sigmundsson, "Influence of surface load variations on eruption likelihood: Application to two Icelandic subglacial volcanoes, Grmsv otn and Katla," *Geophysical Journal International*, vol. 181, pp. 1510–1524, 2010.

[109] S. D. Angelis and S. R. McNutt, "Degassing and hydrothermal activity at Mt. Spurr, Alaska during the summer of 2004 inferred from the complex frequencies of long-period events," *Geophysical Research Letters*, vol. 32, no. L12312, 2005.

[110] M. L. Coombs, C. A. Neal, R. L. Wessels, and R. G. McGimsey, "Geothermal disruption of summit glaciers at Mount Spurr volcano, 20046: An unusual manifestation of volcanic unrest," Professional Paper 1732-B, United States Geologic Survey, 2005.

[111] A. Bonaccorso, A. Bonforte, F. Guglielmino, M. Palano, and G. Puglisi, "Composite ground deformation pattern forerunning the 2004-2005 Mount Etna eruption," *Journal of Geophysical Research*, vol. 111, 2006.

[112] M. Lisowski, D. Dzursin, R. P. Denlinger, and E. Y. Iwatsubo, "Analysis of GPS-measured deformation associated with the 2004-2006 dome-building eruption of Mount St. Helens, Washington," Professional Paper 1750, United States Geologic Survey, 2008.

[113] P. F. Cervelli, T. Fournier, J. Freymueller, and J. A. Power, "Ground deformation associated with the precursory unrest and early phases of the January 2006 eruption of Augustine Volcano, Alaska," *Geophysical Research Letters*, vol. 33, no. L18304, 2006.

[114] C. A. Neal, R. G. McGimsey, J. P. Dixon, A. Manevich, and A. Rybin, "2006 Volcanic activity in Alaska, Kamchatka, and the Kurile Islands: Summary of events and response of the Alaska Volcano Observatory," Scientific Investigations Report 20085214, United States Geologic Survey, 2009.

[115] R. G. McGimsey, C. A. Neal, J. P. Dixon, N. Malik, and M. Chibisova, "2007 Volcanic activity in Alaska, Kamchatka, and the Kurile Islands: Summary of events and response of the Alaska Volcano Observatory," Scientific Investigations Report 20105242, United States Geologic Survey, 2011.

[116] Z. Lu, D. Dzurisin, C. Wicks, and J. Power, "Diverse deformation patterns of Aleutian volcanoes from InSAR." European Space Agency Presentation.

[117] S. S. Jakobsdottir, M. J. Roberts, G. B. Gudmundsson, H. Geirsson, and R. Slunga, "Earthquake swarms at Upptyppingar, North-East Iceland: A sign of magma intrusion," *Studia Geophysica et Geodaetica*, vol. 52, no. 4, pp. 513–528, 2008.

[118] W. L. Chang, R. B. Smith, J. Farrell, and C. M. Puskas, "An extraordinary episode of Yellowstone caldera uplift, 2004-2010, from GPS and InSAR observations," *Geophysical Research Letters*, vol. 37, no. L23302, 2010.

[119] T. J. Fournier, M. E. Pritchard, and S. N. Riddick, "Duration, magnitude, and frequency of subaerial volcano deformation events: New results from Latin America using InSAR and a global synthesis," *Geochemistry, Geophysics, and Geosystems*, vol. 11, no. 1, 2010.

[120] J. D. amd T. Arnadottir, A. Hooper, H. Geirsson, F. Sigmundsson, M. Keiding, B. G. Ofeigsson, S. Hreinsdottir, P. Einarsson, P. LaFemina, and R. A. Bennett4, "InSAR and GPS measurements of the 29 May 2008 South Iceland earthquake sequence," in *Proceedings of the Fringe Workshop*, 2009.

[121] Z. Lu., T. Masterlark, and D. Dzurisin, "Interferometric synthetic aperture radar InSAR study of Okmok Volcano, Alaska, 1992-2003: Magma supply dynamics and postemplacement lava flow deformation," *Journal of Geophysical Research*, vol. 110, no. B2, 2005.

[122] N. A. Ruppert, S. Prejean, and R. A. Hansen, "Seismic swarm associated with the 2008 eruption of Kasatochi Volcano, Alaska: Earthquake locations and source parameters," *Journal of Geophysical Research*, vol. 116, 2011.

[123] F. Sigmundsson, S. Hreinsdottir, A. Hooper, T. Arnadottir, R. Pedersen, M. J. Roberts, N. Oskarsson, A. Auriac, J. Decriem, P. Einarsson, H. Geirsson, M. Hensch, B. G. Ofeigsson, E. Sturkell, H. Sveinbjornsson, and K. L. Feigl, "Intrusion triggering of the 2010 Eyjafjalljokull," *Nature*, vol. 468, 2010.

[124] S. C. Moran and W. A. Thelen, "Characterizing and comparing seismicity at Cascade Range (USA) volcanoes," in *Abstract S13B-1989 presented at the 2010 Fall Meeting, AGU, San Francisco, CA*, 13-17 Dec.

[125] W. N. Junek, W. L. Jones, and M. T. Woods, "Detecting developing volcanic unrest (accepted)," in *IEEE SouthEastCon Proceedings*, 2012.

[126] N. A. Weiss, *Introductory Statistics*. Addison Wesley, 2007.

[127] S. Institute, "Global volcanism program web page." `http://www.volcano.si.edu/`.

[128] W. N. Junek, W. L. Jones, and M. T. Woods, "Locating incipient volcanic vents using multidisciplinary remote sensing data and source modeling information (under review)," *IEEE Geoscience and Remote Sensing Letters*.

[129] T. A. Lasko, J. G. Bhagwat, K. H. Zou, and L. Ohno-Machado, "The use of receiver operating characteristic curves in biomedical informatics," *Journal of Biomedical Informatics*, vol. 38, pp. 404–415, 2005.

[130] Z. Lu and D. Dzurisin, "Ground surface deformation patterns, magma supply, and magma storage at Okmok volcano, Alaska, from InSAR analysis: 2. coeruption deformation, July-August 2008," *Journal of Geophysical Research*, vol. 115, no. B00B03, 2010.

[131] J. P. Dixon and S. D. Stihler, "Catalog of earthquake hypocenters at Alaskan volcanoes: January 1 through December 31, 2008," Open File Report 467, United States Geologic Survey, 2009.

[132] J. Larsen, C. Neal, P. Webley, J. Freymueller, M. Haney, S. McNutt, D. Schneider, S. Prejean, J. F. Larsen, and R. Wessels, "Eruption of Alaska volcano breaks historic pattern," *EOS Transactions AGU*, vol. 90, no. 20, 2009.

[133] C. A. Neal, J. F. Larsen, and J. G. Schaefer, "The July-August 2008 hydrovolcanic eruption of Okmok Volcano, Umnak Island, Alaska," *Alaska Geological Society Newsletter*, 2009.

[134] C. M. Paskus, R. B. Smith, C. M. Meertens, and W. L. Chang, "Crustal deformation of the Yellowstone-Snake River plain volcano-tectonic system: Campaign and continuous GPS observations, 1987-2004," *Journal of Geophysical Research*, vol. 112, p. 19, 2007.

[135] C. M. Meertens and R. B. Smith, "Crustal deformation of the Yellowstone caldera from first GPS measurements: 1987-1989," *Geophysical Research Letters*, vol. 18, no. 9, pp. 1763–1766, 1991.

[136] R. Showstack, "Iceland's Grimsvotn volcano erupts," *EOS Transactions AGU*, vol. 92, no. 22, 2011.

[137] "Icelandic meteorological office website for the 2011 grimsvotn eruption." `http://hraun.vedur.is/ja/vatnajokulsvoktun/english.html`.

[138] "Institute of earth science website for the 2011 grimsvotn eruption." http://earthice.hi.is.page/ies_GV2011_eruption/.

[139] "World organization of volcano observatories WOVOdat: A database of volcanic unrest." http://www.wovodat.org/.

[140] "Computer vision and remote sensing group, berlin university of technology." http://srv-43-200.bv.tu-berlin.de/rat/index.php.

[141] "Visual information solutions, itt corporation." http://www.ittvis.com/ProductServices/IDL.aspx.

[142] Delft Institute for Earth-oriented Space Research (DEOS), Delft University of Technology, *Delft Object-oriented Radar Interferometric Software User's manual and technical documentation*, 2008.

[143] T. A. Herring, R. W. King, and S. C. McClusky, "Introduction to Gamit/Globk." http://www-gpsg.mit.edu/~simon/gtgk/index.htm.